SCIENCE AND APPLICATIONS OF COASTAL REMOTE SENSING

EDITED BY: Kevin Ross Turpie, Tiffany Kay Moisan, Kristin B. Byrd and Steven G. Ackleson

PUBLISHED IN: Frontiers in Marine Science

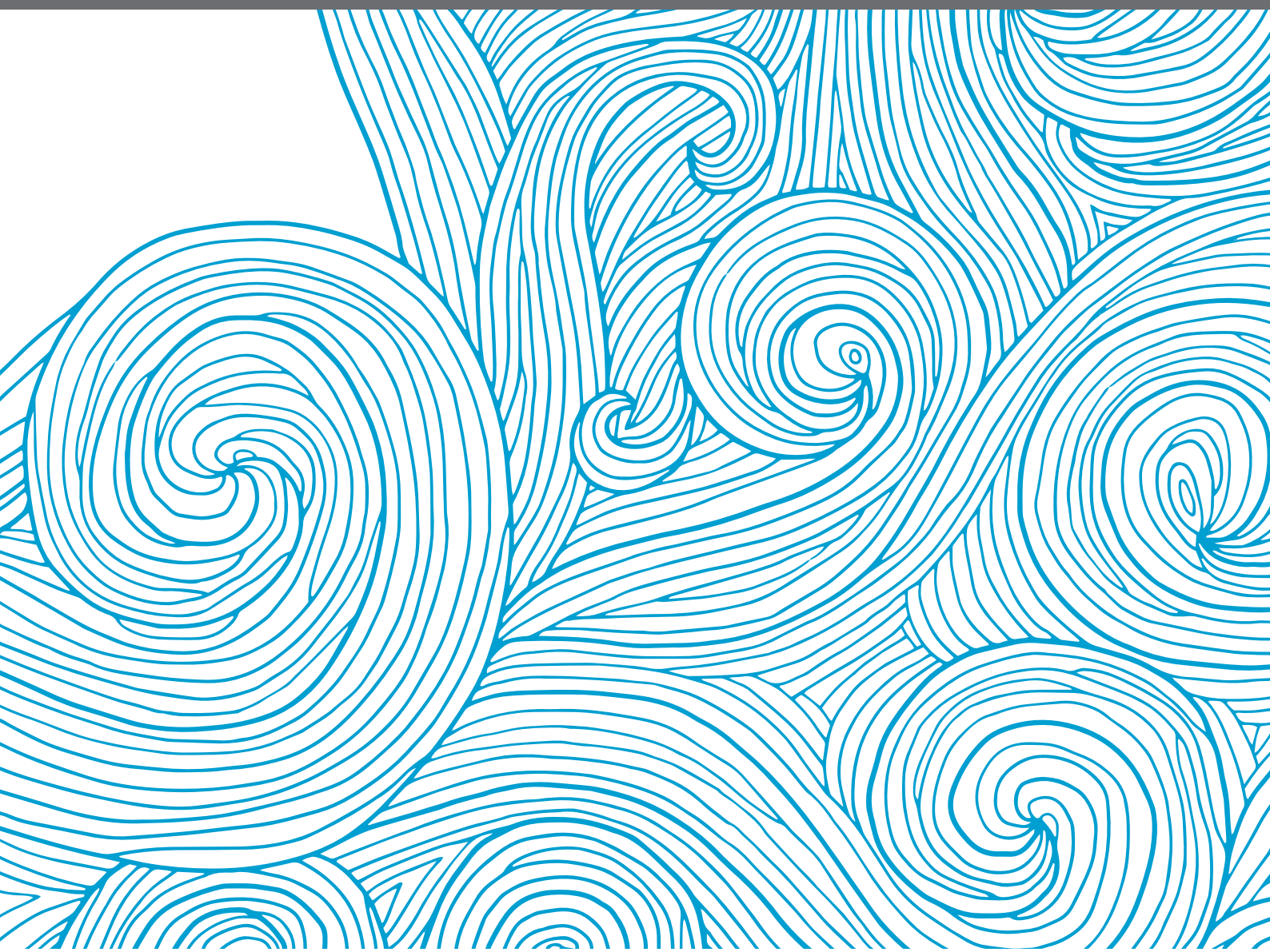

frontiers Research Topics

ISSN 1664-8714
ISBN 978-2-88966-832-8
DOI 10.3389/978-2-88966-832-8

About Frontiers

Frontiers is more than just an open-access publisher of scholarly articles: it is a pioneering approach to the world of academia, radically improving the way scholarly research is managed. The grand vision of Frontiers is a world where all people have an equal opportunity to seek, share and generate knowledge. Frontiers provides immediate and permanent online open access to all its publications, but this alone is not enough to realize our grand goals.

Frontiers Journal Series

The Frontiers Journal Series is a multi-tier and interdisciplinary set of open-access, online journals, promising a paradigm shift from the current review, selection and dissemination processes in academic publishing. All Frontiers journals are driven by researchers for researchers; therefore, they constitute a service to the scholarly community. At the same time, the Frontiers Journal Series operates on a revolutionary invention, the tiered publishing system, initially addressing specific communities of scholars, and gradually climbing up to broader public understanding, thus serving the interests of the lay society, too.

Dedication to Quality

Each Frontiers article is a landmark of the highest quality, thanks to genuinely collaborative interactions between authors and review editors, who include some of the world's best academicians. Research must be certified by peers before entering a stream of knowledge that may eventually reach the public - and shape society; therefore, Frontiers only applies the most rigorous and unbiased reviews.
Frontiers revolutionizes research publishing by freely delivering the most outstanding research, evaluated with no bias from both the academic and social point of view. By applying the most advanced information technologies, Frontiers is catapulting scholarly publishing into a new generation.

What are Frontiers Research Topics?

Frontiers Research Topics are very popular trademarks of the Frontiers Journals Series: they are collections of at least ten articles, all centered on a particular subject. With their unique mix of varied contributions from Original Research to Review Articles, Frontiers Research Topics unify the most influential researchers, the latest key findings and historical advances in a hot research area! Find out more on how to host your own Frontiers Research Topic or contribute to one as an author by contacting the Frontiers Editorial Office: frontiersin.org/about/contact

SCIENCE AND APPLICATIONS OF COASTAL REMOTE SENSING

Topic Editors:
Kevin Ross Turpie, University of Maryland, United States
Tiffany Kay Moisan, National Aeronautics and Space Administration (NASA), United States
Kristin B. Byrd, United States Geological Survey (USGS), United States
Steven G. Ackleson, United States Naval Research Laboratory, United States

IN MEMORIAL: This Research Topic is dedicated to our co-editor Dr. Tiffany Moisan, a well-regarded ocean color remote sensing scientist, who unexpectedly passed away during its preparation. Dr. Moisan was a dear friend, and upbeat and enthusiastic colleague and a scientist committed to the use of remote sensing to improve our understanding of marine microbiology and phytoplankton ecology. She was a strong supporter of the development of remote sensing capabilities and applications for coastal and inland waters, and we know that she would have wanted this Research Topic to provide her colleagues an opportunity to share and promote their work in this area. A voice in our community is now quiet. Let the chorus of our shared song continue with her memory. Dr. Tiffany Moisan is survived by her loving family, including her husband, Dr. John Moisan and her two daughters.

Citation: Turpie, K. R., Moisan, T. K., Byrd, K. B., Ackleson, S. G., eds. (2021). Science and Applications of Coastal Remote Sensing. Lausanne: Frontiers Media SA. doi: 10.3389/978-2-88966-832-8

Table of Contents

frontiers in Marine Science

EDITORIAL
published: 06 April 2021
doi: 10.3389/fmars.2021.641029

Editorial: Science and Applications of Coastal Remote Sensing

Kevin R. Turpie[1]*, *Steven G. Ackleson*[2], *Kristin B. Byrd*[3] and *Tiffany A. H. Moisan*[4†]

[1] Joint Center for Earth Systems Technology (JCET), University of Maryland, Baltimore, MD, United States, [2] United States Naval Research Laboratory, Washington, DC, United States, [3] Western Geographic Science Center, United States Geological Survey, Moffett Field, CA, United States, [4] Wallops Flight Facility, NASA, Accomack County, VA, United States

Keywords: remote sensing, coastal water areas, marine ecosystems, coastal processes, turbid and shallow water

Editorial on the Research Topic

Science and Applications of Coastal Remote Sensing

The Earth has been aptly described as a coastal planet (Martínez et al., 2007). The coastal zone, defined as land where proximity to the coast is <100 km and elevation is <10 m above sea level, is a linear interface sprawling the Earth's surface between the planet's water bodies and land masses, with a length over 1.6 million kilometers. This significant feature of the Earth's surface is so long that it would wrap around the equator 402 times (Martínez et al., 2007) or stretch to the Moon and back twice. Although the coastal ocean spans 8% of the global ocean surface area (Cracknell, 1999), it accounts for 14–30% of the total marine organic matter (Gattuso et al., 1998). Coastal oceans, defined as ocean areas between the shore and the continental shelf edge, and associated coastal environments are on the front lines of a warming climate. A warming atmosphere driven by a rising carbon dioxide concentration, the annual average of which is now approaching 420 ppm (https://www.esrl.noaa.gov), is driving sea level rise and possibly changes in coastal hydrology, currents and weather. Sea level rise due to melting glaciers and ice caps threaten inundation of coastal communities (Vitousek et al., 2017) as well as increased coastal erosion (Zhang et al., 2004), and warming ocean waters are expected to enhance the severity of tropical cyclones (Sobel et al., 2016). Disruptions in marine ecosystem biodiversity have been documented as tropical species shift poleward in response to warming trends (Pinsky et al., 2013) and coral reefs undergo mass bleaching (Heron et al., 2017).

Added to climate factors are the stresses imposed by growing coastal human populations on the marine services that they require to survive and thrive. Currently, 27% of the global population lives within the coastal zone (Kummu et al., 2016). This population is expected to nearly double by mid-century (Neumann et al., 2015), which will increase stressors on this changing coastal environment. Human dependency and exploitation of coastal resources has produced increasingly dramatic changes to coastal and inland aquatic habitats in the last 100 years (Turpie et al., 2017). Presently, the global per capita consumption of seafood represents 6% of all animal protein and is the most highly traded international food commodity (Smith et al., 2010). Aquaculture constitutes a growing portion of the consumer seafood supply. This trend is expected to continue with projected population growth and climate change (Wells et al., 2015).

In addition, stresses on coastal aquatic habitats have resulted in the emergence of many species of phytoplankton that are pernicious to both humans and aquatic ecosystems (Anderson et al., 2002). For example, aquaculture produces waste nutrients that fuel the formation of harmful algal blooms (HAB). The introduction of toxic HAB and the overgrowth of non-toxic or invasive phytoplankton species disrupt ecosystem functionality, and affect food and water resources. These changes stem largely from anthropogenic eutrophication (Glibert et al., 2005; Anderson, 2009). Excessive amounts of algae can decrease light penetration, negatively affecting water-column, and benthic photosynthesis. Some algal blooms can grow faster than natural grazers can consume them.

Edited and reviewed by:
Marta Marcos, University of the Balearic Islands, Spain

***Correspondence:**
Kevin R. Turpie
kturpie@umbc.edu

†Deceased

Specialty section:
This article was submitted to Coastal Ocean Processes, a section of the journal Frontiers in Marine Science

Received: *13 December 2020*
Accepted: *01 February 2021*
Published: *06 April 2021*

Citation:
Turpie KR, Ackleson SG, Byrd KB and Moisan TAH (2021) Editorial: Science and Applications of Coastal Remote Sensing. Front. Mar. Sci. 8:641029. doi: 10.3389/fmars.2021.641029

TABLE 1 | List of eBook chapters.

Authors	Title	DOI
S. Ackleson, J. P. Smith, L. M. Rodriguez, W. J. Moses, and B. J. Russell	Autonomous Coral Reef Survey in Support of Remote Sensing	https://doi.org/10.3389/fmars.2017.00325
D. Chapple and I. Dronova	Vegetation Development in a Tidal Marsh Restoration Project during a Historic Drought: A Remote Sensing Approach	https://doi.org/10.3389/fmars.2017.00243
J. Headley, B. J. Russell, K. Randolph, M. Á. Pérez-Castro, R. M. Vásquez-Elizondo, S. Enríquez, and H. M. Dierssen	Remote Sensing of Seagrass Leaf Area Index and Species: The Capability of a Model Inversion Method Assessed by Sensitivity Analysis and Hyperspectral Data of Florida Bay	https://doi.org/10.3389/fmars.2017.00362
W. Jiang, B. R. Knight, C. Cornelisen, P. Barter, and R. Kudela	Simplifying Regional Tuning of MODIS Algorithms for Monitoring Chlorophyll-a in Coastal Waters	https://doi.org/10.3389/fmars.2017.00151
Z. Lee, S. Shang, and R. Stavn	AOPs Are Not Additive: On the Biogeo-Optical Modeling of the Diffuse Attenuation Coefficient	https://doi.org/10.3389/fmars.2018.00008
J. Lehrter and C. Le	Satellite Derived Water Quality Observations Are Related to River Discharge and Nitrogen Loads in Pensacola Bay, Florida	https://doi.org/10.3389/fmars.2017.00274
M. Marrari, A. R. Piola, and D. Valla	Variability and 20-Year Trends in Satellite-Derived Surface Chlorophyll Concentrations in Large Marine Ecosystems around South and Western Central America	https://doi.org/10.3389/fmars.2017.00372
T. Moisan, K. M. Rufty, J. R. Moisan, and M. A. Linkswiler	Satellite Observations of Phytoplankton Functional Type Spatial Distributions, Phenology, Diversity, and Ecotones	https://doi.org/10.3389/fmars.2017.00189
T. Moisan and B. G. Mitchell	Modeling Net Growth of Phaeocystis antarctica Based on Physiological and Optical Responses to Light and Temperature Co-limitation	https://doi.org/10.3389/fmars.2017.00437
J. Ortiz, D. Avouris, S. Schiller, J. C. Luvall, J. D. Lekki, R. P. Tokars, R. C. Anderson, R. Shuchman, M. Sayers, and R. Becker	Intercomparison of Approaches to the Empirical Line Method for Vicarious Hyperspectral Reflectance Calibration	https://doi.org/10.3389/fmars.2017.00296
A. Reisinger, J. C. Gibeaut, and P. E. Tissot	Estuarine Suspended Sediment Dynamics: Observations Derived from over a Decade of Satellite Data	https://doi.org/10.3389/fmars.2017.00233
J. Snyder, E. Boss, R. Weatherbee, A. C. Thomas, D. Brady, and C. Newell	Oyster Aquaculture Site Selection Using Landsat 8-Derived Sea Surface Temperature, Turbidity, and Chlorophyll a	https://doi.org/10.3389/fmars.2017.00190
A. Trembanis, A. L. Forrest, B. M. Keller, and M. R. Patterson	Mesophotic Coral Ecosystems: A Geoacoustically Derived Proxy for Habitat and Relative Diversity for the Leeward Shelf of Bonaire, Dutch Caribbean	https://doi.org/10.3389/fmars.2017.00051
R. Trinh, C. G. Fichot, M. M. Gierach, B. Holt, N. K. Malakar, G. Hulley, and J. Smith	Application of Landsat 8 for Monitoring Impacts of Wastewater Discharge on Coastal Water Quality	https://doi.org/10.3389/fmars.2017.00329

When they die, the bloom sinks and decomposes, and the resulting bacterial respiration takes up dissolved oxygen, causing hypoxic, and anoxic "dead zones," which can devastate fisheries and benthic communities (Anderson et al., 2000; Rabalais et al., 2002).

To better understand the mounting ecological pressures on coastal environments, ecosystem scientists and natural resource managers have increasingly turned to remote sensing for timely and spatially coherent information. In response, Earth imaging sensor technologies aboard satellites and aircraft have advanced rapidly from multispectral systems offering a small number of broad, discontiguous spectral bands in the visible and infrared portions of the spectrum to imaging spectrometers with continuous, high-resolution coverage throughout the visible and near-infrared spectrum (VNIR), e.g., between 400 nm and 1 μm and spectral bandwidth <10 nm. Such sensors are referred to as imaging spectrometers or *hyperspectral* imaging systems. The next generation of space-based Earth imagers, such as the U.S. National Aeronautics and Space Administration (NASA) Ocean Color Imager (OCI), a component of the Plankton, Aerosol, Cloud and ocean Ecosystem mission (PACE) (Gorman et al., 2019), and the NASA Surface Biology and Geology (SBG) designated observable (National Academies of Sciences, 2018) and the Geosynchronous Littoral Imaging and Monitoring Radiometer (GLIMR) (National Aeronautics Space Administration, 2019), will serve to extend the heritage of global ocean color imagery and will be designed for hyperspectral coverage to address a wide range of societal problems. Coincident with the large, national, multi-community efforts, miniaturized systems are rapidly under development that may be deployed on small unmanned aerial vehicles controlled by a single research group or even an individual researcher. As such, they may more accurately be described as embedded systems because they are integral to specific, small-scale research and management efforts and would not exist were it not for those activities.

With the availability of more spectrally complex imagery, new algorithmic approaches have emerged to retrieve more useful information from the data. Advances in coastal remote sensing technology are well-documented in recent review articles (De Moraes Rudorff and Kampel, 2012; Duffy et al., 2013; Blondeau-Patissier et al., 2014; Mouw et al., 2015; Palmer et al., 2015; Hedley et al., 2016; Werdell et al., 2018).

The lynchpin for any environmental remote sensing operation is the coincidental collection of high quality, *in situ* observations

of direct relevance to the calibration and validation of image-based products. This requirement is particularly challenging within coastal environments where the temporal and spatial correlation scales can be quite short (Hedley et al., 2012; Moses et al., 2016). Traditional methods of collecting *in situ* observations from floating platforms can be compromised by water depth, either by restricting access or causing re-suspension of bottom sediments. In applications to benthic cover, such as coral reef surveys, observations with SCUBA have proven effective for collecting high quality data, but operations are slow, laborious, expensive, and require a high level of specialized training. To address these problems, researchers have developed autonomous methods of collecting *in situ* observations (Moline et al., 2005; Ryan et al., 2010). Autonomous *in situ* survey systems offer key advantages over traditional methods including lower survey costs (excluding the initial infrastructure investment) and orders of magnitude more data with greater dimensionality and aerial coverage, often representing environmental conditions that would prohibit safe, human-based operations.

The purpose of this Frontiers in Marine Science eBook focuses on remote sensing of the coastal ocean is to provide a condensed forum to sample areas of notable technological advance. It provides a sample of such innovations and considerations contributed from the coastal remote sensing community. Given the *a priori* emphasis placed on environmental problems, the papers included in this eBook largely address processes, methods and technology pertaining to biological resources. The eBook is comprised of 14 chapters representing the work and thoughts of 62 authors (**Table 1**). Remote sensing technology covers multispectral to hyperspectral systems applied to environments ranging from wetlands to the pelagic ocean. Many of the papers include a large component of radiative transfer modeling and algorithm development and several of the papers address new autonomous methods to survey the coastal ocean in support of algorithm development, validation, and verification. One paper explores the use of acoustic remote sensing to improve studies of coastal ecosystems. Papers address multiple coastal remote sensing themes and applications, including remote sensing of coastal ecosystems (coral reefs: Trembanis et al.; Ackleson et al.; tidal marsh: Chapple and Dronova; seagrass: Hedley et al.), water quality (Reisinger et al.; Jiang et al.; Snyder et al.; Lehrter and Le; Trinh et al.), phytoplankton abundance and diversity (Moisan et al.; Moisan and Mitchell; Marrari et al.), and improvements to calibration and radiative transfer modeling (Ortiz et al.; Lee et al.). Water quality papers address a range of topics including suspended sediments in estuaries (Reisinger et al.), eutrophication, as indicated by chlorophyll-a (Jiang et al.), aquaculture site selection (Snyder et al.), and effects of river discharge and nutrient loads (Lehrter and Le; Trinh et al.).

DEDICATION

This eBook is dedicated to our co-editor Dr. Tiffany Moisan, a well-regarded ocean color remote sensing scientist, who unexpectedly passed away during its preparation. Dr. Moisan was a dear friend, and upbeat and enthusiastic colleague and a scientist committed to the use of remote sensing to improve our understanding of marine microbiology and phytoplankton ecology. Tiffany was a strong supporter of coastal remote sensing science and applications and wanted this publication to provide her colleagues a forum to share and promote their most recent accomplishments. Let the chorus of our shared song continue with her memory. Dr. Moisan is survived by her loving family, including her husband, Dr. John Moisan, and her two daughters.

AUTHOR CONTRIBUTIONS

All authors have contributed in equal amounts to this manuscript. All authors contributed to the article and approved the submitted version.

REFERENCES

Anderson, D. M. (2009). Approaches to monitoring, control and management of harmful algal blooms (HABs). *Ocean Coast. Manage.* 52, 342–347. doi: 10.1016/j.ocecoaman.2009.04.006

Anderson, D. M., Glibert, P. M., Burkholder, J. M. (2002). Harmful algal blooms and eutrophication: nutrient sources, composition, and consequences. *Estuaries* 25, 704–726. doi: 10.1007/BF02804901

Anderson, D. M., Kaoru, Y., and White, A. W. (2000). *Estimated Annual Economic Impacts from Harmful Algal Blooms (HABs) in the United States*. No. WHOI-2000-11. Norman: National Oceanic and Atmospheric Administration, National Severe Storms Lab.

Blondeau-Patissier, D., Gower, J. F. R., Dekker, A. G., Phinn, S. R., and Brando, V. E. (2014). A review of ocean color remote sensing methods and statistical techniques for the detection, mapping and analysis of phytoplankton blooms in coastal and open oceans. *Prog. Oceanogr.* 123, 123–144. doi: 10.1016/j.pocean.2013.12.008

Cracknell, A. P. (1999). Remote sensing techniques in estuaries and coastal zones – an update. *Int. J. Remote Sens.* 19, 485–496.

De Moraes Rudorff, N., and Kampel, M. (2012). Orbital remote sensing of phytoplankton functional types: a new review. *Int. J. Remote Sens.* 33, 61967–61990. doi: 10.1080/01431161.2011.601343

Duffy, J. E., Amaral-Zettler, L. A., Fautin, D. G., Paulay, G., Rynerson, T. A., Sosik, H. M., et al. (2013). Envisioning a marine biodiversity observation network. *BioScience* 63, 350–361. doi: 10.1525/bio.2013.63.5.8

Gattuso, J. P., Frankignoulle, M. M., and Wollast, R. (1998). Carbon and carbonate metabolism in coastal aquatic ecosystems. *Ann. Rev. Ecol. Sys.* 29, 405–434. doi: 10.1146/annurev.scolsys.29.1.405

Glibert, P., Anderson, D., Gentein, P., Granéli, E., and Sellner, K. G. (2005). The global complex phenomena of harmful algal blooms. *Oceanography* 18, 136–147. doi: 10.5670/oceanog.2005.49

Gorman, E. T., Kubalak, D. A., Patel, D., Dress, A., Mott, D. B., Meister, G., et al. (2019). "The NASA Plankton, Aerosol, Cloud, ocean Ecosystem (PACE) mission: an emerging era of global, hyperspectral Earth system remote sensing," *Proceedings Volume 11151, Sensors, Systems, and Next-Generation Satellites, Vol. 23* (Strasbourg: Palais de la Musique et des Congrés) 111510G. doi: 10.1117/12.2537146

Hedley, J. D., Roelfsema, C. M., Chollett, I., Harborne, A. R., Heron, S. F., Weeks, S. J., et al. (2016). Remote sensing of coral reefs for monitoring and management: a review. *Remote Sens.* 8:118. doi: 10.3390/rs8020118

Hedley, J. D., Roelfsema, C. M., Phinn, S. R., and Mumby, P. J. (2012). Environmental and sensor limitations in optical remote sensing of coral reefs: Implications for monitoring and sensor design. *Remote Sen.* 4, 271–302. doi: 10.3390/rs4010271

Heron, S. F., Eakin, C. M., and Douvere, F. (2017). *Impacts of Climate Change on World Heritage Coral Reefs: A First Scientific Assessment*. Paris: UNESCO World Heritage Center, 12.

Kummu, M, de Moel, H., Salvucci, G., Viviroli, D., Ward, P. J., and Varis, O. (2016). Over the hills and further away from coast: global geospatial patterns of human and environment over the 20th−21st centuries. *Environ. Res. Lett.* 11:034010. doi: 10.1088/1748-9326/11/3/034010

Martínez, M. L., Intralawan, A., Vázquez, G., Pérez-Maqueo, O., Sutton, P., Landgrave, R. (2007). The coasts of our world: Ecological, economic and social importance. *Ecol. Econ.* 63, 254–272. doi: 10.1016/j.ecolecon.2006.10.022

Moline, M. A., Blackwell, S. M., van Alt, C., Allen, B., Austin, T., Case, J., et al. (2005). Remote environmental monitoring units: an autonomous vehicle for characterizing coastal environments. *J. Atmos. Ocean. Tech.* 22:1797–1808. doi: 10.1175/JTECH1809.1

Moses, W. J., Ackleson, S. G., Hair, J. W., Hostetler, C. A., and Miller, W. D. (2016). Spatial scales of optical variability in the coastal ocean: Implications for remote sensing and in situ sampling. *J. Geophys. Res. Oceans* 121, 4194–4208. doi: 10.1002/2016JC011767

Mouw, C. B., Greb, S., Aurin, D., DeGiacomo, P. M., Lee, Z., Twardowski, M., et al. (2015). Aquatic color radiometry remote sensing of coastal and inland waters: Challenges and recommendations for future satellite missions. *Remote Sens. Envirion.* 160, 15–30. doi: 10.1016/j.rse.2015.02.001

National Academies of Sciences, Engineering, and Medicine (2018). *Thriving on Our Changing Planet: A Decadal Strategy for Earth Observation from Space*. Washington, DC: The National Academies Press. doi: 10.17226/24938

National Aeronautics and Space Administration (2019). *NASA Targets Coastal Ecosystems with New Space Sensor*. ed K. Northon. NASA Press Release written by Felicia Chou. Available online at: https://www.nasa.gov/press-release/nasa-targets-coastal-ecosystems-with-new-space-sensor (accesssed August 1, 2019).

Neumann, B., Vafeidis, A. T., Zimmermann, J., and Nicholis, R. J. (2015). Future coastal population growth and exposure to sea-level rise and coastal flooding – a global assessment. *PLoS ONE* 10:e0118571. doi: 10.1371/journal.pone.0118571

Palmer, S. C. J., Kutser, T., and Hunter, P. D. (2015). Remote sensing of inland waters: challenges, progress, and future directions. *Remote Sens. Environ.* 157, 1–8. doi: 10.1016/j.rse.2014.09.021

Pinsky, M. L., Worm, B., Fogarty, M. J., Sarmiento, J. L., and Levin, S. A. (2013). Marine taxa track local climate velocities. *Science* 341, 1239–1242. doi: 10.1126/science.1239352

Rabalais, N. N., Turner, R. E., and Wiseman, W. J. (2002). Gulf of Mexico Hypoxia, A.K.A. "The Dead Zone". *Ann. Rev. Ecol. Syst.* 33, 235–263. doi: 10.1146/annurev.ecolsys.33.010802.150513

Ryan, J. P., Johnson, S. B., Sherman, A., Rajan, K., Py, F., Thomas, H., et al. (2010). Mobile autonomous process sampling within coastal ocean observing systems. *Limnol. Oceanogr. Meth.* 8, 394–402. doi: 10.4319/lom.2010.8.394

Smith, M. D., Roheim, C. A., Crowder, L. B., Halpern, B. S., Turnipseed, M., Anderson, J. L., et al. (2010). Sustainability and global seafood. *Science* 327, 784–786. doi: 10.1126/science.1185345

Sobel, A. H., Camargo, S., J., Hall, T., M., C.-Lee, Y., Tippett, M., K., and Wing, A., A. (2016). Human influence on tropical cyclone intensity. *Science* 353:242–246. doi: 10.1126/science.aaf6574

Turpie, K. R., Ackleson, S., Bell, T., Dierssen, H. M., Goodman, J., Green, R., et al. (2017). Spectroscopy for global observation of coastal and inland aquatic habitats. *2017 IEEE International Geoscience and Remote Sensing Symposium (IGARSS)* (Fort Worth, TX), 3051–3054. doi: 10.1109/IGARSS.2017.8127642

Vitousek, S., Barnard, P. L., Fletcher, C. H., Frazer, N., Erikson, L., and Storlazzi, C. D. (2017). Doubling of coastal flooding frequency within decades due to sea-level rise. *Sci. Rep.* 7:1399. doi: 10.1038/s41598-017-01362-7

Wells, M. L., Trainer, V. L., Smayda, T. J., Karlson, B. S. O., Trick, C. G., Kudela, R. M., et al. (2015). Harmful algal blooms and climate change: Learning from the past and present to forecast the future. *Harmful Algae* 49, 68–93. doi: 10.1016/j.hal.2015.07.009

Werdell, P. J., McKinna, L. I. W., Boss, E., Ackleson, S. G., Craig, S. E., Gregg, W. W., et al. (2018). An overview of approaches and challenges for retrieving marine inherent optical properties from ocean color remote sensing. *Prog. Oceanogr.* 160, 186–212. doi: 10.1016/j.pocean.2018.01.001

Zhang, K., Douglas, B. C., and Leatherman, S. P. (2004). Global warming and coastal erosion. *Clim. Change* 64, 41–58. doi: 10.1023/B:CLIM.0000024690.32682.48

Conflict of Interest: The authors declare that the research was conducted in the absence of any commercial or financial relationships that could be construed as a potential conflict of interest.

frontiers in Marine Science

ORIGINAL RESEARCH
published: 01 March 2017
doi: 10.3389/fmars.2017.00051

Mesophotic Coral Ecosystems: A Geoacoustically Derived Proxy for Habitat and Relative Diversity for the Leeward Shelf of Bonaire, Dutch Caribbean

Arthur C. Trembanis[1], Alexander L. Forrest[2], Bryan M. Keller[1] and Mark R. Patterson[3]*

[1] Robotics Discovery Laboratories, School of Marine Science and Policy, College of Earth, Ocean, and Environment, University of Delaware, Newark, DE, USA, [2] Department of Civil and Environmental Engineering, University of California Davis, Davis, CA, USA, [3] Marine Science Center, Northeastern University, Nahant, MA, USA

Current trends demonstrate coral reef health in serious decline worldwide. Some of the most well-preserved coral reefs in the Caribbean basin are located in the waters surrounding Bonaire, in the Dutch Caribbean. In many places on the leeward side on islands dominated by trade winds, the shallow reef systems extend into deeper water where they are known as Mesophotic Coral Ecosystems (MCE). Autonomous Underwater Vehicles (AUVs) were used to collect geoacoustic data of these leeward reefs at multiple sites as part of an ocean exploration project. AUV swath bathymetry and side-scan sonar data were analyzed for depth, acoustic backscatter intensity, seafloor slope, and rugosity. These geomorphic metrics were then used as inputs to generate a composite synthetic index of bottom-type to delineate MCE features. A confusion matrix statistical analysis of the acoustic class map showed an overall accuracy of the acoustic classes at 66%, with accuracy of the hard coral class the highest at 83%, and the sandy-bottom class the lowest at 55. The hard coral class was also the statistically most reliable, at over 80%, with the noise class coming in as the least reliable. This morphologic habitat index is a potentially useful new tool in quantifying the extent of MCE located in proximity to Marine Protected Areas (MPAs).

Keywords: Mesophotic Coral Ecosystem (MCE), Autonomous Underwater Vehicle (AUV), Acoustic Ground Discrimination System (AGDS), Caribbean, side-scan sonar, swath bathymetry, seafloor rugosity

OPEN ACCESS

Edited by:
Steven G. Ackleson, Naval Research Laboratory, USA

Reviewed by:
Joaquin Rodrigo Garza-Pérez, National Autonomous University of Mexico (UNAM), Mexico
Bryan Costa, National Oceanic and Atmospheric Administration (NOAA), USA

****Correspondence:***
Arthur C. Trembanis
art@udel.edu

Specialty section:
This article was submitted to Coral Reef Research, a section of the journal Frontiers in Marine Science

Received: *30 September 2016*
Accepted: *14 February 2017*
Published: *01 March 2017*

Citation:
Trembanis AC, Forrest AL, Keller BM and Patterson MR (2017) Mesophotic Coral Ecosystems: A Geoacoustically Derived Proxy for Habitat and Relative Diversity for the Leeward Shelf of Bonaire, Dutch Caribbean. Front. Mar. Sci. 4:51. doi: 10.3389/fmars.2017.00051

INTRODUCTION

Coral reefs surrounding the island of Bonaire, Dutch Caribbean, are arguably some of the most well-preserved in the Caribbean. Nevertheless, there has been recent evidence of coral mortality, decline in live coral reef cover and changing ecosystem dynamics as compared to previous decades (Steneck and McClanahan, 2004; Bak et al., 2005; Stokes et al., 2010). Most ecosystem research in Bonaire has been focused primarily along the shallow (<12 m water depth), near-shore reef communities. For example, van Duyl (1985) mapped out bottom types and benthic community structure around the leeward perimeter of the island from the shoreline to a depth of ~10 m. There have been limited observations of reefs in Bonaire at greater depths and almost no work has been

done to date at depths where Mesophotic Coral Ecosystems (referred to in the research literature as MCEs) exist. A recent study by De Bakker et al. (2016) reported pressures and declines in coral assemblages even in depths of 30–40 m off Bonaire and Curaçao thus emphasizing the need to locate and characterize coral reef assemblages in mesophotic depths. MCEs in Bonaire have been shown to extend from 30 to 150 m water (De Meyer and MacRae, 2006; Keller, 2011).

MCEs are known to: (1) exist at multiple locations around the world (e.g., Fricke and Meischner, 1985; Bridge et al., 2011a); (2) extend deeper than the shallow reefs (beginning at 30 m deep) to the bottom of the photic zone (>75 m) depending on the light penetration through the water column (Bridge et al., 2011b); (3) provide potentially important refugia for deep- and shallow-water fishes and coral species (Brockovich et al., 2008; Lesser et al., 2009; Bridge et al., 2013; Harris et al., 2013); and, (4) act as important sources and sinks of shallow coral larvae and thus can affect the recovery time of damaged coral reefs (Bongaerts et al., 2010). The systems are comprised mainly of zooxanthellate scleractinian and octocorallian taxa, sponges, and rhodolith assemblages and very greatly from region to region as noted in the exhaustive review by Kahng et al. (2010). The presence and structure of the MCE are influenced by additional factors such as light availability (PAR), nutrient levels, and hydrodynamic processes (e.g., waves and currents) that drive physical mixing at depth in the water column. The physical process generated turbulent energy has ramifications for the ecology associated with MCEs (Leichter et al., 1998).

Recent advances in diving technologies (e.g., closed-circuit rebreathers, application of mixed gases, etc.), field robotics (e.g., Autonomous Underwater Vehicles -AUVs, Remotely Operated Vehicles, -ROVs), and survey techniques (e.g., sonar and benthic optical imagery) from towed bodies allow MCEs to be explored in an unprecedented way (Armstrong et al., 2006; Locker et al., 2010; Williams et al., 2010; Relles and Patterson, 2011; Bridge et al., 2011a; Smale et al., 2012). The use of AUVs as data collection platforms decouples data collection from a surface vessel allowing higher frequency and shorter pulse length sonars to be brought closer to the seabed (lower altitude) in deeper waters than would be possible from a surface vessel mounted sonar system. This inherently improves the resolution of the sonar based survey data to decimeter horizontal and vertical scale resolution even at depths well-beyond 100 m (Patterson and Relles, 2008; Williams et al., 2010; Forrest et al., 2012; Trembanis et al., 2012). This increased level of precision provided by subsea robotic platforms allows for bottom features, such as coral reef morphologic structures, to be resolved from small (0.1–0.5 m) to large (>1 m) scale over broad areas of the seabed (1–10s of km). Benthic imagery concurrently collected by AUVs allows the measured acoustic backscatter to be ground-truthed in such a way that was previously only possible through logistically challenging field campaigns (Locker et al., 2010). Other aspects of the marine environment can also be surveyed. For example, nekton can be identified from acoustic returns (Fernandes et al., 2003; Patterson et al., 2007) and water quality parameters can also be simultaneously surveyed from AUVs (Moline et al., 2005).

This study aims to identify and characterize through remote sensing the mesophotic reef ecosystem at eight sites along the insular, leeward side, of Bonaire. Dutch Caribbean. Bathymetric sonar, side-scan sonar, and benthic imagery surveys collected from an AUV at each site down to depths of >200 m provide the basis of the geoacoustic data used for the subsequent benthic classification. Substrate classification was conducted using an Acoustic Ground Discrimination System (AGDS) using a new synthetic index for feature discrimination. This classification was then ground-truthed against images concurrently collected from above the seabed. The resulting geoacoustic classification is then used to show the presence of and geomorphic distribution and characteristics of MCEs at some of the test sites. Distribution charts of the MCEs are developed in this work and then presented along with a comparison of MCE presence in the Bonaire Marine Park as compared to sites receiving regular tourist diving in the shallower reef. Implications of these findings for MCE distribution are discussed.

MATERIALS AND METHODS

Study Area

This study was part of a larger National Oceanic and Atmospheric Association (NOAA) Signature Expedition in 2008 to Bonaire, Dutch Caribbean (Patterson et al., 2008). Bonaire is located in the Caribbean Sea immediately north of Venezuela (**Figure 1**—Insert). The island municipality of Bonaire is comprised of the main island of Bonaire and then the smaller uninhabited island of Klein Bonaire, which is located on the leeward, western side of the main island (**Figure 1**). While the eastern (windward) side of Klein Bonaire is occasionally subject to large swell from hurricanes passing through the Caribbean, the western (leeward) side sees infrequent events (Bries et al., 2004). The western side of the island is also exposed to smaller wave energy environments (levels are numbered in **Figure 1**; adapted from van Duyl, 1985). The study sites (**Figure 1**—filled squares) range from indexed wave energy states of 4–6 (i.e., the lower end of the wave spectrum) and correspond to wave heights up to 1 m. As wave heights along the western side of the island are lower than the eastern, the shallow reefs are better preserved (Steneck and McClanahan, 2004) and more routinely explored.

Data Collection by AUV

At each of the sites, a phase-measuring bathymetric sonar (PMBS) and a side-scan sonar (SSS) data were acquired using a Teledyne Gavia AUV as the survey platform (**Figure 2**). The depth rating (200 m) allowed missions over a large range of the mesophotic zone. Note that while strictly speaking the mesophotic zone operatively extends to the bottom of the photic zone, here functionally we set our analysis to between the 30 and 150 m isobath (Lesser et al., 2009). Powered with a 1 kW h lithium-ion battery pack (**Figure 2A2**), the AUV has a mission duration of c. 4 h at a swimming speed of $\sim$1.8 m s^{-1}, or greater than 25 km of trackline in a given mission. This AUV utilized a Kearfott T-24 INS Inertial Navigation System (INS) aided with a 1,200 kHz RDI Doppler Velocity Log (DVL) for navigation (**Figure 2A4**). The navigational solution has less than 0.05% error

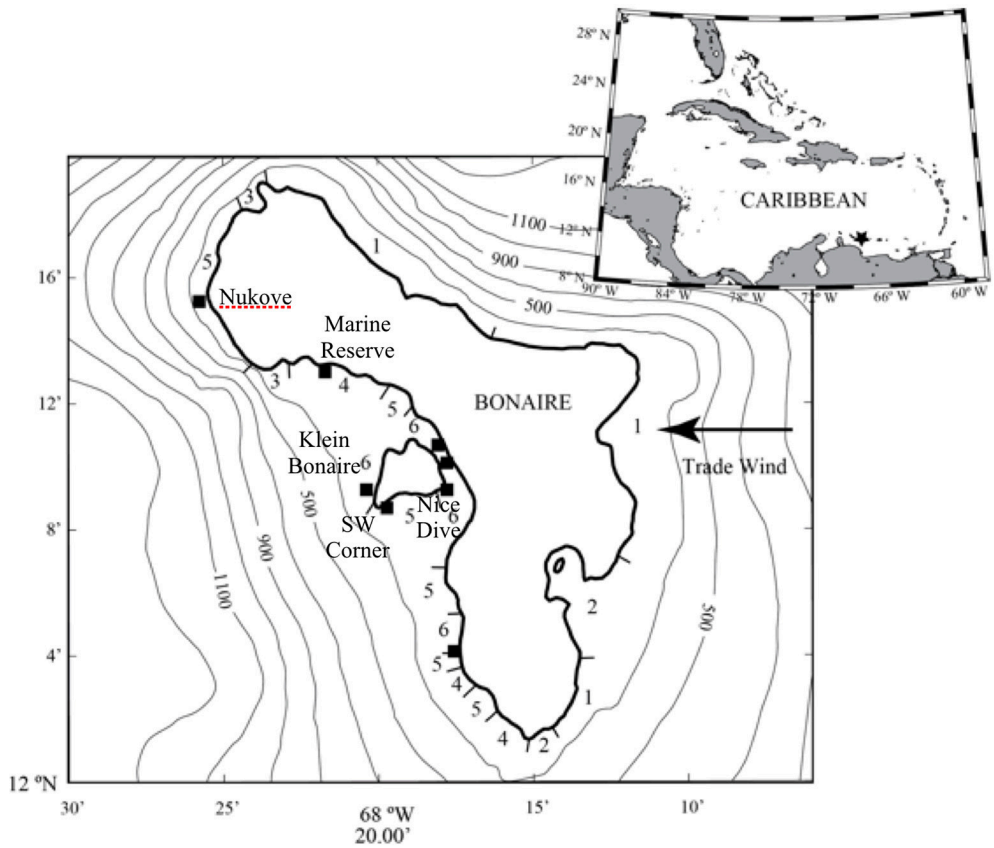

FIGURE 1 | Chart of Bonaire, Dutch Caribbean (global location marked in inset) with surrounding bathymetry and index of wave level environments around the shoreline indicated (Level 1: Wave height 2–3.5 m; 2: 1.5–2 m; 3: 1–1.5 m; 4: 0.5–1 m; 5: 0.3–0.5; 6: 0.0–0.3 m, as adapted from van Duyl, 1985). Survey sites indicated around the island (filled squares). For reference Nukove is the northernmost site. Klein Bonaire is the smaller island to west of main island.

by distance traveled resulting in ∼3.0 m positional uncertainty after completing an hour of submerged trackline (Trembanis et al., 2012).

The key scientific payloads on the AUV were the camera, the phase-measuring bathymetric sonar (PMBS), and a side-scan sonar (SSS). Fitted into the nose module (**Figure 2A1**) of the AUV was a Point Gray Scorpion 20SO digital camera that has an image capture rate of ∼ 4 Hz. At the survey speed of ∼1.8 m s^{-1}, this frame rate results in one image every 0.45 m and ∼40% overlap between frames for typical flight altitudes of the AUV. With geophysical surveys commanded at vehicle altitudes of 15 m, this fixed in-water field of view of the camera of 54°, features of 6–12 cm were resolvable in the resulting images. Camera gain, aperture, and exposure were set to be fully automatic rather than fixed contrary to recommendations for imagery in low light environments (Pike, 2011). The phase measuring bathymetric sonar was a GeoSwath module manufactured by Kongsberg Maritime (**Figure 2A3**). The 500 kHz operating frequency provides 20 cm horizontal resolution in the final acoustic backscatter mosaic, with 1.0 m horizontal resolution in the associated gridded bathymetric surface. Side-scan sonar data were also collected with a 900/1,800 kHz Marine Sonic Technology Sea Scan module (**Figure 2A5**). Side-scan sonar data were collected exclusively at 900 kHz, which provides 18 cm horizontal resolution in the gridded backscatter mosaic.

Between January 13 and 25, 2008, nearly 200 h and over 160 km of trackline survey data were collected. The AUV was programmed to follow a constant altitude of typically 15 m for bathymetric surveys, with survey lines run roughly parallel to known bathymetric contours (using known bathymetry for mission planning). Alternating line spacing of 30 and 60 m was used with sonar set to achieve swath widths of 70 m. These acquisition settings resulted in data with ∼150% port and starboard overlap on successive survey lines. Identical acquisition settings with this same AUV have been used by the authors successfully in several similar studies (Raineault et al., 2012; and Trembanis et al., 2012, 2013).

Data Processing

Phase-measuring bathymetric data were processed with commercial processing software including GS+ (GeoAcoustics Ltd) and SonarWiz (Chesapeake Technology Inc.) with an established workflow (**Figure 3**) for removing outliers caused by noise within the water column and generating bathymetry and backscatter representation of the seafloor. Geocoder software, a component of the Fledermaus software suite was

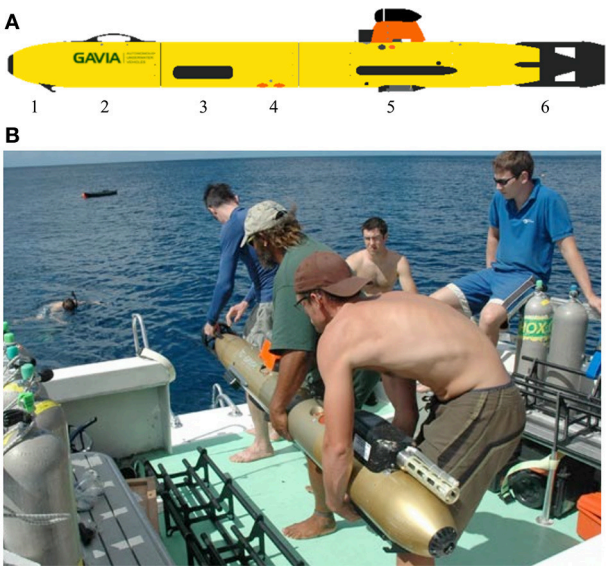

FIGURE 2 | The gavia autonomous underwater vehicle (A) as assembled for these survey dives and **(B)** being launched from the surface vessel. Numbers delineate each of the modules of the AUV. 1, Nose Cone where the camera view port is located; 2, Battery Module; 3, Phase Measuring Bathymetric Sonar Module; 4, Inertial Navigation System Module; 5, Control Module with side-scan sonar transducers; 6, Propulsion Module.

used to generate backscatter mosaics including geometric and radiometric corrections in addition to the motion compensation provided by the INS data. These data were then imported to a data visualization software package Fledermaus (QPS BV) and gridded onto a user-specified grid, in this case a cell size of 1.0 m, using a moving average that included three nearest neighbors (Keller, 2011). Acoustic backscatter data were processed and quantitatively compared using an additional seabed Acoustic Ground Discrimination System (AGDS) software package called QTC SWATHVIEW (Quester Tangent, Saanichton BC) following the methods and approach of other recent investigators e.g., Brennan et al. (2012) and Raineault et al. (2012). Class maps of similar acoustic image properties are generated with SWATHVIEW and are then ground truthed from seabed photos for each of the investigated sites (**Figure 4**). Seabed characteristics for a defined class are assumed to be reasonably constant (i.e., consistent between study sites based on similar setting and the consistent sonar settings used for each survey) and distinct from other class characteristics.

Classification in this manner reduces the amount of ground-truthing data (**Figure 5**) that must be collected in order to verify that a specific substrate segmentation coincides with a specific sediment type (i.e., only a small nominal number of ground-truthing samples from each class are adequate to define the entire class). QTC SWATHVIEW has been widely used in acoustic habitat studies and further theoretical information and example studies (Preston et al., 2001; Quester Tangent, 2010; Brennan et al., 2012; Raineault et al., 2012, 2013). As shown in **Figures 4**, **5**, for all of the datasets, the final output was Keyhole Markup Language (.kml) files, which could be imported directly into Google Earth. In addition to acoustic class maps and sonar mosaics, gridded Digital Elevation Models (DEMs) were generated from the bathymetric data.

Synthetic Bottom-Type Index

Biological diversity (e.g., Shannon's diversity index, H',) is a measure of information entropy, however, there were no direct estimations of taxa (genus or species) observed in the benthic imagery as a result of the higher AUV flight altitudes designed to maximize sonar coverage (cf. analyses done from AUV sampling in Bridge et al., 2011a,b). Nevertheless, a new quantitative synthetic index proxy of diversity potential was created. This index H'_{SC}, was related to the geomorphology and the biological complexity, by combining the geoacoustic classes from the QTC principal components analysis together with the benthic photographic imagery and morphologic measurements of slope, rugosity, and depth from the sonar mapping measurements.

The synthetic bottom-type index, H'_{SC}, is given by:

$$H'_{SC} = (R * (dmid/d) * sin(slope) + C_{weight} * (dmid/d) * sin(slope)) \quad (1)$$

where R is the estimated rugosity (based on Jenness, 2004), d is the depth (m), d_{mid} is the mid-point depth of the survey site region (here 50 m), s is slope of the seafloor in the absolute value (degrees) relative to a horizontal plane), and C_{weight} is the weighted classification (**Figure 6**) of the different bottom-type acoustic classes that were previously identified by QTC SWATHVIEW, following a similar methodology as employed in other geoacoustic studies (Brennan et al., 2012; Raineault et al., 2013). Note that the d_{mid}/d term places more emphasis on shallow compared to deeper depths. C_{weight} allows different acoustic cluster classes to have different weightings. For example, coral bottom substrates will have a significantly higher index value than sand or macroalgae. Diversity weightings, C_{weight}, (**Figure 6**) were assigned according to previously published diversity indices for Caribbean reefs with values of 3.5, 3.2, 1.9, and 0.1 assigned to the hard coral, coral rubble, macro algae, and sandy bottom cluster classes, respectively (computed as bits and reported by Porter, 1972). It should be noted that the "unknown" noise class identified in the geoacoustic classification was assigned a value of 0, as it was most similar to sand. Based on the location of this class, with respect to vessel trackline, it is suspected to be purely acoustic noise.

These map datasets were then input into Eq. 1 in order to produce composite maps of H'_{SC} on a 4 m grid (**Figure 11**) for Klein Bonaire from ~ 0–135 m depth (see **Figure 10** for depth profile). This larger grid resolution was required because the acoustic classes are calculated over multiple pixels of the underlying side-scan sonar mosaic.

The depth of many of the Bonaire site locations exceeds 200 m, well-beyond the nominal depth of scientific diving activity (~40 m). Many of the MCEs identified in this study were found in depths greater than 70 m, the simultaneous collection of sonar and benthic imagery provides additional information in assessing MCE characteristics and distribution. Furthermore, the camera

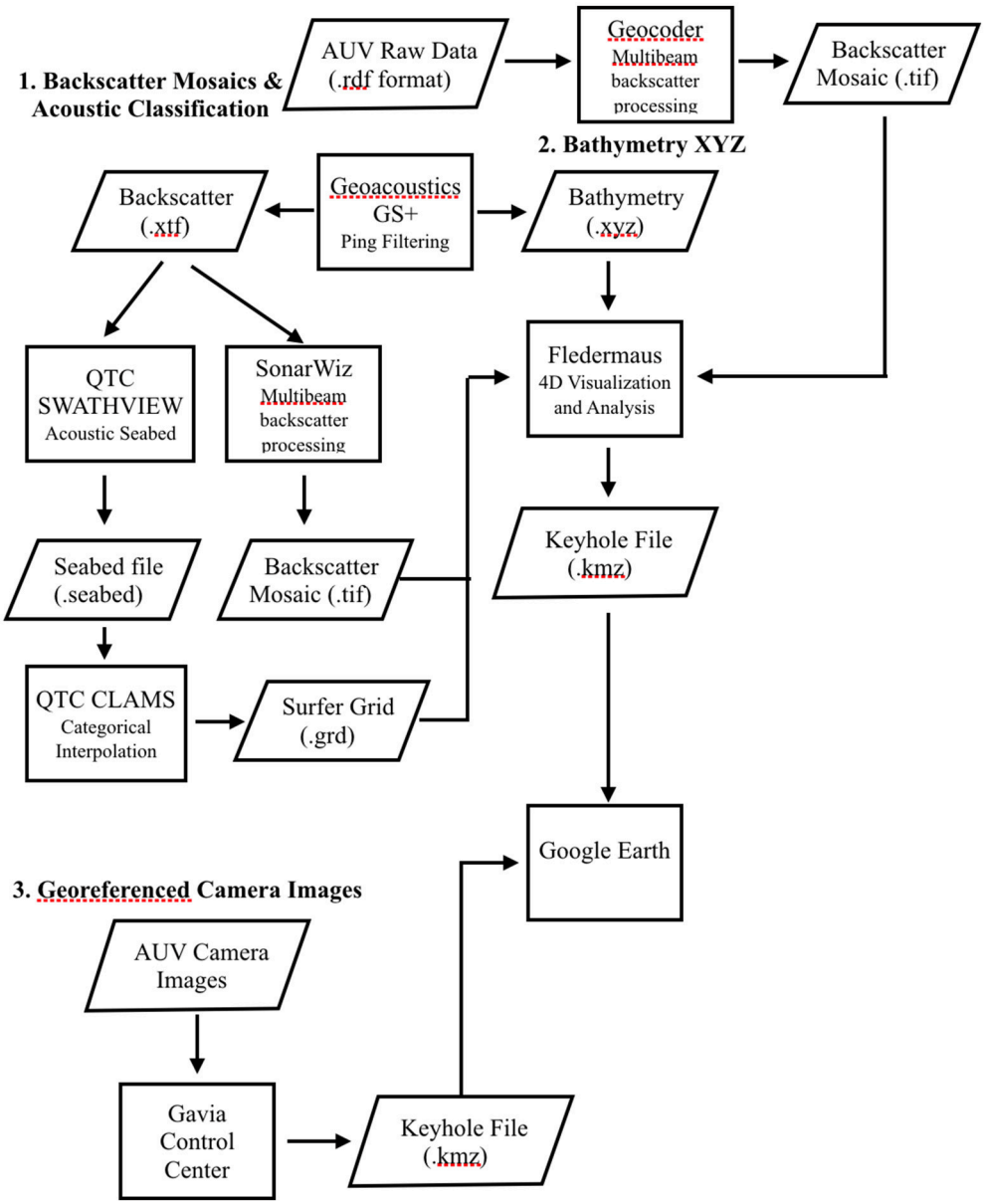

FIGURE 3 | Data processing workflow for the generation of (1) Backscatter mosaics (2) XYZ bathymetry ad (3) georeferenced camera images. All of the resulting products are then integrated and visualized together for analysis in Matlab and Google Earth.

images are valuable for ground-truthing acoustic class maps. The AUV camera records frames at approximately two frames per second and, during the Bonaire surveys, collected nearly 73,000 images. Given the speed of the vehicle, the overlap in consecutive images, and a nominal autocorrelation length scale of 10 m the image database reduces down to ∼5,800 images that could be considered independent measurements of the seabed habitat composition. Using the Gavia Control Center software, and the metadata contained within each image, these camera images were georeferenced and exported to .kml, which could be imported directly into Google Earth for overlay onto the sonar and class maps. An example of a set of georeferenced images gathered with the downward facing AUV camera is provided in **Figures 4**, **5**. A subset of 1,500 images from the photo collection were used to perform a statistical analysis of the accuracy and reliability of the acoustic class map and are reported in the results section. Operationally higher altitudes are preferred in order to optimize the sonar swath width, however, we found that camera image resolution degrades with increasing altitude above the bed as the image footprint covers and increasingly wider area, which allows to us distinguish habitat type but not to the level of species and genus.

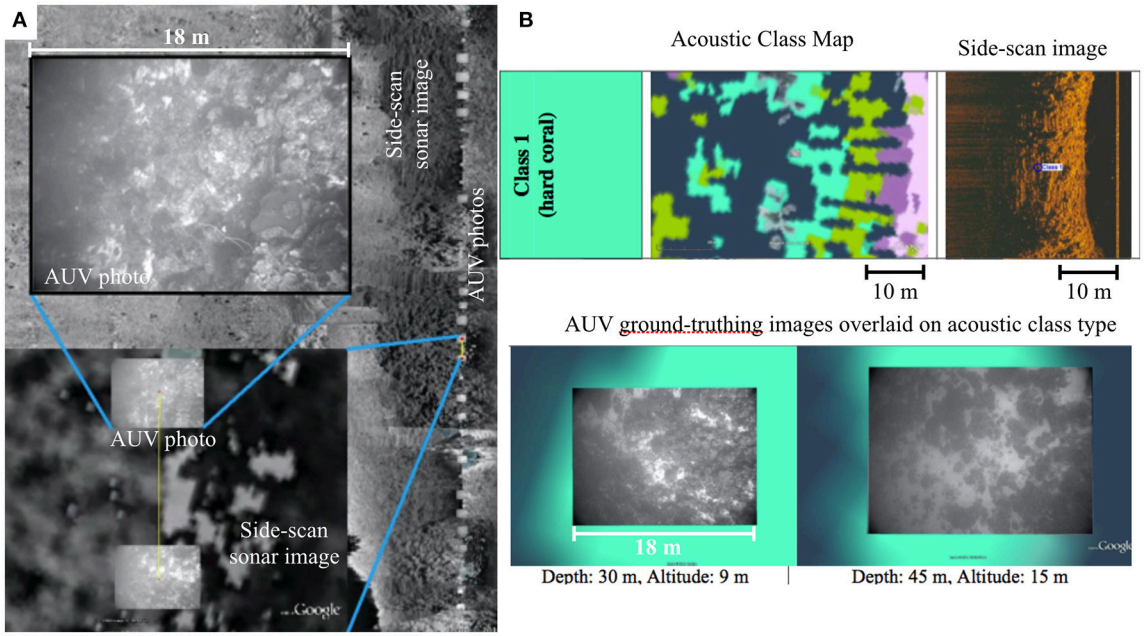

FIGURE 4 | (A) AUV benthic images from the Nukove Bonaire (northern most survey site) displaying the photo size and spacing in Google Earth. Note: Display interval above set to show only every tenth photo. Approximate Image Footprint = 18 × 13 m. **(B)** Example of acoustic class map highlighting class 1 hard coral (turquoise color) along with representative side-scan sonar image of class 1 and AUV camera photos used to ground-truth and classify class 1 as indicative of hard coral cover.

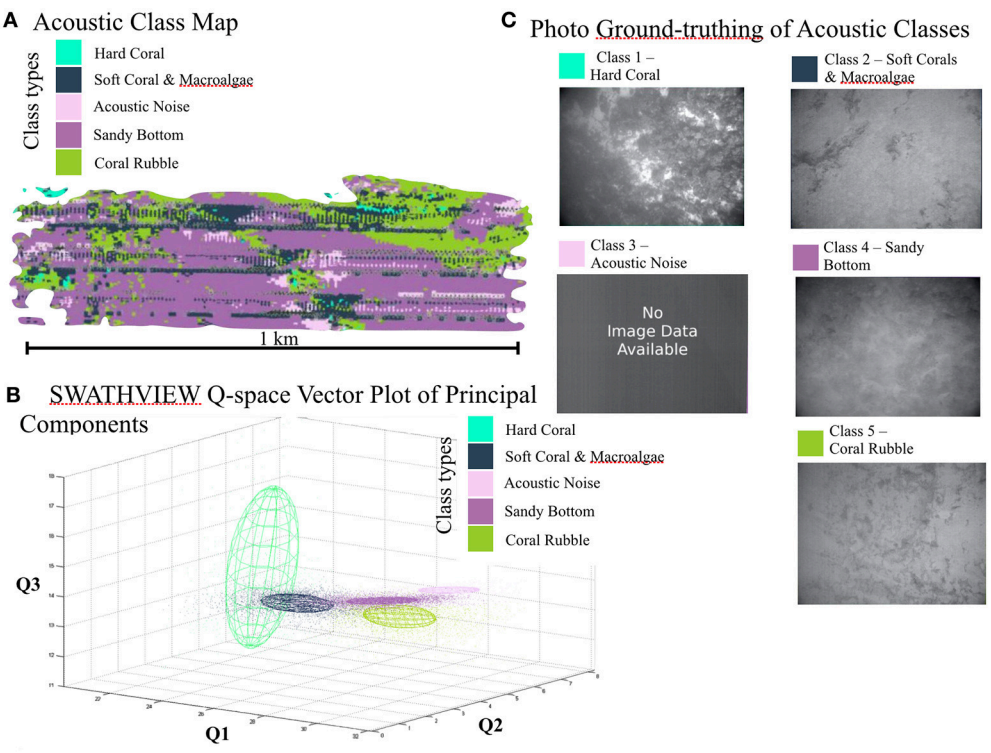

FIGURE 5 | QTC SWATHVIEW acoustic classifications of the combined Bonaire MCE survey database. (A) Acoustic Class map of the southwest Klein Bonaire site (cf **Figure 6**). **(B)** Q-Space vector plot of each point in the survey map in the three-dimensional principle component space with each class type colored and outlined in the vector space. **(C)** Examples of AUV ground-truthing photos of each acoustic class type used to specify the class composition.

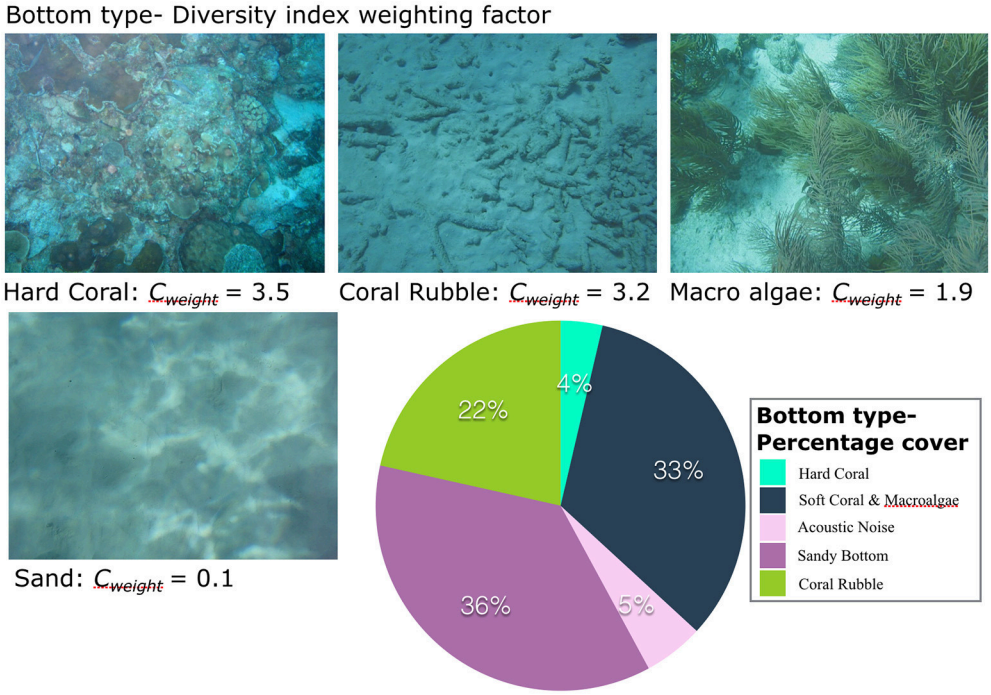

FIGURE 6 | Representative photos of each bottom type class along with the diversity index values assigned for each class type computed as bits using values reported by Porter (1972). Distribution of each class type as a percentage of the mapped seafloor.

AUV camera imagery was used to ground-truth different sediment types associated with each particular SWATHVIEW seafloor classification (**Figure 5**). The mission altitudes that were selected to maximize for acoustic swath coverage produce images that can be used to distinguish bulk habitat class types (e.g., sandy bottom vs. hard coral vs. noise) but are not of sufficient resolution from these survey altitudes to distinguish genus or species. Ground-truthing was achieved by loading a class map into Google Earth as a layer and then loading overlay images of that particular type. For each class three hundred images were examined to validate the acoustic class type (Keller, 2011). This method was used to validate the SWATHVIEW acoustic classifications collected from the surveys (**Figures 4B**, **5C**).

RESULTS

SWATHVIEW Classification

Based upon multiple runs of SWATHVIEW, it was determined that five acoustic classifications best fit the available data, as they included all of the known bottom types (**Figure 5B**). Based on the available AUV ground-truthing image data, Class 1 is associated with clearly defined hard coral structures, including both massive head corals, and foliaceous corals (e.g., *Agaricia agaricites*). Class 2 is associated with soft coral (e.g., *Pseudopterogorgia acerosa*) and macroalgae. No image data are available for Class 3 as it is an acoustical noise class (accounting for only 5% of total class coverage). Class 4 is associated with sandy bottom areas with few distinct characteristics. Class 5 is associated with coral rubble and sparse macroalgae (**Figure 5**). These conclusions about bottom type were made by comparison of the AUV imagery data to photos taken by van Duyl (1985) and also from diver photos taken during the 2008 field campaign and represent bulk habitat class determinations.

Using equation 1 and the aforementioned class weightings, H'_{SC} shows its highest value when coral substrate is found with high rugosity and steep slope in shallower water. This index proved useful in delineating features seen in the acoustic imagery because features created by coral produce complex topography with the highest values using this new combinatorial formulation scheme. Operationally, H'_{SC} ranges from 0 to c. 2.5 for the weighting scheme we used in this work. Note that this synthetic proxy index has dimensions only of bits as the other units all cancel out; thus the absolute magnitude of values computed at a specific seafloor location cannot be directly transferred to another location, but this proxy metric method does prove operationally useful for landscape-level classifications to locate MCE and prioritize within a given location. Other schemes for weighting the bottom types could be used to achieve similar results.

Two of the survey sites were selected as being representative of the two dominant type of shelf profile observed: Klein Bonaire was chosen to represent Type I (**Figure 11**), and Nukove was chosen to represent Type II (**Figure 12**). At each of the sites, estimates of slope, rugosity, and geoacoustic classification were

generated for the surveyed region and combined into the H'_{SC} relative diversity proxy value.

Figure 12 shows similar composite index results for Nukove (Type II) from ∼ 0–225 m depth (see **Figure 10** for depth profile) with a similar submerged structure running parallel to shore as was observed at the Klein Bonaire (Type I) site. However, in contrast to the previous site, this submerged reef occurred at 100 m depth. These greater depths will decrease the value of H'_{SC}. For example the average value for the deep submerged reef at the Nukove (Type II) site is ∼ 1.75 in contrast to an computed value of ∼ 2.25 at the Klein Bonaire site (Type I).

Fully 55.6% of all data points collected in Bonaire fall within the mesophotic zone; however, this includes both flat sandy bottoms as well as coral substrate. To better understand the distribution of coral structures in Bonaire, both the classification data as well as the calculated rugosity values must be interpreted. A high rugosity value is often indicative of the presence of coral structures (Prada et al., 2008), in fact 11.8% of all data points had a rugosity ratio of 1.3 or greater and were found within the inferred hard coral acoustic class (**Figure 6**). In **Figure 6**, the classifications assigned to each data point are shown along with the percentage of the seabed coverage that each class accounted for. Classes 1 (Hard Coral) and 2 (Soft Corals and Macroalgae) are indicative of live coral substrate. These two geoacoustic classes account for 37% of all data points.

Accuracy Metrics of Habitat Classification

In order to assess the accuracy and reliability of the acoustically derived class maps, 1500 independent images were analyzed using a confusion matrix approach (**Table 1**). These images represent ∼25% of the total independent images in the presented survey areas. For the accuracy and reliability assessment images were selected from the areas presented here in the results (**Figures 11**, **12**) with 300 non-overlapping images in each acoustic class domain randomly selected and then the image based bottom type was recorded into a confusion matrix for statistical analysis. The statistical analysis showed an overall accuracy of the acoustic classes at 66%, with accuracy of the hard coral class the highest at 83%, and the sandy-bottom class the lowest at 55. The hard coral class was also the statistically most reliable, at over 80%, with the noise class coming in as the least reliable.

TABLE 1 | Confusion matrix.

	Hard coral	Soft coral macroalgae	Sandy bottom	Coral rubble	Noise
Hard coral	247	33	15	5	0
Soft coral macroalgae	34	227	28	8	3
Sandy bottom	11	31	197	46	15
Coral rubble	4	26	37	203	30
Noise	0	21	83	72	124
Accuracy %	83.4	67.2	54.7	60.8	72.1
Reliability %	82.3	75.7	65.7	67.7	41.3

DISCUSSION

This work detailed the use of an AUV for a high-resolution remote sensing survey of nearly two square kilometers of seafloor around Bonaire in a short 7-day period. Many of the areas mapped in this survey have never been explored in detail before now owing to the depths being beyond traditional SCUBA diver limits. In addition to the commonly visited shallow reef, observations of a second reef which exists from 75 to 100 m on much of the leeward coast from a time that sea level was lower than its current state. Significant deep-water features were discovered at several locations. Their existence was likely unknown, as these depths are greater than traditional scuba diving is capable of achieving. Over half of all the observed reef structures are found outside of the designated Marine Protected Area, and do not benefit from the conservation efforts that exist to protect the shallow reef. **Figure 13** shows a conceptual diagram profile of the leeward shoreline of Bonaire, based on the bathymetry and classification data from all the AUV survey locations. This figure summarizes where specific features and bottom types were found by our AUV surveys and estimated from the data fusion of geomorphologic and acoustic class metrics using a new synthetic proxy index for inferred diversity.

Classes 1 (Hard Coral) and 2 (Soft Corals and Macroalgae), when found at depths beyond 40–50 m (**Figure 7**) these two classes represent inferred areas of MCE. These geoacoustically inferred MCE substrates are fairly discontinuous, and change in width and depth depending on location around the island. Most sites have very low rugosity at depths greater than 100 m; however, Just a Nice Dive, Southwest Corner, and the Marine Park each have significant roughness features indicative of possible MCE sites. The two Klein Bonaire sites show evidence of reef-like structures existing at depths greater than 175 m with no other structures nearby (**Figure 8**). By examining the slope map, these features shows a trail directly behind them trending up into shallower water. This suggests that at least some amount of slumping of the reef structure downslope has likely occurred. This escarpment is fairly continuous and is thus indicative of a submerged reef rather than a collapsed fragment from the modern reef. These calculations of H'_{SC} show that this submerged reef is a potential viable MCE community at ∼60 m depth, although likely not as diverse as the shallow modern reef based on the proxy diversity index calculation. There is also evidence of a feature on the northern side of the plot that is not part of this continuous feature. At 100 m, this feature is much deeper than the submerged reef and is inferred to be a submerged collapsed feature, which may also act as potential deepwater habitat.

A large pile of coral rubble was discovered at the marine reserve site at a depth of 170 m. This pile was measured to be 10 m in height, with a width of nearly 300 m, and surrounded by sand (Class 4; **Figure 9**). It is unlikely that this coral was originally found at this location, as it does not display a shape congruent with a patch reef. Although no significant break in the shallow reef can be distinguished from the available data, it appears to have originated in shallow water. Morton et al. (2008) found a significant onshore ridge deposit at this location, with

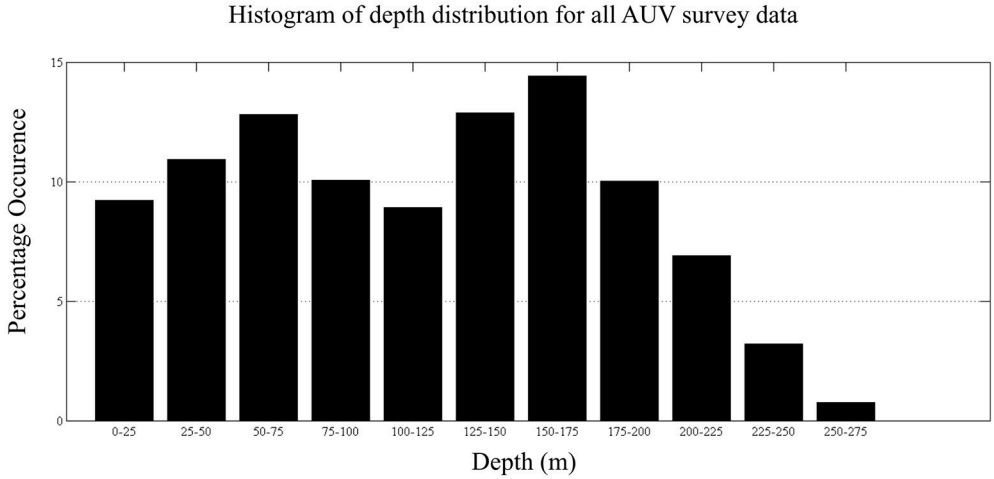

FIGURE 7 | Histogram distribution of bathymetry from all Bonaire survey locations in this study. Portions of the survey within the mesophotic zone comprise 57% of the data and are found in the depth intervals between 50–150 m.

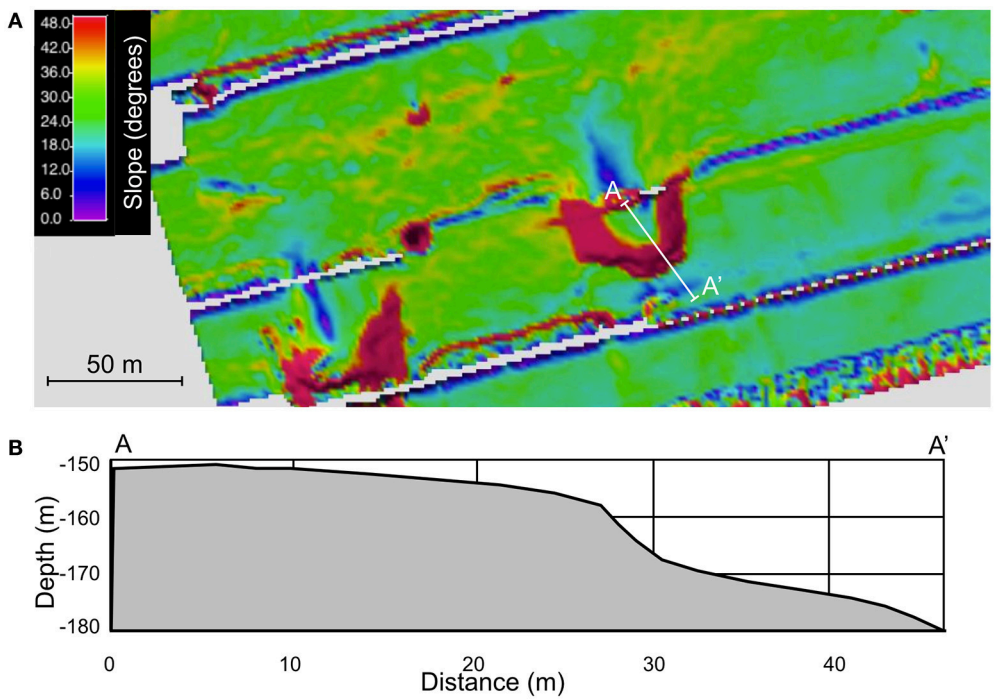

FIGURE 8 | (A) Slope map of the southern section of the Southwest Corner site (cf **Figure 1**) showing trails behind two the deep water reef-like features. **(B)** Close-up bathymetric profile over the deep mound structure. Profile ends refer to A and A′ in panel **A**.

a width of 60–70 m and a thickness of 3 m, consisting of mostly pebbles to cobbles, with some sand and fine boulders. Formations such as these are often indicative of single or multiple significant wave events (Morton et al., 2008). If a large wave event did create this ridge formation onshore, it is likely that substantial damage was also done to the underwater environment, which may have generated this large pile of coral rubble from downslope transport.

These potentially gravity-driven slump features, whether storm or tsunamigenic in origin, provide a transport pathway for the movement of shallow reef species to depth and at the very least would provide new exploitable structural substrate for deep tolerant species to take. These pathways could potentially allow these deposits to serve as conduits to deeper reef banks, or to serve as refugia themselves for any shallow water corals transported with the slump

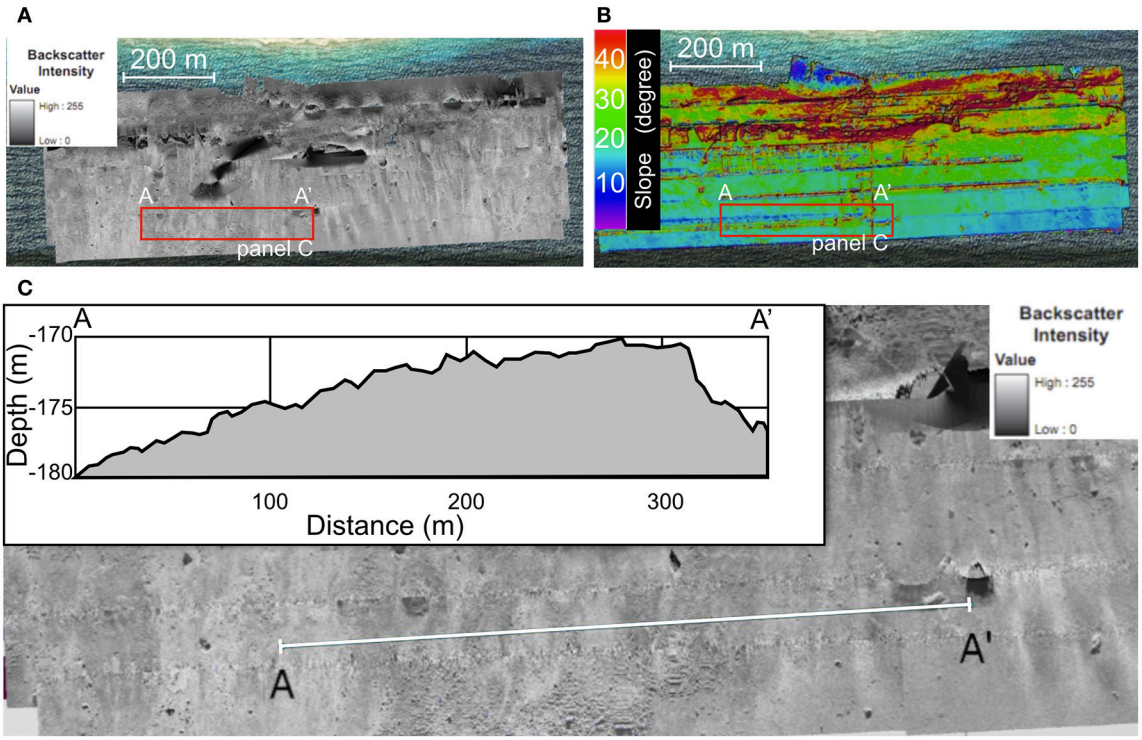

FIGURE 9 | (A) Backscatter mosaic map of the Marine Reserve site. **(B)** Slope map of the Marine Reserve site. **(C)** Profile of bathymetry data overlaid with a backscatter mosaic showing a large mound, ~10 m in height, with a rough acoustically bright surface, and a horizontal width of nearly 300 m.

block that are capable of still thriving at the new depths (Bongaerts et al., 2010). Harriott and Banks (2002) and Harris et al. (2013) found that the presence of hard substrate was essential for coral development. Therefore, we infer that antecedent geology, or more recent event transport mechanisms that can introduce hard substrate at depth, may both provide potential value to MCE development that can be characterized by careful high-resolution remote sensing combining sonar and camera imagery from autonomous underwater vehicles.

One of the original hypotheses associated with this work was that differences in the extent of MCE would be related to the index of wave environments zones proposed by van Duyl (1985). The eight survey sites spanned index values 4–6 according to the van Duyl classification, which covers all of the zones on the leeward side of the island (c.f. **Figure 1**). There appears to be minimal correlation between wave environment zone and the typical observed cross-shore profiles collected at each site (**Figure 10**). Slopes at almost all the locations were relatively shallow ($<5°$) until the reef break 100–125 m from shore and then dropped quite steeply ($>20°$). As shown, the profiles at each of sites can be generalized into one of two different morphologic types (**Figure 10**): Type I—steep initial slope to 50 m with a minor secondary shelf break; and, Type II—steep initial slope to 125 m depth followed by a lower slope inflection. We hypothesized that MCE features associated with the Type I shelf form would be submerged reefs with higher index values whereas Type II shelf forms would more likely be collapse features with lower index values. From this analysis, it is possible to conclude that MCE occurring in regions that have a depth profiles similar to a Type I profile are more likely to have greater index values than on Type II slopes. Utilizing this approach of fusing remote sensing information on morphology and class type to produce composite indices provides a quantitative way to determine areas of interest for follow-up investigation by divers or remotely operated vehicles.

Although these newly mapped MCE are nominally below the depth of the Bonaire MPA (60 m isobath) they may represent significant and important contributors to the health of the reef within the MPA jurisdiction. These deep reef formations have little direct significance to the diving tourism industry, as they fall well-beyond the range of recreational SCUBA diving; however, they may play a vital role to the continued health of the shallower reef. The mesophotic zone for this study is defined as the region between 30 and 150 m and has been shown to support growth of some coral species. The entirety of the deeper coral reef found in Bonaire lies within this zone and has been suggested by numerous studies (Brockovich et al., 2008; Lesser et al., 2009; Bridge et al., 2013; Harris et al., 2013) to serve as refugia and to play an important role in the recovery of damaged shallow water coral reefs.

A follow-up survey of Bonaire would be beneficial as a measure of tracking how the reef has changed since the last

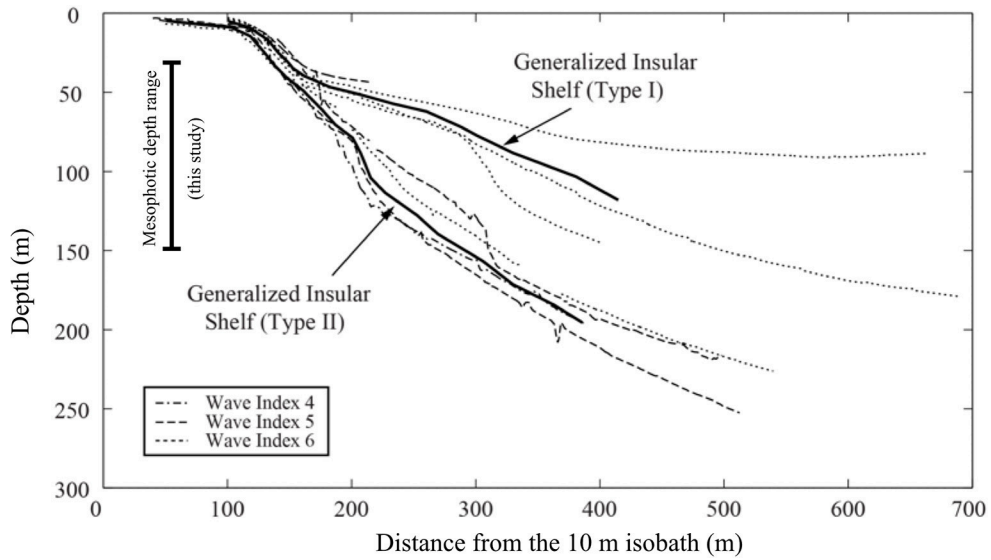

FIGURE 10 | Depth profiles from each study site along the leeward side of Bonaire with the two observed generalized shelf types based on averages of the other profiles.

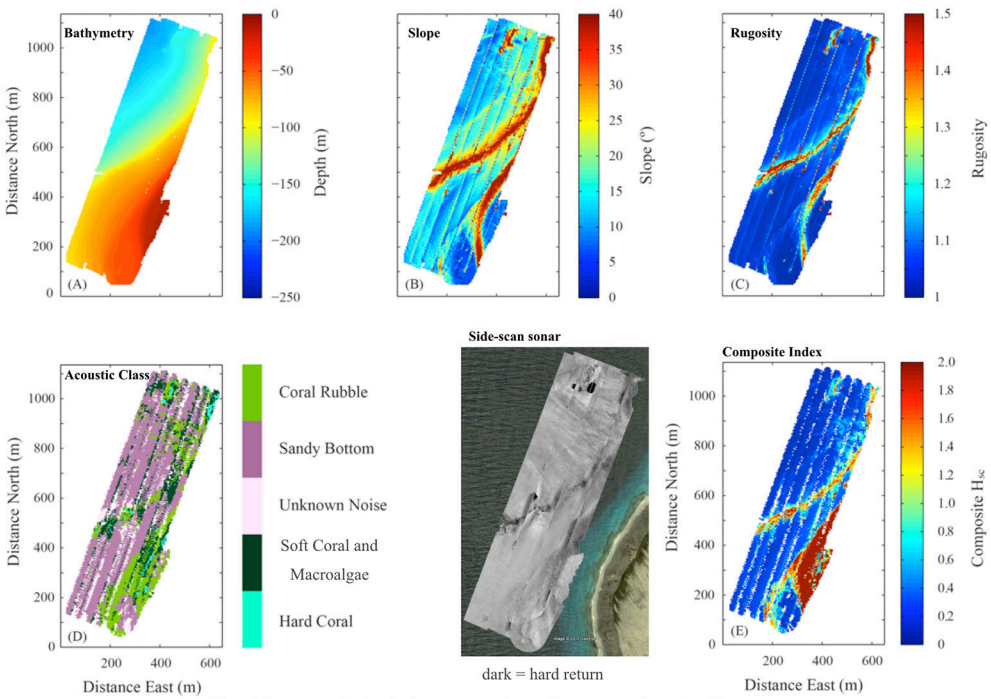

FIGURE 11 | Synthetic bottom type-diversity index, H'_{SC} for the Klein Bonaire site based on composite summary of bathymetry, rugosity, slope, and acoustic class type. Color scale indicates magnitude of synthetic bottom-type diversity index (cf. Equation 1).

survey, especially with the damage caused by Hurricane Omar in October 2008. Several of the significant deep water features were located on the edge of the maps, so these areas could also be further explored in more detail to see how the features relate to the areas around them. These data, along with additional coordinated onshore surveys to determine the locations of wave deposits, could be used to better determine and study possible extreme events that may have generated many of the features

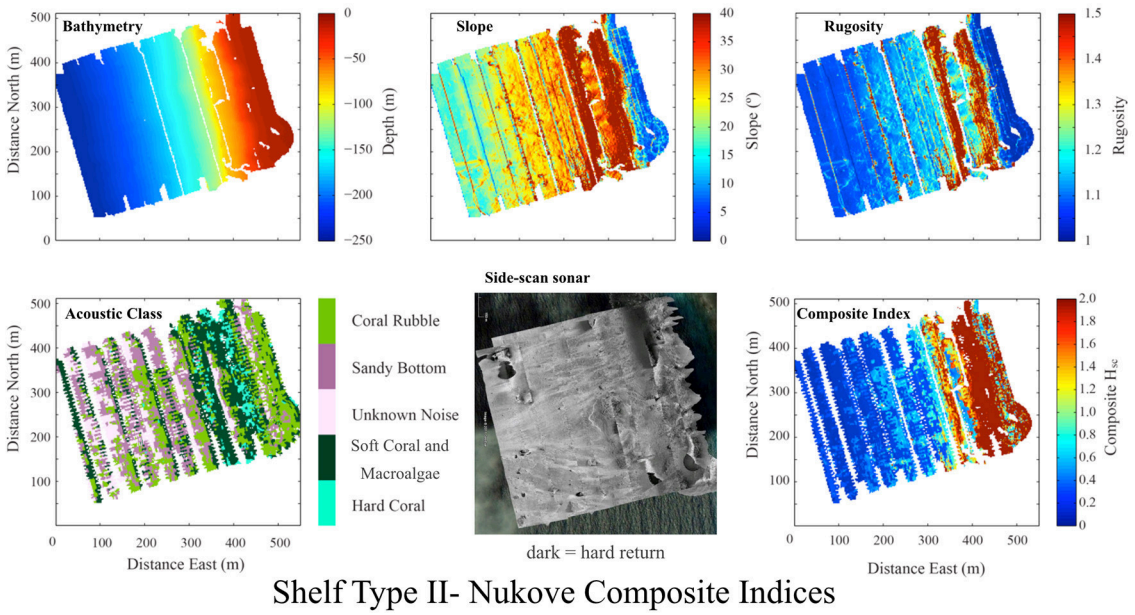

FIGURE 12 | Synthetic bottom type-diversity index for the Nukove Bonaire site based on composite summary of bathymetry, rugosity, slope, and acoustic class type. Color scale indicates magnitude of synthetic bottom-type diversity index (cf. Equation 1).

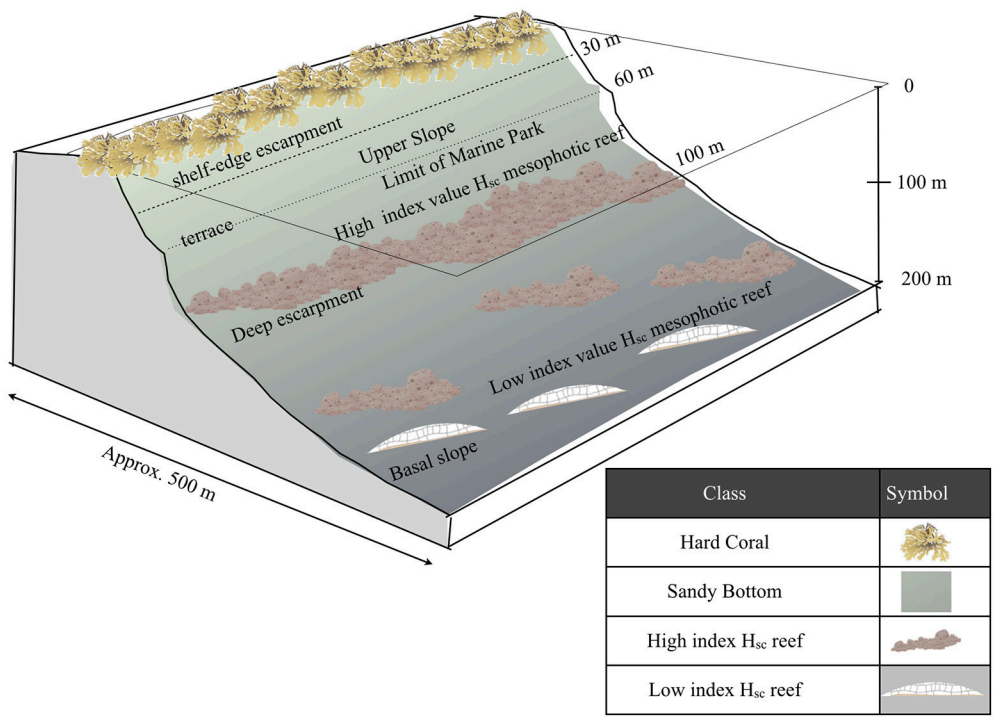

FIGURE 13 | Conceptual diagram of an idealized profile of the insular shelf of Bonaire based on the AUV acoustic data and synthetic diversity maps of mesophotic bottom types.

shown in these surveys. Similar studies could also be conducted on the neighboring islands of Curaçao and Aruba, due to their close proximity.

Confusion matrix based statistical analysis of the remotely sensed geoacoustic class types provided additional insights into the strengths and challenges associated with any form

of pixel based seabed classification from automated ground discrimitation system (AGDS) approaches such as the QTC SWATHVIEW system employed in this study. The AGDS system was seen to have the highest accuracy (83.4%) and reliability (82.3%) for the hard coral class, which is a beneficial finding for studies focused on identifying and assessing hard coral communities. It may be inferred that the generally higher amplitude of acoustic return and shadow created from the relief of hard coral heads compared to other benthic class types makes it more readily distinguishable from the other classes. It was the "Soft Coral and Macroalgae" which had the next highest combination of reliability and accuracy, perhaps intuitively congruent, as this habitat type presents a structural response to ensonification making it fairly easy to distinguish. Acoustic noise, which can come from a variety of sources including inherent design and geometries of the sonar system and environmental variables, showed a farily high accuracy but the lowest reliability, meaning that it could generally be found but that it was also readily confused with either the "Sandy Bottom" or "Coral Rubble" classes perhaps a result of the low amplitude reflection of the former and the somewhat scattered and specular nature of the latter. Of importance to this study, the ADGS was able to clearly distinguish between noise and hard coral classes with no occurrences of noise having been classed as hard coral according to the statistical analysis.

Ground-truthing data, including georeferenced photographs taken closer to the seabed, should be collected to better associate the QTC SWATHVIEW classifications with sediment type and to derive direct species-level measurement indices of diversity to compare to the inferred composite index developed here in this study.

MCEs at Bonaire provide a potential buffer against pressures such as climate change and storms. MCEs throughout the ABC islands (Aruba, Bonaire, and Curaçao) and many others in the Caribbean still remain largely unexamined. Further research is required to determine the full extent and condition of the MCE grounds both on the leeward and particularly the largely unexplored windward portion of the island. Our results suggest that the potential reef habitat of Bonaire may be underestimated. Our summary finding is that geoacoustic surveys from robotic platforms can be used to accurately discriminate between different habitat types/ecological communities in deep waters that are otherwise difficult to survey, and that this type of remote sensing habitat mapping tool provides valuable information for the management of coral reef/MCE ecosystems here and elsewhere.

AUTHOR CONTRIBUTIONS

AT was the Co-PI of the project and lead the design of the experiment, field effort, and supervised the analysis of the data. He advised the graduate student involved and helped write the manuscript and draft the figures. AF helped execute the field collection of the AUV data and to develop the post-processing analysis and to write the paper. BK was the graduate student involved in the data analysis and interpretation and helped write the manuscript. MP was the project Co-PI and helped lead the design of the overall project and to conduct the field work.

ACKNOWLEDGMENTS

This work was supported by a NOAA Office of Ocean Exploration and Research Award #NA07OAR4600291. Expert field assistance was provided by project co-PIs J. Leichter, and M. D. Stokes, and expedition members C. Cocarro, K. Collins, S. Genovese, T. Hiller, D. Jones, B. Laval, E. Magnússon, J. Mallinson, K. McCole, D. Miller, N. and A. Relles, O. Rutten, H. Stevens, and R. Yeo. E. Beukenboom and R. de Leon of STINAPA Bonaire provided logistical help, field assistance, and boat access. F. van Slobbe, Department of Environment and Natural Resources, and the Honorable H. Domacassé, Lt. Governor of the Government of the Island Territory of Bonaire provided insights into development trends and political support for the expedition.

REFERENCES

Armstrong, R. A., Singh, H., Torres, J., Nemeth, R. S., Can, A., Roman, C., et al. (2006). Characterizing the deep insular shelf coral reef habitat of the Hind Bank marine conservation district (US Virgin Islands) using the Seabed autonomous underwater vehicle. *Cont. Shelf Res.* 26, 194–205. doi: 10.1016/j.csr.2005.10.004

Bak, R. P. M., Nieuwland, G., and Meesters, E. H. (2005). Coral reef crisis in deep and shallow reefs: 30 years of constancy and change in reefs of Curaçao and Bonaire. *Coral Reefs* 24, 475–479. doi: 10.1007/s00338-005-0009-1

Bongaerts, P., Ridgway, T., Sampayo, E., and Hoegh-Guldberg, O. (2010). Assessing the "deep reef refugia" hypothesis: focus on Caribbean reefs. *Coral Reefs* 29, 309–327. doi: 10.1007/s00338-009-0581-x

Brennan, M. L., Robert, D. B., Roman, C., Bell, K. L. C., Buxton, B., Coleman, D. F., et al. (2012). Evaluation of the modern submarine landscape off southwestern Turkey through the documentation of ancient shipwreck sites. *Cont. Shelf Res.* 43, 55–70. doi: 10.1016/j.csr.2012.04.017

Bridge, T. C. L., Done, T. J., Friedman, A., Beaman, R. J., Williams, S. B., Pizarro, O., et al. (2011b). Variability in mesophotic coral reef communities along the Great Barrier Reef, Australia. *Mar. Ecol. Prog. Ser.* 428, 63–75. doi: 10.3354/meps09046

Bridge T. C. L., Done, T., Beaman, R., Friedman, A., Williams, S., Pizarro, O., et al. (2011a). Topography, substratum and benthic macrofaunal relationships on a tropical mesophotic shelf margin, central Great Barrier Reef, Australia. *Coral Reefs* 30, 143–153. doi: 10.1007/s00338-010-0677-3

Bridge, T., Hughes, T., Guinotte, J., and Bongaerts, P. (2013). Call to protect all coral reefs. *Nat. Clim. Change* 3, 528–530. doi: 10.1038/nclimate1879

Bries, J. M., Debrot, A. O., and Meyer, D. L. (2004). Damage to the leeward reefs of Curaçao and Bonaire, Netherlands Antilles from a rare storm event: Hurricane Lenny, November 1999. *Coral Reefs* 23, 297–307. doi: 10.1007/s00338-004-0379-9

Brockovich, E., Einbinder, S., Shashar, N., Kiflawi, M., and Kark, S. (2008). Descending to the twilight zone: changes in coral reef fish assemblages along a depth gradient down to 65 m. *Mar. Ecol. Prog. Ser.* 371, 253–262. doi: 10.3354/meps07591

De Bakker, D. M., Meesters, E. H., Bak, R. P. M., Nieuwland, G., and Van Duyl, F. C. (2016). Long-term shifts in coral communities on shallow to deep reef slopes of Curaçao and Bonaire: are there any winners? post-hoc. *Mar. Sci.* 3:247. doi: 10.3389/fmars.2016.00247

De Meyer, K., and MacRae, D. (2006). *Bonaire National Marine Park Management Plan. Part 1. Background.* The Dutch Caribbean Nature Alliance (Bonarte) and

Coastal Zone Management. Available online at: http://ec.europa.eu/ourcoast/download.cfm?fileID=865

Fernandes, P. G., Stevenson, P., Brierley, A. S., Armstrong, F., and Simmonds, E. J. (2003). Autonomous underwater vehicles: future platforms for fisheries acoustics. *ICES J. Mar. Sci.* 60, 684–691. doi: 10.1016/S1054-3139(03)00038-9

Forrest, A. L., Trembanis, A. C., and Todd, W. L. (2012). Ocean floor mapping as a precursor for space exploration. *J. Ocean Technol.* 7, 71–87.

Fricke, H., and Meischner, D. (1985). Depth limits of Bermudan scleractinian corals: a submersible survey. *Mar. Biol.* 88, 175–187. doi: 10.1007/BF00397165

Harriott, V. H., and Banks, S. B. (2002). Latitudinal variation in coral communities in eastern Australia: a qualitative biophysical model of factors regulating coral reefs. *Coral Reefs* 21, 83–94. doi: 10.1007/s00338-001-0201-x

Harris, P. T., Bridge, T. C. L., Beaman, R. J., Webster, J. M., Nichol, S. L., and Brooke, B. P. (2013). Submerged banks in the Great Barrier Reef, Australia, greatly increase available coral reef habitat. *ICES J. Mar. Sci.* 70, 284–293. doi: 10.1093/icesjms/fss165

Jenness, J. S. (2004). Calculating landscape surface area from digital elevation models. *Wild Soc. Bull.* 32, 829–839. doi: 10.2193/0091-7648(2004)032[0829:CLSAFD]2.0.CO;2

Kahng, S. E., Garcia-Sais, J. R., Spalding, H. L., Brokovich, E., Wagner, D., Weil, E., et al. (2010). Community ecology of mesophotic coral reef ecosystems. *Coral Reefs* 29, 255–275. doi: 10.1007/s00338-010-0593-6

Keller, B. M. (2011). *Imaging the Twilight Zone: the Morphology and Distribution of Mesophotic Zone Features, a Case Study from Bonaire, Dutch Caribbean*. MSc thesis, University of Delaware, 168.

Leichter, J. J., Shellenbarger, G., Genovese, S. J., and Wing, S. R. (1998). Breaking internal waves on a Florida (USA) coral reef: a plankton pump at work? *Mar. Ecol. Prog. Ser.* 166, 83–97. doi: 10.3354/meps166083

Lesser, M. P., Slattery, M., and Leichter, J. J. (2009). Ecology of mesophotic coral reefs. *J. Exp. Mar. Biol. Ecol.* 375, 1–8. doi: 10.1016/j.jembe.2009.05.009

Locker, S., Armstrong, R., Battista, T., Rooney, J., Sherman, C., and Zawada, D. (2010). Geomorphology of mesophotic coral ecosystems: current perspectives on morphology, distribution, and mapping strategies. *Coral Reefs* 29, 329–345. doi: 10.1007/s00338-010-0613-6

Moline, M. A., Blackwell, S. M., Allen, B., Austin, T., Forrester, N., Goldsborogh, R., et al. (2005). Remote Environmental Monitoring UnitS: an autonomous vehicle for characterizing coastal environments. *J. Atmos. Ocean. Technol.* 22, 1798–1809. doi: 10.1175/jtech1809.1

Morton, R. A., Richmond, B. M., Jaffe, B. E., and Gelfenbaum, G. (2008). Coarse-clast ridge complexes of the Caribbean: a preliminary basis for distinguishing tsunami and storm-wave origins. *J. Sed. Res.* 78, 624–637. doi: 10.2110/jsr.2008.068

Patterson, M. R., and Relles, N. J. (2008). "Autonomous underwater vehicles resurvey bonaire: a new tool for coral reef management," in *Proceedings of the 11th International Coral Reef Symposium,* Vol. 1 (Lauderdale, FL), 546–550.

Patterson, M. R., Doolittle, D. F., Rahman, Z., and Mann, R. L. (2007). *Method for Identification and Quantification of Biological Sonar Targets in Liquid Medium*. U. S. Patent 7,221,621. Washington, DC: U.S. Patent and Trademark Office.

Patterson, M., Hiller, T., and Trembanis, A. (2008). Exploring coral reef sustainability. *Hydro Int.* 12, 10–15.

Pike, W. J. (2011). *Optical Benthic Imagery Survey in a Lacustrine Basin Using an Autonomous Underwater Vehicle.* MSc thesis, University of British Columbia, Vancouver, BC.

Porter, J. W. (1972). Patterns of species diversity in Caribbean reef corals. *Ecology* 53, 745–748. doi: 10.2307/1934796

Prada, M. C., Appeldoorn, R. S., and Rivera, J. A. (2008). Improving coral reef habitat mapping of the Puerto Rico insular shelf using side scan sonar. *Mar. Geod.* 31, 49–73. doi: 10.1080/01490410701812170

Preston, J. M., Christey, A. C., Bloomer, S. F., and Beaudet, I. L. (2001). "Seabed classification of multibeam sonar images," *Proceedings of the MTS/IEEE Conference,* 01.

Quester Tangent (2010). *QTC SWATHVIEW 1.0 User Manual and Reference: DMN-SWVW-0000-R00*. Saanichton.

Raineault, N. A., Trembanis, A. C., and Miller, D. (2012). Mapping benthic habitats in Delaware Bay and the coastal Atlantic: acoustic techniques provide greater coverage and high resolution in complex shallow-water environments, *Estuar. Coasts* 35, 682–699. doi: 10.1007/s12237-011-9457-8

Raineault, N. A., Trembanis, A. C., Miller, D. C., and Capone, V. (2013). Interannual changes in seafloor surficial geology at an artificial reef site on the inner continental shelf. *Cont. Shelf Res.* 58, 67–78. doi: 10.1016/j.csr.2013.03.008

Relles, N. J., and Patterson, M. R. (2011). "AUVs (ROVs)," in *Encyclopedia of Modern Coral Reefs,* ed D. Hopley (Dordrecht: Springer), 71–75.

Smale, D. A., Kendrick, G. A., Harvey, E. S., Langlois, T. J., Hovey, R. K., Van Niel, K. P., et al. (2012). Regional-scale benthic monitoring for ecosystem-based fisheries management (EBFM) using an autonomous underwater vehicle (AUV). *ICES J. Mar. Sci.* 69, 1108–1118. doi: 10.1093/icesjms/fss082

Steneck, R., and McClanahan, T. (2004). *A Report on the Status of the Coral Reefs of Bonaire with Advice on the Establishment of fish Protection Areas*. Pew Charitable Trust Report.

Stokes, M. D., Leichter, J. J., and Genovese, S. J. (2010). Long-term declines in coral cover at Bonaire, Netherlands Antilles. *Atoll Res. Bull.* 582, 1–21. doi: 10.5479/si.00775630.582.1

Trembanis, A. C., DuVal, C., Beaudoin, J., Schmidt, V., Miller, D., and Mayer, L. (2013). A detailed seabed signature from hurricane sandy revealed in bedforms and scour. *Geochem. Geophys. Geosyst.* 14, 4334–4340. doi: 10.1002/ggge.20260

Trembanis, A. C., Forrest, A. L., Miller, D. C., Lim, D. S. S., Gernhardt, M. L., and Todd, W. L. (2012). Multiplatform ocean exploration: insights from the NEEMO space analog mission. *J. Mar. Technol. Soc.* 46, 7–19. doi: 10.4031/MTSJ.46.4.2

van Duyl, F. C. (1985). *Atlas of the Living Reefs of Curaçao and Bonaire (Netherlands Antilles).* Vrije Universiteit, Utrecht.

Williams, S. B., Pizarro, O., Webster, J. M., Beaman, R. J., Mahon, I., Johnson-Roberson, M., et al. (2010). Autonomous underwater vehicle-assisted surveying of drowned reefs on the shelf edge of the Great Barrier Reef, Australia. *J. Field Robot.* 27, 675–697. doi: 10.1002/rob.20356

Conflict of Interest Statement: The authors declare that the research was conducted in the absence of any commercial or financial relationships that could be construed as a potential conflict of interest.

frontiers in Marine Science

ORIGINAL RESEARCH
published: 29 May 2017
doi: 10.3389/fmars.2017.00151

Simplifying Regional Tuning of MODIS Algorithms for Monitoring Chlorophyll-*a* in Coastal Waters

Weimin Jiang[1], *Benjamin R. Knight*[1]*, *Chris Cornelisen*[1], *Paul Barter*[1] and *Raphael Kudela*[2]

[1] Coastal and Freshwater Group, Cawthron Institute, Nelson, New Zealand, [2] Kudela Lab, Department of Ocean Sciences, University of California, Santa Cruz, Santa Cruz, CA, United States

Monitoring of the phytoplankton pigment chlorophyll-*a* is often used as an indicator of eutrophication in coastal waters. Improved water quality monitoring using data sourced from MODIS (Moderate Resolution Imaging Spectroradiometer)-sourced data allows for infrequently sampled sites to be interrogated for long-term trends. Despite the wide availability and good spatial and temporal coverage of MODIS data, these data have had little use in operational coastal monitoring of chlorophyll-*a* in New Zealand. This is in part due to the poor performance of global oceanic algorithms applied in the coastal waters. Accessible algorithm tuning methods that can be validated by *in situ* measurements may assist the uptake of satellite data for coastal monitoring. This study presents results from regional tuning and validation of two empirical algorithm approaches, including a new simple exponential model, to estimate chlorophyll-*a* for two coastal locations in New Zealand. A novel method of training chlorophyll-*a* models using smoothed *in situ* data to match spatial scales of satellite observations was applied, and shows promise for improving tuned model performance. This approach shows potential for lowering barriers for researchers and coastal managers wishing to make use of the growing satellite data resource in their coastal environments.

Keywords: remote sensing, satellite, biological oceanography, New Zealand, water quality

OPEN ACCESS

Edited by:
Kevin Ross Turpie,
University of Maryland, United States

Reviewed by:
Mukesh Gupta,
Institut de Ciències del Mar (CSIC), Spain
Maria João Costa,
University of Évora, Portugal

***Correspondence:**
Benjamin R. Knight
ben.knight@cawthron.org.nz

Specialty section:
This article was submitted to Environmental Informatics, a section of the journal Frontiers in Marine Science

Received: *28 February 2017*
Accepted: *03 May 2017*
Published: *29 May 2017*

Citation:
Jiang W, Knight BR, Cornelisen C, Barter P and Kudela R (2017) Simplifying Regional Tuning of MODIS Algorithms for Monitoring Chlorophyll-a in Coastal Waters. Front. Mar. Sci. 4:151. doi: 10.3389/fmars.2017.00151

INTRODUCTION

Chlorophyll-*a* (chl-*a*) concentrations provide a valuable measure of phytoplankton biomass in the marine environment. Phytoplankton biomass can provide an indicator of trophic state in marine systems due to an association with anthropogenic nutrient pressures (Smith et al., 1999). Consequently chl-*a* is commonly monitored, particularly in coastal marine environments, as part of a wider suite of indicators (Bricker et al., 2003; Giovanardi and Vollenweider, 2004). However, field monitoring and analysis of chl-*a* is a resource-intensive process which may limit the temporal and spatial coverage of monitoring by relevant authorities.

A traditional way of monitoring chl-*a* in aquatic systems involves field analysis of *in situ* chl-*a* fluorescence. For logistical reasons, field sampling is often unable to match the spatial and temporal scale of variability in phytoplankton biomass. Since the launch of ocean-color sensors such as the Coastal Zone Color Scanner (CZCS) in the 1970s, multispectral and hyperspectral satellite remote sensing data are routinely processed to estimate oceanic water chl-*a* concentrations. Many satellite sensors are currently available to monitor chl-*a*, making them potentially useful tools for

management, but the use of the data in coastal waters requires local calibration and validation (IOCCG, 2000).

The rewards from successful satellite algorithm development for coastal waters are high. For example the MODIS (Moderate Resolution Imaging Spectroradiometer) Aqua and Terra satellite datasets have been collected daily from 1999, with some of these data easily viewable through webtools such as Worldview (https://worldview.earthdata.nasa.gov/) and CawthronEye (http://www.cawthron.org.nz/apps/cawthroneye). Consequently there is the potential to access over a decade of twice daily surface data at a spatial resolution of about 1 km^2. As well as the MODIS datasets, there are several other accessible satellite datasets. The MERIS (MEdium Resolution Imaging Spectrometer) instrument offered additional insights due to a greater number of spectral bands, and provides a template for the Ocean Land Color Imager (OLCI) launched on Sentinel-3. However, MERIS is not currently operational and so it has limited opportunities for calibration to contemporary datasets. Similarly the LandSat satellites also offer high spatial resolution (30 m), but have a limited number of relevant spectral bands for aquatic research and only a 16-day temporal resolution. Consequently we selected MODIS satellite data for use in this study.

In order to quantify radiance across many spectral bands, the receiving satellite sensor relies on sunlight penetrating the atmosphere and the surface ocean water. The incident light will be affected by various factors in the water that interfere and change the intensity of light of different wavelengths that arrive at the satellite sensor. These factors include absorbance by waterborne constituents and atmospheric aerosols and can include other factors such as ocean surface waves or bottom reflectance. It is these spectral modifications that can affect the estimation of properties, such as chl-*a* concentrations in surface waters.

Accurate estimation of chl-*a* concentration, from satellite-sensed data cannot be tested and validated without substantial field datasets, which equates to a large effort for an unknown result. This is particularly true for chl-*a* in optically complex coastal waters. The common issue to overcome is the overlap in the spectral response with other water constituents such as colored dissolved organic matter (CDOM; IOCCG, 2000). Internationally, freely accessible satellite-derived chl-*a* data in coastal waters are increasingly being used with newly developed algorithms. However, little application of satellite data to New Zealand coastal waters has occurred, with only a limited number of studies undertaken for coastal monitoring (Jones et al., 2013). We suspect the limited uptake may be associated with the risk of unsuccessful results and lack of access to tools and advice to assist with calibration of satellite data algorithms for estimating chl-*a* in coastal waters. Indeed a recent survey study by Schaeffer et al. (2013) identified a number of factors that limit the use of satellite data globally.

Many algorithms have been developed for estimating chl-*a* from MODIS and SeaWiFS (Sea viewing Wide Field-of-view Sensor) data, ranging from empirical to more physically realistic "semi-empirical" algorithm approaches. Examples of commonly used global empirical algorithms are: the OC3M algorithm (Carder et al., 2004) for MODIS, the OC2 and OC4 algorithms for SeaWiFS, and the OC4Me for MERIS (O'Reilly et al., 1998, 2000; Morel et al., 2007). These algorithms have been routinely used to process satellite images for oceanic (referred to here as Case 1) waters (IOCCG, 2000), where phytoplankton and their derivatives predominantly determine the optical properties (Morel, 1988). For most coastal and inland (Case 2) waters, where sediments or dissolved yellow substance make an important or dominant contribution to the optical properties (Morel, 1988), the algorithms may fail to produce accurate estimates (Ruddick et al., 2000; Moses et al., 2009). For more reliable estimates of chl-*a* concentrations, the application of algorithms to Case 2 waters will need to be locally validated (Kahru et al., 2014).

The present study explores the potential usage of readily accessible MODIS multispectral data for describing chl-*a* variability in coastal waters of New Zealand at two locations (Hawke Bay and Tasman Bay; **Figure 1**). The study relies on long-term near surface data collected using morred sensors to determine *in situ* conditions and to investigate the suitability of these data for satellite algorithm development in New Zealand.

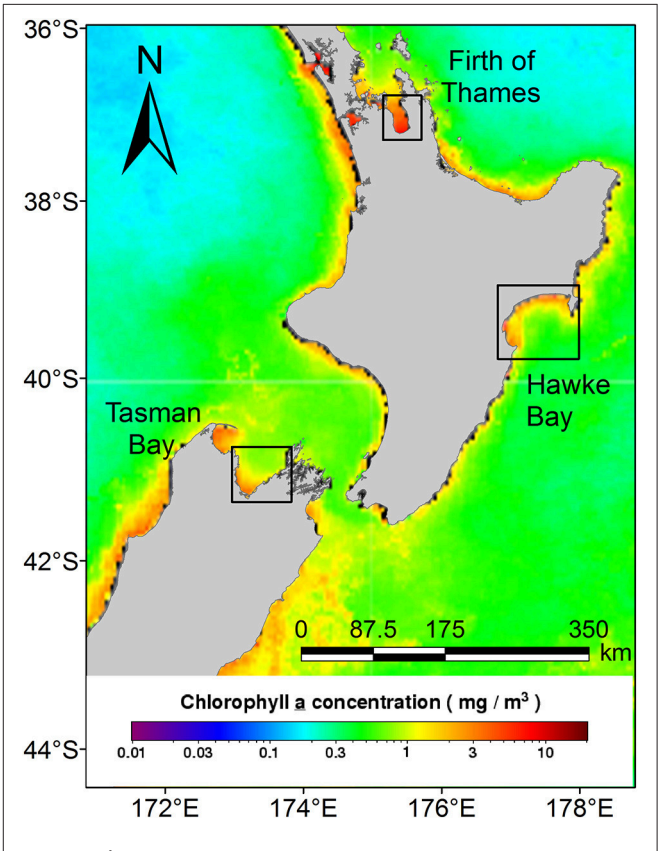

FIGURE 1 | The two New Zealand coastal regions (Tasman and Hawke bays) that are the focus of the study are shown in the two southern boxes with an additional Firth of Thames region (northern-most box) which is discussed, but which is not analyzed in detail here. Mean annual global chlorophyll-*a* concentrations from the Case 1 OC3M algorithm are shown for 2012. Chlorophyll-*a* data were sourced at a spatial resolution of 4 km (level 3 data) from the Ocean Color website (https://oceancolor.gsfc.nasa.gov/).

MATERIALS AND METHODS

Satellite Data

The present study uses MODIS Aqua Level 2 (L2) data, which can be downloaded on request from the OceanColor website (NASA, 2013). Although MODIS Terra data products were also available for this study, these were excluded from our analysis due to identified issues with the data collected by this instrument (Franz et al., 2007). MODIS Level 2 data products have a spatial resolution of about 1 km^2 and are atmospherically corrected using the standard Near-Infrared (NIR) algorithm for oceanic (Case 1) waters (Gordon and Wang, 1994). For turbid coastal waters, the water-leaving radiance in the near-infrared bands is significantly greater than zero due to suspended particles. Applying the default atmospheric correction algorithm can therefore lead to over-correction of the reflectance and result in negative values for some pixels. Alternative algorithms of atmospheric correction of Case 2 waters can improve radiance reflectance accuracy in turbid coastal waters. For example, using the assumption of negligible water-leaving reflectance in the near-infrared region of the spectrum (Bailey et al., 2010). However, this procedure would require additional processing of less refined Level 1 (L1) data (Aiken and Moore, 1997; Ruddick et al., 2000; Wang and Shi, 2007). Because of aims of this study to consider accessible methods that will improve accessibility of data, additional atmospheric processing of L1 data has not been undertaken for this study.

The L2 data quality was checked before use by inspection of the provided quality flags for atmosphere, land, glint and cloud (specific flags used were: ATMFAIL, LAND, HIGLINT, HILT, CLDICE, CHLFAIL, and ATMWARN). Any flagged data were excluded from future analysis and remaining remote sensing reflectance data with negative values were excluded from the subsequent analyses.

Level 2 processed data files were sourced from the OceanColor website and also included chl-*a* estimates based on a global OC3M algorithm (Carder et al., 2004; NASA, 2013). The global OC3M chl-*a* algorithm (Default OC3M) was developed for Case 1 waters and were used for comparison with locally calibrated chl-*a* algorithms (Local OC3M) developed in this study.

Field Data

Two locations around New Zealand, Tasman Bay and Hawke Bay (**Figure 1**), were assessed using available water quality data. Several sources of time-series data from moored sensors, and data from discrete water sampling were used to locally calibrate and assess the performance of satellite data algorithms.

In Tasman Bay, a 2 year dataset (April 2011 to March 2013) was available through sensors attached to a moored monitoring buoy named TASCAM (41.058°S 173.091°E, **Figure 2**). The TASCAM monitoring buoy contained a fluorescent chl-*a* sensor (Weblabs Eco-FLNTUS), which uses a 470/695 nm excitation-emission frequency to characterize the fluorescent signal with a stated chl-*a* sensitivity of 0.025 mg/m^3. Two chl-*a* sensors were used over the 2 year deployment period. Both sensors were initially calibrated at the factory (www.wetlabs.com) on the 2nd of August 2010 at an ambient temperature of 22.3°C and were deployed from new to the TASCAM site. The second sensor replaced the initial sensor deployment and was deployed in April 2012. Both sensors were deployed at a depth of 8 m and contained an integrated copper anti-fouling Bio-wiper™ which was closed when no measurements were being taken to prevent fouling. Antifouling was used on the sensor housings, with *in situ* diver cleaning occurring approximately every 3 months at the site. A 60 min sampling interval was used over the deployment period, with a single fluorescent measurement reported.

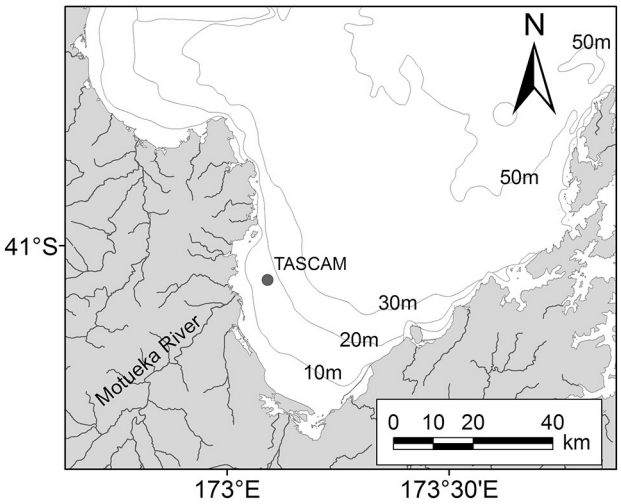

FIGURE 2 | Map showing the location of the TASCAM (dot) monitoring buoy in Tasman Bay and the Motueka River to the south-east of the buoy. Bathymetric depth contours also shown (gray lines).

Hawke Bay chl-*a* data was accessed from another moored bouy, HAWQi (Hawke Bay water quality information), (39.386°S 176.949°E, **Figure 3**). This bouy was identical to TASCAM and used the same chl-*a* sensor (i.e., a WETLabs Eco-FLNTUS with an integrated anti-fouling Bio-wiper™). The chl-*a* sensor was also deployed from new with factory calibration and cleaned with approximately three-monthly visits to the site. A single sensor at the HAWQi buoy was deployed at a depth of 5 m. Both 30 and 60 min sampling intervals were used over the period December 2012–October 2013, with a single florescent measurement reported. Field accuracy of the chl-*a* sensor was checked by comparing *in situ* readings to Van Dorn collected seawater samples from near to the sensor. Processing of *in situ* samples for chl-*a* concentrations were obtained following the procedures specified by Lorenzen (1967).

Chlorophyll-*a* sampling for the period 2002–2013 from a number of other locations was also collated for Hawke Bay. These data were collected by the Hawke's Bay Regional Council using individual laboratory-analyzed water samples (**Figure 3**). Due to issues associated with a coarse temporal sampling scale of the data and the proximity of the sampling sites to the coast, these data were excluded from model training. The data were instead used to assess the skill of the algorithm for different areas of the bay to assess the applicability of the algorithm for wider use.

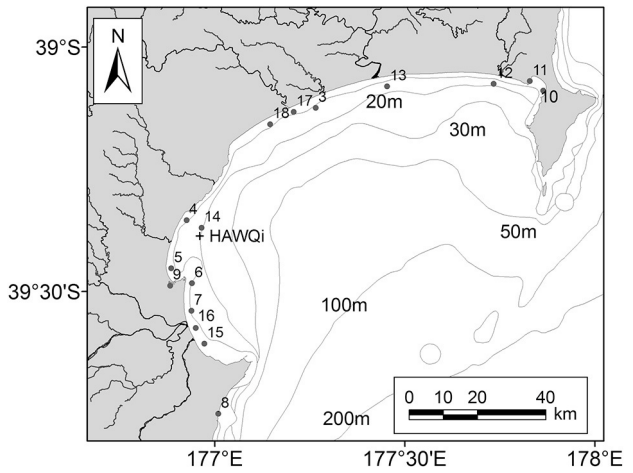

FIGURE 3 | Moored data site of the Hawke Bay water quality information monitoring buoy (HAWQi; +), and State of the Environment (SOE; dots) water sampled sites (3–18) used in this study. Bathymetric depth contours also shown (gray lines).

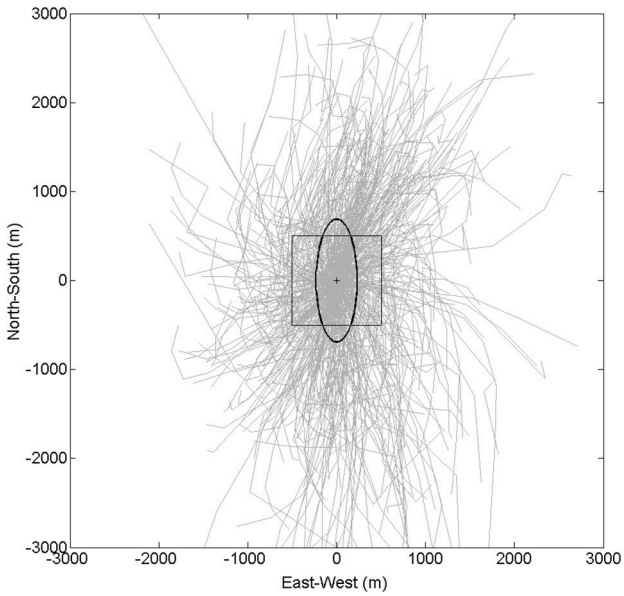

FIGURE 4 | Progressive vectors (light gray) showing estimated surface advection length-scales over a 6 h periods at the TASCAM mooring site. Note the ellipse shows mean advection distances over 6 h and the thin black square shows the 1 km^2 resolution of satellite data used in the study.

To ensure data from the moored sensors were compatible with the 1 km^2 resolution satellite data, temporal smoothing using a centered 6 h window moving box mean was applied to both the reported TASCAM and HAWQi buoy data. In the case of the TASCAM data, this equated to a moving box window of six data points. For the higher temporal resolution sampling in the HAWQi time series (i.e., 30 min sampling), 12 data points were averaged. The smoothing over a 6 h time window was undertaken to approximate the 1 km^2 scale of satellite estimates by accounting for water moving past the moored sensor. The chosen temporal widths equate to movement of 1 km for an average water movement speed of about 4.6 cm/s.

A 6 h time window for both the Tasman and Hawke bays' buoy data balanced the need for spatial smoothing, whilst ensuring that the time period was not too long (i.e., greater than a day). It was recognized that growth or grazing factors could significantly influence the measurements if longer averaging periods were used. Comparison with a progressive vector showed the 6 h window was appropriate for the Tasman Bay site (**Figure 4**). Comparison to current data for the Hawke Bay site was not possible due to a current meter failure at the site, but mean depth averaged current speeds of 5.6 cm/s observed at a nearby site (39.319°S, 177.090°E) over a 3 month period imply the selected 6 h window was appropriate (Cawthron unpublished data).

While it is more common to use stringent quasi-simultaneous and spatially collocated match-ups (Gordon and Wang, 1994; Moses et al., 2009; Kahru et al., 2014) to increase the availability of data for comparison, those methods can end up excluding a large fraction of the data for comparison. This can be due to issues such as cloud cover and adjacency to land (Kahru et al., 2014). This approach can also introduce some bias if large gradients exist over small spatial scales (i.e., at or less than the satellite sensor resolution) and there exists a risk that *in situ* measurements may be matched to optically different water than was sampled (Moses et al., 2009). Because moored sensors allow continuous sampling, our approach aimed to reduce the variability that exists between *in situ* point-scale measurements and 1 km^2 satellite retrievals.

In order to prepare *in situ* samples for the smoothed model development, a nearest temporal match of the closest satellite data product pixel was undertaken to the mean sample time. Typically this time difference was <1 h between the observed chl-*a* satellite remote sensing time and the smoothed sensor time. But allowance was made for time differences of <3 h either side of a satellite observation to increase the availability of data from the model for construction and testing. This is consistent with time differences from other studies (Gordon and Wang, 1994; Moses et al., 2009; Kahru et al., 2014). As a check of the smoothed-data approach, the single closest-time datum was also used to train separate models for comparison. However, it is important to note that each of the closest-time and smoothed models are predicting different parameters, specifically point-in-time chl-*a* and smoothed chl-*a*, respectively.

Models applied in the present study used two empirical approaches for fitting satellite remote sensing reflectance data to observed chl-*a* concentrations. These models were, a linear model, based on the OC3M algorithm (hereafter: Local OC3M), and a novel non-linear exponential model (hereafter: Exponential) developed for this study.

The Local OC3M takes the form of:

$$\log_{10}(chl\,a) = a_0 + a_1.R + a_2.R^2 + a_3.R^3 + a_4.R^4$$

Where $R = \log_{10}(\max(\text{Rrs443, Rrs488})/\text{Rrs555})$, and Rrs443, Rrs488 and Rrs555 refer to remote sensing reflectance at the wavebands centered on 443, 488, and 555 nm, respectively. Model coefficients are defined as *a0* to *a4* in the equation.

The model coefficients were fitted to both closest-time chl-*a* and 6 h mean (smoothed) chl-*a* data and the corresponding satellite remote sensing reflectance ratios (R) using the generalized least-squares linear model fitting routine (glm) from the R software package (R Core Team, 2014).

The remote sensing reflectance ratio, R, of the max(Rrs443, Rrs488) to Rrs555 provides a ratio of light at the peak blue (i.e., 443 nm) chl-*a* absorbance to a minimum chl-*a* absorbance (555 nm). Unabsorbed light can be reflected, contributing to the remote reflectance signal, therefore chl-*a* concentrations are expected to decrease under increasing R (i.e., less 443 nm light is absorbed and more is reflected, relative to 555 nm light). However, phytoplankton specific absorbance is also known to decrease non-linearly (through a power relationship) with increasing chl-*a* (Bricaud et al., 1995). In order to capture this non-linearity, a simple exponential model was also tested against the data. This exponential model takes the form:

$$chl\ a = ae^{-kS}$$

where a and k are model coefficients and $S = 10^{R}$. R is the same as defined in the OC3M linear modeling approach, so S = max(Rrs443, Rrs488)/Rrs555. In formulating S, we chose to remove the logarithm from R, as it is redundant in an exponential model. Furthermore, as S will always be positive (provided negative Rrs values are removed) this insures that chl-*a* estimates cannot be less than zero, which is a benefit over the OC 4th order polynomial approach.

Coefficients for the Exponential model were fit to both the closest-time chl-*a* and 6 h mean chl-*a* data and the corresponding satellite remote sensing reflectance ratios (S). Model fitting was undertaken using the non-linear least squares (nls) model fitting routine from the R software package (R Core Team, 2014). In the case of the Tasman Bay data, a limited range to the chl-*a* data was observed over the sampling period (maximum chl-$a = 2.76$ mg/m^3). This was a value that is lower than the observed range of chl-*a* values in the region which have been noted to be up to about 10 mg/m^3 (MacKenzie and Gillespie, 1986). As the coefficient, a, in the model provides a constraint on the maximum predictable order to allow for model fitting to higher values in the case of Tasman Bay a fixed value of 10 was also selected for the coefficient a to allow prediction of maximum observed values.

For all model constructions, each dataset was split into two parts, where two-thirds of the data were randomly selected for model training and the remaining one-third was used for evaluation of model performance (i.e., "test" data). Although the initial derivation of the data split was random, the same division of the data were used for both the closest-time and smoothed data models to allow comparative performance to be assessed.

The accuracy of different models was assessed using several measures used in other remote sensing (IOCCG, 2006; Moore et al., 2009) and modeling studies (Zhang et al., 2010). Calculation of the regression parameters for the observed vs. derived data (i.e., slope and intercept), the deviance explained (r square), the root mean square error (RMSE) and the average absolute percentage error (ε) were reported for the smoothed data, with a subset, deviance explained and RMSE only calculated for closest match data.

The relevant calculations for RMSE and average absolute percentage error (ε) are specified here:

$$RMSE = \sqrt{\frac{1}{n}\sum [\log_{10}(chl\ a_{observed}) - \log_{10}(chl\ a_{derived})]^2}$$

$$\varepsilon = \frac{1}{n}\sum \frac{|chl\ a_{derived} - chl\ a_{observed}|}{chl\ a_{observed}} \times 100$$

where n is sample size.

Another measure, the relative central frequency (RCF), which reports the proportion of percentage error that lies within ± 50% of observed values, is also calculated (Zhang et al., 2010). All analyses were conducted using the R software package (R Core Team, 2014).

RESULTS

Results of model training to 6 h averaged and closest-time matchups are both presented here, along with their performance information within their respective regions. Overview statistics for the chl-a datasets from the two regions are presented in **Table 1**.

Six-Hour Mean Models

Tasman Bay

After matching TASCAM chl-*a* data with the corresponding satellite remote sensing reflectance data, a total of 394 data points were available. The two models (Local OC3M and Exponential) were then trained on the random two-thirds of the total dataset. TASCAM chl-*a* data were used as the dependent variable and the ratios of satellite remote sensing reflectance (R) as independent variables. **Table 2** provides the summary of the output of the two models.

Validation using the remaining one-third of the data showed that both locally fitted models performed better than the global Case 1 OC3M (Default OC3M) model (**Figure 5**). The two local models displayed significant improvement over the global OC3M algorithm in all performance measures used (**Table 3**). For example, deviance explained increased from 0.09 for the global algorithm to 0.49 and 0.52 for the local models. The RMSE decreased from 0.71 for the global algorithm to ∼0.22 and 0.24 for the local algorithms. The average percentage error decreased significantly from 465% for the global algorithm, to 48 and ∼56% for the two local algorithms (**Table 3**).

Comparison of predicted chl-*a* with field data (**Figure 6**) shows that, though the model can underestimate the peaks, it generally follows time series and therefore may be useful in monitoring trends in the coastal water environments of the bay. Despite the long period of deployment for the sensors at the TASCAM site, no clear drift in sensor response was apparent over the deployment period (**Figure 6**).

Hawke Bay

A total of 174 data points were used for training and testing of the satellite models. Two-thirds of the dataset ($N = 114$) was used for

model construction, and the remaining one-third ($N = 58$) for the evaluation model performance. The model summary is given in **Table 4**.

Model validation using the remaining one third of the HAWQi dataset shows that both local algorithms performed better than the global OC3M model (**Figure 7**). Typically, the two models achieved significantly higher deviance explained, lower percent error (ε) and RMSE (**Table 5**). For example, the average percentage error for the local OC3M model reached 32%, which is within an acceptable upper limit of 35% (IOCCG, 2006; Moore et al., 2009). Although the exponential algorithm produced a higher average percentage error (47%) than the local OC3M model, the exponential model exhibited less bias when compared to *in situ* data from the test dataset (**Figure 7**, **Table 5**).

Comparison of the predicted time series with HAWQi buoy data also shows that both the local models performed reasonably well (**Figure 8**). The modeled chl-*a* was able to track observed trends in the buoy data for most of the time series, with the exception of a short period in September 2013 (**Figure 8**). Similarly *in situ* seawater sample results taken beside the sensor were generally comparable to the mooring sensor result, highlighting the accuracy of the sensor over the deployment period (**Figure 8**).

When applied to other areas of the bay using additional water sample data from the region, the algorithms did not compare well with the collected data at most sites (**Figure 9**, **Table 6**). Although the two local algorithms performed better than the global OC3M algorithm, there was a high average percentage error (**Figure 9**, **Table 6**).

TABLE 1 | Statistics for the two chlorophyll-*a* datasets (mg/m^3) used for algorithm development.

Location (data source)	Mean	Minimum	10th percentile	90th percentile	Max
Tasman Bay (TASCAM)	0.47	0.04	0.11	0.92	2.76
Hawke Bay (HAWQi)	1.32	0.05	0.12	3.70	9.10

TABLE 2 | Summary of results of the two locally-tuned models for Tasman Bay trained on 6 h averaged data.

	Deviance explained					
Model	**Train**	**Test**	**Coefficient**	**Estimate**	**SE**	***p***
Local OC3M	0.45	0.48	a_0	−0.339	0.022	< 0.001
			a_1	−1.604	0.122	< 0.001
			a_2	−0.678	0.543	0.213
			a_3	3.599	0.636	< 0.001
			a_4	2.911	1.166	0.013
Exponential	0.39	0.51	a	1.552 (10)	0.128	< 0.001
	(0.28)	(0.19)	k	1.02 (3.99)	0.087 (0.1249)	< 0.001

SE, standard error; p, probability. Values given in parentheses for the exponential model are for the fixed coefficient model (a = 10).

Closest-Time Models

Tasman Bay

Using the closest match data to train the two local models produced different coefficients to the models built using smoothed data (**Table 7**). The model performance on the test data

TABLE 3 | Comparison of accuracy of the default (global Case 1) and local model predictions using the TASCAM monitoring buoy test dataset; *n* = sample size and significance test results are shown in brackets.

Model	*n*	Intercept	Slope	Deviance explained	RMSE	ε	RCF
Default OC3M	131	0.34 (s)	0.04 (s)	0.22	0.71	465	6
Local OC3M	131	0.03 (ns)	1.04 (ns)	0.49	0.22	48	66
Exponential	131	−0.03 (ns)	1.05 (ns)	0.52	0.24	56	60

For intercept, (s) indicates significantly different from 0; for slope, (s) indicates significantly different from 1; for both, (ns) indicates not significant; RMSE and ε are defined in equations (3) and (4); RCF is the relative central frequency.

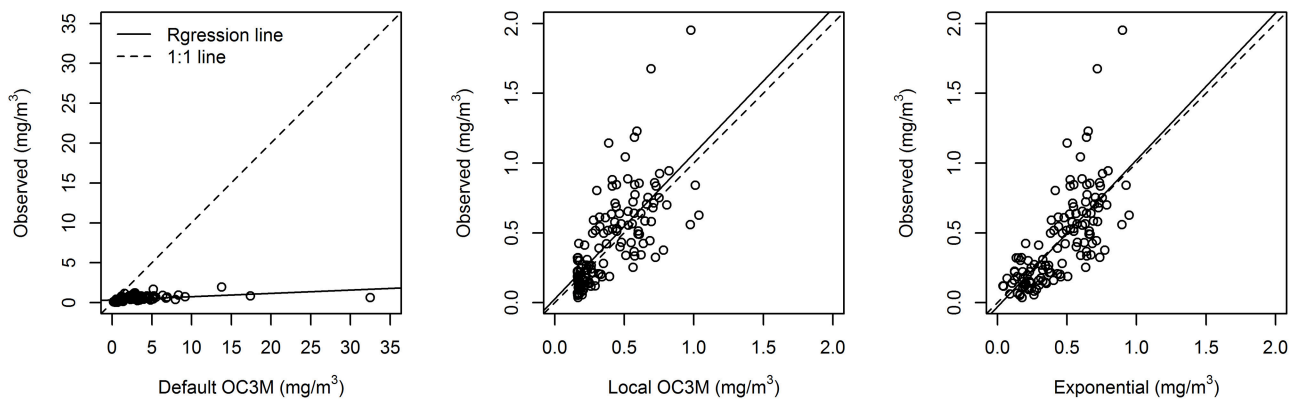

FIGURE 5 | Default (global Case 1) and local model predictions vs. 6-h averaged *in situ* TASCAM monitoring buoy chlorophyll-*a* test dataset for the three different model approaches in Tasman Bay. Note that a different scale is used for the global Default OC3M model results.

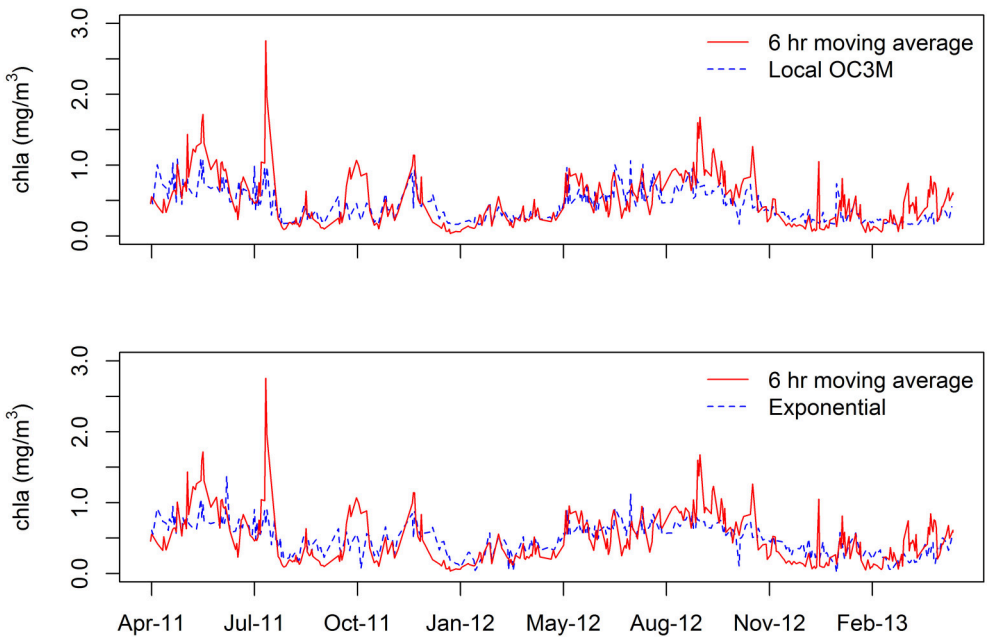

FIGURE 6 | Comparison of the 6 h averaged TASCAM monitoring buoy data with model predicted chlorophyll-*a* (chla) using Local OC3M (upper) and Exponential model (lower).

TABLE 4 | Summary of the locally-tuned model outputs for the Hawke Bay water quality information (HAWQi) monitoring buoy for the 6 h averaged data.

	Deviance explained					
Model	**Train**	**Test**	**Coefficient**	**Estimate**	**SE**	***p***
Local OC3M	0.86	0.75	a_0	0.091	0.041	0.028
			a_1	−2.651	0.192	<0.001
			a_2	−2.58	0.934	0.007
			a_3	2.8	0.722	<0.001
			a_4	5.287	2.311	0.025
Exponential	0.64	0.79	a	14.791	2.167	<0.001
			k	2.217	0.227	<0.001

SE, Standard error; p, probability.

was also decreased when compared to the smoothed data models. Specifically, deviance explained decreased from 0.48 to 0.26 for the OC3M model and from 0.51 to 0.41 for the Exponential model (**Tables 2**, **7**). These results were mirrored in the RMSE results, which also showed increases from 0.23 to 0.34 for the OC3M model and from 0.24 to 0.28 for the Exponential model (**Table 3**).

Hawke Bay

Using the closest match data also produced different coefficients to the models built using smoothed data at the Hawke Bay site (**Table 8**). However, at this site, the model performance decline on the test data was generally less pronounced than the smoothed data models. Specifically, deviance explained decreased from 0.75 to 0.28 for the OC3M model and from 0.51 to 0.41 for the Exponential model (**Tables 4, 8**). The decrease in performance was more pronounced in the RMSE results, which also showed error increases from 0.17 to 0.58 for the OC3M model and 0.22 to 0.60 for the Exponential model (**Table 5**).

DISCUSSION

The present study compared estimates of chl-*a* concentrations from freely available ocean color data (MODIS Aqua Level 2) with long-term field measurements. The study shows that the standard global OC3M algorithm over-estimated chl-*a* concentrations at all coastal study sites. The average percentage error ranged between 150 and ∼500%. This is in agreement with previous findings that showed that the chl-*a* retrievals from standard Case 1 MODIS algorithms typically over-estimate chl-*a* concentration for turbid coastal waters (Darecki and Stramski, 2004; Magnuson et al., 2004; Werdell et al., 2009). Although the global Case 1 OC3M algorithm typically over-estimated chl-*a* concentration for coastal waters in our study, it appears that aspects of the model may still be useful in coastal environments provided the model is locally tuned.

In the case of the two locations analyzed for this study, there were potentially different optical regimes in place based on the composition of the respective catchments that drain into these locations. In the case of Tasman Bay, the site is located about 8 km from the mouth of the Motueka River (**Figure 2**). This river drains a catchment with a large proportion of native vegetation cover and subsequently high inputs of colored dissolved organic

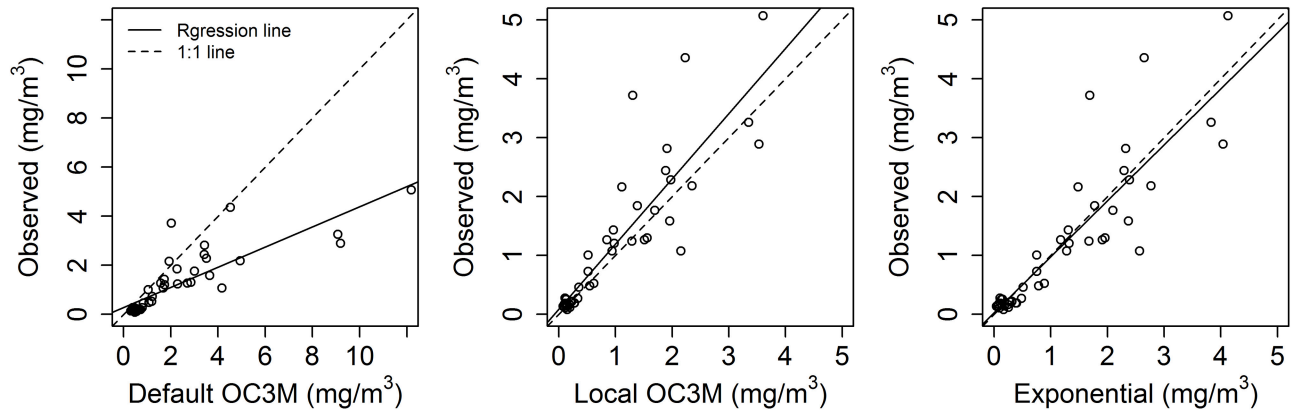

FIGURE 7 | Default (global Case 1) and local model predictions vs. 6 h averaged *in situ* HAWQi (Hawke Bay water quality information monitoring buoy) chlorophyll-*a* concentrations using test dataset for the three different model approaches. Note that a different scale is used for the global Default OC3M results.

TABLE 5 | Comparison of accuracy of the default (global Case 1) and local model predictions using the Hawke Bay water quality information monitoring buoy (HAWQi) test dataset; *n* = sample size and significance test results are shown in brackets.

Model	*n*	Intercept	Slope	Deviance explained	RMSE	ε	RCF
Default OC3M	58	0.28 (ns)	0.41 (s)	0.70	0.42	159	24
Local OC3M	58	0.09 (ns)	1.11 (ns)	0.77	0.17	32	80
Exponential	58	0.03 (ns)	0.95 (ns)	0.78	0.22	47	72

For intercept, (s) indicates significantly different from 0; for slope, (s) indicate significantly different from 1; for both, (ns) indicates not significant; RMSE and ε are defined in equation (3) and (4); RCF is the relative central frequency.

material which may affect the optical properties of the site. The catchments around the Hawke Bay site are largely associated with pastoral farming and the HAWQi buoy was located further away from major rivers, consequently differing signal to noise ratios in the chl-*a* response to incoming solar radiation were likely.

Modeling Approaches

Differing coefficients were observed in each model formulation, which is due in part to both optical differences inherent at the two sites, and the range of observed chl-*a* at each site. The local OC3M model may provide a preferred approach based on its historical use and because this model generally achieved lower average percentage error (ε) than the exponential model (**Tables 2**, **4**, **5**). However, the exponential model better captured the deviance in the observations of chl-*a* based on a higher deviance explained values (**Tables 2**, **4**, **5**). Such contradictions based on different measures, shows the need for the use of several measures to evaluate model performance and careful selection based on relevant scientific, or management, objectives for the data. For example, a bias error could have greater impacts on long-term trend analysis.

While the simple exponential model applied in this study does not have the historical use of the OC3M approach, it is clear that it has a similar performance and there are fewer degrees of freedom. The reduced flexibility for fitting the exponential model implies that it would be less likely to result in statistical over-fitting of the model. This is consistent with the results presented here, which show that deviance explained for the exponential model is higher in both test dataset results (i.e., **Tables 2, 4**) and with the results of the comparison with independent datasets. Given the similar performance of the empirical approaches across the two case studies presented, we consider that local calibration of the exponential model is potentially a more robust approach to construction of empirical locally calibrated chl-*a* models. As indicated by the results of a naïve fitting of the exponential model to the Tasman Bay data, clearly any model needs to be checked for its relevance to the region of interest. In the case of the Tasman Bay, the Exponential model will only able to estimate chl-*a* concentrations up to 1.55 mg /m^3 (i.e., the *a* coefficient value), this is limited when compared to measured historical maxima of 10 mg chl-*a*/m^3 (MacKenzie and Gillespie, 1986).

Fitting using an informed coefficient may be one way to avoid this issue; however comparison of the two exponential models constructed for Tasman Bay shows a coincident reduction in the deviance explained by a second model which used a fixed coefficient (**Table 2**). Consequently, this method may be appropriate for producing a useful model in the absence of representative data, but should ideally be updated as more representative data become available. Setting a bounded maximum in the model also further reduces the degrees of freedom for the fitting process, potentially further reducing over-fitting. While a value of 10 mg chl-*a*/m^3 has been used in Tasman Bay, it is possible that higher concentrations could also have occurred but have not been recorded. Therefore, the use of predetermined fixed coefficients appropriate to the environments of the models (e.g., oligiotrophic coastal temperate, eutrophic coastal tropical environments etc.) could be considered. For example, the Hawkes Bay Exponential model also has an artificial limit (14.79 mg chl-*a*/m^3; **Table 4**); while this is a reasonable limit for this region, the model will not be able to resolve higher

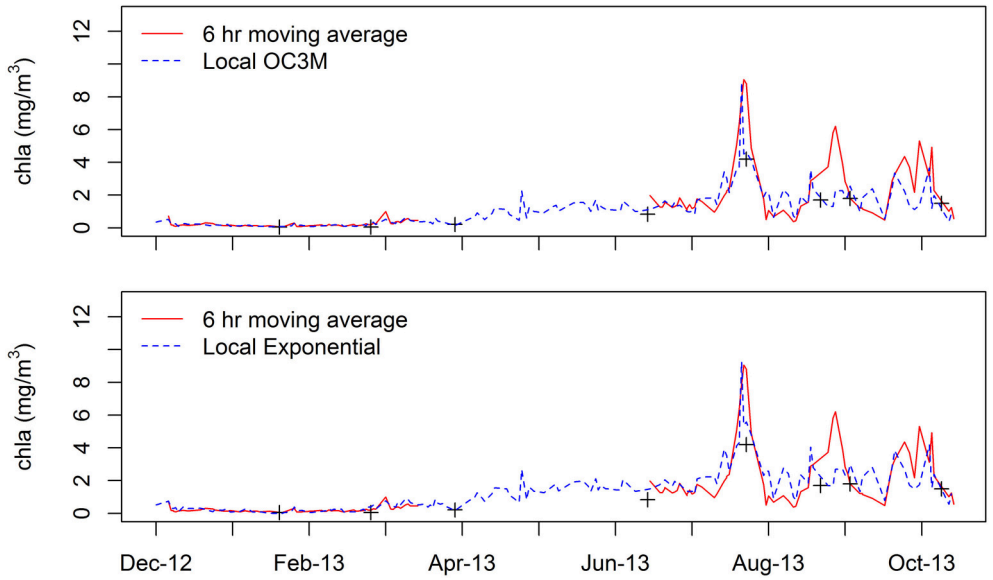

FIGURE 8 | Comparison of 6 h averaged HAWQi data with predicted chlorophyll-a (chl*a*) concentrations using Local OC3M model (upper) and Exponential model (lower). Also shown is the field sampled data (+) collected from beside the chlorophyll-*a* sensor at the site.

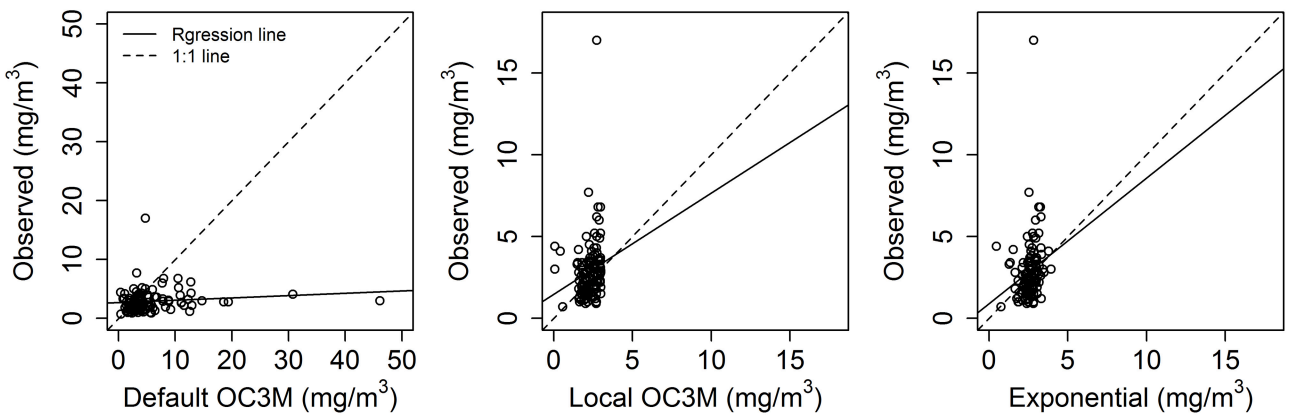

FIGURE 9 | Default (global Case 1) and local model predictions vs. 6 h averaged *in situ* State of the Environment (SOE) chlorophyll-*a* concentrations for the three different model approaches. Note: the different scale for the global OC3M comparison.

concentrations. Therefore, pre-classification of the environment and the use of an appropriate coefficient for the environment under consideration may be a worthwhile undertaking. The use of predetermined coefficients has the potential to introduce some bias to the tuning process, but the incorporation of this prior knowledge could also yield some benefits to the models. Consequently, while it is worthy of future research, it is not possible to recommend this approach at this time.

The Effect of Spatial Smoothing on Model Training

Despite the issues noted in the modeling of the Tasman Bay site, the results of the effects of smoothing were consistently better across both models and sites. Improved model fit to test data was seen at the TASCAM and HAWQi sites, with better performance observed in both the RMSE and deviance explained performance measures. However, the effect differed at the two sites, suggesting that the benefits may vary. For this reason we would recommend training both smoothed and closest-time models and selecting the best performing model against independent data.

Accuracy of the Models

In considering the measured performance of the algorithms against *in situ* sensor data, it is important to recognize that the fluorescence data are themselves an estimate of the "true" chl-*a* concentrations at the sites. The sensors in this study were factory calibrated and new at the time of deployment and we saw no evidence of issues that can affect the accuracy of *in situ* fluorometric sensors (e.g., quenching, fouling etc.). However, the

TABLE 6 | Model comparison with Hawke Bay water sample data; *n* = sample size and significance test results are shown in brackets.

Site	*n*	Model	Intercept	Slope	Deviance explained	RMSE (mg chl-a/m^3)	ε(%)	RCF (%)
3	37	Default OC3M	0.63(s)	0.13(*s*)	0.19	0.53	246	14
		Local OC3M	0.41(s)	0.43(*s*)	0.26	0.32	83	41
		Exponential	0.34(ns)	0.38(*s*)	0.25	0.37	123	14
4	34	Default OC3M	0.40(s)	0.13(*ns*)	0.68	0.76	2,054	15
		Local OC3M	0.14(ns)	0.54(*ns*)	0.51	0.54	1,045	35
		Exponential	0.08(ns)	0.47(*ns*)	0.5	0.65	1,515	29
5	30	Default OC3M	0.96(s)	0.06(*s*)	0.12	0.61	346	7
		Local OC3M	0.09(ns)	0.64(*ns*)	0.31	0.31	97	43
		Exponential	0(ns)	0.56(*s*)	0.29	0.39	141	23
6	36	Default OC3M	0.95(s)	0.07(*s*)	0.12	0.75	3,784	14
		Local OC3M	0.39(ns)	0.52(*s*)	0.23	0.57	2,203	36
		Exponential	0.33(ns)	0.45(*s*)	0.21	0.62	2,925	33
7	33	Default OC3M	0.81(ns)	0.26(*s*)	0.35	0.52	240	21
		Local OC3M	−2.32(s)	2.16(*s*)	0.73	0.29	80	48
		Exponential	−2.52(s)	1.82(*s*)	0.8	0.34	109	45
8	36	Default OC3M	0.29(s)	0.16(*s*)	0.55	0.49	205	14
		Local OC3M	0.29(s)	0.32(*s*)	0.54	0.27	69	44
		Exponential	0.25(s)	0.28(*s*)	0.55	0.36	113	19
9	28	Default OC3M	0.93(s)	0.04(*s*)	0.01	0.84	767	4
		Local OC3M	0.68(ns)	0.23(*s*)	0.02	0.58	288	25
		Exponential	0.64(ns)	0.20(*s*)	0.02	0.65	381	11
Overall	234	Default OC3M	0.66(s)	0.13(*ns*)	0.2	0.65	1,121	13
		Local OC3M	−0.18(ns)	0.87(*ns*)	0.34	0.43	572	39
		Exponential	−0.35(ns)	0.78(*ns*)	0.37	0.5	768	25

For intercept, (s) indicates significantly different from 0; for slope, (s) indicates significantly different from 1; for both, (ns) indicates not significant. RMSE and ε are defined in equations (3) and (4); RCF is the relative central frequency (only sample size <10 were included for the model validation).

TABLE 7 | Summary of results of the two locally-tuned models for Tasman Bay trained on closest-time data.

	Deviance explained					
Model	**Train**	**Test**	**Coefficient**	**Estimate**	**SE**	***p***
Local OC3M	0.49	0.26	a_0	−0.3313	0.025	<0.001
			a_1	−0.8497	0.064	<0.001
			a_2	−0.3866	0.130	0.003
			a_3	0.4779	0.075	<0.001
			a_4	0.2391	0.058	<0.001
Exponential	0.37	0.41	a	1.6287	0.240	<0.001
			k	1.0347	0.157	<0.001

SE, Standard error; p, probability.

TABLE 8 | Summary of locally-tuned model output for the HAWQi monitoring buoy trained on closest-time data.

	Deviance explained					
Model	**Train**	**Test**	**Coefficient**	**Estimate**	**SE**	***p***
Local OC3M	0.87	0.28	a_0	0.01274	0.0409	0.756
			a_1	−2.95666	0.1995	<0.001
			a_2	−1.9285	0.956	0.047
			a_3	3.38598	0.735	<0.001
			a_4	4.04635	2.363	0.091
Exponential	0.68	0.73	a	16.6099	2.280	<0.001
			k	2.4437	0.224	<0.001

SE, Standard error; p, probability.

quality of these underlying data is critical and the differences in the resulting parameterization of the models suggests that there are optical differences between sites. This does not appear to have affected our results (and we aim to study the underlying optical regimes in more detail in future), but we offer this modeling approach as a first step to allow naïve tuning of readily available satellite data to existing datasets.

The accuracy of the local models in the present study significantly improved on the results of the standard Case 1 OC3M algorithm, particularly in the case of Tasman and Hawke bays. In Hawke Bay, the Local OC3M algorithm achieved an average error of 32%. This is within the lower limit for the margin of error set by NASA for retrieving chl-*a* of within 35% accuracy for the global open oceans (Hooker et al., 1992; Le et al., 2013). The Hawke Bay water sample dataset comparison showed average errors in the range of 40–60%, but were of limited use due to reasons stated previously (e.g., turbid near shore locations, point-in-time samples). Despite the issues, it was interesting to see that the model estimates for some of the Hawke Bay sites (e.g., sites 7 and 8; **Table 6**) still compared well to data. These results are comparable to the accuracy achieved in other studies for turbid waters (Le et al., 2013) and better than those reported by Shang et al. (2014), where the average percent errors from locally-tuned algorithms were typically in the range of 60–130%. Consequently, the algorithms developed for the HAWQi site presented in this study can be considered satisfactory for future use. Although the Exponential model for the TASCAM site achieved a satisfactory error metric, unfortunately a lack of representative data from a wide range of conditions means that the model is likely only to be accurate for low chl-*a* conditions. While we have only presented results from two sites, the algorithm fitting approaches presented here will be useful for other coastal water investigations.

The modeling approach presented here (i.e., Tasman Bay and Hawke Bay) generally performed well at the locations and data they were tuned to, but the application of the approach to another region located in the North of New Zealand (the Firth of Thames; **Figure 1**) was not successful. The Firth of Thames is a similar environment to the Tasman and Hawke bays, but the main difference was that Firth of Thames chl-*a* data was provided from 15 m vertically-integrated seawater samples taken at fortnightly and monthly frequencies (Jones et al., 2013). Despite a lack of high temporal resolution fluorometric data, available data for the Firth of Thames were plentiful and were comprised of lab analyzed water samples for the period 2002 to 2013, which equated to about 1,300 samples across five sites. The results of Firth of Thames are not presented here, but we note that the results of a similar study (Jones et al., 2013) yielded a model with a low deviance explained (0.15).

We consider a likely explanation for the difficulty in training accurate models at the Firth of Thames site was the lack of higher frequency data available at that time. The field data for Tasman and Hawke bays were collected continuously at least every hour and could therefore either be smoothed to approximate the spatial resolution of the satellite (i.e., 1 km^2), or closely matched in time. This was not possible with the data available in the Firth of Thames. In this regard, it appears continuous buoy data can facilitate local satellite algorithm development, ideally with lab-processed data used to check sensor accuracy. The difficulty of matching in-water data to satellite observations in dynamic coastal regions has been extensively discussed (e.g., Gordon and Wang, 1994), with issues arising from both temporal matchups and spatial variability at a subpixel (<300 m) level. While temporal smoothing, or closer time matching, of the buoy data does not solve all of these issues, it may help to match spatial and temporal variability in regions where more restrictive criteria (Bailey and Werdell, 2006; Kahru et al., 2014) would limit potential matchups.

Uptake of Satellite Data in the New Zealand Context

Several factors may have prevented wider application of the freely accessible satellite data for coastal waters around New Zealand. While chl-*a* data for Case 1 coastal waters are readily available, our research shows these are not applicable to the Case 2 coastal waters around New Zealand without additional tuning. Several specific Case 2 algorithms have been developed for other studies that have successfully improved chl-*a* data retrieval for coastal waters (Ahn and Shanmugam, 2006; Cannizzaro and Carder, 2006; Shanmugam, 2011; Simon and Shanmugam, 2012; Le et al., 2013). While these models were successful, they are regionally specific and may be complex to calibrate locally without specialist equipment and additional targeted studies. Consequently we propose alternate methods that may allow use of existing long-term datasets to begin to unlock previously under-utilized historical data from satellites.

Development of generalized algorithms applicable for coastal waters in different regions requires not only an understanding of the optical properties of phytoplankton, but also other particles and dissolved material. This can be problematic, as it may involve greater resource requirements; e.g., collection of concurrent *in situ* measurements of pigment concentration and radiometric reflectance (IOCCG, 2000). As a result, the potentially invaluable information provided by satellite reflectance has not been widely utilized in New Zealand to date. It also seems that this is a wider issue than just New Zealand, as recognized by Schaeffer et al. (2013) who note that more effort is required to ensure that managers are aware of the value in the data, and that real and perceived hurdles need to be overcome to improve the uptake of remotely sensed data.

Our study provides evidence of some successful outcomes based on two case studies in New Zealand and that local calibration of empirical chl-*a* algorithms from pre-processed L2 data products is feasible in New Zealand coastal waters. It also shows that these locally calibrated algorithms may be validated in new regions with optically different properties. Furthermore, the methods we have employed can be achieved using readily accessible techniques and freely available software reducing barriers to the use of the data.

Local calibration of chl-*a* model in coastal environments may be more likely to succeed if the following recommendations are considered:

- If possible, use high temporal resolution data (at least hourly) to improve the availability of data for model training.
- *In situ* data should be collected across all seasons (i.e., a year) to ensure a wide range of local optical conditions are observed for model building.
- *In situ* collection depths are important, because satellite sensors only provide optical information from surface waters. Where coastal waters are turbid and stratified, measurements

will need to be close to the surface, but if possible multiple depths should be collected to assess vertical variability.
- Bottom reflections in shallow water have the potential to complicate algorithm development. Similar issues may also occur in turbid waters, with Raman scattering of about 8% previously reported (Gupta, 2015). For this reason data collection for algorithm development should be carried out in optically deep waters (i.e., low reflection and scattering) if possible.
- Empirical fitting of the OC3M algorithm may be prone to over-fitting when compared to a simpler exponential model presented in this study. This could limit its use outside of the training period and location; consequently testing on a leave-out (or "test") or completely independent dataset is highly recommended.
- The use of the simple exponential model approach is recommended given it generally performed better than a locally calibrated OC3M algorithm with the same data.
- Even if a reasonable level of fit is achieved to reflectance ratio data, assess the utility of the model for estimating the full range of conditions in the region should be assessed, not just the period of data for which the model was trained.
- If high temporal resolution data are available, consider averaging the data to match the spatial-scales for model building and compare to a closest-time approach. While our results differed between sites and the model applied, smoothing generally improved our models when compared to independent data.

Future Implications

Successful calibration of satellite data over ∼1 year potentially offers access to over a decade of data at daily (or more frequent) temporal resolution. Using the methods presented here, long-term trends in chl-*a* concentrations can be interrogated at sites that have perhaps been poorly sampled in the past. Because chl-*a* is a common indicator of primary production and symptoms of eutrophication, this information can then provide important insights into coastal health.

In the case of New Zealand, expansion of land-based farming is leading to large changes in the flow of nutrients to coastal environments (e.g., Heggie and Savage, 2009). These new pressures have the potential to affect the health of downstream coastal waters, but historical environment monitoring records are limited in their spatial and temporal extent. In order to allow for improved planning decisions on land and in the sea, long-term reliable datasets at many locations will be required to ensure that trends can be detected early and managed appropriately. Consequently remotely-sensed satellite data will play an increasingly important role in providing ongoing information on the state of surface waters for New Zealand. The initial studies presented here highlight that existing field datasets may be able to help assist in unlocking satellite data for such purposes. However, ideally empirical modeling methods (such those presented here) should be continued to be improved upon, as resources and data become available. This will ensure that modeled datasets are robust outside of both the times and areas that they are tuned for.

CONCLUSIONS

Simplified methods for regional tuning of satellite algorithms that can produce comparable water quality results to *in situ* samples are required to improve the uptake of satellite data for coastal monitoring. This study presents results from the local calibration and validation of two empirical algorithm approaches for chl-*a*, including a simple exponential model developed for this study. There appear to be benefits from the novel method of training the models to spatially-matched data scales, which suggests this approach is worth considering if the available data are appropriate for this purpose. Key to this approach is the use of high-frequency data from moored sensors, which can help to overcome issues with match-up limitations that have previously documented in highly dynamic coastal regions (Gordon and Wang, 1994; Kahru et al., 2014).

Good performance of a simple empirical model trained from high frequency data from moored sensors and standard satellite reflectance products illustrates that local calibration and operational use of readily available satellite data products for coastal waters is feasible. Further research and data collection will be required to more fully validate the methods presented in this study, but we note that pragmatic advice to assist in the application and use of satellite data in coastal waters is currently limited which could restrict the uptake of these valuable datasets. While successful calibration cannot always be guaranteed for satellite datasets, we have identified simple steps that appear to improve model performance.

AUTHOR CONTRIBUTIONS

WJ undertook the majority of statistical analysis of this work, the production of figures and initially suggested the use of simpler models for development in this project consequently his efforts have been recognized with primary authorship for this paper. Recent health issues have limited WJ's recent involvement in this work, nevertheless he has read and accepted this submission. BK has undertaken the majority of the writing for this manuscript and has helped guide the development of the work undertaken in the study. CC has contributed to sections in this submission and acted in an oversight role. PB was responsible for the data collection used in this study and the methods associated with this submission. The efforts of RK have mirrored that of CC and he has brought an large amount background knowledge to this study. Early versions of this manuscript also drew on RK's extensive knowledge of US datasets with which model were tested against truly independent datasets. Although these data were ultimately removed, they helped provide all authors with additional confidence to progress with publishing this work and represent a significant contribution.

FUNDING

Cawthron Institute Internal Investment Fund (Grant Number 15954) provided the majority of funding for this work.

ACKNOWLEDGMENTS

NASA and the team at the Ocean Biology Processing Group (OBPG) are thanked for the provision of the MODIS satellite data used in this study and the tools used to acquire these data. Kent Headley, Paul Cohen, and the rest of the team at the Monterey Bay Aquarium Research Institute are thanked for their time and assistance in developing the technology used in the TASCAM and HAWQi buoy platforms. Waikato Regional Council, particularly Hilke Giles and the late Vernon Pickett are thanked for their support of the initial research that was applied to the Firth of Thames in which many of the methods developed in this paper where initially established. The Hawke's Bay Regional Council, particularly Oliver Wade and Anna Madarasz-Smith are thanked for the timely provision of data and support in the initial HAWQi model development. The Ministry for Business Innovation and Employment Envirolink programme provided support for aspects of the Hawke Bay research (Grant number: 1436-HBRC199). We wish to thank the Wilsons Bay Area A Consortium for their provision of data used in Jones et al. (2013), while these data are not presented in this study it proved helpful for identifying the shortcomings of coarse temporal measurements in satellite model development. Preparation of this paper was supported by the Cawthron Institute Internal Investment Fund and the Ministry of Business Innovation & Employment Catalyst Leaders Fund (Grant number: ILF-CAW1601). Lastly we would like to thank Dr Paul Gillespie and Gretchen Rasch for their valuable comments on the drafts of this paper, and the efforts of peer reviewers and editorial staff that have contributed to this publication.

REFERENCES

Ahn, Y. H., and Shanmugam, P. (2006). Detecting the red tide blooms from satellite ocean color observations in optically complex Northeast—Asia Coastal waters. *Remote Sens. Environ.* 103, 419–437. doi: 10.1016/j.rse.2006.04.007

Aiken, J., and Moore, G. (1997). *MERIS algorithm Theoretical Basis Document: Case 2 (S) Bright Pixel Atmospheric Correction*, Rep. PO-TN-MEL-GS-0005, Plymouth Marine Laboratory, Plymouth.

Bailey, S. W., Franz, B. A., and Werdell, P. J. (2010). Estimation of near-infrared water-leaving reflectance for satellite ocean color data processing. *Opt. Express* 18, 7521–7527. doi: 10.1364/OE.18.007521

Bailey, S. W., and Werdell, P. J. (2006). A multi-sensor approach for the on-orbit validation of ocean color satellite data products. *Remote Sens. Environ.* 102, 12–23. doi: 10.1016/j.rse.2006.01.015

Bricaud, A., Babin, M., Morel, A., and Claustre, H. (1995). Variability in the chlorophyll-specific absorption coefficients of natural phytoplankton: analysis and parameterization. *J. Geophys. Res.* 13, 321–13, 332. doi: 10.1029/95jc00463

Bricker, S., Ferreira, J., and Simas, T. (2003). An integrated methodology for assessment of estuarine trophic status. *Ecol. Model.* 169, 39–60. doi: 10.1016/S0304-3800(03)00199-6

Cannizzaro, J. P., and Carder, K. L. (2006). Estimating chlorophyll a concentrations from remote-sensing reflectance in optically shallow waters. *Remote Sens. Environ.* 101, 13–24. doi: 10.1016/j.rse.2005.12.002

Carder, K. L., Chen, F. R., Cannizzaro, J. P., Campbell, J. W., and Michell, B. G. (2004). Performance of the MODIS semi-*a*nalytical ocean color algorithm for chlorophyll-*a*. *Adv. Space Res.* 33, 1152–1159. doi: 10.1016/S0273-1177(03)00365-X

Darecki, M., and Stramski, D. (2004). An evaluation of MODIS and SeaWiFS bio-optical algorithms in the Baltic Sea. *Remote Sens. Environ.* 89, 326–350. doi: 10.1016/j.rse.2003.10.012

Franz, B. A., Kwiatkowska, E. J., Meister, G., and McClain, C. R. (2007). "Utility of MODIS-Terra for ocean color applications," in *Proc. SPIE 6677, Earth Observing Systems, XII, 66770Q* (San Diego, CA). Available online at: http://spie.org/Documents/ConferencesExhibitions/SPIE-Optics-and-Photonics-2007-Final.pdf

Giovanardi, F., and Vollenweider, R. A. (2004). Trophic conditions of marine coastal waters: experience in applying the trophic index TRIX to two areas of the Adriatic and Tyrrhenian seas. *J. Limnol.* 63, 199–218. doi: 10.4081/jlimnol.2004.199

Gordon, H. R., and Wang, M. (1994). Retrieval of water-leaving radiance and aerosol optical thickness over the oceans with SeaWiFS: a preliminary algorithm. *Appl. Opt.* 3, 443–452. doi: 10.1364/ao.33.000443

Gupta, M. (2015). Contribution of Raman scattering in remote sensing retrieval of suspended sediment concentration by empirical modeling. *IEEE J-STARS* 8, 398–405. doi: 10.1109/jstars.2014.2361336

Heggie, K., and Savage, C. (2009). Nitrogen yields from New Zealand coastal catchments to receiving estuaries. *N. Z. J. Mar. Freshwater Res.* 43, 1039–1052. doi: 10.1080/00288330.2009.9626527

Hooker, S. B., Esaias, W. E., Feldman, G. C., Gregg, W. W., and McClain, C. R. (1992). *An Overview of SeaWiFS and Ocean Color*. NASA Tech. Memo., Vol. 104566. National Aeronautics and Space Administration, Goddard Space Flight CenterGreenbelt, M. D.

IOCCG (2000). "Remote sensing of ocean colour in coastal, and other optically-complex waters," in *Reports of the International Ocean Colour Coordinating Group No. 3*, ed S. Sathyendranath (Dartmouth, NS: IOCCG), 1–140.

IOCCG (2006). "Remote sensing of inherent optical properties: Fundamentals, tests of algorithms, and applications," in *Reports of the International Ocean-Colour Coordinating Group, No. 5*, ed Z. P. Lee (Dartmouth, NS: IOCCG), 1–126.

Jones, K., Jiang, W. M., and Knight, B. R. (2013). *A Review of Sources and Applications of Satellite Data for Coastal Waters of the Waikato region. Prepared for Waikato Regional Council*. Cawthron Report No. 2334.

Kahru, M., Kudela, R. M., Anderson, C. R., Manzano-Sarabia, M., and Mitchell, B. G. (2014). Evaluation of satellite retrievals of ocean chlorophyll-*a* in the California Current. *Remote Sens.* 6, 8524–8540. doi: 10.3390/rs6098524

Le, C. F., Hu, C. M., English, D., Cannizzaro, J., Chen, Z. Q., Feng, L., et al. (2013). Towards a long-term chlorophyll-*a* data record in a turbid estuary using MODIS observations. *Progr. Oceanogr.* 109, 90–103. doi: 10.1016/j.pocean.2012.10.002

Lorenzen, C. J. (1967). Vertical distribution of chlorophyll and phaeopigments: Baja California. *Deep-Sea Res.* 14, 735–745.

MacKenzie, A., and Gillespie, P. (1986). Plankton ecology and productivity, nutrient chemistry, and hydrography of Tasman Bay, New Zealand, 1982–1984. *N. Z. J. Mar. Freshwater Res.* 20, 365–395. doi: 10.1080/00288330.1986.9516158

Magnuson, A., Harding, L. W., Mallonee, M. E., and Adolf, J. E. (2004). Bio-optical model for Chesapeake Bay and the Middle Atlantic Bight. *Estuar. Coast. Shelf. S.* 61, 403–424. doi: 10.1016/j.ecss.2004.06.020

Moore, T. S., Campbell, J. W., and Dowell, M. D. (2009). A class-based approach to characterizing and mapping the uncertainty of the MODIS ocean chlorophyll product. *Remote Sens. Environ.* 113, 2424–2430. doi: 10.1016/j.rse.2009.07.016

Morel, A. (1988). Optical modeling of the upper ocean in relation to its biogenous matter content(case I waters). *J. Geophys. Res.* 93, 749–710. doi: 10.1029/jc093ic09p10749

Morel, A., Huot, Y., Gentili, A., Werdell, P. J., Hooker, S. B., and Franz, B. A. (2007). Examining the consistency of products derived from various ocean color sensors in open ocean (Case 1) waters in the perspective of a multi-sensor approach. *Remote Sens. Environ.* 111, 69–88. doi: 10.1016/j.rse.2007.03.012

Moses, W. J., Gitlson, A. A., Berdnikow, S., and Povazhnyy, V. (2009). Estimation of chlorophyll-*a* concentration in case II waters using MODIS and MERIS data – successes and challenges. *Environ. Res. Lett.* 4, 1–8. doi: 10.1088/1748-9326/4/4/045005

NASA (2013). *Goddard Space Flight Center Ocean Biology Distributed Active Archive Center*. MODIS-Aqua Level 2 Ocean Color Data, Reprocessing version

2013.1, NASA OB.DAAC. Available online at: https://oceancolor.gsfc.nasa.gov/ (Accessed Nov 4, 2013).

O'Reilly, J. E., Maritorena, S., Siegel, D., and O'Brien, M. C. (2000). "Ocean color chlorophyll a algorithms for SeaWiFS, OC2, and OC4: version 4," in *SeaWiFS Postlaunch Technical Report Series, Vol. 11, SeaWiFS Postlaunch Calibration and Validation Analyses, Part 3*, eds S. B. Hooker and E. R. Firestone (Greenbelt, MA: NASA Goddard Space Flight Center), 9–23.

O'Reilly, J., Maritorena, S., Mitchell, B. G., Siegel, D., Carder, K. L., Garver, S., et al. (1998). Ocean color chlorophyll algorithms for SeaWiFS. *J. Geophys. Res.* 103, 24937–24953.

R Core Team (2014). *R: A Language and Environment of Statistical Computing*. Vienna: R Foundation for Statistical Computing. Available online at: http://www.R-project.org/

Ruddick, K. G., Ovidio, F., and Rijkeboer, M. (2000). Atmospheric correction of SeaWiFS imagery for turbid coastal and inland waters. *Appl. Opt.* 39, 897–912. doi: 10.1364/AO.39.000897

Schaeffer, B. A., Schaeffer, K. G., Keith, D., Lunetta, R. S., Conmy, R., and Gould, R. W. (2013). Barriers to adopting satellite remote sensing for water quality management. *Inter. J. Remote Sens.* 34, 7534–7544. doi: 10.1080/01431161.2013.823524

Shang, S. L., Dong, Q., Hu, C. M., Lin, G., Li, Y. H., and Shang, S. P. (2014). On the consistency of MODIS chlorophyll a products in the northern South China Sea. *Biogeosciences* 11, 269–280. doi: 10.5194/bg-11-269-2014

Shanmugam, P. (2011). A new bio-optical algorithm for the remote sensing of algal blooms in complex ocean waters. *J. Geophys. Res.* 116, 1–12. doi: 10.1029/2010jc006796

Simon, A., and Shanmugam, P. (2012). An algorithm for classification of algal bloom using MODIS Aqua data in oceanic waters around India. *Adv. Remote Sens.* 1, 35–51. doi: 10.4236/ars.2012.12004

Smith, V., Tilman, G., and Nekola, J. (1999). Eutrophication: impacts of excess nutrient inputs on freshwater, marine, and terrestrial ecosystems. *Environ. Pollut.* 100, 179–196. doi: 10.1016/S0269-7491(99)00091-3

Wang, M., and Shi, W. (2007). The NIR-SWIR combined atmospheric correction approach for MODIS ocean color data processing. *Opt. Express* 15, 15722–15733. doi: 10.1364/oe.15.015722

Werdell, P. J., Bailey, S. W., Franz, B. A., Harding, L. W. Jr., Feldman, G. C., and McClain, C. R. (2009). Regional and seasonal variability of chlorophyll-*a* in Chesapeake Bay as observed by SeaWiFS and MODIS-Aqua. *Remote Sens. Environ.* 113, 1319–1330. doi: 10.1016/j.rse.2009.02.012

Zhang, A., Hess, K. W., and Aikman, F. (2010). User-based skill assessment techniques for operational hydrodynamic forecast systems. *J. Oper. Oceanogr.* 3, 11–24. doi: 10.1080/1755876x.2010.11020114

Conflict of Interest Statement: The authors declare that the research was conducted in the absence of any commercial or financial relationships that could be construed as a potential conflict of interest.

frontiers in Marine Science

ORIGINAL RESEARCH
published: 19 June 2017
doi: 10.3389/fmars.2017.00189

Satellite Observations of Phytoplankton Functional Type Spatial Distributions, Phenology, Diversity, and Ecotones

Tiffany A. Moisan[1†], Kay M. Rufty[2], John R. Moisan[1] and Matthew A. Linkswiler[3]*

[1] Wallops Flight Facility, NASA Goddard Space Flight Center, Wallops Island, VA, United States, [2] Global Science and Technology, Inc., Wallops Flight Facility, NASA Goddard Space Flight Center, Wallops Island, VA, United States, [3] AECOM, Wallops Flight Facility, NASA Goddard Space Flight Center, Wallops Island, VA, United States

Phytoplankton functional diversity plays a key role in structuring the ocean carbon cycle and can be estimated using measurements of phytoplankton functional type (PFT) groupings. Concentrations of 18 phytoplankton pigments were calculated using a linear matrix inversion algorithm, with an average r^2 value of 0.70 for all pigments with *p*-values below the statistical threshold of 0.05. The inversion algorithm was then used with a chlorophyll-based absorption spectra model and Moderate Resolution Imaging Spectroradiometer (MODIS-Aqua) chlorophyll observations to calculate phytoplankton pigment concentrations in an area of the Atlantic Ocean off the United States east coast. Pigment distributions were analyzed to assess the distribution of PFTs. Five unique PFTs were found and delineated into three distinct offshore, transition, and open ocean groups. Group 1 (Diatoms) had highest abundance along the coast. Group 2 (prymnesiophytes, prokaryotes, and green algae) was a year-round stable offshore community that extended at reduced levels into the coast. Group 3 (dinoflagellates) dominated offshore between the Groups 1 and 2. Phytoplankton communities were delineated into coastal and offshore populations, with Group 2 having a dampened seasonal cycle, relative to the coastal populations. Shannon Diversity Indices (H) for the PFTs showed both spatial and temporal variability and had a clear non-linear relationship with chlorophyll. Diversity levels varied seasonally with changes in chlorophyll a levels. Peak PFT H was observed on the shelf where frontal features dominate, with diversity levels declining nearshore and offshore. This region marks an ecotone for phytoplankton in the study domain, and is associated with the coastal-side boundary of dinoflagellate dominance. Highest levels of diversity were observed in the tidally well-mixed regions of the Gulf of Maine and along a band that ran along the shelf region of the study area that was narrowest in the summer periods and broadened during the winter. These peak diversity zones were associated with moderate levels (~0.8 mg m^{-3}) of chlorophyll a. While the sign in the linear trends in chlorophyll between 2002 and 2016 varied depending on the region, the trends in the PFT H values were nearly all negative due to the non-linear relationship between chlorophyll levels and H.

Keywords: phytoplankton, absorption, diversity, phytoplankton functional type, phytoplankton community, pigments, biodiversity, climate change

OPEN ACCESS

Edited by:
Astrid Bracher, Alfred-Wegener-Institute Helmholtz Center for Polar and Marine Research, Germany

Reviewed by:
Hongyan Xi, Helmholtz-Zentrum Geesthacht Centre for Materials and Coastal Research (HZG), Germany
Guoqing Wang, University of Massachusetts System, United States

****Correspondence:***
John R. Moisan
john.r.moisan@nasa.gov

[†] Deceased 5 June, 2016.

Specialty section:
This article was submitted to Ocean Observation, a section of the journal Frontiers in Marine Science

Received: *31 March 2017*
Accepted: *31 May 2017*
Published: *19 June 2017*

Citation:
Moisan TA, Rufty KM, Moisan JR and Linkswiler MA (2017) Satellite Observations of Phytoplankton Functional Type Spatial Distributions, Phenology, Diversity, and Ecotones. Front. Mar. Sci. 4:189. doi: 10.3389/fmars.2017.00189

INTRODUCTION

Climate change will alter the timing and magnitude of oceanic forcing conditions that affect phytoplankton biomass and productivity, both critical elements of the ocean carbon cycle (Levitus et al., 2000). Warmer ocean temperatures are expected to alter primary production rates, vertical stratification, mixing, and entrainment of nutrients from beneath deep mixed layers (Sarmiento et al., 2004). There is now ample evidence on the ecological impacts of recent climate change conditions at all latitudes, but especially in polar environments. The responses of both flora and fauna span an array of ecosystem and organizational hierarchies in both terrestrial and marine environments (Walther et al., 2002; Cermeño et al., 2008; Iglesias-Rodriguez et al., 2008). These observed changes are strong motivators for developing remote sensing approaches to observe the base of the food chain in order to monitor alterations in ecosystem function and to help improve biogeochemical and primary productivity models (Edwards et al., 2006; Striebel et al., 2009; Boyce et al., 2010).

Analysis of phytoplankton taxonomic composition in relation to satellite-derived chlorophyll a (Chl_{SAT}) provides an ecological approach to understand the role of past and future climate changes on ecosystem function (Boyce et al., 2010). Knowledge of the spatial and temporal variability of various Phytoplankton Functional Types (PFTs) is critical for improving primary productivity models which estimate biologically mediated fluxes of elements between the ocean's mixed layer and its deep interior (Falkowski and Raven, 1997), and for understanding potential climate-linked feedbacks. Improved performance and accuracy has already been observed in marine biogeochemical models that have incorporated PFTs into their ecosystem dynamics (Gregg et al., 2003).

Our current knowledge about the global distribution and seasonality of PFTs originates from shipboard and satellite observations (Alvain et al., 2008; Hirata et al., 2011; IOCCG, 2014; Bracher et al., 2015). Several new approaches for detecting phytoplankton biomass and specific PFTs, including coccolithophores (Balch et al., 1991, 1996; Bracher et al., 2015), Trichodesmium (Subramaniam and Carpenter, 1994; Subramaniam et al., 1999a,b, 2002; Hu et al., 2010), and diatoms (Sathyendranath et al., 2004; Soppa et al., 2014) have been developed. Other algorithms characterize size class distributions (Ciotti et al., 2002; Mouw and Yoder, 2005, 2010; Kostadinov et al., 2009; Brewin et al., 2010; Devred et al., 2011; Hirata et al., 2011; Organelli et al., 2013; Roy et al., 2013), PFT groups (Alvain et al., 2005; Hardman-Mountford et al., 2008; Bracher et al., 2009; Hirata et al., 2011; Moisan et al., 2011; Sadeghi et al., 2012; Campbell et al., 2013; IOCCG, 2014; Navarro et al., 2014) and select pigment concentrations (Pan et al., 2010), while others have utilized abundance based approaches (Uitz et al., 2006; Hirata et al., 2011; Chase et al., 2013).

A fundamental goal of phytoplankton biogeography is to describe the phenology of different PFTs and understand their interannual variability, and how these patterns relate to processes that control phytoplankton community structure and primary production (Longhurst, 2010). Phytoplankton biogeography influences how climate is regulated on a seasonal basis and also controls carbon flux processes (Oliver and Irwin, 2008). The diversity of the PFTs modulates the biological processes and controls ecosystem linkages within the carbon cycle. Understanding how they are modulated requires a better understanding of how the base of the food web is controlled by environmental conditions, which are impacted by climate change scenarios. Community developed algorithms for taxonomic marker pigments and size distribution (Balch et al., 1996; Alvain et al., 2005; Hu et al., 2010; Mouw and Yoder, 2010; Hirata et al., 2011; Moisan et al., 2011) continue to increase in their number and applications for the study of ocean ecosystem dynamics and biogeochemistry processes.

Algorithm development for PFTs using remote sensing observations has historically been based on bio-optical inherent optical properties such as backscatter and absorption (Nair et al., 2008). Absorption is often utilized in algorithm development because of its dominant role in regulating spectral variability of remote sensing reflectance due to changes in pigmentation (Moisan et al., 2011; Chase et al., 2013; Wang et al., 2016). In addition, sophisticated algorithms focus on ecological patterns of the phytoplankton community in relation to many factors such as climate change and meteorological conditions (Sathyendranath et al., 2004; Alvain et al., 2005; Hardman-Mountford et al., 2008; Raitsos et al., 2008; D'Ortenzio and Ribera d'Alcalà, 2009).

Many theories have been developed regarding the processes that govern marine biological diversity and stability and the impact that these have in evolving ecosystem community dynamics (Sommer et al., 1993). Recent advances in genomic observations and evolutionary/dynamic models are causing a surge in interest for this topic (Bruggeman and Kooijman, 2007; Terseleer et al., 2014). Indicators of phytoplankton functional diversity can be used to observe the response of marine ecosystems to climate change and its relationship to human activities (Platt and Sathyendranath, 2008; Platt et al., 2009). Past satellite studies, primarily focused on the North Atlantic, have shown phenological characteristics of bloom initiation and peak productivity (Siegel et al., 2002; Ueyama and Monger, 2005; Henson et al., 2006; Pan et al., 2010, 2011). Documenting additional phenological markers may lead to a better understanding of the processes that affect the phytoplankton community and help in monitoring the response of PFT processes to changes in the environment.

This paper presents results from a study that uses *in situ* observations of phytoplankton absorption spectra and High-Performance Liquid Chromatography (HPLC) chlorophyll-a pigment measurements (Chl_{HPLC}) to develop a satellite-based model for PFTs. In previous work, an inverse model technique was developed that used HPLC pigments and phytoplankton absorption spectra to create a method to retrieve 18 phytoplankton pigment estimates using phytoplankton absorption spectra (Moisan et al., 2011). An extension of this work used a linear model for phytoplankton absorption spectra, based on satellite observations of Chl_{SAT}, photosynthetically available radiation, and temperature to estimate pigments within a region along the northeastern U.S. coastal ocean (Moisan et al., 2013). Previous studies have utilized inversion

methods and demonstrated their value in calculating a wide variety of oceanographic information such as inherent optical properties (Hoge and Lyon, 1996; Garver and Siegel, 1997), pigment absorption spectra (Lee and Carder, 2004), and chlorophyll retrievals (Hoogenboom et al., 1998). This present study modified and expanded these techniques to generate phytoplankton pigment maps across the larger ocean domain of the Northeast Atlantic over the period from 2002 to 2016. The resulting phytoplankton pigment maps were then used with pigment-based PFT algorithms (Hirata et al., 2011) to calculate maps of PFTs. These PFT estimates were then used to calculate the PFT diversity using the Shannon Diversity Index (H).

MATERIALS AND METHODS

Ocean Color Data Retrieval

Satellite (MODIS Aqua) chlorophyll a OCI algorithm, Chl_{SAT}, estimates were obtained for the period of 2002-2016 from the NASA GSFC Ocean Color Processing Group. The validation of satellite products using quasi-simultaneous and spatially collocated measurements (match-ups) of satellite and *in situ* data followed the general procedures of previous studies (Werdell and Bailey, 2005; Bailey and Werdell, 2006). Observations for Chl_{SAT} were obtained using the 8-day averaged, 9 km spatial resolution, mapped, level 3 products.

Laboratory Analysis

Data was collected from a variety of geographical areas, which included both coastal eutrophic and oligotrophic waters (**Figures 1A,B**). A total of 172 water samples for phytoplankton absorption spectra, a_{ph} (λ), and HPLC were collected at depths between 0 and 29 meters during different cruises from the open ocean and two U.S. eastern coastal ocean regions: (1) Delaware, Maryland and Virginia and (2) the coastal waters within the Gulf of Maine and near Martha's Vineyard (**Figures 1A,B**). The data set includes all seasons for the Delaware/Maryland/Virginia (USA) region during 2006 and 2007 and spring samples from the Gulf of Maine during 2007.

Phytoplankton Absorption Spectra

Phytoplankton absorption samples were processed using the filter pad technique that partitions absorption into the particulate and detrital fraction (Kishino et al., 1985) to yield a phytoplankton absorption coefficient (m^{-1}; Mitchell, 1990). Absorption spectra were acquired on a Perkin Elmer LS800 UV/VIS Spectrophotometer at 1 nm intervals from 300 to 800 nm using a 4 nm slit-width.

Fluorometric Chlorophyll a

Water samples were filtered with 0.7 μm Whatman GF/F filter (USA), stored in Histoprep tissue capsules, and flash frozen in liquid nitrogen until processing. Chlorophyll a fluorescence was then measured using a Turner Model 10-AU fluorometer (Sunnyvale, USA) according to the method of Welschmeyer (1994). Phytoplankton absorption values were converted to specific absorption (m^2 mg $chla^{-1}$) using fluorometric chlorophyll a measurements. Fluorometric chlorophyll a compared well to Chl_{HPLC} values with an r^2 of 0.94.

High-Performance Liquid Chromatography (HPLC) Pigments

Samples were collected from the same Niskin bottles as phytoplankton absorption samples and filtered onto 0.7 μm Whatman GF/F filters. Samples were placed in Histoprep tissue capsules and stored in liquid nitrogen. Phytoplankton pigment concentrations were measured by

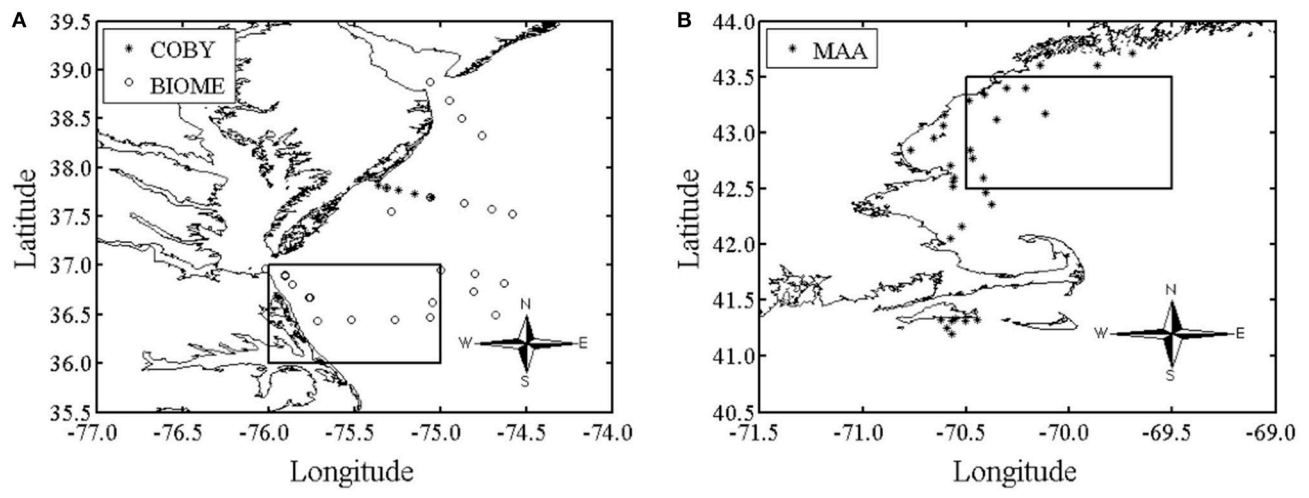

FIGURE 1 | The oceanographic study region was located in: **(A)** the Delaware, Maryland and Virginia (Delmarva) coastal waters [BIOME and COBY (Bio-physical Interactions in Ocean Margin Ecosystems and Coastal Ocean Buoy Transect), $N = 82$ samples] during all seasons in 2006 and 2007 and. The square is the area averaged over to represent BIOME in **Figure 10**. **(B)** The coastal waters within the Gulf of Maine and near Martha's Vineyard (MAA (Mycosporine-like amino acid), $N =$ 90 samples) during spring of 2007. The data set includes all seasons for the Delmarva region in 2006 and 2007 and only spring samples from the Gulf of Maine in 2007. Both sample regions are along the eastern coast of the United States. The square is the area averaged over to represent MAA in **Figure 10**.

HPLC on a C18 column using the procedure described by Van Heukelem et al. (2002) at Hornpoint Laboratory. A total of 25 pigment groupings were identified in each of the samples, 18 are calculated in this model, and 8 are used as marker pigments in this study (**Table 1**). The model pigments are: chlorophyll c, chlorophyllide, phaeophorbide, peridinin, 19′butanoyloxyfucoxanthin, fucoxanthin, neoxanthin, violaxanthin, 19′hexanoyloxyfucoxanthin, diadinoxanthin, alloxanthin, diatoxanthin, zeaxanthin, lutein, chlorophyll b, chlorophyll a, phaeophytin a, and carotenoids (α-carotene, B-carotene, diatoxanthin, diadinoxanthin, alloxanthin, zeaxanthin, lutein, fucoxanthin, peridinin, violoxanthin, 19′butanoyloxyfucoxanthin, and 19′hexanoyloxyfucoxanthin) (Barlow et al., 2007).

Methods for Modeling Phytoplankton Absorption Spectra and Pigments

Modeled Total Phytoplankton Absorption by Multiple Linear Regression

Total phytoplankton absorption spectra, a_{ph} (λ, m^{-1}), was modeled as a second order function of chlorophyll a such that

$$a_{ph}(\lambda) = C_0(\lambda) + C_C(\lambda)\,Chl\,a + C_{C2}(\lambda)\,Chl\,a^2, \qquad (1)$$

where Chl a is the concentration of chlorophyll a [mg m^{-3}] and C_0, C_C, and C_{C2} are the wavelength-dependent coefficients in the multiple linear regression. The Levenberg-Marquardt non-linear least squares minimization routine (Marquardt, 1963) was used to perform the linear fits using *in situ* Chl_{HPLC} and a_{ph} (λ).

In order to account for pigment packaging effects, the phytoplankton absorption spectra were "normalized" to 675 nm by a normalization term based on the expected unpackaged absorption at 675 nm. The unpackaged or "normalized" absorption spectra is calculated with,

$$\hat{a}_{ph}(\lambda) = a_{ph}(\lambda)\left(\frac{\sum_{i=1}^{n} c_i a_i^*(675nm)}{a_{ph}(675nm)}\right), \qquad (2)$$

where c_i is the concentration of the individual pigments derived from the HPLC analysis and $a_i^*(\lambda = 675\ nm)$ is the pigment-specific (a.k.a. weight-specific) absorption coefficient at 675 nm for the individual phytoplankton pigments, obtained courtesy of Annick Bricaud (Bricaud et al., 2004).

TABLE 1 | Diagnostic pigments used in the present study as biomarkers for phytoplankton functional types (Barlow et al., 1999; Vidussi et al., 2001; Wright and Jeffrey, 2006).

Diagnostic pigments	Abbreviations	Taxonomic significance	Phytoplankton size class
Fucoxanthin	Fuco	Diatoms	Microplankton
Peridinin	Perid	Dinoflagellates	Microplankton
19′-hexanoyloxyfucoxanthin	Hexa	*Phaeocystis*, coccolithophorids	Nanoplankton
19′-butanoyloxyfucoxanthin	Buta	Chrysophyte, Chromophytes,	Nanoplankton
Alloxanthin	Allo	Pelagophytes cryptophytes	Nanoplankton
Violaxanthin	Viol	Prasinophytes	Picoplankton
Chlorophyll *b*	Chl *b*	chlorophytes, prochlorophytes prasinophytes	picoplankton nanoplankton
Zeaxanthin	Zea	Cyanobacteria prochlorophytes	Picoplankton

Modeled Phytoplankton Pigment-Specific Spectra by Matrix Inversion

A goal in modeling phytoplankton absorption spectra, $a_{ph}(\lambda)$ (m^{-1}), is to make use of the reconstruction models to estimate phytoplankton pigments directly from the observed phytoplankton absorption spectra (Moisan et al., 2011). By combining phytoplankton pigment concentrations and pigment-specific absorption spectra, it is possible to reconstruct the total phytoplankton absorption spectra a_{ph} (λ) for the sample, such that

$$a_{ph}(\lambda) = \sum_{i=1}^{n} c_i a_i^*(\lambda), \qquad (3)$$

where c_i (mg pigment m^{-3}) is the concentration of the individual pigments and $a_i*(\lambda)$ (m^2/mg) are phytoplankton pigment-specific absorption coefficients. When a large number (n) of phytoplankton absorption spectra and HPLC observations are available it becomes possible to relate the pigment-specific absorption coefficients and HPLC pigment concentrations to the total phytoplankton absorption measured at a specific wavelength as,

$$\begin{bmatrix} c_{i=1,j=1} & \cdots & c_{i=m,j=1} \\ \vdots & \ddots & \vdots \\ c_{i=1,j=n} & \cdots & c_{i=m,j=n} \end{bmatrix} \begin{bmatrix} \tilde{a}_{i=1}^*(\lambda) \\ \vdots \\ \tilde{a}_{i=m}^*(\lambda) \end{bmatrix} = \begin{bmatrix} a_{ph,j=1}(\lambda) \\ \vdots \\ a_{ph,j=n}(\lambda) \end{bmatrix} \qquad (4)$$

where $c_{i,j}$ is the observed pigment concentration of the i^{th} pigment and the j^{th} sample, $\tilde{a}_i^*(\lambda)$ is the derived pigment-specific absorption for the i^{th} pigment, and $a_{ph,j}(\lambda)$ is the total absorption due to phytoplankton for the j^{th} sample and at a given wavelength (λ). At this point the various concentrations and absorption terms are members of a system of linear equations that can be inverted successively using the Singular Value Decomposition (SVD, Press et al., 1987) inversion technique on each wavelength to solve for each of the modeled pigment-specific absorption spectra, $\tilde{a}_i^*(\lambda)$.

Pigment Concentrations from Observed and Modeled $a_{ph}(\lambda)$ Spectra

Once estimates for pigment-specific absorption coefficients are available, either through laboratory measurements (Bidigare et al., 1990; Bricaud et al., 2004) or through the numerical inversions such as the SVD approach outlined above, they can be used with phytoplankton total absorption spectra,

$a_{ph}(\lambda)$, to estimate the individual pigment concentrations using a second matrix inversion application (Moisan et al., 2011). In this study, we utilized SVD-derived pigment-specific absorption and measured total absorption in the process of estimating phytoplankton pigment concentrations. By expanding the phytoplankton absorption spectra reconstruction technique (Equation 3) of Bidigare et al. (1990) into matrix form, total phytoplankton absorption for a suite of (n) samples can be written as

$$\begin{bmatrix} \tilde{a}^{*}_{i=1}(\lambda=1)\cdots\tilde{a}^{*}_{i=m}(\lambda=1) \\ \vdots\ddots\vdots \\ \tilde{a}^{*}_{i=1}(\lambda=L)\cdots\tilde{a}^{*}_{i=m}(\lambda=L) \end{bmatrix} \begin{bmatrix} \tilde{c}_{i=1,j=1\ldots n} \\ \vdots \\ \tilde{c}_{i=m,j=1\ldots n} \end{bmatrix} = \begin{bmatrix} a_{ph\ j=1\ldots n}(\lambda=1) \\ \vdots \\ a_{ph\ j=1\ldots n}(\lambda=L) \end{bmatrix} \quad (5)$$

where $\tilde{a}^{*}_{i}(\lambda)$ is the estimated pigment-specific absorption of the i^{th} pigment for a given wavelength (λ) obtained from the SVD inversion described in the preceding section, c a_i is the estimated concentration of i^{th} pigment for the j^{th} sample, and $a_{ph}(\lambda)$ is the measured total absorption due to phytoplankton at a given wavelength for each j sample.

Phytoplankton pigments were estimated using the resulting pigment-specific absorption spectra obtained from SVD inversion with observed $a_{ph}(\lambda)$. Because solutions to SVD inversions are not guaranteed to produce positive concentrations (negative pigment concentrations have yet to be measured in the ocean), the Non-Negative Least Squares (NNLS, Lawson and Hanson, 1974) inversion method was used to estimate the pigment concentrations to guarantee positive solutions. Moisan et al. (2011) demonstrated that out of all the inversion models tested, SVD-NNLS gave the best results when comparing modeled and measured pigment concentrations. Similarly, this technique has previously been verified in Moisan et al. (2011) through random division of the phytoplankton absorption spectra and pigment measurement pairs. Two independent pools of data were created by randomly separating the full data set in order to carry out the inversions to calculate the pigment-specific absorption spectra and the other to estimate pigment concentrations using the second inversion procedure to validate the model.

In order to apply this matrix inversion technique to satellite data and generate pigment maps, the MODIS Aqua Ocean Color chlorophyll a (Chl_{SAT}) was used with the resulting coefficients from the multiple linear absorption spectra model (Equation 1) to generate predictions of the mapped absorption spectra. These modeled absorption spectra were then inverted, pixel-by-pixel, using the SVD-derived pigment specific absorption spectra from Equation 4 and the NNLS inversion model (Equation 5) to yield maps of pigment concentration for the ocean region of the northeastern United States. Both the linear regression coefficients from Equation 1 and pigment-specific absorption spectra from Equation 4 were obtained using the normalized *in situ* $a_{ph}(\lambda)$ (Equation 2) and HPLC pigment data. A flowchart of the method summary is detailed in **Figure 2**.

The matrix inversion technique applied to satellite data uses modeled instead of *in situ* absorption. In order to assess how the pigment inversions are affected by the use of modeled absorption, the results from the inversion model using modeled versus measured absorption spectra is compared.

Phytoplankton Functional Type Maps and Diversity

Once maps of the various 18 phytoplankton pigments were obtained, they were used to generate estimates of the various PFTs for the region by using the estimation formulas outlined in Table 1 of Hirata et al. (2011) for diatoms, dinoflagellates, prymnesiophytes, prokaryotes, and green algae (**Table 2**). The pigments necessary as inputs for these algorithms included: fucoxanthin, peridinin, chlorophyll-b, 19-butanoyloxyfucoxanthin, 19-hexanoyloxyfucoxanthin, alloxanthin, and zeaxanthin. Maps of these functional types were calculated for all of the MODIS Aqua data used in this study domain and period.

After calculation of the PFT fields, the PFTs Diversity was calculated using the Shannon Diversity Index (H) equation,

$$H = -\sum_{i=1}^{N} p_i \ln\left(p_i\right), \quad (6)$$

where p_i is the i^{th} proportionality of the N phytoplankton functional groups (Shannon, 1948). Proportionality values, p_i, were defined as the resulting PFT values, the ratio of chlorophyll for that functional type versus the total chlorophyll within a sample. While the Shannon Diversity equation was developed to use specific cell or organism counts, a sensitivity study was conducted that used randomly chosen cell to biomass ratios in order to see what the impact of this had on the resulting H values, assuming that the conversion factors were constant throughout the study's time and space domain. The results showed little impact on the resulting H values meaning that the method used in calculation of the proportionality values was justified.

TABLE 2 | Phytoplankton Functional Type (PFT) equations (Hirata et al., 2011) used in this study.

PFT	Pigments used	Estimation formula
Diatoms	Fucoxanthin (Fuco)	$1.41Fuco/(\sum DP^{*})^2$
Dinoflagellates	Peridinin (Perid)	$1.41Fuco/\sum DP^2$
Green Algae	Chlorophyll-b (Chl-b)	$1.01Chl\text{-}b/\sum DP^2$
Prymnesiophytes	19-Hexanoyloxyfucoxanthin (Hex), Chl-b, Alloxanthin (Allo) 19′-Butanoyloxyfucoxanthin (But),	$(\delta^{\oplus}1.27Hex + 1.01Chl\text{-}b + 0.35But + 0.60Allo)/\sum DP^3 - 1.01Chl\text{-}b/\sum DP^2$
Prokaryotes	Zeaxanthin (Zea)	$0.86Zea/\sum DP^2$

$^{*}\sum DP = 1.41Fuco + 1.41Perid + 1.27Hex + 0.6Allo + 0.35But + 1.01Chl\text{-}b + 0.86Zea$.
$\oplus\delta$ *quantifies the proportion of nanoplankton contribution in Hex, (Brewin et al., 2010).*

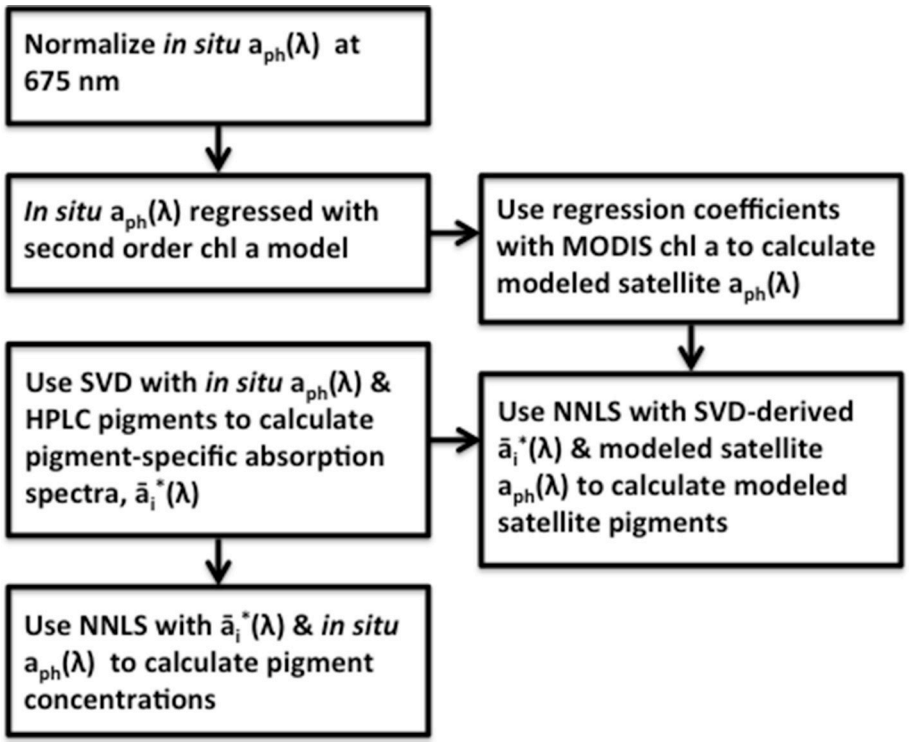

FIGURE 2 | Flow chart of the method utilized in this study to calculate 18 different pigment concentrations along the eastern shore of the United States. The linear absorption spectra model developed in Moisan et al. (2013) is modified and used with the matrix inversion techniques developed in Moisan et al. (2011) in order to extend the matrix inversion technique for use with satellite data.

RESULTS

Observations of Absorption Spectra

Values of $a_{ph}(\lambda)$ showed large variability in the ultraviolet (UV) and visible region (**Figure 3**). UV absorption was high, presumably due to mycosporine-like amino acids (MAAs, Moisan and Mitchell, 2001) and was commensurate with a Phaeocystis-dominated community in the Gulf of Maine. MAA absorption peaked at the surface of the ocean and is most likely controlled by irradiance and nutrient concentration (Whitehead and Vernet, 2000). Phytoplankton maximum absorption in the UV region ranged from 0.28 to 0.85 m^{-1}. Maximum values of $a_{ph}(\lambda)$ in the visible ranged from 0.03 to 0.37 m^{-1} (**Figure 3**). Values of $a_{ph}(436{:}676)$, the red and blue absorption peaks of chlorophyll a, varied by an order of magnitude, with highest levels associated with elevated levels of carotenoids, indicating growth in a high-light environment. Minimum and maximum values for $a_{ph}(436{:}676)$ are 0.006 and 0.369 and 0.003 and 0.198, respectively.

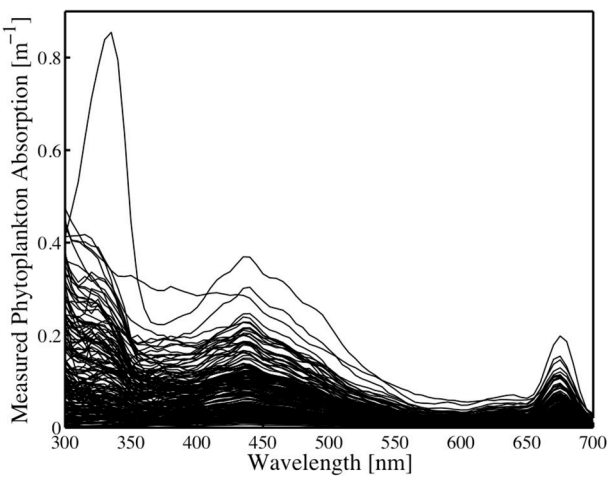

FIGURE 3 | *In situ* phytoplankton absorption (m^{-1}) from samples collected during the study.

Modeling of the Total Absorption Spectra

In order to model the absorption spectra, the spectrally-dependent, linear model coefficients from Equation 1 were used with Chl_{HPLC} values. The r^2 values of *in situ* versus modeled absorption, when normalized to 675 nm, are between 0.76 and 1.00 from 400 to 700 nm and drop by about 25%, as calculated by dividing the mean r^2 of UV and visible groups, in the ultraviolet region (**Figure 4**) where MAAs provide sun screening to phytoplankton and increase the observed value of $a_{ph}(\lambda)$. Accuracies were substantially improved using the "normalized"

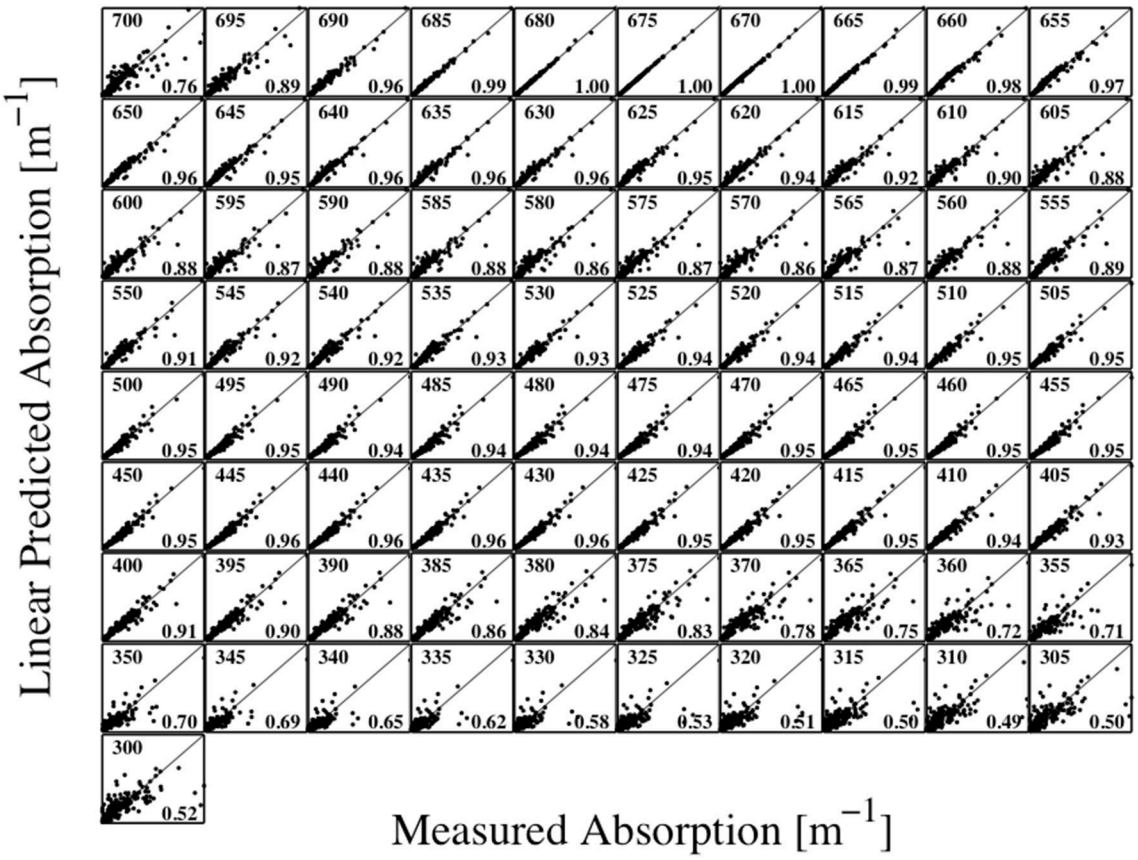

FIGURE 4 | Measured total absorption (m^{-1}) normalized to 675 nm (horizontal axis) versus the predicted total absorption (m^{-1}) (vertical axis) using the multiple linear regression of Chl_{HPLC} and $Chl_{HPLC}{}^2$.

absorption spectra in Equation 1, compared to original *in vivo* absorption spectra (Moisan et al., 2011).

To assess how much of the variability in the absorption curve is accounted for in the absorption model, the root mean square error (RMSE) was calculated for the first, second, and third order absorption models. The RMSE is the square root of the mean of the square of all the error. The variance drops by half from the observed spectra to the first order modeled spectra (RMSE = 0.113 and 0.063, respectively), and only slightly decreases with the second and third orders (RMSE = 0.063 and 0.060, respectively). Beyond the first order regression model there are only small improvements in modeling the absorption spectra. However, while the second order model is only slightly better than the first order in representing the variability of the absorption spectra, a larger improvement is observed in the pigment retrieval solutions. This may be because small improvements in modeling the absorption spectra can have a significant impact on the solution of those pigments that have smaller contributions to the total absorption spectra. The second order Chl_{HPLC} model was chosen because there are only marginal difference between first, second, and third order in modeling absorption and second order produces the best pigments retrievals.

Observations of Pigments in Relation to Absorption Spectra

The contribution of each of the 18 pigments estimated by the inverse model to total absorption was determined by reconstructing the absorption spectra following the technique developed by Bidigare et al. (1990) and utilizing the pigment-specific absorption coefficients from Bricaud et al. (2004) and the *in situ* HPLC pigment measurements (**Figure 5A**). The standard deviation of these individual absorption spectra (not shown) scale directly with the standard deviation of the various pigments observed, which is considerable. An analysis of the individual pigment contributions to the total absorption spectra, shown as a cumulative function, demonstrated that Chl_{HPLC}, fucoxanthin, chlorophyll c, diadinoxanthin and carotenoids together account for more than 90% of the observed *in vivo* absorption (**Figure 5B**). Coincidentally, these pigments were shown to have the highest predictive capability for the SVD-NNLS model that yields pigment-specific absorption spectra and HPLC pigment estimates (**Figure 5B**). Those pigments that contributed significantly to $a_{ph}(\lambda)$ and account for the majority the absorption were also those that were best predicted using the SVD-NNLS inversion model.

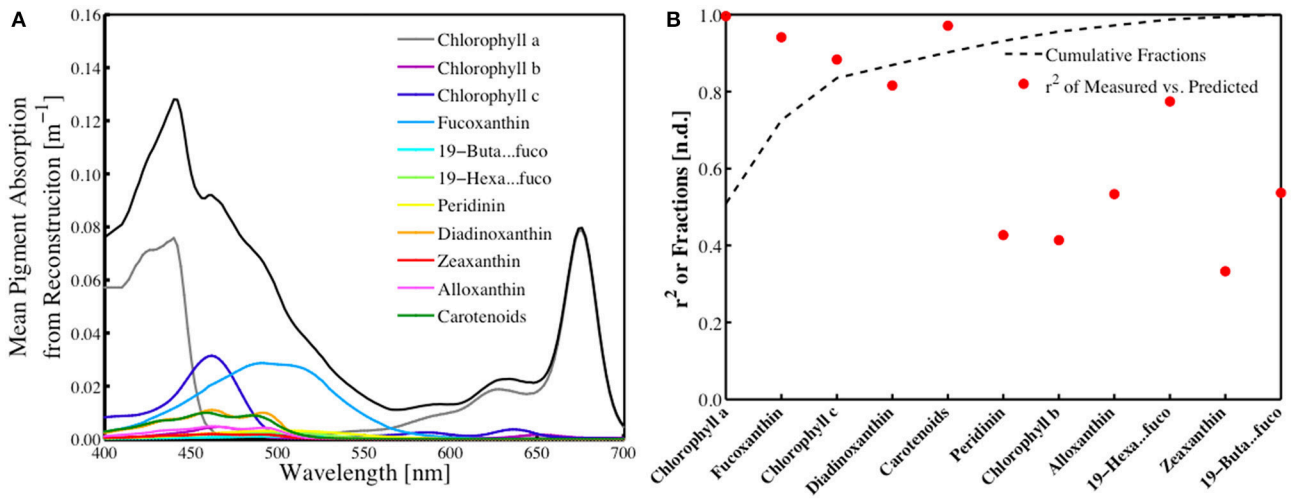

FIGURE 5 | (A) Reconstructed mean pigment-specific total absorption spectra (m^{-1}) of the different pigment biomarkers resolved in this study. The black line is the total absorption of all pigments. The lowest standard deviation values were insignificant, while higher standard deviation values for the pigments ranged from 0.0015 to 0.0686. **(B)** Cumulative fraction of the reconstructed pigment absorption to total absorption compared to the r^2 from the inverse model versus predicted HPLC pigments from SVD-NNLS.

Individual Photosynthetic and Photo-Protective Pigment Retrievals

Pigments were estimated by the NNLS matrix inversion (Equation 5) with the SVD-derived pigment-specific absorption from Equation 4 and *in situ* absorption spectra. A comparison of *in situ* measured to SVD-NNLS-derived HPLC pigments shows varying results with coefficients of determination ranging from very high (near 1.0) for chlorophyll a (Chl^{MOD}_{HPLC}) to a low of 0.33 for zeaxanthin (**Figure 6**). While 18 different pigments were estimated, only 10 had r^2 values greater than 0.68. The *p*-values of the algorithm were calculated with a threshold value of 0.05. All pigments had *p*-values of less than 0.001, demonstrating that the results are significant (**Table 3**). Similarly, the pigment concentrations on a normal scale produced relatively small RMSE for most pigments, with normalized RMSE less than 22% for all pigments, except zeaxanthin and lutein. Normalized RMSE is the RMSE divided by the pigment range and bias is the tendency of a statistic to overestimate or underestimate a parameter. Pigments that correlate best with Chl_{HPLC}, such as chlorophyll c, fucoxanthin, and carotenoids, along with Chl_{HPLC} account for the majority of the total absorption spectra (**Figure 5B**). These pigments are also shown to have the best prediction results when modeled pigment concentrations are compared with *in situ* concentrations: they have the highest r^2 values, their slopes are very close to 1 with y-intercepts close to 0, normalized RMSE below 5%, and all have *p*-values below the 0.05 threshold. While the coefficients of determination for the predicted pigments vary, all are within the acceptable range of algorithms that predict PFTs (Hirata et al., 2008, 2011; Bracher et al., 2009; Mouw and Yoder, 2010; Mouw et al., 2012; Soppa et al., 2014). In addition, even with the known uncertainties, the resulting maps of PFTs can be useful for phenological functional diversity studies.

Applying Inversion Model to Satellite Data

Modeling phytoplankton absorption spectra at every 5 nm using satellite chlorophyll a observations allows for extrapolation of observed relationships and can account for changes due to spectral shape, pigment composition, and pigment packaging (**Figure 4**). To apply the inversion model to satellite data, we calculated absorption (Equation 1) and inverted the modeled absorption values to obtain estimates for 18 HPLC pigments over a series of remote sensing images of the northeastern US coastal ocean. To demonstrate that the modeled absorption (as opposed to *in situ* absorption) would not have a significant effect on the pigment retrievals, we ran the SVD-NNLS inversion model using HPLC pigments and absorption modeled from Equation 1 and compared the resulting modeled pigment concentrations with *in situ* concentrations. While the r^2 values in general decreased and the normalized RMSEs increased, compared to the inversion with *in situ* absorption, the r^2 values of the predicted pigments that are addressed in detail in the analysis were not significantly less (**Table 2**). The statistical comparison of the two methods demonstrated that using modeled absorption in the satellite inversions does not significantly impact the pigment retrievals.

The results from the satellite-based inversion model show that the resulting estimates of chlorophyll a (Chl^{MOD}_{SAT}) maps are similar to those from the standard MODIS Aqua Chl_{SAT} product (data not shown). A linear comparison of Chl_{SAT} and Chl_{SAT} results in an r^2 of 1.00. While the OC-4 algorithm, applied to any of the NASA ocean color satellites (SeaWiFS, MODIS Terra and Aqua) has known issues with predicting chlorophyll a in coastal regions, the results from this study demonstrate that on a larger regional scale the features for both the OC-4 algorithm and the SVD-NNLS model solutions have very similar spatial scales and features.

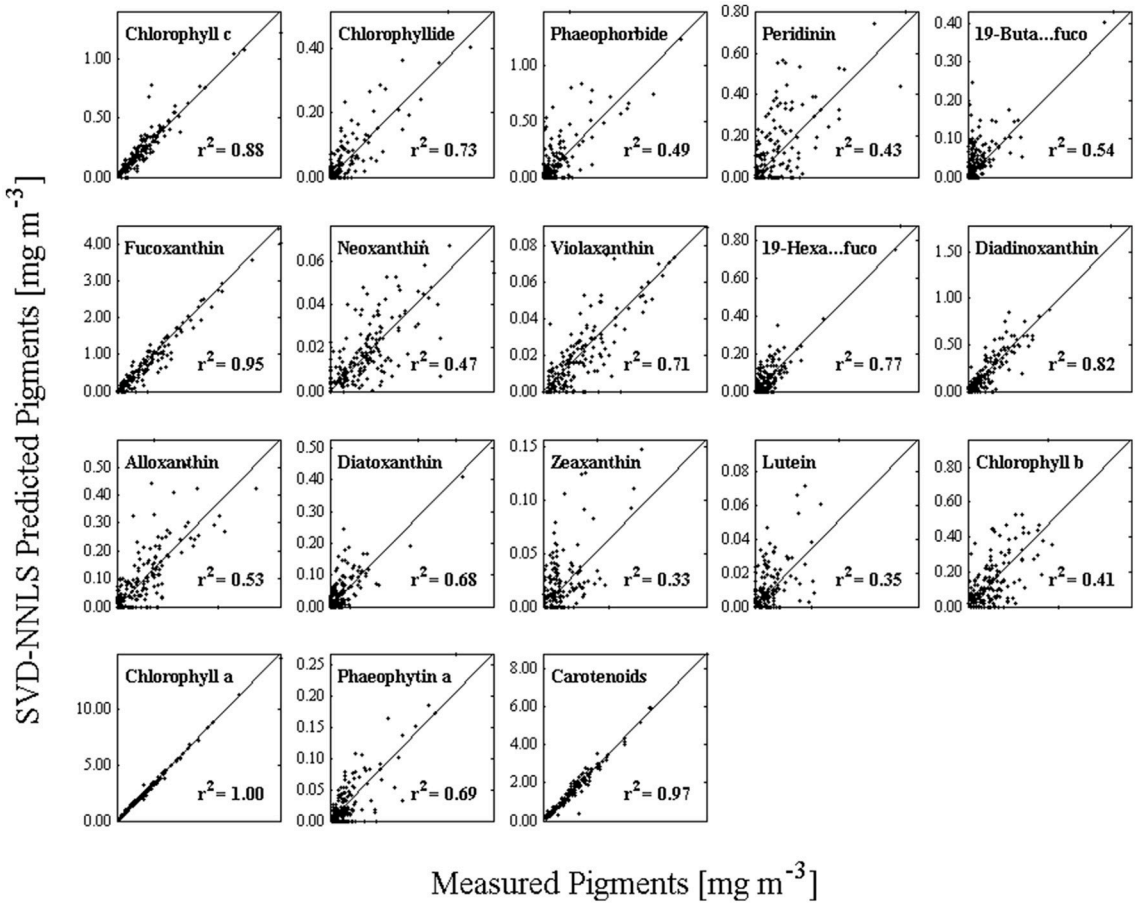

FIGURE 6 | HPLC measured pigments (horizontal axis) versus the predicted pigments (vertical axis) using SVD to obtain the pigment-specific absorption spectra and NNLS to obtain pigment estimates.

To quantify the inherent error of using Chl_{SAT} in the inversion model, we gradually introduced normal random error ranging from zero to a level comparable to the MODIS Aqua Chl_{SAT} (r^2 ~0.75) into the Chl_{HPLC} and ran it through the SVD-NNLS inversion model. After hundreds of iterations, our mean r^2 values for pigment retrieval dropped by 15–30 percent when errors were compatible to the satellite error which implied that the introduction of the satellite error does not greatly diminish the results of the inversion analysis (**Figure 7**).

In addition to Chl_{SAT}^{MOD}, inversion of absorption spectra over a larger regional domain yielded estimates of 18 photosynthetic and photo-protective pigments for the year 2007 (**Table 2**). A number of these are useful as biomarkers for certain PFTs and can aid in resolving phytoplankton community structure (**Table 1**). Maps of pigments normalized to biomass (using Chl_{SAT}^{MOD}) are markers for the distribution of PFTs within a region (**Figure 8**).

Chlorophyll a Distribution

Modeled Chl_{SAT}^{MOD} distribution from the SVD-NNLS inversion process compares well with MODIS Aqua Chl_{SAT} distribution with r^2 value of 1.00, and they both were inversely correlated to observed MODIS Aqua SST (data not shown), with highest (coldest) levels of Chl_{SAT} (SST) located along the coast and over the well tidally-mixed region of the Grand Banks, with lowest (warmest) levels offshore to the southeast near the Gulf Stream Province, as noted by Longhurst (2010). However, while the inverse model solutions compare well with the satellite observations, the technique does not eliminate the inaccuracies inherent in using satellite observations. A recent study comparing in situ chlorophyll a measurements and MODIS-Aqua chlorophyll a OC3 retrievals (Kahru et al., 2014) shows that the coefficient of determination (R^2) values were 0.86 for all measurements but that R^2 dropped to 0.35 for comparisons matchups with chlorophyll levels > 1.0 mg Chla m^{-3}. In addition, an earlier work by Thomas et al. (2003) focusing on the region of the Gulf of Maine (a subdomain of our study) notes that summertime matchups of log-transformed in situ chlorophyll to SeaWiFS chlorophyll have an r^2 of 0.55. Most of the errors in these estimates seem to be limited to the higher chlorophyll regions (>1.0 mg m-3) regions along the coast, which were only a small part of the overall study domain. For the most part, MODIS-Aqua underestimates the higher chlorophyll

TABLE 3 | Statistical values derived from comparison of measured pigment concentrations with those estimated from the SVD-NNLS inversions using the measured (modeled) absorption spectra.

Diagnostic Pigments	r^2-Values	Slope	Intercept	RMSE	Normalized RMSE	Bias	*p*-Values
Chlorophyll a	1.00 (0.99)	0.99 (1.01)	−0.00 (−0.01)	0.14 (0.15)	0.01 (0.01)	0.03 (−0.01)	<0.001
Chlorophyll b	0.41 (0.43)	0.79 (0.83)	0.03 (0.07)	0.12 (0.12)	0.22 (0.23)	0.00 (−0.04)	<0.001
Chlorophyll c	0.88 (0.86)	0.98 (0.96)	0.03 (−0.02)	0.14 (0.16)	0.05 (0.06)	−0.02 (0.04)	<0.001
Chlorophyllide	0.73 (0.40)	1.01 (0.82)	0.02 (0.01)	0.11 (0.15)	0.10 (0.14)	−0.02 (0.01)	<0.001
Phaeophorbide	0.49 (0.68)	0.89 (0.79)	0.03 (0.01)	0.17 (0.14)	0.13 (0.12)	−0.02 (0.01)	<0.001
Peridinin	0.43 (0.34)	0.88 (0.94)	0.03 (0.04)	0.12 (0.15)	0.17 (0.21)	−0.02 (−0.03)	<0.001
19′-butanoyloxy-fucoxanthin	0.54 (0.55)	0.95 (0.86)	0.02 (0.02)	0.04 (0.05)	0.11 (.012)	−0.02 (−0.02)	<0.001
Fucoxanthin	0.95 (0.92)	0.96 (0.96)	−0.06 (−0.06)	0.21 (0.32)	0.05 (0.07)	0.09 (0.10)	<0.001
Neoxanthin	0.47 (0.38)	0.77 (0.68)	0.01 (0.01)	0.01 (0.01)	0.14 (0.17)	−0.00 (−0.01)	<0.001
Violaxanthin	0.71 (0.60)	0.94 (0.91)	−0.00 (0.01)	0.01 (0.01)	0.12 (0.14)	0.00 (−0.00)	<0.001
19′-hexanoyloxy-fucoxanthin	0.77 (0.64)	0.99 (0.86)	0.00 (0.03)	0.05 (0.07)	0.07 (0.08)	−0.00 (−0.02)	<0.001
Diadinoxanthin	0.82 (0.66)	1.02 (1.01)	−0.01 (0.01)	0.10 (0.14)	0.07 (0.09)	0.00 (−0.01)	<0.001
Alloxanthin	0.53 (0.41)	0.85 (0.83)	0.02 (0.04)	0.08 (0.10)	0.16 (0.20)	−0.01 (−0.03)	<0.001
Diatoxanthin	0.68 (0.63)	1.06 (0.89)	0.01 (0.02)	0.04 (0.04)	0.10 (0.10)	−0.01 (−0.01)	<0.001
Zeaxanthin	0.3 (0.02)	1.03 (0.22)	0.01 (0.05)	0.05 (0.06)	0.26 (0.31)	−0.01 (−0.02)	<0.001
Lutein	0.35 (0.27)	0.95 (0.80)	0.00 (0.01)	0.01 (0.01)	0.24 (0.26)	−0.00 (−0.00)	<0.001
Phaeophytin a	0.69 (0.70)	0.99 (1.04)	−0.00 (−0.00)	0.02 (0.02)	0.12 (0.11)	0.00 (0.00)	<0.001
Carotenoids	0.97 (0.94)	1.00 (0.94)	−0.03 (0.17)	0.21 (0.30)	0.02 (0.03)	0.03 (−0.08)	<0.001

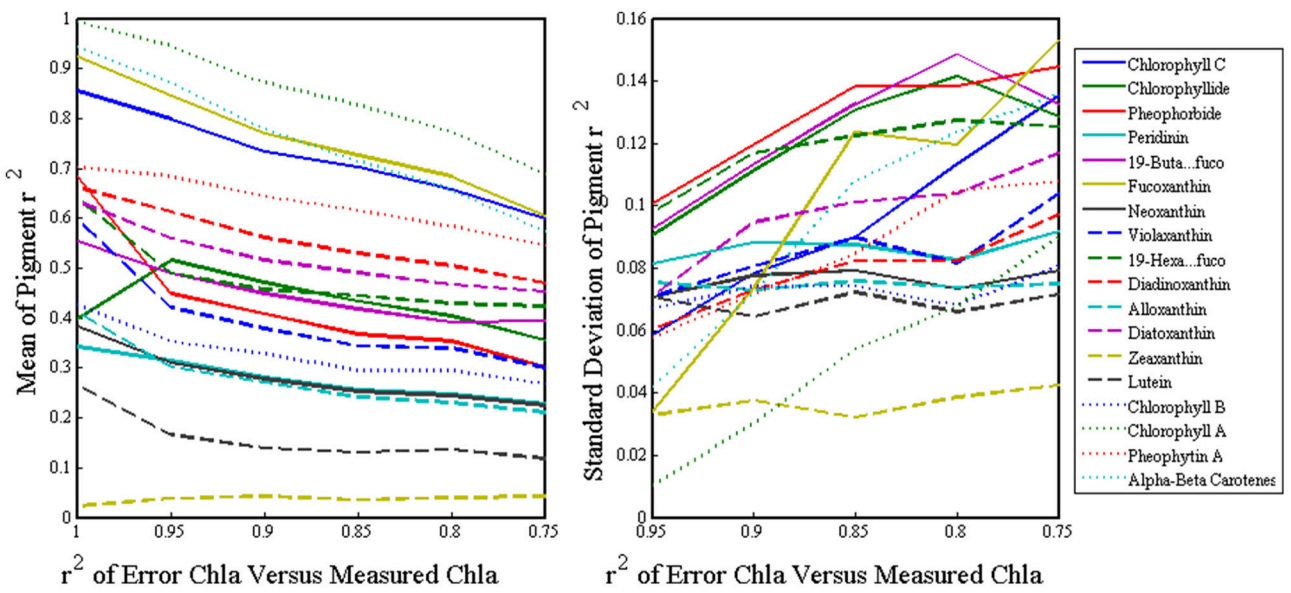

FIGURE 7 | The x-axes are the r^2 of the Chl_{HPLC} versus the Chl_{HPLC} with normal random error added, where 1 is Chl_{HPLC} with no error and 0.75 is equivalent to the error of Chl_{SAT}. The y-axes depict the mean **(left)** and standard deviation **(right)** of the r^2 values of the measured versus predicted pigment concentrations after the inversions are run with errored Chl_{HPLC} for hundred of iterations.

a levels observed in the coastal region and underestimates the lower chlorophyll a values found in the offshore region, thereby reducing the overall gradients in the true chlorophyll a fields. Such a cross-domain bias serves only to distort the resulting pigment retrievals by diminishing the gradients, while keeping distinguishable the larger scale pigment patterns and time series variability.

Phytoplankton Functional Type Marker Pigment Distributions

Identification of the presence of specific PFTs using marker pigments has been shown to be possible for a number of functional types (Wright, 2005). Although most pigments are not unique to specific phytoplankton taxa, and only a limited number are unambiguous pigments for specific phytoplankton

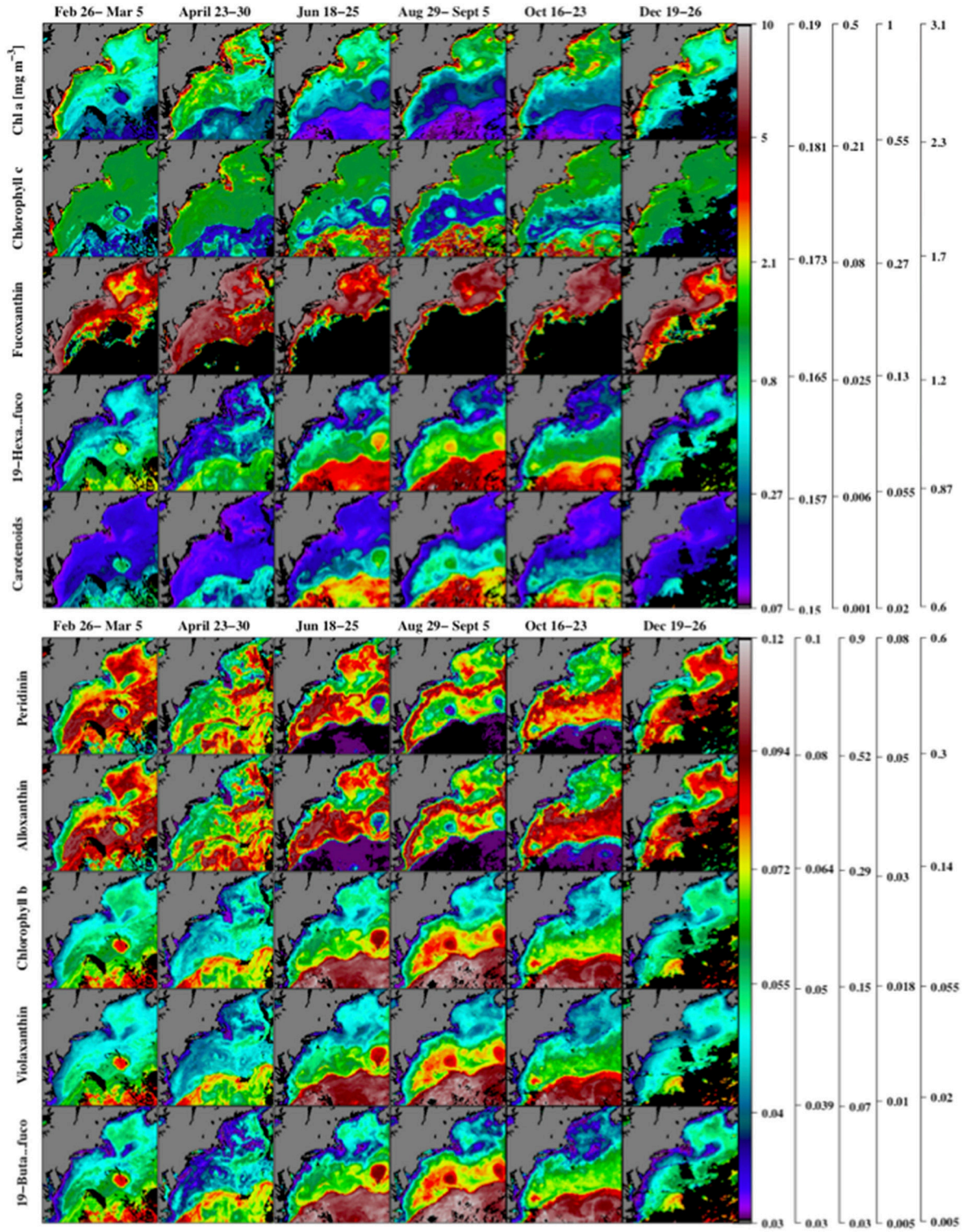

FIGURE 8 | Maps of the satellite-based inversion model estimates of chlorophyll a, Chl^{MOD}_{SAT} and the ratios of chlorophyll c, fucoxanthin, 19′hexanoyloxyfucoxanthin, carotenoids (α-carotene, B-carotene, diatoxanthin, diadinoxanthin, alloxanthin, zeaxanthin, lutein, fucoxanthin, peridinin, violoxanthin, 19′butanoyloxyfucoxanthin, and 19′hexanoyloxyfucoxanthin) to Chl^{MOD}_{SAT} (upper panel) using MODIS Aqua 2007 chlorophyll a observations. Similar ratios of peridinin, alloxanthin, chlorophyll b, violaxanthin, and 19′butanoyloxyfucoxanthin to Chl^{MOD}_{SAT} are shown in the lower panel. Note that the nonlinear colored scale bars differ for each pigment, and the scales from left to right are associated with the pigments from top to bottom. Regions where the inverse model yielded zero concentrations are shown in black.

taxa (Nair et al., 2008), it is possible to make valid inferences using in situ field measurements for verification of functional type distributions.

Maps of several key PFT marker pigments, normalized to chlorophyll a, obtained from the inverse model (**Figure 8**) solutions for 2007 show a range of different spatial distributions over the study region. A small group of pigments (notably chlorophyll a, and fucoxanthin) show a strong spatial correlation with chlorophyll levels, and are highest in the coastal regions and lowest offshore. Fucoxanthin is primarily a marker pigment for diatoms, though it is also associated with other phytoplankton types and therefore has been argued to be ambiguous as a marker pigment (Nair et al., 2008). A second group of marker pigments (peridinin and alloxanthin) shows highest pigment to chlorophyll a ratios in the mid-shelf region of the study area. Peridinin is a marker pigment for Type-I dinoflagellates (Ornótfsdóttir et al., 2003) and alloxanthin is a marker pigment for Cryptophytes (Wright, 2005). A third larger grouping of marker pigments (19′hexanoyloxyfucoxanthin, chlorophyll-b, violaxanthan, and 19′butanoyloxyfucoxanthin) and carotenoids show highest pigment to chlorophyll levels in the offshore region of the study area. All of these pigments are ambiguous marker pigments, but have been used in prior studies to infer distributions of haptophytes (Mackey et al., 1996).

Spatial Distribution and Phenology of Phytoplankton Marker Pigments

The seasonality of the functional type marker pigments (**Figure 8**) co-varied strongly with phytoplankton biomass levels, estimated by chlorophyll a concentrations, even though the ratios of the marker pigment concentrations to biomass levels varied spatially over the study region. Three specific regions related to the MAA sample area (coastal Gulf of Maine), the BIOME sample area (coastal region of the mid-Atlantic Bight), and for an open ocean region near the southeast associated with the Gulf Stream Extension domain were chosen as representative study regions (not shown). MODIST Aqua Chl_{SAT} from 2002 to 2016 was taken for these three square areas and run through the inversion method to calculate 18 pigment concentrations that were averaged over each region. The spatially-averaged time series of the phenologically related marker pigments within each of the three regions from 2002 to 2016 (not shown) demonstrates that these key pigments vary differently from region to region.

Chl_{SAT}^{MOD} levels for all regions showed seasonal variability, but no similarities (**Figure 8**). A review of the Chl_{SAT}^{MOD} variability in this region is given by O'Reilly and Zetlin (1998). The BIOME region showed peaks in Chl_{SAT}^{MOD} during its noted wintertime-spring bloom that is associated with the well-mixed water column. The open ocean region shows bloom levels of Chl_{SAT}^{MOD} rising more than two fold, with a larger peak bloom occurring in the spring followed by a less dramatic bloom in the fall. The coastal Gulf of Maine (MAA) region shows late spring blooms marked by lowest Chl_{SAT}^{MOD} levels in mid-winter.

Fucoxanthin to Chl_{SAT}^{MOD} ratios, a marker pigment for diatoms, showed high variance and an inverse correlated with SST over the time series (2002–2016) analyzed. The open ocean region showed the highest variance and a bi-annual peak in ratios in the spring and fall, possibly due to spring and fall diatom blooms. The BIOME region (northern coastal) showed high, low variance and nearly constant ratios during the fall through winter period, with a decrease during the summer seasons only. Finally, the MAA (southern coastal) had the highest observed variability, which, like the BIOME region, showed large decreases, but timed to occur primarily during the winter periods.

The 19′hexanoyloxyfucoxanthin to Chl_{SAT}^{MOD} ratios (prymnesiophytes, Phaeocystis pouchetii and coccolithophorids) covaried with SST, with peak levels observed in the open ocean during the summer months, followed by the BIOME, with lowest peaks at the MAA site.

Peridinin: Chl_{SAT}^{MOD} ratios (dinoflagellates) on the other hand showed an inverse correlation with SST except in the Biome region, peaking in concentration in the winter months when temperatures were at their lowest and mixed layer depths were at their greatest. Like the phenology of the 19′hexanoyloxyfucoxanthin-related PFTs, peridinin showed highest ratios in the open ocean site. However, higher peaks in the ratios were observed for the MAA region with lower levels in the BIOME region, noting that the dinoflagellates preferred more northerly coastal regions.

Phytoplankton Functional Type Distributions, Phenology, and Diversity

Maps of five PFTs (diatoms, dinoflagellates, prymnesiophytes, prokaryotes, and green algae) calculated using the equations developed by Hirata et al. (2011; **Table 1**) were generated using the resulting pigment maps obtained from the inverse model using the MODIS-Aqua chlorophyll observations from the study region.

Diatom Distributions

Diatom distribution was assessed by utilizing fucoxanthin as its biomarker pigment. Fucoxanthin is a useful marker for the bacillariophyceae or diatoms (**Table 1**) and also occurs in the raphidophytes and some prymnesiophytes (Jeffrey and Vest, 1997). Quantile regression analysis of HPLC fucoxanthin relative to 19′hexanoloxyfucoxanthin observations, as carried out in Devred et al. (2011), revealed slightly elevated concentrations of fucoxanthin relative to 19′hexanoloxyfucoxanthin, indicating a negligible contribution of fucoxanthin to prymnesiophytes. After the calculation of microplankton and nanoplankton percentages from pigment concentrations, fucoxanthin on average accounts for about 20% of nanophytoplankton and 80% of microphytoplankton (data not shown, Devred et al., 2011). The diatom's marker pigment, fucoxanthin, had a high correlation coefficient ($r^2 = 0.95$) between *in situ* and modeled values (**Table 2**). Other accessory pigments found in diatoms, such as chlorophyll c and photo-protective pigments, had average r^2 values of ∼0.97. The observations show that diatoms were taxonomically dominant throughout the year (**Figure 9**), with fall and spring peaks in their biomass as shown in the chlorophyll a observations (**Figure 8**). This has been shown previously in this region using radiance measurements to estimate PFTs (Pan et al.,

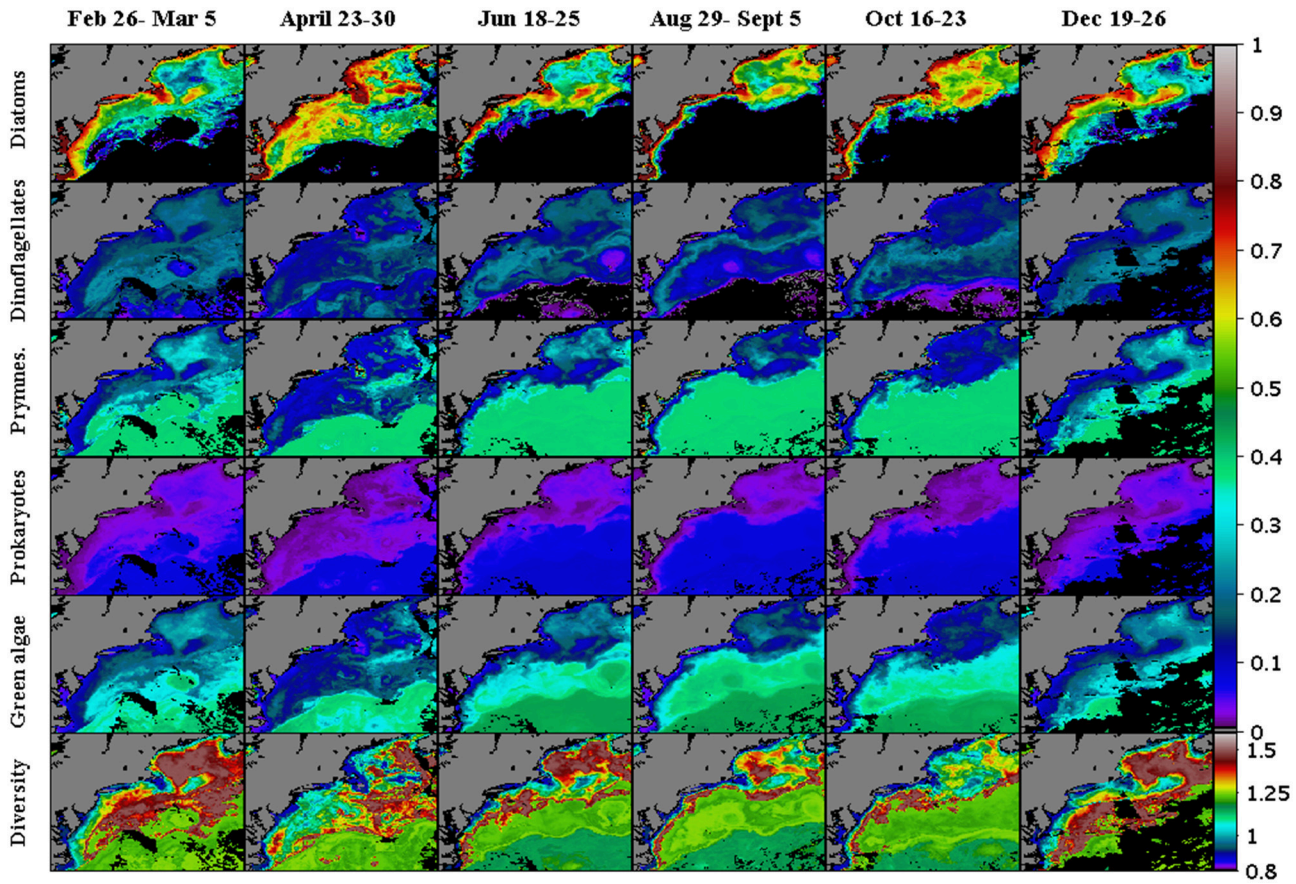

FIGURE 9 | Modeled weekly-mean phytoplankton functional types and calculated Shannon Diversity Index during 2007. Starting from the upper row of images are distribution maps of Diatoms, Dinoflagellates, Prymnesiophytes, Prokaryotes, and Green Algae (% chlorophyll a). Weekly maps of the Shannon Index (H; n.d.) for the PFT diversity are shown along the lower row of panels. Regions where the inverse model yielded zero concentrations are shown in black.

2010). Diatoms were the dominant coastal region functional type, accounting for well over half of the phytoplankton biomass, relative to chlorophyll a levels. The time series of the diatom populations averaged over three separate regional areas in the study site (**Figure 10**) and the climatology between 2006 and 2011, shows that the diatom population has highest concentrations in the coastal Gulf of Maine (**Figure 1B**, MAA) region, with a slight decrease during the summer stratified season. High levels are also observed in the coastal Delmarva region (**Figure 1A**, BIOME), but with two nearly similar peaks, one in the spring and the other in the fall. The open ocean region (not shown, site domain is 69°–68° west longitude and 38°–39° north latitude) diatom levels are lowest of the entire domain but exhibit relatively strong spring and modest late fall blooms. For much of the summer periods in the open ocean region, chlorophyll levels are below the ∼0.45 mg chla m^{-3} cutoff levels, below which fucoxanthin pigments are not retrieved in the inverse model solutions. For those periods of time the diatom levels are estimated to be minimal or irrelevant relative to the rest of the PFT population.

Within the study region, diatoms played a dominant role in shaping the diversity in areas with chlorophyll levels greater than 0.45 mg chla m^{-3} (**Figure 11**). A peak of ∼1.5 in diversity levels is observed at chlorophyll levels of ∼0.82 mg chla m^{-3} which is driven entirely by the rise in contribution in total biomass from the diatom fraction of the PFTs. Below the 0.45 mg chla m^{-3}, diatoms play little to no role in determining the functional type diversity levels.

Dinoflagellate Distributions

Peridinin was the biomarker pigment used to calculate the distribution of dinoflagellates (**Table 1**) according to Hirata et al. (2011; **Table 1**). Concentrations of both measured and modeled peridinin were generally less than 0.8 mg peridinin m^{-3}, with a modest 0.49 r^2 (**Figure 6**) in the one-to-one comparisons. In terms of its importance to total absorption reconstruction, it ranks sixth. Maps of the modeled pigment to chlorophyll a ratios of peridinin were low and ranged from 0.00 to 0.12 (mg peridinin/mg chla, (**Figure 8**). Maps of the dinoflagellate populations show that they were present in highest concentrations in the mid-shelf regions of the study site (**Figure 9**), being at their highest concentrations in the winter months for the MAA and open ocean regions but at lower and less variable levels in the BIOME domain

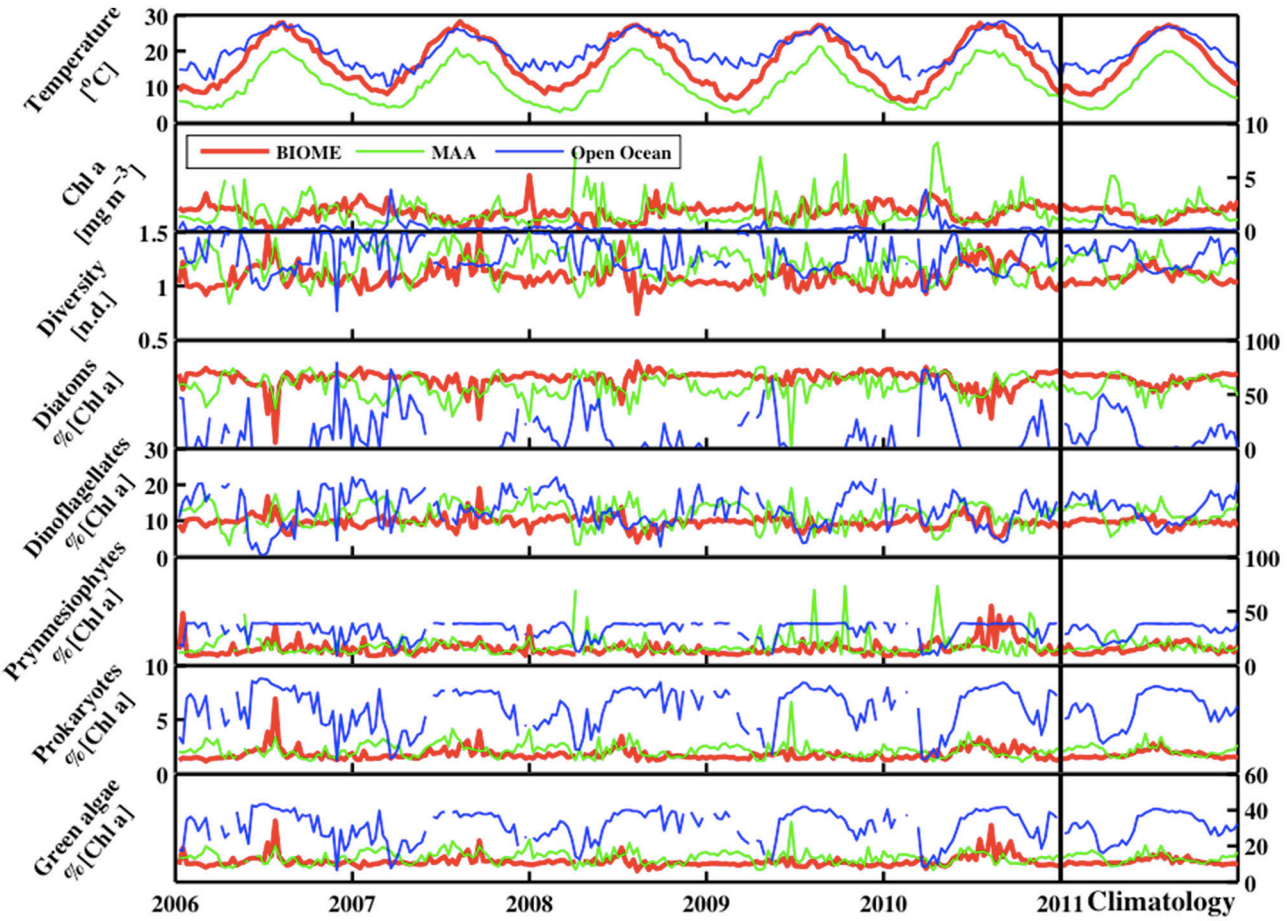

FIGURE 10 | The temporal distribution for sea surface temperature (°C), Chl_{SAT}, Shannon Diversity Index (H; n.d.), and phytoplankton functional types (% chlorophyll a) for Diatoms, Dinoflagellates, Prymnesiophytes, Prokaryotes, and Green Algae from 2006 to 2011 for three stations including the Mid Atlantic Bight, Gulf of Maine, and open ocean.

where no seasonal variability was observable. Lowest levels of dinoflagellates were estimated to be present in the late spring for the MAA region and in the mid-summer for the BIOME region. Late summer maximum levels retreated to a region running along the shelf front along the outer region of the Gulf of Maine and south along the coast (**Figure 9**).

Unlike the diatom populations, dinoflagellates influence diversity across all levels of biomass. Their peak influence in diversity occurs at chlorophyll levels of 0.45 mg chla m^{-3}, which is where the diatom populations, or more correctly where fucoxanthin estimates go to zero. At lower phytoplankton biomass, or chlorophyll levels below the peak, the contribution of dinoflagellates to phytoplankton functional diversity levels decreases to zero at chlorophyll a concentrations of 0.1 mg chla m^{-3}. At higher phytoplankton biomass or chlorophyll levels above the peak, the contribution of dinoflagellates to PFT diversity also decreases but at a much slower rate, reaching a near constant level at the higher chlorophyll levels.

Green Algae

Green algae is a large, diverse and informal group, in the planktonic ocean realm this group is composed primarily of chlorophytes (Prasinophyceae (i.e. *Ostreococcus*), micromonas). The distribution of this PFT's taxonomic importance closely resembles that of the Prokaryotes and Prymnesiophytes. Concentrations of green algae were estimated according to Hirata et al. (2011; **Table 1**) using estimates of chlorophyll-b concentrations. Maps of the green algae distribution (**Figure 9**) show that the green algae were the dominant PFT in the open ocean, where they accounted for nearly 40% of the phytoplankton biomass (**Figures 10**, **12**). In this offshore domain, large spring and smaller fall diatom blooms correlated with a decrease in the green algae levels during those periods. Green algae contributions to the PFT diversity was highest (∼38%) in the open ocean, low chlorophyll a domain and remained relatively constant with increasing chlorophyll a levels until it encountered the transition region where the diatom population begins to appear in the solutions. For chlorophyll levels above 0.45 mg chla m^{-3}, the green algae biomass (**Figure 11**) and their contributions to the

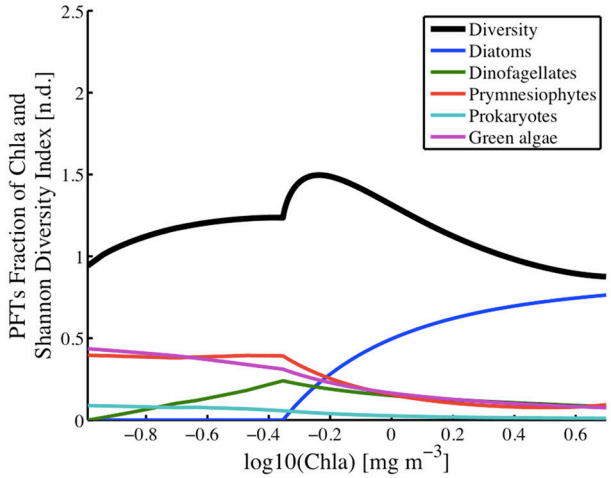

FIGURE 11 | Phytoplankton functional types (fraction of chlorophyll a) for Diatoms, Dinoflagellates, Prymnesiophytes, Prokaryotes, and Green Algae, and Shannon Diversity Index (H; n.d.) plotted against the log of Chl_{SAT} over the whole study region.

PFT diversity continued to decline with increasing levels of chlorophyll a.

Prymnesiophyte (Haptophyte) Distributions

Concentrations of haptophytes were estimated according to Hirata et al. (2011; **Table 1**) using estimates of 19′hexanoyloxyfucoxanthin and 19′butanoyloxyfucoxanthin concentrations to estimate total nanoplankton from which the estimates of green algae are subtracted. While 19′hexanoyloxyfucoxanthin is an ambiguous marker pigment for functional types, it is associated with prymnesiophytes, i.e., Phaeocystis pouchetii, and coccolithophorids (**Table 1**). Both Phaeocystis sp. and the diatom Skeletonema costatum dominated the bloom in the Gulf of Maine during April, 2007, where a mesoscale bloom was persistent during the spring (**Figure 8**). The results show that when diatom blooms occur the importance of Prymnesiophytes within the phytoplankton population declines relative to the diatom levels both in terms of concentrations (**Figure 10**) and their contribution to the diversity levels (**Figure 11**). Prymnesiophytes generally were found to be higher in the offshore ocean regions and diminished onshore relative to the per unit chlorophyll levels in each region. Seasonally, Prymnesiophytes showed broadly varying seasonal cycles in the BIOME and MAA regions, with peaks in percent chlorophyll levels occurring in late summer. The open ocean levels were predominantly flat except when the spring diatom bloom appeared.

Prymnesiophytes influence the PFT diversity levels (**Figure 11**) only at chlorophyll levels greater than 0.45 mg chla m^{-3}, with highest influence at this transition chlorophyll concentration and a minimal impact at chlorophyll levels of ∼3.2 mg chla m^{-3}. Below 0.45 mg chla m^{-3}, its contribution to the PFT diversity is equal to that of the green algae and constant at around 35%. Prymnesiophytes and the green algae showed strong correlations in terms of their spatial distribution and their contribution to PFT diversity as a function of chlorophyll a levels.

Prokaryotes

Maps of the prokaryotes (cyanobacteria) show distributional patterns that correlate strongly with the patterns observed in the green algae and Prymnesiophyte distributions. Estimates of the distribution of this group shows that they are more taxonomically important in the warmer, more stratified region of the study domain, and highest concentrations in the southeastern region where low nutrient gulf stream waters are found. In terms of percent chlorophyll, the Prokaryotes accounted for the lowest percentage of total biomass, with the highest percentages found in the offshore southeastern domain with values near 5%, and diminishing to near 2% for both the MAA and BIOME regions. During the warmer season, when nutrients are lower and stratification is high they have been observed to thrive in the coastal regions that have highly stratified water, such as the coastal areas off the Delmarva Peninsula region (Moisan et al., 2010). The seasonal cycles of both the MAA and BIOME regions showed modest peaks in the winter and summer time periods. Overall, prokaryote distributions over time were similar to that of the prymnesiophytes and green algae, and they varied inversely with the concentrations in diatom populations.

Phytoplankton Functional Type Diversity

Maps of the PFT diversity (**Figure 9**), calculated using the Shannon Diversity Index (H, Equation 6) and PTF proportionality values of the various five (diatoms, dinoflagellates, prymnesiophytes, prokaryotes, and green algae), show that a dynamic field of PFT diversity exists in the study domain. Highest levels of diversity are seen between the nearshore high chlorophyll regions and the offshore oligatrophic regions, with the most extensive areas showing up during the winter and spring time and having lowest extent in the summer when the region is isolated to the Gulf of Maine and along the coastal shelf region along the entire study domain.

Because of the methods used to generate PFT estimates, the suites of phytoplankton pigment estimates, the PFT concentrations, and the Shannon Diversity Index (H) are all non-linear functions of chlorophyll a concentrations (**Figure 11**). The results show that the majority of the PFT concentrations or relative abundances vary smoothly across chlorophyll levels ranging from 0.01 to 10.0 mg chla m^{-3}. A peak in the diversity is seen at chlorophyll levels of 0.63 mg chla m^{-3}, with diversity levels decreasing at lower and higher concentrations of chlorophyll a. The peak itself is part of a localized higher (>0.8) diversity estimate for chlorophyll levels ranging between ∼0.45 and ∼1.0 mg chla m^{-3}. This high PFT diversity region is located along the shelf at all times of the year and within the majority of the Gulf of Maine except along the near coastal areas. The overall area of high diversity expands to larger open ocean areas in the winter (**Figure 9**), when diatom levels are lower and become closer to the concentrations of the green algae, dinoflagellates and prymnesiophytes.

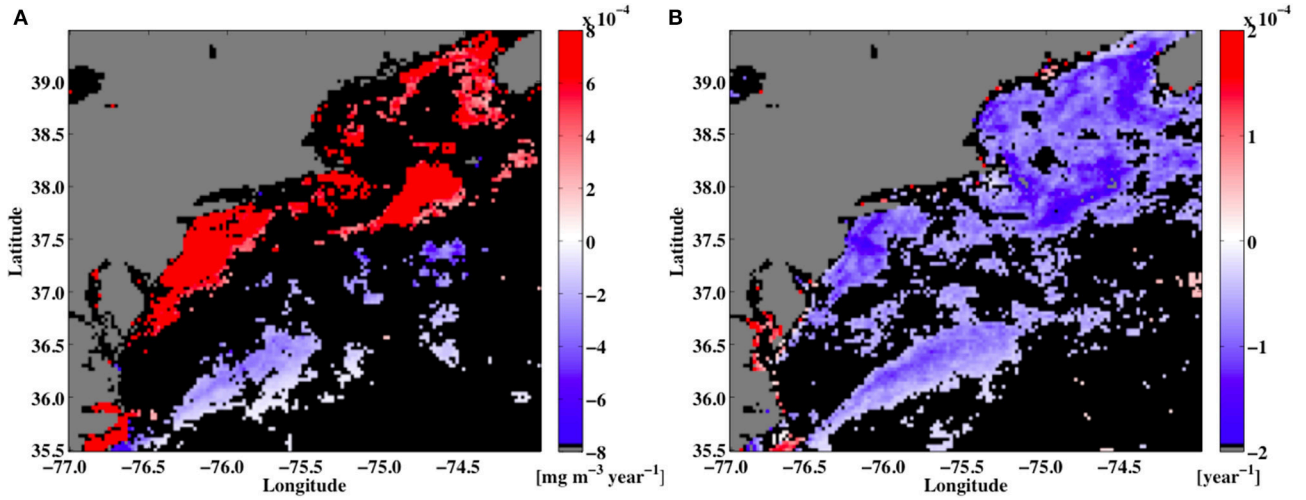

FIGURE 12 | The trend line slopes of **(A)** seatellite chlorophyll a [mg chla m^{-3} year^{-1}] and **(B)** shannon Diversity Index [H; year^{-1}] at each point over a 15-year period (2002–2016) in the study region. Regions where the slopes were insignificant are shown in black.

The local time series dynamics of both the PFTs and the resulting H show a wide range of variability (**Figure 10**). Overall, along the southern coastal BIOME region, the climatology in H shows a smooth seasonally varying relationship with a maximum level of diversity in the summer season. In the coastal Gulf of Maine MAA domain, the seasonal cycle in the H values shows high levels in the winter and summer season, with lows in the spring and fall due to the diatom bloom. In both the MAA and BIOME regions, increases in H are directly correlated with decreases in chlorophyll a or phytoplankton biomass. In the open ocean, chlorophyll a levels fluctuate around the peak in the H versus chlorophyll a relationship (**Figure 11**), leading to a much more variable climatology in H for this region. For instance, during the start of the spring bloom period in the open ocean domain, when the diatom population begin blooms and the winter population of prymnesiophytes, prokaryotes, and green algae are in decline, H increases until the chlorophyll a levels pass beyond the 0.63 mg chla m^{-3} level, above which H levels drop as the diatom population continues to bloom. This peak in the H versus phytoplankton biomass or chlorophyll a levels creates a much more complex H climatology for areas of the domain where the mean chlorophyll a levels are at this peak in H. Surprisingly enough, this chlorophyll a level is very near the peak in the histogram (not shown) of the chlorophyll a values for the domain. The belief is that this is merely serendipity from the choice in the domain under study, and not an ecological observation.

In addition to the complexities arising from the non-linear relationship between chlorophyll a levels and PFT diversity, the impact of climate-scale changes in the chlorophyll a field can also result in changes in PFT H values. For instance, for the 3 × 3 pixel region of the MODIS Aqua data centered on the location of the Woods Hole Oceanographic Institution's Air-Sea Interaction Tower (ASIT; 41° 19.5′ N, 70° 34.0′ W), the PFT diversity time series (not shown) has a seasonal cycle and a significant (p-value was 0.028) negative trend in the overall PFT diversity for that location. This trend is due to changes in the chlorophyll a levels during that period of time.

Maps of chlorophyll a linear trends for the study domain (not shown) reveal that the coastal ocean areas have positive trends in chlorophyll levels but negative trends are seen in the open ocean regions. The majority of the domain (∼70%) shows no significant trends in the chlorophyll a levels. So for the study domain, some areas have observed rising chlorophyll a levels (along the coast) and in other regions chlorophyll a levels fall (open ocean). However, because the relationship between chlorophyll a levels and PFT diversity is non-linear, the long-term trends in PFTs can also vary. So, while the resulting trends in the chlorophyll maps for the region showed some areas of positive and negative trends, the trends for the PFT H values were nearly all negative.

DISCUSSION

The aim of this study is to demonstrate how a technique that uses both an inverse model (Moisan et al., 2011) and a pigment-dependent algorithm (Hirata et al., 2011) to predict phytoplankton biodiversity can be used to estimate PFT diversity over a much larger area than was sampled, while maintaining robust results that retain the unique spatial and temporal features of the MODIS-Aqua Chl_{SAT} data. The key to retaining original features of the chlorophyll a data is the second order chlorophyll a model and matrix inversion model that convert Chl_{SAT} into phytoplankton absorption from 300 to 700 nm at a high resolution of 5 nm which is then converted into 18 different marker pigments (Moisan et al., 2011, 2013). Using total absorption spectra derived for a variety of coastal and open ocean environments, the algorithm was able to predict phytoplankton absorption and pigments in Longhurst (2010) provinces including the Gulf Stream Province, N. Atlantic Subtropical Gyral Province, and the NW Atlantic Shelves Province. Interestingly, the phytoplankton community did not

necessarily follow Longhurst's provinces, but is divided into a delineated coastal community, offshore community, and one that moves offshore and onshore with the seasons. The results have implications for understanding how different phytoplankton groups compete with each other in different biological provinces within the ocean.

The accuracy in terms of r^2 of the pigments predictions from inverting absorption spectra are highest when *in situ* data are used (**Table 2**). The accuracies increase when regressing absorption spectra with an additional pigment packaging parameter (O'Reilly and Zetlin, 1998; Alvain et al., 2005). An increase in the accuracy of the predicted phytoplankton absorption and pigments was retrieved when pigment package effects were parameterized (Johnsen et al., 1994; Bricaud et al., 1995; Ciotti et al., 2002) by "normalization" of the measured absorption spectra to the expected absorption at 675 nm. The spectral shape of the pigment package effect shows modest variability across the spectrum (Morel and Bricaud, 1981). Inaccuracies are factored into the equation when pigment package effects are taken into account. Also, Bricaud et al. (2004) claims that a term is missing when reconstructing the *in vivo* absorption spectrum of natural populations from pigment concentrations. Another factor that introduces error into the pigment estimates are the linear regression technique that has a fair r^2 value of 0.76 to 1.0 of modeled to *in situ* absorption from 400 to 700 nm. The matrix inversion method produced estimates of marker pigments that compared well against the measured HPLC pigment observations, with r^2 values averaging 0.70. The technique was robust for all pigments except zeaxanthin and lutein (**Figure 6**). The resulting range of r^2 values obtained in this study (r^2 0.33–1.0) are similar to those obtained by Pan et al. (2010) from a related study that estimated pigment concentrations (r^2 0.4–0.8) using in-water radiometry measurements off the northeast U.S. continental shelf. The satellite data driven $a_{ph}(\lambda)$ model accurately captured the variability with respect to its shape and magnitude caused by pigment concentrations, variable pigment ratios, and pigment packaging (Moisan and Mitchell, 1999).

The techniques's use of pigments estimates with algorithms for PFTs should be used with caution because pigment ratios can vary with phytoplankton species composition, light history, and acclimation to temperature and nutrients (Moisan and Mitchell, 1999; Louanchi and Najjar, 2001; Woodward and Rees, 2001; McGillicuddy et al., 2003; Geider et al., 2014). In this paper, PFTs are reported in terms of pigments to Chl_{SAT}^{MOD} ratios in order to be comparable with past HPLC studies and to reduce possible pigment estimate bias errors (Roy et al., 2011).

Distribution, Seasonality, and Biodiversity in the Phytoplankton Community

The PFTs can be roughly divided into three groups, based on their contribution to PFT diversity as a function of total chlorophyll a (**Figure 11**). On a large scale, the phytoplankton community was delineated into coastal, mixed and open ocean populations, with open ocean populations having reduced seasonal cycles in terms of biomass but not in terms of PFT diversity. Group 1 consisted of the diatoms. This group dominates the high chlorophyll regions along the coast. This group's distribution becomes insignificant at chlorophyll a levels below 0.45 mg chla m^{-3}. Group 2 is made up of the dinoflagellates, who are found across the coastal and out into the open ocean, but flourish best in the mid ocean shelf region, at the region where diatom disappear. Group 3 is composed of the green algae and the prymnesiophytes and prokaryotes. This group dominates the open ocean region and transitions in the mid-shelf regions to a less dominant group in the coastal region. Although Pan et al. (2010) did not divide their region into sub-groups, they generally found high concentrations along the coast that decreased toward the open ocean. There were significant differences in the phenology of individual PFTs over the nearly fifteen-year period of time that this study focused on, 2002–2016. This is also the case for the distributions of all of the groups, however, normalization of the groups by Chl_{SAT}^{MOD}, reduces the large cross-shelf trend in biomass and allows the regions for the various groups to be easier resolved (**Figures 10–12**). Overall, the results showed seasonality in PFTs and their geographic boundaries were either nearly static or expanded and contracted depending on the season. The modeled PFTs were discriminated geographically based on their association with coastal versus offshore distribution and their association with Gulf Stream and North Atlantic Gyre waters.

Diatoms (Group 1) play a major quantitative role in the coastal zone and had a high relative contribution to total $a_{ph}(\lambda)$ (**Figure 5B**). Seasonal variability of diatoms was observed in all of the study domain, with much larger variability in the open ocean region associated with the shelf zone, where they dominated in the spring bloom and nearly again in the late fall blooms when they co-existed with the dinoflagellates and prymnesiophytes. In both coastal regions, the diatoms dominated throughout the year and showed much milder seasonal cycles in terms of their relative importance to the chlorophyll levels. In terms of overall biomass, the dominance of diatoms in this highly productive coastal region was high during winter and was lower in the summer (Marshall and Cohn, 1983; O'Reilly and Zetlin, 1998; Filippino et al., 2011; Makinen and Moisan, 2012). Dominance by diatoms extended into the Grand Banks and well into the Gulf of Maine and along the entire coastal region. We observed a narrow feature of nanoplankton and net diatoms along the coast and its extent is likely limited due to the availability of nitrogen/nutrients (Filippino et al., 2011) that controls the likelihood of success for these r-selected diatoms (Margalef, 1978). All other PFT groups (in relation to Chl_{SAT}^{MOD} show minimal concentrations and time variability along the coast because they are outcompeted by diatoms. Although microscopy was not available for the entire region, the coastal time series in eutrophic waters showed that the diatom community was dominated by Skeletonema, Rhizosolenia, and Pseudonitzschia pungens throughout the year (Makinen and Moisan, 2012). The study suggests that the diatom community is fast growing and able to respond to events such as upwelling/downwelling, estuarine outflows, and processes that encourage eutrophication (O'Reilly and Zetlin, 1998).

The seasonal and spatial variability in the relative dominance (% chlorophyll a) of Group 2 (dinoflagellates) is limited primarily to the shelf regions of the domain, where they are present

throughout the year and with a spatial expansion of the population in the fall and winter. They have been found at modest levels in the open ocean ranging from ∼200 to 800 cells mL-1 (Makinen and Moisan, 2012). Group 2 algae were found to be most dominant (∼35% of chlorophyll a) at chlorophyll levels of 0.45 mg chla m^{-3}, which was the transition region from coastal diatom dominance to the open ocean populations. Diversity levels peaked at chlorophyll levels on the higher side of this transition region, marking this region as an ocean ecotone within this study region. The specific location of this ecotone is best shown in the narrow maximum of the August 29—September 5 color map of the dinoflagellate distribution (**Figure 9**). The location of the ecotone is just inshore of the peak in the narrow maximum band that runs along the shelf and offshore along the mouth of the Gulf of Maine.

Group 3 algae (prymnesiophytes [coccolithophorids and Phaeocystis], prokatyotes [cyanobacteria] and green algae) are dominant algae in the open ocean regions of the study domain. Of the three PFTs, the prymnesiphytes and green algae are nearly equally important, each accounting for ∼40% of the chlorophyll a field. Prokaryotes contributed to only about 10% of chlorophyll a levels and was observed in offshore shore waters and was near absent in onshore coastal waters.

In terms of the biomass (chlorophyll a) levels, the spatial and temporal variance appears to be lower in offshore waters, implying a year-round, stable community (Stramma and Siedler, 1988; Holligan et al., 1993). But relative to their contributions to the total phytoplankton pool, the summer and late fall blooms of diatoms reduced their levels of importance significantly, especially for the green algae and the prokaryote. These particular taxa are well adapted for this balanced, quasi steady-state region (Stramma and Siedler, 1988). The low nutrient and high light affinities of coccolithophorids gives them a competitive advantage over larger phytoplankton such as diatoms, showing a shift in size distribution from large/onshore to small/offshore (Marañón et al., 2001; Litchman et al., 2007). The distributional pattern of this group covaries with the distribution of photo-protective pigments (α-carotene, B-carotene, diatoxanthin, diadinoxanthin, neoxanthin, alloxanthin, zeaxanthin, and lutein) and degradation products (phaeophytin and chlorophyllide). Coccolithophorids also increased in abundance during summer months in the Gulf Stream region and were near absent in this region during December and February (Schoemann et al., 2005; Verity et al., 2007). Phaeocystis was present in the Gulf of Maine and blooms of this organism spanned the area down to Cape Cod from February to April (Moisan et al., 2013). Cyanobacteria showed the same distributional pattern throughout the study region except for the enhanced concentrations in the Mid Atlantic Bight (Moisan et al., 2010; Makinen and Moisan, 2012).

Phenology of Diatoms, Prymnesiophytes, Green Algae, and Dinoflagellates

Climate change will alter environmental conditions within the ocean and invoke a response in the timing and magnitude of phytoplankton diversity, biomass and primary production. The seasonal cycles of the PFTs shows that diatoms had a broad summer minima while prymnesiophytes had a summer peaking maxima and dinoflagellates had a very weak seasonal cycle. PFTs were distributed into unique biomes in the Atlantic Ocean, with one PFT marking the location of the PFT ecotone that has a strong correlation to SST. The seasonality of the pigments that are markers for PFTs was linked to temperature in different ways, with some peaking at a maximal temperature while others responded to a decrease in temperature with increases in biomass (**Table 4**). Predicted phytoplankton marker pigments revealed seasonal changes in individual PFTs with respect to timing of initiation, peak duration, and demise (**Figure 8**, **Table 4**). To understand the phenology of the phytoplankton community over time, three sites of interest were chosen including the Mid-Atlantic Bight, the Gulf of Maine and open ocean, to observe seasonal shifts in phytoplankton community by running the PFT calculations with inputs of MODIS Aqua Chl_{SAT} for nearly fifteen years (2002-2016). Three regions were chosen that represented two coastal and an open ocean regimes. In studying the trends of the time series, we found that the timing of the PFT maxima was different for the three groupings of PFTs and some peaks were sharp while others were broad. The phenology of the phytoplankton communities was related to the oceanographic conditions within each region.

Diatoms were present in highest concentrations along the coasts and dominated the phytoplankton community and were at a minimum during summer in all zones. During spring and summer, values of 19′hexanoyloxyfucoxanthin (prymnesiophytes) peaked, suggesting that they competed better against the diatoms (**Figure 8**). Diatoms appeared to tolerate deep mixed layers and cool temperatures during their winter maxima in both coastal and open ocean regions (Longhurst, 2010). It appears that their phenology is dependent on both light intensity and photoperiod (Edwards and Richardson, 2004). Diatom spring blooms occur once warming temperatures and weakening winter winds induce upper ocean stratification (Townsend et al., 1994). In late spring (May), diatoms reached their maximal abundance. Edwards and Richardson (2004) reported that this sudden increase is predominantly controlled by light availability in the euphotic zone because the day length and light intensity increase as the degree of mixing gradually declines. The diatoms are the first PFT to be seeded into the phytoplankton community due to their high chlorophyll a per cell with high pigment packaging (**Figure 9**).

Dinoflagellates showed a similar seasonal trend as the diatoms, but with more variability, especially in the open ocean where their fall bloom was relatively stronger than the higher biomass diatoms. Dinoflagellates were closely linked to temperature with higher concentrations at the coast from December to February, with concentrations decreasing in this region during warm summer months. Dinoflagellate concentrations to Chl_{SAT}^{MOD} ratios peaked in the Gulf of Maine and open ocean around January and decreased in summer. Surprisingly, dinoflagellates appear low in concentration in the Mid Atlantic Bight and showed a dampened seasonality. Dinoflagellates may not only be responding physiologically to temperature, but may also respond to temperature indirectly if stratified conditions appear early in the season (Edwards and Richardson, 2004). The

TABLE 4 | Phenology of certain PFT markers in the study region for 2006 as defined by the dates of the initiation, peak and termination of the seasonal maximum/bloom period.

Marker pigment	Location	Duration of initiation	Duration of peak	Duration of termination
Chlorophyll a	BIOME	July 28–August 4	January 17–24	July 20–27
	MAA	January 24–February 1	April 15–22	January 17–24
	Open Ocean	June 26–July 3	March 30–April 6	June 18–25
Fucoxanthin	BIOME	July 11–18	January 17–24	July 3–10
	MAA	March 6–13	April 23–30	February 26–March 5
	Open Ocean	September 14–21	March 22–29	September 6–13
Peridinin	BIOME	July 28–August 4	May 17–24	July 20–27
	MAA	August 13–20	January 17–24	August 5–12
	Open Ocean	August 13–20	February 2–9	August 5–12
19′-Hexa-fuco	BIOME	February 18–25	August 5–12	February 2–9
	MAA	January 17–24	August 21–28	January 9–16
	Open Ocean	March 22–29	August 5–12	March 14–21

geographic extent of the modeled dinoflagellates in coastal and near coastal cooler waters appeared to contract and expand within a geographic region bounded by sea surface temperatures. A boundary appeared to clearly delineate their distribution between cooler waters that marks the edge of the shelf front to the northwest and the Gulf Stream. This region near the shelf front boundary was the location of the ecotone for the coastal (diatoms) and open ocean phytoplankton populations and also the location for the maximum concentrations of dinoflagellates. It marks the ecotone for the PFTs in the study domain.

Prymnesiophytes (19′hexanoyloxyfucoxanthin), a major feature in the North Atlantic, showed distinct peaks in biomass during the summer (July) with an initiation of their bloom in February at all sites (Holligan et al., 1993). The prymnesiophytes represented in the coastal Mid-Atlantic and open ocean are probably the coccolithophorids, Emiliania huxleyi. Whereas, the Gulf of Maine probably is represented by both coccolithophorids and Phaeocystis. Unfortunately, the marker pigment, 19′hexanoyloxyfucoxanthin, does not differentiate between coccolithophorids and Phaeocystis. However, we hypothesize that Phaeocystis probably blooms in early spring (February) in the Gulf of Maine (Moisan et al., 2013) and reaches its maximal in August. Whereas, coccolithophorids were found in high concentration at the coast and in the open ocean south of the Gulf Stream and peaked in late summer and are dominant feature in remote sensing of Ocean Color (Holligan et al., 1993).

General mechanistic explanations for the phenology of certain PFTs are still controversial, as most phenology has focused on chlorophyll a biomass (Siegel et al., 2002; Ji et al., 2010). Ecological explanations for the presence of individual PFTs include the following: (1) coastal upwelling events, (2) seasonal freshwater fluxes from major estuaries or rivers, (3) variability in the intensity of fall and winter storms which reduce/enhance mixing-induced vertical nutrient fluxes resulting in decreased/increased chlorophyll a levels in fall/winter, and, (4) stronger than usual wind stress curl in the summer, which can shoal the thermocline offshore and deliver nutrients to the upper photic zone, producing local phytoplankton blooms (Foukal and Thomas, 2014). One-dimensional models have proven helpful in revealing the underlying mechanisms driving the phenological shifts in the phytoplankton community when local forcing controls the mixing/stratification dynamics (Olivieri and Chavez, 2000).

Phytoplankton Functional Type Diversity and Climate

A review of the various methods presently in use to estimate PFTs using remote sensing observation (IOCCG, 2014) notes that while it is possible to quantify phytoplankton pigments by differentiation of phytoplankton absorption spectra (Bricaud et al., 2007; Moisan et al., 2011), the requirement for high spectral resolution remote sensing data sets limits its application. A method to estimate various PFTs using hyperspectral observations has been developed (PhytoDOAS, Bracher et al., 2009) that has been able to retrieve global-scale observations of two important PFTs. But, these sophisticated satellite-based applications require hyperspectral data sets. In this study, hyperspectral absorption spectra were modeled as a function of chlorophyll a, using in situ observations of absorption spectra and HPLC pigments. By using an inverse modeling technique to yield pigment estimates from hyperspecral absorption spectra (Moisan et al., 2011, 2013), the method allows us to estimate phytoplankton pigment suites from satellite chlorophyll a measurements. The use of pigment-dependent algorithms to estimate the PFT concentrations (Hirata et al., 2011) demonstrates the potential for developing these types of relationships for various ocean areas. The need to develop such regional relationships was one of the gaps identified by Bracher et al. (2017) in a recent review on obtaining phytoplankton diversity from ocean color data.

The assessment of the PTF diversity patterns in the study domain is the first study that has been done which utilizes a number of techniques to yield PFT estimates from phytoplankton absorption spectra modeled using satellite observations. There are a number of recent studies that have created PFT diversity

maps using other techniques, including models. Phytoplankton diversity was compared to primary productivity estimates in the California Current region (Goebel et al., 2013) using an NPZ-type model with 78 phytoplankton types (Goebel et al., 2010). The results from this study calculated the Shannon Diversity Index (H) and species richness and showed that there was very high diversity offshore of the California upwelling regions where production was very high. In addition, north of the west wind drift region H showed very low values in this High Nutrient, Low Chlorophyll region. No clear patterns where observed when comparing H to primary production levels. However the study did note that a number of commonly observed relationships between diversity and productivity did exist, including: monotonic increase; monotonic decrease; a unimodal or hump-backed relationship or a hump-backed envelope that denotes the maximum in the data sets. The results from this study show that non-monotonic diversity versus biomass relationships may exist along the coastal regions of the U.S. east coast, including the Gulf of Maine and extending beyond the shelf front regions where the diversity was estimated to be highest in the areas of the eddy-rich shelf frontal regions. Higher phytoplankton diversity within frontal regions was also calculated in the eddy rich regions of the Gulf Stream Extension (Lévy et al., 2015), which is located due east of this paper's study region. The patterns and locations of the higher H values were similar to those encountered in this study. In this present study highest H values were observed in the frontal regions of the shelf frontal zone and in the central region of the Gulf of Maine, while moderate levels of H offshore can be seen extending eastward with the Gulf Stream extension and contain variability associated with the mesoscale features of the warm core Gulf Stream rings.

Are these satellite-derived estimates of H more informative than the traditional species-resolved H estimates, which the Goebel et al. (2013) and Lévy et al. (2015) studies simulated using a complex species-based model? Does the number of species versus the range of species function determine the functioning capability of the ocean ecosystem? Do we need to know the complexity of species numbers or can we just resolve the functionality of the ecosystem in order to understand it? Some ecologists will argue that both the diversity of the species and the functional types are equally important (Tilman et al., 2001). But a study by Diaz and Cabido (2001) argues that because of the functional nature of the processes that each functional type contributes to ecosystem the functional diversity of the ecosystem is more important to its overall function. Therefore, generating satellite maps of phytoplankton functional diversity even at the course 5-component functional type scale developed in this effort can be useful for monitoring marine ecosystem function over time.

In addition to assessments of the ecosystem function for various ocean regions, maps of PFT diversity can be used to monitor any changes to the ocean's ecosystem over longer time. An analysis of satellite chlorophyll a observations demonstrated that while there is no significant trend in the global scale chlorophyll a levels, there are regions in the ocean where chlorophyll levels have increased and decreased over the SeaWiFS satellite lifetime, 1998-2012 (Gregg et al., 2005; Vantrepotte and Melin, 2009; Henson et al., 2010; Siegel et al., 2013; Gregg and Rousseaux, 2014). Additionally, Boyce et al. (2010) have argued that the ocean's chlorophyll a levels observed have been in decline over the past century. Although this observed decline has been thought to possibly arise from data bias from blending data sets or other errors in the analysis (Mackas, 2011; McQuatters-Gollop et al., 2011; Rykaczewski and Dunne, 2011), any systematic long-term changes in ocean phytoplankton biomass should be reflected in changes to the PFTs and the resulting PFT diversity. An analysis of the local linear trends in the MODIS-Aqua chlorophyll a product from 2002-2016 showed that for the majority of the region used in this study significant trends were observed in about 25% of the domain, with increasing trends in areas along the coast and decreasing chlorophyll levels in the open ocean (**Figure 12A**). A similar linear trend analysis of the PFT H time series showed that for both those regions the H values had a negative trend (**Figure 12B**), meaning that diversity decreased in both areas regardless of the fact that the chlorophyll trends were opposite signs in two areas. The reason for this is that the PFT diversity function (**Figure 11**) shows hump-backed relationship, so that at low chlorophyll values, as observed in the open ocean regions, any decrease in chlorophyll levels leads to a decrease in H, and in the coastal region, where chlorophyll levels are highest an increase in chlorophyll levels also leads to a decrease in H. Such non-linear relationships in the biomass to H relationships can have an interesting impact in the predicted climate scale changes in H.

CONCLUSION

In summary, the process of inverting modeled phytoplankton absorption spectra generated using satellite chlorophyll observations into biomarker pigments and then utilizing the Hirata et al. (2011) PFT algorithms to estimate PFT diversity demonstrates unique patterns of individual PFTs in the Northwest Atlantic region in addition to large scale and dynamic patterns in PFT diversity. The distribution of the phytoplankton community can be divided into a number of groupings that are all related cross-shelf variability, ranging from coastal ocean to shelf-front/mesoscale-feature dominated, to oligatrophic open ocean regions. The temporal distribution of these PFTs shows phenological variability in these ocean regions, which vary with timing of their seasonal maxima and minima. These regional analyses demonstrate the importance of developing methods to remotely observe PFTs and their H in order to improve knowledge on the temporal and spatial distribution of the major phytoplankton groups and perhaps ecosystem stability at the regional scale, and to potentially quantify the impacts of climate variability on ecosystems. In the future, once greater numbers of global *in situ* measurements are available, such methods may be expanded to encompass larger areas to serve as a model for analyzing PFTs and diversity trends across the world's oceans. The algorithm's versatility in utilizing available satellite data enables potential applications for providing larger scale estimates to support ecosystem models that attempt to model PFTs explicitly.

AUTHOR CONTRIBUTIONS

TM was the senior author of the manuscript and contributed to understanding the relationship between absorption and pigmentation in order to understand diversity in the phytoplankton community. TM was an ecologist who sought to understand the linkages between phytoplankton diversity and Carbon Cycle science. She utilized inherent optical properties to link to satellite oceanography to understand biogeochemical cycles in the ocean. KR is a programmer who participated in all of the mathematical calculations that linked phytoplankton optics to community dynamics in the ocean. She is responsible for all of the graphics and calculations for the paper. She is an early oceanographer budding into satellite oceanography. JM is a physical oceanographer and is responsible for formulating the calculations for the biodiversity of phytoplankton. He is responsible for overseeing mathematical calculations and putting them into an ecological framework to understand carbon Cycle Science. His interest is in understanding climate change and how it relates to phytoplankton diversity. ML participated in the collection and processing of samples from ocean cruises. He also worked with JM and TM in developing the matrix inversion algorithms.

FUNDING

Funding for this research was provided for by the NASA Ocean Biology and Biogeochemistry Research Program, NASA Goddard Space Flight Center, and The Gordon and Betty Moore Foundation. Grant Number 3292 for Gordon and Betty Moore Foundation and 600-14-4316 for Ocean Biology and Biogeochemistry Research Program.

ACKNOWLEDGMENTS

We thank Ms. Kristin Golmon for earlier testing and development of our inversion algorithm through the NASA USRP Student Program. We thank Carla Makinen and Kristen Blattner participation in filtration and cruise logistics. John Morrow helped to deploy the PRR-800 on several of the BIOME cruises. Our HPLC samples (BIOME, COBY, and MAA cruises) were processed through Laurie van Heukelum (HPEL). The authors wish to thank the Ocean Color Processing Group (OBPG) at the NASA Goddard Space Flight Center (Code 616.0), Greenbelt, Maryland for the production and distribution of the MODIS-Aqua data. We thank our reviewers including Astrid Bracher for their excellent and generous comments that improved our work. Our work was partially funded by the NASA Biodiversity Program 05-TEB/05-0016 and NOAA. The paper was prepared under award #NA03NOS4730220 from NOAA, U.S. Department of Commerce and NASA Climate Adaptation Science Initiative (CASI). The statements, findings, and conclusions are those of the authors and do not necessarily reflect the views of NOAA or the U.S. Department of Commerce.

REFERENCES

Alvain, S., Moulin, C., and Dandonneau, Y. (2005). Remote sensing of phytoplankton groups in case 1 waters from global SeaWiFS imagery. *Deep Sea Res.* 52, 1989–2004. doi: 10.1016/j.dsr.2005.06.015

Alvain, S., Moulin, C., Dandonneau, Y., and Loisel, H. (2008). Seasonal distribution and succession of dominant phytoplankton groups in the global ocean: A satellite view. *Glob. Biogeochem. Cycles* 22, GB3001–GB3015. doi: 10.1029/2007GB003154

Bailey, S. W., and Werdell, P. J. (2006). A multi-sensor approach for the on-orbit validation of ocean color satellite data products. *Rem. Sens. Environ.* 102, 12–23. doi: 10.1016/j.rse.2006.01.015

Balch, W., Holligan, P. M., Ackleson, S. G., and Voss, K. J. (1991). Biological and optical properties of mesoscale coccolithophore blooms. *Limnol. Oceanogr.* 36, 629–643. doi: 10.4319/lo.1991.36.4.0629

Balch, W., Kilpatrick, K. A., Holligan, P. M., and Trees, C. (1996). The 1991 coccolithophore bloom in the central north Atlantic I—Optical properties and factors affecting their distribution. *Limnol. Oceanogr.* 41, 1669–1683. doi: 10.4319/lo.1996.41.8.1669

Barlow, R. G., Mantoura, R. F. C., and Cummings, D. G. (1999). Monsoonal influence on the distribution of phytoplankton pigments in the Arabian Sea. *Deep Sea Res. II Top. Stud. Oceanogr.* 46, 677–699. doi: 10.1016/S0967-0645(98)00123-4

Barlow, R., Stuart, V., Lutz, V., Sessions, H., Sathyendranath, S., Platt, T., et al. (2007). Seasonal pigment patterns of surface phytoplankton in the subtropical southern hemisphere. *Deep Sea Res. I Oceanogr. Res. Pap.* 54, 1687–1703. doi: 10.1016/j.dsr.2007.06.010

Bidigare, R. R., Ondrusek, M. E., Morrow, J. H., and Kiefer, D. H. (1990). *In vivo* absorption properties of algal pigments. *Proc. SPIE* 1302, 290–302. doi: 10.1117/12.21451

Boyce, D. G., Lewis, M. R., and Worm, B. (2010). Global phytoplankton decline over the past century. *Nature* 466, 591–596. doi: 10.1038/nature09268

Bracher, A., Bouman, H. A., Brewin, R. J. W., Bricaud, A., Brotas, V., Ciotti, A. M., et al. (2017). Obtaining phytoplankton diversity from ocean color: a scientific roadmap for future development. *Front. Mar. Sci.* 4:55. doi: 10.3389/fmars.2017.00055

Bracher, A., Taylor, M., Taylor, B., Dinter, T., Roettgers, R., and Steinmetz, F. (2015). Using empirical orthogonal functions derived from remote sensing reflectance for the prediction of phytoplankton pigments concentrations. *Ocean Sci.* 11, 139–158. doi: 10.5194/os-11-139-2015

Bracher, A., Vountas, M., Dinter, T., Burrows, J. P., Röttgers, R., and Peeken, I. (2009). Quantitative observation of cyanobacteria and diatoms from space using PhytoDOAS on SCIAMACHY data. *Biogeosciences* 6, 751–764. doi: 10.5194/bg-6-751-2009

Brewin, R., Sathyendranath, S., Hirata, T., Lavender, S., Barciela, R., and Hardman-Mountford, N. (2010). A three-component model of phytoplankton size class for the Atlantic Ocean. *Ecol. Modell.* 221, 1472–1483. doi: 10.1016/j.ecolmodel.2010.02.014

Bricaud, A., Babin, M., Morel, A., and Claustre, H. (1995). Variability in the chlorophyll-specific absorption coefficients of natural phytoplankton: analysis and parameterization. *J. Geophys. Res.* 100, 13321–13332. doi: 10.1029/95JC00463

Bricaud, A., Claustre, H., Ras, J., and Oubelkheir, K. (2004). Natural variability of phytoplanktonic absorption in oceanic waters: Influence of the size structure of algal populations. *J. Geophys. Res.* 109:C11010-1. doi: 10.1029/2004JC002419

Bricaud, A., Mejia, C., Blondeau-Patissier, D., Claustre, H., Crepon, M., and Thiria, S. (2007). Retrieval of pigment concentrations and size structure of algal populations from their absorption spectra using multilayered perceptrons. *Appl. Opt.* 46, 1251–1260. doi: 10.1364/AO.46.001251

Bruggeman, J., and Kooijman, S. A. L. M. (2007). A biodiversity-inspired approach to aquatic ecosystem modeling. *Limnol. Oceanogr.* 52:1533. doi: 10.4319/lo.2007.52.4.1533

Campbell, L., Henrichs, D. W., Olson, R. J., and Sosik, H. M. (2013). Continuous automated imaging-in-flow cytometry for detection and early warning of Karenia brevis blooms in the Gulf of Mexico. *Environ. Sci. Pollut. Res.* 20, 6896–6902. doi: 10.1007/s11356-012-1437-4

Cermeño, P., Dutkiewicz, S., Harris, R. P., Follows, M., Schofield, O., and Falkowski, P. G. (2008). The role of nutricline depth in regulating the ocean carbon cycle. *Proc. Natl. Acad. Sci. U.S.A.* 105, 20344–20349. doi: 10.1073/pnas.0811302106

Chase, A., Boss, E., Zaneveld, R., Bricaud, A., Claustre, H., Ras, J., et al. (2013). Decomposition of in situ particulate absorption spectra. *Methods Oceanogr.* 7, 110–124. doi: 10.1016/j.mio.2014.02.002

Ciotti, A. M., Lewis, M. R., and Cullen, J. J. (2002). Assessment of the relationships between dominant cell size in natural phytoplankton communities and the spectral shape of the absorption coefficient. *Limnol. Oceanogr.* 47, 404–417. doi: 10.4319/lo.2002.47.2.0404

Devred, E., Sathyendranath, S., Stuart, V., and Platt, T. (2011). A three component classification of phytoplankton absorption spectra: Application to ocean-color data. *Rem. Sens. Environ.* 115, 2255–2266. doi: 10.1016/j.rse.2011.04.025

Diaz, S., and Cabido, M. (2001). Vive le difference: Plant functional diversity matters to ecosystem processes. *Trends Evol.* 16, 646–655, doi: 10.1016/S0169-5347(01)02283-2

D'Ortenzio, F., and Ribera d'Alcalà, M. (2009). On the trophic regimes of the Mediterranean Sea: a satellite analysis. *Biogeosciences* 6, 139–148. doi: 10.5194/bg-6-139-2009

Edwards, M., Johns, D. G., Leterme, S. C., Svendsen, E., and Richardson, A. J. (2006). Regional climate change and harmful algal blooms in the northeast Atlantic. *Limnol. Oceanogr.* 51, 820–829. doi: 10.4319/lo.2006.51.2.0820

Edwards, M., and Richardson, A. J. (2004). Impact of climate change on marine pelagic phenology and trophic mismatch. *Nature* 430, 881–884. doi: 10.1038/nature02808

Falkowski, P. G., and Raven, J. A. (1997). *Aquatic Photosynthesis*. Malden, MA: Blackwell Science, 375.

Filippino, K. C., Mulholland, M. R., and Bernhardt, P. W. (2011). Nitrogen uptake and primary productivity rates in the Mid-Atlantic Bight (MAB). *Estuar. Coast. Shelf Sci.* 91, 13–23. doi: 10.1016/j.ecss.2010.10.001

Foukal, N. P., and Thomas, A. C. (2014). Biogeography and phenology of satellite-measured phytoplankton seasonality in the California current. *Deep Sea Res. I Oceanogr. Res. Pap.* 92, 11–25. doi: 10.1016/j.dsr.2014.06.008

Garver, S. A., and Siegel, D. A. (1997). Inherent optical property inversion of ocean color spectra and its biogeochemical interpretation: 1. Time series from the Sargasso Sea. *J. Geophys. Res.* 102, 18607–18625. doi: 10.1029/96JC03243

Geider, R. J., Moore, C. M., and Suggett, D. J. (2014). "Ecology of Marine Phytoplankton," in *Ecology and the Environment*, ed R. K. Monson (New York, NY: Springer Science+Business Media), 483–531.

Goebel, N. L., Edwards, C. A., Zehr, J. P., Follow, M. J., and Morgan, S. G. (2013). Modeled phytoplankton diversity and productivity in the California current system. *Ecol. Modell.* 264, 37–47. doi: 10.1016/j.ecolmodel.2012.11.008

Goebel, N. L., Edwards, C. A., Zehr, J. P., and Follows, M. J. (2010). An emergent community ecosystem model applied to the California current system. *J. Mar. Syst.* 83, 221–241. doi: 10.1016/j.jmarsys.2010.05.002

Gregg, W. W., Casey, N. W., and McClain, C. R. (2005). Recent trends in global ocean chlorophyll. *Geophys. Res. Lett.* 32:L03606, doi: 10.1029/2004GL021808

Gregg, W. W., Ginoux, P., Schopf, P. S., and Casey, N. W. (2003). Phytoplankton and iron: validation of a global three-dimensional ocean biogeochemical model. *Deep Sea Res. II Top. Stud. Oceanogr.* 50, 3143–3169. doi: 10.1016/j.dsr2.2003.07.013

Gregg, W. W., and Rousseaux, C. S. (2014). Decadal trends in global pelagic ocean chlorophyll: a new assessment integrating multiple satellites, in situ data, and models. *J. Geophys. Res.* 119, 5921–5933. doi: 10.1002/2014jc010158

Hardman-Mountford, N. J., Hirata, T., Richardson, K. A., and Aiken, J. (2008). An objective methodology for the classification of ecological pattern into biomes and provinces for the pelagic ocean. *Remote Sens. Environ.* 112, 3341–3352. doi: 10.1016/j.rse.2008.02.016

Henson, S. A., Robinson, I., Allen, J. T., and Waniek, J. J. (2006). Effect of meteorological conditions on interannual variability in timing and magnitude of the spring bloom in the Irminger Basin, North Atlantic. *Deep Sea Res. I Oceanogr. Res. Pap.* 53, 1601–1615. doi: 10.1016/j.dsr.2006.07.009

Henson, S. A., Sarmiento, J. L., Dunne, J. P., Bopp, L., Lima, I., Doney, S. C., et al. (2010), Detection of anthropogenic climate change in satellite records of ocean chlorophyll and productivity, *Biogeosciences* 7, 621–640. doi: 10.5194/bg-7-621-2010

Hirata, T., Aiken, J., Hardman-Mountford, N., Smyth, T. J., and Barlow, R. G. (2008). An absorption model to determine phytoplankton size classes from satellite ocean colour. *Remote Sens. Environ.* 112, 3153–3159. doi: 10.1016/j.rse.2008.03.011

Hirata, T., Hardman-Mountford, N., Brewin, R., Aiken, J., Barlow, R., Suzuki, K., et al. (2011). Synoptic relationships between surface Chlorophyll-a and diagnostic pigments specific to phytoplankton functional types. *Biogeosciences* 8, 311–327. doi: 10.5194/bg-8-311-2011

Hoge, F. E., and Lyon, P. E. (1996). Satellite retrieval of inherent optical properties by linear matrix inversion of oceanic radiance models: an analysis of model and radiance measurement errors. *J. Geophys. Res.* 101, 16631–16648. doi: 10.1029/96JC01414

Holligan, P. M., Fernández, E., Aiken, J., Balch, W. M., Boyd, P., Burkill, P. H., et al. (1993). A biogeochemical study of the coccolithophore, Emiliania huxleyi, in the North Atlantic. *Glob. Biogeochem. Cycles* 7, 879–900. doi: 10.1029/93GB01731

Hoogenboom, H. J., Dekker, A. G., and De Haan, J. F. (1998). Retrieval of chlorophyll and suspended matter from imaging spectrometry data by matrix inversion. *Can. J. Remote Sens.* 24, 144–152. doi: 10.1080/07038992.1998.10855234

Hu, C., Cannizzaro, J., Carder, K. L., Muller-Karger, F. E., and Hardy, R. (2010). Remote detection of Trichodesmium blooms in optically complex coastal waters: Examples with MODIS full-spectra data. *Remote Sens. Environ.* 114, 2048–2058. doi: 10.1016/j.rse.2010.04.011

Iglesias-Rodriguez, M. D., Halloran, P. R., Rickaby, R. E., Hall, I. R., Colmenero-Hidalgo, E., Gittins, J. R., et al. (2008). Phytoplankton calcification in a high-CO_2 world. *Science* 320, 336–340. doi: 10.1126/science.1154122

IOCCG (2014). *Phytoplankton Functional Types from Space*. ed S. Sathyendranath, Reports of the International Ocean Colour Coordinating Group, No. 15, IOCCG, (Dartmouth, NS).

Jeffrey, S. W., and Vest, M. (1997). "Introduction to marine phytoplankton and their pigment signatures," in Phytoplankton Pigments in Oceanography, eds F. S. Jeffrey, F. C. Mantoura, S. W. Wright (Paris: UNESCO), 37–84.

Ji, R., Edwards, M., Mackas, D. L., Runge, J. A., and Thomas, A. C. (2010). Marine plankton phenology and life history in a changing climate: current research and future directions. *J. Plankton Res.* 32, 1355–1368. doi: 10.1093/plankt/fbq062

Johnsen, G., Samset, O., Granskog, L., and Sakshaug, E. (1994). *In-vivo* absorption characteristics in 10 classes of bloom-forming phytoplankton-taxonomic characteristics and responses to photoadaptation by means of discriminant and HPLC analysis. *Mar. Ecol. Prog. Ser.* 105, 149–157. doi: 10.3354/meps105149

Kahru, M., Kudela, R. M., Anderson, C. R., Manzano-Sarabia, M., and Mitchell, B. G. (2014). Evaluation of satellite retrievals of ocean chlorophyll-a in the California Current, Remote Sens., 6, 8524–8540. doi: 10.3390/rs6098524

Kishino, M., Takahashi, M., Okami, N., and Ichimura, S. (1985). Estimation of the spectral absorption coefficients of phytoplankton in the sea. *Bull. Mar. Sci.* 37, 634–642.

Kostadinov, T. S., Siegel, D. A., and Maritorena, S. (2009). Retrieval of the particle size distribution from satellite ocean color observations. *J. Geophys. Res.* 114:C09015. doi: 10.1029/2009jc005303

Lawson, C. L., and Hanson, R. J. (1974). *Solving Least Squares Problems, Vol. 161,* Englewood Cliffs, NJ: Prentice-hall.

Lee, Z., and Carder, K. L. (2004). Absorption spectrum of phytoplankton pigments derived from hyperspectral remote-sensing reflectance. *Remote Sens. Environ.* 89, 361–368. doi: 10.1016/j.rse.2003.10.013

Levitus, S., Antonov, J. I., Boyer, T. P., and Stephens, C. (2000). Warming of the world ocean. *Science* 287, 2225–2229. doi: 10.1126/science.287.5461.2225

Lévy, M., Jahn, O., Dutkiewicz, S., Follows, M. J., and d'Ovidio, F. (2015). The dynamical landscape of marine phytoplankton diversity. *J. R. Soc. Interface* 12:20150481. doi: 10.1098/rsif.2015.0481

Litchman, E., Klausmeier, C. A., Schofield, O. M., and Falkowski, P. G. (2007). The role of functional traits and trade-offs in structuring phytoplankton communities: scaling from cellular to ecosystem level. *Ecol. Lett.* 10, 1170–1181. doi: 10.1111/j.1461-0248.2007.01117.x

Longhurst, A. (2010). *Ecological Geography of the Sea, 2nd Edn*, San Diego, CA: Academic Press, 542.

Louanchi, F., and Najjar, R. G. (2001). Annual cycles of nutrients and oxygen in the upper layers of the North Atlantic Ocean. *Deep Sea Res. II Top. Stud. Oceanogr.* 48, 2155–2171. doi: 10.1016/S0967-0645(00)00185-5

Mackas, D. L. (2011). Does blending of chlorophyll data bias temporal trend? *Nature* 472, E4–E5, doi: 10.1038/nature09951

Mackey, M. D., Mackey, D. J., Higgins, H. W., and Wright, S. W. (1996). CHEMTAX—a program for estimating class abundances from chemical markers: application to HPLC measurements of phytoplankton. *Mar. Ecol. Prog. Ser.* 144, 265–283. doi: 10.3354/meps144265

Makinen, C. P., and Moisan, T. A. (2012). Phytoplankton assemblage patterns in the southern Mid-Atlantic Bight. *Bot. Mar.* 55, 445–457. doi: 10.1515/bot-2012-0110

Marañón, E., Holligan, P. M., Barciela, R., González, N., Mouri-o, B., Paz,ó, M. J., et al. (2001). Patterns of phytoplankton size structure and productivity in contrasting open-ocean environments. *Mar. Ecol. Prog. Ser.* 216, 43–56. doi: 10.3354/meps216043

Margalef, R. (1978). Life-forms of phytoplankton as survival alternatives in an unstable environment. *Oceanologica Acta* 1, 493–509.

Marquardt, D. W. (1963). An algorithm for least-squares estimation of nonlinear parameters. *J. Soc. Indust. Appl. Math.* 11, 431–441. doi: 10.1137/0111030

Marshall, H. G., and Cohn, M. S. (1983). Distribution and composition of phytoplankton in northeastern coastal waters of the United States. *Estuar. Coast. Shelf Sci.* 17, 119–131. doi: 10.1016/0272-7714(83)90057-4

McGillicuddy, D. J. Jr., Anderson, L. A., Doney, S. C., and Maltrud, M. E. (2003). Eddy-driven sources and sinks of nutrients in the upper ocean: Results from a 0.1° resolution model of the North Atlantic, Global Biogeochem. *Cycles* 17, 1035. doi: 10.1029/2002GB001987

McQuatters-Gollop, A., Reid, P. C., Edwards, M., Burkill, P. H., Castellani, C., Batten, S., et al. (2011). Is there a decline in marine phytoplankton. *Nature* 472, E6–E7. doi: 10.1038/nature09950

Mitchell, B. G. (1990). Algorithms for determining the absorption coefficient of aquatic particulates using the quantitative filter technique (QFT). *SPIE, Ocean Optics X* 1302, 137–148. doi: 10.1117/12.21440

Moisan, J. R., Moisan, T. A., and Linkswiler, M. A. (2011). An inverse modeling approach to estimating phytoplankton pigment concentrations from phytoplankton absorption spectra. *J. Geophys. Res.* 116:C09018. doi: 10.1029/2010jc006786

Moisan, J. R., Moisan, T. A., Linkswiler, M. A., and Steinhardt, R. A. (2013). Algorithm development for predicting biodiversity based on phytoplankton absorption. *Cont. Shelf Res.* 55, 17–28. doi: 10.1016/j.csr.2012.12.011

Moisan, T. A., Blattner, K. L., and Makinen, C. P. (2010). Influences of temperature and nutrients on *Synechococcus abundanc*e and biomass in the southern Mid-Atlantic Bight. *Cont. Shelf Res.* 30, 1275–1282. doi: 10.1016/j.csr.2010.04.005

Moisan, T. A., and Mitchell, B. G. (1999). Photophysiological acclimation of Phaeocystis antarctica Karsten under light limitation. *Limnol. Oceanogr.* 44, 247–258. doi: 10.4319/lo.1999.44.2.0247

Moisan, T. A., and Mitchell, B. G. (2001). UV absorption by mycosporine-like amino acids in Phaeocystis antarctica Karsten induced by photosynthetically available radiation. *Mar. Biol.* 138, 217–227. doi: 10.1007/s002270000424

Morel, A., and Bricaud, A. (1981). Theoretical results concerning light absorption in a discrete medium, and application to specific absorption of phytoplankton. *Deep Sea Res. A Oceanogr. Res. Pap.* 28, 1375–1393. doi: 10.1016/0198-0149(81)90039-X

Mouw, C. B., and Yoder, J. A. (2005). Primary production calculations in the Mid-Atlantic Bight, including effects of phytoplankton community size structure. *Limnol. Oceanogr.* 50, 1232–1243. doi: 10.4319/lo.2005.50.4.1232

Mouw, C. B., and Yoder, J. A. (2010). Optical determination of phytoplankton size composition from global SeaWiFS imagery. *J. Geophys. Res.* 115:C12018. doi: 10.1029/2010jc006337

Mouw, C. B., Yoder, J. A., and Doney, S. C. (2012). Impact of phytoplankton community size on a linked global ocean optical and ecosystem model. *J. Mar. Syst.* 89, 61–75. doi: 10.1016/j.jmarsys.2011.08.002

Nair, A., Sathyendranath, S., Platt, T., Morales, J., Stuart, V., Forget, M. H., et al. (2008). Remote sensing of phytoplankton functional types. *Remote Sens. Environ.* 112, 3366–3375. doi: 10.1016/j.rse.2008.01.021

Navarro, G., Alvain, S., Vantrepotte, V., and Huertas, I. E. (2014). Identification of dominant phytoplankton functional types in the Mediterranean Sea based on a regionalized remote sensing approach. *Remote Sens. Environ.* 152, 557–575. doi: 10.1016/j.rse.2014.06.029

Oliver, M. J., and Irwin, A. J. (2008). Objective global ocean biogeographic provinces. *Geophys. Res. Lett.* 35:L15601. doi: 10.1029/2008GL034238

Olivieri, R. A., and Chavez, F. P. (2000). A model of plankton dynamics for the coastal upwelling system of Monterey Bay, California. *Deep-Sea Res. II* 47, 1077–1106. doi: 10.1016/S0967-0645(99)00137-X

O'Reilly, J. E., and Zetlin, C. (1998). *Seasonal, Horizontal, and Vertical Distribution of Phytoplankton Chlorophyll a in the Northeast US Continental Shelf Ecosystem*. NOAA Technical Report NMFS, 139.

Organelli, E., Bricaud, A., Antoine, and, D., and Uitz, J. (2013). Multivariate approach for the retrieval of phytoplankton size structure from measured light absorption spectra in the Mediterranean Sea (BOUSSOLE site). *Appl. Opt.* 52, 2257–2273. doi: 10.1364/AO.52.002257

Ornótfsdóttir, E. B., Pinckney, J. L., and Tester, P. A. (2003). Quantification of the relative abundance of the toxic dinoflagellate, Karenia brevis (*Dinophyta*), using unique photopigments. *J. Phycol.* 39, 449–457. doi: 10.1046/j.1529-8817.2003.01219.x

Pan, X., Mannino, A., Marshall, H., Filippino, K., and Mulholland, M. (2011). Remote sensing of phytoplankton community composition along the northeast coast of the United States. *Remote Sens. Environ.* 115, 3731–3747. doi: 10.1016/j.rse.2011.09.011

Pan, X., Mannino, A., Russ, M., Hooker, S., and Harding, L. (2010). Remote sensing of phytoplankton pigment distribution in the United States northeast coast. *Remote Sens. Environ.* 114, 2403–2416. doi: 10.1016/j.rse.2010.05.015

Platt, T., and Sathyendranath, S. (2008). Ecological indicators for the pelagic zone of the ocean from remote sensing. *Remote Sens. Environ.* 112, 3426–3436. doi: 10.1016/j.rse.2007.10.016

Platt, T., White, G. N., Zhai, L., Sathyendranath, S., and Roy, S. (2009). The phenology of phytoplankton blooms: ecosystem indicators from remote sensing. *Ecol. Model.* 220, 3057–3069. doi: 10.1016/j.ecolmodel.2008.11.022

Press, W. H., Flannery, B. P., Teukolsky, S. A., Vetterling, W. T., and Gould, H. (1987). Numerical recipes, the art of scientific computing. *Am. J. Phys.* 55, 90–91. doi: 10.1119/1.14981

Raitsos, D. E., Lavender, S. J., Maravelias, C. D., Haralabous, J., Richardson, A. J., and Reid, P. C. (2008). Identifying four phytoplankton functional types from space: an ecological approach. *Limnol. Oceanogr.* 53, 605–613. doi: 10.4319/lo.2008.53.2.0605

Roy, S., Llewellyn, C., Egeland, E., and Johnsen, G. (eds.). (2011). *Phytoplankton Pigments: Characterization, Chemotaxonomy and Applications in Oceanography*. Cambridge: Cambridge University Press, 845.

Roy, S., Sathyendranath, S., Bouman, H., and Platt, T. (2013). The global distribution of phytoplankton size spectrum and size classes from their light-absorption spectra derived from satellite data. *Remote Sens. Environ.* 139, 185–197. doi: 10.1016/j.rse.2013.08.004

Rykaczewski, R. R., and Dunne, J. P. (2011). A measured look at ocean chlorophyll trends. *Nature* 472, E5–E6, doi: 10.1038/nature09952

Sadeghi, A., Dinter, T., Vountas, M., Taylor, B., Altenburg-Soppa, M., and Bracher, A. (2012). Remote sensing of coccolithophore blooms in selected oceanic regions using the PhytoDOAS method applied to hyper-spectral satellite data. *Biogeosciences* 9, 2127–2143. doi: 10.5194/bg-9-2127-2012

Sarmiento, J. L., Gruber, N., Brzezinski, M. A., and Dunne, J. P. (2004). High-latitude controls of thermocline nutrients and low latitude biological productivity. *Nature* 427, 56–60. doi: 10.1038/nature02127

Sathyendranath, S., Watts, L., and Devred, E. (2004). Discrimination of diatoms from other phytoplankton using ocean-colour data. *Mar. Ecol. Prog. Ser.* 272, 59–68. doi: 10.3354/meps272059

Schoemann, V., Becquevort, S., Stefels, J., Rousseau, V., and Lancelot, C. (2005). Phaeocystis blooms in the global ocean and their controlling mechanisms: a review. *J. Sea Res.* 53, 43–66. doi: 10.1016/j.seares.2004.01.008

Shannon, C. E. (1948). A mathematical theory of communication. *Bell Syst. Techn. J.* 27, 379–423. doi: 10.1002/j.1538-7305.1948.tb01338.x

Siegel, D. A., Behrenfeld, M. J., Maritorena, S., McClain, C. R., Antoined, D., Bailey, S. W., et al. (2013). Regional to global assessments of phytoplankton dynamics from the SeaWiFS mission. *Remote Sens. Environ.* 135, 77–91. doi: 10.1016/j.rse.2013.03.025

Siegel, D. A., Doney, S. C., and Yoder, J. A. (2002). The North Atlantic spring phytoplankton bloom and Sverdrup's critical depth hypothesis. *Science* 296, 730–733. doi: 10.1126/science.1069174

Sommer, U., Padisak, J., Renolds, C. S., and Juhasz-Nagy, P. (1993). Hutchinson's heritage: the diversity-disturbance relationship in phytoplankton. *Hydrobiologia* 249, 1–7. doi: 10.1007/BF00008837

Soppa, M., Hirata, T., Silva, B., Dinter, T., Peeken, I., Wiegmann, S., et al. (2014). Global retrieval of diatom abundance based on phytoplankton pigments and satellite data. *Remote Sens.* 6, 10089–10106. doi: 10.3390/rs61010089

Stramma, L., and Siedler, G. (1988). Seasonal changes in the North Atlantic subtropical gyre. *J. Geophys. Res.* 93, 8111–8118. doi: 10.1029/JC093iC07p08111

Striebel, M., Behl, S., and Stibor, H. (2009). The coupling of biodiversity and productivity in phytoplankton communities: consequences for biomass stoichiometry. *Ecology* 90, 2025–2031. doi: 10.1890/08-1409.1

Subramaniam, A., Brown, C. W., and Hood, R. R. (2002). Detecting Trichodesmium blooms in SeaWiFS imagery. *Deep-Sea Res. II* 49, 107–121. doi: 10.1016/S0967-0645(01)00096-0

Subramaniam, A., and Carpenter, E. J. (1994). An empirically derived protocol for the detection of blooms of the marine cyanobacterium Trichodesmium using CZCS imagery. *Int. J. Remote Sens.* 158, 1559–1569. doi: 10.1080/01431169408954191

Subramaniam, A., Carpenter, E. J., Karentz, P. G., and Falkowski, P. G. (1999a). Optical properties of the marine diazotrophic cyanobacteria *Trichodesmium* spp. I. Absorption and spectral photosynthetic characteristics. *Limnol. Oceanogr.* 44, 608–617. doi: 10.4319/lo.1999.44.3.0608

Subramaniam, A., Carpenter, E. J., and Falkowski, P. G. (1999b). Optical properties of the marine diazotrophic cyanobacteria *Trichodesmium* spp. II. Reflectance model for remote sensing. *Limnol. Oceanogr.* 44, 618–627. doi: 10.4319/lo.1999.44.3.0618

Terseleer, N., Bruggeman, J., Lancelot, C., and Gypens, N. (2014). Trait-based representation of diatom functional diversity in a plankton functional type model of the eutrophied southern North Sea. *Limnol. Oceanogr.* 59, 1958–1972. doi: 10.4319/lo.2014.59.6.1958

Thomas, A. C., Townsend, D. W., and Weatherbee, R. (2003). Satellite-measured phytoplankton variability in the Gulf of Maine. *Cont. Shelf Res.* 23, 971–989. doi: 10.1016/S0278-4343(03)00086-4

Tilman, D., Reich, P. B., Knops, J., Wedin, D., Mielke, T., and Lehman, C. (2001). Diversity and productivity in a long-term grassland experiment. *Science* 294, 843–845. doi: 10.1126/science.1060391

Townsend, D. W., Cammen, L. M., Holligan, P. M., Campbell, D. E., and Pettigrew, N. R. (1994). Causes and consequences of variability in the timing of spring phytoplankton blooms. *Deep Sea Res. I Oceanogr. Res. Pap.* 41, 747–765. doi: 10.1016/0967-0637(94)90075-2

Ueyama, R., and Monger, B. C. (2005). Wind-induced modulation of seasonal phytoplankton blooms in the North Atlantic derived from satellite observations. *Limnol. Oceanogr.* 50, 1820–1829. doi: 10.4319/lo.2005.50.6.1820

Uitz, J., Claustre, H., Morel, A., and Hooker, S. B. (2006). Vertical distribution of phytoplankton commu,ities in open ocean: An assessment based on surface chlorophyll. *J. Geophys. Res.* 111:C08005. doi: 10.1029/2005JC003207

Van Heukelem, L., Thomas, C. M., and Gilbert, P. M. (2002). "Sources of variability in chlorophyll analysis by fluorometry and high performance liquid chromatography in a SIMBIOS inter-calibration exercise," in *NASA Technical Memorandum 2002-211606*. Greenbelt, MD: Goddard Space Flight Center, 50.

Vantrepotte, V., and Melin, F. (2009). Temporal variability of 10-year global SeaWiFS time-series of phytoplankton chlorophyll a concentration. *ICES J. Mar. Sci.* 66, 1547–1556. doi: 10.1093/icesjms/fsp107

Verity, P. G., Brussaard, C. P., Nejstgaard, J. C., van Leeuwe, M. A., Lancelot, C., and Medlin, L. K. (2007). Current understanding of Phaeocystis ecology and biogeochemistry, and perspectives for future research. *Biogeochemistry* 83, 311–330. doi: 10.1007/s10533-007-9090-6

Vidussi, F., Claustre, H., Manca, B. B., Luchetta, A., and Marty, J. C. (2001). Phytoplankton pigment distribution in relation to upper thermocline circulation in the eastern Mediterranean Sea during winter. *J. Geophys. Res.* 106, 19939–19956. doi: 10.1029/1999JC000308

Walther, G. R., Post, E., Convey, P., Menzel, A., Parmesan, C., Beebee, T. J. C., et al. (2002). Ecological responses to recent climate change. *Nature* 416, 389–395. doi: 10.1038/416389a

Wang, G., Lee, Z., Mishra, D. R., and Ma, R. (2016). Retrieving absorption coefficients of multiple phytoplankton pigments from hyperspectral remote sensing reflectance measured over cyanobacteria bloom waters. *Limnol. Oceanogr.* 14, 432–447. doi: 10.1002/lom3.10102

Welschmeyer, N. A. (1994). Fluorometric analysis of chlorophyll a in the presence of chlorophyll b and pheopigments. *Limnol. Oceanogr.* 39, 1985–1992. doi: 10.4319/lo.1994.39.8.1985

Werdell, P. J., and Bailey, S. W. (2005). An improved in-situ bio-optical data set for ocean color algorithm development and satellite data product validation. *Remote Sens. Environ.* 98, 122–140. doi: 10.1016/j.rse.2005.07.001

Whitehead, K., and Vernet, M. (2000). Influence of mycosporine-like amino acids (MAAs) on UV absorption by particulate and dissolved organic matter in La Jolla Bay. *Limnol. Oceanogr.* 45, 1788–1796. doi: 10.4319/lo.2000.45.8.1788

Woodward, E. M. S., and Rees, A. P. (2001). Nutrient distributions in an anticyclonic eddy in the northeast Atlantic Ocean, with reference to nanomolar ammonium concentrations. *Deep Sea Res. II.* 48. 775–793. doi: 10.1016/S0967-0645(00)00097-7

Wright, S. W. (2005). *Analysis of Phytoplankton Populations Using Pigment Markers*. Workshop of pigment analysis of Antarctic microorganisms, University of Malaya, June 20-July 1.

Wright, S. W., and Jeffrey, S. W. (2006). Pigment markers for phytoplankton production. *Mar. Organ. Matter* 2, 71–104. doi: 10.1007/698_2_003

Conflict of Interest Statement: The authors declare that the research was conducted in the absence of any commercial or financial relationships that could be construed as a potential conflict of interest.

frontiers in Marine Science

ORIGINAL RESEARCH
published: 29 June 2017
doi: 10.3389/fmars.2017.00190

Oyster Aquaculture Site Selection Using Landsat 8-Derived Sea Surface Temperature, Turbidity, and Chlorophyll *a*

Jordan Snyder[1], Emmanuel Boss[1], Ryan Weatherbee[2], Andrew C. Thomas[2], Damian Brady[3] and Carter Newell[4]*

[1] Marine In-situ Sound and Color Lab, School of Marine Sciences, University of Maine, Orono, ME, United States, [2] Satellite Oceanography Data Lab, School of Marine Sciences, University of Maine, Orono, ME, United States, [3] Darling Marine Center, School of Marine Sciences, University of Maine, Walpole, ME, United States, [4] Maine Shellfish Research and Development, Damariscotta, ME, United States

Remote sensing data is useful for selection of aquaculture sites because it can provide water-quality products mapped over large regions at low cost to users. However, the spatial resolution of most ocean color satellites is too coarse to provide usable data within many estuaries. The Landsat 8 satellite, launched February 11, 2013, has both the spatial resolution and the necessary signal to noise ratio to provide temperature, as well as ocean color derived products along complex coastlines. The state of Maine (USA) has an abundance of estuarine indentations (~3,500 miles of tidal shoreline within 220 miles of coast), and an expanding aquaculture industry, which makes it a prime case-study for using Landsat 8 data to provide products suitable for aquaculture site selection. We collected the Landsat 8 scenes over coastal Maine, flagged clouds, atmospherically corrected the top-of-the-atmosphere radiances, and derived time varying fields (repeat time of Landsat 8 is 16 days) of temperature (100 m resolution), turbidity (30 m resolution), and chlorophyll *a* (30 m resolution). We validated the remote-sensing-based products at several *in situ* locations along the Maine coast where monitoring buoys and programs are in place. Initial analysis of the validated fields revealed promising new areas for oyster aquaculture. The approach used is applicable to other coastal regions and the data collected to date show potential for other applications in marine coastal environments, including water quality monitoring and ecosystem management.

Keywords: remote sensing, Landsat 8, oyster aquaculture, atmospheric correction, habitat suitability index, sea surface temperature, turbidity, chlorophyll

OPEN ACCESS

Edited by:
Steven G. Ackleson, United States Naval Research Laboratory, United States

Reviewed by:
Nima Pahlevan, Goddard Space Flight Center (NASA), United States
Sabine Schmidt, Centre National de la Recherche Scientifique (CNRS), France

****Correspondence:***
Jordan Snyder
jordan.snyder@maine.edu

Specialty section:
This article was submitted to Coastal Ocean Processes, a section of the journal Frontiers in Marine Science

Received: *28 February 2017*
Accepted: *01 June 2017*
Published: *29 June 2017*

Citation:
Snyder J, Boss E, Weatherbee R, Thomas AC, Brady D and Newell C (2017) Oyster Aquaculture Site Selection Using Landsat 8-Derived Sea Surface Temperature, Turbidity, and Chlorophyll a. Front. Mar. Sci. 4:190. doi: 10.3389/fmars.2017.00190

INTRODUCTION

Oyster aquaculture of the American oyster, *Crassostrea virginica*, is an expanding industry in coastal Maine, USA, with landings worth $4.8 million dollars in 2015, up from $0.6 million in 2003 and increasing by 250% between 2011 and 2015 (Maine DMR commercial landings 2016, www.maine.gov/dmr/). To meet the growing demand for high quality oysters, identification of new sites with the most optimal biophysical conditions for oyster growth is needed. To decrease the risk of choosing an unproductive site, it is crucial that growers have the right tools for site

selection. Currently, the method for selecting a suitable site for bivalve aquaculture is largely based on proximity to existing sites or trial and error. These methods are inefficient because they may not consider the specific temperature and nutritional conditions needed for the species to grow, each of which affect how fast it takes to reach market size (Rheault and Rice, 1996; Hawkins et al., 2013b). Recent advances in remote sensing techniques enable satellite imagery to help in site selection (e.g., Thomas et al., 2011). By visually inspecting information products calculated from processed Landsat 8 satellite images, estuaries that reach relatively warm temperatures (above 20°C), support high levels of chlorophyll in the summer (above 1 μg Chl l^{-1}), and exhibit low turbidity (below 8 NTU) can be efficiently identified as potential oyster growing areas.

The spatial resolution of standard global ocean color satellites (typically 1 × 1 km) is too coarse to provide usable data within the many estuaries and embayments along coastal Maine where much of the suitable habitat for oyster aquaculture is located. The Thermal Infrared Sensor (TIRS) and the Operational Land Imager (OLI) are sensors on the Landsat 8 satellite, launched February 11, 2013. These sensors have both the spatial resolution (100 m for infrared data and 30 m for multi spectral visible data) and the necessary signal to noise ratio to provide useful temperature as well as ocean color derived products along the Maine coastline (Vanhellemont and Ruddick, 2014). In this paper, we used a combination of empirical and analytical approaches to derive temperature, turbidity and chlorophyll products from Landsat 8 data for the coast of Maine.

Although, it was designed for terrestrial monitoring, Landsat 8 data was shown to be useful for marine applications, provided that a reliable atmospheric correction is applied (Pahlevan et al., 2014; Franz et al., 2015). An atmospheric correction is necessary for satellite remote sensing because in the visible wavelengths, the majority of the signal observed by the satellite is from gas and aerosol particles in the atmosphere (e.g., Mobley et al., 2016). We used the NASA[1] software platform SeaDAS, and algorithms implemented within it, together with an empirical approach to derive chlorophyll *a* and turbidity.

As with any instrument, there are limitations to using Landsat 8 imagery for coastal monitoring. Compared to other space-borne instruments such as AVHRR and MODIS, that have daily coverage, the temporal resolution of Landsat 8 is low. The 16 day repeat coverage makes it insufficient to observe short-term changes (due to weather, storm events, etc.), but it is useful for describing patterns such as seasonal changes, which is informative for monitoring long-term conditions and relative spatial differences between sites. Additionally, cloud cover decreases the probability of clear overpasses; most of the clear images we retrieved come from summer and fall months (June through November), the seasons with the least amount of cloud cover. Fortunately, this is also the critical time of year for oyster aquaculture as it overlaps the growing season.

Ocean color measurements can be used to describe components of water quality, such as turbidity and chlorophyll-*a* (Chl *a*) concentration (O'Reilly et al., 1998). Algorithms have been developed that can estimate concentrations of these components by (1) retrieving radiant flux from the satellite which includes both target surface and atmosphere components, (2) correcting for the signal from the atmosphere, (3) transforming radiant energy collected by the satellite sensor into remote sensing reflectance (R_{rs}), and (4) converting R_{rs} values into products. Reflectance in the red wavelengths of light is used to estimate suspended particulate matter (Vanhellemont and Ruddick, 2014; Dogliotti et al., 2015), while reflectance in the blue and green wavelengths is used to estimate Chl *a* biomass (a proxy of phytoplankton biomass) (Franz et al., 2015; Mobley et al., 2016). Remote sensing products have been used for monitoring in several sites around the world (Radiarta et al., 2008; Wang et al., 2010; Thomas et al., 2011; Aguilar Manjarrez and Crespi, 2013; Gernez et al., 2014) to assess the impacts of turbidity and Chl *a* on aquaculture.

Optimal conditions for oyster growth have been determined primarily through the use of various types of ecophysical models. Habitat suitability models were first applied to the restoration of the American oyster, *Crassostrea virginica*, on the warm southeast Atlantic coast of the U.S. (Cake, 1983; Soniat and Brody, 1988; Barnes et al., 2007). These models considered bottom substrate and suitable salinities to maximize oyster survival in relation to siltation and protozoan parasites. More recently, Carrasco and Barón (2010) used satellite imagery to map temperatures which defined the potential range for Pacific oyster populations in South America. Statistical models relating organism growth, biomass and economic yield illustrate the importance of site specific environmental variables (water velocity, food concentration) on farm yields (Pérez-Camacho et al., 2014). Powell et al. (1992) and Hoffmann et al. (1992) modeled American oyster filtration rate and growth as a function of animal size, water temperature and total particulate matter, with a negative effect at high suspended loads, although selection for organic matter by the oyster when producing pseudofeces (Newell and Jordan, 1983) was not considered. Gernez et al. (2014) used 300 m pixel-size suspended particulate distributions derived from MODIS to assess the impact of suspended particulate matter concentration on oyster farming sites, and Gernez et al. (2017) improved on this study by using Sentinel 2 with a 10 m resolution.

Crassostrea virginica is somewhat unusual in that its filtration rate is a strong function of temperature (from 8°C to a maximum at 30°C; Loosanoff, 1958) compared to other bivalves where the filtration rate is relatively independent of water temperature. Therefore, temperature is of primary importance in site selection for oyster aquaculture in the relatively heterogeneous and strongly seasonal sea surface temperature regime of the colder Maine waters. Bivalve feeding and growth is also a positive function of phytoplankton concentration (Hawkins et al., 2013b), so chlorophyll *a* is considered the next most important factor for site selection. In general, total suspended particulate matter has a negative effect on bivalve growth by diluting the organic matter at high levels (Widdows et al., 1979; Barillé et al., 1997). For bivalves, the proportion of phytoplankton in the suspended particles is a key aspect of site suitability (Newell et al., 1989).

[1]NASA (2016). Available online at: https://oceancolor.gsfc.nasa.gov/atbd/chlor_a/

Another important factor in oyster site selection is water velocity, which delivers food to populations of oysters and other bivalves at commercial-scale densities. Congleton et al. (1999) developed a GIS system that included water velocity and intertidal elevation to predict optimal locations for clam (*Mya arenaria*) mariculture. Within a coastal bay, ShellGIS (Newell et al., 2013) used the growth model Shellsim (Hawkins et al., 2013a) to predict oyster growth and yield as a function of water quality (temperature, salinity, and food concentration), husbandry and seeding density, and water velocity on a 50 m farm scale. Water velocity is not a limiting factor in the coast of Maine where tidal amplitudes and currents are large. Hence, the primary screening variables of temperature, chlorophyll *a*, and turbidity are effective tools to identify suitable locations on the scale of bays and estuaries, and provide novel opportunities for mapping potential zones for aquaculture development over large and complex coastal regions such as Maine.

In this paper, we demonstrate a methodology to obtain SST and calibrated water quality products from the TIRS and OLI sensors on board Landsat 8, and validate them with measurements in coastal Maine waters. We compute uncertainties based on match-ups between local data and that derived from satellites and discuss how temporal and spatial sampling and adjacency effects affect the accuracy of remote sensing products. These processed satellite products are then used to establish an oyster suitability index and its distribution in mid-coast Maine. The consistency between high values of the index and sites of existing oyster farms provides validation for the oyster suitability index derived here.

METHODS

Study Area

The coast of Maine includes a series of fjards (shallow and broad fjords) and jagged embayments carved by receding glaciers during the Pleistocene epoch. *In situ* samples were collected and monitoring buoy systems were maintained in two of these estuaries, the Damariscotta River and Harpswell Sound, over the course of several years and we used them here to validate Landsat 8-derived products on the Maine coast (triangles on **Figure 1**). We chose to focus on the Damariscotta River because it has existing aquaculture operations (currently 75% of the oysters produced in Maine, Maine DMR, 2015) and suitable sampling access. The Damariscotta River Estuary is 29 km long, has a mean summer flushing time of 4–5 weeks, and is dominated by strong tides with amplitudes of up to 3.35 m (McAlice, 1977). Sediment resuspension in this estuary is highest at low tide, and lowest at high tide. The estuary is highly saline, ranging from 25 to 32.5 psu, with a small amount of fresh water input from Damariscotta Lake into Salt Bay at its northern reach. The bottom substrate is a soft mud, composed of clay to sandy silts with an average water depth of 15.25 m. These attributes, combined with suitable water temperatures, turbidity, and Chl *a* concentrations, make the Damariscotta River an ideal place for growing market-size oysters and other bivalve species, and make it an excellent reference point for expanding the aquaculture industry along the coast of Maine.

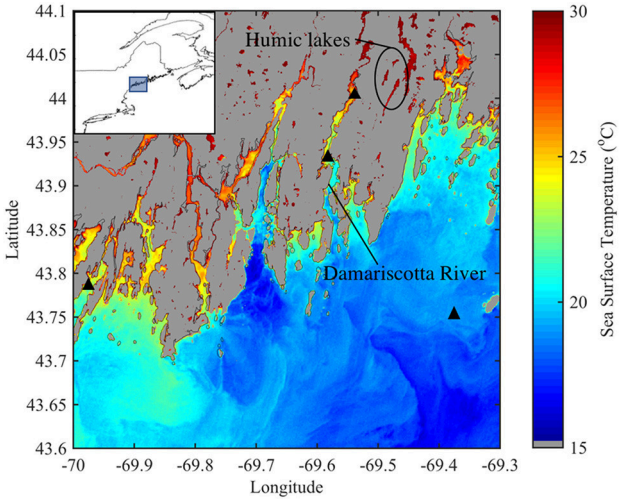

FIGURE 1 | Sea surface temperature on the coast of Maine, USA, on July 14, 2013 from Landsat 8 infrared data. Triangles indicate locations of validation buoys. Freshwater lakes used for the atmospheric correction are circled at ~44′N, −69.5′E.

Processing of Sea Surface Temperature

All applicable raw data from Landsat 8 were downloaded from the USGS Earth Explorer website from the period 2013 to 2016 (USGS, 2016). To calculate SST, we used brightness temperature values from Landsat 8's Thermal Infrared Sensor (TIRS) Band 10. There are stray light issues associated with the two TIRS bands (Band 10 and Band 11) due to the curvature of the optical lens (Montanaro et al., 2014). Of these two bands, we chose to use thermal Band 10 because it has lesser issues of the two (see Discussion Section). Each image was processed in the NASA SeaDAS platform up to level 2 to retrieve latitude and longitude arrays, a geo-registered image, and the associated land/cloud mask (georeferencing is maintained, as it is provided from USGS).

Regressions between coincident, atmospherically corrected NOAA AVHRR satellite derived SST and that derived from Landsat 8's brightness temperature were used to create an SST product from each Landsat 8 image (similar to Thomas et al., 2002). This regression process, de-facto, acts as the atmospheric correction for the Landsat SST product assuming that (1) the atmosphere does not change in the time interval between AVHRR and Landsat data acquisition and (2) the atmosphere is homogenous across the Landsat scene. Example results from this procedure are displayed on **Figure 1** above. Of the four to eight AVHRR images captured on the same day as each Landsat 8 overpass, we subjectively chose the image with the least amount of cloud cover, best geolocation, and most realistic SST patterns, for the regression (see Section A in Supplementary Material for detailed description). The data for the regression were selected from cloud free and offshore areas to accommodate the lower AVHRR resolution (1 km vs. Landsat 8 100 m resolution). The best results were achieved using cloud free areas with a high dynamic range in SST. The resulting regression equation between

the signal of Landsat's Band 10 and the AVHRR-based SST was then applied to the full resolution Landsat 8 image.

On average, there are approximately four AVHRR images per day. Due to changing cloud cover and orbit configuration between available AVHRR images, it was sometimes necessary to use an image more distant in time (but less cloudy) from the Landsat 8 overpass, despite a temporally more proximate one being available. However, because Gulf of Maine SST patterns change relatively slowly (<0.4°C over 12 h at buoy 44005, www.neracoos.org), we consider this an acceptable tradeoff to maximize the number of quality AVHRR pixels that were used in the regression. The mean offset time between the Landsat 8 and AVHRR overpasses was 6.8 h, with a minimum of 2.3 h, a maximum of 30.2 h, and a standard deviation of 5.8 h. The entire area of spatial overlap between AVHRR ocean pixels and Landsat 8 ocean pixels is used for most scenes. Landsat 8 images were subsampled to every 10th pixel in both x and y dimensions to reduce the data volume for the regressions. Depending on the distribution of clouds, the regression area was restricted to areas without cloud contamination (or poorly masked clouds) in some instances. Cloud and land were dilated by two pixels in the AVHRR image to reduce occurrences of cloud ringing artifacts and nearshore land contamination. The regression process was iterative. After each iteration, all Landsat 8 and coincident AVHRR pixels that were >1 standard deviation from the linear best fit line of the relationship were removed and the regression was re-calculated with the remaining data. The iteration process was repeated until the Pearson correlation coefficient for the two datasets stabilized or started to worsen (which is due to uncertainties in the approach). The final regression equation was then applied to each Landsat 8 B10 pixel to obtain a Landsat SST image.

Ocean Color

Ocean color multispectral data, which responds to the effects of oceanic particles and dissolved matter, are measured from space by the Operational Land Imager (OLI) radiometer on board Landsat 8. The radiance measured includes contributions from the target (the surface water column), the air-water interface, and the background (particles and gases from nearby pixels and particles in the atmosphere) (Mobley et al., 2016). To obtain information on the oceanic constituents, the atmospheric contribution to the signal needs to be removed (a process known as "atmospheric correction," see below). From the corrected water-leaving radiance, we computed the reflectance (denoted as R_{rs}) from which the products of turbidity and Chl *a* are derived.

Atmospheric Correction for R_{rs}

Given the low turbidity in our area of investigation (see Section Retrieval of Turbidity below), we chose to use a combination of the Near Infrared (NIR) and Short Wave Infrared (SWIR) channels for atmospheric correction in SeaDAS. The NIR was important to use because of its higher signal/noise ratio (NIR band had a ratio of 67 in low turbidity waters, while SWIR bands had ratios of 9 and 10), and the SWIR was important because it has the strongest absorption for water which helps differentiate in-water sediments from atmospheric aerosol particles (Franz et al., 2015; Pahlevan et al., 2017). Applying this atmospheric correction over a scene resulted in a per-pixel correction, each with its own angstrom coefficient. The angstrom coefficient is the exponent of a power-law fit to the spectral aerosol optical thickness. We adjusted this coefficient because the automatic per-pixel retrievals provided by SeaDAS resulted in negative reflectance values at several freshwater bodies that were used as black body targets for our atmospheric correction scheme. These lakes should have near-zero or positive retrievals at the 443 nm band. The primary reason for adjusting the angstrom coefficient is that the aerosol models used for processing data from satellites such as SeaWiFs and MODIS (Ahmad et al., 2010), do not represent the aerosol conditions for our study area, the coast of Maine (Pahlevan et al., 2017). We then chose a single angstrom coefficient per scene (from within the distribution of inverted angstrom values), by requiring that the minimal value of $R_{rs}(443)$ in a scene, measured in a very humic lake, be zero. Most freshwater lakes on the coast of Maine are humic and have high levels of chromophoric dissolved organic matter, CDOM, which gives them a brown hue and attenuates light quickly (Rasmussen et al., 1989; Roesler and Culbertson, 2016) and are not turbid. Several freshwater lakes with high CDOM within our study region (Muddy Pond, Biscay Pond, and Damariscotta Pond circled in **Figure 1**) were selected as suitable reference targets to correct the entire Landsat 8 scene. In each individual satellite image, the darkest lake (where $R_{rs}(443)$ is near zero) was used to determine the angstrom coefficient. Analysis of a sample of water from one of these lakes verified that the expected $R_{rs}(443)$ is zero within the uncertainty of the satellite retrieval (Table B1 in Supplementary Material). We subsequently applied the retrieved angstrom in SeaDAS to the entire scene to recalculate R_{rs} at every wavelength. Resulting R_{rs} values were then used to compute turbidity and Chl *a*.

Retrieval of Turbidity

Turbidity, T, [note that 1 mg l^{-1} of suspended particulate matter, SPM, is similar, within the range of values found in our study area, to a turbidity of 1 NTU (Pfannkuche and Schmidt, 2003)], was calculated over the entire satellite scene using atmospherically corrected $R_{rs}(655)$ following Nechad et al. (2010):

$$\mathrm{T} = \mathrm{A}^{\rho}\frac{\rho_{\mathrm{w}}}{1-\rho_{\mathrm{w}}/\mathrm{C}^{\rho}}[\mathrm{gm}^{-3}] \quad (1)$$

where $\rho_w = R_{rs}(655)^{*}\pi$ is the atmospherically corrected and derived water leaving reflectance, $A^{\rho} = 289.1$ and $C^{\rho} = 16.86$ (Nechad et al., 2010).

Retrieval of Chlorophyll- *a*

Chl *a* was calculated using the OC3 algorithm (O'Reilly et al., 1998) from the NASA Ocean Biology Processing Group, using the above-calculated R_{rs}:

$$\log_{10}(\mathrm{Chl}\,a) = \mathrm{a}_0 + \sum_{\mathrm{i}=1}^{4}\mathrm{a}_{\mathrm{i}}\log_{10}\left(\frac{\mathrm{R_{rs}}(\lambda_{\mathrm{blue}})}{\mathrm{R_{rs}}(\lambda_{\mathrm{green}})}\right)^{\mathrm{i}} \quad (2)$$

where a_0 and a_i are sensor specific coefficients, and R_{rs} (λ_{blue}) and R_{rs} (λ_{green}) are the greatest of values from 443 > 483 and 555 nm, respectively, on the OLI sensor aboard Landsat 8 (NASA, 2016)[1]. (Note: SeaDAS applies coefficients to convert broad band Landsat 8-based R_{rs} to 11 nm narrow bands for which this equation was developed).

Validation with *In situ* Data

Validation was carried out for SST, turbidity, and Chl *a*, using data from water samples and three oceanographic buoy observing systems. Historical data was downloaded from the NERACOOS (Northeastern Regional Association of Coastal Ocean Observing Systems) buoys E01 and I01 operated by the University of Maine in the Gulf of Maine, a Land/Ocean Biogeochemical Observatory (LOBO) buoy operated by Bowdoin College in Harpswell Sound, and two LOBO buoys at the University of Maine's Darling Marine Center in the Damariscotta River (**Figure 1**. Note: NERACOOS Buoy I01 is outside the map). The LOBO buoys were equipped with sensors that remain at a depth of 1.5 m and maintained and cleaned to prevent biofouling approximately every 2 weeks. Temperature data were collected from all three observing systems and compared to Landsat 8 SST. A total of 52 matchups were identified originating from 31 clear overpasses from 2013 to 2016.

In situ turbidity measurements were used to validate satellite-derived turbidity during eight overpasses in 2015 and 2016. Data were collected from the LOBO buoys in the Damariscotta River, and were measured by a WETLabs WQM sensor capable of measuring turbidity from 0 to 25 NTU (using a backscattering sensor measuring light scattered in the back direction at a 20 nm bandwidth around 700 nm). This sensor was vicariously calibrated against a Hach turbidity sensor (which conform to the ISO 7027:1999 turbidity standard). The buoy data were calibrated using a regression between Hach turbidity samples and the LOBO turbidity using a factor of 1.58 (Table B2 in Supplementary Material).

In situ Chl *a* was used to validate satellite-derived Chl *a* during the same eight overpasses in 2015 and 2016. *In situ* Chl *a* data were measured by the Damariscotta River LOBO buoys' WETLabs fluorescent sensor capable of measuring Chl *a* concentrations from 0 to 50 $\mu g l^{-1}$. The buoy data were calibrated using a regression between extracted Chl *a* samples and the LOBO Chl *a* using a factor of 1.71. Water samples were collected in triplicate, at the surface, and in opaque bottles within 30 min of each overpass and filtered for extraction on a Turner 10 AU fluorometer per standard protocol (Holm-Hansen and Riemann, 1978). Statistics were calculated for regressions between the *in situ* and satellite-derived data: Root mean square difference, RMSD, root mean square relative difference, RRMSD, and coefficient of determination, r^2 (see **Figures 2–4** below).

Satellite Imagery for Oyster Suitability Index

An Oyster Growth Suitability Index (OSI) was designed using the satellite-derived SST, turbidity, and Chl *a*. A weighting and indexing procedure of these three physical parameters described ideal, moderate, and poor conditions for growing

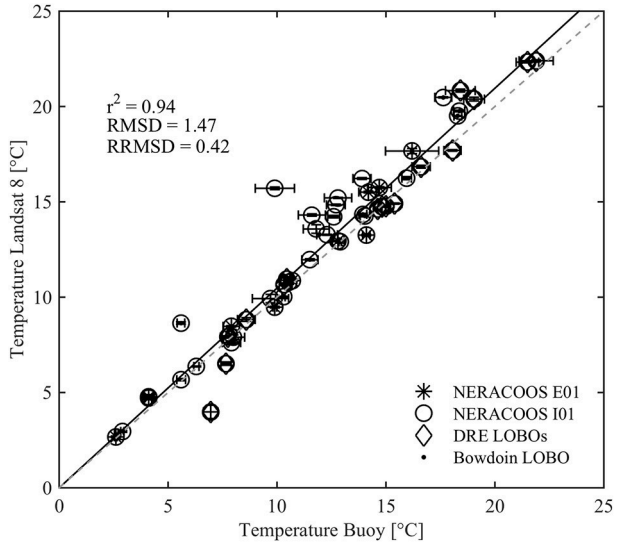

FIGURE 2 | Type II linear regression (black line) between Landsat 8-derived SST and SST measured by sensors on oceanographic buoys. Different symbols represent measurements by the three different observing systems. Vertical error bars are the standard deviation of a 5 × 5 pixel box. Horizontal error bars are the standard deviation of daily temperature at each buoy. Dashed gray line is 1:1.

market sized oysters in surface culture. The criteria for the index were chosen based on published studies of environmental effects on oyster growth, recognizing that the concentration of organic detritus, known to be an important component of oyster diet, was not available. Temperature is the most important variable for oyster growth, especially in the cold waters of coastal Maine as it controls the filtration rate of oysters [and therefore given an importance weight factor of 80% in our OSI; (Loosanoff, 1958; Hoffmann et al., 1992; Ehrich and Harris, 2015)]. Oyster clearance of algae is a positive function of algae concentration, as large amounts of pseudofeces are produced at high algal concentrations. Because of this, we weighted Chl *a* at 15%, with poor conditions as <1 or >10 μg Chl l^{-1}, moderate conditions as 1 to 3 μg Chl l^{-1}, and ideal conditions as 3 to 10 μg Chl l^{-1} (Epifanio and Ewart, 1977; Hawkins et al., 2013b). Turbidity, an index of suspended particulate matter, has a negative effect on oyster feeding when at high concentrations, by diluting algal cells with largely inorganic matter. Haven and Morales-Alamo (1966) observed large amounts of pseudofeces production by Eastern oysters at concentrations of suspended particulate matter above 10 mg l^{-1}. Thus, we gave turbidity a weight of 5% and designated poor conditions as >10 mg l^{-1}, moderate conditions between 8 and 10 mg l^{-1} and ideal conditions <8 mg l^{-1}. Hoffmann et al. (1992) also modeled oyster filtration as a positive function of water temperature and a negative function of high suspended loads.

These weights are subjective and were chosen as a starting point for an OSI. They could be refined in the future (Gong et al., 2012), based on sensitivity analysis of the relative importance of these factors measured simultaneously with growth measurements *in situ*. The resulting OSI is the sum of the weighted conditions on a scale from 0 to 1, where pixels with

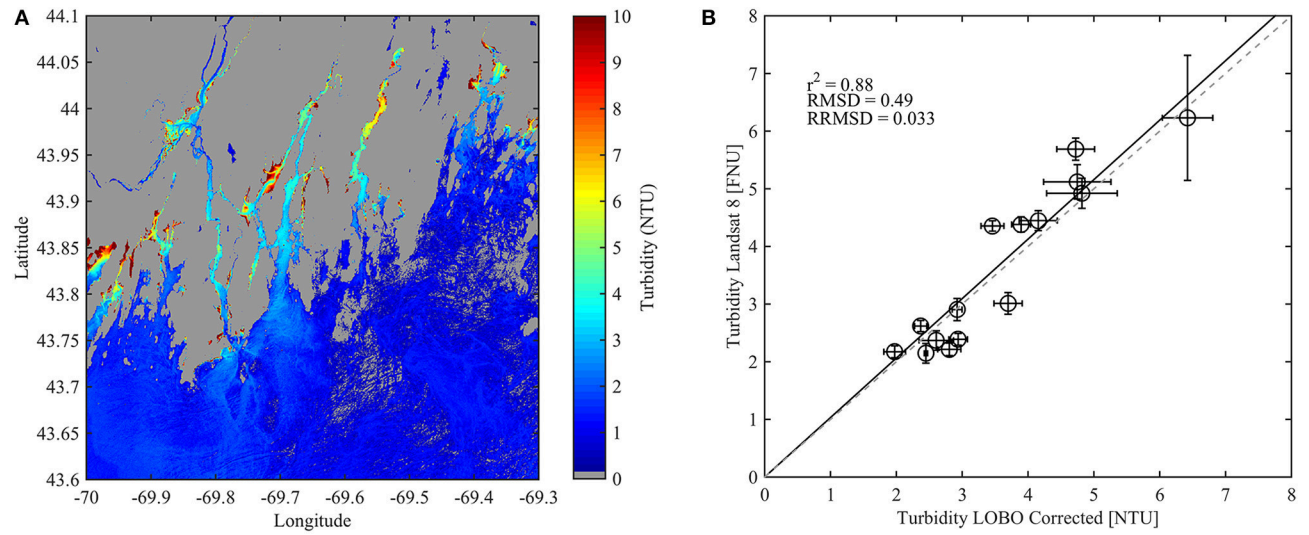

FIGURE 3 | (A) Landsat 8-derived turbidity along mid-coast Maine on July 14, 2013. **(B)** Type II linear regression (black line) between Landsat 8-derived turbidity and turbidity measured by LOBO buoys. Vertical error bars are the standard deviation of a 5 × 5 pixel box centered at the *in situ* measurement. Horizontal error bars are the standard deviation of turbidity for 4 h at each buoy. Dashed gray line is 1:1.

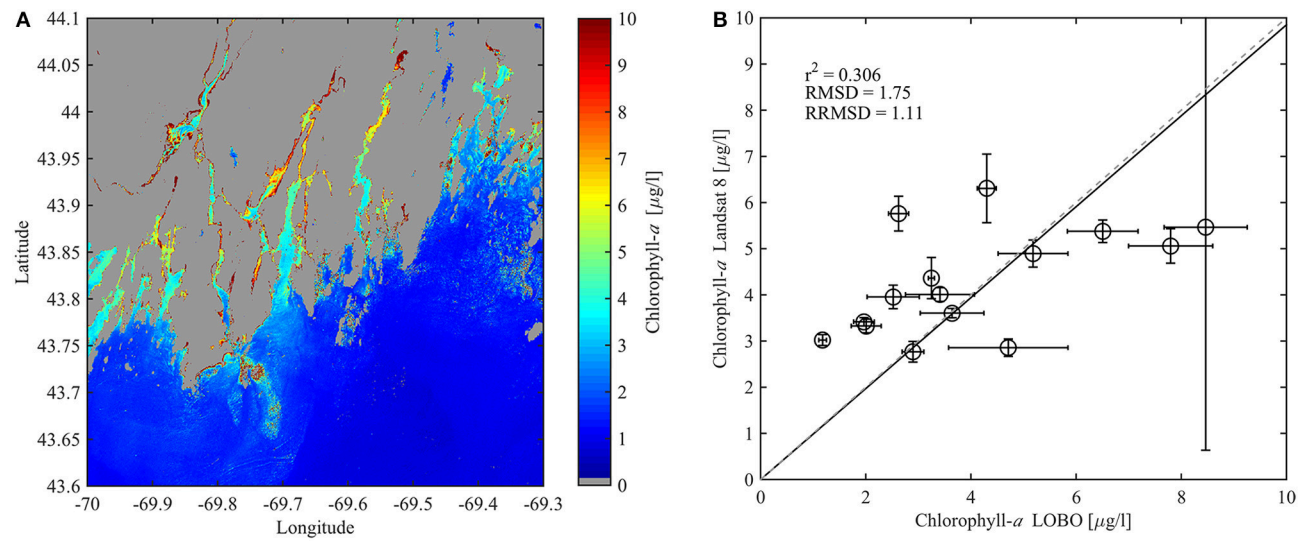

FIGURE 4 | (A) Landsat 8-derived chlorophyll-*a* along mid-coast Maine on July 14, 2013. **(B)** Type II linear regression (black line) between Landsat 8 derived chlorophyll-*a* and chlorophyll-*a* measured by LOBO buoys. Vertical error bars are the standard deviation of a 5 × 5 pixel box centered at the *in situ* measurement. Horizontal error bars are the standard deviation of chlorophyll-*a* for 4 h at each buoy. Buoy chlorophyll-*a* was calibrated with chlorophyll extraction samples. Dashed gray line is 1:1.

a value of 1 represent waters where an oyster is likely to grow to market size within 2 years:

$$\mathrm{OSI} = \sum_{i=1}^{n} \mathrm{SI_i} \times \mathrm{w_i} \quad (3)$$

where $\mathrm{SI_i}$ is the value of the environmental variable i, $\mathrm{w_i}$ is the weight of the variable i, and n is the number of environmental variables (three in our case). At any location where one of the three indices reported poor conditions, the OSI was set to zero. We combined images from each year during the same month to create a monthly averaged index.

RESULTS

Validation with *In situ* Data

The Landsat 8 SST retrievals correlated well with *in situ* temperatures (RMSD is 0.82°C, RRMSD is 4%, $r^2 = 0.94$)

with, on average, 1°C higher SST values than those measured by the buoy sensors, especially in warmer waters (**Figure 2**). However, variability of the buoy measurements is larger at higher temperatures when horizontal gradients in temperature were also larger.

The Landsat 8 turbidity estimates correlated well with *in situ* turbidities (RMSD 0.49 NTU, RRMSD 3%, max absolute deviation is 0.96 and maximal relative deviation is 15%, $r^2 = 0.88$), with an uncertainty of 0.5 NTU, on average (**Figures 3A,B**). Uncertainties are larger at higher turbidities for both the buoy and the satellite algorithm.

Landsat 8 based Chl *a* did not correlate well with *in situ* Chl *a* (RMSD is 1.75 μg Chl l^{-1}, RRMSD is 110%, max absolute deviation is 3.14 μg Chl l^{-1}, max relative deviation is 156%, $r^2 = 0.31$). Below 5 μg Chl l^{-1}, the OC3 algorithm produced higher Chl *a* values than those measured by the buoy sensors (**Figures 4A,B**). Above 5 μg Chl l^{-1}, the buoy measurements were higher than the satellite-derived Chl *a*. Uncertainties are larger at higher Chl *a* for the buoys and the satellite algorithm. Out of the three parameters derived from Landsat 8, this algorithm has the highest relative deviation of 156%, with an average relative difference of 110%, which is significantly worse than the average relative difference of 30% for chlorophyll algorithms in the open ocean (but see Discussion).

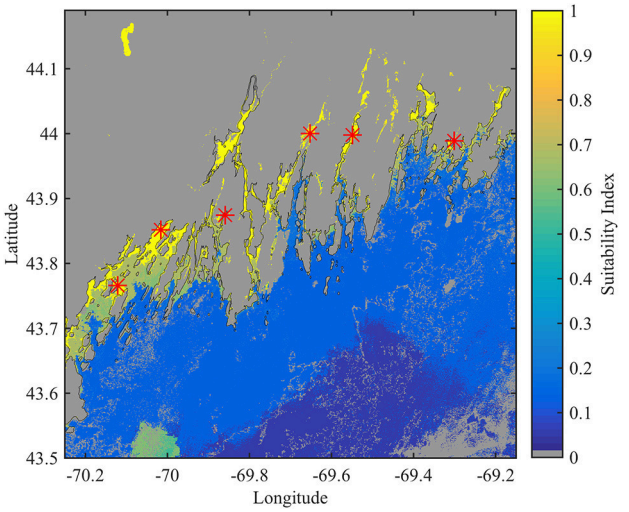

FIGURE 5 | Oyster suitability map based on Landsat 8-derived SST, turbidity, and chlorophyll-*a*. Map is an average of all images in the month of July. Yellow areas indicate ideal conditions, green areas indicate moderate conditions, and blue areas indicate poor conditions. Red stars indicate existing oyster farms. Index criteria is given in Section B in Supplementary Material.

Satellite Imagery for Oyster Growth Conditions

Monthly maps of Oyster Suitability Index (**Figure 5**) were created using averaged monthly satellite images (Section B in Supplementary Material). Most existing oyster aquaculture areas (indicated by red stars on **Figure 5**) fall within the highest suitability index during the month of July. Suitability maps for August and September exhibit a similar pattern of ideal, moderate, and poor growing areas as the map for July (**Figure 5**), but, in general, with slightly lower values due to colder temperatures (average monthly temperatures were highest during July). The Oyster Suitability Index map provides two important findings: (1) it is consistent in its finding that the Damariscotta River as a suitable place to grow oysters in aquaculture and therefore an important test and verification site for using remote sensing tools, and (2) it maps many new locations along the coast that host similar conditions (Table B2 in Supplementary Material).

DISCUSSION

Satellite Imagery

The correspondence between the Landsat 8 satellite-derived products and *in situ* measurements demonstrates the capability of generating SST, turbidity, and Chl *a* maps along the jagged coast of Maine. While these data show encouraging results, there are several factors from our study that could improve the present algorithms. Stray light issues arise if the temperature from an object outside of the field of view of the imager affects the pixel within the field of view. Fortunately, most water along the coast of Maine is vigorously tidally mixed (~3 m tidal range), and thus data from the center of channels can be used to infer SST throughout those channels (Thornton and Mayer, 2015). Within the estuaries, however, a TIRS pixel (which is three times as wide as an OLI pixel) next to land may be incorrectly colder (if the land is colder) or warmer (if the land is warmer). However, our match-ups with temperature and turbidity products suggest adjacency and stray light have not degraded the data significantly, and differences are likely due to noise as opposed to systematic bias.

Limitations in Validation Process

Validation of Landsat 8 products with *in situ* measurements is necessary to assess the accuracy of the algorithms for retrieving bio-physical products. Some of the discrepancy in matchups between *in situ* data and satellite-derived products can be explained, while others require further investigation. One reason that Landsat 8 SST values may be higher than most buoy measurements (**Figure 2**) is because the SST estimates come from radiation emitted from the top few micrometers of the sea surface, while the buoy sensors are located about 1.5 m below the surface. In the daytime images, the subsurface water is likely cooler than the surface skin due to physical and environmental factors (Donlon et al., 2002; Ward, 2006; Padula et al., 2010). Despite this bias, the Landsat 8 SST (derived by regressing with atmospherically-corrected AVHRR SST) performed well along the coast of Maine and our results suggest that our approach could be used as a tool for measuring SST where high spatial resolution is desired.

A vigorous semi-diurnal tide characterizes the Damariscotta River and delivers shelf water into the upper reaches of the estuary. The tidal cycle was evident in the daily turbidity signal (not shown) from the LOBO buoys: at low tide, there are elevated levels of turbidity whereas at high tide there is less turbidity

(due to the increase in turbidity from the mouth to the end of the estuary). The horizontal error bars in **Figure 3** represent the variability during a 4-h period around each satellite overpass time, and highlight the importance of simultaneous sampling for *in situ*—satellite matchups. The turbidity algorithm performs well within our uncertainties in this context.

Landsat 8-derived Chl *a* often differs significantly from the LOBO buoy measurements. We note that there are significant uncertainties associated with both measurement techniques (Cullen, 2008). Landsat 8-derived Chl *a* is retrieved from R_{rs} using an algorithm calibrated in the open ocean, whereas the LOBO buoys measure Chl *a* fluorescence which is regressed against chlorophyll measured on water samples. Estimating Chl *a* from fluorescence is the most common way to measure Chl *a* but is affected by several processes that contribute to uncertainty. These include changes in fluorescence yield due to variability in the algal taxonomy, nutrient stress, and photo-acclimation, to name a few (Cullen, 1982). In addition, concentrations of phytoplankton have been observed in the Damariscotta River to vary on time scales of hours (Thompson and Perry, 2006) potentially making mismatches in time problematic.

Non-photochemical quenching (NPQ; when phytoplankton decrease their fluorescence at a maximum light harvesting level, e.g., Cullen, 1982) contributes to variability. However, we find nighttime measurements to be comparable to daytime measurements (Figure B1 Supplementary Material) for the Damariscotta River. Therefore, the offset in Chl *a* is likely not due to errors induced by NPQ. Another potential error is associated with the OC3 algorithm, which estimates Chl *a* as a ratio of R_{rs} in the blue and green channels. The blue channel is especially influenced by colored dissolved organic material (CDOM). Independent changes of CDOM will affect the OC3 chlorophyll estimate (Siegel et al., 2005). Along the coast of Maine, where there are coastal forests and marshes, CDOM is in high concentration and variable (Roesler and Culbertson, 2016). In coastal areas and estuaries rich in CDOM it is likely that absorption by dissolved organic matter would bias the OC3 algorithm. It is likely that a local algorithm that takes local CDOM concentration into account, could improve Chl *a* retrievals from Landsat 8.

Oyster Suitability Index

The OSI provided in this paper is intended to supplement other tools that determine optimal oyster growing areas. The satellite images, due to their low temporal resolution, provide a climatological monthly average of coastal temperature, which does not resolve the day degree input necessary in models for temperature-dependent shellfish growth. In addition, other important environmental factors such as salinity, water depth, bottom type, and water velocity (necessary for oyster growing), are not considered (Theuerkauf and Lipcius, 2016). Organic detritus is known to be an important component of bivalve diets (Dame and Patten, 1981; Bayne et al., 1993; Barillé et al., 1997), but currently cannot be measured using satellite imagery. It is conceivable that detritus could be related to the ratio of turbidity and Chl *a*, after light acclimation has been accounted for. Our index therefore provides guidance on suitable water quality conducive to rapid growth, but not sufficient information to model site specific production capacity for suspended or bottom culture.

Although, satellite thermal data is only sensitive to the temperature of the top few micrometers of water, and ocean color is sensitive only to one optical depth (which varies, but on the Maine coast is usually the top 1 or 2 m), these data are relevant to the whole water column if the water column is often vertically well-mixed. Indeed, many estuaries on the Maine coast are well-mixed (e.g., the Sheepscot and Medomak Rivers, Mayer, 1996; Thornton and Mayer, 2015), which makes it relevant for our OSI (Table B2 in Supplementary Material). Finally, local knowledge is invaluable for the expansion of an existing industry on the coast of Maine, and stakeholder input is essential for improving such an index with local information such as site accessibility, town ordinances, etc.

Future Work

Continued sampling during the spring and summer of 2017 will provide a more complete dataset for optimizing Landsat-derived products in Maine. A local algorithm for Landsat 8-derived Chl *a* along the coast of Maine could be constructed with additional *in situ* samples collected during satellite overpasses. There are several approaches to tune a local algorithm. An empirical approach, such as the OC3 algorithm, uses a relationship between *in situ* measurements and ratios of the satellite sensor bands. A second method involves using a generalized inherent optical properties inversion (GIOP, Werdell et al., 2013). This method solves for Chl *a*, SPM, and CDOM using known spectral shapes of optical properties (for phytoplankton and non-algal absorption and backscattering by particles) and known values of absorbance and backscattering of water (which are weak functions of salinity and temperature). Databases of collection sites located in the Damariscotta River and Harpswell Sound could tune the shapes of IOPs for the GIOP algorithm and provide an estimate of Chl *a* in these two estuaries. Furthermore, *in situ* samples from various locations along the coast will validate the local algorithm so that its use can be expanded from the Damariscotta River to other places along the coast.

Obtaining more parameters from Landsat 8, such as colored dissolved organic matter (CDOM), would provide additional information to growers and ecosystem managers. Franz et al. (2015) and Slonecker et al. (2015) describe the potential of using Landsat 8 for remote sensing of CDOM in conjunction with *in situ* measurements. A reliable CDOM product would also improve the algorithm for Chl *a*, as the presence of CDOM often contributes to an overestimation of Chl *a*. Furthermore, high levels of CDOM are correlated with low salinity in estuaries (Carder et al., 1989; D'Sa et al., 2002; Mayer, pers. commun.). CDOM would therefore be helpful to identify areas with significant freshwater influx because these often bring concentrations of bacteria that negatively affect clamming and other fisheries (Shumway et al., 1988; Kleindinst et al., 2014).

Validation of our OSI is provided by the fact that current farms are all located where the OSI is high. Further validation and refinement with direct measurements of oyster growth, will likely improve on this OSI. Note: OSI does not include

information about site closures, bottom depth, or residential restrictions. Future work should include this information for a more comprehensive index.

CONCLUSION

A satellite-derived Oyster Suitability Index can act as a powerful tool for oyster aquaculture site selection and the expansion of the shellfish farming industry. It shows that suitable biophysical conditions for oyster growth exist in many areas of the Maine coast. Suitability indices for other bivalve species, such as mussels, scallops, and finfish along the coast, or other applications requiring high spatial resolution, can be developed based on the algorithms presented here.

Our results show that Landsat 8-derived data are useful for retrieving SST, turbidity, and Chl *a* in coastal waters of Maine, USA, and can be applied to other narrow estuaries around the world. The novelty of using Landsat 8 in this context offers a unique opportunity to map and monitor coastal waters at an unprecedented spatial resolution. Inclusion of data from other satellites with complimentary sensor suites such as Sentinel 2A, and the recently launched Sentinel 2B, could improve both the spatial and temporal coverage of coastal waters, as they will provide five-day or better coverage and more visible bands to derive products with (unfortunately, Sentinel 2A and B do not have thermal bands), and be used to study oyster growing facilities (Gernez et al., 2017). SST data from Landsat 8 is especially useful for aquaculture site prospecting. We recommend adding thermal bands to high resolution instruments on future missions. Future work improving biogeochemical local algorithms, refining the atmospheric correction, and adding other parameters such as CDOM, will further advance the use of high resolution remote-sensing for coastal applications.

AUTHOR CONTRIBUTIONS

EB, AT, CN, and DB provided contributions for the design of the work. JS, RW, and EB contributed to data acquisition and analysis. JS was responsible for conducting field work and buoy maintenance in the Damariscotta River. JS, RW, EB, and CN were responsible for drafting the work, and all authors were responsible for revisions and final approval.

FUNDING

This project is supported by National Sea Grant award E-14-EA-2, the National Science Foundation award #11A-1355457 to Maine EPSCoR at the University of Maine, the NASA Ocean Biology and Biogeochemistry program Grant #NNX14AP66G, and the NASA EPSCoR program to Maine Space Grant.

ACKNOWLEDGMENTS

Thank you to Catherine Coupland, Nicolas DelPrete, Tiega Martin, Chris Rigaud, Matthew Grey, and Robbie Downs for their assistance maintaining the LOBO buoys at the Darling Marine Center. Thank you to Nils Haëntjens for assistance with data processing. Thank you to Jocelyn Runnebaum, Kevin Staples, and Nils Haëntjens for the helpful edits. Thank you to the SEANET project at University of Maine for providing LOBO buoy data and travel support. We thank our two reviewers for their input which resulted in a better manuscript.

SUPPLEMENTARY MATERIAL

The Supplementary Material for this article can be found online at: http://journal.frontiersin.org/article/10.3389/fmars.2017.00190/full#supplementary-material

REFERENCES

Aguilar Manjarrez, J., and Crespi, V. (2013). *Aquaculture Newsletter 55*, September 2016. Rome: FAO.

Ahmad, Z., Franz, B. A., McClain, C. R., Kwiatkowska, E. J., Werdell, J., Shettle, E. P., et al. (2010). New aerosol models for the retrieval of aerosol optical thickness and normalized water-leaving radiances from the SeaWiFS and MODIS sensors over coastal regions and open oceans. *Appl. Opt.* 49:5545. doi: 10.1364/ao.49.005545

Barillé, L., Prou, J., Héral, M., and Razet, D. (1997). Effects of high natural seston concentrations on the feeding, selection, and absorption of the oyster *Crassostrea gigas* (Thunberg). *J. Exp. Mar. Biol. Ecol.* 212, 149–172. doi: 10.1016/S0022-0981(96)02756-6

Barnes, T. K., Volety, A. K., Chartier, K., Mazzotti, F. J., and Pearlstine, L. (2007). A habitat suitability index model for the eastern oyster (*Crassostrea virginica*), a tool for restoration of the Caloosahatchee Estuary, Florida. *J. Shellfish Res.* 26, 949–959. doi: 10.2983/0730-8000(2007)26[949:AHSIMF]2.0.CO;2

Bayne, B. L., Iglesias, J. I. P., Hawkins, A. J. S., Navarro, E., Heral, M., and Deslous-Paoli, J. M. (1993). Feeding behaviour of the mussel, *Mytilus edulis*: responses to variations in quantity and organic content of the seston. *J. Mar. Biol. Assoc. United Kingdom* 73, 813–829. doi: 10.1017/S0025315400034743

Cake, E. W. Jr. (1983). *Habitat Suitability Index Models: Gulf of Mexico American Oyster* (No. 82/10.57). U.S. Fish and Wildlife Service.

Carder, K. L., Steward, R. G., Harvey, G. R., and Ortner, P. B. (1989). Marine humic and fulvic acids: their effects on remote sensing of ocean chlorophyll. *Limnol. Oceanogr.* 34, 68–81. doi: 10.4319/lo.1989.34.1.0068

Carrasco, M. F., and Barón, P. J. (2010). Analysis of the potential geographic range of the Pacific oyster *Crassostrea gigas* (Thunberg, 1793) based on surface seawater temperature satellite data and climate charts: the coast of South America as a study case. *Biol. Invasions* 12, 2597–2607. doi: 10.1007/s10530-009-9668-0

Congleton, W. R., Pearce, B. R., Parker, M. R., and Beal, B. F. (1999). Mariculture siting: a GIS description of intertidal areas. *Ecol. Model.* 116, 63–75. doi: 10.1016/S0304-3800(98)00158-6

Cullen, J. J. (1982). The deep chlorophyll maximum: comparing vertical profiles of chlorophyll a. *Can. J. Fish. Aqu. Sci.* 39, 791–803. doi: 10.1139/f82-108

Cullen, J. J. (2008). "Observation and prediction of harmful algal blooms," in *Real-Time Coastal Observing Systems for Ecosystem Dynamics and Harmful Algal Blooms*, eds M. Babin, C. S. Roesler, and J. J. Cullen (Paris: UNESCO).

Dame, R. F., and Patten, B. C. (1981). Analysis of energy flows in an intertidal oyster reef. *Mar. Ecol. Prog. Ser.* 5, 115–124. doi: 10.3354/meps005115

Dogliotti, A. I., Ruddick, K. G., Nechad, B., Doxaran, D., and Knaeps, E. (2015). A single algorithm to retrieve turbidity from remotely-sensed data in all coastal and estuarine waters. *Remote Sens. Environ.* 156, 157–168. doi: 10.1016/j.rse.2014.09.020

Donlon, C. J., Minnett, P. J., Gentemann, C., Nightingale, T. J., Barton, I. J., Ward, B., et al. (2002). Toward improved validation of satellite sea surface

skin temperature measurements for climate research. *J. Climate* 15, 353–369. doi: 10.1175/1520-0442(2002)015<0353:TIVOSS>2.0.CO;2

D'Sa, E., Hu, C., Muller-Karger, F., and Carder, K. (2002). Estimation of colored dissolved organic matter and salinity fields in case 2 waters using SeaWiFS: examples from Florida Bay and Florida Shelf. *J. Earth Syst. Sci.* 111, 197–207. doi: 10.1007/BF02701966

Ehrich, M. K., and Harris, L. A. (2015). A review of existing eastern oyster filtration rate models. *Ecol. Model.* 297, 201–212. doi: 10.1016/j.ecolmodel.2014.11.023

Epifanio, C. E., and Ewart, J. (1977). Maximum ration of four algal diets for the oyster *Crassostrea virginica* Gmelin. *Aquaculture* 11, 13–29. doi: 10.4319/lo.1966.11.4.0487

Franz, B. A., Bailey, S. W., Kuring, N., and Werdell, P. J. (2015). Ocean color measurements with the operational land imager on landsat-8: implementation and evaluation in SeaDAS. *J. Appl. Remote Sens.* 9:96070. doi: 10.1117/1.JRS.9.096070

Gernez, P., Doxaran, D., and Barille, L. (2017). Shellfish Aquaculture from Space: potential of Sentinel2 to monitor tide-driven changes in turbidity, chlorophyll concentrations and oyster physiological response at the scale of an oyster farm. *Front. Mar. Sci.* 4:137. doi: 10.3389/fmars.2017.00137

Gernez, P., Lerouxel, A., Mazeran, C., Lucas, A., and Barill, L. (2014). Remote sensing of suspended particulate matter in turbid oyster-farming ecosystems. *J. Geophys. Res.* 119, 7277–7294. doi: 10.1002/2014jc010055

Gong, C., Chen, X., Gao, F., and Chen, Y. (2012). Importance of weighting for multi-variable habitat suitability index model: a case study of winter-spring cohort of *Ommastrephes bartramii* in the Northwestern Pacific Ocean. *J. Ocean Univers. China* 11, 241–248. doi: 10.1007/s11802-012-1898-6

Haven, D. S., and Morales-Alamo, R. (1966). Aspects of biodeposition by oysters and other invertebrate filter feeders. *Limnol. Oceanogr.* 11, 487–498. doi: 10.4319/lo.1966.11.4.0487

Hawkins, A. J. S., Pascoe, P. L., Parry, H., Brinsley, M., Black, K. D., McGonigle, C., et al. (2013a). Shellsim: a generic model of growth and environmental effects validated across contrasting habitats in bivalve shellfish. *J. Shellfish Res.* 32, 237–253. doi: 10.2983/035.032.0201

Hawkins, A. J. S., Pascoe, P. L., Parry, H., Brinsley, M., Cacciatore, F., Black, K. D., et al. (2013b). Comparative feeding on chlorophyll-rich versus remaining organic matter in bivalve shellfish. *J. Shellfish Res.* 32, 883–897. doi: 10.2983/035.032.0332

Hoffmann, E. E., Powell, E. N., Klinck, J. M., and Wilson, E. A. (1992). Modeling oyster populations III. Critical feeding periods, growth. *J. Shellfish Res.* 11, 399–416.

Holm-Hansen, O., and Riemann, B. (1978). Chlorophyll a determination: improvements in methodology. *Oikos* 30, 438–447. doi: 10.2307/3543338

Kleindinst, J. L., Anderson, D. M., McGillicuddy, D. J., Stumpf, R. P., Fisher, K. M., Couture, D. A., et al. (2014). Categorizing the severity of paralytic shellfish poisoning outbreaks in the Gulf of Maine for forecasting and management. *Deep Sea Res. II* 103, 277–287. doi: 10.1016/j.dsr2.2013.03.027

Loosanoff, V. L. (1958). Some aspects of behavior of oysters at different temperatures. *Biol. Bull.* 114, 57–70. doi: 10.2307/1538965

Mayer, L. M. (1996). *The Kennebec, Sheepscot and Damariscotta River Estuaries: Seasonal Oceanographic Data*. University of Maine at Orono and University of Maine/University of New Hampshire Sea Grant College, Program. Orono, ME: Dept. of Oceanography, University of Maine.

McAlice, B. J. (1977). *A Preliminary Oceanographic Survey of Damariscotta River Estuary, Lincoln County, Maine*. Washington: US National Oceanic and Atmospheric Administration.

Mobley, C. D., Werdell, J., Franz, B., Ahmad, Z., and Bailey, S. (2016). *Atmospheric Correction for Satellite Ocean Color Radiometry A Tutorial and Documentation NASA Ocean Biology Processing Group*.

Montanaro, M., Gerace, A., Lunsford, A., and Reuter, D. (2014). Stray light artifacts in imagery from the landsat 8 thermal infrared sensor. *Remote Sens.* 6, 10435–10456. doi: 10.3390/rs61110435

Nechad, B., Ruddick, K. G., and Park, Y. (2010). Calibration and validation of a generic multisensor algorithm for mapping of total suspended matter in turbid waters. *Remote Sens. Environ.* 114, 854–866. doi: 10.1016/j.rse.2009.11.022

Newell, C. R., Hawkins, A. J. S., Morris, K., Richardson, J., Davis, C., and Getchis, T. (2013). ShellGIS: a dynamic tool for shellfish farm site selection. *World Aquacult.* 44, 50–53. Available online at: http://www.was.org/magazine/Contents.aspx?Id=47

Newell, C. R., Shumway, S., Cucci, T. L., and Selvin, R. (1989). The effects of natural seston particle size and type on feeding rates, feeding selectivity and food resource availability for the mussel *Mytilus edulis* Linnaeus, 1758 at bottom culture sites in Maine. *J. Shellfish Res.* 8, 187–196.

Newell, R. I. E., and Jordan, S. J. (1983). Preferential ingestion of organic material by the American oyster *Crassostrea virginica*. *Mar. Ecol. Prog. Ser. Oldendorf* 13, 47–53. doi: 10.3354/meps013047

O'Reilly, J. E., Maritorena, S., Mitchell, B. G., Siegel, D. A., Carder, K. L., Garver, S. A., et al. (1998). Ocean color chlorophyll algorithm for SeaWiFS. *J. Geophys. Res.* 103, 24937–24953.

Pahlevan, N., Lee, Z., Wei, J., Schaaf, C. B., Schott, J. R., and Berk, A. (2014). On-orbit radiometric characterization of OLI (Landsat-8) for applications in aquatic remote sensing. *Remote Sens. Environ.* 154, 272–284. doi: 10.1016/j.rse.2014.08.001

Pahlevan, N., Roger, J.-C., and Ahmad, Z. (2017). Revisiting short-wave-infrared (SWIR) bands for atmospheric correction in coastal waters. *Opt. Express* 25, 6015–6035. doi: 10.1364/OE.25.006015

Pérez-Camacho, A., Aguiar, E., Labarta, U., Vinseiro, V., Fernández-Reiriz, M. J., and Álvarez-Salgado, X. A. (2014). Ecosystem-based indicators as a tool for mussel culture management strategies. *Ecol. Indic.* 45, 538–548. doi: 10.1016/j.ecolind.2014.05.015

Pfannkuche, J., and Schmidt, A. (2003). Determination of suspended particulate matter concentration from turbidity measurements: particle size effects and calibration procedures. *Hydrol. Process.* 17, 1951–1963. doi: 10.1002/hyp.1220

Powell, E. N., Hofmann, E. E., Klinck, J. M., and Ray, S. M. (1992). Modeling oyster populations 1. A commentary on filtration rate. Is faster always better? *J. Shellfish Res.* 1, 387–398.

Padula, F. P., Schott, J. R., Barsi, J. A., Raqueno, N. G., and Hook, S. J. (2010). Calibration of Landsat 5 thermal infrared channel: updated calibration history and assessment of the errors associated with the methodology. *Can. J. Remote Sens.* 36, 617–630. doi: 10.5589/m10-084

Radiarta, I. N., Saitoh, S. I., and Miyazono, A. (2008). GIS-based multi-criteria evaluation models for identifying suitable sites for Japanese scallop (*Mizuhopecten yessoensis*) aquaculture in Funka Bay, southwestern Hokkaido, Japan. *Aquaculture* 284, 127–135. doi: 10.1016/j.aquaculture.2008.07.048

Rasmussen, J. B., Godbout, L., and Schallenburg, M. (1989). The humic content of lake water and its relationship to watershed and lake morphometry. *Limnol. Oceanogr.* 34, 1336–1343. doi: 10.4319/lo.1989.34.7.1336

Rheault, R. B., and Rice, M. A. (1996). Food-limited growth and condition index in the eastern oyster, *Crassostrea virginica* (Gmelin 1791), and the bay scallop, *Argopecten irradians* irradians (Lamarck 1819). *J. Shellfish Res.* 15, 271–283.

Roesler, C., and Culbertson, C. (2016). "Lake transparency: a window into decadal variations in dissolved organic carbon concentrations in lakes of Acadia National Park, Maine," in *Aquatic Microbial Ecology and Biogeochemistry: A Dual Perspective*, eds P. M. Glibert and T. M. Kana (Springer International Publishing Switzerland), 225–236. doi: 10.1007/978-3-319-30259-1

Shumway, S. E., Sherman-Caswell, S., and Hurst, J. (1988). Paralytic shellfish poisoning in Maine: monitoring a monster. *J. Shellfish Res.* 7, 643–652.

Siegel, D. A., Maritorena, S., Nelson, N. B., and Behrenfeld, M. J. (2005). Independence and interdependencies among global ocean color properties: reassessing the bio-optical assumption. *J. Geophys. Res. C* 110, 1–14. doi: 10.1029/2004jc002527

Slonecker, E. T., Jones, D. K., and Pellerin, B. A. (2015). The new Landsat 8 potential for remote sensing of colored dissolved organic matter (CDOM). *Mar. Pollut. Bull.* 107, 518–527. doi: 10.1016/j.marpolbul.2016.02.076

Soniat, T. M., and Brody, M. S. (1988). Field validation of a habitat suitability index model for the American oyster. *Estuaries Coasts* 11, 87–95. doi: 10.2307/1351995

Theuerkauf, S. J., and Lipcius, R. N. (2016). Quantitative validation of a habitat suitability index for oyster restoration. *Front. Mar. Sci.* 3:64. doi: 10.3389/fmars.2016.00064

Thomas, A., Byrne, D., and Weatherbee, R. (2002). Coastal sea surface temperature variability from Landsat infrared data. *Remote Sens. Environ.* 81, 262–272. doi: 10.1016/S0034-4257(02)00004-4

Thomas, Y., Mazurié, J., Alunno-Bruscia, M., Bacher, C., Bouget, J. F., Gohin, F., et al. (2011). Modelling spatio-temporal variability of *Mytilus edulis* (L.) growth by forcing a dynamic energy budget model with satellite-derived environmental data. *J. Sea Res.* 66, 308–317. doi: 10.1016/j.seares.2011.04.015

Thompson, B. P., and Perry, M. J. (2006). *Temporal and Spatial Variability of Phytoplankton Biomass in the Damariscotta River Estuary, Maine, U.S.A*. Thesis, Department of Marine Sciences.

Thornton, K., and Mayer, L. (2015). *Maine Coastal Observing Alliance*. Summary Report 2014.

USGS (2016). *L8 OLI/TIRS Product*. Available online at: https://earthexplorer.usgs.gov

Vanhellemont, Q., and Ruddick, K. (2014). Turbid wakes associated with offshore wind turbines observed with Landsat 8. *Remote Sens. Environ.* 145, 105–115. doi: 10.1016/j.rse.2014.01.009

Wang, H., Hladik, C. M., Huang, W., Milla, K., Edmiston, L., Schalles, J. F., et al. (2010). Detecting the spatial and temporal variability of chlorophyll-a concentration and total suspended solids in Apalachicola Bay, Florida using MODIS imagery. *Int. J. Remote Sens.* 31, 439–453. doi: 10.1080/01431160902893485

Ward, B. (2006). Near-surface ocean temperature. *J. Geophys. Res.* 111, 1–18. doi: 10.1029/2004jc002689

Werdell, P. J., Franz, B. A., Bailey, S. W., Feldman, G. C., Boss, E., Brando, V. E., et al. (2013). Generalized ocean color inversion model for retrieving marine inherent optical properties. *Appl. Optics* 52, 2019–2037. doi: 10.1364/AO.52.002019

Widdows, J., Fieth, P., and Worrall, C. M. (1979). Relationships between seston, available food and feeding activity in the common mussel Mytilus edulis. *Mar. Biol.* 50, 195–207. doi: 10.1007/bf00394201

Conflict of Interest Statement: The authors declare that the research was conducted in the absence of any commercial or financial relationships that could be construed as a potential conflict of interest.

frontiers in Marine Science

ORIGINAL RESEARCH
published: 10 August 2017
doi: 10.3389/fmars.2017.00243

Vegetation Development in a Tidal Marsh Restoration Project during a Historic Drought: A Remote Sensing Approach

Dylan Chapple[1]* *and Iryna Dronova*[2]

[1] Department of Environmental Science, Policy and Management, University of California, Berkeley, Berkeley, CA, United States, [2] Department of Landscape Architecture and Environmental Planning, University of California, Berkeley, Berkeley, CA, United States

Tidal wetland restoration efforts can be challenging to monitor in the field due to unstable local conditions and poor site access. However, understanding how restored systems evolve over time is essential for future management of their ecological benefits, many of which are related to vegetation dynamics. Physical attributes, such as elevation and distance to channel play important roles in governing vegetation expansion in developing tidal wetlands. However, in Mediterranean ecosystems, drought years, wet years, and their resulting influence on salinity levels may also play a crucial role in determining the trajectory of restoration projects, but the influence of weather variability on restoration outcomes is not well-understood. Here, we use object-based image analysis (OBIA) and change analysis of high-resolution IKONOS and WorldView-2 satellite imagery to explore whether mean annual rates of change from mudflat to vegetation are lower during drought years with higher salinity (2011–2015) compared to years with lower salinity (2009–2011) at a developing restoration site in California's San Francisco Bay. We found that vegetation increased at a mean rate of 1,979 m^2/year during California's historic drought, 10.4 times slower than the rate of 20,580 m^2/year between 2009 and 2011 when the state was not in drought. Vegetation was significantly concentrated in areas closer to channel edges, where salinity stress is ameliorated, and the magnitude of the effect increased in the 2015 image. In our image analysis, we found that different distributions of water, mud, and algae between years led to different segmentation settings for each set of images, highlighting the need for more robust and reproducible OBIA strategies in complex wetlands. Our results demonstrate that adaptive monitoring efforts in variable climates should take into account the influence of weather on tidal wetland ecosystems, and that high-resolution remote sensing can be an effective means of assessing these dynamics.

Keywords: tidal wetland, restoration ecology, drought, remote sensing, satellite imagery, object-based image analysis, climate variability

OPEN ACCESS

Edited by:
Kristin B. Byrd, United States Geological Survey, United States

Reviewed by:
Athanasios Thomas Vafeidis, University of Kiel, Germany
Shari L. Gallop, Macquarie University, Australia

***Correspondence:**
Dylan E. Chapple
dylanchapple@berkeley.edu

Specialty section:
This article was submitted to Coastal Ocean Processes, a section of the journal Frontiers in Marine Science

Received: *31 March 2017*
Accepted: *18 July 2017*
Published: *10 August 2017*

Citation:
Chapple D and Dronova I (2017) Vegetation Development in a Tidal Marsh Restoration Project during a Historic Drought: A Remote Sensing Approach. Front. Mar. Sci. 4:243. doi: 10.3389/fmars.2017.00243

INTRODUCTION

Tidal wetland ecosystems worldwide are threatened by a range of human activities (Zedler and Kercher, 2005; Erwin, 2009; Klemas, 2013) and have been in steady decline for the last 150 years in California (Goals Project, 2015). In recent years, significant efforts have been undertaken to reverse this widespread loss and alteration. To effectively implement and plan restoration efforts, detailed understandings of system dynamics are necessary for driving adaptive management approaches (Spencer et al., 2016). To date, studies of restoration projects have focused more on the physical aspects of vegetation development and how they relate to sediment supply, initial elevation, and landscape context (Williams and Orr, 2002; Kelly et al., 2011; Brand et al., 2012). However, due to a variety of interacting factors, restoration projects may not proceed in a simple linear manner over time (Holmgren and Scheffer, 2001; Peters et al., 2004; Holmgren et al., 2006; Scheffer et al., 2009; Sitters et al., 2012; Chapple et al., 2017). Rates of restoration change over time and the factors that influence these transitions are critical yet understudied aspects of the restoration process. Since restoration projects increasingly use iterative, data-driven adaptive management strategies to plan projects, an improved understanding of how systems change over longer time periods is necessary.

Due to its Mediterranean-type climate and variable weather between years, California's San Francisco Bay (SF Bay) is an interesting location to study how climate variability influences restoration projects (Chapple et al., 2017). Between 2011 and 2015, California experienced an extreme drought event with an essentially incalculable return period (Robeson, 2015). This extended dry period has led to changes in other plant communities across the state (Asner et al., 2016; Copeland et al., 2016), and has likely influenced restoration project trajectories (Holmgren and Scheffer, 2001; Chapple et al., 2017). At the broad scale, plant communities in SF Bay tidal wetlands are primarily influenced by the salinity of tide waters (Malamud-Roam and Ingram, 2004; Callaway et al., 2007), which are influenced by snowpack levels and a complex series of upstream interactions across the state (Dettinger and Cayan, 2003). Anthropogenic sources of atmospheric carbon appear to be contributing to reduced snow pack in the state, which is expected to continue declining (Berg and Hall, 2017). These shifts will likely have major impacts on salinity and plant community dynamics throughout the estuary (Malamud-Roam and Ingram, 2004; Callaway et al., 2007) and will play a role in determining how restoration trajectories progress (Chapple et al., 2017). An improved understanding of how extreme events like California's historic drought impact restoration efforts is essential for future management (Holmgren and Scheffer, 2001; Holmgren et al., 2006; Callaway et al., 2007; Sitters et al., 2012; Zedler et al., 2012), given that increased climate variability is a major projected outcome of climate change (Pachauri et al., 2014).

In the SF Bay, the restoration of tens of thousands of acres of tidal wetland are planned or in process (Goals Project, 2015). Tidal wetlands in the area are inundated twice daily by tidal water, and the ambient salinity of Bay water is the primary determinant of tidal wetland plant community structure at the broad scale (Callaway et al., 2007; Chapple et al., 2017). At the site-level scale, salinity interacts with tidal channel structure and elevation to determine vegetation patterns (Sanderson et al., 2000; Schile et al., 2011; Chapple et al., 2017). Previous studies on the role of freshwater dynamics in California's tidal wetlands have focused on field-collected data, finding that salinity can play a pronounced role in plant productivity and community dynamics (Zedler, 1983; Callaway and Sabraw, 1994; Chapple et al., 2017). To improve management outcomes, understanding vegetation trends at larger scales is critical, and remote sensing of aerial imagery provides a cost-effective means of monitoring tidal wetland sites where access may be challenging. In particular, object-based image analysis (OBIA) is a promising technique for monitoring tidal salt marshes (Dronova, 2015), and has been applied to looking at vegetation across spatial scales in these ecosystems (Tuxen and Kelly, 2008; Moffett and Gorelick, 2013, 2016), but has only recently been used to explore change over time (Campbell et al., 2017). Previous geospatial work using aerial imagery has largely taken place in the North SF Bay, where freshwater river runoff buffers Bay salinity (Tuxen and Kelly, 2008; Tuxen et al., 2008). While large-scale manipulation of freshwater in restoring tidal wetlands is not feasible, remotely sensed data allows for retrospective consideration of how drought has influenced restoration trajectories.

Ecological trends are often hard to predict in heavily modified restoration sites (Suding et al., 2004; Zedler, 2007), which makes monitoring a crucial aspect of iterative restoration design (Bernhardt et al., 2007; Kondolf et al., 2007; Zedler et al., 2012; Chapple et al., 2017). These uncertainties are compounded by climate variability, but the influence of year-effects on restoration outcomes is under-represented in the literature (Vaughn and Young, 2010). Site conditions in developing tidal wetlands can be particularly challenging for ground surveys owing to tides, mud, and limited access options (Watson, 2008; Diggory and Parker, 2011). Remote sensing of satellite imagery allows for the monitoring of large wetland areas at a fraction of the cost and time associated with field monitoring, but it is still under-utilized as a restoration tool (Klemas, 2013). To effectively track the fine scale trends required by most tidal wetland restoration projects, high resolution (<4 m) imagery is needed to analyze surface trends (Dronova, 2015).

High-resolution satellite imagery also presents certain challenges for accurately characterizing restoration targets, such as vegetation cover. Due to high spatial complexity caused by fine-scale patterning of water, algae, topography, and other features, high-resolution imagery can be challenging to interpret. Often, pixel-based approaches are hampered by their inability to consider both the pixel identity and spatial context in classifying landscapes (Tuxen and Kelly, 2008). To account for these issues, object-based approaches are increasingly used to categorize heterogeneous landscapes like tidal wetlands (Wang et al., 2004; Tuxen and Kelly, 2008; Moffett and Gorelick, 2013, 2016; Dronova, 2015; Campbell et al., 2017). In tidal wetland restoration projects, sediment is highly dynamic over time, imagery must be gathered at low tide for optimal visualization while surface water and debris can vary greatly between images (Tuxen and Kelly, 2008; Fulfrost et al., 2012). Further, vegetation

patches may be heterogeneous, leading to salt-and-pepper speckle artifacts that confuse delineation and interpretation of cover types (Moffett and Gorelick, 2013). By smoothing local noise and allowing for supervised classification for each year, OBIA can help address some of these issues (Dronova, 2015), but it has rarely been used for monitoring restoration outcomes (but see Campbell et al., 2017).

OBIA methods are effective because they rely on multi-scale interpretations of images instead of simple pixel measures (Schiewe et al., 2001). By nature, pixels represent a fixed area of the ground surface, defined by the pixel size, or resolution. Object-based approaches integrate pixel information with spatial information, as pixels closer together in space are more likely to be related (Blaschke and Hay, 2001). Further, the shape of objects can be incorporated and controlled in the OBIA process flow, allowing for more detailed pattern analysis (Blaschke et al., 2000; Schiewe et al., 2001). A comparison of pixel-based and object based analyses of IKONOS imagery in a tidal system found that object-based methods repeatedly outperformed pixel-based methods (Wang et al., 2004).

Object-based methods rely on a mix of the parameter classes listed above to segment images for analysis. Scale and shape parameters capture the spatial attributes of the study system, while spectral bands from the imagery capture variation in visual and often infrared sensor bands (Dronova, 2015). The process of segmentation incorporates user-specified weights for each of these parameters and divides the images into discrete objects. Based on how well these objects capture variation across the landscape, the user varies parameters to arrive at an appropriate set of objects (Moffett and Gorelick, 2013). Once the appropriate objects are defined, the user classifies a subset of objects into classes. This subset of points is then used to classify the entire image. Despite its strong potential, change analysis is less frequently implemented in tidal wetland ecosystems using OBIA. The most frequent use of this has been in mapping mangrove ecosystems (Conchedda et al., 2008; Gaertner et al., 2014; Son et al., 2015), where Conchedda et al. found that increases in mangrove ecosystems in Senegal may be attributable to increased precipitation in the region over the study period (Conchedda et al., 2008). Campbell et al. were able to track the influence of Hurricane Sandy on vegetation dynamics across a range of wetlands in New York (Campbell et al., 2017). These studies highlight the potential to use these methods to discern the influence of weather variability on vegetation change.

Tidal wetland restoration has been underway in the SF Bay since the mid-1970s (Williams and Faber, 2001). Early projects showed that the proper elevation range was crucial for plant establishment, but that pre-filling sites to their target elevations prevented the development of tidal channels, leading to inferior quality habitat (Williams and Faber, 2001; Philip Williams & Associates, Ltd., and Faber, 2004). As such, tidal wetlands in the SF Bay are typically restored through a hybrid process, whereby the topography in a target area is altered to insure proper drainage before returning tidal influence, but the mudflats accrete sediment passively from the tide over time to reach target elevations for vegetation development (Williams and Orr, 2002; Kelly et al., 2011; Brand et al., 2012). This allows for the development of tidal channel networks that convey tidal waters in and out of these sites. Both channel structure and elevation play key roles in determining vegetation patterning, largely due to the reduction of salinity in higher elevation areas and areas closer to channel edges (Sanderson et al., 2000; Tuxen et al., 2011; Brand et al., 2012). Channel proximity also influences salinity levels: poorly drained areas in the interior of the marsh exhibit lower biomass production when ambient salinity levels are higher, while channel edges appear to buffer the negative influences of ambient salinity, allowing for similar levels of biomass production across different salinity levels in areas adjacent to channels (Schile et al., 2011). Biomass production influences the speed of restoration, which in turn influences the resilience of developing restoration projects to sea level rise (Goals Project, 2015); it is thus critical to understand how restoration sites change over time.

Despite a developed conceptual framework on the spatial development of marshes from mudflats based on sediment and elevation, the influence of weather variability and extreme events like drought over time is less well-understood. In California tidal salt marshes, freshwater added by El Nino events (Zedler, 1983; Chapple et al., 2017) and experimental manipulations (Callaway and Sabraw, 1994; Schile et al., 2011; Woo and Takekawa, 2012) has been shown to influence biomass production and species identity. Freshwater impacts can also influence plant dynamics at restoration sites (Chapple et al., 2017), but these impacts have not been explored at larger spatial scales. To better understand the influence of drought on vegetation development over time, we performed change analysis at a developing restoration site in the South Bay Salt Pond Restoration Project (SBSPRP) in Hayward, CA during California's historic drought (2011–2015) and a period of average precipitation (2009–2011). In the SF Bay, earlier change detection efforts have largely relied on using spectral indicators, such as NDVI to track restoration site changes over time (Tuxen et al., 2008; Kelly et al., 2011; Fulfrost et al., 2012). The goals of our study are three-fold: (1) compare rates of annual vegetation change during the drought period to a period with greater freshwater influence (2009–2011), (2) assess how channel structure influences vegetation patterning across different years, and (3) discern the utility of OBIA classification and change analysis to detect changes in a tidal wetland restoration project.

METHODS

Study Area

Our study focused on a single marsh (North Creek Marsh, 37°36′40.20″N, 122°6′43.94′W) at Eden Landing Ecological Reserve in Hayward, CA, part of the South Bay Salt Pond Restoration Project (**Figure 1**). The SBSPRP is an adaptively-managed effort to restore over 15,000 acres of former salt-evaporation ponds to a mosaic of tidal wetlands and managed ponds (Trulio et al., 2007). North Creek Marsh is a 37.32 Ha restoration site initiated in 2006. The site was historically tidal wetland and was converted to industrial salt-evaporation in the late nineteenth century (Stanford et al., 2013). Tidal influence was returned to the area by breaching a levee at the southern end of the site. The restoration process is driven by tidal transport of sediment building the marsh plain to the appropriate

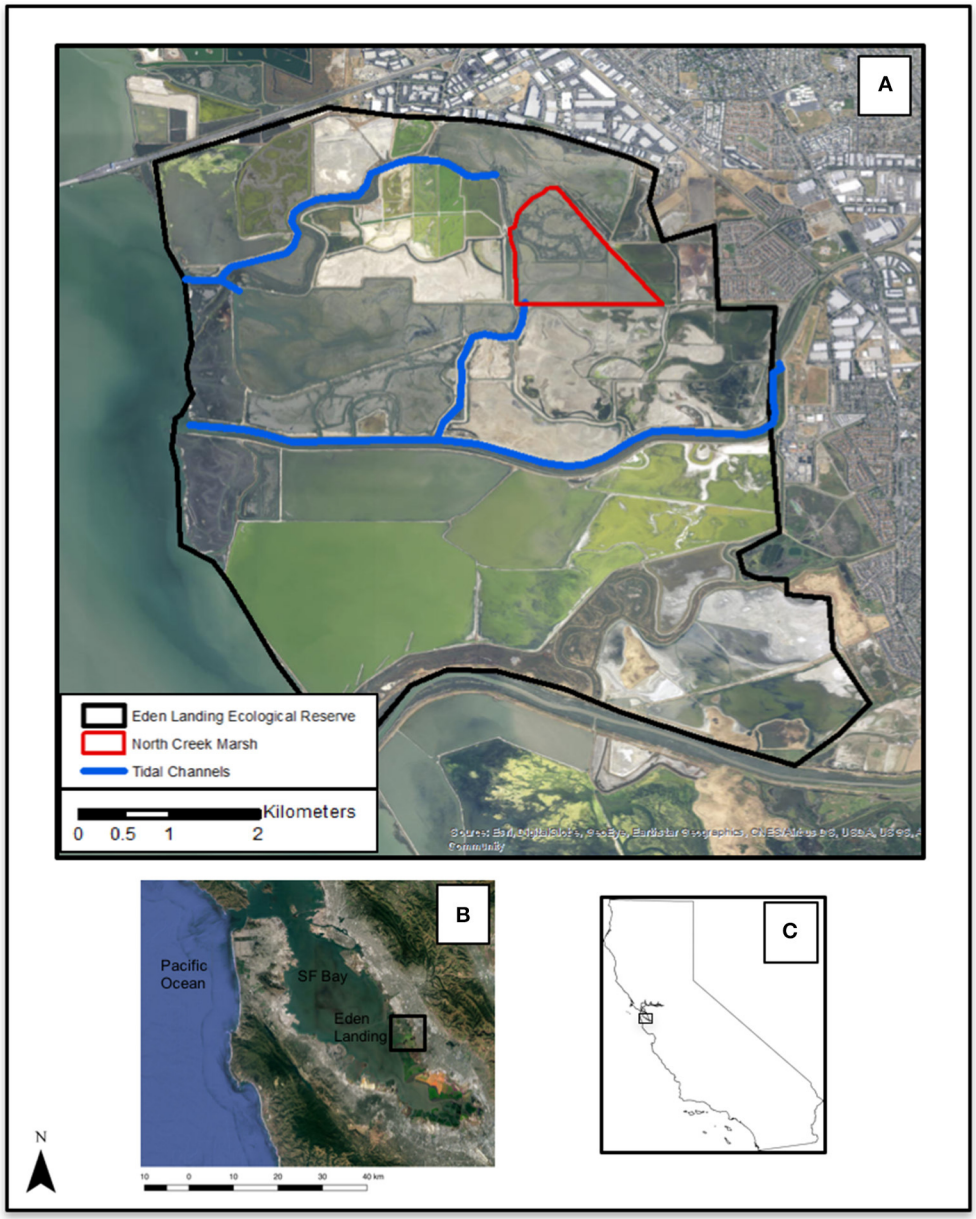

FIGURE 1 | (A) Eden Landing Ecological Reserve (CA Dept. Fish and Wildlife), Hayward, California, USA. **(B)** South San Francisco Bay, Eden Landing Ecological Reserve outlined **(C)** California state outline. Aerial images reproduced with permission from ©Google, 2017.

level (Brew and Williams, 2010), then seed dispersal via tidal hydrochory driving the development of vegetation (Diggory and Parker, 2011). In addition to the passive restoration process via seed dispersal, the Invasive Spartina Project actively planted selected portions of the site with the native cordgrass *Spartina foliosa*, *Distichlis spicata* (saltgrass), and *Grindelia stricta* (marsh gumplant) (Hammond, 2016).

Salinity Data Analysis

We determined mean annual salinity for each rain year (October–September) between 2009 and 2015 using Station 30 from the USGS SF Bay water quality archive (Cloern and Schraga, 2016). To explore potential differences between tidal heights, we determined mean higher high water (MHHW) and monthly maximum tide from the NOAA Redwood City Tide Gauge, the closest tide station with continuous data over the study period (https://tidesandcurrents.noaa.gov/). For salinity and MHHW, we subset the data for rain years 2009–2011 and 2012–2015 to correspond to the dates of our imagery and California's historic drought. To determine differences between the two periods, we performed a non-parametric Kruskal–Wallis test for salinity, MHHW and monthly maximum tide. To determine directional

trends in salinity during the two periods, we used non-parametric generalized additive models to analyze salinity levels over time using the *gam* package in R (Hastie, 2013). Non-parametric tests were used due to non-normality of salinity data.

Remote Sensing Data and Image Pre-processing

For 2009 and 2011, we obtained 0.8 m pan sharpened IKONOS imagery of the South Bay Salt Pond Restoration Project from the San Francisco Estuary Institute (©Digital Globe Inc., 2011). For 2015, we obtained 0.5 m WorldView-2 imagery (©Digital Globe Inc., 2015). Each set of imagery contained four spectral bands: red, green, blue, and near-infrared (NIR). To ensure phenological continuity between collection dates, all images were collected near peak biomass (June 23 2009, July 7 2011, and June 21 2015) at low tide to ensure maximum visibility of vegetation. The timing of collection is essential because tidal water frequently covers landscape features, such as vegetation patches, essential to change detection. To double check that intermediate years at our site did not exhibit anomalous vegetation growth that is not accounted for in our analysis, we reviewed Google Earth imagery (©Google, 2017) for all available dates between June 2009 and June 2015. We did not find evidence of anomalous change or loss in the periods between our high resolution images.

To prepare the images for analysis, we re-projected the 2009 image from the GCS 1984 datum to the NAD 1983 datum to match the 2011 and 2015 images. We down-sampled all images to 0.8 m pixel resolution to match the lowest resolution images. We then geocorrected all images, resulting in an offset of 0.5 pixel maximum. Images were imported into eCognition (©Trimble Inc.) software to perform OBIA. To allow for the most effective interpretation of vegetation patches, bands 4, 3, and 2 were visualized as RGB, respectively, and the Histogram Equalization stretch was applied across the image.

Object-Based Image Classification

Object-based analyses were performed in eCognition Developer software version 8.8 (©Trimble Inc.). As a first step, we generated primitive image objects as spatial units for wetland classification using the Multiscale Resolution Segmentation (MRS) tool which requires the parameters of scale, shape and compactness to control object size and heterogeneity. For all images, we used the red, green, blue, and infrared bands to classify imagery. To determine their values for our objectives, we worked through a series of scale parameter values in increments of 5, and both shape and compactness parameters in increments of 0.1. We assessed each combination of settings by trial and error to determine which combination of parameters best matched the visual distribution of vegetation at the site. Notably, due to the differences in the original resolution of image datasets, we had to individually adjust their MRS parameters to obtain primitive objects of comparable size. For the 2011 image, using a scale of 10 resulted in unrealistically small objects. Using scales of 40 and above did not capture enough of the surface variation, and after comparison of incremental steps, we determined that a scale of 30 most effectively captured the vegetation patterning on the marsh surface. We selected a scale of 25 for the 2015 image and a scale of 6 for the 2009 image. For all images, shape was given low weight (0.1) in the final classification, as shapes in wetland vegetation are highly dependent on patch size and do not conform to regular patterns across the marsh surface (Moffett and Gorelick, 2013). Compactness was given a medium weight (0.5). For all images, the four bands were given equal weight.

Following the segmentation process, we manually identified at least 50 training samples for each of the three main categories: Water/Channels, Mudflat, and Vegetation. Vegetation is included as a simple category since the majority of vegetation at the site consists of *Salicornia pacifica*, an early-colonizing marsh dominant (Krause, 2016). *Jaumea carnosa* (Fleshy Jaumea), *Frankenia salina* (Alkali Heath), the annual *Salicornia europaea* (common glasswort), *G. stricta* (marsh gumplant), and *S. foliosa* (California cordgrass) are present in lower densities due to natural recruitment (Krause, 2016) and planting (Hammond, 2016), but our imagery did not allow for differentiation between species. Samples were selected by examining the imagery and cross-referencing these observations with checks of Google Earth (©2015 Google) imagery to verify vegetation patterns. This information was combined with expert knowledge on vegetation patterns from field visits conducted between 2013 and 2015. Once samples were selected, images were classified by including a supervised nearest neighbor process algorithm with the mean brightness, mean NIR and standard deviation of the red band selected as class-discriminating features. We initially included the Normalized Difference Vegetation Index (NDVI), which uses the red and infrared bands to detect green vegetation, as a classification parameter. However, this led to spurious identification of algae as vegetation, and misclassified vegetated areas with apparent mudfilms as mudflat, so we elected not to include it in the final process decision tree. Following sample selection and implementation of the nearest neighbor algorithm, images from all years were separately classified into the three categories using the classification algorithm in eCognition. Once images from each year had been classified, the resulting classifications were imported into ENVI to perform change detection analysis via simple spatial overlay. Images were masked to include only the marsh-plain area.

To perform accuracy assessment, we used the Random Points tool (Standard C Rand function) in ArcGIS v. 10.3 (Esri Inc.) to select between 54 and 87 points per category per year, excluding training samples, and visually identified cover categories. Samples that fell along object edges were excluded from the random point selection. Google Earth images (©2015 Google) from each year were used to manually verify sample collection points. These points were imported as Regions of Interest (ROI) into ENVI v.5.2 (Harris Geospatial Inc.) software to perform accuracy analysis. The ROIs were used to populate the Confusion Matrix tool, which calculates standard accuracy metrics (overall accuracy, kappa, user's, and producer's accuracies for different classes) of a classified image based on verified samples.

Following classification, we analyzed vegetation patch dynamics. To determine the relationship between vegetation presence and channel structure, we digitized a vector of the

major channels at the site, then created a distance raster using the Euclidean Distance tool in ArcGIS v. 10.3 (Esri Inc.). This tool calculates the distance from a specified feature and outputs a continuous raster with corresponding values. We generated 1,000 random points using the Random Points tool in ArcGis and extracted the vegetation layer from our classification for each year. Based on this data we used vegetation presence (1) and absence (0) to run a generalized linear model with a binomial distribution using the lme4 package in R (Bates et al., 2017). To determine changes in patch configuration across the three images, we ran patch statistics using FragStats v. 4 (McGarigal et al., 2015).

RESULTS

Salinity and Tides

Our results show that salinity was significantly higher during California's historic drought, and the magnitude of mean annual vegetation change was 10.4 times slower during this period compared to the lower salinity period that preceded it (**Figures 2**, **3**). Mean salinity was 25.64 ppt for 2009–2010, and 23.99 ppt for 2010–2011, with an overall mean of 24.82 ppt (CV = 0.198) between 2009 and 2011. Mean salinity was 26.08 ppt for 2011–2012, 28.18 ppt for 2012–2013, 30.12 ppt for 2013–2014, and 29.50 ppt for 2014–2015, with a mean salinity of 28.47 ppt (CV = 0.10) between 2011 and 2015 (**Figure 5**). Salinity was significantly different between these two periods ($p < 0.001$, $\chi^2 = 18.40$). Salinity significantly decreased between 2009 and 2011 ($p < 0.001$, $F = 18.69$) and significantly increased between 2011 and 2015 ($p < 0.001$, $F = 16.50$). Neither MHHW ($p = 0.354$, $\chi^2 = 0.86$) nor monthly maximum tide was significantly different between the two periods ($p = 0.354$, $\chi^2 = 43.87$) (**Figure 2**).

Remote Sensing Classification Accuracy

We obtained high classification accuracy for each of our cover categories in each year. For 2009, we obtained an overall accuracy of 92.42% and a Kappa Coefficient of 0.88. For 2011, we obtained an overall accuracy of 95.02% and a Kappa Coefficient of 0.92. For 2015, we obtained an overall accuracy of 96.83% and a Kappa Coefficient of 0.95. The lower overall accuracy in the 2009 image was due to over-classification of water on the marsh surface (**Table 1**). Vegetation, the focal target of post-restoration monitoring, was consistently classified with high user's and producer's accuracy exceeding 92% at all times (**Table 1**). It was most commonly misclassified with water in 2009 and 2015 and mudflat in 2011. Some of the overall classification error also occurred due to misclassification of water and mudflats that did not correspond to vegetation *per se* and thus was of lower concern for our objectives.

Changes in Vegetation Cover and Distribution

Total vegetation cover increased from 58,154 m^2 of the study area to 99,315 m^2 from 2009 to 2011, an increase of 70.77% at a mean rate of 20,580 m^2/year. In contrast, vegetation cover increased from 99,315 m^2 in 2011 to 107,232 m^2 in 2015, a 7.97% change from the 2011 cover at a mean rate of 1,979 m^2/year (**Figures 3**, **4**). For all years, vegetation presence was significantly related to distance from channel, with areas closer to channel more likely to support vegetation, but the magnitude of the effect

TABLE 1 | Accuracy assessment for each cover category for 2009, 2011, and 2015.

	2009		2011		2015	
	Overall accuracy: 92.42%		Overall accuracy: 95.02%		Overall accuracy: 96.83%	
Class	**Producer's**	**User's**	**Producer's**	**User's**	**Producer's**	**User's**
Channels/ Water	96	82.76	94.12	96	91.8	98.25
Vegetation	98.08	94.44	95.89	92.11	98.67	96.1
Mudflat	87.5	97.67	94.81	98.65	98.82	96.55

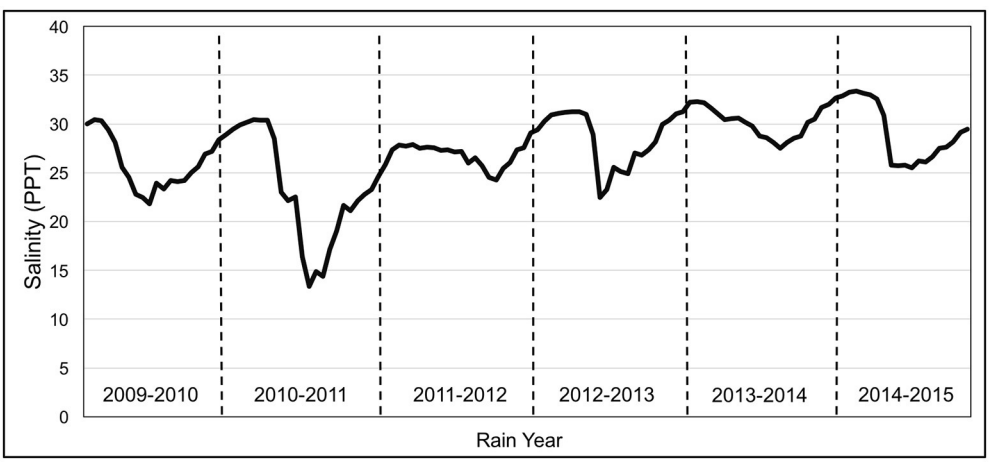

FIGURE 2 | SF Bay Salinity, rain years 2009–2015. Data were taken from Station 30 of the bi-monthly USGS Water Quality Cruise (Cloern and Schraga, 2016).

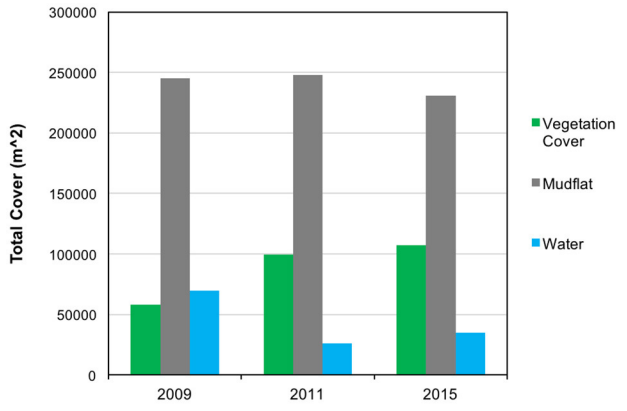

FIGURE 3 | Cover type change. Mudflat was the dominant cover type across all 3 years. Vegetation increased at a rate of 20,580 m^2/year between 2009 and 2011, and 1,979 m^2/year between 2011 and 2015.

was notably larger in the 2015 image (2009: $p < 0.001$, $z = -3.49$; 2011: $p = 0.002$, $z = -2.98$; 2015: $p < 0.001$, $z = -6.33$). In the 2011 image, we observed some vegetation colonization of interior mudflat areas that did not persist in the 2015 image (**Figures 4**, **5**). The overall number of patches decreased from 2009 (394 patches) to 2011 (282 patches) and increased in 2015 (473 patches). Mean patch area was the largest in 2011 (352 m^2), intermediate in 2015 (226 m^2), and smallest in 2009 (147 m^2; **Table 2**).

Among non-vegetated surfaces, mudflats were the most prevalent cover class across all years, declining slightly in 2015, with total cover of 245,413 m^2 in 2009, 247,685 m^2 in 2011, and 230,752 m^2 in 2015. Since the amount of water in aerial images is highly dependent on the timing of image, tidal phase, and other stochastic factors, changes in water coverage should be interpreted with caution. In our images, water accounted for 69,764 m^2 in 2009, 26,188 m^2 in 2011, and 34,787 m^2 in 2015 (**Figures 3**, **4**).

DISCUSSION

Post-restoration Vegetation Dynamics in Tidal Wetlands

Our results demonstrate that drought may impact vegetation change rates in Mediterranean-type tidal wetland restoration projects, leading to non-linear recovery patterns. At North Creek Marsh, vegetation cover increased from 2009 to 2011 and from 2011 to 2015, but the mean annual rate of change during the first period, when Bay salinity was lower, was more than 10 times as rapid as change during the second period, when historic drought conditions elevated salinity levels in the Bay. By employing remotely sensed imagery to study this progression, we were able to scale up from previous field efforts that demonstrated the effect of lowered salinity on plant productivity (Zedler, 1983; Schile et al., 2011; Woo and Takekawa, 2012), and restoration trajectories (Chapple et al., 2017). Previous work from Southern California documented increased rates of *S. foliosa* establishment in response to increased sedimentation rates brought on by El Nino events (Ward et al., 2003) and increased *Spartina* biomass and structure in response to lowered salinity brought on by El Nino events (Zedler, 1983; Zedler et al., 1986). Our results show that freshwater availability may also influence the rate of vegetation expansion in recently restored wetlands dominated by *S. pacifica*. These larger-scale observations are supported by experimental results that demonstrate that increased salinity levels reduced *S. pacifica* biomass production (Schile et al., 2011; Woo and Takekawa, 2012). In contrast to our site, a similar restoration project in a more freshwater marsh without a notable drought period reached 90% vegetated over a 10 year period, with no evidence of slowing pace after initial gains (Tuxen et al., 2008). This indicates that restoration projects in higher salinity regions may exhibit more variable, less linear trajectories due to interannual variability in salinity. While increased inundation during periods of higher rainfall could be another factor influencing vegetation change, we found no significant difference in MHHW or monthly maximum tide between the two periods.

Our results also demonstrate that channel structure is a key determinant of where vegetation establishes, and may be even more important during periods of elevated salinity. Vegetation was significantly associated with channel proximity for all years, but between 2011 and 2015, the strength of the interaction between vegetation presence and channel proximity more than doubled. We also visually observed establishment of new vegetation patches in interior marsh areas in 2011 (**Figure 4**), but these patches did not persist in 2015. Channels drive the restoration process by improving drainage across the marsh surface and lowering salinity (Sanderson et al., 2000; Williams and Orr, 2002; Wallace et al., 2005; O'Brien and Zedler, 2006). Biomass production of *S. pacifica* is significantly influenced by elevated salinity in in poorly drained areas, but has no effect in well-drained areas adjacent to channels (Schile et al., 2011). Our results indicate that salinity levels likely interact with the channel structure at the site, allowing vegetation to persist and expand in areas adjacent to channels but precluding development in poorly drained interior areas. Under projected climate change scenarios, increased prevalence of drought is likely to reduce snowpack and increase salinity (Callaway et al., 2007). This may slow the overall rate of vegetation change and increase the importance of channel structure in the restoration process.

The Potential of OBIA for Wetland Monitoring and Future Research Needs

Our results also show how OBIA can be used to overcome some of the challenges with high resolution data to map vegetation change over time in developing tidal wetlands. The dynamic nature of tidal processes mean that images are often different from each other based on how mud and water appear in the image, which can present problems for comparing images from different years (Dronova, 2015; Campbell et al., 2017). Furthermore, local noise and spectral variation, especially pronounced at higher spatial resolution, pose considerable challenges for delineating wetland cover type patches as semantic

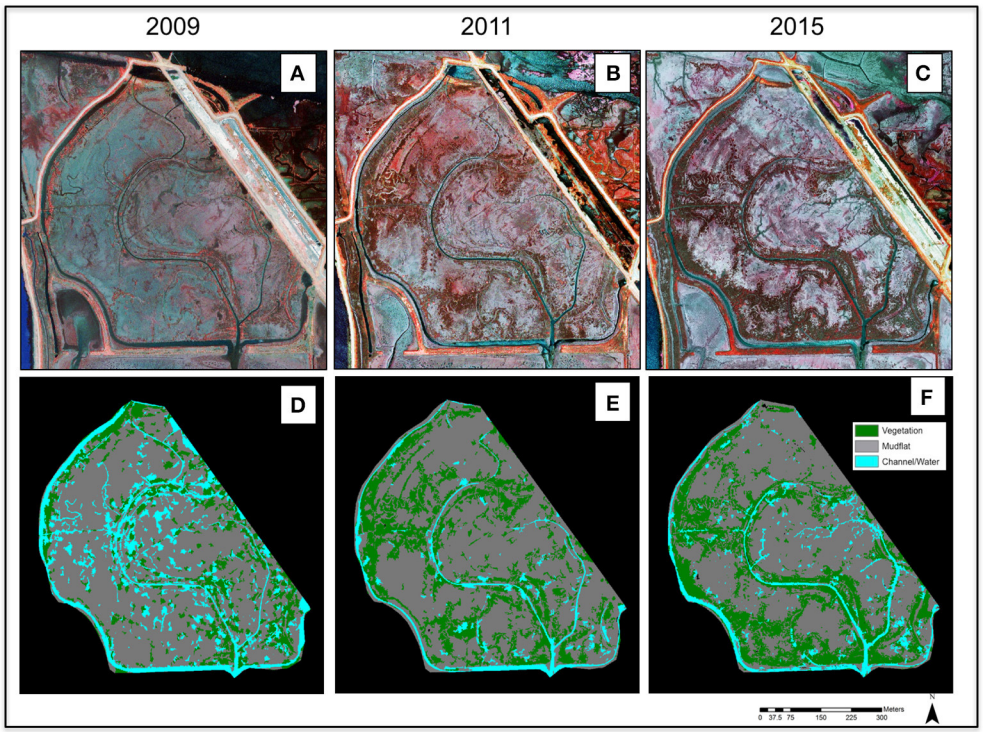

FIGURE 4 | Change over time at North Creek Marsh. **(A–C)** False color imagery for 2009, 2011, and 2015. **(D–F)** Classifications of cover types for 2009, 2011, and 2015. Aerial images reproduced with permission from ©DigitalGlobe, 2017.

entities (Moffett and Gorelick, 2013), particularly at early post-restoration stages with higher spatial heterogeneity (Tuxen and Kelly, 2008; Tuxen et al., 2008; Kelly et al., 2011). By using object-based methods, we were able to create realistic objects for our cover types that produced high levels of accuracy, allowing for comparison between years at high spatial resolution. While NDVI has historically been employed as a means of detecting vegetation, we found that classification parameters that relied too heavily on NDVI led to classification of areas with green algae on the mudflat surface as vegetation. By also taking into account spatial parameters, our object-based approach minimized spurious mapping of vegetation that may occur when using pixel-based change methods. Our results highlight the distinct benefit of using OBIA in assessing early stages of restoration project development to capture fine scale change and to streamline semi-automated vegetation detection despite some degree of required specificity of methods and parameters at individual dates. Although OBIA benefits in wetland analyses have long been recognized (Tuxen and Kelly, 2008; Dronova, 2015), this methodology is still under-utilized in the context of restoration monitoring (Klemas 2013) and offers powerful opportunities for cost-effective, spatially comprehensive, and repeated characterizations of vegetation development and landscape structure.

Notably, different algorithm parameters were needed for each image to produce images with the highest accuracy. We were able to attain a high level of accuracy across all three images, but accuracy was slightly lower in the in the 2009 imagery, when algae and surface water led to more confusion between classes, highlighting the importance of date-specific conditions on wetland surface analysis in tidal systems. Distributions of water and mud across the landscape were mapped differently in different years, due to different tidal heights at the time of collection and evolving morphology of landscape topography that likely led to retention of water in different areas across the years. We suggest that changes between mudflat and water should be interpreted with caution, since they are highly temporally variable and sensitive to when imagery was collected. While vegetation increased overall, there were also notable areas of localized vegetation loss (particularly in areas farther from channels), which indicates that the site is still evolving. We expect that efforts to monitor multiple restoration sites will likely need to create separate classifications for each site to minimize the impact of unique surface conditions at a given tidal stage and surface variability on classification effectiveness.

Limitations and Future Directions

In addition to the effects of wet years and drought, the trends we observed are likely influenced by a combination of other factors. In the commonly accepted models of tidal wetland development, sedimentation rates are expected to slow as the marsh plain reaches equilibrium with tidal inundation (Morris et al., 2002; Williams and Orr, 2002; D'Alpaos et al., 2012; Schile et al.,

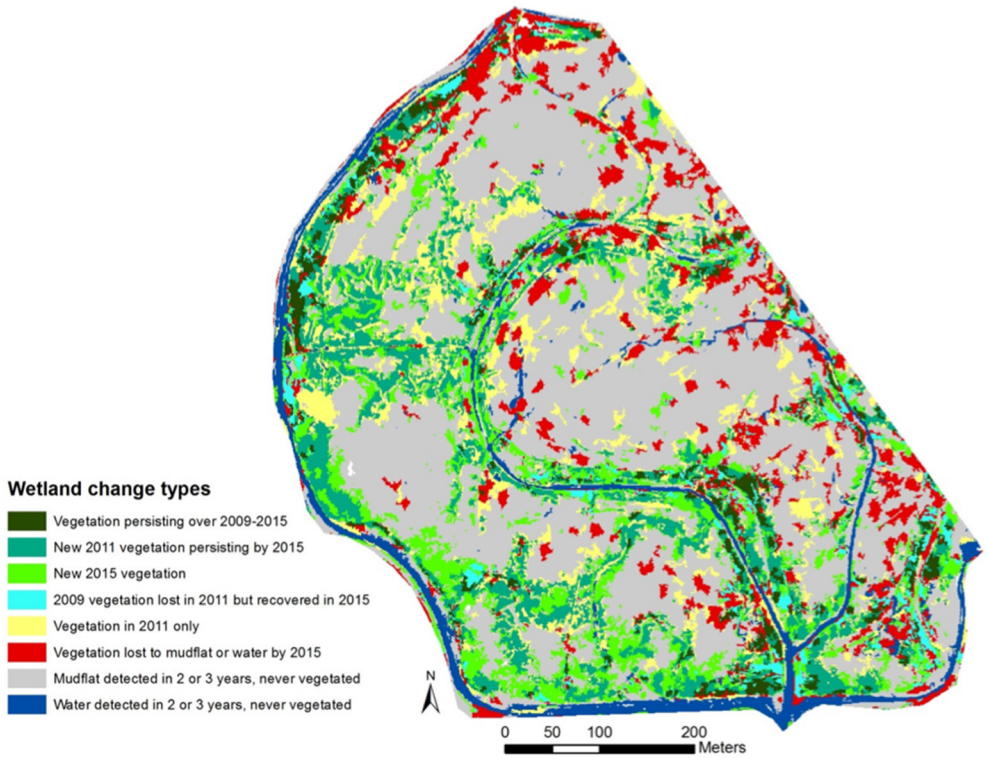

FIGURE 5 | Change detection image at North Creek Marsh, 2009–2011. Vegetation is largely concentrated along channel edges. Interior areas are largely persistent mudflat over the entire study period. Some interior areas away from channels contain vegetation in the 2011 classification only that is subsequently lost in 2015.

TABLE 2 | Patch statistics for 2009, 2011, and 2015.

Year	Number of patches	Mean patch area, m^2	Maximum patch area, m^2	Standard deviation patch area, m^2	Coefficient of variation
2009	394	147.6	4,682.24	385.79	2.61
2011	282	352.18	25,623.7	1,641.05	4.66
2015	473	226.71	21,194.9	1,351.44	5.96

2014), which could explain the observed decrease in the rate of vegetation expansion we observed. However, sedimentation data collected at the site shows that annual sedimentation rates between the breach date in 2006 and 2013 were marginally slower (1.21 cm/year) than between 2013 and 2016 (1.33 cm/year), when drought conditions persisted (Krause, 2016). This indicates that the decreased rate of vegetation expansion is not due to decreased rates of sedimentation. Further, between 2012 and 2015, *S. foliosa* was planted across the study site (Hammond, 2016). Since these plantings were largely adjacent to areas of existing vegetation, they may have contributed to the expansion we observed, which means that rates of natural expansion during the drought years may have been even lower than our results indicate. Lastly, our analysis of tidal height data shows that differences in tidal inundation did not differ between the wet and dry periods.

The inability to detect species-level trends is an important limitation of our study. In addition to the *S. foliosa* plantings, the tidal wetland sub-dominant species *F. salina* (Alkali Heath) and *J. carnosa* (Fleshy Jaumea) were also present at the site in very low densities (Krause, 2016). Work from older restoration and reference sites in the north SF Bay indicates that Bay salinity can also influence the dynamics of sub-dominant species (Chapple et al., 2017), which may be a promising direction for future studies in these areas. However, *S. pacifica* is the dominant species in the early stages of restoration in the area, and is responsible for the majority of vegetation cover. One of the major implications of rates of vegetation change is the ability of developing restoration projects to keep pace with sea level rise (Goals Project, 2015), so for the purposes of our study understanding overall rates of vegetation change is appropriate. Advancing this OBIA-based monitoring framework to develop a capacity to detect species-level transitions in the future is an important research need that could benefit from the advances in high-resolution hyperspectral platforms (Santos et al., 2011; Lucieer et al., 2014).

Implications for Restoration and Adaptive Management

Our results demonstrate that considering non-linear post-restoration site development trajectories that are dependent on weather may be crucial for structuring adaptive management decisions in variable climates. A detailed understanding of how weather interacts with site geomorphology to influence outcomes is important for planning effective restoration efforts (Holmgren and Scheffer, 2001; Vaughn and Young, 2010; Sitters et al., 2012; Chapple et al., 2017). Importantly, slower progress of vegetation is not entirely negative, as the intermediate habitat mosaic of vegetation, mudflat, and water provides habitat for a number of avian species (Moss, 2015). However, given that the rapid re-vegetation of tidal wetland restoration projects is considered to be one of the best means of allowing developing sites to keep pace with sea-level rise (Goals Project, 2015), understanding the role of weather in determining these rates will be essential for managing projects that are resilient to climate change.

Developing reproducible remote sensing techniques is a promising, potentially cost effective means of monitoring change in these projects over time. Future efforts should explore change over multiple sites to discern how generalized these weather-dependent trends are and how transferable image classification settings are between sites. Sampling restoration sites across a range of salinity levels in the SF Bay would allow for an exploration of how the spatial context of sites might influence their temporal development. Since field sampling is limited by time, scale, funding, and spatial resolution, remotely sensed products hold high promise for addressing these issues.

From a restoration management perspective, our findings supported other work demonstrating that channel edges are hotspots of vegetation development (Sanderson et al., 2000; Wallace et al., 2005; O'Brien and Zedler, 2006). Attempts to add diversity into developing marshes should focus on these areas, a practice which is already in place in the SF Bay (Hammond, 2016). Since we show that interior mudflat areas away from channels may be slow to develop vegetation, proactive manipulation of elevation in these areas prior to restoring tidal access may be one way to speed vegetation development. Further, efforts to actively manipulate channel structure may also help speed the development of vegetation establishment. These actions are likely to be more necessary in areas where salinity levels are currently higher, but may become necessary across a range of sites as climate change shifts salinity distributions in the SF Bay (Callaway et al., 2007). Proactive geomorphic intervention is likely to make these projects more resilient to the impacts of sea level rise.

AUTHOR CONTRIBUTIONS

DC and ID conceived of the research. DC analyzed the data. DC and ID wrote and revised the manuscript.

FUNDING

DC's work on the project was supported by the NSF GRFP program (DGE 1106400) and UC Berkeley's Sponsored Projects for Undergraduate Research Program.

ACKNOWLEDGMENTS

Thanks to Adina Merenlender, Katie Suding, Maggi Kelly, Laurel Larsen, John Krause, John Bourgeois, Kristin Byrd, Brian Fulfrost, Micah Levi, Manda Au, and Christian Tettlebach. Image registration was done by Sean Hogan at the UCANR Informatics and GIS Program. CA Department of Fish and Wildlife provided site access and the San Francisco Estuary Institute provided imagery for 2009 and 2011. Two reviewers provided feedback that greatly improved the manuscript. Appropriate permissions have been obtained from copyright holders for all reproduced imagery.

REFERENCES

Asner, G. P., Brodrick, P. G., Anderson, C. B., Vaughn, N., Knapp, D. E., and Martin, R. E. (2016). Progressive forest canopy water loss during the 2012–2015 California drought. *Proc. Natl. Acad. Sci. U.S.A.* 113, E249–E255. doi: 10.1073/pnas.1523397113

Bates, D., Maechler, M., Bolker, B., and Walker, S. (2017). *lme4: Linear Mixed-Effects Models Using EIGEN and S4*. Available online at: http://CRAN.R-project.org/package=lme4

Berg, N., and Hall, A. (2017). Anthropogenic warming impacts on California snowpack during drought. *Geophys. Res. Lett.* 44, 2511–2518. doi: 10.1002/2016GL072104

Bernhardt, E. S., Sudduth, E. B., Palmer, M. A., Allan, J. D., Meyer, J. L., Alexander, G., et al. (2007). Restoring rivers one reach at a time: results from a survey of US river restoration practitioners. *Restor. Ecol.* 15, 482–493. doi: 10.1111/j.1526-100X.2007.00244.x

Blaschke, T., and Hay, G. J. (2001). Object-oriented image analysis and scale-space: theory and methods for modeling and evaluating multiscale landscape structure. *Int. Arch. Photogramm. Remote Sens.* 34, 22–29.

Blaschke, T., Lang, S., Lorup, E., Strobl, J., and Zeil, P. (2000). Object-oriented image processing in an integrated GIS/remote sensing environment and perspectives for environmental applications. *Environ. Informat. Plann. Politic. Public* 2, 555–570.

Brand, L. A., Smith, L. M., Takekawa, J. Y., Athearn, N. D., Taylor, K., Shellenbarger, G. G., et al. (2012). Trajectory of early tidal marsh restoration: elevation, sedimentation and colonization of breached salt ponds in the northern San Francisco Bay. *Ecol. Eng.* 42, 19–29. doi: 10.1016/j.ecoleng.2012.01.012

Brew, D. S., and Williams, P. B. (2010). Predicting the impact of large-scale tidal wetland restoration on morphodynamics and habitat evolution in south San Francisco Bay, California. *J. Coastal Res.* 26, 912–924. doi: 10.2112/08-1174.1

Callaway, J. C., Thomas Parker, V., Vasey, M. C., and Schile, L. M. (2007). Emerging issues for the restoration of tidal marsh ecosystems in the context of predicted climate change. *Madroño* 54, 234–248. doi: 10.3120/0024-9637(2007)54[234:EIFTRO]2.0.CO;2

Callaway, R. M., and Sabraw, C. S. (1994). Effects of variable precipitation on the structure and diversity of a California salt marsh community. *J. Veget. Sci.* 5, 433–438. doi: 10.2307/3235867

Campbell, A., Wang, Y., Christiano, M., and Stevens, S. (2017). Salt Marsh Monitoring in Jamaica Bay, New York from 2003 to 2013: a decade of change from restoration to hurricane sandy. *Remote Sens.* 9:131. doi: 10.3390/rs9020131

Chapple, D. E., Faber, P., Suding, K. N., and Merenlender, A. M. (2017). Climate variability structures plant community dynamics in mediterranean restored and reference tidal wetlands. *Water* 9:209. doi: 10.3390/w9030209

Cloern, J. E., and Schraga, T. S. (2016). *USGS Measurements of Water Quality in San Francisco Bay (CA), 1969-2015, Version 2.* U.S. Geological Survey Release. U.S. Geological Survey.

Conchedda, G., Durieux, L., and Mayaux, P. (2008). An object-based method for mapping and change analysis in mangrove ecosystems. *Isprs J. Photogramm. Remote Sens.* 63, 578–589. doi: 10.1016/j.isprsjprs.2008.04.002

Copeland, S. M., Harrison, S. P., Latimer, A. M., Damschen, E. I., Eskelinen, A. M., Fernandez-Going, B., et al. (2016). Ecological effects of extreme drought on Californian herbaceous plant communities. *Ecol. Monogr.* 86, 295–311. doi: 10.1002/ecm.1218

D'Alpaos, A., Da Lio, C., and Marani, M. (2012). Biogeomorphology of tidal landforms: physical and biological processes shaping the tidal landscape. *Ecohydrology* 5, 550–562. doi: 10.1002/eco.279

Dettinger, M. D., and Cayan, D. R. (2003). Interseasonal covariability of Sierra Nevada streamflow and San Francisco Bay salinity. *J. Hydrol.* 277, 164–181. doi: 10.1016/S0022-1694(03)00078-7

Diggory, Z. E., and Parker, V. T. (2011). Seed supply and revegetation dynamics at restored tidal marshes, Napa River, California. *Restor. Ecol.* 19, 121–130. doi: 10.1111/j.1526-100X.2009.00636.x

Dronova, I. (2015). Object-based image analysis in wetland research: a review. *Remote Sens.* 7:6380–6413. doi: 10.3390/rs70506380

Erwin, K. L. (2009). Wetlands and global climate change: the role of wetland restoration in a changing world. *Wetlands Ecol. Manag.* 17, 71. doi: 10.1007/s11273-008-9119-1

Fulfrost, B., Thomson, D., Archibald, G., Loy, C., and Fourt, W. (2012). *Habitat Evolution Monitoring Program: South Bay Salt Pond Restoration Project, Final Report (2009-2011).* Prepared for California Coastal Conservancy.

Gaertner, P., Foerster, M., Kurban, A., and Kleinschmit, B. (2014). Object based change detection of Central Asian Tugai vegetation with very high spatial resolution satellite imagery. *Int. J. Appl. Earth Observ. Geoinform.* 31, 110–121. doi: 10.1016/j.jag.2014.03.004

Goals Project (2015). *The Baylands and Climate Change: What We Can Do. Baylands Ecosystem Habitat Goals Science Update 2015*. San Francisco Bay Area Wetlands Ecosystem Goals Project, California State Coastal Conservancy.

Hammond, J. (2016). *San Francisco Estuary Invasive Spartina Project Revegetation Program 2014–2015 Installation Report and 2015-2016 Revegetation Plan*. Oakland, CA: California State Coastal Conservancy.

Hastie, T. (2013). *gam: Generalized Additive Models, R Package, Version 0.98*. Available online at: www.r-project.com

Holmgren, M., and Scheffer, M. (2001). El Niño as a window of opportunity for the restoration of degraded arid ecosystems. *Ecosystems* 4, 151–159. doi: 10.1007/s100210000065

Holmgren, M., Stapp, P., Dickman, C. R., Gracia, C., Graham, S., Gutiérrez, J. R., et al. (2006). Extreme climatic events shape arid and semiarid ecosystems. *Front. Ecol. Environ.* 4, 87–95. doi: 10.1890/1540-9295(2006)004[0087:ECESAA]2.0.CO;2

Kelly, M., Tuxen, K. A., and Stralberg, D. (2011). Mapping changes to vegetation pattern in a restoring wetland: finding pattern metrics that are consistent across spatial scale and time. *Ecol. Indic.* 11, 263–273. doi: 10.1016/j.ecolind.2010.05.003

Klemas, V. (2013). Using remote sensing to select and monitor wetland restoration sites: an overview. *J. Coast. Res.* 29, 958–970. doi: 10.2112/JCOASTRES-D-12-00170.1

Kondolf, G. M., Anderson, S., Lave, R., Pagano, L., Merenlender, A., and Bernhardt, E. S. (2007). Two decades of river restoration in California: what can we learn? *Restor. Ecol.* 15, 516–523. doi: 10.1111/j.1526-100X.2007.00247.x

Krause, J. (2016). *CDFW Marsh Monitoring Field Form: Vegetation and Sediment*. Sacramento, CA: California Department of Fish and Wildlife.

Lucieer, A., Malenovsky, Z., Veness, T., and Wallace, L. (2014). HyperUAS—imaging spectroscopy from a multirotor unmanned aircraft system. *J. Field Robot.* 31, 571–590. doi: 10.1002/rob.21508

Malamud-Roam, F., and Ingram, B. L. (2004). Late Holocene δ 13 C and pollen records of paleosalinity from tidal marshes in the San Francisco Bay estuary, California. *Q. Res.* 62, 134–145. doi: 10.1016/j.yqres.2004.02.011

McGarigal, K., Cushman, S. A., Neel, M. C., and Ene, E. (2015). *FRAGSTATS: spatial Pattern Analysis Program for Categorical Maps. Computer Software Program Produced by the Authors at the University of Massachusetts, Amherst*. Available online at: http://www.umass.edu/landeco/research/fragstats/fragstats.html

Moffett, K. B., and Gorelick, S. M. (2013). Distinguishing wetland vegetation and channel features with object-based image segmentation. *Int. J. Remote Sens.* 34, 1332–1354. doi: 10.1080/01431161.2012.718463

Moffett, K. B., and Gorelick, S. M. (2016). Alternative stable states of tidal marsh vegetation patterns and channel complexity. *Ecohydrology* 9, 1639–1662. doi: 10.1002/eco.1755

Morris, J. T., Sundareshwar, P. V., Nietch, C. T., Kjerfve, B., and Cahoon, D. R. (2002). Responses of coastal wetlands to rising sea level. *Ecology* 83, 2869–2877. doi: 10.1890/0012-9658(2002)083[2869:ROCWTR]2.0.CO;2

Moss, B. (2015). Mammals, freshwater reference states, and the mitigation of climate change. *Freshwater Biol.* 60, 1964–1976. doi: 10.1111/fwb.12614

O'Brien, E. L., and Zedler, J. B. (2006). Accelerating the restoration of vegetation in a southern California salt marsh. *Wetlands Ecol. Manag.* 14, 269–286. doi: 10.1007/s11273-005-1480-8

Pachauri, R. K., Allen, M. R., Barros, V. R., Broome, J., Cramer, W., Christ, R., et al. (2014). *Climate Change 2014: Synthesis Report. Contribution of Working Groups I, II and III to the fifth Assessment Report of the Intergovernmental Panel on Climate Change.* Geneva: IPCC. Available online at: http://epic.awi.de/37530/ (Accessed October 18, 2016).

Peters, D. P., Pielke, R. A., Bestelmeyer, B. T., Allen, C. D., Munson-McGee, S., and Havstad, K. M. (2004). Cross-scale interactions, nonlinearities, and forecasting catastrophic events. *Proc. Natl. Acad. Sci. U.S.A.* 101, 15130–15135. doi: 10.1073/pnas.0403822101

Philip Williams & Associates, Ltd., and Faber, P. M. (2004). *Design Guidelines for Tidal Wetland Restoration in San Francisco Bay* (San Francisco, CA: The Bay Institue).

Robeson, S. M. (2015). Revisiting the recent California drought as an extreme value. *Geophys. Res. Lett.* 42, 6771–6779. doi: 10.1002/2015GL064593

Sanderson, E. W., Ustin, S. L., and Foin, T. C. (2000). The influence of tidal channels on the distribution of salt marsh plant species in Petaluma Marsh, CA, USA. *Plant Ecol.* 146, 29–41. doi: 10.1023/A:1009882110988

Santos, M. J., Anderson, L. W., and Ustin, S. L. (2011). Effects of invasive species on plant communities: an example using submersed aquatic plants at the regional scale. *Biol. Invasions* 13, 443–457. doi: 10.1007/s10530-010-9840-6

Scheffer, M., Bascompte, J., Brock, W. A., Brovkin, V., Carpenter, S. R., Dakos, V., et al. (2009). Early-warning signals for critical transitions. *Nature* 461, 53–59. doi: 10.1038/nature08227

Schiewe, J., Tufte, L., and Ehlers, M. (2001). Potential and problems of multi-scale segmentation methods in remote sensing. *GeoBIT/GIS* 6, 34–39.

Schile, L. M., Callaway, J. C., Morris, J. T., Stralberg, D., Parker, V. T., and Kelly, M. (2014). Modeling tidal marsh distribution with sea-level rise: evaluating the role of vegetation, sediment, and upland habitat in marsh resiliency. *PLoS ONE* 9:e88760. doi: 10.1371/journal.pone.0088760

Schile, L. M., Callaway, J. C., Parker, V. T., and Vasey, M. C. (2011). Salinity and inundation influence productivity of the halophytic Plant *Sarcocornia pacifica*. *Wetlands* 31, 1165–1174. doi: 10.1007/s13157-011-0227-y

Sitters, J., Holmgren, M., Stoorvogel, J. J., and López, B. C. (2012). Rainfall-tuned management facilitates dry forest recovery. *Restor. Ecol.* 20, 33–42. doi: 10.1111/j.1526-100X.2010.00761.x

Son, N.-T., Chen, C.-F., Chang, N.-B., Chen, C.-R., Chang, L.-Y., and Thanh, B.-X. (2015). Mangrove mapping and change detection in Ca Mau Peninsula, Vietnam, using landsat data and object-based image analysis. *IEEE J. Select. Top. Appl. Earth Observ. Remote Sens.* 8, 503–510. doi: 10.1109/JSTARS.2014.2360691

Spencer, T., Schuerch, M., Nicholls, R. J., Hinkel, J., Lincke, D., Vafeidis, A. T., et al. (2016). Global coastal wetland change under sea-level rise and related stresses: the DIVA wetland change model. *Glob. Planet. Change* 139, 15–30. doi: 10.1016/j.gloplacha.2015.12.018

Stanford, B., R. M., Grossinger, J., Beagle, R. A., Askevold, R. A., Leidy, E. E., et al. (2013). *Alameda Creek Watershed Historical Ecology Study*. Richmond, CA: San Francisco Estuary Institute.

Suding, K. N., Gross, K. L., and Houseman, G. R. (2004). Alternative states and positive feedbacks in restoration ecology. *Trends Ecol. Evol.* 19, 46–53. doi: 10.1016/j.tree.2003.10.005

Trulio, L., Clark, D., Richie, S., and Hutzel, A. (2007). *Adaptive Management Plan: Science Team Report for the South Bay Salt Pond Restoration Project.* California Coastal Conservancy.

Tuxen, K. A., Schile, L. M., Kelly, M., and Siegel, S. W. (2008). Vegetation colonization in a restoring tidal marsh: a remote sensing approach. *Restor. Ecol.* 16, 313–323. doi: 10.1111/j.1526-100X.2007.00313.x

Tuxen, K., and Kelly, M. (2008). "Multi-scale functional mapping of tidal marsh vegetation using object-based image analysis," in *Object-Based Image Analysis* (Springer), 415–442. Available online at: http://link.springer.com/chapter/10.1007/978-3-540-77058-9_23 (accessed May 5, 2015).

Tuxen, K., Schile, L., Stralberg, D., Siegel, S., Parker, T., Vasey, M., et al. (2011). Mapping changes in tidal wetland vegetation composition and pattern across a salinity gradient using high spatial resolution imagery. *Wetlands Ecol. Manag.* 19, 141–157. doi: 10.1007/s11273-010-9207-x

Vaughn, K. J., and Young, T. P. (2010). Contingent conclusions: year of initiation influences ecological field experiments, but temporal replication is rare. *Restor. Ecol.* 18, 59–64. doi: 10.1111/j.1526-100X.2010.00714.x

Wallace, K. J., Callaway, J. C., and Zedler, J. B. (2005). Evolution of tidal creek networks in a high sedimentation environment: a 5-year experiment at Tijuana Estuary, California. *Estuar. Coasts* 28, 795–811. doi: 10.1007/BF02696010

Wang, L., Sousa, W. P., and Gong, P. (2004). Integration of object-based and pixel-based classification for mapping mangroves with IKONOS imagery. *Int. J. Remote Sens.* 25, 5655–5668. doi: 10.1080/01431160233129121 5

Ward, K. M., Callaway, J. C., and Zedler, J. B. (2003). Episodic colonization of an intertidal mudflat by native cordgrass (*Spartina foliosa*) at Tijuana Estuary. *Estuar. Coasts* 26, 116–130. doi: 10.1007/BF02691699

Watson, E. B. (2008). Marsh expansion at Calaveras Point Marsh, South San Francisco Bay, California. *Estuar. Coast. Shelf Sci.* 78, 593–602. doi: 10.1016/j.ecss.2008.02.008

Williams, P. B., and Orr, M. K. (2002). Physical evolution of restored breached levee salt marshes in the San Francisco Bay estuary. *Restor. Ecol.* 10, 527–542. doi: 10.1046/j.1526-100X.2002.02031.x

Williams, P., and Faber, P. (2001). Salt marsh restoration experience in San Francisco Bay. *J. Coast. Res.* 27, 203–211.

Woo, I., and Takekawa, J. Y. (2012). Will inundation and salinity levels associated with projected sea level rise reduce the survival, growth, and reproductive capacity of *Sarcocornia pacifica* (pickleweed)? *Aquat. Bot.* 102, 8–14. doi: 10.1016/j.aquabot.2012.03.014

Zedler, J. B. (1983). Freshwater impacts in normally hypersaline marshes. *Estuaries* 6, 346–355. doi: 10.2307/1351393

Zedler, J. B. (2007). Success: an unclear, subjective descriptor of restoration outcomes. *Ecol. Restor.* 25, 162–168. doi: 10.3368/er.25.3.162

Zedler, J. B., and Kercher, S. (2005). Wetland resources: status, trends, ecosystem services, and restorability. *Annu. Rev. Environ. Res.* 30, 39–74. doi: 10.1146/annurev.energy.30.050504.144248

Zedler, J. B., Covin, J., Nordby, C., Williams, P., and Boland, J. (1986). Catastrophic events reveal the dynamic nature of salt-marsh vegetation in Southern California. *Estuaries* 9, 75–80. doi: 10.2307/1352195

Zedler, J. B., Doherty, J. M., and Miller, N. A. (2012). Shifting restoration policy to address landscape change, novel ecosystems, and monitoring. *Ecol. Soc.* 17:36. doi: 10.5751/ES-05197-170436

Conflict of Interest Statement: The authors declare that the research was conducted in the absence of any commercial or financial relationships that could be construed as a potential conflict of interest.

frontiers in Marine Science

METHODS
published: 14 September 2017
doi: 10.3389/fmars.2017.00296

Intercomparison of Approaches to the Empirical Line Method for Vicarious Hyperspectral Reflectance Calibration

Joseph D. Ortiz[1], Dulcinea Avouris[1], Stephen Schiller[2], Jeffrey C. Luvall[3], John D. Lekki[4], Roger P. Tokars[4], Robert C. Anderson[4], Robert Shuchman[5], Michael Sayers[5] and Richard Becker[6]*

[1] Department of Geology, Kent State University, Kent, OH, United States, [2] Department of Physics, South Dakota State University, Brookings, SD, United States, [3] Marshall Space Flight Center (NASA) Huntsville, AL, United States, [4] Glenn Research Center (NASA), Cleveland, OH, United States, [5] Michigan Technological Research Institute, Ann Arbor, MI, United States, [6] Department of Environmental Science, University of Toledo, Toledo, OH, United States

OPEN ACCESS

Edited by:
Kristin B. Byrd, United States Geological Survey, United States

Reviewed by:
Stephanie Schollaert Uz, Goddard Space Flight Center (NASA), United States
Shuisen Chen, Guangzhou Institute of Geography, China

***Correspondence:**
Joseph D. Ortiz
jortiz@kent.edu

Specialty section:
This article was submitted to Coastal Ocean Processes, a section of the journal Frontiers in Marine Science

Received: *28 April 2017*
Accepted: *30 August 2017*
Published: *14 September 2017*

Citation:
Ortiz JD, Avouris D, Schiller S, Luvall JC, Lekki JD, Tokars RP, Anderson RC, Shuchman R, Sayers M and Becker R (2017) Intercomparison of Approaches to the Empirical Line Method for Vicarious Hyperspectral Reflectance Calibration. Front. Mar. Sci. 4:296. doi: 10.3389/fmars.2017.00296

Analysis of visible remote sensing data research requires removing atmospheric effects by conversion from radiance to at-surface reflectance. This conversion can be achieved through theoretical radiative transfer models, which yield good results when well-constrained by field observations, although these measurements are often lacking. Additionally, radiative transfer models often perform poorly in marine or lacustrine settings or when complex air masses with variable aerosols are present. The empirical line method (ELM) measures reference targets of known reflectance in the scene. ELM methods require minimal environmental observations and are conceptually simple. However, calibration coefficients are unique to the image containing the reflectance reference. Here we compare the conversion of hyperspectral radiance observations obtained with the NASA Glenn Research Center Hyperspectral Imager to at-surface reflectance factor using two reflectance reference targets. The first target employs spherical convex mirrors, deployed on the water surface to reflect ambient direct solar and hemispherical sky irradiance to the sensor. We calculate the mirror gain using near concurrent at-sensor reflectance, integrated mirror radiance, and *in situ* water reflectance. The second target is the Lambertian-like blacktop surface at Maumee Bay State Park, Oregon, OH, where reflectance was measured concurrently by a downward looking, spectroradiometer on the ground, the aerial hyperspectral imager and an upward looking spectroradiometer on the aircraft. These methods allows us to produce an independently calibrated at-surface water reflectance spectrum, when atmospheric conditions are consistent. We compare the mirror and blacktop-corrected spectra to the *in situ* water reflectance, and find good agreement between methods. The blacktop method can be applied to all scenes, while the mirror calibration method, based on direct observation of the light illuminating the scene validates the results. The two methods are complementary and a powerful evaluation of the quality of atmospheric correction over extended areas. We decompose the resulting spectra using varimax-rotated, principal component analysis, yielding information about the underlying color producing agents that contribute to the

observed reflectance factor scene, identifying several spectrally and spatially distinct mixtures of algae, cyanobacteria, illite, haematite, and goethite. These results have implications for future hyperspectral remote sensing missions, such as PACE, HyspIRI, and GeoCAPE.

Keywords: hyperspectral remote sensing, PACE, HyspIRI, GeoCAPE, empirical line method, cyanobacterial harmful algal blooms, VPCA, atmospheric correction

INTRODUCTION

The empirical line method (ELM) is well-recognized as an accurate, operational approach for the calibration of aerial and satellite imaging systems to correct multispectral and hyperspectral data from raw digital numbers (DNs) or radiance to at-surface reflectance factors (e.g., Ferrier and Trahair, 1995; Smith and Milton, 1999). If two or more ground targets with a known reflectance factor are placed within a scene, calibration for each spectral band reduces to an uncomplicated process of regressing the observed radiance against the known reflectance factor values. Linearity has been empirically demonstrated to be valid over the full range of low to high reflectance factor targets (Baugh and Groeneveld, 2008). The result is the calculation of gain and offset coefficients that can be applied to all surfaces in the scene, assuming uniform atmospheric conditions. The gain characterizes the sensor response of reflectance factor per unit radiance and the offset characterizes the sky path radiance between the sensor and the surface for a sensor system calibrated to radiance.

As part of a collaborative Cyanobacterial Harmful Algal Bloom (CyanoHAB) monitoring program in the Western Basin of Lake Erie (**Figure 1**) and Sandusky Bay, OH conducted from 2014 to present, we have developed and implemented an approach to apply an empirical atmospheric correction and vicarious reflectance factor calibration to the second generation, National Aeronautics and Space Administration (NASA) John Glenn Research Center's Hyperspectral Imager (HSI2). This manuscript focuses on methods developed at Kent State University (KSU) compared with those employed at Michigan Technological Research Institute (MTRI) and the University of Toledo (UT). Research conducted by MTRI, UT and other collaborators will be presented in greater detail separately. The HSI2 is an aerial imaging spectroradiometer that generates a hyperspectral datacube over the VNIR from 400 to 900 nm. Atmospheric correction is a necessary pre-processing step required prior to further processing to extract information about algal composition from the HSI2 image swaths (Gordon et al., 1988; Gao et al., 2009; Goetz, 2009). For the application presented in this study, the ELM is applied in four ways as described below. Three versions are simplified further to a single-point calibration by assuming that since the NASA Glenn S3 Viking aircraft carrying the spectroradiometer is flying at a low altitude that the path radiance between the surface and aircraft can be assumed to be negligible. The result may introduce an offset in the retrieved spectra compared to the actual surface spectrum, however the general spectral shape of the upwelling surface reflectance factor spectrum is still revealed (Farrand et al., 1994). This allows spectral shape based methods, which are not strongly dependent on absolute reflectance factor values to be effectively employed. The approach that we use here is the KSU visible derivative, Varimax-rotated, Principle Component Analysis (VPCA) spectral decomposition method, (Ali et al., 2013; Ortiz et al., 2013). Our conceptual approach also capitalizes on an innovative reflectance factor reference target, allowing the ELM to be applied directly to observations collected on the lake surface, which is the surface of particular interest for this and other aquatic studies. Application of these methods to the optically complex waters of Lake Erie is a stringent test of the approach because we document its applicability in highly turbid waters. The methods developed here will be applicable in coastal and inland water as well as marine environments imaged by proposed orbital hyperspectral missions such as the: Plankton, Aerosol, Cloud, ocean Ecosystem (PACE) mission, the Hyperspectral Infrared Imager (HyspIRI) mission, and the Geostationary Coastal and Air Pollution Events (GeoCAPE) mission. Deploying these orbital tools will create the opportunity for enhanced estimation of pigment-related biomass and new capabilities to identify algal and cyanobacterial composition based on extraction of pigment spectra by visible derivative spectroscopy.

METHODS

The innovative calibration approach is to employ a floating panel (1.07 m by 1.17 m; 1.25 m^2) composed of 16 convex mirrors (0.26 m diameter with radius of curvature 0.18 m) deployed on the water surface, providing an in-scene lake surface reference for image reflectance factor calibration. The convex mirrors reflect the direct sunlight and hemispherical sky illumination downwelling to the surface of the Earth back up to the HSI2 sensor while it is flying over the target. We can then use the HSI2 response of the mirror targets to normalize the upwelling radiance to percent reflectance factor, if we know the correct calibration gain function for the mirror target that transforms the HSI2 measured at-sensor radiance to a Lambertian surface reflectance factor. This effectively converts the spectroradiometer to a spectrophotometer merely by sacrificing a few scene pixels. An advantage of using convex mirrors deployed on the lake (**Figure 1**) is that their spherical surface produces a constant reflectance factor even when bobbing around on the unstable water surface. We have constructed a series of mirror panels for in scene reflectance factor calibration (**Figure 1B**). These were deployed as floating platforms in the western basin, Sandusky Bay, and a coastal transect along the southern shore of the central basin of Lake Erie using Ohio Division of Natural Resources

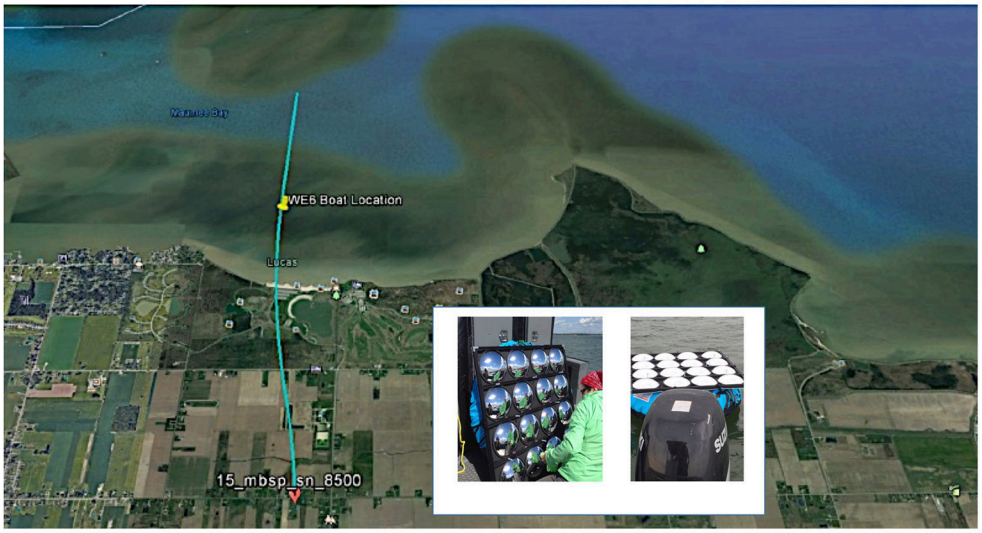

FIGURE 1 | (A) Maumee Bay State Park is the location where the NASA Glenn, second generation Hyperspectral imager (HSI2) swath 15_MBSP was collected on June 21, 2016. Sampling station Western Erie 6 (WE6) is indicated, where measurements were taken from the boat, and the mirror array was deployed. **(B)** Inset: mirror calibration panel being cleaned on deck and deployed behind the vessel in Sandusky Bay (After Figure 4.3 with modification, Lekki et al., 2017).

(ODNR), United States Geological Survey (USGS), or Ohio Sea Grant vessels used as part of regular sampling trips conducted during NASA coincident over flights.

Ground-Based Measurements and Sampling

The image swath analyzed here was collected in the western basin of Lake Erie perpendicular to the coast over Maumee Bay State Park (MBSP), Oregon, OH, one of the surface calibration sites employed in the Lake Erie CyanoHAB monitoring program and includes the offshore sampling station designated WE6 (or sometimes WLE06) shown in **Figure 1**.

Each field site was revisited bi-weekly from early June through mid-October, 2016, via boat, provided that weather conditions were suitable for data collection. An Analytical Spectral Devices™ (ASD) FieldSpec® Handheld 2 (HH2) spectroradiometer was used to measure downwelling irradiance with a cosine-theta receptor. Irradiance data was collected with the cosine-theta receptor shaded and unshaded to obtain diffuse and global irradiance data. Surface water reflectance factor was collected with a 10-degree field of view (10° FOV) receptor calibrated to a 100% Spectralon™ plate that is factory calibrated with the ASD FieldSpec® HH2 spectroradiometer. At specific stations chosen in coordination with the NASA aircraft pilot to ensure coincident operations, the mirror calibration panel was deployed from the research vessel during the overflight.

Image Acquisition

The initial version of the hyperspectral imaging system was developed at NASA Glenn Research Center in fiscal year 2006 and has been flown in three separate aircraft campaigns to study CyanoHABs in collaboration with the National Oceanic and Atmospheric Administration (NOAA) Great Lakes Environmental Research Laboratory (GLERL) (Lekki et al., 2009).

As of 2015, the second generation, NASA Glenn hyperspectral imaging system (HSI2) (Lekki et al., 2017 NASA TM 2017-219071) includes the imager, an Inertial Navigation System (INS), and an upward-looking spectroradiometer. Because reflectance factor measurements are desired for CyanoHAB assessment, starting with the 2015 HSI2 imaging campaign, an ASD FieldSpec® HH2 spectroradiometer was mounted in the aircraft and used to collect downwelling irradiance measurements in order to compute simple, at-sensor reflectance factor values in conjunction with imager radiance. The HH2 spectroradiometer was mounted in the aircraft under a Plexiglas window because it was logistically impractical to modify the fuselage of the aircraft. A cosine receptor foreoptic was attached to the upward-looking HH2 spectroradiometer by a fiber optic cable to directly measure the total hemispherical solar irradiance.

Data recorded during each flight is produced by two systems: the HSI2 control and acquisition computer and the spectroradiometer system. The HSI2 imager and the INS acquire data at 25 Hz while the ASD FieldSpec® HH2 spectroradiometer acquires at 0.033 Hz. Because the HSI2 imager and upward-looking HH2 spectroradiometer are not synchronized, the imager frame times are used as the basis for the INS and spectroradiometer data are interpolated to estimate data values corresponding to the imager frame times. From 2015 and on, for each imaging flight over a point of interest, the output of the hyperspectral data acquisition computer is a binary file containing a number of hyperspectral image frames (also referred to as tracks). Each frame includes an image with data in raw counts. The data files also contain a set of parameter values for

each frame related to GPS time, latitude, longitude, altitude, roll (side to side motion), pitch (nose up to nose down motion) and yaw (motion around a vertical axis). The raw HSI2 image contains 658 spectral bands (arrayed in the along-track direction from the UV to the NIR) and 496 spatial pixels (arrayed in the cross-track ground direction). From the 658 spectral bands, the 510 central bands with the highest signal to noise ratio (SNR) are retained for analysis. The full spectral resolution of the HSI2 sensor is thus ∼0.98 nm per band, with continuous bands through the visible-near infrared (VIS-NIR) range of 400–900 nm.

The calibration of the HSI2 imager takes place at the NASA Glenn Optical Laboratory. Using a Labsphere™ incandescent light source with a radiance profile traceable to the National Institute of Standards and Technology (NIST), a set of calibration frames is acquired with the HSI2 system. The Labsphere™ radiance profile image is then divided by the average of this set of frames to yield a radiance-per-count image. Radiance units are: Watts per square meter per steradian per nanometer. The radiance-per-count image can then be multiplied by each HSI2 image acquired in flight to convert it to radiance.

When applying the radiance-per-count calibration image, a perfect pixel-to-pixel match must be assumed between the radiance-per-count image generated in the laboratory and the in-flight data image. This is frequently not the case with data acquired while airborne. The HSI images have two axes: the wavelength axis and the distance axis. There is evidence that a shift occurs in the airborne data along both axes and that the shift may be different for each axis. To correct this shift, the calibration image may also be shifted to improve the registration before it is applied to the data. The solar "G" line and the O_2 absorption line have been used to determine the wavelength shift. The wavelength axis is stretched and/or translated so that these two spectral features occur at their proper wavelengths in the data image.

Incorrect registration along the distance axis manifests as striping that appears in the along-track direction of the images. The radiance-per-count image may be shifted slightly along the distance axis to minimize the striping effect. When a segment of a track is over water across the whole track, a correlation process can determine the optimum shift based on the maximum from a cross-correlation between the data image and the radiance-per-count image. For the KSU VPCA spectral decomposition method, the data was destriped using the ENVI/IDL SPEAR Vertical Stripe Removal tool.

To reduce the size of the processed files and to satisfy requirements imposed by some CyanoHAB detection algorithms, the HSI images are rebinned along the wavelength axis, decreasing the wavelength resolution from 0.98 to 2.97 nm per pixel. This results in an increase in the SNR of the resulting binned image. The rebinning process is performed both on the raw data and on the calibration images before the radiance calibration is applied. For the KSU VPCA spectral decomposition method, the data is further rebinned to 10 nm resolution.

The georeferencing process requires knowledge of the effective viewing angle for the imager. The total viewing angle is defined as twice the angle from nadir to the angle beyond which the image cuts off. For the imager described here, the total angular width of the image swath was determined to be 12.4°. The accuracy of georeferencing has been used as a validation of this view angle determination. Once the data has been converted to units of radiance with the optimum shifts applied, a set of GPS coordinates is computed for each pixel in the image track. For each frame in the track, the spatial pixels mark a cross track line that is imaged on the surface of the Earth with the GPS coordinates computed for each pixel in the line. Think of the pixels as 496 point sources whose beams are projected across the swath from the Earth surface to the aircraft as the plane overflies an area. The problem is to compute the GPS coordinates of the projected spots for each of the 496 spatial pixels. This would be a relatively simple geometry problem if the imager was always pointing directly down. But, the HSI2 unit is fixed to the airplane structure, so as the plane rolls, pitches and yaws, the HSI2 unit must follow. Finding the GPS coordinates is thus essentially a ray-tracing process. The method used here attempts to trace a ray out from each pixel on the imager through the optical system and down to the surface.

In order to do this ray-tracing computation, some assumptions are made: (1) Traveling out from the image sensor chip, the ray path to the front of the lens includes mirrors, a holographic grating, and then the lens. The rays are not followed through this maze, but are assumed to begin at the lens. (2) A constant angle of view is assumed for the optical system. The 496 imaging pixels are assumed to be spread linearly over the 12.4° viewing angle. This amounts to an angular spacing between pixels of 0.025°. (3) The above-ground-level elevation is also assumed to be constant. This is important because the GPS device provides altitude above sea level. To compute the actual distance to the surface from the aircraft, the ground elevation above sea level is subtracted from the GPS altitude. The constant elevation assumption is reasonable when flying over one of the Laurentian Great Lakes because the elevation is known and is essentially constant. The constant elevation assumption is frequently violated when flying over land. There is currently no way of knowing the elevation before knowing the coordinates; the elevation information must be determined post flight. Thus, there is presently more uncertainty in the geolocation for inland tracks. With these assumptions and measurements of the image platform orientation, the coordinates of the imaged line on the surface can be computed. This georeferencing process was validated using known ground control points.

Because the plane may be pitch, roll or yaw during the data acquisition, it is very likely that the coordinates of some adjacent pixels will overlap. Thus, the process of georeferencing of these images can be very complex. Fortunately, the software package used (Excelis Visual Information Solutions) provides this functionality. The georeferencing routine available computes a footprint using the envelope of all the GPS coordinates in the track. Then the software attempts to fill in the gaps with data pixels. To compute a radiance value for a pixel in a gap, the software looks for data pixels within a 7-pixel neighborhood around the gap pixel and sets the value of the gap pixel to the average of these neighborhood data pixels. For hyperspectral image pixels located on the same geographical location, the

software uses a similar operation to determine the proper data level for that pixel. The roll, pitch, and yaw angles are assumed to apply to the imaging axis. However, small adjustments to the roll, pitch, and yaw values are necessary to achieve optimum georeferencing results. These adjustments remain constant until the mounting configuration is changed. As longitude and latitude is generated for each pixel in a given track, these data are then used to produce a georeferenced data set. The software package (Excelis Visual Information Solutions) used also provides a Google Earth Bridge functionality, which creates a ".kml" file that places the georeferenced image onto a satellite view of the Earth surface.

As a demonstration of the empirical mirror-based correction approaches described below, the technique is applied to NASA HSI2 scene 062116_15_MBSP, where the file name convention for the HSI2 images is: <acquisition date (mmddyy)>_<swath #>_<location ID>. This image was collected on June 21, 2016 over Lake Erie, offshore of MBSP. On this day, the sky conditions were clear and the NASA aircraft flew at an altitude of 8,500 ft. The image swath collected included station WE6, offshore of MBSP where the team deployed a mirror panel and collected surface validation data as described above. The aircraft HSI2 sensor was calibrated preflight for producing absolute radiance imagery as described above. The image used for this analysis was corrected for aircraft motion, georeferenced to obtain proper spatial relationships between pixels, and resampled using a nearest neighbor algorithm to convert rectangular pixels in the raw data to square pixels. The rectangular pixels resulted from an extended along-scan integration time to improve the sensor signal-to-noise at the low water radiance. After processing, the resulting pixel GSD was 3.21 m on a side.

Reflectance Factor Calibration-Inter-Comparison of Four Methods

For this study, we compare four empirical means of removing atmospheric effects by transforming from radiance to reflectance factor (**Table 1**). Three of these make use of data from the floating mirror arrays, while one is based on application of the ELM using parking lot blacktop as the calibration surface.

In the empirical mirror calibration method designated ELM0, the Sun's downwelling irradiance hits the mirror surfaces and is radiated back up to the HSI2 senor flying above the target during an overpass. The ratio of the HSI2 radiance divided by the radiance reflected from the mirror is calculated to yield a biased estimate of the at-sensor reflectance factor. The measurement is biased due to the dispersion of light by the curved mirror surfaces. A gain factor for the mirror is then calculated by dividing the biased estimate of the at-sensor reflectance factor with the 100% Spectralon™-calibrated, at-surface reflectance factor measurement obtained from an ASD FieldSpec® HH2 spectroradiometer to remove the bias. This single-point gain factor is then used to correct the mirror signal to determine a reflectance factor from the HSI2 radiance. This correction depends on knowledge of the observed at-surface reflectance of the target, measured using an ASD FieldSpec® HH2 spectroradiometer. For the single-point empirical mirror calibration method (ELM1), we use a combination of the mirror radiance and the diffuse to global ratio measured using an upward looking ASD FieldSpec® HH2 spectroradiometer equipped with a cosine-theta receptor to determine the mirror gain function. For the two-point empirical mirror calibration method, we add the use of the ASD at-surface lake reflectance factor, which yields the intercept for the reflectance factor in addition to the gain of the relationship. Derivations and equations for the ELM0, ELM1, and ELM2 methods based on radiative transfer theory are described below.

The MTRI blacktop calibration method does not employ mirrors to remove the atmospheric effects. Rather, that method starts with an at-sensor reflectance factor ratio determined by dividing the HSI2 radiance using the at-sensor irradiance measured by the upward looking ASD FieldSpec® HH2 equipped with a cosine theta receptor that is mounted in the aircraft. A gain function is then determined by comparing the at-sensor reflectance factor to the well-known measurement of the reflectance factor of the asphalt blacktop parking lot at MBSP, which is measured routinely by researchers throughout the summer. The cosine theta irradiance data is adjusted to the same time of day as the parking lot reflectance factor data to minimize sun angle offsets.

Because each of these methods employs data from multiple instruments, it is possible that minor path radiance biases may be introduced by the fact that not all measurements are coincident in time or space. The ELM0 method should exhibit minimal path radiance bias because the reflectance factor ratio that removes atmospheric effects is determined using the same instrument, the HSI2. Any offset with this method arises from the calculation of the gain function by comparison with the surface reflectance factor measurement. This effect should be minimal, however, as the surface reflectance factor should vary more slowly than atmospheric measurements. The ELM2 method should yield a better estimate of the absolute reflectance factor than the ELM1 method, since it provides a more complete correction that accounts for both the slope and intercept. Offsets in the MTRI blacktop method could arise from calculation of the at-sensor reflectance factor using three separate instruments, or from the temporal and spatial offset of the path radiance between the measurements over the lake and the calibration data obtained from a nearby ground station.

We used the Kent State University (KSU) Varimax-rotated Principle Component Analysis (VPCA) visible derivative spectral decomposition method to partition the variance of the reflectance factor from the resulting derivative-transformed reflectance images. The resulting VPCA spatial score maps were smoothed with a 9×9 median kernel for presentation. The VPCA method allows us to compare the level of path radiance bias observed in the four, empirical reflectance factor calibration methods. This is a stringent test because the VPCA method is based on the derivative of the spectra and is capable of separating correlated signal from systematic bias and random noise (Ali et al., 2013; Ortiz et al., 2013). The KSU VPCA approach should thus be effective at separating path radiance biases resulting from scattering of light on the blue end of the spectrum from the

TABLE 1 | Reflectance calibration methods employed.

Method designation	Calibration surface	Instrumentation and data
ELM0[a]	Floating, convex mirrors	HSI2[e] at-sensor upwelling radiance, mirrors, ASD[f] at-surface lake reflectance factor
ELM1[b]	Floating, convex mirrors	HSI2 at-sensor upwelling radiance, mirrors, ASD at-surface diffuse to global ratio
ELM2[c]	Floating, convex mirrors	HSI2 at-sensor upwelling radiance, mirrors, ASD at-surface diffuse to global ratio, ASD at-surface lake reflectance factor
MTRI[d] Blacktop	Asphalt parking lot	HSI2 at-sensor upwelling radiance, ASD at-sensor downwelling irradiance, ASD at-surface lake reflectance factor

[a] *Empirical Line Method 0.*
[b] *Empirical Line Method 1.*
[c] *Empirical Line Method 2.*
[d] *Michigan Tech Research Institute.*
[e] *NASA Glenn, second generation Hyperspectral Imager.*
[f] *Analytical Spectral Devices.*

spatially coherent, environmental signals. We predict that the ELM1 and ELM2 methods will yield similar VPCA signals since they differ only by a constant. Because the derivative of a constant is zero, the addition of the second calibration point, while necessary to yield accurate absolute reflectance factor values, should contribute little to the derivative spectra. In the sections that follow, we present theoretical derivations and empirical descriptions of the methods employed to convert from radiance to reflectance and to decompose the complex, mixed signals into independent spectral signatures that can be related to know color producing agents.

Deriving the Effective Lambertian Reflectance Factor of a Spherical Mirror

The empirical calibration of aerial and satellite systems to retrieve surface reflectance factor requires that the reference target have a known Lambertian reflectance factor. To use a ground reference target made of spherical convex mirrors, the specular reflectance factor of the mirror target must be converted to a Lambertian reflectance factor producing an equivalent sensor response in each spectral channel for the view angle recorded in the sensor image. The derivation of the transformation used in this analysis is described in this section. The spherical convex mirrors deployed on the water surface are domes designed to reflect a fraction f of the hemispherical sky toward the sensor as given by

$$f = 1 - \cos 2\theta_m \tag{1}$$

where θ_m is the angular width of the mirror surface as measured from the mirror's center of curvature. A virtual image of the full hemispherical sky ($f = 1$) is seen in the mirror by a nadir looking sensor when $\theta_m = 45^\circ$. Schiller and Silny (2010) have shown that when illuminated by a hemispherical irradiance on a horizontal surface from the sun and the sky ($E_{sun}^{surf}(\lambda) + E_{sky}^{surf}(\lambda)$; Watts m^{-2} nm), that the upwelling radiance (L_m^{surf}; Watts m^{-2} sr^{-1} nm^{-1}) from a panel of N convex mirrors can be calculated knowing the radius of curvature of the mirrors (R_c) and the along-scan and cross-scan ground sample distance (GSD) of the sensor system (GSD_{AS} and GSD_{CS}, respectively) using the equation:

$$L_m^{surf}(\lambda) = \left[E_{sun}^{surf}(\lambda) + E_{sky}^{surf}(\lambda)\right] \frac{f \rho_m(\lambda) {R_c}^2}{4 GSD_{AS} GSD_{CS}} \tag{2}$$

where $\rho_m(\lambda)$ is the specular reflectance of the mirror measured in the laboratory. It is important to note that by using spherical mirrors, there is no foreshortening effect as with a flat diffuse target. Thus, the upwelling radiance signal is constant and independent of the sensor view angle and in principle, the tilt of the sphere representing the mirror's surface. Although the wave motion changes the orientation of the hemisphere reflected by a mirror so that the 180° Field of view may include some of the water surface if $f = 1$, the effect can be minimized by designing the mirrors to reflect a sky fraction slightly <1, if one assumes the integrated diffuse sky is relatively isotropic. As long as the direct solar contribution continues to be reflected at the sensor, a constant upwelling radiance will be maintained even for off-nadir view geometries of <25°.

Next, we establish a hemispherical-directional reflectance factor distribution function, ρ_m^{HDRF}, for the mirror reflectance factor target by taking the ratio of the radiance directed toward the sensor to the horizontal irradiance at the surface (Schaepman-Strub et al., 2006). Since there are no significant directional effects in the upwelling signal, applying Equation (2), one can write:

$$\rho_m^{HDRF}(\lambda) = \frac{L_m^{surf}(\lambda)}{E_{sun}^{surf}(\lambda) + E_{sky}^{surf}(\lambda)} = \left[\frac{1}{\cos\theta_o} + \left(f - \frac{1}{\cos\theta_o}\right) G(\lambda)\right] \frac{N {R_c}^2}{4 GSD_{CS} GSD_{AS}} \rho_m(\lambda). \tag{3}$$

Here, we have included the term $\left[\frac{1}{\cos\theta_o} + \left(f - \frac{1}{\cos\theta_o}\right) G(\lambda)\right]$, which includes the solar zenith angle, θ_o, and the diffuse-to-global ratio illuminating a horizontal surface [$G(\lambda)$]. This term is needed to perform a proper conversion of specular reflectance to an equivalent Lambertian reflectance factor. It corrects for the fact that there is no foreshortening in the solar contribution to the mirror reflected signal compared to a Lambertian surface. A more detailed description of this correction term will be presented in a future publication.

Finally, Palmer (1999) shows that a reflectance factor distribution function, such as ρ_m^{HDRF}, is related to a hemispherical-to-direct Lambertian reflectance factor, ρ_m^{HDRF}, through a simple factor of π steradians. Thus,

$$\rho_m^{HDRF} = \left[\frac{1}{\cos\theta_o} + \left(f - \frac{1}{\cos\theta_o}\right) G(\lambda)\right] \frac{\pi N R_c{}^2}{4GSD_{CS}GSD_{AS}} \rho_m(\lambda). \quad (4)$$

The result is that Equation (4) provides the needed transformation equation for converting the specular reflectance spectrum of the mirror reference target to an equivalent Lambertian reflectance factor needed for the empirical calibration of the sensor image radiance to surface reflectance factor.

Empirical Line Method Reflectance Factor Calibration

The ELM applied to a lake surface image assumes a linear relationship between at-sensor water radiance, $L_w^{sen}(\lambda)$, recorded by the HSI2 imaging system and water surface reflectance factor, $\rho_w^{HDRF}(\lambda)$. This can be expressed for a sensor image calibrated to radiance as:

$$\rho_w^{HDRF}(\lambda) = g_m(\lambda)\,[L_w^{sen}(\lambda) + (L_p(\lambda) + d(\lambda))]. \quad (5)$$

In terms of a linear equation, $g_m(\lambda)$ is the gain function that will be derived from the mirror surface reference target and $g_m(\lambda)\,(L_p(\lambda) + d(\lambda)) = b(\lambda)$ is the linear intercept. The term $L_p(\lambda)$ is the atmospheric path radiance between the aircraft and the surface, while $d(\lambda)$ accounts for any residual sensor calibration dark bias drift and potential processing offset. The empirical line equation follows as:

$$\rho_w^{-surf}(\lambda) = g_m(\lambda)\,L_w^{sen}(\lambda) + b(\lambda). \quad (6)$$

The determination of the gain and bias coefficients is obtained by regressing observed radiance values, recorded by the HSI2 sensor, against known reflectance factor values in each band from at least a high and low reflectance factor target pair in the scene. For the ELM1 solution, the coefficients needed to determine the intercept, $b(\lambda)$ are set to zero, while both the slope and intercept coefficients are used for the ELM2 solution. This allows us to determine the impact that both the slope and intercept have on the solution. The high reflectance factor reference is provided by the convex mirror target deployed on the water and the low reflectance factor reference is recorded by a direct measurement of the water surface reflectance factor from a research vessel in the scene, or measurement from a nearby ground station. Thus, the calibration is based on the two reference points $(L_m^{sen}(\lambda),\ \rho_m^{HDRF})$ and $(L_{w,\,boat}^{sen}(\lambda),\ \rho_{w,\,boat}^{HDRF})$, where $L_m^{sen}(\lambda)$ and $L_{w,\,boat}^{sen}(\lambda)$ are the HSI2 measured reference radiance of the mirror target and water surface and $\rho_{w,\,boat}^{HDRF}$ is the reflectance factor recorded at the location of the research vessel, or nearby ground station.

Thus, for the ELM2 solution, the image calibration equation converting all pixels in the scene from at-sensor radiance, $L_w^{sen}(\lambda)$, to at-surface reflectance factor, $\rho_w^{surf}(\lambda)$, becomes:

$$\rho_w^{surf}(\lambda) = \frac{\rho_m^{HDRF}(\lambda)}{L_m^{sen}(\lambda)} \left[L_w^{sen}(\lambda) - L_{w,\,boat}^{sen}(\lambda)\right] + \rho_{w,\,boat}^{HDRF}(\lambda) \quad (7)$$

and provides an algorithm for performing an atmospheric correction of hyperspectral or multispectral image data. The ratio $\frac{\rho_m^{HDRF}(\lambda)}{L_m^{sen}(\lambda)}$ represents the mirror gain function $g_m(\lambda)$.

One advantage obtained by the use of curved mirrors is that their convex shape disperses the light reflected back to the air- or space-bourne sensor passing over the target. This decreases the possibility that the solar radiance reflected from the surface will saturate the detector. The dispersion factor is determined as part of the calibration process. The approach effectively converts a passive spectroradiometer to an active spectrophotometer by sacrificing a small number of scene pixels. An additional advantage of the mirror targets for deployment is that they are small and generally can be designed to be the size of an instantaneous field of view (IFOV) pixel or smaller. As a result, the deployment of reflectance factor reference targets on water now becomes practical. If actual Lambertian-like targets were placed on the water instead of the mirror targets, their surface area would need to be at least 25 times larger in order to provide a reliable measure of the target radiance. This is due to the blurring resulting from the aircraft motion, the optical point spread function (PSF) and pixel resampling, all of which have the effect of mixing the reference signal with the background. The blurring effects can be seen in (**Figure 2A**), which shows the image of the mirror target deployed on the water surface. Although the target (1.2 m on a side) is smaller than the processed image pixels (3.21 m on a side), the radiance signal recorded by the sensor has been spread out over many pixels around it. Thus, the radiance from the target pixels is a combination of the mirror signal and the background water. However, because the target is small, it can be assumed to be a point source, located on a uniform background. It is thus straightforward to separate the total target radiance from the background water. An integration to remove the background is carried out by placing an integration window containing P pixels around the target centroid enclosing all the radiance from the target (**Figure 2A**, red box), as defined by the system PSF, and calculating the average radiance spectrum, $\overline{L_m^{sen}}(\lambda)$. Outside the perimeter of this window, an average pixel water radiance spectrum is derived, $\overline{L_w^{bkg}}(\lambda)$, to represent the background signal (**Figure 2A**, green box). Thus, the calculation of the background subtracted at-sensor total integrated radiance from the mirror target becomes:

$$L_m^{sen}(\lambda) = P\left[\overline{L_m^{sen}}(\lambda) - \overline{L_w^{bkg}}(\lambda)\right] \quad (8)$$

Equation (8) provides the at-sensor radiance response for completing the calculation of the mirror gain function.

To fully explore parameter space, we also consider a different single-point calibration, the ELM0 method, which is based on

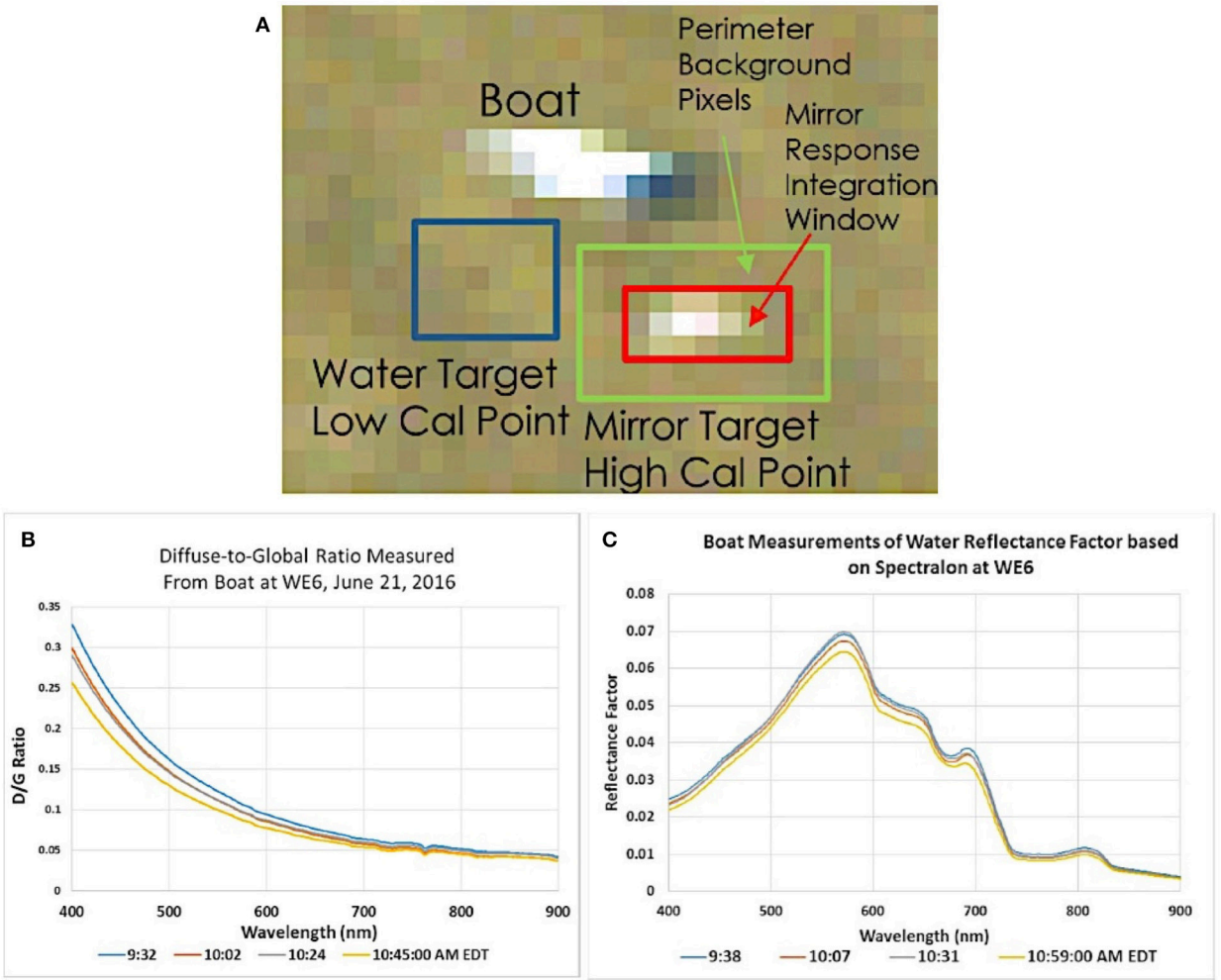

FIGURE 2 | (A) NASA Glenn, second generation Hyperspectral imager (HSI2) image pixels from swath 15_MBSP, acquired on June 21, 2016, of the mirror reflectance target (red box: high calibration point), water (blue box: low calibration point) and boat at station Western Erie 6 WE6. Though the mirror target is smaller than an instantaneous field of view (IFOV) pixel, the energy reflected at the mirror is spread out over multiple pixels due to the aircraft motion, sensor system point spread function and pixel resampling during processing. Pixels included in target integration are indicated by green and red boxes. **(B)** Example diffuse to global ratio spectra, and **(C)** water surface reflectance spectra measurements taken from the boat located at WE6 on June 21, 2016.

the at-surface water reflectance factor, $\rho_{w,\,boat}^{HDRF}$, measured with an ASD FieldSpec® HH2 at the boat location, rather than the mirror target reflectance factor $\rho_m^{HDRF}(\lambda)$. This method first uses the mirror signal to remove the atmosphere by determining a ratio of the water leaving radiance and mirror radiance with both quantities measured directly by the HSI2 sensor. Because that ratio is biased by the mirror dispersion, it is rescaled using the at-surface reflectance factor measured from the boat with an ASD FieldSpec® HH2 spectroradiometer. After algebraic re-arrangement, the mirror terms drop out and the radiance to reflectance conversion equation for the ELM0 has the form:

$$\rho_w^{surf}(\lambda) = \frac{\rho_{w,\,boat}^{HDRF}(\lambda)}{L_{w,\,boat}^{sen}(\lambda)} L_w^{sen}(\lambda). \quad (9)$$

While this transformation will not yield absolute reflectance, it should be scaled so that spectra at various spatial locations in the scene have the correct spectral shape as needed for algorithms based on spectral shape, such as the KSU VPCA spectral decomposition method. We compare the results of the ELM0, ELM1, and ELM2 solutions with the MTRI Blacktop calibration, which is described below.

RESULTS

Application of the Mirror-Based Empirical Line Method

The steps in the analysis of the data include the following for each HSI2 swath. We obtain the subset of the swaths that includes locations of ground-based measurements conducted

by researchers in a vessel on the water or at a nearby ground station. We then identify the location of the research vessel and floating mirror array in the swath (**Figures 1**, **2A**). The pixels associated with the mirror array (**Figure 2A**) are extracted and averaged, as are lake pixels near the mirror array. The image cutout of the mirror target and boat are shown in (**Figure 2A**) identifying the target integration window and pixel locations used to estimate the water background. The mirror correction method for the ELM1 and ELM2 is then applied using Equation (7) as described in the text and for the ELM0 using Equation (9). Validation data collected on the lake included measurements of the diffuse to global ratio obtained from the ratio of shaded to unshaded downwelling solar irradiance measured with an upward looking ASD FieldSpec® HH2 spectroradiometer equipped with a cosine theta receptor (**Figure 2B**) and measurements of the at-surface reflectance factor relative to a 100% Spectralon™ plate measured with a downward looking ASD FieldSpec® HH2 spectroradiometer equipped with a 10° FOV foreoptic (**Figure 2C**). The data in **Figures 2B,C** document the stability of the atmosphere and lake surface during data collection.

With knowledge of the sensor GSD for the image, the calculation of the mirror Lambertian reflectance factor, ρ_m^{HDRF}, can be completed. The specular reflectance spectra of the mirrors were measured at Kent State University using a Konica Minolta CM-2600d Spectrophotometer, which was set to measure the specular component of the reflectance factor relative to daylight with a brightness temperature of 6,500K. The calibration panel consisted of $N = 16$ mirrors deployed on the water surface. The radius of curvature for the mirrors, $R_c = 20.1$ cm, and a hemispherical sky fraction was calculated as $f = 0.878$. The resulting specular reflectance factor and Lambertian equivalent reflectance factor spectra, calculated from Equation (4), are shown in **Figure 3A**. The reference target is spectrally flat, which is ideal for the calibration of a hyperspectral sensor. Note that a calibrated, diffuse reflectance factor flat panel delivering a reflectance factor of 18% as shown in **Figure 3A** would normally saturate a sensor designed to record a high SNR for water leaving radiances. However, since the energy from the curved mirrors is spread over many pixels by the sensor PSF, a small bright target can be recorded without saturation, providing a measurement of the target signal with good precision. **Figure 3B**

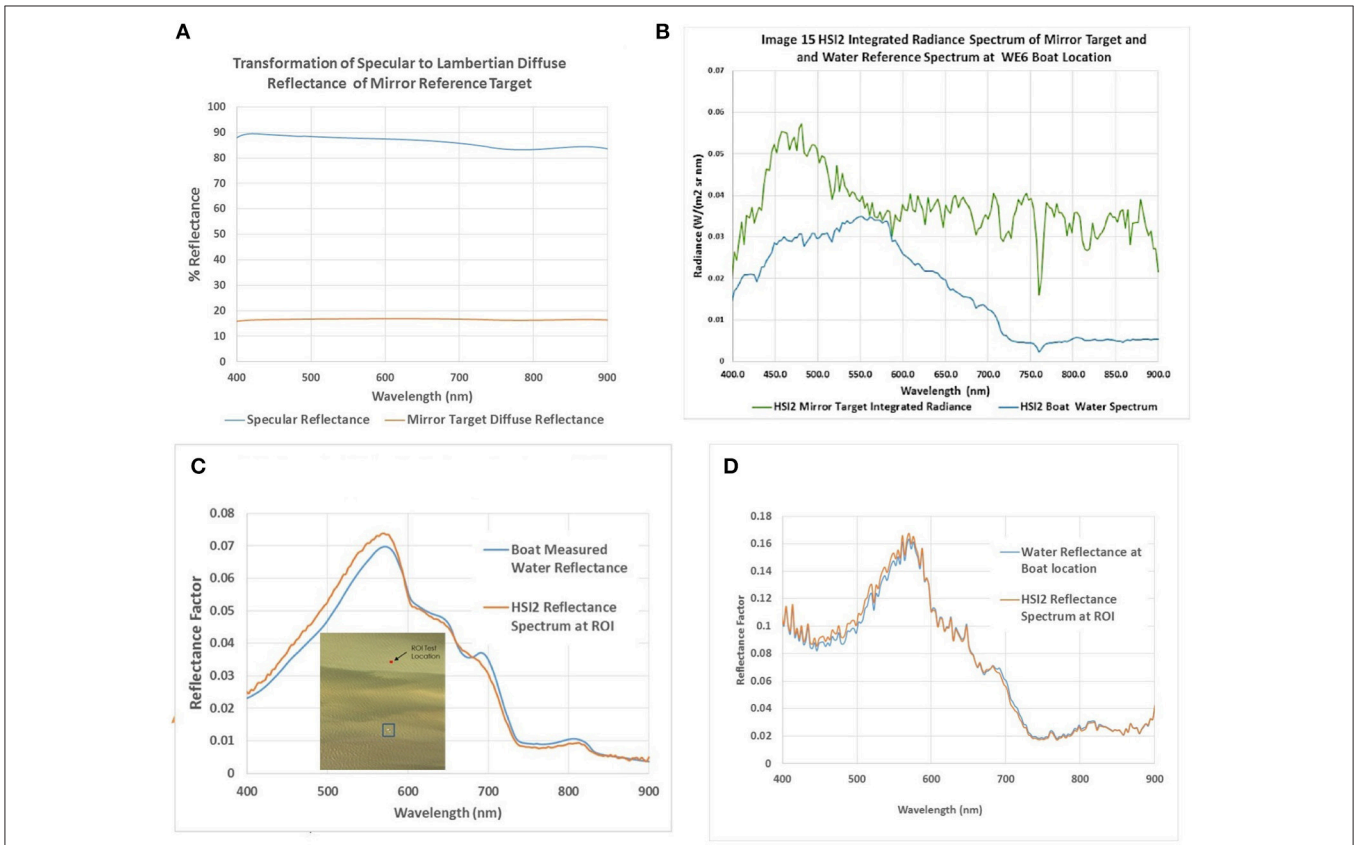

FIGURE 3 | (A) Specular reflectance factor and Lambertian equivalent reflectance factor spectra, calculated from Equation (4). **(B)** Resultant average NASA Glenn, second generation Hyperspectral imager (HSI2) water and mirror radiance spectra representing the low calibration reference spectrum (HSI2 Boat Water Spectrum) and the high cal reference (HSI2 Mirror Target Integrated Radiance). **(C)** Empirical line method 2 (ELM2) transformation reflectance spectra of water pixels extracted from the HSI2 15_MBSP swath (inset, red region of interest; ROI), compared to in situ reflectance spectra measured concurrently using the Analytical Spectral Devices (ASD) FieldSpec HandHeld 2 (HH2) around the boat at station WE6 (insert, blue box). **(D)** Empirical line method 0 (ELM0) transformation reflectance spectra of the same pixels shown in **(C)** for comparison.

shows both the resulting average HSI2 water radiance spectrum representing the low calibration reference spectrum, $L^{sen}_{w,\,boat}(\lambda)$, denoted with the blue box in **Figure 2A** and the net integrated HSI2 target radiance with background subtraction as calculated using Equation (8), $L^{sen}_{m}(\lambda)$, representing the high calibration radiance spectrum. The ratio of the at-surface mirror target reflectance factor spectrum and HSI2 measured at-sensor mirror target integrated radiance spectrum provides the mirror gain function used to convert any HSI2 radiance spectrum to surface reflectance factor in the scene via Equation (7), assuming even illumination throughout the scene.

The at-sensor radiance to surface reflectance factor transformation is demonstrated in **Figure 3C** as the average water radiance spectra, based on HSI2 pixels around the boat and mirror targets that were extracted from a portion of the 062116_15_MBSP swath, which is shown in the inset image in **Figure 3C**. Applying Equation (7) as a two-point calibration (ELM2), the transformation to a predicted at-surface reflectance factor spectrum was calculated and shown in the plot for two locations, the boat location in the blue box and a second, independent region of interest (ROI) in the red box. The result produces an estimated absolute reflectance factor water surface spectrum at each location. The predicted spectrum at the boat is identical to the ASD measured reflectance factor spectrum at the research vessel (10:31 a.m. EDT **Figure 2C**) because it was recorded nearly coincident with the HSI2 overpass (3 min apart) and was used as the low reference reflectance spectrum for calibration and thus sits exactly on the line defined by Equation (7). The second spectrum in red is the resulting reflectance factor spectrum for an independent ROI location. The two spectra represent the absolute appearance of the water reflectance factor spectra at the two locations recorded by the HSI2 sensor as scaled in reflectance units by the mirror gain function. The two-point calibration transformation removes the solar/sky illumination spectrum and the atmospheric transmittance and path radiance effects produced between the sensor and the water surface extracting the water reflectance factor spectrum for the illumination and view geometries at the time of the HSI2 collect. In comparison, **Figure 3D** shows the resulting transformation using only the mirror gain function in a single-point calibration (ELM1) without the bias correction provided by the ASD measured at-surface water reflectance [the terms for $\rho^{HDRF}_{w,\,boat}$ and $L^{sen}_{w,\,boat}(\lambda)$ were set to 0 in Equation (7)]. The resulting spectrum has similar shape, but more noise than the EML2 spectrum from **Figure 3C**, and a higher path radiance contribution on the blue end of the spectrum. The ELM1 calculation will allow us to determine if the KSU VPCA spectral decomposition analysis can still be performed in this way using less ground validation data. The mirror gain function correctly scales the relative difference between the two locations in reflectance units for the ELM2, but a spatially constant reflectance offset in each spectral band still remains as revealed in the difference between the spectra in **Figures 3C,D**. Though the result is not an absolute reflectance spectrum, the ELM1 spectrum can still potentially be used for spatial/spectral decomposition. This will be explored in Section Comparison of the Reflectance factor calibration methods: VPCA Decomposition.

The important result is that the methodology of deploying a single mirror reflectance factor reference target was successful in performing an atmospheric correction of the HSI2 aircraft imagery resulting in the retrieval of the at-surface water reflectance factor spectral profiles based on the image data, sensor metadata, the mirror target properties, measurements of the lake surface reflectance and simple measurements of shaded and unshaded downwelling solar irradiance to establish the diffuse to global ratio. The utility of the derived spectra will be demonstrated in the following sections, where we compare the ELM0, ELM1, and ELM2 reflectance factor estimates with the extraction of water constituents using the KSU VPCA spectra decomposition method. Though random path radiance bias is likely present between the derived HSI2 and the surface validation spectrum due to offsets in time of measurement and/or location, they will mostly drop out in the derivative transformation and decomposition process with minimal effect on the analysis results.

MTRI Blacktop Calibration Results

We compare the three mirror-based reflectance calibration methods with an additional empirical approach to estimate the reflectance factor. The MTRI blacktop vicarious calibration method involves identifying a natural or artificial site that can be measured both by the HSI2 sensor, which requires calibration, and instruments of known calibration, such as the ASD FieldSpec® HH2 spectroradiometers used in our field measurements. The ratio of these measurements is used as the basis for the vicarious calibration. The MBSP parking lot was chosen as a suitable location because the site is located along the immediate shoreline of Lake Erie so that it does not impose an undue burden on flight planning and navigation; the parking lot has a consistent and well-characterized spectral response across both time and space (**Figure 4A**); and is a relatively large feature that can be easily identified in HSI2 imagery at any operational elevation (**Figure 4B**).

The correction factor (**Figure 5**), which is a wavelength-dependent scalar that relates the two reflectance factor measurements, is then calculated using Equation (10), where C is a correction coefficient, λ is wavelength, Cal_{Ref} is the calibrated reflectance factor (i.e., ASD radiance/ASD irradiance measured *in situ* at MBSP), and $Uncal_{\mathrm{Ref}}$ is the uncalibrated reflectance factor (i.e., HSI2 radiance/ASD irradiance upward looking from the S3 Viking aircraft). The correction factor equation will encapsulate the measurement differences between the two sensors, including all sources of measurement error, and can be used to convert measurements from one instrument into the other. Of obvious interest is converting the uncertain sensor to match the well-calibrated instrument.

$$C(\lambda) = \frac{Cal_{\mathrm{Ref}}(\lambda)}{Uncal_{\mathrm{Ref}}(\lambda)} \tag{10}$$

$$Cal_{\mathrm{Ref}}(\lambda) = C(\lambda) * Uncal_{\mathrm{Ref}}(\lambda) \tag{11}$$

Radiance and irradiance spectroradiometer measurements were recorded to calculate an at-sensor surface reflectance factor. Coincident ground data was collected during overflight using ASD FieldSpec® HH2 spectroradiometers set up in the MBSP

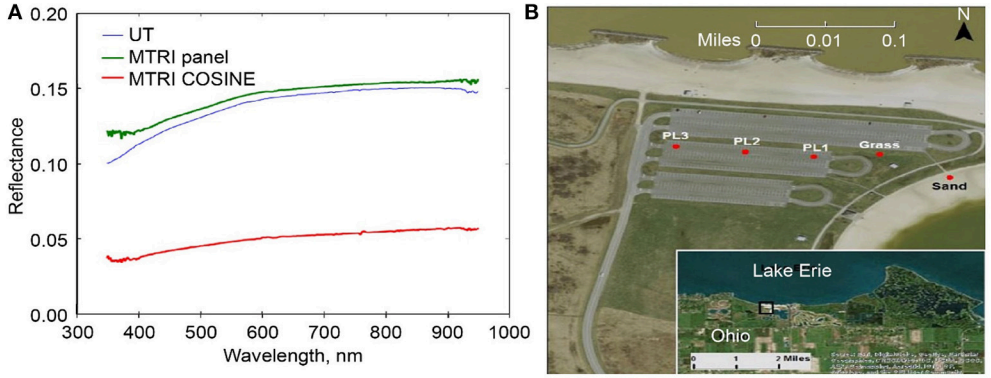

FIGURE 4 | (A) Maumee Bay State Park (MBSP) parking lot blacktop spectral response, as measured by MTRI and the University of Toledo (UT) research teams. **(B)** NASA Glenn, second generation Hyperspectral imager (HSI2) image of MBSP parking lot in relation to Lake Erie (insert) (After Figures 4.2 and 4.3, Lekki et al., 2017).

parking lot. This allows collection of data under the same illumination conditions as the lake surface from a nearby ground station. We account for the effects of solar angle on the diffuse illumination component of radiance when a cosine receptor is used to measure irradiance by applying a time correction. When using a 100% Spectralon™ panel, mirror, or other known reflector to estimate solar radiance, the effect of the diffuse terms will cancel out when computing the reflectance factor. The cosine receptor does not include this term, whereas the radiance measurement does, and will therefore remain in the computed reflectance factor if not addressed. An example of this effect is readily apparent (**Figure 6A**) in the split between the 10:30 and 13:00 measurements from the MTRI ASD FieldSpec® HH2 data collected on August 24, 2015, in which the time correction for solar angle removes most of the offset (**Figure 6B**).

We explore output from the MTRI method using data from a number of swaths collected in 2015. In **Figure 6C**, the parking lot as observed by the HSI2 sensor has a similar shape in spectra extracted from different swaths; the remaining differences are likely atmospheric or time of day effects. This suggests that a single correction factor would be useful even on days for which it was not recomputed, as demonstrated by the manner in which the corrected signals clustering around the observed ASD FieldSpec® HH2 spectra (**Figure 6D**). The two anomalous dates are both flagged as cloudy days (dashed line), their measurement difference could be explained by clouds periodically shadowing the irradiance measurements, which were averaged across the entire track, leading to a higher than normal reflectance factor measurement. The measurements thus likely differ due to variations in the diffuse to global ratio for cloudy vs. clear sky.

Reflectance Factor Inter-Comparison

To explore the hyperspectral nature of the reflectance factor signals, we compare the average reflectance spectra from each reflectance factor calculation and their derivatives (**Figure 7**). To more clearly compare the spectral shapes for each reflectance factor calculation, we convert the averages to *z*-scores, by subtracting the average reflectance value across all wavelengths in the visible and dividing by the standard deviation across all wavelengths in the visible. These standardized reflectance values and standardized derivatives are a useful way to compare the results because the VPCA method is based on analysis of the correlation matrix of the derivative spectra. The four methods of calculating the reflectance factor produce values that range in amplitude from minimum to maximum reflectance by 1.8 to 14.8%. None of the average spectra exhibited negative reflectance factors. The ELM0 method produced the lowest amplitude signal, while the ELM1 method produced the largest amplitude signal. The ELM1 and MTRI exhibited higher reflectance factors on the blue end of the spectrum relative to the ELM0 and ELM2 methods. This is particularly apparent when viewing the *z*-score transformed reflectance factors (**Figure 7B**). When the results were *z*-score transformed, the similarity in spectral shape of the four methods of calculating the reflectance factor is readily apparent as is the increased blue-end reflectance for the ELM1 and MTRI methods relative to the ELM0 and ELM2 methods. The derivative spectra for both the absolute reflectance factor values and the *z*-score transformed observations were similar, exhibiting the same spectral features, although they diverged to some extent toward the blue end of the spectrum.

The ELM2 provides the best estimate of the absolute reflectance as demonstrated by the goodness of fit with the measured at-surface ASD FieldSpec® HH2 surface reflectance factor. The MTRI and ELM0 methods produced reflectance spectra of similar amplitude, while the ELM2 values had higher amplitude. The ELM1 values were considerably higher than the ELM2 estimates because the intercept term in Equation (8) for the ELM1 calculation was intentionally set to zero to explore the impact of the intercept on the solution. In terms of absolute reflectance, there is a bias offset for the ELM0 and MTRI relative to the absolute spectrum produced by the ELM2 transformation, but less offset than for the ELM1 transformation. As predicted, the ELM0 and ELM2 solutions have the same spectral shape as can be seen for the *z*-score transformed results (**Figure 7B**). We further explore the differences between the ELM0, ELM1, ELM2, and MTRI calculations in the following section where

we evaluate the underlying structure of the images using an eigenvalue-eigenvector decomposition method, the KSU VPCA spectral decomposition method.

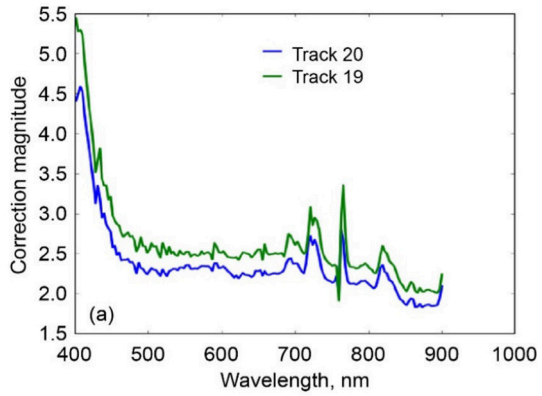

FIGURE 5 | Wavelength-specific correction coefficients derived from comparing to in situ reflectance for two NASA Glenn, second generation Hyperspectral imager (HSI2) tracks (track 19 and 20) (After Figures 4.5, Lekki et al., 2017).

Comparison of the Reflectance Factor Calibration Methods: VPCA Decomposition

The four reflectance factor calculation methods listed in **Table 1** when applied to HSI2 swath 062116_15_MBSP produce reflectance RGB plots that look very similar (not shown) to the radiance RGB plot in **Figure 8A**. The dominant pattern observed in the radiance RGB image for the swath are alternating bands and filaments that run parallel to the coast, which is located at the bottom of the image. There is a strong coastal transition front that marks the end of the reddish-brown coastal waters and the transition into the bluish-green offshore waters of the Western Basin. The coastal water appears more red than the offshore waters, located further into the Western Basin. A second, strong brighter-colored front can be seen toward the top of the swath. This front separates milky blue water to the south in the middle of the image that transition into water of more buff coloration to the north, before transitioning furthest offshore into a darker, blue color. Because of the similarity of the reflectance-derived RGB images, the MTRI reflectance method was used to calculate the Cyanobacterial Index (CI) (Wynne et al., 2010, 2013). The calculation of the widely-used NOAA CI, contributed by collaborators at UT, provides a useful reference for comparison to the components extracted using the VPCA

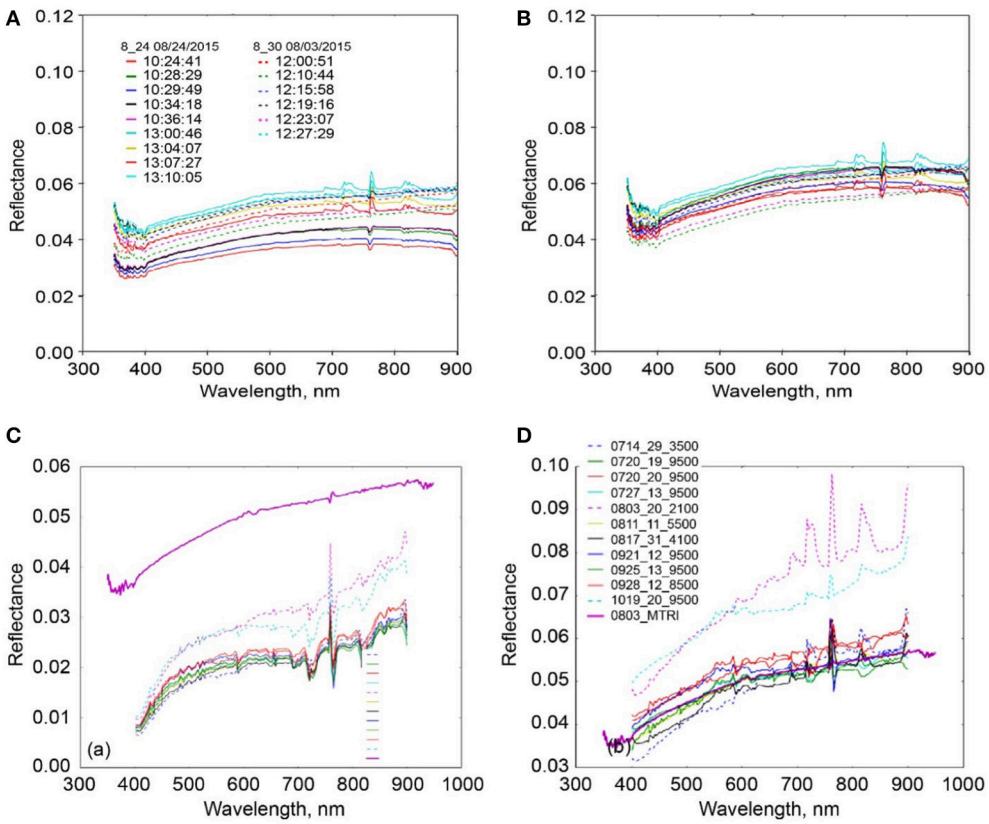

FIGURE 6 | (A) Maumee Bay State Park (MBSP) in situ reflectance before time correction. **(B)** MBSP in situ reflectance after time correction. **(C)** NASA Glenn, second generation Hyperspectral imager (HSI2) parking lot reflectance uncorrected. **(D)** NASA HSI2 parking lot reflectance corrected. *In situ* reflectance is shown in magenta (labeled 0803_MTRI) in **(C,D)** (After Figures 4.4 and 4.6, Lekki et al., 2017).

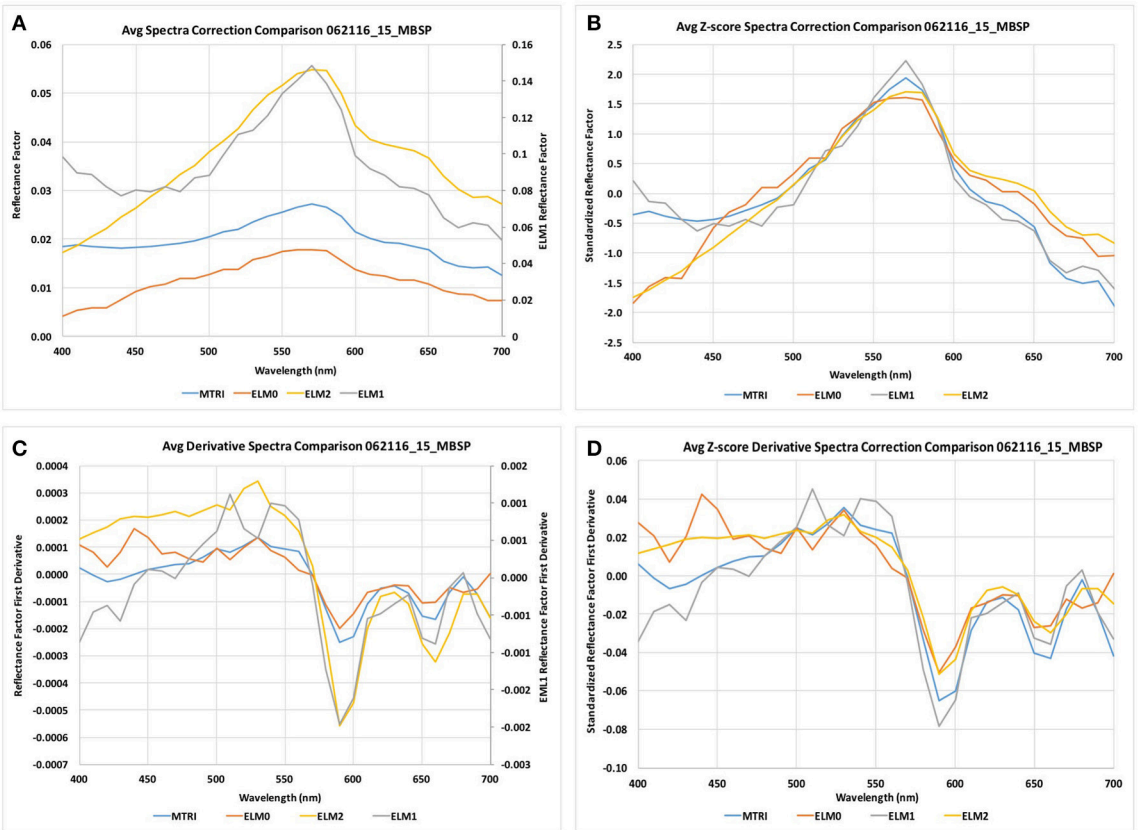

FIGURE 7 | (A) Comparison of average scene spectra for each correction method. **(B)** Comparison of *z*-score correction of average scene spectra. **(C)** Comparison of average derivative scene spectra for each correction method. **(D)** Comparison of *z*-score correction of average derivative scene spectra for each correction method.

decomposition method. For comparison with VPCA score maps, the spatial map of the NOAA CI was smoothed with a 9 × 9 median kernel for presentation as was done with the VPCA score maps.

Application of the KSU VPCA spectral decomposition method following (Ortiz et al., 2013; Lekki et al., 2017) to the four reflectance factor data sets enabled extraction of four to six components that account for a maximum of 92.8–97.4% variance in the four derivative transformed data sets (**Table 2**). One difference among the various solutions is that in some cases, the components extracted were flipped relative to similar components from one of the other calculation methods. This is a function of the varimax rotation. It can be easily addressed by multiplying the component scores and loadings by −1, so that the components with similar shape and spatial pattern have the same sign. This has been done for ease of comparison between components. The ELM0 solution explained the largest amount of variance in the image at 97.4% for five components (**Table 2**). The components extracted from the other reflectance factor methods exhibit subtle differences from each other, but their general similarity is readily apparent (**Figures 8–13**).

To identify the composition of the color producing agents in each component, we standardized the component scores, then matched the components from each data set without replacement to their best visual match (if any) in the other data sets to group them into spectral "patterns." Comparing the various solutions, the components can be matched on the basis of their spectral shapes and spatial patterns into six patterns, labeled A through F (**Table 2**, **Figure 14**). The component loadings for the matches in the patterns were then averaged and compared using forward, least-squares, stepwise regression against a library of known standardized pigments and mineral spectra (Ortiz et al., 2013) to infer their composition. The quality of the identified patterns was determined by the spatial coherence of their component score maps, average spectral loadings $< \pm 3$ standard deviations, and absolute *R*-values for the stepwise regression >0.8.

The key point to address here is the similarity of the structure of the results extracted despite the differences in the atmospheric correction methods applied. All of these patterns (with the exception of Pattern E) exhibit coherent spatial structures, partitioning the variance in the hyperspectral image cube into graceful filaments and bands that run parallel to the coast. The NOAA CI and the VPCA solutions pull out features similar to those seen in the RGB images. The NOAA CI indicates bloom-like conditions offshore and then alternating bands of higher and lower values parallel to the coast, tapering out toward

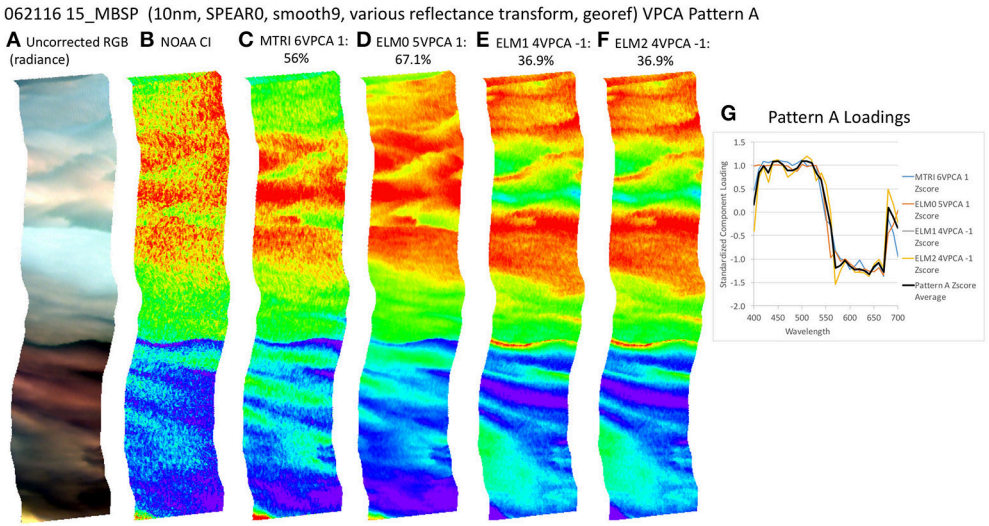

FIGURE 8 | (A) Red, Green, Blue (RGB) image of swath 15_MBSP from June 21, 2016. **(B)** National Oceanic and Aeronautical Administration Cyanobacterial Index (NOAA CI) product calculated after Wynne et al. (2010). **(C)** Spatial distribution of varimax-rotated principal component analysis (VPCA) component pattern A using Michigan Tech Research Institute (MTRI) correction method decomposition. **(D)** Spatial distribution of VPCA component pattern A using Empirical Line Method 0 (ELM0) correction method decomposition. **(E)** Spatial distribution of VPCA component pattern A using Empirical Line Method 1 (ELM1) correction method decomposition. **(F)** Spatial distribution of VPCA component pattern A Using Empirical Line Method 2 (ELM2) correction method decomposition. **(G)** Pattern A Loadings. Negative signs in loading numbers indicate that pattern has been multiplied by −1 for comparison purposes.

TABLE 2 | Correlation of spectral patterns and variance explained.

Component spectral pattern[a]	MTRI[b] 6VPCA[c]	ELM0[d] 5VPCA	ELM1[e] 4VPCA	ELM2[f] 4VPCA
Pattern A: +Illite, +Diatoms and −phycoerythrin	VPCA 1 (56%)	VPCA 1 (67.3%)	VPCA 1 (36.9%)	VPCA 1 (36.9%)
Pattern B: +Haematite, +Green Algae, −α-carotene, and +phycoycanin	VPCA 2 (16.4%)	VPCA 2 (15.5%)	VPCA 3 (26.3%)	VPCA 3 (26.3%)
Pattern C: −Goethite and +haematite	VPCA 3 (10%)	VPCA 3 (7.2%)	VPCA 2 (26.5%)	VPCA 2 (26.5%)
Pattern D: +Haematite and +phycocyanin	VPCA 4 (7.8%)	VPCA 4 (6.4%)	Absent	Absent
Pattern E: Residual Path radiance errors	VPCA 5 (4.4%)	Absent	VPCA 4 (4.3%)	VPCA 4 (4.3%)
Pattern F: −Myxoxanthophyll, +phycocyanin, and –Chl b	VPCA 6 (1.3%)	VPCA 5 (1%)	Absent	Absent
Sum patterns A–C	82.4%	90%	89.7%	89.7%
Sum patterns D, and F	9.1%	7.4%	Absent	Absent
Sum all patterns except E	91.5%	97.4%	89.7%	89.7%
Sum all patterns	95.9%	97.4%	94.0%	94.0%

[a] *Positive or Negative signs indicate a direct or inverse correlation between the component spectral pattern and identified pigment and sediment mixture.*
[b] *Michigan Tech Research Institute.*
[c] *Varimax rotated principal component analysis.*
[d] *Empirical Line Method 0.*
[e] *Empirical Line Method 1.*
[f] *Empirical Line Method 2.*

lower values near the shore. The leading component (Pattern A) extracted from the four data sets has a spatial pattern most similar to the NOAA CI (**Figure 8B**). The first three patterns are found in all four of the solutions and explain between 82.4 and 90% of the variance in the data sets (**Table 2**, **Figures 8–10**). Patterns D, F are each found in two of the four solutions (**Figures 11**, **13**). They represent 6.4 or 7.8%, 1.0 or 1.3%, of the variance in each data set, respectively. The sum of all the coherent spatial patterns, which can be related to environment signals in the images accounted for 88.5–97.4% of the image variance.

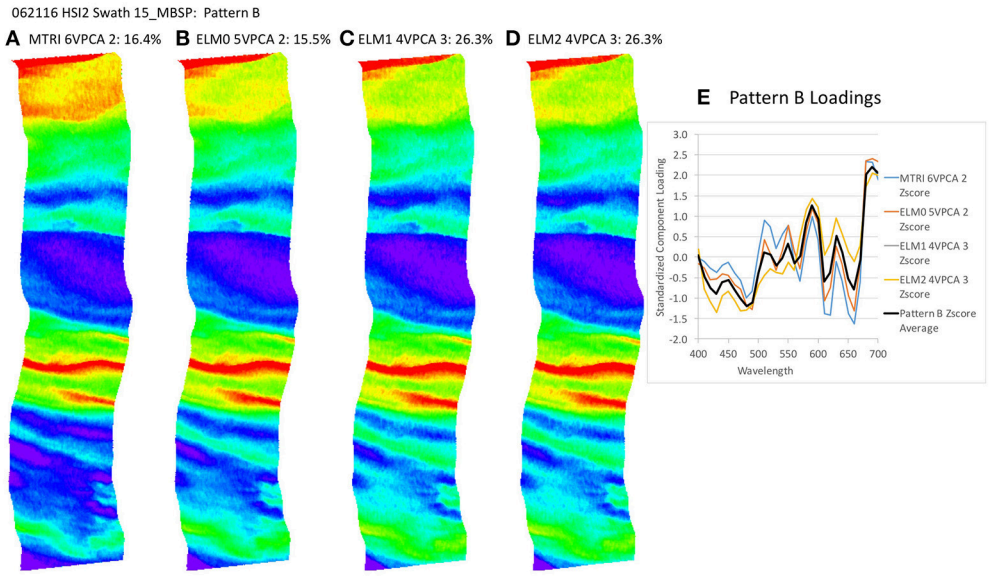

FIGURE 9 | Spatial distribution of varimax-rotated principal component analysis (VPCA) component pattern B. **(A)** Michigan Tech Research Institute (MTRI) correction method decomposition. **(B)** Empirical Line Method 0 (ELM0) correction method decomposition. **(C)** Empirical Line Method 1 (ELM1) correction method decomposition. **(D)** Empirical Line Method 2 (ELM2) correction method decomposition. **(E)** Pattern B Loadings.

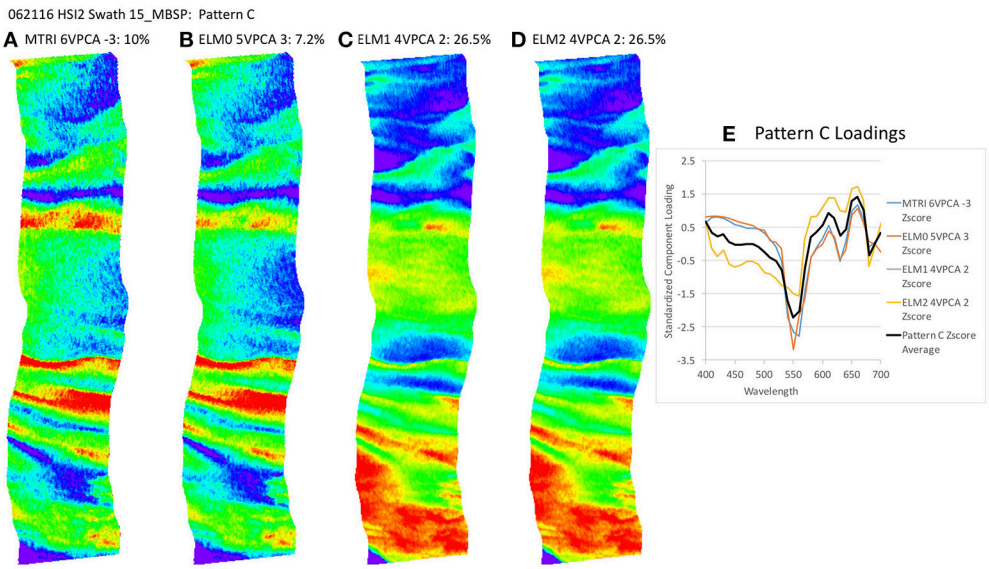

FIGURE 10 | Spatial distribution of varimax-rotated principal component analysis (VPCA) component pattern C. **(A)** Michigan Tech Research Institute (MTRI) correction method decomposition. **(B)** Empirical Line Method 0 (ELM0) correction method decomposition. **(C)** Empirical Line Method 1 (ELM1) correction method decomposition. **(D)** Empirical Line Method 2 (ELM2) correction method decomposition. **(E)** Pattern C Loadings. Negative signs in loading numbers indicate that pattern has been multiplied by -1 for comparison purposes.

These components can be partitioned into spatially coherent environmental signals and random noise. A detailed evaluation of the spectral interpretation of the components is beyond the scope of this paper and will be addressed in a separate paper, but **Table 2** and **Figure 14** identify the most likely composition of the spectral patterns based on stepwise multiple linear regression against known standards. Briefly, the components extracted from the image represent mixtures of sediment (illite, haematite, and goethite), and algal and cyanophyte groups and pigments known to be present in the waters of the western basin of Lake Erie (Ortiz et al., 2013). Matching the features present in the radiance-based true color image (**Figure 8A**), the reddish portions of the image

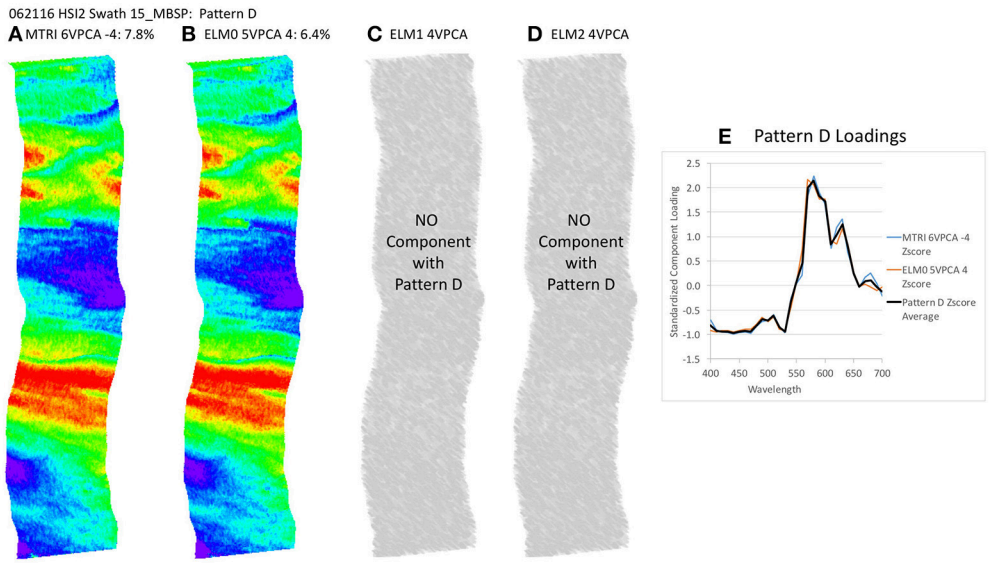

FIGURE 11 | Spatial distribution of varimax-rotated principal component analysis (VPCA) component pattern D. **(A)** Michigan Tech Research Institute (MTRI) correction method decomposition. **(B)** Empirical Line Method 0 (ELM0) correction method decomposition. **(C)** Empirical Line Method 1 (ELM1) correction method decomposition. **(D)** Empirical Line Method 2 (ELM2) correction method decomposition. **(E)** Pattern D Loadings. Negative signs in loading numbers indicate that pattern has been multiplied by -1 for comparison purposes.

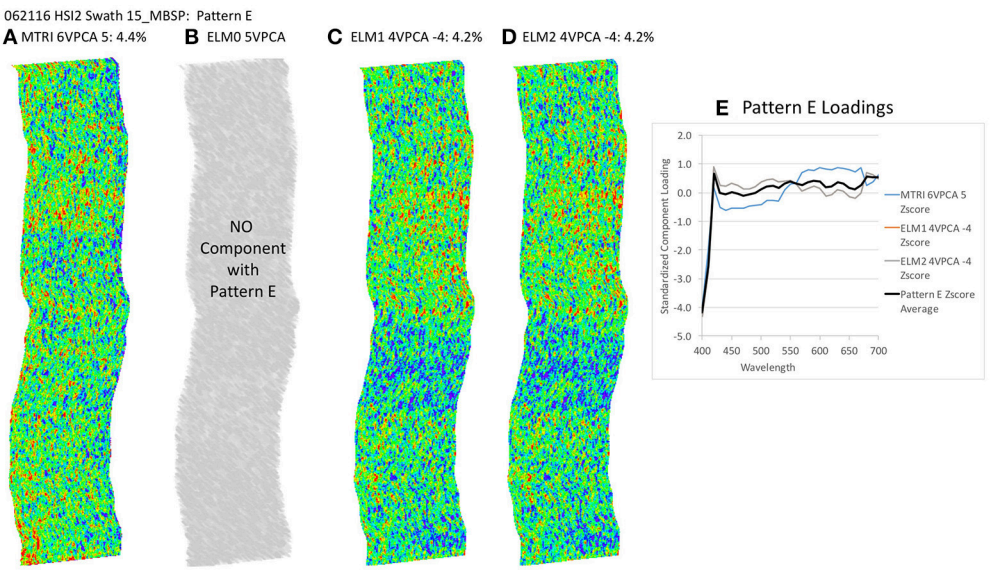

FIGURE 12 | Spatial distribution of varimax-rotated principal component analysis (VPCA) component pattern E. **(A)** Michigan Tech Research Institute (MTRI) correction method decomposition. **(B)** Empirical Line Method 0 (ELM0) correction method decomposition. **(C)** Empirical Line Method 1 (ELM1) correction method decomposition. **(D)** Empirical Line Method 2 (ELM2) correction method decomposition. **(E)** Pattern E Loadings. Negative signs in loading numbers indicate that pattern has been multiplied by -1 for comparison purposes.

were identified as containing iron-bearing minerals as well as autotrophs, while the offshore waters were identified as mixtures of lighter-colored illite, algae, cyanophytes, and various accessory pigments.

One notable difference between the ELM0 solution and the other three solutions is Pattern E, which is absent from the ELM0 solution, but present in each of the other three data sets (**Figure 12**). Pattern E exhibits a random spatial pattern and a spectral pattern with strongest loadings in the blue end of the spectrum. This pattern accounts for 4.3 to 4.4% of the variance in the data sets where it is found. The significance of Pattern E is discussed below. Expanding the MTRI

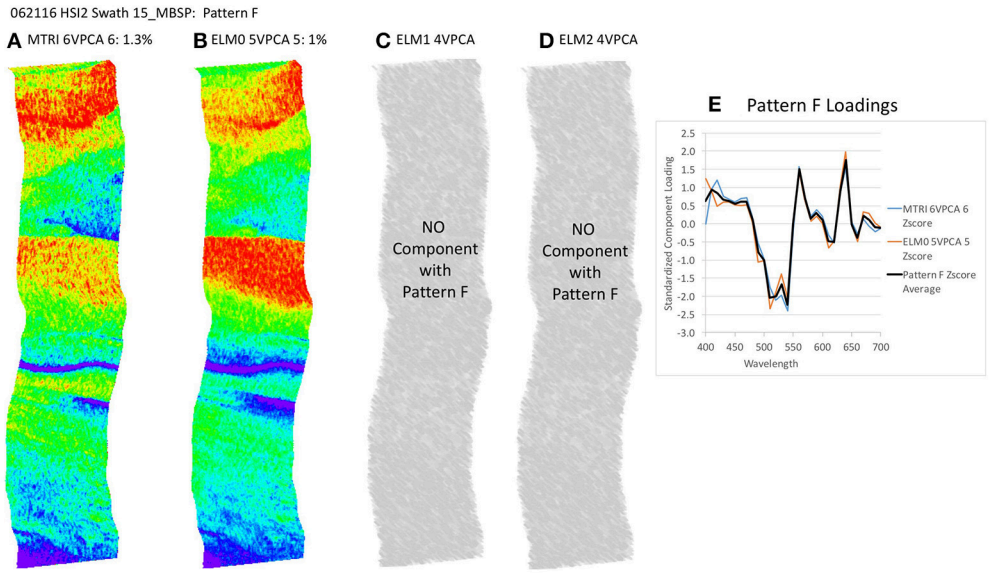

FIGURE 13 | Spatial distribution of varimax-rotated principal component analysis (VPCA) component pattern F. **(A)** Michigan Tech Research Institute (MTRI) correction method decomposition. **(B)** Empirical Line Method 0 (ELM0) correction method decomposition. **(C)** Empirical Line Method 1 (ELM1) correction method decomposition. **(D)** Empirical Line Method 2 (ELM2) correction method decomposition. **(E)** Pattern F Loadings. Negative signs in loading numbers indicate that pattern has been multiplied by -1 for comparison purposes.

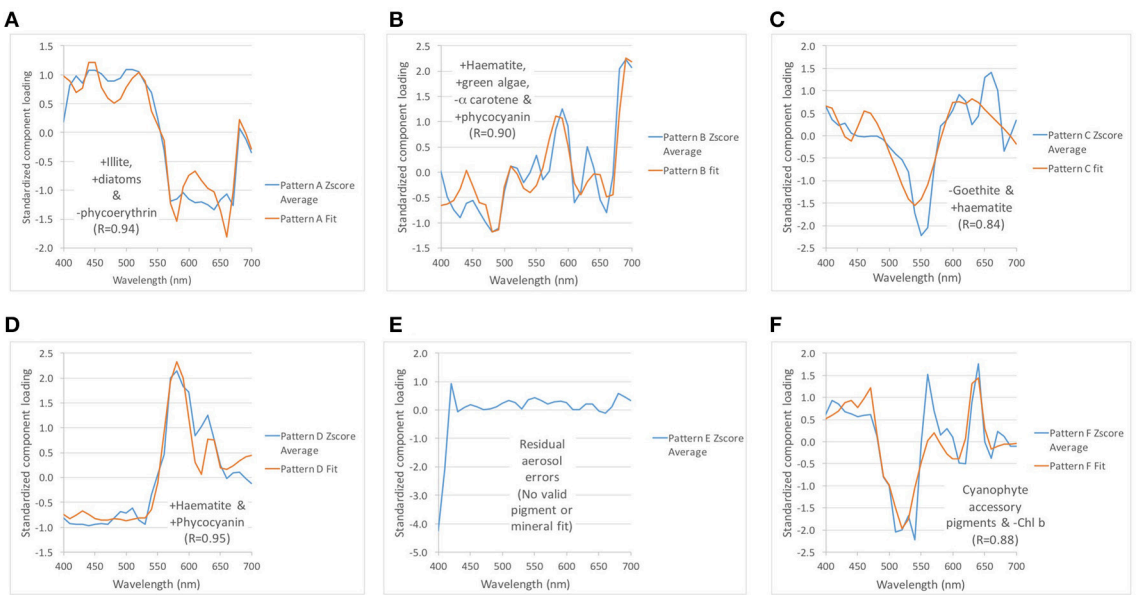

FIGURE 14 | Spectral patterns of varimax-rotated principal component analysis (VPCA) components **(A–F)**, indicating inferred composition based on forward, stepwise least squares regression. Complete description of the composition of each average component spectral pattern is listed in **Table 2**. The quality of the regression fit is indicated by the reported *R*-value.

decomposition to 6 components extracted a 6th component (Pattern F) that was similar to the 5th component in the ELM0 case. Expanding the ELM1 and ELM2 solutions out to a 5th or 6th component extracts a 5th component with a spectral pattern that cannot be matched to any know standards or mixtures in the spectral library in the 5-component case and splits the random noise component (Pattern E) in the 6th component case. This indicates that a 4-component solution is sufficient to capture all the variability in the ELM1 and ELM2 cases.

DISCUSSION

Implications for Reflectance Estimation and Atmospheric Correction

A fundamental challenge associated with analysis of multispectral and hyperspectral visible remote sensing imagery is removal of atmospheric effects. Here we explore several different applications of empirical methods of atmospheric correction, which enables extraction and separation of mixed environmental signals from aquatic data sets. Development of atmospheric correction methods that are effective is important to enable optimal use of future, planned hyperspectral orbital missions, such as PACE, HyspIRI, and GeoCAPE. In this application, the question of interest is to identify the constituents present in the optically complex waters of the Western Basin of Lake Erie. This area develops a perennial CyanoHAB bloom that initiates in the late spring or early summer, depending on the level of runoff to the system (Stumpf et al., 2012; Bullerjahn et al., 2016). In general, the bloom is larger and starts earlier during wet years, and is smaller in dry years (Stumpf et al., 2012). The Maumee River and other rivers in the region deliver significant nutrient loads, suspended sediment and a variety of algal and cyanobacterial taxa into the Western basin (Conroy et al., 2014; Kane et al., 2014; Matisoff and Carson, 2014; Pennuto et al., 2014). As a result, the assumption that the optical properties of the water are controlled only by chlorophyll a is not valid (Ali et al., 2013, 2014; Ali and Ortiz, 2016). Removal of atmospheric effects enables further analysis of the reflectance spectra to determine which constituents are present at any given time. While several approaches have been proposed to do this, spectral shape-based algorithms show promise at partitioning the variance associated with these complex optical mixtures (Simis et al., 2005; Moisan et al., 2011; Chase et al., 2013; Shuchman et al., 2013). Application of these methods in these complex environments suggests that they will be effective at less complex marine applications. Indeed, a similar EOF analysis approach has been applied in the optically complex Baltic Sea (Soja-Woźniak et al., 2017) and the lead author, Ortiz, is applying the VPCA spectral decomposition method effectively using data sets collected in the USVI.

It is in this context that we compare the reflectance factor calculations. In our experience in the Western Basin, the ELM has proven to be very effective at removal of atmospheric effects, with modest amounts of input data (Lekki et al., 2017). We present a theoretical basis to support the ELM based on radiative transfer theory. To evaluate the effectiveness of the ELM method we employed two complementary means of removing the atmospheric effects: one approach used mirrors to directly measure the downwelling irradiance, while the MTRI approach calculates an at-sensor reflectance factor and then generates a gain function using the reflectance of a known surface to reshape the reflectance factor to at-surface values. The two methods are complimentary. The mirror based correction method is based on direct observation of the downwelling irradiance at one or more points in the scene and thus can be used as an effective check on other methods of atmospheric removal. The MTRI approach can be applied broadly in the absence of additional equipment that must be imaged in the scene (the mirrors), which are required to apply the mirror-based correction methods.

All four of the methods produced average reflectance factors that were positive, suggesting the *in situ* calibration data allowed the methods to yield reasonable reflectance factors. When plotted as a function of wavelength, the ELM0 method produced the lowest amplitude reflectance factor, followed by the MTRI, then the ELM2 and finally the ELM1 method, which is known to be biased, because it intentionally does not include an intercept correction (**Figure 7**). By presenting a theoretical explanation for a single-point and two-point ELM correction, we can illustrate the impact of path radiance on the resulting estimated reflectance factor calculations. The two-point ELM2 correction method outperforms the single-point EML1 correction method in terms of recovering absolute reflectance. The MTRI and ELM0 methods underestimated the maximum reflectance response relative to the two-point ELM method, but the ELM0 was able to capture the same spectral shape as the ELM2 method.

To compare the spectral shapes extracted by the four methods, the average reflectance factor for each method was standardized by removal of the spectral mean and then the residual was divided by the spectral standard deviation to calculate z-scores. Several important points arise from this comparison. First all of the values lie within 3 standard deviations, indicating that on average, the spectra did not include individual bands that were biased by extreme outliers. In addition, (**Figure 7B**) documents that all four methods have similar spectral shapes. The ELM0 and ELM2 spectral shapes are consistent throughout the visible. The MTRI and ELM1 spectra are also similar to each other. However, they both exhibit considerably more signal on the blue end of the spectrum than either the ELM0 and ELM2 spectra below ∼475 nm. The MTRI and ELM1 spectra exhibit slightly less reflectance at wavelengths longer than 600 nm than either the ELM0 or ELM2 methods. Comparison of the derivative spectra for the four methods shows similar variability above 540 nm. The curves diverge somewhat toward the UV end of the spectrum. The similarity of the methods is particularly apparent in the derivative of the z-score spectra.

We can make some observations regarding what will happen if additional secondary analysis methods are applied to the reflectance factors to extract environmental information, such as chlorophyll a or other pigment concentrations related to the scene (e.g., Witter et al., 2009). Methods that rely on accurate absolute reflectance values will fail when applied to the ELM1 method, which was presented only to show the importance of the path radiance correction to a valid solution. Based on the strength of the theoretical basis presented, the ELM2 method will yield a stronger response than if either the MTRI or the ELM0 reflectance factor methods are employed. This may be less of an issue for band ratio based methods, particularly ones that operate toward the red end of the spectrum.

Spectral Shape and Identification of Component Patterns

The z-score analysis of the four methods shows that they each extract very similar spectral shapes. Methods that extract information about color producing agents based on a spectral shape will perform similarly with the four methods. To document this, we applied the KSU VPCA spectral decomposition method (Ortiz et al., 2013) to each of the four reflectance

factor calculations presented here. The results presented in **Figures 8–14** demonstrate this well. The leading component extracted in all cases is similar in spatial distribution to the NOAA CI. This is to be expected, because chlorophyll a is found in all taxa of algae and cyanobacteria and thus should dominate the signal. While the NOAA CI pattern look similar to the leading VPCA component for each case, the VPCA results are cleaner, because they are based on a centered, first derivative, rather than a second derivative as for the NOAA CI. Each higher order derivative calculation introduces more error when looking for small differences between large values (Press et al., 1992).

In addition, the VPCA method removes uncorrelated signal from the data set so that features that are not related to a particular pattern show up in other components, or are excluded as noise (Abdi, 2003). For this reason, the VPCA method is relatively insensitive to the noise that was left in the ELM1 solution by setting the intercept term to zero (**Figure 3C** vs. **Figure 3D**). Notice that the ELM1 and ELM2 spatial patterns for the VPCA solutions in **Figures 8–13** are virtually identical because the two solutions differ only by a constant, which drops out during the derivative calculation step in the VPCA.

The VPCA spectral decomposition approach also provides additional information beyond that which the NOAA CI alone can extract. In this application, we were able to extract three to five consistent components with coherent spatial signals. This was true despite difference in the way that the atmospheric effects were removed or due to differences in the absolution reflectance factor estimates. This result strongly suggests that the KSU VPCA method, which is based on extraction of spectral shapes, is relatively insensitive to the need for absolute reflectance values. Atmospheric corrections that are adequate thus can yield valuable, higher-order information about the scene. The reason why this works is because the KSU VPCA spectral decomposition method is based on decomposition of the correlation matrix of the derivative spectra, rather than analysis of absolute reflectance factors. The derivative transformation removes scattering effects, while the correlation analysis decreases the need for stringently correct absolute reflectance factors. Obtaining a valid estimate of the spectral shape—the relationship between bands in the data set—is sufficient to yield useful results.

Correction for Imperfect Atmospheric Removal

Another problem that plagues conversion from radiance to reflectance is a lack of validation data that are precisely coincident with the overflight observations. In our case, the various methods presented require one or more of the following data for calibration or validation: downwelling irradiance, the diffuse to global ratio, and surface reflectance factor measurements of a known calibration surface on land or water for one or more different surface radiance values. Instruments that can simultaneously measure downwelling irradiance and upwelling radiance or reflectance are considerably more expensive than radiometric instruments that can only measure in one orientation at a time. Likewise, labs that maintain more than one instrument often opt to place them at multiple locations in the scene to assess spatial heterogeneity. The lack of strictly coincident data in space and time can thus lead to errors in calculations because the properties of the scene can shift with time as lighting or cloud cover changes.

The KSU VPCA spectral decomposition method provides a means of addressing and quantifying the impact of temporal variability in scene conditions on data acquisition. In our results, three of the four methods of calculating reflectance factors produced a random noise component, with the largest spectral response in the blue end of the spectrum and near zero responses at other wavelengths (**Figures 12**, **14E**). This spectral and spatial pattern is consistent with path radiance effects that likely arise from ancillary data that are not precisely temporally or spatially coincident with the observations from the NASA Glenn HSI2. The only method that did not produce this path radiance component was the ELM0 method. Because the ELM0 method calculated a direct ratio of the downwelling and upwelling radiance measured over the full path length between the surface and the HSI2 sensor using data from that sensor only, this method did not produce a path radiance bias component during the VPCA spectral decomposition, even though its reflectance factor produced the lowest amplitude response. In addition to the temporal and spatial coherence of the measured downwelling and upwelling radiance ratio from the HSI2 used in the ELM0, this result also arises because the measured at-surface water reflectance factor spectrum used as the calibration point for the ELM0 transformation is closer in magnitude to the rest of the water surface across the scene than the higher mirror target reflectance factor used as the at-surface reflectance calibration point in the ELM1 and ELM2 transformation. Even so, the magnitude of the path radiance bias in the other methods was small, amounting to just 4.3–4.4% of the total variance extracted from the image. The ability of the KSU VPCA spectral decomposition method to partition this random bias from the environmental components extracted from the image further documents the usefulness of the method.

The work presented here documents that the empirical line method, used in conjunction with the KSU VPCA decomposition method is sufficiently robust to provide adequate atmospheric correction to hyperspectral visible image data. The use of derivative spectroscopy also provides a way to extract useful information even when the absolute reflectance values are not strictly correct as was demonstrated with the ELM1 test example where we specifically left off the intercept of the radiance to reflectance transformation. The VPCA method also explicitly removes path radiance issues that result from data that is not precisely temporally synchronous. These results are encouraging and indicate that as a field, we have methodologies in place that will enable the community to capitalize on the additional spectral information that can be extracted from proposed orbital hyperspectral sensors on missions such as PACE, HyspIRI, and GeoCAPE. Each of these sensors has been designed for specific missions. PACE will provide global hyperspectral coverage at daily temporal and 1 km spatial resolution. HyspIRI will provide high spatial resolution hyperspectral data (30 m) in the Landsat orbit to provide continuity with legacy Landsat data and the capability for highly enhanced data products.

Finally, GeoCAPE is a proposed geostationary instrument that would image 70% of the illuminated western hemisphere, enabling the collection of time series of hyperspectral data for unprecedented process studies. Deploying these tools will create the opportunity for enhanced determination of pigment-related biomass estimates and new capabilities to identify algal and cyanobacterial composition based on extraction of pigment spectra by visible derivative spectroscopy as well as a host of other applications.

CONCLUSIONS

Our results document the utility of empirical calibration methods, such as the ELM to remove atmospheric errors from hyperspectral remote sensing data sets. We present a theoretical basis for the ELM using radiative transfer theory. The ELM2 and ELM0 methods produced spectral shapes that were consistent across the entire visible spectrum, but the ELM2 was effective at reconstructing the absolute reflectance values. The work presented here documents that the empirical line method, used in conjunction with the KSU VPCA decomposition method is sufficiently robust to provide adequate atmospheric correction to hyperspectral visible image data. The VPCA method extracted more information from the image swaths than the NOAA CI method, with less random error. The use of derivative spectroscopy also provides a way to extract useful information even when the absolute reflectance values are not strictly correct as was demonstrated with the ELM1 test example where we specifically left off the intercept of the radiance to reflectance transformation. In our results, three of the four methods of calculating reflectance factors produced a random noise component, with the largest spectral response in the blue end of the spectrum and near zero responses at other wavelengths. This spectral and spatial pattern is consistent with path radiance effects that likely arise from ancillary calibration data that are not precisely temporally or spatially coincident with the observations from the NASA Glenn HSI2. The only method that did not produce this path radiance component was the ELM0 method. Because the ELM0 method calculated a direct ratio of the downwelling and upwelling radiance measured over the full path length between the surface and the HSI2 sensor, this method did not produce a path radiance bias component during the VPCA spectral decomposition, even though its reflectance factor produced the lowest amplitude response. The VPCA decomposition method was effective at isolating the path radiance issues, thus improving the quality of the resulting retrievals. The VPCA enabled extraction of components that can be identified by quantitative comparison with a spectral library. This approach will enable accurate analysis of how phytoplankton functional groups and suspended sediment distribution vary in space and time, particularly once new hyperspectral sensors are available in orbit.

AUTHOR CONTRIBUTIONS

JDO: Lead for the conceptual basis of the paper, including development of the ELM 0, 1, and 2 methods and theory and the VPCA method; Field data collection and processing. SS and JCL: Development of the ELM 0, 1, and 2 methods and theory; Field data collection and processing. DA: Data processing to implement all 4 calibration methods for the HSI2 swath, and VPCA results; Figure generation; Editing; Field data collection. JDL: PI of NASA Lake Erie CyanoHAB collaboration, development/design, implementation, and initial processing of the HSI2 system and data acquired by the sensor; Description of processing of raw data into swaths. RT and RA: Development/design, implementation, and initial processing of the HSI2 system and data acquired by the sensor; Description of processing of raw data into swaths. RS and MS: Development of MTRI blacktop calibration method, field data sampling and analysis, authorship of section describing the MTRI method. RB: Field data collection and analysis. Calculation of NOAA CI for 15_MBSP HSI2 swath; Editing.

FUNDING

This work was funded by grants to JDO from the National Aeronautics and Space Administration (with separate awards to: JDO- Grant NNC15VB05P; SS- Grant NNC15MF72P; RS- Grant NNC15VA51P; and RB- Grant NNC15MF73P), the Ohio Department of Education (JDO: Grant ODHE-10009090-KSU), and the Ohio Sea Grant College Program, Ohio State University (JDO: Grant R/ES-021-PD).

ACKNOWLEDGMENTS

We thank the captains and crews of the vessels employed in our collaborative work, the staff of the water treatment plants who provided access for instrument placement and the student workers who assisted with sample collection and processing. Funding for the project was provided by NASA, the Ohio Department of Education and Ohio Sea Grant. JDO dedicates this work to his mentor, Dr. John Imbrie (1925–2016), who introduced him to factor analysis and principal component analysis. We thank Drs. Shuisen Chen and Stephanie Schollaert Uz and Dr. Kristin Byrd, editor for comments and suggestions that improved the manuscript.

REFERENCES

Abdi, H. (2003). "Factor rotations in factor analyses," in *Encyclopedia of Social Sciences Research Methods*, eds M. Lewis-Beck, A. Bryman, and T. Futing (Thousand Oaks, CA: Sage), 1–8.

Ali, K. A., and Ortiz, J. D. (2016). Multivariate approach for chlorophyll-a and suspended matter retrievals in Case II type waters using hyperspectral data. *Hydrol. Sci. J.* 61, 200–213. doi: 10.1080/02626667.2014.964242

Ali, K. A., Witter, D., L., and Ortiz, J., D. (2013). Multivariate approach to estimate colour producing agents in Case 2 waters

using first-derivative spectrophotometer data. *Geocarto Int.* 29, 1–26. doi: 10.1080/10106049.2012.743601

Ali, K., Witter, D., and Ortiz, J. (2014). Application of empirical and semi-analytical algorithms to MERIS data for estimating chlorophyll a in Case 2 waters of Lake Erie. *Environ. Earth Sci.* 71, 4209–4220. doi: 10.1007/s12665-013-2814-0

Baugh, W. M., and Groeneveld, D. P. (2008). Empirical proof of the empirical line. *Int. J. Remote Sens.* 29, 665–672. doi: 10.1080/01431160701352162

Bullerjahn, G. S., McKay, R. M., Davis, T. W., Baker, D. B., Boyer G. L., D'Anglada, L. V., et al. (2016). Global solutions to regional problems: collecting global expertise to address the problem of harmful cyanobacterial blooms. A Lake Erie case study. *Harmful Algae* 54, 223–238. doi: 10.1016/j.hal.2016.01.003

Chase, A., Boss, E., Zaneveld, R., Bricaud, A., Claustre, H., Ras, J., et al. (2013). Decomposition of *in situ* particulate absorption spectra. *Methods Oceanogr.* 7, 110–124. doi: 10.1016/j.mio.2014.02.002

Conroy, J. D., Kane, D., D., Briland, R., D., and Culver, D., A. (2014). Systemic, early-season Microcystis blooms in western Lake Erie and two of its major agricultural tributaries (Maumee and Sandusky rivers). *J. Great Lakes Res.* 40, 518–523. doi: 10.1016/j.jglr.2014.04.015

Farrand, W. H., Singer, R. B., and Merényi, E. (1994). Retrieval of apparent surface reflectance from AVIRIS data: a comparison of empirical line, radiative transfer, and spectral mixture methods. *Remote Sens. Environ.* 47, 311–321. doi: 10.1016/0034-4257(94)90099-X

Ferrier, G., and Trahair, N. S. (1995). Evaluation of apparent surface reflectance estimation methodologies. *Int. J. Remote Sens.* 16, 2291–2297. doi: 10.1080/01431169508954557

Gao, B.-C., Montes, M. J., Davis, C. O., and Goetz, A. F. H. (2009). Atmospheric correction algorithms for hyperspectral remote sensing data of land and ocean. *Remote Sens. Environ.* 113, S17–S24. doi: 10.1016/j.rse.2007.12.015

Goetz, A. F. H. (2009). Three decades of hyperspectral remote sensing of the Earth: a personal view. *Remote Sens. Environ.* 113, S5–S16. doi: 10.1016/j.rse.2007.12.014

Gordon, H. R., Brown, O. B., Evans, R. H., Brown, J. W., Smith, R. C., Clark, D. K., et al. (1988). A semianalytic radiance model of ocean color. *J. Geophys. Res.* 93:10909. doi: 10.1029/JD093iD09p10909

Lekki, J., Anderson, R., Avouris, D., Becker, R., Churnside, J., Cline, M., et al. (2017). *Airborne Hyperspectral Sensing of Harmful Algal Blooms in the Great Lakes Region: System Calibration and Validation. From Photons to Algae Information: The Processes in-Between.* NASA/TM-2017-219071, E-19202, GRC-E-DAA-TN29647. Available online at: https://ntrs.nasa.gov/archive/nasa/casi.ntrs.nasa.gov/20170002298.pdf

Lekki, J., Anderson, R., Nguyen, Q-V., Demers, J., Leshkevich, G., Flatico, J., et al. (2009). "Development of hyperspectral remote sensing capability for the early detection and monitoring of Harmful Algal Blooms (HABs) in the Great Lakes," in *Proceedings of AIAA infotech@Aerospace Conference* (AIAA 2009-1978) (Seattle, WA).

Kane, D. D., Conroy, J. D., Peter Richards, R., Baker, D. B., and Culver, D. A. (2014). Re-eutrophication of Lake Erie: correlations between tributary nutrient loads and phytoplankton biomass. *J. Great Lakes Res.* 40, 496–501. doi: 10.1016/j.jglr.2014.04.004

Matisoff, G., and Carson, M. L. (2014). Sediment resuspension in the Lake Erie nearshore. *J. Great Lakes Res.* 40, 532–540. doi: 10.1016/j.jglr.2014.02.001

Moisan, J. R., Moisan, T. A. H., and Linkswiler, M. A. (2011). An inverse modeling approach to estimating phytoplankton pigment concentrations from phytoplankton absorption spectra. *J. Geophys. Res.* 116:C09018. doi: 10.1029/2010JC006786

Ortiz, J. D., Witter, D. L., Ali, K. A., Fela, N., Dull, M., and Mills, L. (2013). Evaluating multiple colour-producing agents in Case II waters from Lake Erie. *Int. J. Remote Sens.* 34, 8854–8880. doi: 10.1080/01431161.2013.853892

Palmer, J. M. (1999). *Radiometry and Photometry FAQ.* Available online at: http://www.optics.arizona.edu/Palmer/rpfag.htm#motivation

Pennuto, C. M., Dayton, L., Kane, D. D., and Bridgeman, T. B. (2014). Lake Erie nutrients: from watersheds to open water. *J. Great Lakes Res.* 40, 469–472. doi: 10.1016/j.jglr.2014.07.002

Press, W. H., Teukolsky, S. A., Vetterling, W. T., and Flannery. B. P. (1992). *Numerical Recipes in Fortran*. New York, NY: Cambridge University Press.

Schaepman-Strub, G., Schaepman, M. E., Painter, T. H., Dangel, S., and Martonchik, J. V. (2006). Reflectance quantities in optical remote sensing—definitions and case studies. *Remote Sens. Environ.* 103, 27–42. doi: 10.1016/j.rse.2006.03.002

Schiller, S. J., and Silny, J. (2010). "The SPecular Array Radiometric Calibration (SPARC) method: a new approach for absolute vicarious calibration in the solar reflective spectrum," in *Proc. of SPIE 7813, Remote Sensing System Engineering III,* 78130E-7813–78130E-7819. doi: 10.1117/12.864071

Shuchman, R. A., Leshkevich, G., Sayers, M. J., Johengen, T. H., Brooks, C. N., and Pozdnyakov, D. (2013). An algorithm to retrieve chlorophyll, dissolved organic carbon, and suspended minerals from Great Lakes satellite data. *J. Great Lakes Res.* 39, 14–33. doi: 10.1016/j.jglr.2013.06.017

Simis, S. G. H., Peters, S. W. M., and Gons, H. J. (2005). Remote sensing of the cyanobacterial pigment phycocyanin in turbid inland water. *Limnol. Oceanogr.* 50, 237–245. doi: 10.4319/lo.2005.50.1.0237

Smith, G.M., and Milton, E. J. (1999). The use of the empirical line method to calibrate remotely sensed data to reflectance. *Int. J. Remote Sens.* 20, 2653–2662. doi: 10.1080/014311699211994

Soja-Woźniak, M., Craig, S., E., Kratzer, S., Wojtasiewicz, B., Darecki, M., and Jones, C. T. (2017). A novel statistical approach for ocean colour estimation of inherent optical properties and cyanobacteria abundance in optically complex waters. *Remote Sens.* 9, 1–22. doi: 10.3390/rs9040343

Stumpf, R. P., Wynne, T. T., Baker, D. B., and Fahnenstiel, G. L. (2012). Interannual variability of cyanobacterial blooms in Lake Erie. *PLoS ONE* 7:e42444. doi: 10.1371/journal.pone.0042444

Witter, D. L., Ortiz, J. D., Palm, S., Heath, R. T., and Budd, J. W. (2009). Assessing the application of SeaWiFS ocean color algorithms to Lake Erie. *J. Great Lakes Res.* 35, 361–370. doi: 10.1016/j.jglr.2009.03.002

Wynne, T. T., Stumpf, R. P., and Briggs, T. O. (2013). Comparing MODIS and MERIS spectral shapes for cyanobacterial bloom detection. *Int. J. Remote Sens.* 34, 6668–6678. doi: 10.1080/01431161.2013.804228

Wynne, T. T., Stumpf, R. P., Tomlinson, M. C., and Dyble, J. (2010). Characterizing a cyanobacterial bloom in Western Lake Erie using satellite imagery and meteorological data. *Limnol. Oceanogr.* 55, 2025–2036. doi: 10.4319/lo.2010.55.5.2025

Conflict of Interest Statement: The authors declare that the research was conducted in the absence of any commercial or financial relationships that could be construed as a potential conflict of interest.

frontiers in Marine Science

ORIGINAL RESEARCH
published: 15 September 2017
doi: 10.3389/fmars.2017.00274

Satellite Derived Water Quality Observations Are Related to River Discharge and Nitrogen Loads in Pensacola Bay, Florida

John C. Lehrter[1,2]* *and Chengfeng Le*[3]

[1] Department of Marine Sciences, University of South Alabama, Mobile, AL, United States, [2] Dauphin Island Sea Lab, Dauphin Island, AL, United States, [3] Ocean College, Zhejiang University, Zhoushan, China

Relationships between satellite-derived water quality variables and river discharges, concentrations and loads of nutrients, organic carbon, and sediments were investigated over a 9-year period (2003–2011) in Pensacola Bay, Florida, USA. These analyses were conducted to better understand which river forcing factors were the primary drivers of estuarine variability in several water quality variables. Remote sensing reflectance time-series data were retrieved from the MEdium Resolution Imaging Spectrometer (MERIS) and used to calculate monthly and annual estuarine time-series of chlorophyll *a* (*Chla*), colored dissolved organic matter (*CDOM*), and total suspended sediments (*TSS*). Monthly MERIS *Chla* varied from 2.0 mg m^{-3} in the lower region of the bay to 17.2 mg m^{-3} in the upper bay. MERIS *CDOM* and *TSS* exhibited similar patterns with ranges of 0.51–2.67 (m^{-1}) and 0.11–8.9 (g m^{-3}). Variations in the MERIS-derived monthly and annual *Chla*, *CDOM*, and *TSS* time-series were significantly related to monthly and annual river discharge and loads of nitrogen, organic carbon, and suspended sediments from the Escambia and Yellow rivers. Multiple regression models based on river loads (independent variables) and MERIS *Chla*, *CDOM*, or *TSS* (dependent variables) explained significant fractions of the variability (up to 62%) at monthly and annual scales. The most significant independent variables in the regressions were river nitrogen loads, which were associated with increased MERIS *Chla*, *CDOM*, and *TSS* concentrations, and river suspended sediment loads, which were associated with decreased concentrations. In contrast, MERIS water quality variations were not significantly related to river total phosphorus loads. The spatially synoptic, nine-year satellite record expanded upon the spatial extent of past field studies to reveal previously unseen system-wide responses to river discharge and loading variation. The results indicated that variations in Pensacola Bay *Chla*, *CDOM*, and *TSS* were primarily associated with riverine nitrogen loads. Thus, reducing these loads may improve water quality issues associated with eutrophication, turbidity, and water clarity in this system.

Keywords: MERIS chlorophyll *a*, CDOM, suspended sediments, estuary, nutrient loads, organic matter loads, sediment loads, Pensacola Bay

OPEN ACCESS

Edited by:
Kevin Ross Turpie, University of Maryland, Baltimore County, United States

Reviewed by:
Michael R. Twiss, Clarkson University, United States
Gerson Araujo De Medeiros, Universidade Estadual Paulista Júlio Mesquita Filho, Brazil
Dongyan Liu, State Key Laboratory of Estuarine and Coastal Research (ECNU), China

***Correspondence:**
John C. Lehrter
jlehrter@disl.org

Specialty section:
This article was submitted to Coastal Ocean Processes, a section of the journal Frontiers in Marine Science

Received: *29 April 2017*
Accepted: *10 August 2017*
Published: *15 September 2017*

Citation:
Lehrter JC and Le C (2017) Satellite Derived Water Quality Observations Are Related to River Discharge and Nitrogen Loads in Pensacola Bay, Florida. Front. Mar. Sci. 4:274. doi: 10.3389/fmars.2017.00274

INTRODUCTION

Like many estuarine and coastal systems worldwide, the Pensacola Bay system in northwest Florida exhibits symptoms of eutrophication associated with watershed nutrient loading. Mean annual primary production in this system of 290 g C m^{-2} y^{-1} (Murrell et al., 2007) is moderately high being in the 70th percentile globally in comparison to other estuaries (Caffrey and Murrell, 2016). Hypoxia (O_2 < 2 mg l^{-1}) occurs in bottom waters over seasonal scales due to both bottom water respiration driven by organic matter supply and strong vertical stratification of the water-column driven by a halocline (Hagy and Murrell, 2007). There have also been large declines in seagrass extent in the bay (Handley et al., 2007) with the present extent of 14.3 km^2 (Yarbro and Carlson, 2013) being about 38% of the extent from the 1960s when seagrass covered 8% of the bay bottom (Caffrey and Murrell, 2016). Though it is still largely unknown what caused this loss of seagrass, restoration activities in the northern Gulf are targeting water clarity improvements as a means to restore seagrass (Conmy et al., 2017). Management strategies for both hypoxia and water clarity are being pursued by targeting non-point source nutrient reductions in the watershed as well as by reducing runoff of sediments in order to reduce bay chlorophyll *a* (*Chla*), colored dissolved organic matter (*CDOM*), and total suspended sediment (*TSS*). Thus, gaining a more quantitative understanding of how bay *Chla*, *CDOM*, and *TSS* dynamics are related to river loads is important for improving our understanding of this system and its management.

Estuarine studies that relate watershed discharges and loads to estuarine water quality have largely relied on empirical studies based on time-series analyses or comparative analyses across systems. For example, there are documented relationships of estuarine *Chla* with river discharge (Harding et al., 2016) and nutrients (Boynton et al., 1982; Monbet, 1992; Lehrter, 2008) and between suspended sediment loads and water clarity (Borkman and Smayda, 1998). However, in most estuarine systems there are insufficient observations to perform these types of analyses. Water quality measures obtained from high temporal and spatial resolution ocean color satellites can therefore be useful for supplementing or establishing baseline water quality conditions and trends.

Further the satellite data allow for characterizing water quality dynamics in relation to time-series of river discharge and inputs of dissolved and particulate constituents (Acker et al., 2005; Green and Gould, 2008; Green et al., 2008; Chen et al., 2013; Le et al., 2014, 2016). In this study, we add to the previous work by examining the relationships of satellite-derived, estuarine water quality constituents with river concentrations, and loads of organic and inorganic nitrogen and phosphorus, organic carbon, and suspended sediment. Specifically, we used a 9-year, water quality time-series of MERIS-derived *Chla*, *CDOM*, and *TSS* to explore relationships of these variables with monthly and annual river discharges, concentrations, and loading dynamics in Pensacola Bay. The application of MERIS for this analysis provided data that were otherwise unavailable and allowed for a synoptic analysis across the entire Pensacola Bay system.

MATERIALS AND METHODS

Study Area

Pensacola Bay is located in the Florida Panhandle of the northern Gulf of Mexico. The bay has an area of 480 km^2 and is comprised of several distinct hydrographic regions including oligohaline and mesohaline regions that are river dominated and polyhaline regions that are more lagoonal in nature (Caffrey and Murrell, 2016). The river-dominated regions include two distinct lobes of the upper bay, namely Escambia Bay and East Bay (**Figure 1**). Escambia Bay receives the freshwater discharge of the Escambia River and East Bay receives the discharge of the Yellow River. The lagoonal region is Santa Rosa Sound. The Lower Bay region exchanges with the Gulf of Mexico with which it shares similar hydrographic characteristics (Hagy and Murrell, 2007). Mean depth in Pensacola Bay is ∼3.0 m with a mean diurnal tide of ∼0.4 m (Caffrey and Murrell, 2016) and an average water residence time of 27 days (Bricker et al., 1999). The Pensacola Bay watershed has an area of 18,100 km^2 and land-use/land-cover is comprised primarily of evergreen (42.6%) and deciduous (10.1%) forest, agriculture (17.1%), rangeland (9.6%), and urban (7.0%) land uses (Le et al., 2015). Human population in the watershed is ∼371,000 (Bricker et al., 1999).

Watershed Discharges and Concentrations and Loads of Nitrate, Phosphorus, Organic Carbon, and Suspended Solids

Mean daily river discharge rates (*Q*) for the largest rivers draining to Pensacola Bay were obtained from the U.S. Geological Survey (USGS) for the study period 2003–2012. Discharge data were retrieved for gaging sites on Escambia River (USGS 02376033), Big Coldwater Creek (USGS 02370500), Blackwater River (USGS 02370000) and Yellow River (USGS 02369600; **Figure 1**). The discharge from the Escambia (mean = 190 m^3 s^{-1}) and Yellow rivers (mean = 64 m^3 s^{-1}) comprised 91% of the total river discharge (279 m^3 s^{-1}) to the bay. The remaining 9% is attributed primarily to the Blackwater River and Big Coldwater Creek, which drain into upper East Bay. Thus, subsequent analyses were restricted to the Escambia and Yellow river data. Because elevated river NO_3^- and Chla were observed under low discharge, baseflow conditions (discussed below), we considered whether baseflow loads may be important explanatory variables of estuarine water quality. Daily baseflow discharges (*Qb*) for Escambia and Yellow rivers were calculated using a hydrograph separation method (Gustard et al., 1992). Briefly, this method consisted of four steps: (1) Divide the daily discharge record into non-overlapping blocks of 5 days and compute the minimum of each block that we call Q_1, Q_2, Q_3,... Q_n. (2) Next we consider the series (Q_1, Q_2, Q_3), (Q_2, Q_3, Q_4),... (Q_{i-1}, Q_i, Q_{i+1}). For each series, if 0.9 × center value < outer values, then we save the center value and its date as a point for the baseflow line. This results in a series of values Qb_1, Qb_2, Qb_3, Qb_n with different time periods between them. (3) Linearly interpolate between Qb_i values to estimate daily values of Qb. (4) For the interpolated series, if $Qb_i > Q_i$ then set $Qb_i = Q_i$.

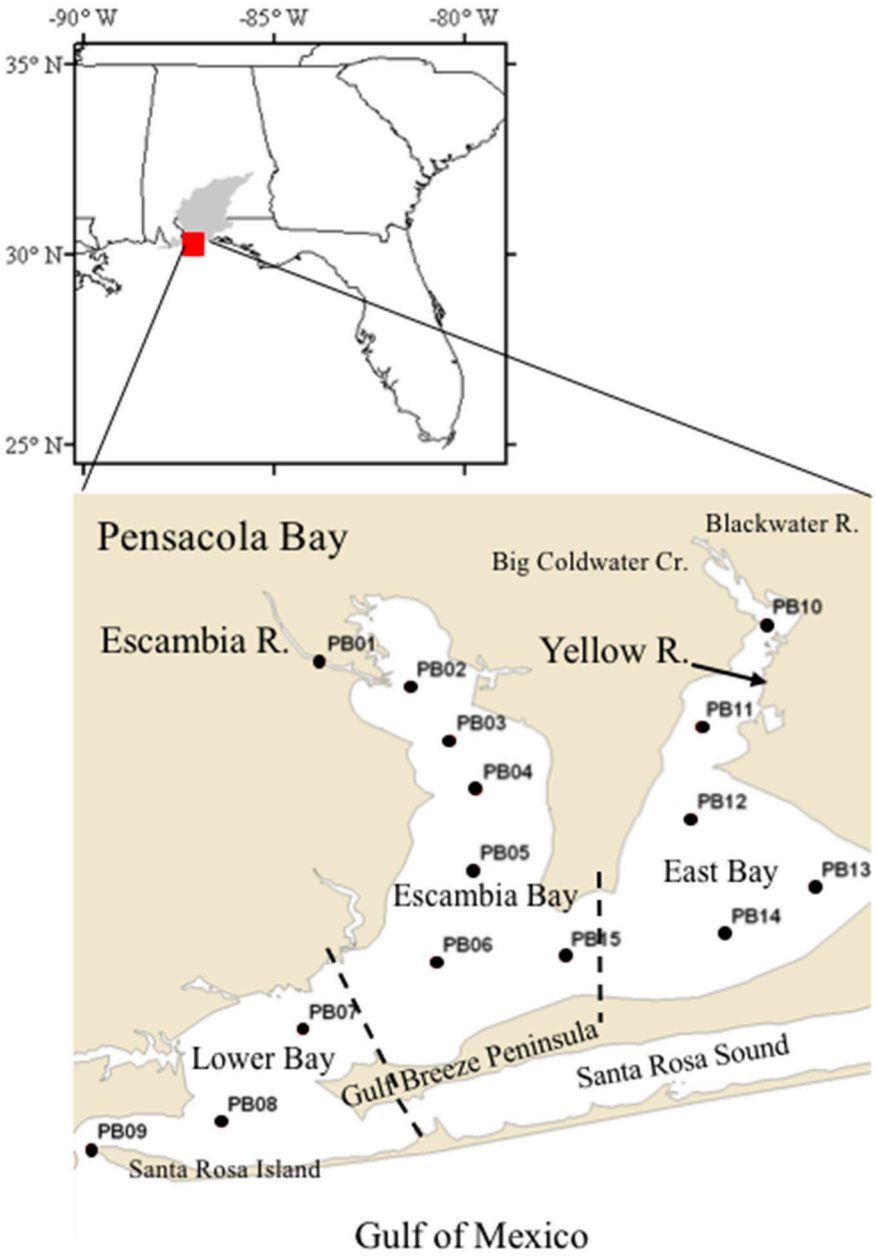

FIGURE 1 | Map of the Pensacola Bay system and sampling sites. Sub-regions of the Bay are delimited by dashed lines between stations PB14 and PB15, which separates East Bay and Escambia Bay, and between PB07 and PB06, which separates Lower Bay and Escambia Bay. The Pensacola Bay watershed is shown in gray in the upper panel.

Observed NO_3^-, total Kjeldahl nitrogen (*TKN*), total phosphorus (*TP*), chlorophyll a ($Chla_{\mathrm{River}}$), total organic carbon (*TOC*), and total suspended sediment (TSS_{River}), collected by the Florida Department of Environmental Protection, were obtained from the U.S. water quality portal (https://www.waterqualitydata.us/). Approximately monthly samples were collected at the Escambia River site (21FLBFA_WQX-33020007), which was co-located with the USGS Escambia River discharge gage. Seasonal samples were collected at the Yellow River site (21FLBFA_WQX-33040003), which was co-located with the USGS Yellow River discharge gage.

In order to calculate monthly averages, a rating curve method was applied to observed NO_3^-, *TKN*, *TP*, $Chla_{\mathrm{River}}$, *TOC*, and TSS_{River} observations (Cohn et al., 1989, 1992). The rating curve regression model equation was

$$\ln(C) = \beta_0 + \beta_1 ln\left(\frac{Q}{Q'}\right) + \beta_2\left(T - T'\right) + \beta_3\left(T - T'\right)^2 + \beta_4 \sin(T) + \varepsilon, \quad (1)$$

where C was a vector of observed constituent concentrations, Q was a vector of daily discharge rates for the dates (T, converted to radians) when C were collected, and Q' and T' were centering variables. C and Q were log transformed to obtain normally distributed residuals. β_0, β_1, β_2, β_3, and β_4 were regression coefficients calculated for each regression model and the last term, ϵ, was the error. Using the regression models, daily concentrations for each constituent were calculated for the study period based on the daily observed discharge rates and time. Then, mean monthly and annual discharge and constituent concentrations were calculated from the daily time-series. Finally, monthly and annual constituent loading time-series were calculated as the products of discharges and constituent concentrations.

Derivation of MERIS *Chla*, *CDOM*, and *TSS*

The *in situ* water quality and optical observations used to develop empirical algorithms for retrieving *Chla*, *CDOM*, and *TSS* from MERIS observations in Pensacola Bay have been described previously (Le et al., 2016; Conmy et al., 2017). Here, a brief summary of the methods is presented for field sampling, laboratory measurements, and validation of satellite observations in comparison to measurements.

Water samples for *Chla*, *CDOM*, and *TSS* analysis (n = 161) were collected from the surface of Pensacola Bay (0.5 m depth) at 15 stations (**Figure 1**) approximately every 6 weeks from September 2009 to December 2011. Water samples were processed on the day of collection and retained sample filter pads and filtrate were stored at −70°C until analysis. *Chla* samples were collected on 25 mm GF/F filters (nominal pore size = 0.7 μm), and then, later, extracted from the filter pad with hot methanol and assayed fluorometrically (Welschmeyer, 1994). *TSS* samples from a measured volume of bay water were collected on pre-weighed, combusted (550°C for 4 h) 47 mm GF/F filters. *TSS* was measured gravimetrically by drying the sample filter pad (105°C), reweighing, and subtracting the initial filter weight. *CDOM* in the filtrate obtained from *TSS* processing was assayed by measuring the specific absorption at 443 nm in a 10-cm quartz cell on a dual-beam scanning spectrophotometer (Shimadzu UV-1700). The absorption spectra from λ = 400–700 nm of dissolved organic matter [$ag(\lambda)$] were further measured on the dissolved fraction (Pegau et al., 2003). Absorption spectra from particles [$ap(\lambda)$] and non-algal detrital particles [$ad(\lambda)$] were quantified on a dual-beam scanning spectrophotometer using the quantitative filter technique (Kiefer and SooHoo, 1982; Kishino et al., 1985). After measuring $ap(\lambda)$, phytoplankton pigments were extracted from the filter with warm methanol and then the spectra of the filter pad was scanned again to obtain $ad(\lambda)$. Phytoplankton absorption spectra [$aph(\lambda)$] were calculated as the difference between $ap(\lambda)$ and $ad(\lambda)$.

Remote sensing reflectance (Rrs) spectral data were measured at each station with a spectroradiometer (HyperSAS, Satlantic Inc., Halifax, Nova Scotia) mounted to the top of the boat, 2 m above the water surface. The HyperSAS collected spectra

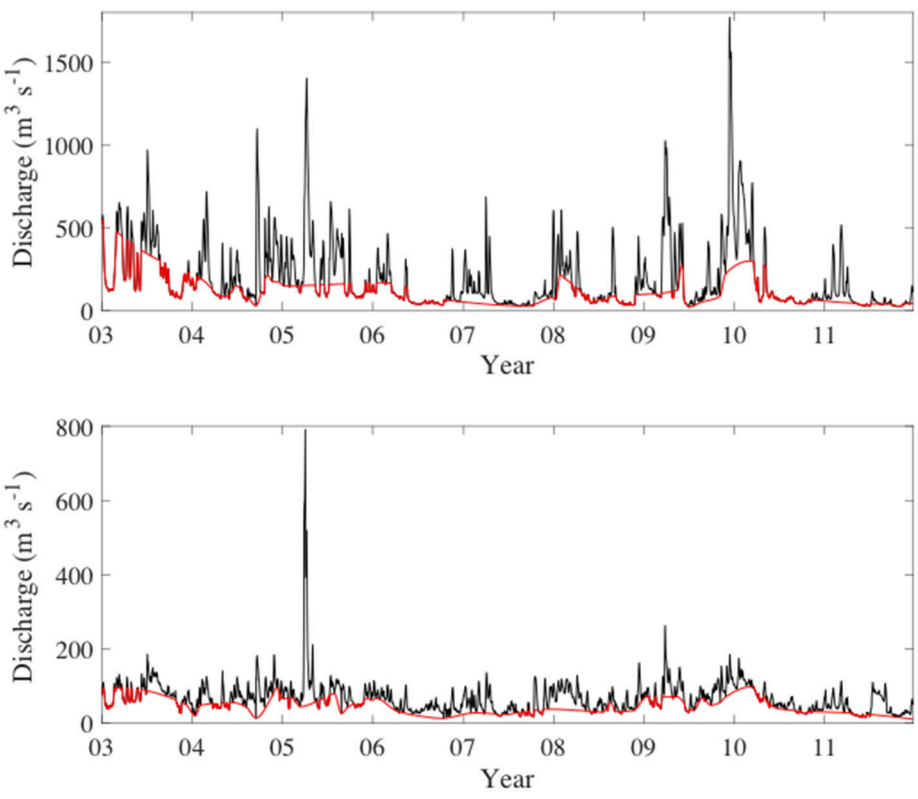

FIGURE 2 | Daily river discharge from the Escambia River (upper) and Yellow River (lower). The red line in both plots shows the calculated baseflow discharge.

(1 nm resolution at λ 350–800 nm) of above-water radiance, sky radiance, and downwelling sky irradiance. At each station, An AC-s (Wet-Labs, Philomath, OR) was used to collect vertical water-column profiles of absorption and beam attenuation. Absorption and beam attenuation were measured at 1 nm resolution from 400 to 735 nm. AC-s absorption, attenuation, and calculated scattering spectra were corrected for changes in salinity and temperature, measured with a Seabird CTD (Wet-Labs; Sullivan et al., 2006). AC-s data were averaged from the surface of the water column to the observed Secchi depth and used to correct the R_{rs} spectra (Gould et al., 1999, 2001).

R_{rs} bands corresponding with MERIS bands were extracted to calculate empirical algorithms relating observed R_{rs} to observed *Chla* (mg m^{-3}), *CDOM* (m^{-1}), and *TSS* (g m^{-3}; Le et al., 2016).

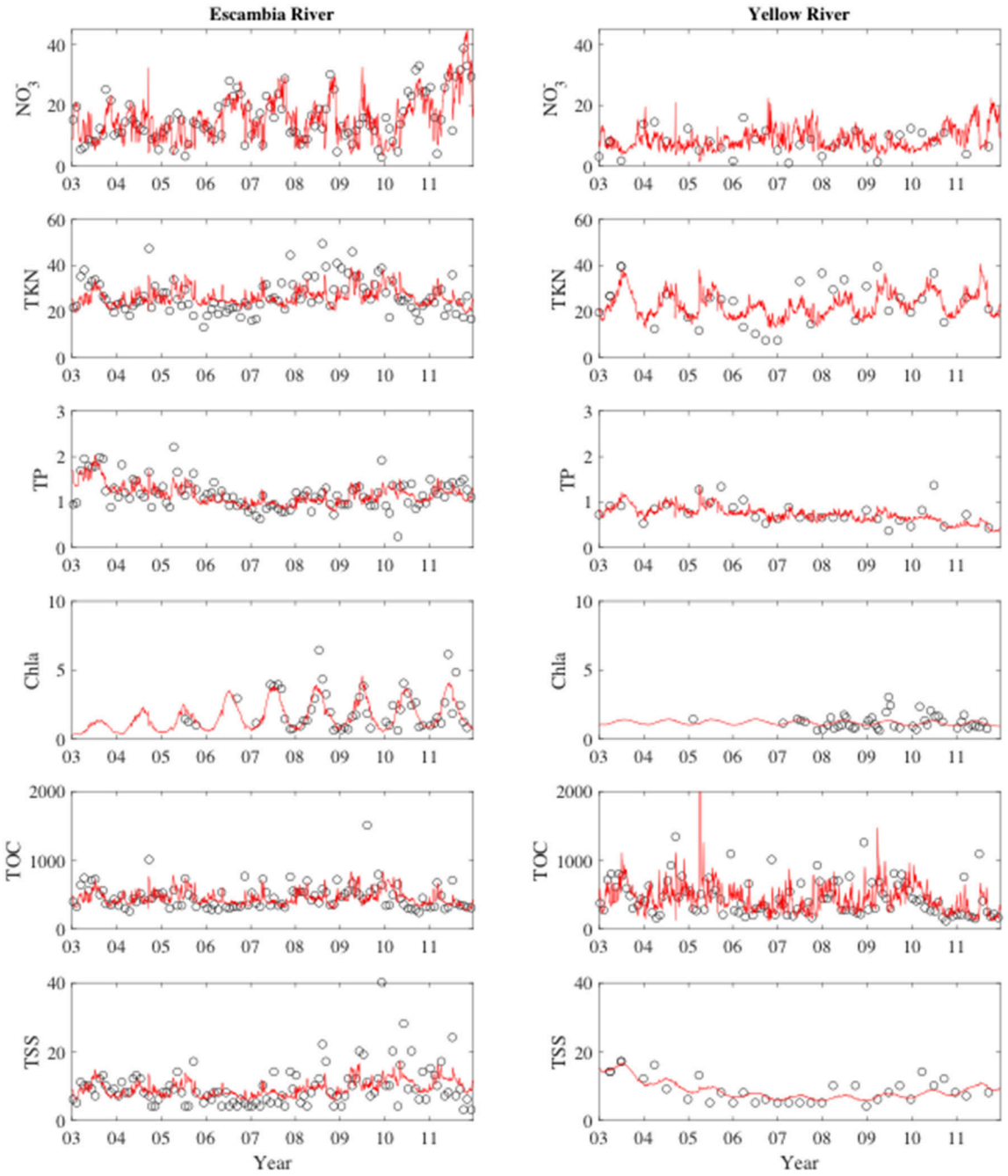

FIGURE 3 | River concentrations during the study period. Left column are the Escambia river time-series and the right column are the Yellow River time-series. Concentration units are mmol m^{-3} for all variables except for Chla (mg m^{-3}) and TSS (g m^{-3}). The solid red lines in each plot show the rating curve model fits to the observations.

Only data collected on cloud-free days and with wind speed $<3\ m\ s^{-1}$ were used to develop algorithms. For *Chla*, the NIR-red band ratio of $R_{rs}(709)/R_{rs}(665)$ was selected in order to minimize interference from *CDOM* and non-algal detritus. For *CDOM*, the NIR-green band ratio of $R_{rs}(709)/R_{rs}(510)$ was used due to uncertainties in the atmospheric correction at blue bands (443 and 490 nm) and interference from phytoplankton absorption in the red bands (665 and 681 nm). For *TSS*, the band ratio $R_{rs}(709)/R_{rs}(681)$ gave the best fit. The equations for the band ratio algorithms were

$$Chla = 29.3\left(\frac{Rrs(709)}{Rrs(665)}\right)^{4.15},\ R^2 = 0.70\ (n = 150) \quad (2)$$

$$CDOM = 1.41\left(\frac{Rrs(709)}{Rrs(510)}\right)^{0.89},\ R^2 = 0.79\ (n = 129) \quad (3)$$

$$TSS = 13.9\left(\frac{Rrs(709)}{Rrs(681)}\right)^{3.67},\ R^2 = 0.71\ (n = 143), \quad (4)$$

where R^2 were the percentage of variation in the observed data explained by the algorithms and n were the number of samples.

Daily MERIS level-2 data were obtained from NASA (http://oceancolor.gsfc.nasa.gov/) for the study period January 1, 2003 to April, 2012. Downloaded products included MERIS $R_{rs}(\lambda)$ in all the spectral bands with 300-m spatial resolution as well as quality control flags for clouds, atmospheric correction warning, and stray light. Pixels along the shoreline with water depths < 2 m were masked to avoid issues with bottom-reflectance. Algorithm Equations (2–4) were then applied to the MERIS R_{rs} time-series to generate MERIS *Chla*, *CDOM*, and *TSS* time-series. To validate the algorithms, MERIS $R_{rs}(\lambda)$ data were extracted for the dates and locations of sampling stations with a time window of ±1 d and calculating a median $R_{rs}(\lambda)$ from a 3 × 3 pixel box centered on the sampling location (Le et al., 2013). For subsequent comparisons with river discharge, concentration, and loading time-series, the MERIS *Chla*, *CDOM*, and *TSS* have been averaged to monthly and annual values for the period from January 2003 to December 2011.

Relating River Discharge, Concentrations, and Loads to MERIS *Chla*, *CDOM*, and *TSS*

On a per pixel basis, Pearson correlations among MERIS monthly *Chla*, *CDOM*, and *TSS* time-series and time-series of *Q*, *Qb*, river concentrations, and river loads were calculated. We examined correlations with concurrent (0-month), 1-month, and 2-month lagged river time-series. In order to further identify how multivariate combinations of river loads could explain variation in MERIS bio-optical water quality, the MERIS data were averaged over discrete regions, namely Escambia Bay, East Bay, and Lower Bay (**Figure 1**), and the regional time-series were then regressed against monthly and annual time-series of river loads. We used a partial least squares (PLS) regression model because of the high degree of correlation between independent variables (described below in Results) and because for the annual time-series there were more independent variables (see Equation 5 below) than annual samples ($n = 9$ years). PLS regression reduces the number of predictor variables by combining the variables into factors similar to principal component analysis. Nine regression models were developed: 3 MERIS water quality variables (i = *Chla, CDOM, and TSS*) by 3 bay regions (j = Escambia, East, and Lower). The regression equation had the form

$$\begin{aligned} MERIS\ WQ_{ij} \sim\ & QNO_3^- + QTKN + QTP + QChl + QTOC \\ & + QTSS + QbNO_3^- + QbTKN + QbTP \\ & + QbChl + QbTOC + QbTSS \end{aligned} \quad (5)$$

where $MERIS\ WQ_{ij}$ were the log transformed MERIS water quality time-series per bay region, and variables on the right hand side were the log transformed time-series of river loads (variables beginning with a *Q*) and baseflow loads (variables beginning with a *Qb*). For Escambia Bay ($j = 1$) and Lower Bay ($j = 3$), the Escambia River loads were used as the independent variables. For East Bay ($j = 2$), the Yellow River loads were used.

TABLE 1 | Mean river concentrations and loads.

	NO_3^-	TKN	TP	Chla	TOC	TSS
Concentrations	**mmol m^{-3}**	**mmol m^{-3}**	**mmol m^{-3}**	**mg m^{-3}**	**mmol m^{-3}**	**g m^{-3}**
Escambia	15.8	26.3	1.17	1.62	454	9.4
Yellow	8.8	22.9	0.73	1.18	448	8.7
Loads	**kg d^{-1}**	**kg d^{-1}**	**kg d^{-1}**	**kg d^{-1}**	**kg d^{-1}**	**kg d^{-1}**
Escambia	3,593	5,981	589	26	88,493	152,686
Yellow	724	1,884	133	7	31,585	51,114
Escambia %	83%	76%	82%	79%	74%	75%

Escambia % is the percentage contribution of the Escambia River load to the combined Escambia + Yellow river loads.

TABLE 2 | Pearson correlation between monthly time (T), river discharge(Q), baseflow discharge (Qb), and concentrations of nitrate (NO_3^-), total Kjeldahl nitrogen (TKN), total phosphorus (TP), chlorophyll *a*, total organic carbon (TOC), and total suspended sediment (TSS).

	T	Q	Qb	NO_3^-	TKN	TP	Chla	TOC	TSS
T	1.00	**−0.27**	**−0.50**	**0.43**	0.12	**−0.42**	0.01	−0.08	**0.42**
Q	**−0.27**	1.00	**0.74**	**−0.76**	**0.71**	**0.59**	**−0.44**	**0.85**	**0.40**
Qb	**−0.50**	**0.74**	1.00	**−0.65**	**0.40**	**0.73**	**−0.35**	**0.57**	**0.23**
NO_3^-	**0.43**	**−0.76**	**−0.65**	1.00	**−0.72**	**−0.44**	**0.32**	**−0.84**	**−0.24**
TKN	0.12	**0.71**	**0.40**	**−0.72**	1.00	**0.40**	−0.05	**0.97**	**0.76**
TP	**−0.42**	**0.59**	**0.73**	**−0.44**	**0.40**	1.00	0.10	**0.51**	**0.54**
Chla	0.01	**−0.44**	**−0.35**	**0.32**	−0.05	0.10	1.00	−0.20	**0.28**
TOC	−0.08	**0.85**	**0.57**	**−0.84**	**0.97**	**0.51**	−0.20	1.00	**0.65**
TSS	**0.42**	**0.40**	**0.23**	**−0.24**	**0.76**	**0.54**	**0.28**	**0.65**	1.00

Bold values are significant correlations (α = 0.05).

RESULTS

Watershed Discharge, Baseflow, Concentrations, and Loads

Watershed discharge was greatest in the winter and spring in both the Escambia and Yellow rivers (**Figure 2**). Notable discharge events occurred during April 2005 and December 2009. April 2005 was the wettest month on record at the time for the city of Pensacola, going back to 1880, with 62 cm of rainfall, which resulted in a mean monthly discharge of 768 m^3 s^{-1} for the Escambia River and 283 m^3 s^{-1} for the Yellow River. Escambia River discharge in December 2009 exceeded April 2005 with a monthly average discharge of 883 m^3 s^{-1}, while Yellow River discharge was 127 m^3 s^{-1} in December 2009. Overall, for the study period the mean discharges from the Escambia and Yellow rivers were 188 and 68 m^3 s^{-1}, respectively. Discharge rates in the two rivers were highly correlated ($r = 0.85$).

Baseflow discharge followed a similar pattern as total discharge with highest baseflow discharge in the winter and spring. For the study period, mean baseflow discharges of the Escambia and Yellow rivers were 109 and 45 m^3 s^{-1}, respectively, which represented 75% of the total discharge in the Escambia River and 72% in the Yellow River. During the summer and fall low discharge periods, the baseflow discharge often accounted for all of the observed river discharge (**Figure 2**). During high discharge periods the baseflow contribution was considerably less. For example, during April 2005 and December 2009, baseflow contributed only 20% and 27%, respectively, of the total discharge from the Escambia River.

Escambia and Yellow river time-series concentrations are shown in **Figure 3**. On average, concentrations were higher in the Escambia River (**Table 1**) where mean concentrations for NO_3^-, *TKN*, *TP*, *Chla*, *TOC*, and *TSS* were 15.8 mmol m^{-3}, 26.3 mmol m^{-3}, 1.17 mmol m^{-3}, 1.62 mg m^{-3}, 454 mmol m^{-3}, and 9.4 g m^{-3}, respectively. NO_3^- and *Chla* concentrations in the rivers were negatively correlated with discharge (**Table 2**). All the other constituent concentrations were positively correlated with discharge. Temporal trends and seasonal patterns were

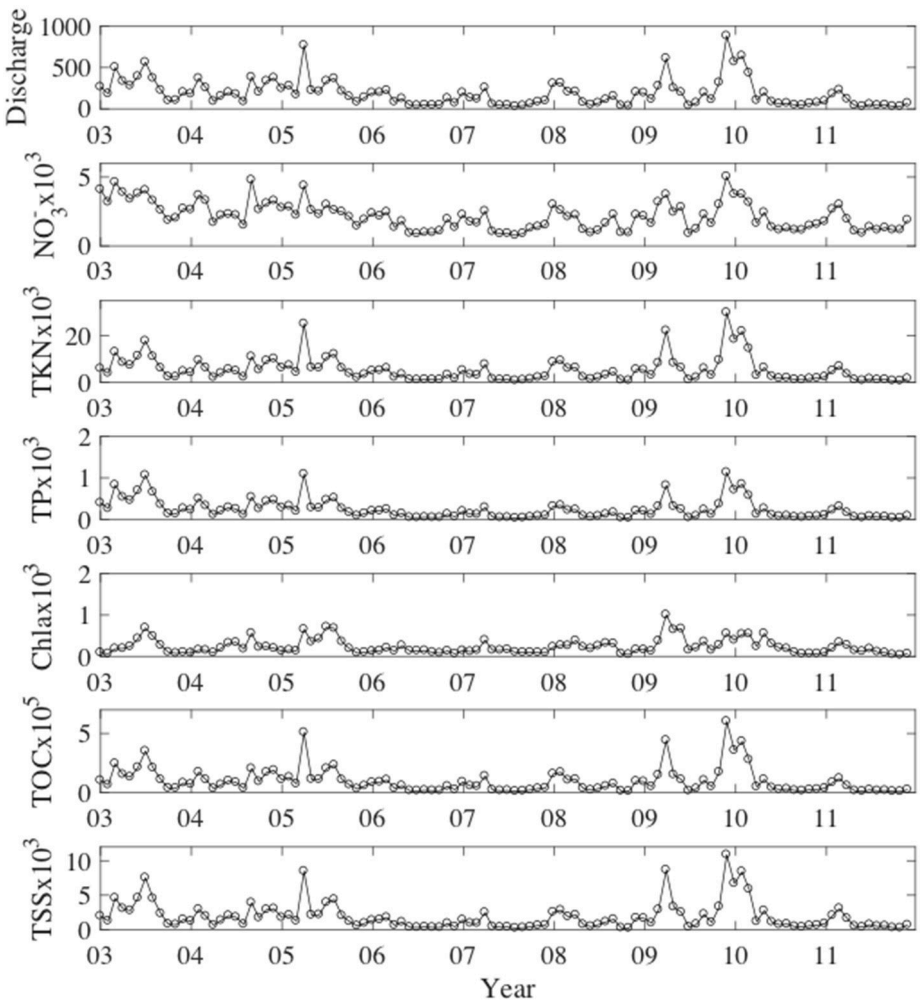

FIGURE 4 | Escambia River monthly mean discharge and loads. River loads of NO_3^-, TKN, TP, and TOC have units of mmol s^{-1}. Loads of Chla have units of mg s^{-1} and loads of TSS have units of g s^{-1}.

also observed in the data. Significant temporal trends occurred in discharge, NO_3^-, *TP*, and *TSS* (**Table 2**). Seasonal patterns were observed in *Chla* and *TKN* with generally higher values in summer than in winter (**Figure 3**). These trends formed the basis for our rating curve regression models. All models were statistically significant ($p < 0.05$) and R^2 ranged from 0.19 for *TSS* to 0.76 for NO_3^-.

River loads to Pensacola Bay were mainly from the Escambia River, which accounted for 74–83% of the total combined constituent loads from Escambia and Yellow rivers (**Table 1**). Mean Escambia River loads of NO_3^-, *TKN*, *TP*, *Chla*, *TOC*, and *TSS* were 3,593, 5,981, 589, 26, 88,493, and 152,686 kg d^{-1}, respectively. Temporal patterns in river loads generally mimicked the patterns of river discharge (**Figure 4**).

Pensacola Bay Observed Data and MERIS Algorithms and Time-Series

We briefly summarize the results from Pensacola Bay optical observations and MERIS algorithm development as these results have been presented previously (Le et al., 2016). Rrs was greatest in East Bay and Escambia Bay and smallest in Lower Bay (Figure S1A). For the wavelengths coincident with the MERIS bands used to generate the algorithms in Equations (2–4), spectral absorption was dominated by *CDOM* at 510 nm, and by a_{ph} and a_d at 665, 681, and 710 nm (Figures S1B–D).

The band ratio algorithms (Equations 2–4) explained 70%, 79%, and 71% of the variability in *Chla*, *CDOM*, and *TSS*, respectively. Validation results (Figure S2) demonstrate a reasonable accuracy for MERIS derived *Chla*, *CDOM*, and *TSS* where error statistics for *Chla* were $R^2 = 0.64$, MRE = 31.9%, $n = 46$; for *CDOM* were $R^2 = 0.80$, MRE = 18.5%, $n = 53$; and for *TSS* were $R^2 = 0.54$, MRE = 42.7%, $n = 53$. MRE (mean relative error) was calculated by

$$\mathrm{MRE} = \frac{1}{n}\sum abs\left(\frac{MERIS - Observed}{Observed}\right)\cdot 100 \qquad (6)$$

Upon application of these algorithms to the retrieved MERIS reflectance, synoptic monthly time-series of MERIS *Chla*, *CDOM*, and *TSS* were derived. As an example, **Figure 5** depicts *Chla* in the summer and fall during a low discharge year in 2007 and a high discharge year in 2009 (**Figure 2**). The fall bloom in 2007 had greater *Chla* than in 2009 despite the lower discharge. This points to other potential mechanisms, besides river forcing, regulating Pensacola Bay *Chla* such as wind-driven resuspension events (Le et al., 2016).

After averaging across the bay sub-regions (**Figure 1**), seasonal patterns in MERIS *Chla*, *CDOM*, and *TSS* were apparent with elevated concentrations in late fall and early winter and lower concentrations in the summer and early fall (**Figure 6**). MERIS *Chla*, *CDOM*, and *TSS* were highly correlated at monthly (**Figure 6**) and annual (Figure S3) time scales; monthly *Chla* and *CDOM* ($r = 0.91$); monthly *Chla* and *TSS* ($r = 0.85$), and monthly *CDOM* and *TSS* ($r = 0.82$); annual *Chla* and *CDOM* ($r = 0.85$);

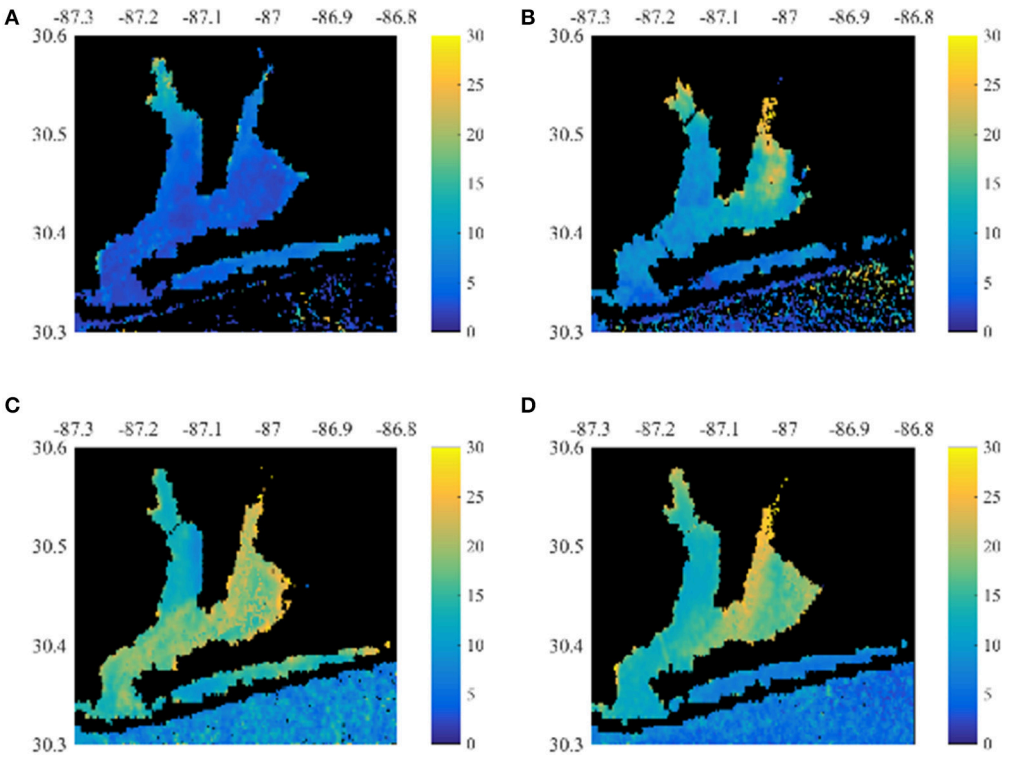

FIGURE 5 | Summer and fall MERIS *Chla* for the Pensacola Bay system. **(A,B)** Show the average *Chla* from August 2007 and August 2009. **(C,D)** Show the average *Chla* from October 2007 and November 2009.

annual *Chla* and *TSS* ($r = 0.79$), and annual *CDOM* and *TSS* ($r = 0.87$).

Relating MERIS Time-Series to River Discharge, Concentration, and Loading Time-Series

Correlation Maps

We examined correlations by pixel between MERIS *Chla, CDOM,* and *TSS* time-series and 0-, 1-, and 2-month lagged time-series of Escambia River and Yellow River discharges, concentrations, and loads of NO_3^-, *TKN*, *TP*, *Chla*, *TOC*, and *TSS*. Correlations were similar using either Escambia River or Yellow River data owing to the strong correlation between river discharge for these two rivers ($r = 0.85$). Thus, as the Escambia River was the largest river input to Pensacola Bay, we present the correlations obtained using the monthly time-series for Escambia River (**Figure 4**). For correlations with 0-month lagged river forcing, MERIS *Chla* was most highly correlated with discharge and baseflow discharge (**Figure 7**). Correlations with river concentrations of NO_3^-, *TP*, and *TKN* were small and correlations with river concentrations of $Chla_{River}$ were mainly negative. Correlations with river TOC and TSS concentrations (not shown) had similar patterns as for TKN. For 1- and 2-month lagged discharge, baseflow discharge, and river concentrations, MERIS *Chla* correlations were smaller than for 0-month (not shown).

To examine spatial patterns of correlation between MERIS water quality time-series and river loading time-series we focused our analysis on 0-month river loads of NO_3^-, *TP*, *TOC*, and *TSS*. We included NO_3^- and *TP* as we expected these nutrient loads to be related to bay *Chla*. We included river *TOC* as it was expected the load would scale with bay *CDOM*. Further, *TOC* and *TKN* concentrations were highly correlated ($r = 0.97$). Thus, *TOC* could act as a surrogate for organic nitrogen. River *TSS* load was expected to scale with bay *TSS*.

MERIS *Chla* had greatest correlation with 0-month lagged NO_3^- loads and *TOC* baseflow loads (**Figure 8**). East Bay pixels had higher correlation with loading rates than other regions. In

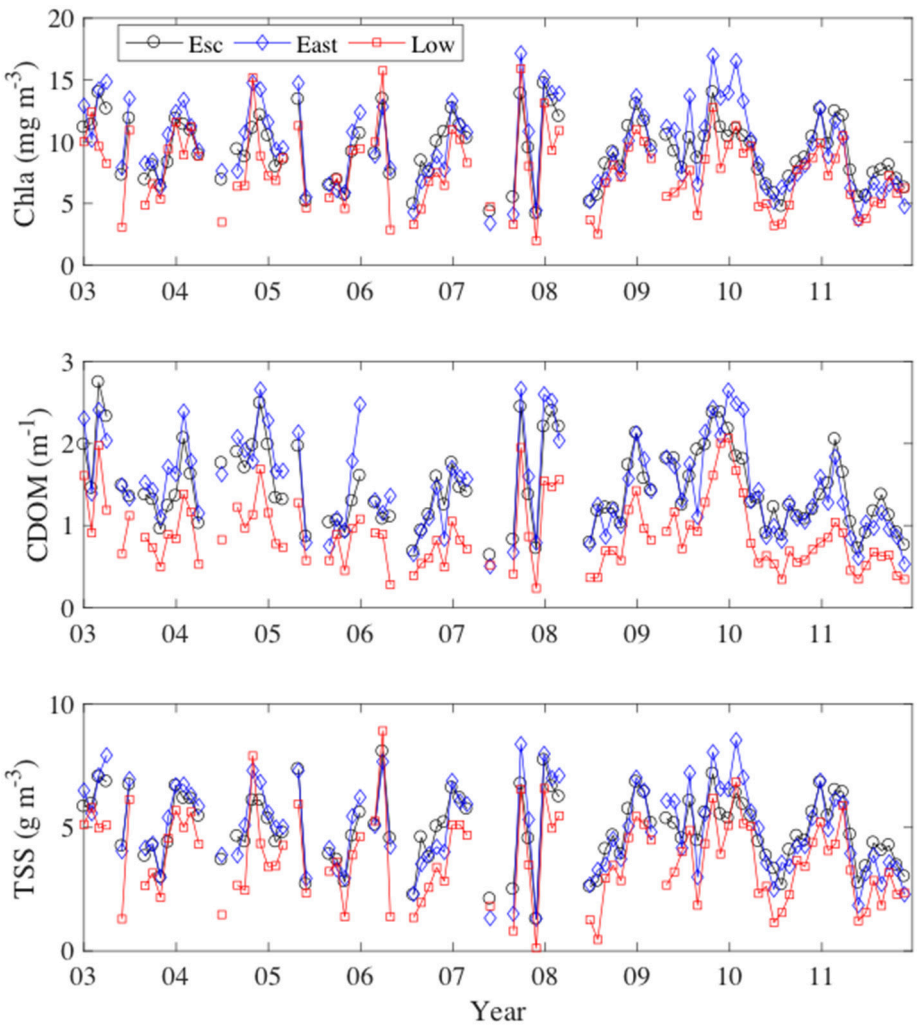

FIGURE 6 | Monthly time-series of MERIS derived Chla, CDOM, and TSS from January 2003 to December 2011.

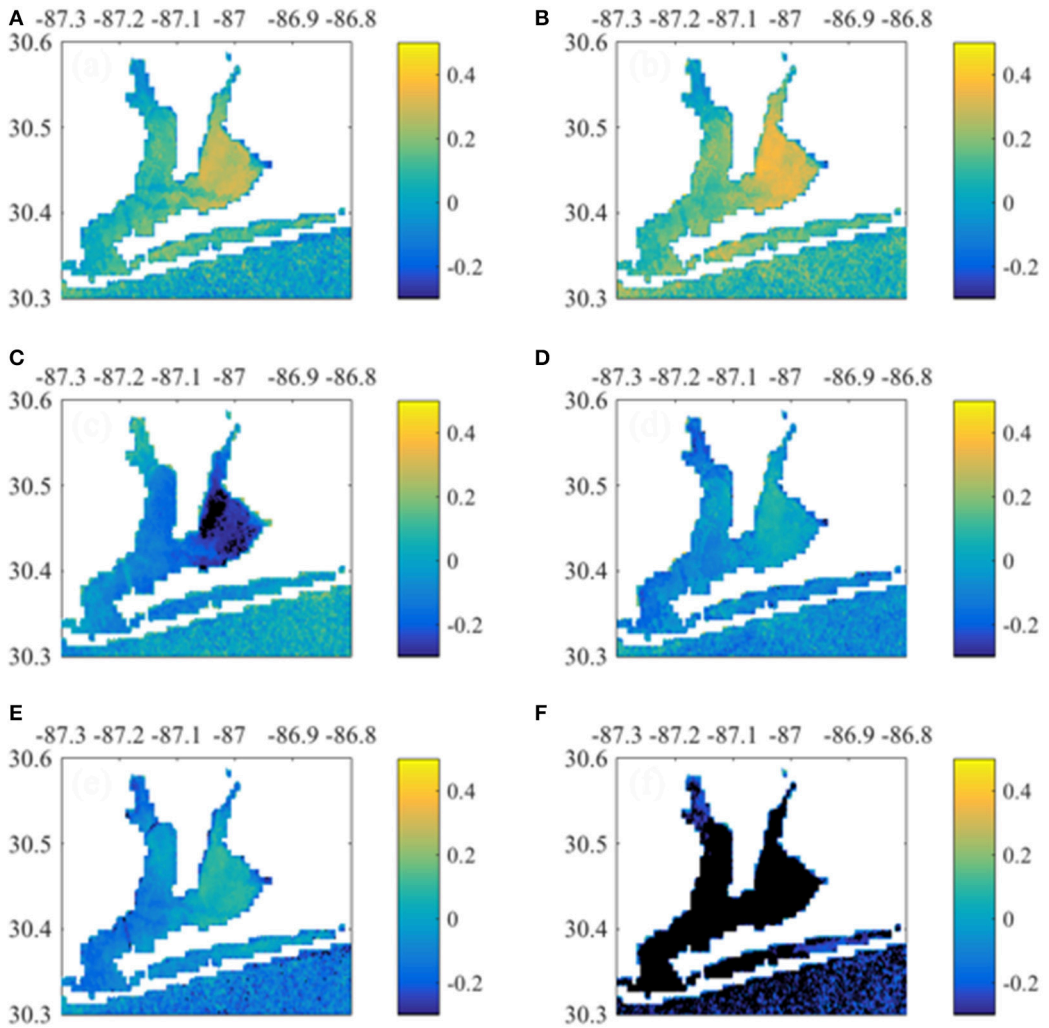

FIGURE 7 | Correlations between monthly Chla time-series (per pixel) with 0-month lagged Escambia River discharge and concentrations. Shown are Chla correlation with **(A)** discharge, **(B)** baseflow discharge, and concentrations of **(C)** river NO_3^-, **(D)** river TKN, **(E)** river TP, and **(F)** river Chl.

contrast, Santa Rosa Sound and the nearshore Gulf of Mexico pixels had higher correlation with 1-month lagged loads (Figure S4). MERIS *CDOM* also correlated with concurrent NO_3^- load and *TOC* baseflow load (**Figure 9**). Correlations were apparent throughout Escambia Bay, East Bay, and Lower Bay, although the upper-most reaches of both Escambia and East bays had weak correlation. *CDOM* correlations with 1-month lagged loads had greater correlation in Santa Rosa Sound and nearshore Gulf of Mexico (Figure S5). MERIS *TSS* had highest correlation with NO_3^- loads, both total and baseflow loads, and with baseflow *TOC* load (**Figure 10**). Correlations exhibited similar spatial patterns with highest correlations in East Bay for 0-month loads and in Santa Rosa Sound and nearshore Gulf of Mexico for 1-month loads (Figure S6).

Partial Least Squares Regression Results

At monthly time-scales, the PLS regression models explained 23–59% of the monthly variability in bay water quality (**Figure 11**). At the annual scale, PLS models explained 20–62% of the variability (**Figure 12**). By evaluating more parsimonious forms of Equation (5), we determined that that the following reduced equation could represent most of the variability in MERIS *Chla*, *CDOM*, and *TSS*

$$MERIS\ WQ_{ij} \sim QNO_3^- + QTKN + QTSS \quad (7)$$

Our justification for this reduced equation was based on several lines of reasoning: (1) the correlation between discharge and baseflow ($r = 0.74$, **Table 2**) suggested we could eliminate baseflow loads, (2), the weak correlations of MERIS water quality with either river TP (**Figures 8–10**) or river Chl (**Figure 7F**) indicated these loads made an insignificant contribution, and (3) the strong correlation between TKN and TOC ($r = 0.97$, **Table 2**) indicated that TKN could be substituted for TOC (discussed further below in Methodological Considerations see Section Methodological Considerations). This reduced form of the model

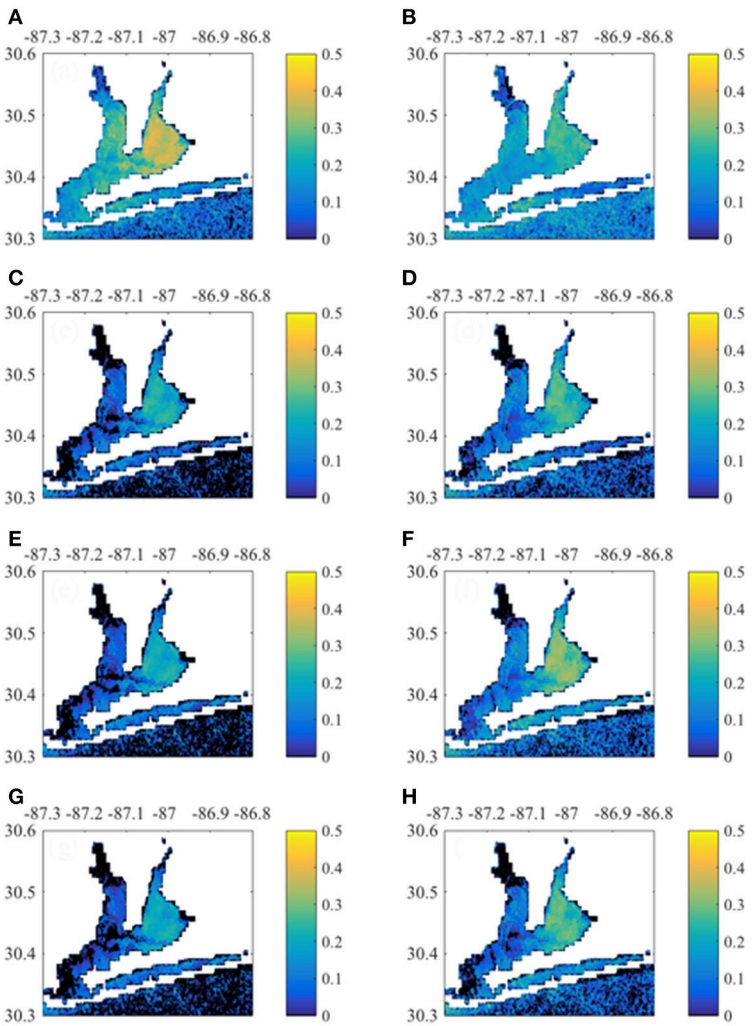

FIGURE 8 | Correlation between monthly Chla time-series per pixel with 0-month lagged Escambia River loads. **(A,B)** Correlation with NO_3^- load and baseflow NO_3^- load, respectively. **(C,D)** Correlation with TP load and baseflow TP load, respectively. **(E,F)** Correlation with TOC load and baseflow TOC load, respectively. **(G,H)** Correlation with TSS load and baseflow TSS load, respectively.

explained 17–56% of the monthly variability in MERIS water quality and 17–62% of the annual variability. Based on **Table 3** of PLS component loadings, component 1, which included a linear combination of *QTKN* and *QTSS* (equal weights) and QNO_3^- (lower weight), was the strongest driver of variability in the MERIS *Chla*, *CDOM*, and *TSS* in the three bay regions. Component 2, which had the highest loading from QNO_3^-, also contributed significantly to the total variance explained in East Bay (**Table 3**), and to a lesser extent in Escambia and East Bay.

DISCUSSION

In many estuarine and coastal systems, observational data are insufficient to link estuarine water quality responses to anthropogenic changes in adjacent watersheds. As a supplemental data source, and in some cases the only data source, ocean color satellites are emerging as powerful tools for monitoring and studying estuarine water quality properties that can be measured optically. Previous work has further demonstrated that satellite derived water quality is useful for quantifying the effects of river forcing. Several studies have assessed the responses of satellite-derived estuarine *Chla*, *CDOM,* and *TSS* to variations in river discharge (Acker et al., 2005; Green et al., 2008; Chen et al., 2013; Le et al., 2016) and nutrient loads (Green and Gould, 2008; Chen et al., 2013; Le et al., 2014). To our knowledge, no previous studies have used the satellite data to investigate multivariate relationships between riverine loads of nutrients, organic matter, and sediments and satellite-derived *Chla*, *CDOM,* and *TSS*, nor have previous studies been conducted in small to moderate sized estuaries such as Pensacola Bay (SCOPUS search for keywords: satellite ocean color, estuary, and multivariate water quality on Aug 8, 2017).

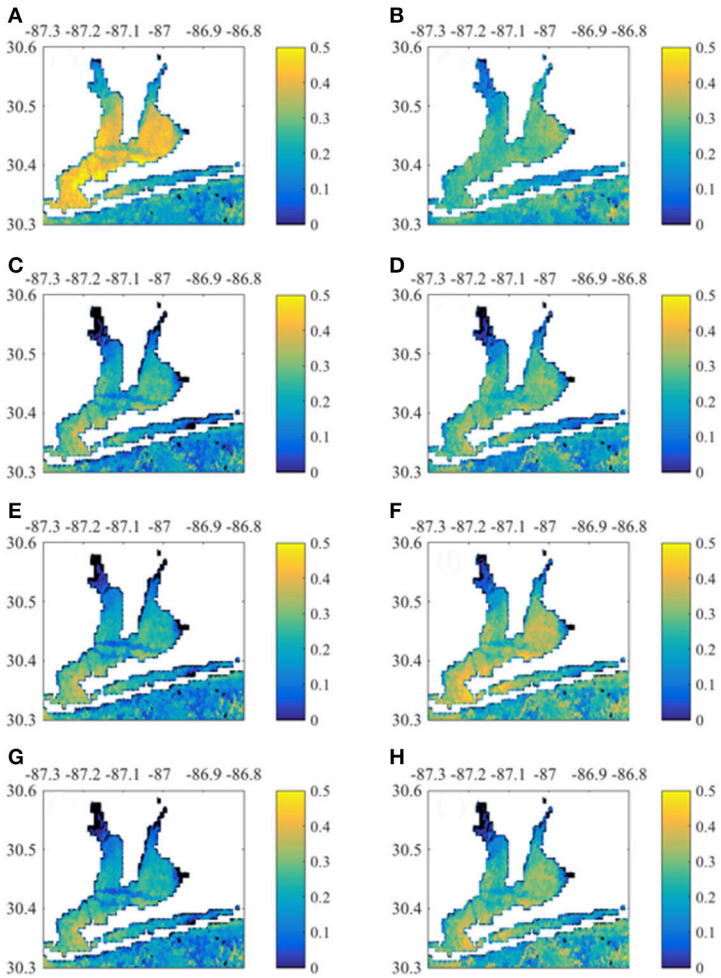

FIGURE 9 | Correlation between monthly CDOM time-series per pixel with 0- month lagged Escambia River loads. **(A,B)** Correlation with NO_3^- load and baseflow NO_3^- load, respectively. **(C,D)** Correlation with TP load and baseflow TP load, respectively. **(E,F)** Correlation with TOC load and baseflow TOC load, respectively. **(G,H)** Correlation with TSS load and baseflow TSS load, respectively.

MERIS *Chla*, *CDOM,* and *TSS* Relationships to River Forcing

Based on correlation and PLS analyses, the river variables that explained the most variation in MERIS *Chla, CDOM,* and *TSS* were *Q*, *Qb*, and NO_3^-, *TKN,* and *TSS* loads (**Figures 7**, **8**, **Table 3**). This held true for all regions of the Bay, but in East Bay the influence of QNO_3^- was greater than in either Escambia or Lower Bay (**Table 3**). In terms of baseflow river loads, MERIS CDOM and TSS, exhibited correlations with baseflow river loads (**Figures 9**, **10**) but *Chla* had a muted response to baseflow loads (**Figure 8**). This latter response is odd given that Chla was modestly correlated to baseflow discharge, especially in East Bay (**Figure 7**). Overall, though, MERIS *Chla*, *CDOM*, and *TSS* had lower correlations with baseflow loads indicating that the total loads were more important throughout the Pensacola Bay system. We had speculated that baseflow loads may be important because the most elevated river NO_3^- and *Chla* concentrations occurred under low discharge, baseflow conditions (**Table 2**).

Correlations with 1-month lagged loads and baseflow loads of NO_3^-, *TP*, *TOC*, and *TSS* suggested that East Bay and Santa Rosa Sound had the greatest response to lagged river loads (Figures S4–S6). Highest correlations occurred in nearshore areas around the Gulf Breeze Peninsula and into Santa Rosa Sound. Pixels in the nearshore Gulf of Mexico, outside of Pensacola Bay, also exhibited higher correlations with 1-month lagged watershed loads. The lagoonal region of Santa Rosa Sound and the areas in the nearshore Gulf of Mexico may have longer water residence times than other regions of Pensacola Bay owing to the lack of direct river discharges. The nearshore Gulf region may be responding to outflows from Pensacola Bay or to larger regional scale (northern Gulf watersheds) loading to the coastal zone.

PLS regression models based on QNO_3^-, *QTKN*, and *QTSS* were relatively good predictors of MERIS *Chla*, *CDOM*, and *TSS* in the three bay regions at both monthly (**Figure 11**) and annual (**Figure 12**) time scales. For Pensacola Bay, these empirical models provide a means to evaluate how changes in nitrogen

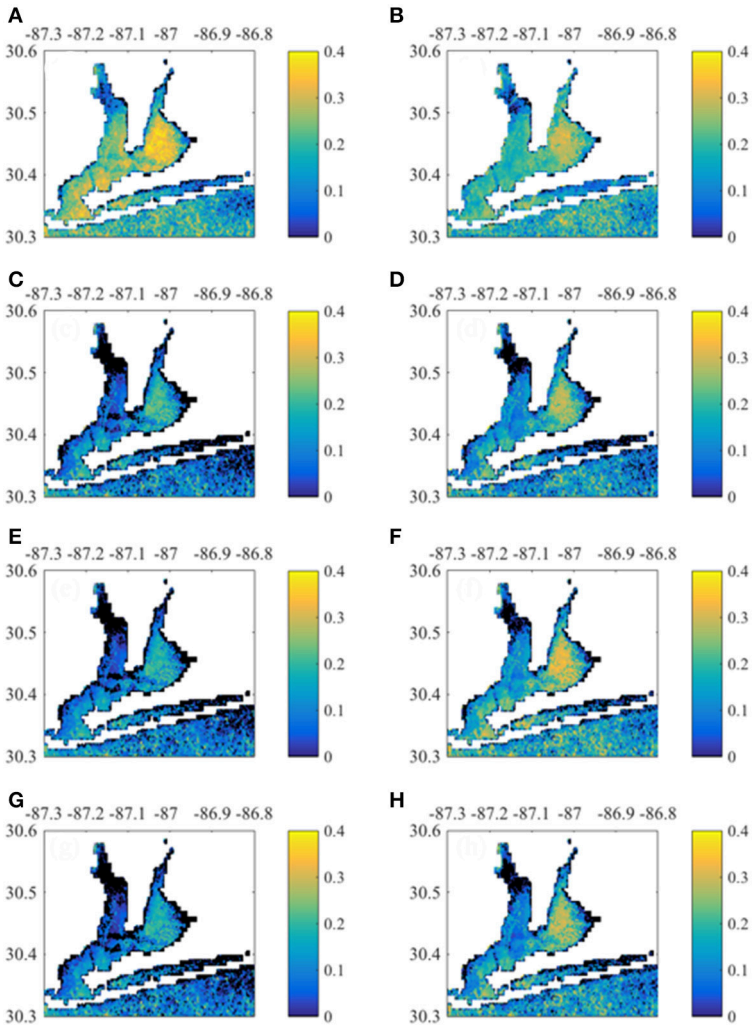

FIGURE 10 | Correlation between monthly TSS time-series by pixel with 0-month lagged Escambia River loads. **(A,B)** Correlation with NO_3^- load and baseflow NO_3^- load, respectively. **(C,D)** Correlation with TP load and baseflow TP load, respectively. **(E,F)** Correlation with TOC load and baseflow TOC load, respectively. **(G,H)** Show correlation with TSS load and baseflow TSS load, respectively.

and suspended loads may impact *Chla*, *CDOM*, and *TSS*. Such an analysis is beyond the scope of the present study, but may be of interest for managers who need to determine loading reductions required to achieve water quality targets in the bay. Furthermore, the covariations exhibited among MERIS *Chla*, *CDOM*, and *TSS* in the three bay regions (**Figure 6**) indicate that load reductions aimed at reducing *Chla*, *CDOM*, and *TSS* are likely to be effective across the entire Bay.

There are few previous studies relating river forcing to field-based observations of water quality in Pensacola Bay. One study found a similar pattern of increased *Chla* in the bay as a result of increased river discharge (Murrell et al., 2007). Studies of nutrient limitation have resulted in mixed results. In one study, phosphorus limitation of primary production was observed based on nutrient and phosphorus addition experiments at two sites, one in an oligohaline and one in a mesohaline region of the bay (Murrell et al., 2002). In another study, nitrogen limitation of primary production was reported from one polyhaline site in Santa Rosa Sound (Juhl and Murrell, 2008). In the present study, river nitrogen (NO_3^- and *TKN*) loads explained most of the variability in MERIS *Chla* as well as in *CDOM* and *TSS*, and, thus, supported nitrogen as being more important as a limiting nutrient. Neither river concentrations nor loads of TP were significantly correlated with *Chla* (**Figures 7D**, **8D**).

In the present study we did not examine the effects of wind on water quality patterns. However, previously wind speed was observed to be significantly correlated (positive) to the MERIS water quality variables in Escambia Bay and East Bay, but not in lower Bay, but correlations were weak ($r < 0.29$) at a monthly scale (Le et al., 2016). Thus, the percentage of variation explained by the PLS regressions for Escambia and East bays could be improved by including wind as an independent variable for these regions of the bay.

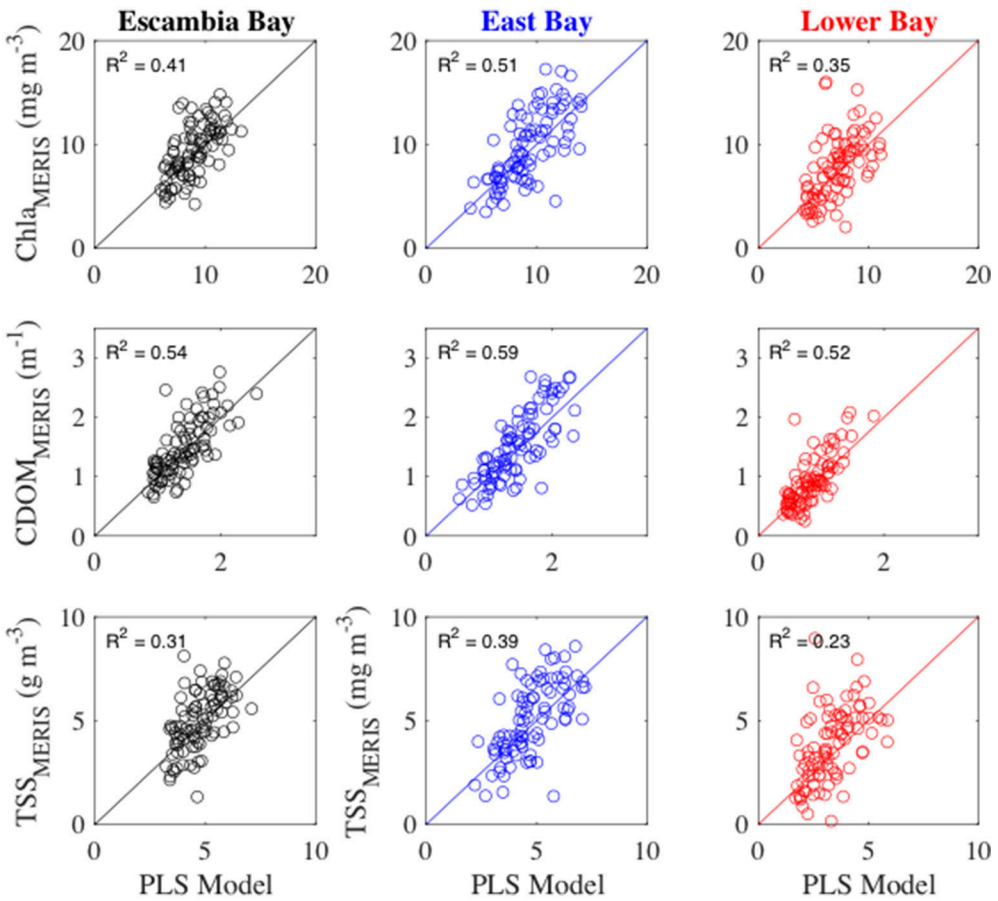

FIGURE 11 | MERIS monthly water quality variables vs. partial least squares regression models (PLS Model). Monthly MERIS water quality time-series for Escambia Bay (left column) and Lower Bay (right column) are compared to the PLS model that was based upon Escambia River monthly loads. Monthly MERIS water quality time-series for East Bay (middle column) are compared to the PLS model that was based upon Yellow River monthly loads. The solid line is the 1:1 line. R^2 values provide the fraction of variability explained by the PLS models.

Methodological Considerations

There are several potential errors in our analysis. First of these was the accuracy of the MERIS satellite-derived *Chla*, *CDOM*, and *TSS*. While the algorithms used here appeared to be robust (Section Pensacola Bay Observed Data and MERIS Algorithms and Time-Series), the mean relative errors between field observations and satellite-derived values were 18.5% for *CDOM*, 31.9% for Chla, and 42.7% for *TSS*. In coastal waters, further work is required to improve the algorithms that equate remote sensing reflectance and other optical properties to water quality variables.

A second source of potential error was from the strong correlations between river discharges and concentrations (**Table 2**). For example, *TKN* and *TOC* were highly correlated ($r = 0.97$). These correlations dictated our use of PLS regression when relating monthly and annual river time-series to MERIS water quality. Though PLS is an alternative to typical least squares regression when independent variables are highly correlated, the interpretation of the PLS results is not straightforward. For example, due to the correlation between TKN and TOC we could have used *TOC* loads in Equation (7) instead of *TKN* loads with little change in the percent variance explained in the dependent water quality variables. Further, there was a high degree of covariation between monthly time-series of MERIS *Chla*, *CDOM*, and *TSS* as observed in **Figure 6**, which limits our ability to tease apart the factors controlling these variables. For example, high *CDOM* or *TSS* may limit light availability for phytoplankton photosynthesis and in turn limit *Chla* concentration, yet at the same time *Chla, CDOM* and *TSS* were all correlated with nitrogen loading, thus light limitation did not appear to have a significant impact on *Chla* in surface waters in comparison to the effect of nitrogen loads.

A third issue was the choice of averaging the river and satellite data to a monthly time scale. We chose this averaging period for the practical reason that there may be large gaps in the satellite record at the daily time step due to cloud cover and/or other quality control issues. Also, the river concentration data were collected at monthly to seasonal scales. Averaging at the monthly scale, however, may obscure estuarine patterns related to episodic

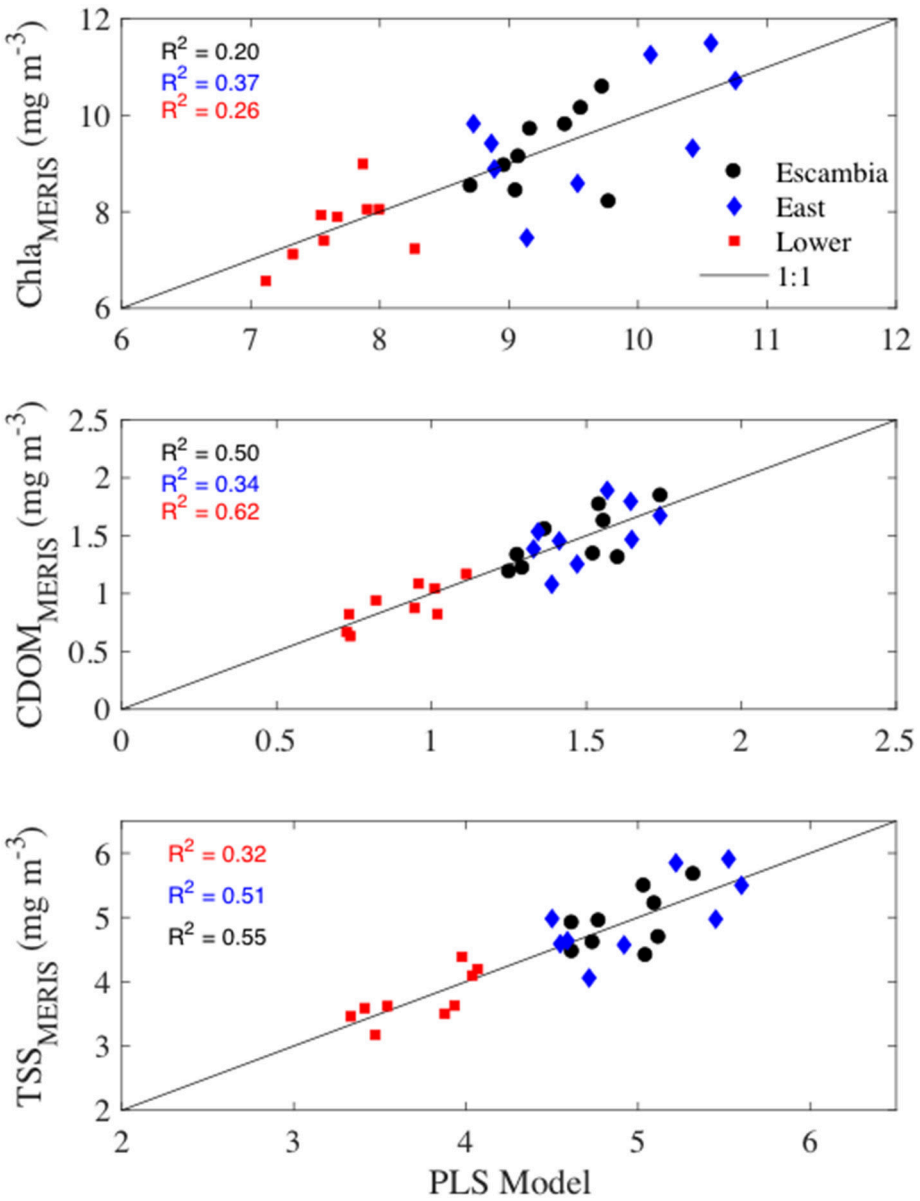

FIGURE 12 | MERIS annual water quality variables vs. partial least squares regression models based upon Escambia River annual loads of NO_3^-, TKN, and TSS. The solid line is the 1:1 line. R^2 values provide the fraction of variability explained by the PLS models.

events such as a tropical storms (Hagy et al., 2006) or peak river discharges (Murrell et al., 2007) that can rapidly flush Pensacola Bay. In future studies, the issue of obtaining greater temporal sampling from satellite may be overcome by including data from other ocean color satellites such as MODIS. A challenge to blending these products is the development of algorithms for each satellite. Including MODIS data in our analysis of Pensacola Bay may not have worked since the spatial resolution and wavelengths of reflectance captured by MODIS are different than MERIS. The greater spatial resolution of MERIS (300 m vs. 1 km for MODIS) and the unique spectral band at 709 nm was the reason that MERIS was applied to Pensacola Bay (Le et al., 2016).

CONCLUSIONS AND FUTURE DIRECTIONS

In this study, we demonstrated the utility of long-term and spatially synoptic satellite data for examining the effects of river forcing on estuarine water quality. This is the first study to apply a multi-variate approach to examine this problem and first to do so with MERIS in small to moderate size estuary, Pensacola Bay. The approach to retrieve water quality from MERIS and to analyze the factors driving water quality variability are readily portable to other similar sized estuaries globally. Our primary conclusion was that MERIS *Chla*, *CDOM*, and *TSS* dynamics

TABLE 3 | Mean PLS loadings for components 1, 2, and 3 of multiple regression model and the percentage of variance explained in the dependent variables.

	Comp 1	Comp 2	Comp 3
QNO3	4.03	1.12	−0.66
QTKN	8.36	0.16	0.73
QTSS	8.31	−0.83	−0.41
	% Explained		
Chla_Esc	24%	7%	0%
Chla_East	22%	18%	6%
Chla_Low	11%	12%	1%
CDOM_Esc	48%	2%	0%
CDOM_East	33%	18%	5%
CDOM_Low	46%	3%	0%
TSS_Esc	22%	3%	0%
TSS_East	19%	12%	4%
TSS_Low	14%	4%	0%

observed in Pensacola Bay were significantly related to riverine nitrogen loads. However, the analyses also indicated that some of the sub-regions of the bay had different responses to the magnitude and timing of river loads. Overall, the MERIS data provided unprecedented spatial and temporal coverage beyond that of past boat-based efforts in Pensacola Bay and revealed previously unobserved spatial and temporal patterns of responses to river forcing.

A similar approach to the one used in this study could also be applied to water column light absorption and attenuation, which are related measures of water clarity. Improving water clarity is a common water quality goal in Florida estuaries for both ecological and economic reasons. Water clarity is a key ecological attribute in Pensacola Bay that controls primary production (Murrell et al., 2009) and likely the spatial distribution of seagrass habitats in the bay. The MERIS-derived water quality variables used in this study could be applied to better understand controls on water clarity. *Chla* and *TSS* scale to the inherent optical properties a_{ph} and a_d, respectively, in Pensacola Bay (Conmy et al., 2017), and, thus, as *CDOM* (a_g) is already measured in units of absorption (m^{-1}), it is possible to construct a total absorption (a_t) budget by summing a_{ph} (obtained by converting from *Chla*), a_d (obtained by converting from *TSS*), and a_g. Also, as a_t is linearly related to light attenuation (m^{-1}, Conmy et al., 2017), it will be possible in future work to extrapolate the MERIS derived *Chla*, *CDOM*, and *TSS* to water clarity targets such as percent of surface solar radiation required to support seagrass habitats.

AUTHOR CONTRIBUTIONS

JL conceived the study, performed data analyses, and wrote the manuscript. CL developed the satellite algorithms, generated the satellite time-series data, and provided comments and edits to manuscript drafts.

FUNDING

Funding for this work was provided by NASA Applied Science Grant number NNH10AN14I and the U.S. EPA Safe and Sustainable Water Resources Research Program.

ACKNOWLEDGMENTS

The authors acknowledge J. Aukamp, D. Beddick, R. Conmy, A. Duffy, G. Craven, B. Jarvis, B. Schaeffer, and D. Yates for their contributions to the collection, analysis, and management of the Pensacola Bay optical data. The authors thank the three reviewers and the editor for constructive comments that improved this manuscript.

SUPPLEMENTARY MATERIAL

The Supplementary Material for this article can be found online at: http://journal.frontiersin.org/article/10.3389/fmars.2017.00274/full#supplementary-material

REFERENCES

Acker, J. G., Harding, L. W., Leptoukh, G., Zhu, T., and Shen, S. (2005). Remotely-sensed chl α at the Chesapeake Bay mouth is correlated with annual freshwater flow to Chesapeake Bay. *Geophys. Res. Lett.* 32:L05601. doi: 10.1029/2004GL021852

Borkman, D. G., and Smayda, T. J. (1998). Long-term trends in water clarity revealed by Secchi-disk measurements in lower Narragansett Bay. *ICES J. Mar. Sci.* 55, 668–679. doi: 10.1006/jmsc.1998.0380

Boynton, W., Kemp, W., and Keefe, C. (1982). "A comparative analysis of nutrients and other factors influencing estuarine phytoplankton production," in *Estuarine Comparisons,* ed V. S. Kennedy (New York, NY: Academic Press), 69–90.

Bricker, S. B., Clement, C. G., Pirhalla, D. E., Orlando, S. P., and Farrow, D. R. (1999). *National estuarine Eutrophication Assessment: Effects of Nutrient Enrichment in the Nation's Estuaries*. US National Oceanographic and Atmospheric Administration, National Ocean Service, Special Projects Office and the National Center for Coastal Ocean Science.

Caffrey, J. M., and Murrell, M. C. (2016). "A Historical Perspective on Eutrophication in the Pensacola Bay Estuary, FL, USA," in *Aquatic Microbial Ecology and Biogeochemistry: A Dual Perspective,* eds P. Glibert and T. Kana (Cham: Springer), 199–213.

Chen, C., Jiang, H., and Zhang, Y. (2013). Anthropogenic impact on spring bloom dynamics in the Yangtze River Estuary based on SeaWiFS Mission (1998–2010) and MODIS (2003–2010) observations. *Int. J. Remote Sens.* 34, 5296–5316. doi: 10.1080/01431161.2013.786851

Cohn, T. A., Caulder, D. L., Gilroy, E. J., Zynjuk, L. D., and Summers, R. M. (1992). The validity of a simple statistical model for estimating fluvial constituent loads: an empirical study involving nutrient loads entering Chesapeake Bay. *Water Resour. Res.* 28, 2353–2363. doi: 10.1029/92WR01008

Cohn, T. A., Delong, L. L., Gilroy, E. J., Hirsch, R. M., and Wells, D. K. (1989). Estimating constituent loads. *Water Resour. Res.* 25, 937–942. doi: 10.1029/WR025i005p00937

Conmy, R. N., Schaeffer, B. A., Schubauer-Berigan, J., Aukamp, J., Duffy, A., Lehrter, J. C., et al. (2017). Characterizing light attenuation within Northwest Florida Estuaries: implications for RESTORE Act water quality

monitoring. *Mar. Pollut. Bull.* 114, 995–1006. doi: 10.1016/j.marpolbul.2016.11.030

Gould, R., Arnone, R., and Sydor, M. (2001). Absorption, scattering, and, remote-sensing reflectance relationships in coastal waters: testing a new inversion algorith. *J. Coast. Res.* 328–341.

Gould, R. W., Arnone, R. A., and Martinolich, P. M. (1999). Spectral dependence of the scattering coefficient in case 1 and case 2 waters. *Appl. Opt.* 38, 2377–2383. doi: 10.1364/AO.38.002377

Green, R. E., and Gould, R. W. (2008). A predictive model for satellite-derived phytoplankton absorption over the Louisiana shelf hypoxic zone: effects of nutrients and physical forcing. *J. Geophys. Res.* 113:C06005. doi: 10.1029/2007JC004594

Green, R. E., Gould, R. W., and Ko, D. S. (2008). Statistical models for sediment/detritus and dissolved absorption coefficients in coastal waters of the northern Gulf of Mexico. *Cont. Shelf Res.* 28, 1273–1285. doi: 10.1016/j.csr.2008.02.019

Gustard, A., Bullock, A., and Dixon, J. (1992). *Low Flow Estimation in the United Kingdom*. Institute of Hydrology.

Hagy, J. D., Lehrter, J. C., and Murrell, M. C. (2006). Effects of hurricane Ivan on water quality in Pensacola Bay, Florida. *Estuaries and Coasts* 29, 919–925.

Hagy, J. D., and Murrell, M. C. (2007). Susceptibility of a northern Gulf of Mexico estuary to hypoxia: an analysis using box models. *Estuar. Coast. Shelf Sci.* 74, 239–253. doi: 10.1016/j.ecss.2007.04.013

Handley, L., Altsman, D., and DeMay, R. (2007). "*Seagrass Status and Trends in the Northern Gulf of Mexico: 1940-2002.*" US Geological Survey.

Harding L. Jr., Gallegos, C., Perry, E., Miller, W., Adolf, J., Mallonee, M., et al. (2016). Long-term trends of nutrients and phytoplankton in Chesapeake Bay. *Estuar. Coasts* 39, 664–681. doi: 10.1007/s12237-015-0023-7

Juhl, A. R., and Murrell, M. C. (2008). Nutrient limitation of phytoplankton growth and physiology in a subtropical estuary (Pensacola Bay, Florida). *Bull. Mar. Sci.* 82, 59–82.

Kiefer, D. A., and SooHoo, J. B. (1982). Spectral absorption by marine particles of coastal waters of Baja California. *Limnol. Oceanogr.* 27, 492–499. doi: 10.4319/lo.1982.27.3.0492

Kishino, M., Takahashi, M., Okami, N., and Ichimura, S. (1985). Estimation of the spectral absorption coefficients of phytoplankton in the sea. *Bull. Mar. Sci.* 37, 634–642.

Le, C., Hu, C., English, D., Cannizzaro, J., Chen, Z., Feng, L., et al. (2013). Towards a long-term chlorophyll-a data record in a turbid estuary using MODIS observations. *Prog. Oceanogr.* 109, 90–103. doi: 10.1016/j.pocean.2012.10.002

Le, C., Lehrter, J. C., Hu, C., Murrell, M. C., and Qi, L. (2014). Spatiotemporal chlorophyll-a dynamics on the Louisiana continental shelf derived from a dual satellite imagery algorithm. *J. Geophys. Res.* 119, 7449–7462. doi: 10.1002/2014JC010084

Le, C., Lehrter, J. C., Hu, C., Schaeffer, B., MacIntyre, H., Hagy, J. D., et al. (2015). Relation between inherent optical properties and land use and land cover across Gulf Coast estuaries. *Limnol. Oceanogr.* 60, 920–933. doi: 10.1002/lno.10065

Le, C., Lehrter, J. C., Schaeffer, B. A., Hu, C., Murrell, M. C., Hagy, J. D., et al. (2016). Bio-optical water quality dynamics observed from MERIS in Pensacola Bay, Florida. *Estuar. Coast. Shelf Sci.* 173, 26–38. doi: 10.1016/j.ecss.2016.02.003

Lehrter, J. C. (2008). Regulation of eutrophication susceptibility in oligohaline regions of a northern Gulf of Mexico estuary, Mobile Bay, Alabama. *Mar. Pollut. Bull.* 56, 1446–1460. doi: 10.1016/j.marpolbul.2008.04.047

Monbet, Y. (1992). Control of phytoplankton biomass in estuaries: a comparative analysis of microtidal and macrotidal estuaries. *Estuar. Coasts* 15, 563–571. doi: 10.2307/1352398

Murrell, M. C., Campbell, J. G., Hagy, J. D., and Caffrey, J. M. (2009). Effects of irradiance on benthic and water column processes in a Gulf of Mexico estuary: Pensacola Bay, Florida, USA. *Estuar. Coast. Shelf Sci.* 81, 501–512. doi: 10.1016/j.ecss.2008.12.002

Murrell, M. C., Hagy, J. D., Lores, E. M., and Greene, R. M. (2007). Phytoplankton production and nutrient distributions in a subtropical estuary: importance of freshwater flow. *Estuar. Coasts* 30, 390–402. doi: 10.1007/BF02819386

Murrell, M. C., Stanley, R. S., Lores, E. M., DiDonato, G. T., Smith, L. M., and Flemer, D. A. (2002). Evidence that phosphorus limits phytoplankton growth in a Gulf of Mexico estuary: Pensacola Bay, Florida, USA. *Bull. Mar. Sci.* 70, 155–167.

Pegau, S., Zaneveld, J. R. V., Mitchell, B. G., Mueller, J. L., Kahru, M., Wieland, J., et al. (2003). *Ocean Optics Protocols for Satellite Ocean Color Sensor Validation, revision 4, Volume IV: INHERENT Optical Properties: Instruments, Characterizations, Field Measurements and Data Analysis Protocols*. NASA Tech. Memo 211621.

Sullivan, J. M., Twardowski, M. S., Zaneveld, J. R. V., Moore, C. M., Barnard, A. H., Donaghay, P. L., et al. (2006). Hyperspectral temperature and salt dependencies of absorption by water and heavy water in the 400-750 nm spectral range. *Appl. Opt.* 45, 5294–5309. doi: 10.1364/AO.45.005294

Welschmeyer, N. A. (1994). Fluorometric analysis of chlorophyll a in the presence of chlorophyll b and pheopigments. *Limnol. Oceanogr.* 39, 1985–1992. doi: 10.4319/lo.1994.39.8.1985

Yarbro, L. A., and Carlson, P. (2013). "Seagrass integrated mapping and monitoring program," in *Mapping and Monitoring Report No. 1. Florida.* (Fish and Wildlife Research Institute).

Conflict of Interest Statement: The authors declare that the research was conducted in the absence of any commercial or financial relationships that could be construed as a potential conflict of interest.

frontiers in Marine Science

ORIGINAL RESEARCH
published: 24 October 2017
doi: 10.3389/fmars.2017.00325

Autonomous Coral Reef Survey in Support of Remote Sensing

Steven G. Ackleson[1], Joseph P. Smith[2], Luis M. Rodriguez[2], Wesley J. Moses[1] and Brandon J. Russell[3]*

[1] *Naval Research Laboratory, Washington, DC, United States,* [2] *United States Naval Academy, Annapolis, MD, United States,* [3] *Department of Marine Sciences, University of Connecticut, Avery Point, Groton, CT, United States*

An autonomous surface vehicle instrumented with optical and acoustical sensors was deployed in Kane'ohe Bay, HI, U.S.A., to provide high-resolution, *in situ* observations of coral reef reflectance with minimal human presence. The data represented a wide range in bottom type, water depth, and illumination and supported more thorough investigations of remote sensing methods for identifying and mapping shallow reef features. The *in situ* data were used to compute spectral bottom reflectance and remote sensing reflectance, $R_{rs,\lambda}$, as a function of water depth and benthic features. The signals were used to distinguish between live coral and uncolonized sediment within the depth range of the measurements (2.5–5 m). *In situ* $R_{rs,\lambda}$ were found to compare well with remotely sensed measurements from an imaging spectrometer, the Airborne Visible and Infrared Imaging Spectrometer (AVIRIS), deployed on an aircraft at high altitude. Cloud cover and *in situ* sensor orientation were found to have minimal impact on *in situ* $R_{rs,\lambda}$, suggesting that valid reflectance data may be collected using autonomous surveys even when atmospheric conditions are not favorable for remote sensing operations. The use of reflectance in the red and near infrared portions of the spectrum, expressed as the red edge height, REH_λ, was investigated for detecting live aquatic vegetative biomass, including coral symbionts and turf algae. The REH_λ signal from live coral was detected in Kane'ohe Bay to a depth of approximately 4 m with *in situ* measurements. A remote sensing algorithm based on the REH_λ signal was defined and applied to AVIRIS imagery of the entire bay and was found to reveal areas of shallow, dense coral and algal cover. The peak wavelength of REH_λ decreased with increasing water depth, indicating that a more complete examination of the red edge signal may potentially yield a remote sensing approach to simultaneously estimate vegetative biomass and bathymetry in shallow water.

Keywords: coral reef, Kane'ohe Bay, autonomous survey, hyperspectral remote sensing, red edge height

OPEN ACCESS

Edited by:
Jesús Ernesto Arias González, Center for Research and Advanced Studies of the National Polytechnic Institute (CINVESTAV), Mexico

Reviewed by:
Stuart Phinn, University of Queensland, Australia
Charles Alan Jacoby, St Johns River Water Management District, United States

****Correspondence:***
Steven G. Ackleson
steve.ackleson@nrl.navy.mil

Specialty section:
This article was submitted to Coral Reef Research, a section of the journal Frontiers in Marine Science

Received: *30 June 2017*
Accepted: *29 September 2017*
Published: *24 October 2017*

Citation:
Ackleson SG, Smith JP, Rodriguez LM, Moses WJ and Russell BJ (2017) Autonomous Coral Reef Survey in Support of Remote Sensing. Front. Mar. Sci. 4:325. doi: 10.3389/fmars.2017.00325

INTRODUCTION

Coral reefs are among the most diverse and productive ecosystems worldwide (Odum and Odum, 1955) and provide a variety of goods and services to many tropical and sub-tropical coastal nations (Spurgeon, 1992; Moberg and Folke, 1999). Coral reef health and diversity are on the decline worldwide in response to local human impacts and global changes in climate (Hughes et al., 2003) and this trend is expected to continue (Kleypas et al., 1999; Anthony et al., 2008; Hoegh-Guldberg, 2011). In response, programs to monitor the health of coral reef ecosystems have been and continue to be implemented, including remote sensing in the visible and near infrared portions of the

light spectrum (Dekker et al., 2011). Likewise, more capable remote sensing systems are planned with features that are designed to enhance coral reef monitoring on a global scale. For example, the NASA Hyperspectral Infrared Imager (HyspIRI) is envisioned as an imaging spectrometer operating in the visible to the near infrared region of the spectrum (0.38–2.5 μm, 10 nm channels) with a nadir spatial resolution of 30 m (Lee et al., 2015).

The success of any remote sensing application depends upon the collection of key environmental information that can be used to vicariously calibrate at-sensor radiance, test atmospheric correction procedures, and develop, test, and validate product algorithms. For shallow water aquatic applications, data sets that include water optical properties, depth, and benthic cover are needed that span appropriate length scales (e.g., >1,000 m) and with sufficient spatial resolution (e.g., <1 m). This is especially true of spatially complex coral reef ecosystems, but the collection of such observations with diver-based approaches alone is not feasible. *in situ* measurements of benthic reflectance using diver-operated spectrometers have, for example, highlighted the spectral differences between various coral reef components and aided assessments of remote sensing systems for coral reef mapping (Hochberg and Atkinson, 2000; Hochberg et al., 2003; Kutser et al., 2003), but field operations are laborious and inefficient for surveying purposes. *In situ* photogrammetric and spectral imaging approaches to mapping coral reef structure have been reported using diver-operated and towed systems (e.g., Gleason et al., 2007; Lirman et al., 2007; Shihavuddin et al., 2013). While these approaches have yielded high-quality photo mosaics and thematic images of benthic features that can be used to validate remote sensing products, such as benthic cover, the data are generally qualitative from a radiometric perspective and of limited use in developing and testing shallow-water light models.

To address these limitations, this research explored the use of an autonomous surface vessel (ASV) instrumented with calibrated radiometers and a side-scan sonar for surveying large areas of shallow coral reef environments in high spatial resolution in support of remote sensing operations. To illustrate the potential utility of the data from a remote sensing perspective, a coral biomass detection algorithm was developed based on reflectance features within the red and near-infrared portions of the spectrum and applied to data collected in the same time frame using an airborne imaging spectrometer deployed at high-altitude. It was shown that high resolution optical and acoustical surveys can be conducted with minimal human presence resulting in high-quality data necessary to support remote sensing operations and algorithm development. The work was conducted in Kane'ohe Bay, Hawai'i, to assess the potential application of HyspIRI data in studies of coral reef health in support of planning for the NASA HyspIRI mission (https://hyspiri.jpl.nasa.gov).

MATERIALS AND METHODS

The approach consisted of instrumenting a small ASV with synchronized optical and acoustical sensors, deploying the system to collect *in situ* observations in high spatial resolution on and around a small patch reef within Kane'ohe Bay, using the observations to derive shallow benthic properties of ecological importance, including water depth, benthic cover and reflectance, relating these properties to computations of water column reflectance, and comparing the *in situ* measurements with similar remotely sensed observations corrected for atmospheric effects. Measurements of water optical properties, collected manually, were used to aid the analysis of the autonomous data. The data processing procedures and underpinning radiative transfer theory are presented briefly in the following sections.

Study Site

Kane'ohe Bay is a semi-enclosed embayment (surface area of 41.4 km^2) located on the east coast of O'ahu, Hawai'i. The bay is bounded on the eastern side by a barrier reef that is cut by two tidal channels that bracket a semi-exposed barrier island, Ahu O Laka. The bay is flushed with clear oceanic waters driven by waves topping the barrier reef and tidal exchange through the channels. Seaward of the barrier island, within the depth range 0.3–1.2 m, the bottom consists almost entirely of mixed corals and sand (Jokiel, 1991). Landward of the barrier island, the bay is characterized as an estuarine lagoon of average depth 19 m and highlighted by numerous patch reefs with depths of less than 1 m that are partially exposed during extreme spring tides. Shallow fringing reefs are present along most of the shoreline. Bottom sediments within the bay are composed of coral rubble and gray coral mud.

The study was focused primarily on a 33,000 m^2 patch reef located southeast of Moku o Lo'e (Coconut Island) in the southern portion of Kane'ohe Bay (centered at 21.4304°N latitude and 157.7849°W longitude, **Figure 1**). The reef, referenced as the coconut patch reef, forms a nearly flat plateau that rises abruptly from the surrounding bay floor to an average depth of between 3 and 4 m. The reef was dredged during World War II in order to make room for a seaplane base (Hunter and Evans, 1995). Since that time, the area has become partially recolonized by coral and associated reef organisms that have gradually built up portions of the reef to within 2.5 m of the surface.

Measurements

Physical and optical data were collected *in situ* on 12 February 2017 using sensors deployed with a small, commercially available, coastal kayak equipped for autonomous operations (**Figure 2**) and described in detail by Curcio et al. (2005) and Wood et al. (2007). The ASV received GPS signals and navigated to pre-defined waypoints by controlling the speed and orientation of an articulating electric trolling motor located in the stern and powered with a 12 V marine battery. Autonomous control was achieved with a 3D Robotics Pixhawk auto-controller and GPS with compass and mission planning and execution was conducted using Mission Planner software. A Lowrance Structure Scan 3-D side-scan sonar and depth finder was mounted through the center of the keel and operated at 800 KHz, yielding bathymetry and high-resolution acoustical images of the surrounding bay floor. SonarTRX Pro side-scan sonar software was used to process and view sonar images as geo-referenced

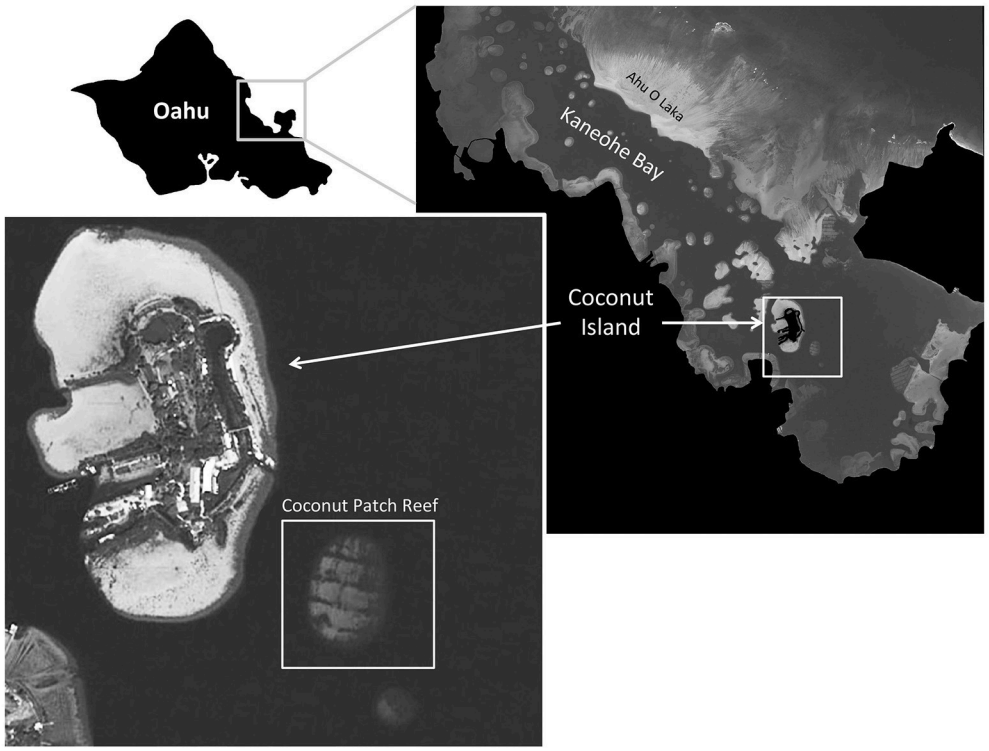

FIGURE 1 | The study location, Kane'ohe Bay, is located on the east coast (windward side) of O'ahu, Hawai'i. *In situ* physical and optical measurements were collected across a shallow patch reef located off the southeast shore of Coconut Island in the southern portion of the bay.

mosaics and to extract bathymetric information including water depth and benthic roughness. Surfer v.11 2D & 3D mapping and visualization software was used to create geo-referenced, 2-D bathymetric contour plots and 3-D bathymetric contour surfaces using Kriging interpolation.

A Satlantic HyperPro hyperspectral radiometer buoy was attached to the ASV with a power and communications cable and towed at a trailing distance of approximately 3 m, in order to avoid shadows cast by the ASV hull. The system measured downwelling irradiance above the water surface $E_{d,\lambda}(0+)$ and upwelling radiance just below the surface at a depth of 0.24 m $L_{u,\lambda}(0.24)$ in 137 spectral bands between 349 nm and 804 nm with an average half-power bandwidth of 3.34 nm. The $E_{d,\lambda}(0+)$ sensor was fitted with a diffuse cosine collector. The in-water field of view (FOV) of the $L_{u,\lambda}(0.24)$ sensor was 8.5°. A weighted keel of length 1 m was built into the radiometer buoy and provided a relatively stable, vertical orientation. A tilt and roll sensor provided deviations in radiometer orientation (measured in degrees) from a horizontal plane in two orthogonal directions. A Teledyne Benthos PSA-916 acoustical depth sounder was attached to the keel of the radiometer at a depth of 0.95 m, and it measured the distance to the bottom D_r m beneath the radiometer with an accuracy of ±0.01 m. Therefore, the total water column depth was computed as $D = D_r + 0.95$.

A down-looking GoPro camera (GP1), enclosed in a watertight housing, was affixed to the bottom of the radiometer keel, and it provided high definition photographic documentation of shallow benthic features. The in-water FOV of the camera was determined to be 83.4° in the long direction and 63.9° in the short direction. It was uncertain precisely where the radiometer sampled within the GP1 imagery. However, care was taken to visually aligned the camera with the radiometer keel to ensure that the radiometer subsampled the GP1 frames simultaneously. A second GoPro camera (GP2) was affixed to the aft deck of the ASV and pointed toward the stern to provide simultaneous photographic documentation regarding the orientation of the radiometer, the sea state, and atmospheric conditions. All data were collected at 1 Hz or greater and time-stamped for post processing.

The ASV survey consisted of a 3 km track, starting within a small boat basin on the southeast shore of Coconut Island, extending out of the basin through a narrow cut and to the study area, where nine East-West transects (labeled T1 through T9 from South to North) were conducted over the coconut patch reef before returning to the boat basin (**Figure 3**). The average speed of the ASV was approximately 1.8 km h^{-1}, yielding a set of optical and acoustical measurements every 0.5 m.

Water column properties within 2 m of the surface, including spectral absorption ($a_{pg,\lambda}$ m^{-1}), attenuation ($c_{pg,\lambda}$ m^{-1}), and backscatter ($b_{bp,\lambda}$ m^{-1}) due to particulate and dissolved impurities, were collected over the coconut patch reef from a small boat several days after the ASV survey, on 17 February

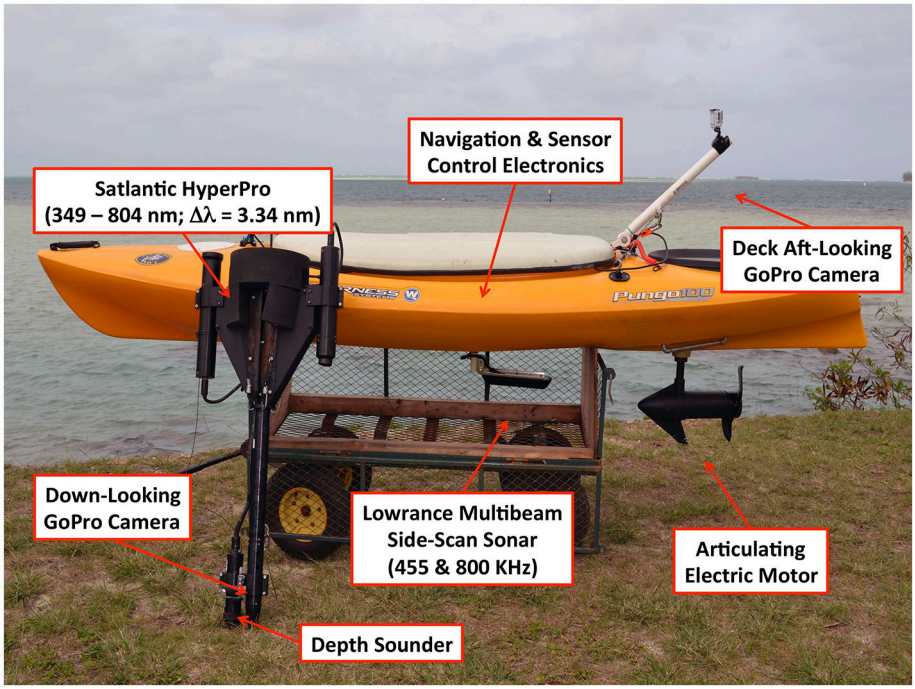

FIGURE 2 | A survey of the coconut patch reef was conducted on 12 February 2017 using an instrumented, autonomous kayak capable of navigating pre-planned routes and collecting simultaneous optical and acoustical observations of benthic features in high spatial resolution.

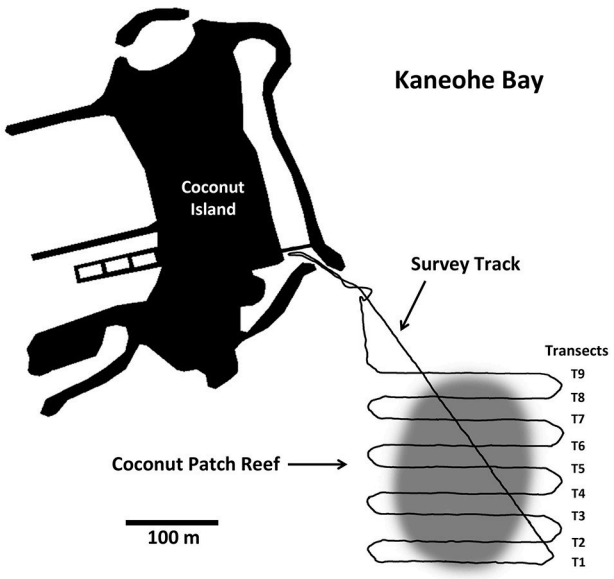

FIGURE 3 | The ASV survey route (black line) on 12 February 2017, included nine East-West transects over the coconut patch reef labeled T1 through T9 from South to North.

2017, using equipment and methods reported by Dierssen and Russell (2017). In addition, fluorometric chlorophyll, (F_{chl} mg m^{-3}), water temperature t°C, and salinity s psu were collected on 16 and 18 February using a pre-calibrated, self-logging YSI EXO2 water quality sonde deployed by hand from a second, manned kayak.

A hyperspectral image of the study site was collected on 3 March 2017 using the Jet Propulsion Laboratory Airborne Visible Infrared Imaging Spectrometer-Classic sensor (AVIRIS) deployed on the NASA ER-2 aircraft at an altitude of approximately 19.8 km (**Figure 4**). AVIRIS measures radiance in 224 contiguous bands between 400 nm and 2,500 nm with a nominal spectral channel full-width at half maximum and sampling interval of 10 nm (Vane et al., 1993). At the deployed altitude, the ground sampling distance was approximately 7 m. The overflight occurred at 19:00 GMT, 09:00 local time, with the sky partly cloudy, but clear over most of Kane'ohe Bay, including the coconut patch reef.

Theoretical Considerations and Computations

In Situ Observations

Radiometer buoy data were used to compute in-water radiance reflectance at 0.24 m depth as

$$r_{rs,\lambda}(0.24) = L_{u,\lambda}(0.24)/E_{d,\lambda}(0.24)\,. \quad (1)$$

In order to perform this computation, the downwelling irradiance at 0.24 m must be computed from the measured downwelling irradiance impinging upon the surface and knowledge of the optical properties of the water;

$$E_{d,\lambda}(0.24) = n_w\,(1-\mathcal{R}_d)\,E_{d,\lambda}(0+)\,e^{-0.24\,K_{d,\lambda}}, \quad (2)$$

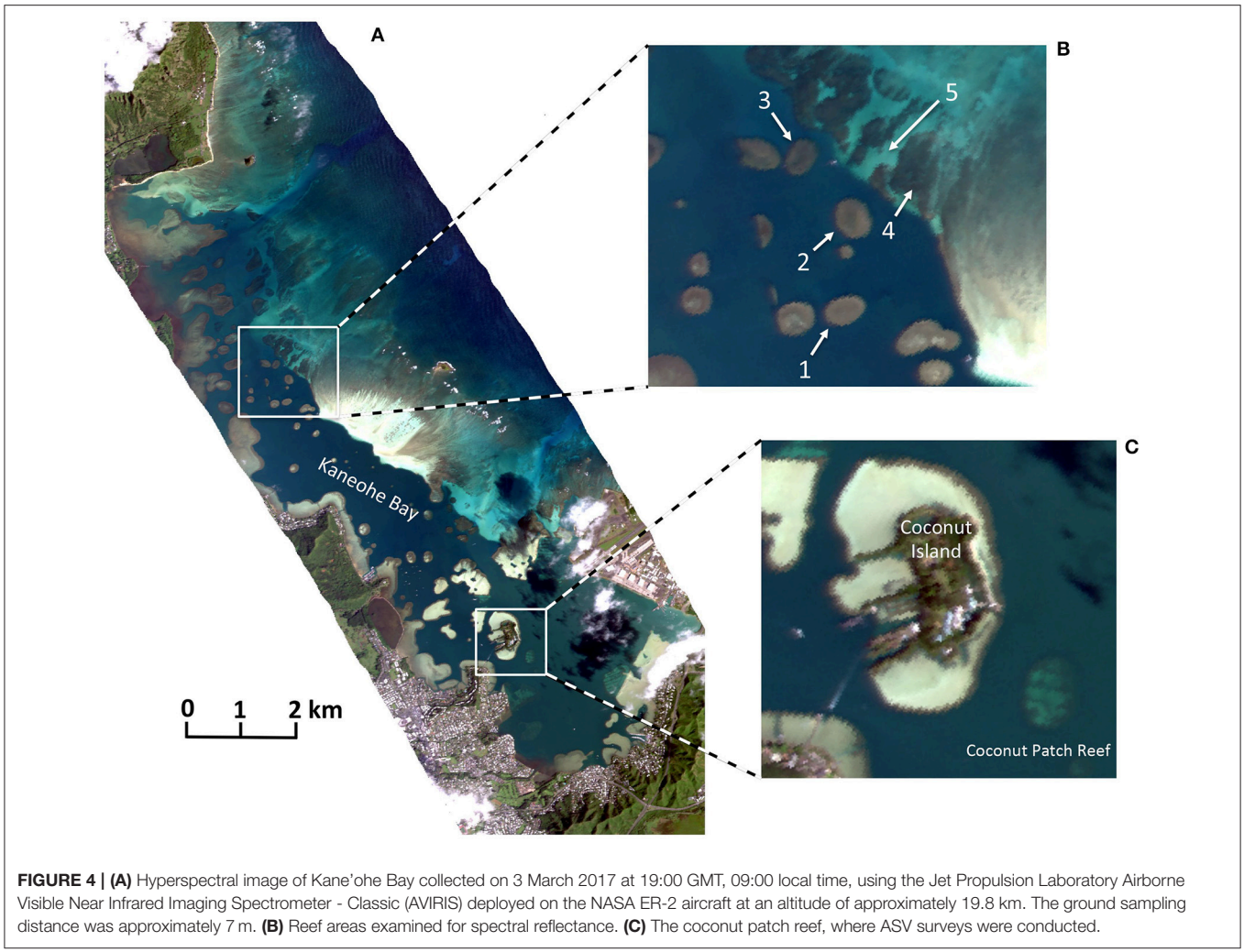

FIGURE 4 | (A) Hyperspectral image of Kane'ohe Bay collected on 3 March 2017 at 19:00 GMT, 09:00 local time, using the Jet Propulsion Laboratory Airborne Visible Near Infrared Imaging Spectrometer - Classic (AVIRIS) deployed on the NASA ER-2 aircraft at an altitude of approximately 19.8 km. The ground sampling distance was approximately 7 m. **(B)** Reef areas examined for spectral reflectance. **(C)** The coconut patch reef, where ASV surveys were conducted.

where n_w is the real portion of the refractive index of water relative to air ($\approx$1.34), $\mathcal{R}_d$ is the surface reflectance of downwelling irradiance illuminating the surface ($\approx$0.02), and $K_{d,\lambda}$ is the diffuse attenuation of downwelling irradiance within the top 0.24 m of the water column. The exponential term in Equation (2) defines how much downwelling irradiance is transmitted to the depth of the down-looking radiometer and $K_{d,\lambda}$ is a function of the absorbing and scattering properties of the water, including particulate and dissolved matter (Mobley, 1994 and references cited therein). Kirk (1984) reported an empirical relationship for $K_{d,\lambda}$ based on numerical simulations of radiative transfer;

$$K_{d,\lambda} \approx \frac{a_\lambda}{\mu_d}\left[1 + (0.425\,\mu_d - 0.19)\,\frac{b_\lambda}{a_\lambda}\right]^{\frac{1}{2}}, \qquad (3)$$

where a_λ ($= a_{w,\lambda} + a_{pg,\lambda}$) is the total absorption coefficient of the water mixture and b_λ ($= b_{w,\lambda} + c_{pg,\lambda} - a_{pg,\lambda}$) is the total scattering coefficient of the water mixture. The subscript w refers to pure water, the properties of which are considered constant (Smith and Baker, 1981; Pope and Fry, 1997), and μ_d is the average cosine of the in-water, near-surface, down-welling radiance distribution. In relatively clear water, as is the case in Kane'ohe Bay, μ_d may be approximated as the cosine of the in-water solar zenith angle θ_s, i.e., after refraction at the water surface; $\mu_d = \cos\left[\sin^{-1}\left(\sin\theta_s/n_w\right)\right]$.

Following shallow water radiative transfer theory and modeling reported by Philpot (1987, 1989) and Maritorena et al. (1994), the in-water reflectance at 0.24 m depth may be expressed as

$$r_{rs,\lambda}(0.24) = r_{rs,\lambda,\infty}(0.24) + [\frac{\rho_{b,\lambda}}{\pi} - r_{rs,\lambda,\infty}(0.24)]e^{-(K_{d,\lambda}+K_{u,\lambda})\,(D-0.24)}, \qquad (4)$$

where the subscript ∞ refers to the reflectance of an optically deep water column and $\rho_{b,\lambda}$ is the irradiance reflectance of the ocean floor. The diffuse attenuation for upwelling irradiance $K_{u,\lambda}$ was computed using Eqn. (3) and replacing μ_d with $u_u = 0.7$, the approximate average cosine for upward propagating light. As $D \Rightarrow \infty$, $r_{rs,\lambda}(0.24)$ approaches the optically deep solution, while as $D \Rightarrow 0.24$, the depth of the in-water radiometer, $r_{rs,\lambda}(0.24)$

approaches $\frac{\rho_b}{\pi}$, the radiance reflectance of the bottom substrate. Rearranging Equation (4) for benthic reflectance yields

$$\rho_{b,\lambda} = \pi \left[\left(r_{rs,\lambda}(0.24) - r_{rs,\lambda,\infty}(0.24) \right) e^{(K_{d,\lambda}+K_{u,\lambda})\,(D-0.24)} + r_{rs,\lambda,\infty}(0.24) \right]. \quad (5)$$

The unknown quantity in Equations (4, 5) is the reflectance of optically deep water. While the maximum depth encountered within the study site was approximately 14 m, this may not be deep enough to provide an accurate deep-water signal, especially in the green portion of the spectrum where transmittance is expected to be greatest and where the bottom substrate, uncolonized calcareous sediment, can be highly reflective. Gordon et al. (1988) provides an accurate empirical representation of $r_{rs,\lambda,\infty}$ as a function of $X = b_b \left(a + b_b\right)^{-1}$, where b_b ($= b_{bp} + b_{bw}$) is the total backscatter coefficient for the water mixture;

$$r_{rs,\lambda,\infty} = \sum_{i=1}^{2} g_i X^i \quad (6)$$

and g_i are coefficients empirically derived from a Monte Carlo radiative transfer model. Lee et al. (1999) provided updated values based on a large number of simulations using the community model Hydrolight (Mobley and Sundman, 2012); $g_1 = 0.084$ and $g_2 = 0.125$. Thus, benthic irradiance reflectance was computed from measured above water irradiance illumination, in-water, upwelling radiance, water depth, and estimated values of diffuse attenuation and deep-water reflectance from independent measurements of water optical properties.

In-water reflectance of optically shallow water was computed using $\rho_{b,\lambda}$, $r_{rs,\lambda,\infty}$, and D to constrain Equation (5);

$$r_{rs,\lambda} = r_{rs,\lambda,\infty} + [\frac{\rho_{b,\lambda}}{\pi} - r_{rs,\lambda,\infty}] e^{-(K_{d,\lambda}+K_{u,\lambda})\,(D)}. \quad (7)$$

The implicit assumption in Equation (7) is that the deep-water reflectance measured at 0.24 m below the surface is equal to the reflectance measured immediately below the surface (zero depth). While reflectance is a function of radiance distribution and both μ_d and u_u are known to change with depth independent of the water optical properties (Mobley, 1994 and references cited), changes between the surface and 0.24 m in the absence of strong bottom effects are expected to be negligible.

Finally, following Lee et al. (1999), above-water remote sensing reflectance, $R_{rs} = L_u(0+)/E_d(0+)$, was computed from the in-water reflectance as

$$R_{rs,\lambda} = \frac{0.52\, r_{rs,\lambda}}{1 - 1.7\, r_{rs,\lambda}}. \quad (8)$$

Remote Sensing Observations

In order to compare the remotely sensed observations with the ASV observations, AVIRIS measurements of at-sensor radiance, $L_{s,\lambda}$, must be corrected for atmospheric effects and the resulting radiances converted to remote sensing reflectance, $[R_{rs,\lambda}]_{AVIRIS}$. Since no field measurements were collected at the time of the AVIRIS overpass, the atmospheric correction procedure must be completely image-based. Following procedures summarized by Chavez (1996),

$$[R_{rs,\lambda}]_{AVIRIS} = \frac{L_{s,\lambda} - L_{a,\lambda}}{\tau\, E_{o,\lambda}(0+)\, \cos(\theta_s)}, \quad (9)$$

where τ is the atmospheric transmittance in the direction of the sensor, $E_{o,\lambda}(0+)$ is the downwelling solar irradiance at the water surface on a plane perpendicular to the solar direction, and θ_s is the solar zenith angle at the location and time of imaging. Chavez estimated that under a clear atmosphere, $\tau \approx 0.81$ for Landsat TM Bands 1 through 4, which span the spectral range 450–900 nm. $L_{a,\lambda}$ is approximated with the at-sensor radiance representing dark pixels within the image for which surface reflectance is nearly zero; $[L_{s,\lambda}]_{dark} \approx L_{a,\lambda}$. Substituting the estimates for τ and $L_{a,\lambda}$ into Equation (9) yields.

$$[R_{rs,\lambda}]_{AVIRIS} = \frac{L_{s,\lambda} - [L_{a,\lambda}]_{dark}}{0.8\, E_{o,\lambda}(0+)\, \cos(\theta_s)}. \quad (10)$$

For the AVIRIS image of Kane'ohe Bay, a dark shadow cast upon a deep water area by a cloud, located slightly south of the coconut patch reef, was used to compute $[L_{s,\lambda}]_{dark}$. Note that this likely yielded a slight over-adjustment as the shadowed water-leaving radiance, while quite small, is not zero. Finally, AVIRIS reflectance was corrected for sunglint, i.e., light reflected from the water surface, using methods reported by Hedley et al. (2005).

Equation (10) has been shown to work reasonably well over land where targets may be treated as Lambertian reflectors. However, over water where $R_{rs,\lambda}$ is affected by reflectance and transmittance at the air/water interface, the amount of light entering the water and, thus, available to be reflected must also be taken into consideration. For $\theta_s < 30^\circ$, surface reflectance, ρ_s, ≈ 0.02 and about 98% of the energy enters the water. However, as θ_s increases, so does ρ_s according to the equations of Fresnel (see (Mobley, 1994) and citations referenced). Replacing $E_{o,\lambda}(0+)$ in Equation (10) with $(1 - \rho_s)\, E_{o,\lambda}(0+)$ yields.

$$[R_{rs,\lambda}]_{AVIRIS} = \frac{L_{s,\lambda} - [L_{a,\lambda}]_{dark}}{0.8\,(1 - \rho_s)\, E_{o,\lambda}(0+)\, \cos(\theta_s)}. \quad (11)$$

At the time of the AVIRIS overflight, $\theta_s \approx 61.4^\circ$ and the corresponding Fresnel reflectance of unpolarized light, assuming the water surface to be flat, was $\rho_s \approx 0.067$. Equation (11) was used to compute reflectance for all cloud-free water pixels within the AVIRIS image.

RESULTS

The ASV survey of coconut reef was conducted under a clear to partly cloudy sky and low wind. The sea surface varied between smooth and slightly choppy. Acoustical measurements indicated that the reef rose up abruptly from the surrounding bay floor from a depth of approximately 14 m to an average depth on the reef plateau of 3.4 ± 0.57 m. (The confidence range, here and throughout the remainder of the paper, is expressed as plus or minus one standard deviation.) The side-scan sonar recorded higher acoustic backscatter in the central portion of the reef (i.e.,

lighter tones in the sonar image) and lower returns (i.e., darker tones in the sonar image) in areas mostly around the periphery (**Figure 5**). Imagery from the GP1 camera revealed benthic features down to approximately $D = 5$ m. Visual inspection of the imagery indicated that the higher acoustical returns represented uncolonized sediment while the lower returns represented areas colonized by coral. Coral areas tended to be shallower than adjacent areas of uncolonized sediment as a result of the coral structures having been built up over time by reef-forming organisms.

Water Properties

In situ measurements made several days after the ASV survey indicated stable, near-surface temperatures, ranging between 23.5° and 24.6°C, and salinities, ranging between 33.45 and 33.6 psu. Total absorption due to impurities increased toward the blue portion of the spectrum, e.g., $a_{pg,414} = 0.186$ m^{-1}, and indicated the presence of small quantities of colored dissolved organic matter (CDOM). Fluorometric chlorophyll concentrations ranged from $F_{chl} = 0.2$ to $F_{chl} = 0.8$ mg m^{-3}. Light scatter due to suspended particulate matter was relative low, e.g., $b_{p,400} = 0.82$ m^{-1}, indicating relatively clear water, and decreased non-linearly with increasing wavelength, as is typical of coastal marine particles (Babin et al., 2003). Likewise, backscatter measured at three discrete wavelengths decreased with increasing wavelength; $b_{bp,470} = 0.0106 \pm 0.0007$ m^{-1}, $b_{bp,532} = 0.0096 \pm 0.0005$ m^{-1}, and $b_{bp,660} = 0.0065 \pm 0.0004$ m^{-1}. The average fractional backscatter, $\tilde{b}_b = \frac{b_b}{b}$, at each wavelength was $\tilde{b}_{b,470} = 0.0149$, $\tilde{b}_{b,532} = 0.0141$, and $\tilde{b}_{b,660} = 0.0117$.

Equation (3) was used to compute near-surface K_d for optically deep water using total absorption and light scatter computed from *in situ* measurements of a_{pg} and $b_p = c_{pg} - a_{pg}$, literature values for pure water (Smith and Baker, 1981; Pope and Fry, 1997), and the average solar zenith angle during the February 12 survey, $\theta_s = 54.6°$ (**Figure 6**). A slight rise in K_d within the blue portion of the spectrum was likely due to the combined effects of absorption by small quantities of CDOM while the shape of the spectrum within the red portion was attributed to absorption by pure water. Likewise, in-water optically deep reflectance was computed using Equation (6), where $b_{b,\lambda} = \tilde{b}_b b_\lambda$ and $\tilde{b}_b$ was the spectrally averaged fraction of light scatter in the backward direction (≈0.0136). Equation (8) was used to compute $R_{rs,\lambda,\infty}$. Similar to the K_d spectrum, the spectral shape of $R_{rs,\lambda,\infty}$ indicated that the water column was relatively clear (low reflectance) but, contained small quantities of CDOM (e.g.,

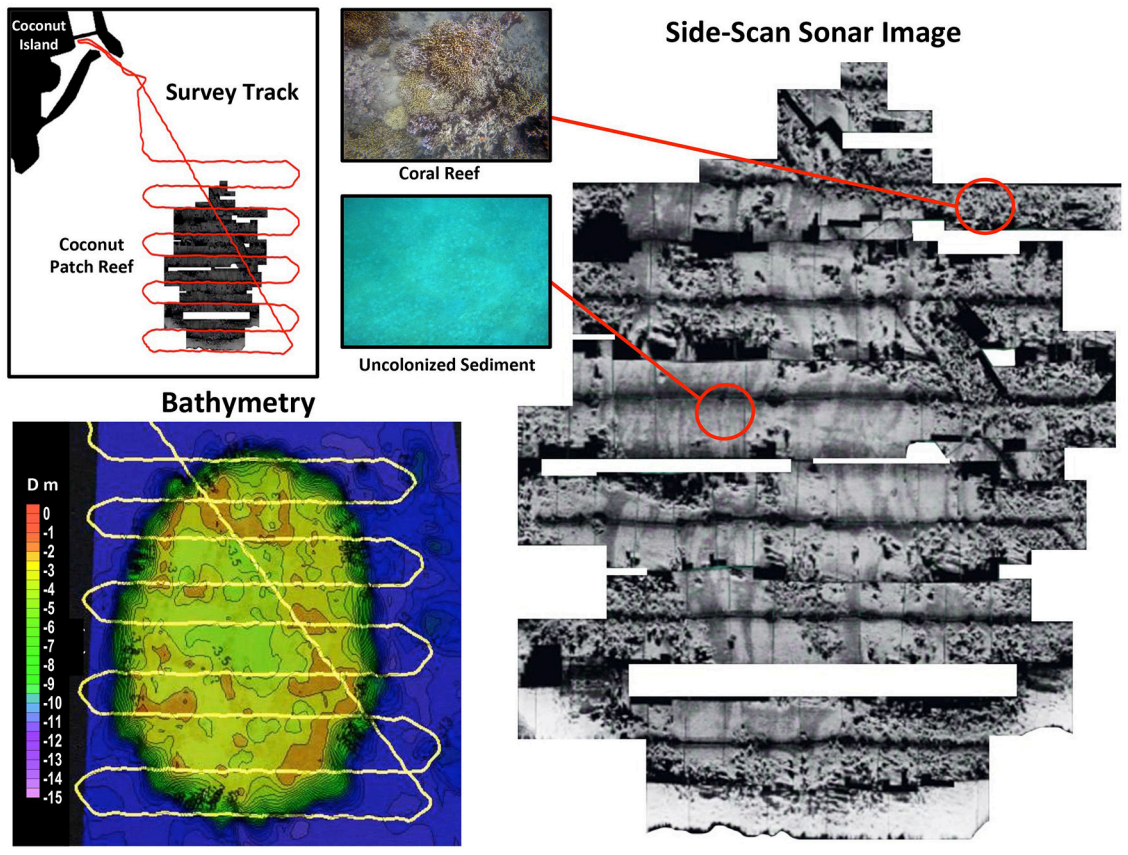

FIGURE 5 | Acoustical data from an autonomous survey was used to map bathymetry within and around the coconut patch reef and identify areas colonized by coral (dark, heterogeneous tones in acoustical backscatter) and uncolonized sediment (lighter, more homogeneous tones). Visual inspection of imagery from a down-looking, in-water camera (GP1) was used to validate the interpretation of the acoustical backscatter signals.

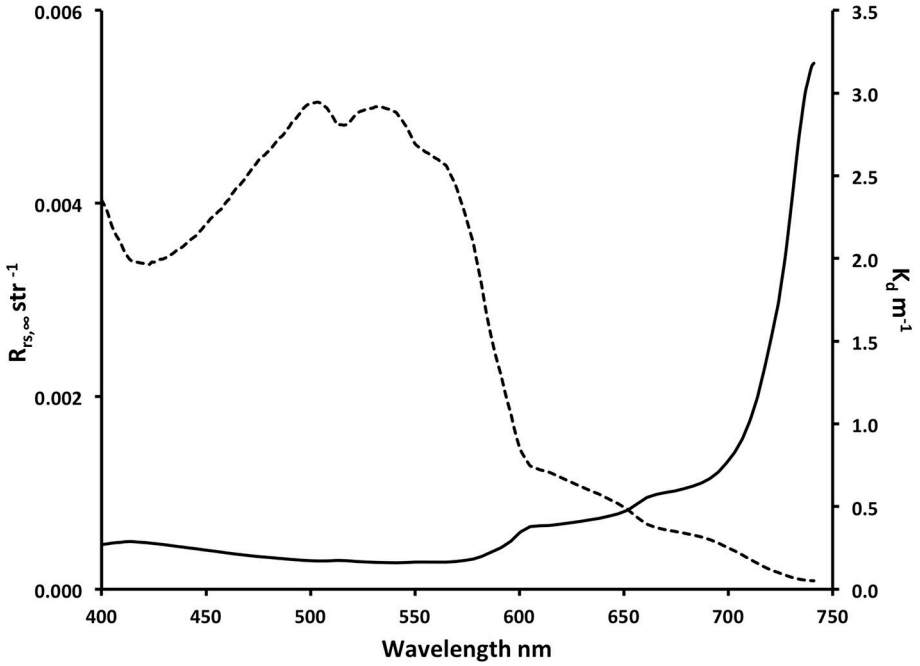

FIGURE 6 | Remote sensing reflectance $R_{rs,\infty}$ str^{-1} (dashed curve) and diffuse attenuation of downwelling irradiance $K_{d,\lambda}$ m^{-1} (solid curve) computed from near-surface, *in situ* optical measurements collected over the coconut patch reef.

slightly depressed reflectance at wavelengths < 500 nm), and low concentrations of suspended particles (e.g., slightly elevated reflectance at wavelengths > 500 nm).

ASV Survey

In-Water Reflectance

In-water reflectance was highly variable as the radiometer passed over shallow areas of the coconut patch reef due to reflectance from benthic features (e.g., $r_{rs,550}$, shown in **Figure 7A**).

In comparison, adjacent deep-water areas, $D \approx 14$ m, were consistently darker than the shallow reef features and much less variable.

Along the course of the ASV survey, the *in situ* radiometer orientation changed with the tow direction (**Figure 7B**) and variability was attributed to how the radiometer interacted with the local wave field. Along eastward transects (T2, T4, T6, and T8), the radiometer deviated an average of 3.6° from a vertical orientation and the maximum deviation at times exceeded 10°. When towed in a westward direction (T1, T3, T5, T7, and T9), the average radiometer deviation from a vertical orientation increased to 6.9° and the maximum deviation exceeded 20°. In order to assess the impact of sensor orientation on the computed reflectance, subsets of the data were examined where tow direction resulted in large changes in radiometer orientation and, at the same time, the effects of bottom reflectance were small and surface illumination was relatively stable. This situation occurred within the time interval between 12.95 and 13.14 h (shaded area within the right hand side of **Figure 7B**) when the radiometer was over deep water. The sky was fairly overcast, but illumination was reasonably stable. Radiometer orientation changed on average more than 10° as the ASV turned from the eastward T8 track to the westward T9 track and then back toward the boat basin. At the same time, variability in $r_{rs,550}(0.24)$ was small, with the exception of a slight increase at 13.05 h when the radiometer passed over the northern edge of the reef and D decreased to 5 m. Thus, within the observed range of radiometer motion, radiometer orientation appeared to have a minor impact on computed reflectance relative to the dominant environmental factors, i.e., water depth and bottom type.

In addition to radiometer orientation, illumination due to clouds changed significantly along the course of the survey (**Figure 7C**). Downwelling irradiance, e.g., $E_{d,550}$, varied by a factor of four, ranging from approximately 0.5 W m^{-2} nm^{-1} under clouds to >2 W m^{-2} nm^{-1} under direct, un-obstructed sunlight. At the same time, as in the case of the radiometer orientation, the response of $r_{rs,550}(0.24)$ was quite small, as illustrated by the observations within the time interval between 11.96 and 12.12 h (i.e., the shaded area on the left hand side of **Figure 7C**).

Benthic Cover

The in-water, down-looking imagery (GP1 data) effectively documented the condition of the shallow bottom where $D <$ 5 m (**Figure 8**). Visual inspection of the imagery indicated that, within the boat basin, the bottom was dominated by turf algae, mixed debris of terrigenous origin, and the frequent presence of benthic fauna, such as the sea cucumber *O. spectabilis*. The floor of the coconut patch reef, on the other hand, was either

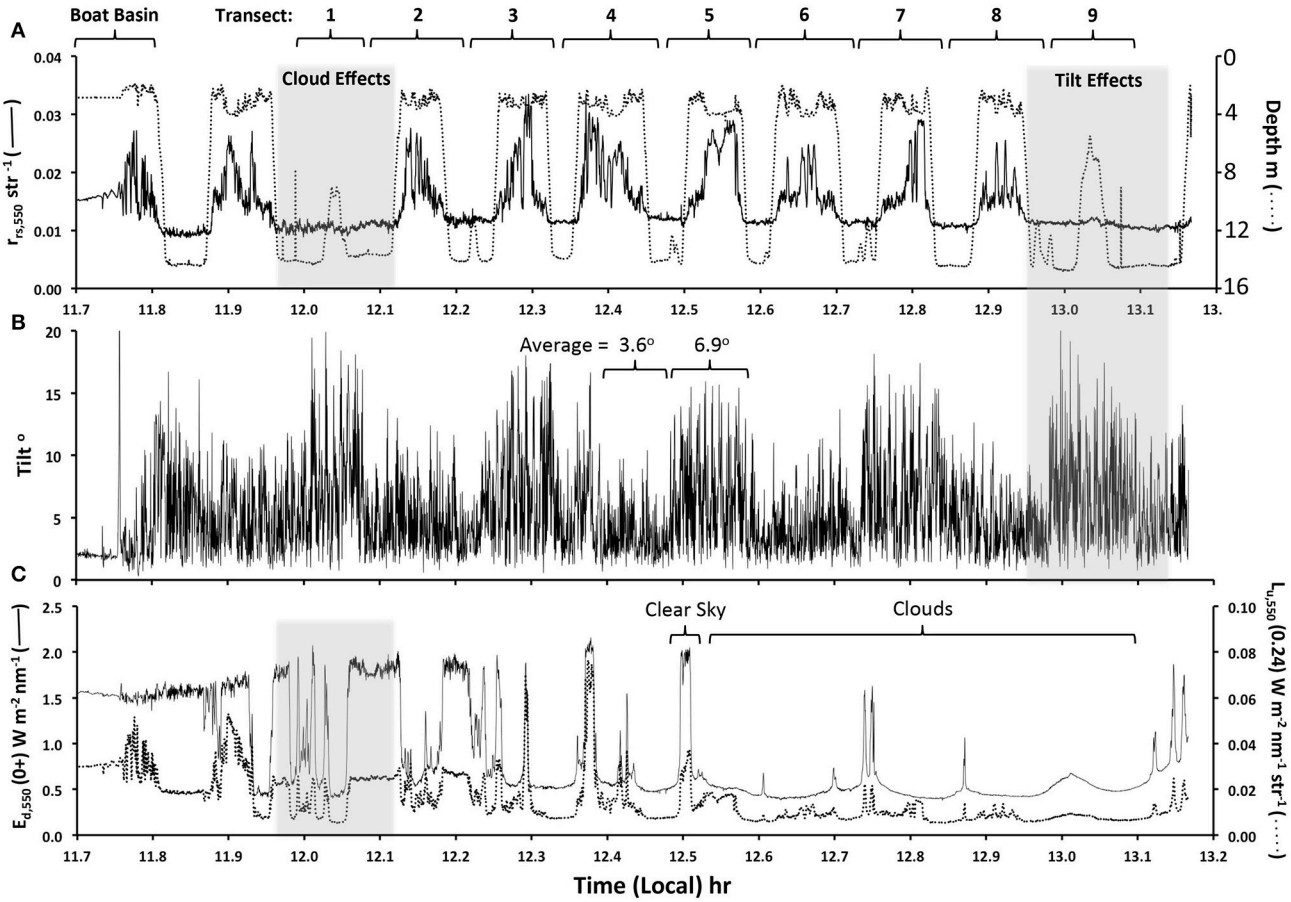

FIGURE 7 | Radiometer data collected along the entire ASV survey course. The boat basin and transects over the coconut patch reef are indicated at the top of the figure and shaded areas indicate portions of the data where variability in cloud effects and radiometer orientation were apparent. **(A)** In-water reflectance (solid curve) and water bottom depth (dotted curve) along the ASV survey course. **(B)** Deviation of the radiometer from vertical. **(C)** Downwelling irradiance, $\lambda = 550$ nm, measured above the water surface (solid curve) and in-water, upwelling radiance measured at a depth of 0.24 m.

comprised of a mixed community of coral, dominated by *Porites*, or uncolonized sediment and silt.

Benthic Reflectance

Benthic reflectance, $\rho_{b,\lambda}$, was computed according to Equation (5) for all areas where $D \leq 5$ m, the maximum depth at which benthic features could be identified within the GP1 imagery. In order to assess variability in $\rho_{b,\lambda}$ as a function of bottom type, spectra representing coral and uncolonized sediment were selected based on visual inspection of the GP1 imagery. Given the uncertainty in the location of the radiometer sampling within the GP1 FOV (the approximate size of the radiometer FOV is shown as a circle in center of the upper right panel of **Figure 8**), radiometer data were selected for which the entire corresponding GP1 frame appeared to represent the bottom type of interest, i.e., the FOV was either all coral or all uncolonized sediment. Data representing images with a mixture of bottom type were not included in the analysis. Benthic reflectance representing the two bottom types indicated two distinct reflectance spectra with little overlap throughout the visible and near infrared spectrum (**Figure 9**). The average water depth for coral was $D = 3.0 \pm 0.5$ m, and for uncolonized sediment the average was $D = 3.9 \pm 0.6$ m.

The coral reflectance spectra were similar to the lower range in reflectance of brown hermatypic coral and the uncolonized sediment spectra were similar to terrigenous mud and lower than the reflectance typical of calcareous sand (Hochberg et al., 2003). The low reflectance of the uncolonized sediment was in agreement with previous descriptions of bottom sediments in Kane'ohe Bay as coral ruble, sand, and "gray coral mud" (Bahr et al., 2015 and references cited therein). While the spectra were parsed based upon the apparent dominate bottom type within the GP1 images, it was likely that each spectrum represents a combination of bottom types. For example, gray colored sediment was often apparent within the GP1 imagery covering small spaces between coral features. Furthermore, the benthic environment had a heterogeneous appearance, such that the likelihood of obtaining a pure spectrum for either bottom type decreased with increasing benthic area viewed by the radiometer. Given the field of view of the down-looking radiometer (8.5°), a

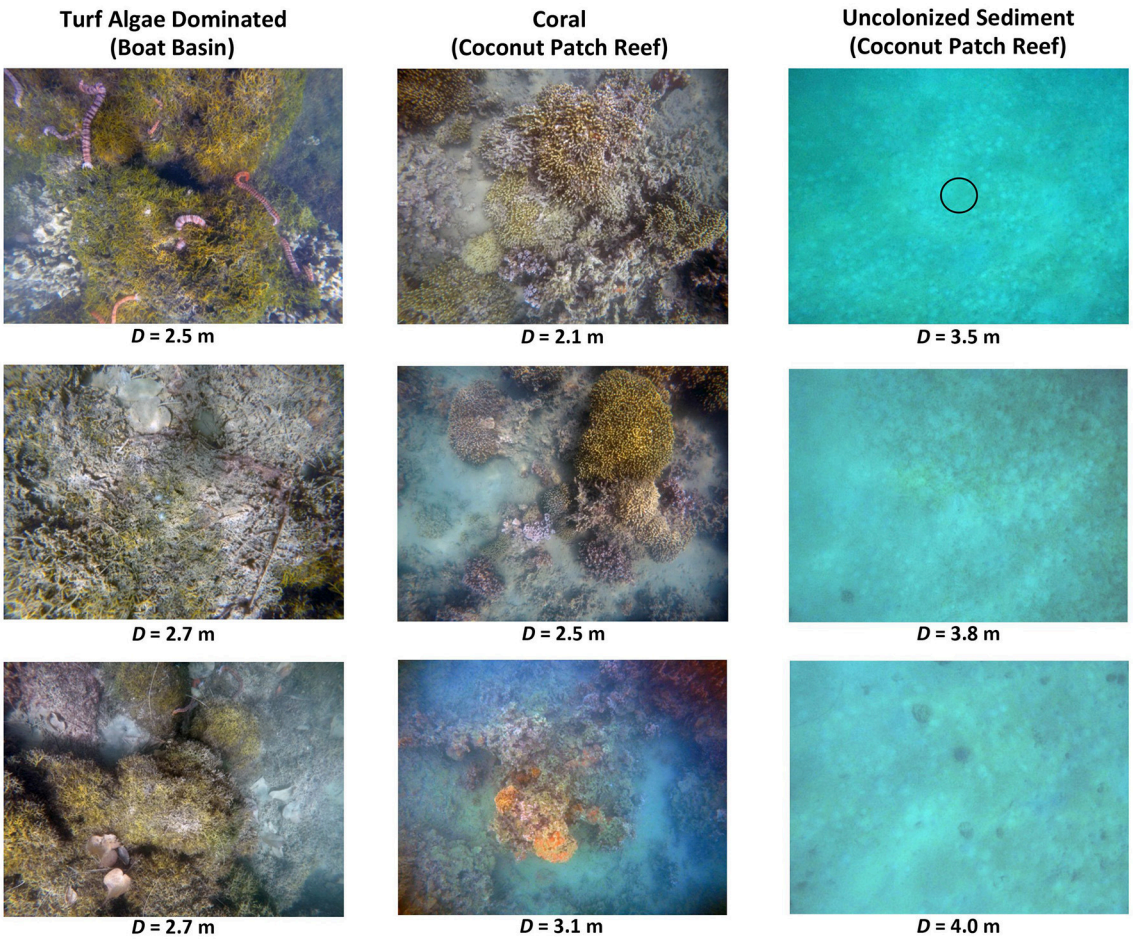

FIGURE 8 | In-water, down-looking imagery (GP1 camera) of selected benthic conditions along the ASV survey track over the coconut patch reef. The approximate field of view of the in-water, down-looking radiometer is shown as a circle centered on the top right plate representing uncolonized sediment at a depth of 3.5 m.

measurement 2 m from the bottom would integrate $\rho_{b,\lambda}$ across an area of 0.08 m^2 (horizontal length scale = 0.31 m), while a measurement made at an altitude of 4 m from the bottom would integrate over 0.31 m^2 (horizontal length scale = 0.63 m).

Similar to published *in situ* measurements, $\rho_{b,\lambda}$ increased rapidly for both uncolonized sediment and coral within the red portion of the spectrum, $\lambda > 680$ nm. When live vegetative biomass is present, the absorption of light by chlorophyll leads to a depression in reflectance within a narrow spectral region centered at roughly 675 nm, resulting in an abrupt increase in reflectance at longer wavelengths. This feature, often referred to as the red edge (e.g., Gates et al., 1965), is well documented for healthy terrestrial plants and aquatic grasses (Felella and Penuelas, 1994; Fyfe, 2003; Zimmerman, 2003) and it is apparent in published measurements of $\rho_{b,\lambda}$ for both live coral and, to a lesser extent, uncolonized sediment (Hochberg et al., 2003).

In Situ Remote Sensing Reflectance

Remote sensing reflectance $R_{rs,\lambda}$ was computed for each observation along the ASV track using Equation (8), where $D < 5$ m. The results represented the combined effects of $\rho_{b,\lambda}$ and bottom depth, assuming stable water optical properties. Parsing the data into primary bottom types using the GP1 imagery indicated that $R_{rs,\lambda}$ representing coral, turf algae, and uncolonized sediment remained distinct within the depth range observed ($2 \text{ m} \leq D \leq 5$ m) and that each was distinguishable from the adjacent deep water signature (**Figure 10**).

The reflectance spectra were slightly depressed in the blue portion of the spectrum, $\lambda < 550$ nm, typical of absorption by CDOM. Variability around the mean of each class represented the combined effects of $\rho_{b,\lambda}$ and bottom depth, assuming that water optical properties were stable and that the influences of sensor orientation and illumination were small. Areas of uncolonized sediment were quite bright relative to the coral, turf algae, and deep-water reflectance, where $\lambda \leq 600$ nm. Reflectance from coral and algae were generally greater than the deep-water signals, where $\lambda \leq 550$ nm. While there were areas within the spectra where bottom type was indistinguishable, there were also areas where each bottom type was unique. All bottom types, for example, were similar in reflectance at 600 nm, but they exhibited little overlap at shorter wavelengths.

AVIRIS Remote Sensing Reflectance

AVIRIS remote sensing reflectance $[R_{rs,\lambda}]_{AVIRIS}$ was computed using Equation (11). Downwelling solar irradiance measured during the ASV survey representing clear sky conditions was used to estimate downwelling irradiance with the sun at nadir; $E_{o,\lambda}(0+) = [E_{d,\lambda}(0+)]_{ASV}\ \left[\cos(\theta_{s,ASV})\right]^{-1}$, where $\theta_{s,ASV}$ is the solar zenith angle at the time of the kayak survey. $[R_{rs,\lambda}]_{AVIRIS}$ was in agreement with *in situ* determinations of remote sensing reflectance, $[R_{rs,\lambda}]_{ASV}$, representing coral and uncolonized sediment within the coconut patch reef and adjacent deep water (**Figure 11**). The magnitude of the AVIRIS reflectance tended to be greater than the *in situ* determinations, especially in the blue portion of the spectrum and, for the adjacent deep water, at all visible wavelengths. This was not surprising as Kane'ohe Bay is influenced by runoff from the adjacent land areas during rain events that transports particulate and dissolved matter into the bay. Light scatter from suspended particles impacted all wavelengths while the effects of impurity absorption were mostly constrained to wavelengths $\lesssim$550 nm. However, for the shallow coral and sand areas, where benthic reflectance dominated the signal, the *in situ* and remotely sensed measurements for $\lambda >$ 600 nm were similar in both magnitude and spectral shape.

The red edge spectral feature was evident in both the coral and sediment reflectance along the ASV survey route as an increase in red and near-infrared reflectance (**Figures 10**, **11**). The feature was also apparent, but to a lesser extent, within the surrounding deep water area and was likely the result of phytoplankton absorption. An examination of the AVIRIS reflectance from selected reef features within the northern portion of Kane'ohe Bay (locations 1 through 5 indicated in **Figure 4**) revealed red edge features associated with coral that were far more pronounced than in the coconut patch reef (**Figure 12**). The patch reefs in the northern bay are very shallow, occasionally piercing the water surface during low tide, and the coral cover tends to be greater than on the coconut patch reef due to the absence of dredging. Also, the water in the northern portion

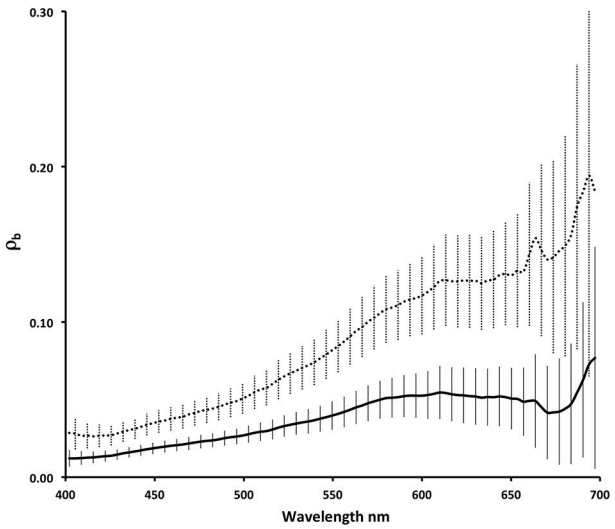

FIGURE 9 | Mean benthic reflectance of coral (solid curve) and uncolonized sediment (dotted curve) within the coconut patch reef computed using Equation (5), where $D < 5$ m. Data were parsed based on manual interpretation of in-water imagery (GP1 camera). Vertical bars indicated ±1 standard deviation relative to the mean.

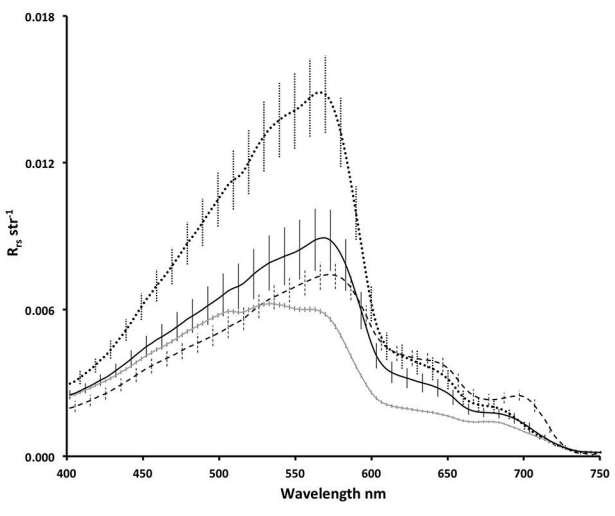

FIGURE 10 | Mean remote sensing reflectance of coral (solid black curve) and uncolonized sediment (dotted black curve) on the coconut patch reef where $D < 5$ m, turf algae within the boat basin on Coconut Island, $D < 2$ m (dashed black curve), and over deep water, $D > 14$ m (solid gray curve), adjacent to the patch reef. Data representing shallow water were parsed on bottom type gleaned from manual interpretation of in-water imagery (GP1 camera). Vertical bars indicated ±1 standard deviation relative to the mean.

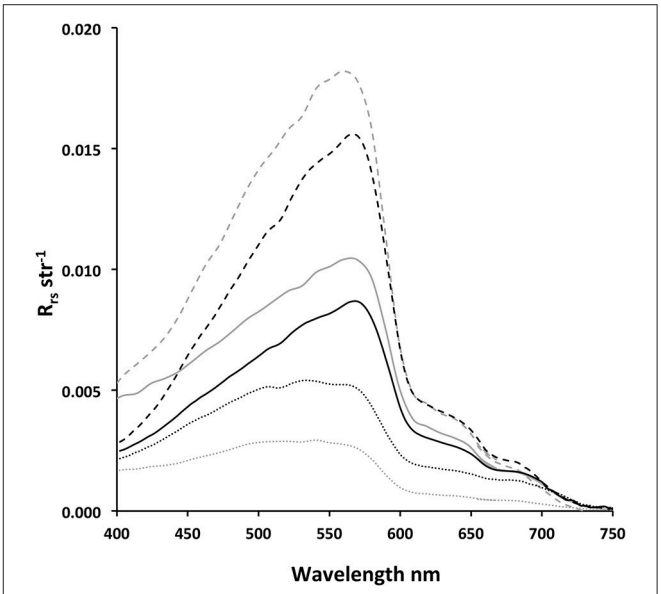

FIGURE 11 | Comparison of remote sensing reflectance derived from *in situ* measurements of the coconut patch reef collected on 12 February 2017 (black curves) and high-altitude AVIRIS imagery collected on 3 March 2017 (gray curves) representing coral (solid curves), uncolonized sediment (dashed curves) and deep water adjacent to the reef (dotted curves).

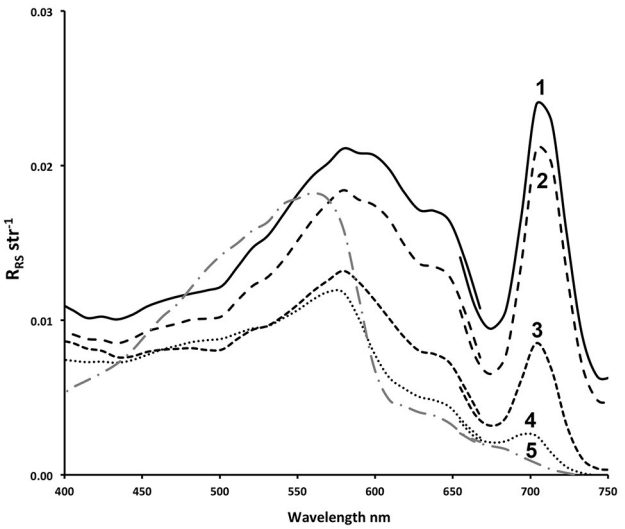

FIGURE 12 | Reflectance from selected shallow reef features in northern Kane'ohe Bay derived from AVIRIS imagery, collected on 3 March 2017; black curves, labeled 1 through 4 (see labeled areas in **Figure 4B**), represent patch reefs colonized by coral and algae and the gray curve, labeled 5, represents an area that appears to be uncolonized sediment.

of the bay tends to be clearer due to more efficient flushing by adjacent Pacific Ocean water. Thus, the larger red edge signals in the northern bay were attributed to greater coral biomass and less water attenuation of the benthic signal by the relatively clear, shallow water column.

Red Edge Height

Given that the waters in the Kane'ohe Bay, and on coral reefs in general, are typically very low in chlorophyll concentration, the red edge feature can potentially be used as a proxy for shallow, benthic vegetative biomass. In order to examine the red edge feature further, the red edge height, REH_λ, was defined as the difference between the measured reflectance and a baseline reflectance, computed as a cord connecting the endpoints of the spectral region of interest; $R_{rs,\lambda 1}$ at the shorter wavelength end and $R_{rs,\lambda 2}$ at the longer wavelength end;

$$REH_\lambda = R_{rs,\lambda} - R'_{rs,\lambda}, \tag{12}$$

where

$$R'_{rs,\lambda} = \frac{R_{rs,\lambda 2} - R_{rs,\lambda 1}}{\lambda_2 - \lambda_1} \cdot (\lambda - \lambda_1) + R_{rs,\lambda 1}. \tag{13}$$

Based upon inspection of the *in situ* and AVIRIS reflectance data, the lower and upper wavelengths bounds of the red edge feature were defined as $\lambda_1 = 675$ nm and $\lambda_2 = 740$ nm, respectively. Positive values of REH_λ were expected to indicate the presence of live, photosynthetic biomass.

Computations of REH_λ with *in situ* measurements over the coconut patch reef representing both coral and uncolonized sediment was positive at shorter wavelengths, $\lambda < 710$ nm, and negative at longer wavelengths (**Figure 13**). The curves representing coral decreased in amplitude with increasing water depth and appeared to converge upon the deep-water signal. This result was to be expected since deeper water, i.e., a longer optical path length, will result in greater attenuation of the benthic signal at longer wavelengths. Furthermore, the wavelength of maximum REH_λ representing coral decreased with increasing water depth from approximately 690 nm, where $2\,\text{m} \leq D \leq 3\,\text{m}$, to approximately 688 nm, where $3\,\text{m} \leq D \leq 4\,\text{m}$. The peak REH_λ wavelength for uncolonized sediment, where $3.5\,\text{m} \leq D \leq 4.5\,\text{m}$, was approximately 687 nm. REH_λ computed from AVIRIS data collected over the coconut patch reef yielded results that were similar to both coral and uncolonized sediment, where $D > 3\,\text{m}$. AVIRIS data representing shallow patch reefs in the northern portion of the bay yielded REH_λ values that were as much as 2 orders of magnitude greater than the coconut patch reef and values were generally positive for all wavelengths within the computation range. AVIRIS data representing adjacent bright areas within the image that appeared to be shallow uncolonized sediment yielded REH_λ values that were similar to the *in situ* results for uncolonized sediment on the coconut patch reef. Furthermore, the maximum REH_λ values for the northern bay patch reefs were shifted to longer wavelengths relative to the coconut patch reef results, $702\,\text{nm} \leq \lambda \leq 708\,\text{nm}$, suggesting that the northern patch reefs were shallower and perhaps more densely covered with coral.

As an operational means of detecting and mapping the distribution of live vegetation biomass associated with coral, a REH_λ-based algorithm was defined as

$$REH_N = \frac{REH_{705}}{R'_{rs,705}}, \tag{14}$$

where the magnitude of the red edge height at 705 nm was normalized to the computed base reflectance at that wavelength. This approach was necessary to reduce the effects of the magnitude of the baseline reflectance, e.g., high reflectance over areas of very shallow, bright sand, such as the Ahu O Laka barrier island. Applying Equation (14) to the *in situ* data revealed areas of coral cover along each transect across the coconut patch reef (**Figure 14**). For $D < 5\,\text{m}$, $REH_N > 0$ and positive values tended to occur in shallower areas, where the GP1 imagery and sonar data indicated the presence of coral, i.e., dark acoustical returns due to increased benthic roughness associated with coral cover (**Figure 5**). The maximum depth at which positive REH_N values were detected was between 3 and 4 m. Parsing the data between coral-dominated and sediment-dominated observations, $[REH_N]_{\text{CORAL}} = 0.06 \pm 0.13$ and $[REH_N]_{\text{SAND}} = -0.13 \pm 0.05$. Where $D \leq 3\,\text{m}$, $[REH_N]_{\text{CORAL}} = 0.12 \pm 0.33$.

The REH_λ signal was used to estimate coral cover as the fraction of observations exceeding a defined threshold value. Defining the threshold as $[REH_N]_{\text{CORAL}} \geq 0.057$ (the mean $[REH_N]_{\text{CORAL}}$ minus one standard deviation) and constraining the analysis to *in situ* measurements over the coconut patch reef where $D \leq 5\,\text{m}$, the percent coral cover along the combined nine ASV transects was 25.2% ($N = 2{,}039$). Hunter and Evans (1995) reported on decadal changes in coral cover at selected

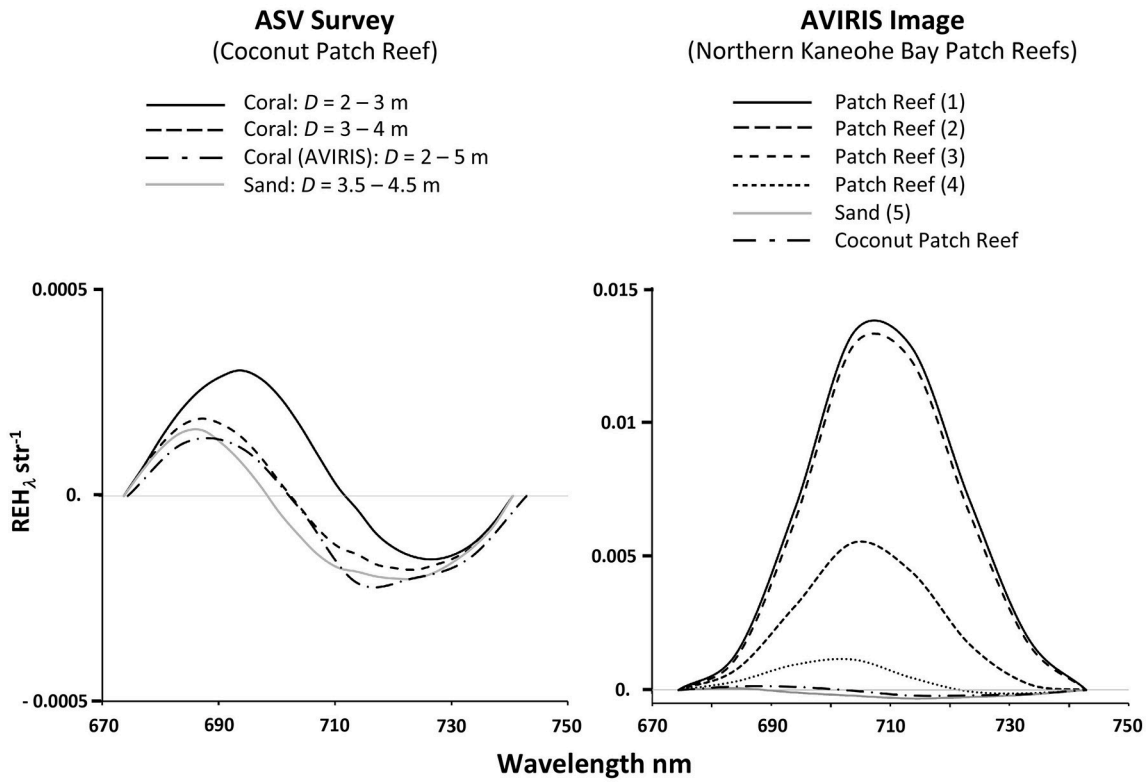

FIGURE 13 | Red edge height computed for data collected during the *in situ* survey of the coconut patch reef on 12 February 201 (**left**) and selected patch reefs in the northern Kane'ohe Bay imaged by AVIRIS on 3 March 2017 (**right**; locations indicated in **Figure 4B**). For comparison, the AVIRIS REH_λ signal is also plotted with the ASV data (dash-dot curve in both panels).

sites within Kane'ohe Bay, including the coconut patch reef, in response to sewage exposure using traditional diver-based methods. The coconut patch reef was found to have increased in coral coverage, from 1.2% in 1971, when the bay was impacted by sewage outflow, to 33.3% in 1990, after the sewage outflow was diverted to deeper waters outside of the bay. In addition, the percent coral cover generally increased with decreasing depth to a maximum cover of >40% where $D = 2$ m. From the ASV survey of the coconut patch reef, the percent coral cover was also found to increase as depth decreased; coral cover was 28.4% ($N = 1{,}800$) where $D \leq 4$ m and 63.4% ($N = 688$) where $D \leq 3$ m.

As a further test of the utility of the red edge algorithm, Equation (14) was applied to the AVIRIS image of the entire Kane'ohe Bay (**Figure 15**). The results indicated areas of high vegetative biomass that were in agreement with the reported distribution of near-surface coral cover (e.g., Bahr et al., 2015 and references cited therein). Highest REH_N values were found fringing many of the shallow banks bordering the coastline, including Coconut Island, and over many of the small patch reefs in the northern bay. Shallow, bright areas that were relatively barren of healthy coral were generally characterized as low REH_N. While the central portions of the Ahu O Laka barrier island indicated relatively low REH_N values, the seaward side of the island, where the bottom gradually falls off to the deeper waters of the adjacent Pacific Ocean, revealed a broad area of moderate REH_N.

Contrary to the patch reefs in the northern portion of the bay, the coconut patch reef did not stand out within the AVIRIS imagery as higher REH_N values relative to the surrounding deeper water, even though data from the ASV survey indicated slightly enhanced red edge features detectable at depths of between 3 and 4 m, (**Figure 11**). This result may have been due to the observed heterogeneity of benthic features across the coconut patch reef. Coral cover and vibrancy in dredged areas of the southern portion of the bay had not yet recovered to pre-dredging conditions (Jokiel, 1991). Thus, less coral cover, deeper average coral depth, and less clear water resulted in more subtle differences between the remotely sensed signals from coral and the adjacent deep water. In addition, the *in situ* measurements represent reflectance averaged across a much smaller area (0.08–0.31 m^2) compared with a typical AVIRIS pixel (49 m^2). The averaging of coral and sediment signals across an AVIRIS pixel would have tended to decrease REH_N. Thus, the useful depth of remotely sensed REH_N was somewhat less than 3 m within the southern portion of the bay. The depth limit for detecting REH_N from healthy coral was expected to be deeper within the northern portion of the bay where coral cover was greater, the water was more transparent due to flushing with adjacent ocean waters, and the reefs had not been impacted by dredging activities.

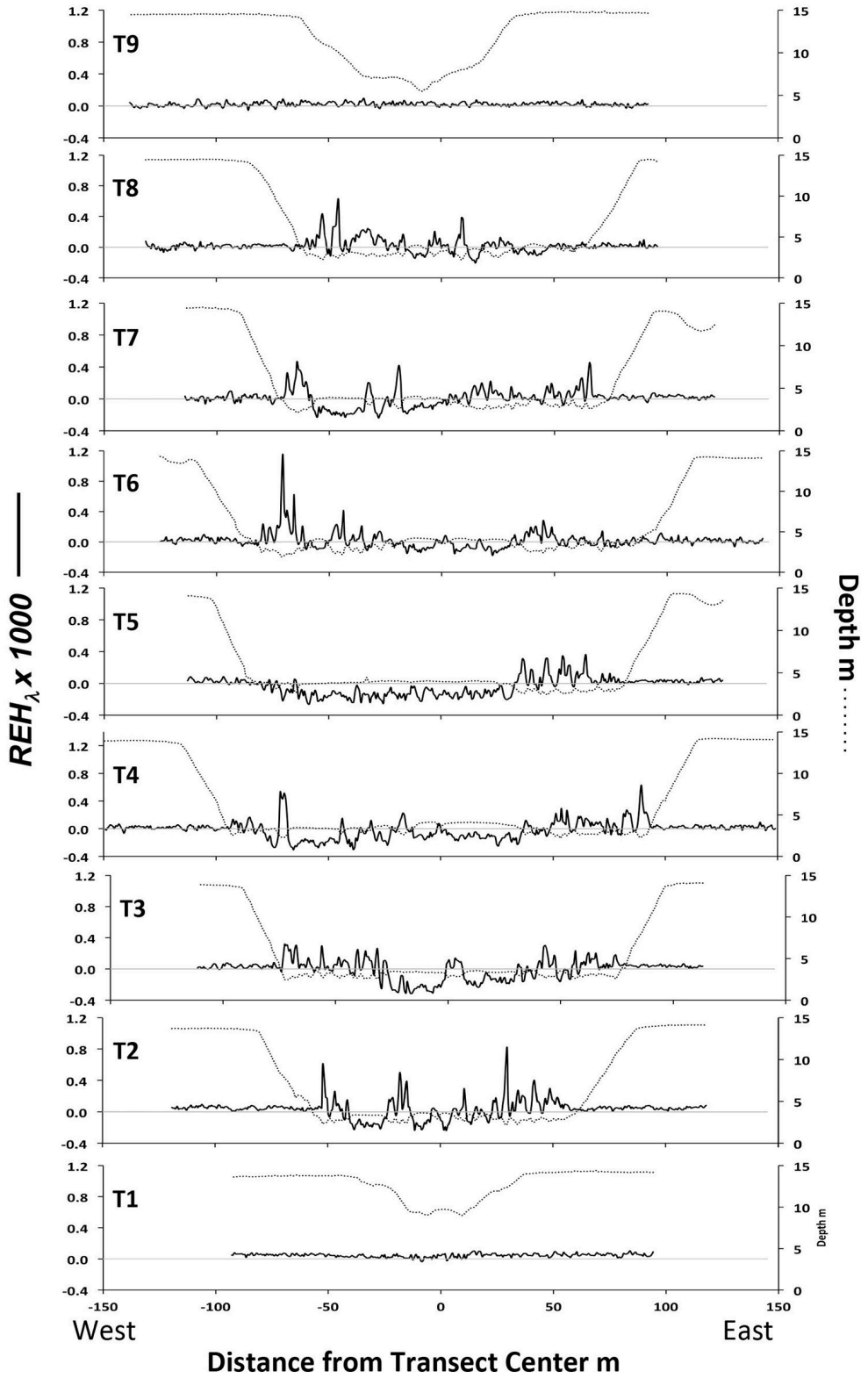

FIGURE 14 | Red edge height (REH_λ, solid curves) and depth (dotted curves) representing observations collected by the ASV along transects across the coconut patch reef.

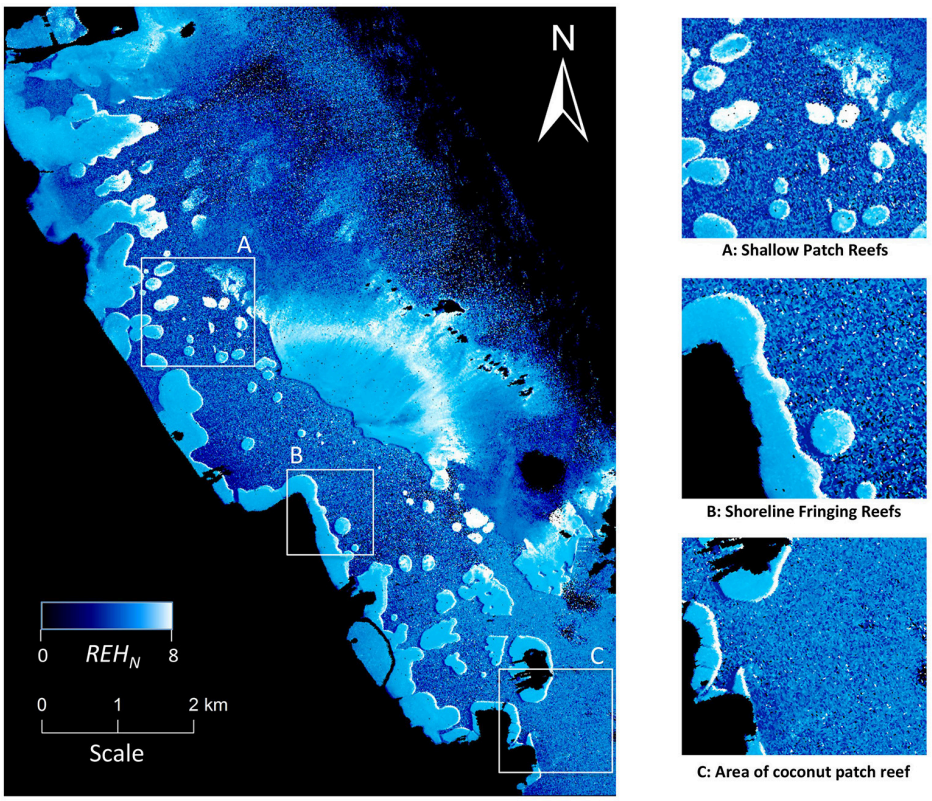

FIGURE 15 | REH_N derived from AVIRIS imagery of Kane'ohe Bay collected on 3 March 2017. Land, clouds, and values of $REH_N < 0$ are displayed as black. **(A)** Shallow patch reefs in the northern bay yielded some of the largest signals. **(B)** Narrow fringing reefs along the coastline are well resolved. **(C)** REH_N from the area of the coconut patch reef, where $D > 3$ m, was not significantly different than the surrounding deep water.

DISCUSSION

The ASV was shown to rapidly survey physical and optical properties of the coconut patch reef in high spatial resolution. Simultaneous measurements of bathymetry and reflectance from acoustical sensors were in agreement with optical signals and in-water photographic evidence of bottom features associated with coral and uncolonized sediment. *In situ* measurements of remote sensing reflectance were shown to reasonably match surface reflectance derived from atmospherically corrected measurements from an imaging spectrometer deployed at high altitude. *In situ* data, collected over the course of a 2 h autonomous survey, comprised over 10,000 sets of simultaneous optical and acoustical observations representing a diverse combination of bottom type and cover, water depth, sea state, and illumination. Highly diverse data sets, such as this, should permit more scientific and technical questions to be addressed than would be possible with traditionally sparse and less diverse data sets collected manually by divers. Additionally, the sampling error associated with radiometer orientation and cloud cover was determined to be small and to have no discernable impact on *in situ* remote sensing reflectance. Consequently, these results suggested that valid field surveys could be conducted under more diverse environmental conditions, including those that would confound high-altitude aircraft or satellite-based remote sensing operations. The insensitivity of remote sensing reflectance to cloud cover also suggested that under-cloud remote sensing, e.g., the application of drone-based sensors, is possible with minimal impact on algorithm performance.

Autonomous observations of high resolution spectral and spatial measurements of the visible and near infrared spectrum with radiometers positioned above and below the water surface provided detailed information regarding a large range in reef environmental conditions and permitted the investigation of a potential remote sensing algorithm and the associated limits of application. The red edge signal, characteristic of healthy vegetation, was shown to reveal the presence of live coral and turf algae and provided a means of distinguishing between benthic vegetation and uncolonized sediments within shallow water. While the REH_N was shown to decrease with depth due to attenuation of the light reflected from benthic features, the signal was detectable over the coconut patch reef at depths of between 3 m and 4 m using *in situ* observations. However, the REH_N signal over the coconut patch reef computed from AVIRIS imagery, while similar to the *in situ* determinations, were not significantly different from the surrounding deep water signal, and suggested that remote determinations may be limited to areas where $D < 3$ m, at least in the southern portions of the bay. The REH_N algorithm applied to the AVIRIS image of the entire Kane'ohe Bay revealed shallow areas known to contain moderate to dense

coral cover. These results, including the negative results over the coconut patch reef, were in general agreement with a previous application of AVIRIS imagery to map coral and algae within Kane'ohe Bay using spectral matching techniques (Goodman and Ustin, 2007).

The detailed hyperspectral signal was necessary to optimize the wavelength range for the REH_N algorithm, but once determined, only three wavelengths were required for an effective algorithm; two wavelengths bracketing the red edge signal, e.g., 675 and 740 nm, and one wavelength representing the *REH* peak, e.g., 705 nm. Any remote sensor meeting these requirements should be able to detect the red edge signal from shallow coral environments, assuming that the spatial resolution is appropriate. The Landsat series of satellites, for example, with 30 m spatial resolution, have been used to map coral reefs (e.g., Palandro et al., 2008) and the most recent Landsat multispectral sensor to date, the Operational Land Imager (OLI) onboard Landsat-8, has five bands spread across the visible and near-infrared spectrum. Within the red edge region, band 4 (centered at 655 nm, $\Delta\lambda = 50$ nm) and band 5 (centered at 865 nm, $\Delta\lambda = 40$ nm) could potentially serve to bracket the red edge region, but there is no appropriate intermediate band coinciding with the peak REH_λ wavelengths. The Multispectral Imager (MSI) onboard the Sentinel-2 satellite, on the other hand, has a higher spatial resolution, between 10 and 20 m, compared to OLI data, and it includes several bands that could satisfy an REH_N algorithm; band 4 (665 nm, $\Delta\lambda = 10$ nm), band 5 (705 nm, $\Delta\lambda = 10$ nm), and band 6 (740 nm, $\Delta\lambda = 10$ nm). In fact, MSI bands 5 and 6 were selected specifically for detecting red edge signals from terrestrial vegetation. However, spatial convolution of the benthic signal across a 10 m ground sampling distance may reduce the maximum depth of red edge detection where coral coverage is sparse, as was the case with the AVIRIS data (with 7 m spatial resolution) collected over the coconut patch reef. Thus, the optimum spatial resolution for coral reef remote sensing remains an open question.

However, in order to measure the peak *REH* wavelength, which is expected to be sensitive to the depth of the vegetative material, the entire red and near-infrared portion of the spectrum must be measured in high spectral resolution. To date, there are no operational satellite systems capable of providing such data.

One limitation of the REH_N algorithm was that it could not alone distinguish between the type of vegetation responsible for the signal. Coral, turf algae, sea grass, and any floating vegetation would all result in similar signals. Therefore, application of the REH_N algorithm would require a level of a priori knowledge about the study site that may not exist for remote locations. While this can be problematic for remote observations, an *in situ* autonomous system that includes in-water imagery, such as the system developed for this project, provides a degree of benthic classification capability that can be used to parse the data and provide class-specific statistics.

We have illustrated the utility of a low-cost, commercially available, coastal kayak, modified for autonomous operations and instrumented with optical and acoustical sensors to survey coral reefs in support of remote sensing operations. We examined the utility of the red edge height as an indicator of live coral and algae and, based on the results, constructed a remote sensing algorithm to map corals in shallow water within Kane'ohe Bay. A more complete examination of the red edge signal may potentially yield information regarding benthic cover and biomass, e.g., as a function of REH_λ amplitude, and water depth derived from the peak REH_λ wavelength. While these results are encouraging, the details of REH_λ response to physical conditions (e.g., water depth and optical properties) and vegetation type (e.g., coral and algae species), cover, and health (e.g., the effects of coral bleaching) remain to be elucidated.

DATA AVAILABILITY

All data are freely available through public access repositories; the *in situ* radiometer and inherent optical property data may be downloaded from the NASA SeaBASS ocean optics data repository (https://seabass.gsfc.nasa.gov) and AVIRIS data may be obtained from the NASA Jet Propulsion Laboratory (https://aviris.jpl.nasa.gov). All acoustical data are available from the authors upon request.

AUTHOR CONTRIBUTIONS

All authors contributed significantly to the writing and/or final editing of the manuscript. SA was the lead author and was responsible for integration and analysis of all data and the writing of the manuscript. JS was the lead for the development, testing, and operations of the ASV and was responsible for the analysis of all of the acoustical and navigation data associated with the *in situ* survey. LR was responsible for analysis of the acoustical and YSI EXO2 data. WM was responsible for the analysis of the AVIRIS hyperspectral data, including implementation of the REH_N algorithm. BR was responsible for the collection and analysis of the *in situ* water optical properties data.

FUNDING

Financial support for this project was provided by the National Aeronautic and Space Administration HyspIRI Program through grants NNH15AB471 and NNX16AB05G, the U.S. Naval Research Laboratory, and the Midshipman Research Office at the U.S. Naval Academy.

ACKNOWLEDGMENTS

The authors are grateful to Dr. Ruth Gates and the University of Hawai'i Marine Biological Laboratory for their generous time and logistical support while operating out of Coconut Island, Dr. Art Tremabanis and Mr. Timothy Pilegard of the University of Delaware, and Mr. Andrew Keppel, MIDN Brian Laboy, and MIDN Michael Madigan of the U. S. Naval Academy Oceanography Department for their support of the ASV development, testing, and operations, Joseph Rhea of the U. S. Naval Research Laboratory, Remote Sensing Division, for his aid in managing the *in situ* field data, and the Jet Propulsion Laboratory for timely access to the AVIRIS imagery collected over Kane'ohe Bay. Without their efforts, this project would not have been possible.

REFERENCES

Anthony, K. R. N., Kline, D. I., Diaz-Pulido, G., Dove, S., and Hoegh-Guldberg, O. (2008). Ocean acidification causes bleaching and productivity loss in coral reef builders. *Proc. Natl. Acad. Sci. U.S.A.* 105, 442–446. doi: 10.1073/pnas.0804478105

Babin, M., Morel, A., Fournier-Sicre, V., Fell, F., and Stramski, D. (2003). Light scattering properties of marine particles in coastal and open ocean waters as related to the particle mass concentration. *Limnol. Oceanogr.* 48, 843–859. doi: 10.4319/lo.2003.48.2.0843

Bahr, K. D., Jokiel, P. L., and Toonen, R. J. (2015). The unnatural history of Kane'ohe Bay: coral reef resilience in the face of centuries of anthropogenic impacts. *PeerJ* 3:e950. doi: 10.7717/peerj.950

Chavez, P. S. (1996). Image-based atmospheric corrections - revisited and improved. *Photogr. Eng. Rem. Sens.* 62, 1025–1036.

Curcio, J., Leonard, J., and Patrikalakis, A. (2005). "SCOUT - A low cost autonomous surface platform for research in cooperative autonomy," in *Proceedings of MTS/IEEE OCEANS* (Washington, DC).

Dekker, A. G., Phinn, S. R., Anstee, J., Bissett, P., Brando, V. E., Casey, B., et al. (2011). Intercomparison of shallow water bathymetry, hydro-optics, and benthos mapping techniques in Australian and Caribbean coastal environments. *Limnol. Oceanogr. Methods* 9, 396–425. doi: 10.4319/lom.2011.9.396

Dierssen, H., and Russell, B. (2017). *Coral Reef Airborne Laboratory. SeaWiFS Bio-optical Archive and Storage System (SeaBASS).* NASA. doi: 10.5067/SeaBASS/CORAL/DATA001

Felella, I., and Penuelas, J. (1994). The red edge position and shape as indicators of plant chlorophyll content, biomass and hydric status. *Int. J. Rem. Sens.* 15, 1459–1470.

Fyfe, S. K. (2003). Spatial and temporal variation in spectral reflectance: Are seagrass species spectrally distinct? *Limnol. Oceanogr.* 48(pt. 2), 464–479. doi: 10.4319/lo.2003.48.1_part_2.0464

Gates, D. M., Keegan, H. J., Schleter, J. C., and Weidner, V. R. (1965). Spectral properties of plants. *Appl. Opt.* 4, 11–20. doi: 10.1364/AO.4.000011

Gleason, A. C. R., Reid, R. P., and Voss, K. J. (2007). "Automated classification of underwater multispectral imagery for coral reef monitoring," in *Proceedings of Oceans* 2007 (Vancouver, BC).

Goodman, J. A., and Ustin, S. L. (2007). Classification of benthic composition in a coral reef environment using spectral unmixing. *J. Appl. Re. Sens*. 1:011501. doi: 10.1117/1.2815907

Gordon, H. R., Brown, O. B., Evans, R. H., Brown, J. W., Smith, R. C., Baker, K. S., et al. (1988). A semianalytic radiance model of ocean color. *J. Geophys. Res.* 93, 10909–910924. doi: 10.1029/JD093iD09p10909

Hedley, J. D., Harborne, A. R., and Mumby, P. J. (2005). Simple and robust removal of sun glint for mapping shallow-water benthos. *Int. J. Rem. Sens*. 26, 2107–2112. doi: 10.1080/01431160500034086

Hochberg, E. J., and Atkinson, N. J. (2000). Spectral discrimination of coeal reef benthic communities. *Coral Reefs* 19, 164–171. doi: 10.1007/s003380000087

Hochberg, E. J., Atkinson, N. J., and Andréfouët, S. (2003). Spectral reflectance of coral reef bottom-types worldwide and implications for coral reef remote sensing. *Rem. Sens. Env*. 85, 159–173. doi: 10.1016/S0034-4257(02)00201-8

Hoegh-Guldberg, O. (2011). "The impact of climate change on coral reef ecosystems," in *Coral Reefs: An Ecosystem in Transition*, eds Z. Dubinsky and N. Stambler (Dordrecht: Springer), 391–403.

Hughes, T. P., Baird, A. H., Bellwood, D. R., Card, M., Connolly, S. R., Folke, C., et al. (2003). Climate change, human impacts, and the resilience of coral reefs. *Science* 301, 929–933. doi: 10.1126/science.1085046

Hunter, C. L., and Evans, C. W. (1995). Coral reefs in Kane'ohe Bay, Hawai'i: Two centuries of western influence and two decades of data. *Bull. Mar. Sci.* 57, 501–515.

Jokiel, P. L. (1991). *Jokiel's Illustrated Scientific Guide to Kane'ohe Bay*. Kaneohe: University of Hawaii.

Kirk, J. T. O. (1984). Dependence of relationship between inherent and apparent optical properties of water on solar altitude. *Limnol. Oceanogr*. 29, 350–356.

Kleypas, J. A., McManus, J. W., and Menez, L. A. B. (1999). Environmental limits to coral reef development: Where do we draw the line? *Am. Zool.* 39, 146–159.

Kutser, T., Dekker, A. G., and Skirving, W. (2003). Modeling spectral discrimination of Great Barrier Reef benthic communities by remote sensing instruments. *Limnol. Oceanogr*. 48(1, part 2), 497–510. doi: 10.4319/lo.2003.48.1_part_2.0497

Lee, C. M., Cable, M. L., Hook, S. J., Green, R. O., Ustin, S. L., Mandl, D. J., et al. (2015). An introduction to the NASA Hyperspectral Infrared Imager (HyspIRI) mission and preparatory activities. *Rem. Sens. Environ*. 167, 6–19. doi: 10.1016/j.rse.2015.06.012

Lee, Z. P., Carder, K. L., Mobley, C. D., Steward, R. G., and Patch, J. S. (1999). Hyperspectral remote sensing for shallow waters: 2. Deriving bottom depths and water properties by optimization. *Appl. Opt*. 38, 3831–3843.

Lirman, D., Gracias, N. R., Gintert, B. E., Gleason, A. C., Reid, R. P., Negahdaripour, S., et al. (2007). Development and application of a video-mosaic survey technology do document the status of coral reef communities. *Environ. Monit. Assess*. 125, 59–73. doi: 10.1007/s10661-006-9239-0

Maritorena, S., Morel, A., and Gentili, B. (1994). Diffuse reflectance of oceanic shallow waters: influence of water depth and bottom albedo. *Limnol. Oceanogr*. 39, 1689–1703.

Moberg, F., and Folke, C. (1999). Ecological goods and services of coral reef ecosystems. *Ecolog. Econom*. 29, 215–233.

Mobley, C. D. (1994). *Light and Water*. San Diego, CA: Academic Press.

Mobley, C. D., and Sundman, L. K. (2012). *Hydrolight 5.1 Ecolight 5.1 Users Guide*. Bellevue, WA: Sequoia Sequoia Scientific.

Odum, H. T., and Odum, E. P. (1955). Trophic structure and productivity of a windward coral reef community on Eniwetok Atoll. *Ecol. Monogr*. 25, 291–320.

Palandro, D. A., Andréfouët, S., Hu, C., Hallock, P., Muller-Karger, F. E., Dustan, P., et al. (2008). Quantification of two decades of challoe-water reef habitat decline in the Florida Kys National Marine Sanctuary using Landsat data (1984-2002). *Rem. Sens. Environ*. 112, 3388–3399. doi: 10.1016/j.rse.2008.02.015

Philpot, W. D. (1987). Radiative transfer in stratified waters: a single-scattering approximation of irradiance. *Appl. Opt*. 26, 4123–4132. doi: 10.1364/AO.26.004123

Philpot, W. D. (1989). Bathymetric mapping with passive multispectral imagery. *Appl. Opt*. 28, 1569–1578.

Pope, R. M., and Fry, E. S. (1997). Absorption spectrum (380–700 nm) of pure water. II. Integrating cavity measurements. *Appl. Opt*. 36, 8710–8723. doi: 10.1364/AO.36.008710

Shihavuddin, A. S. M., Gracias, N., Garcia, R. Gleason, A. C. R., and Gintert, B. (2013). Image-based coral reef classification and thematic mapping. *Rem. Sens*. 5, 1809–1841. doi: 10.3390/rs5041809

Smith, R. C., and Baker, K. S. (1981). Optical properties of the clearest natural waters (200-800 nm). *Appl. Opt*. 20, 177–184.

Spurgeon, J. P. G. (1992). The economic value of coral reefs. *Mar. Pol. Bull*. 24, 529–536.

Vane, G., Green, R. O., Chrien, T. G., Enmark, H. T., Hansen, E. G., and Porter, W. M. (1993). The airborne visible/infrared imaging spectrometer (AVIRIS). *Rem. Sens. Environ*. 44, 127–143.

Wood, S., Rees, M., and Pfeiffer, Z. (2007). "An autonomous self-mooring vehicle for littoral and coastal observations," in *OCEANS 2007* (Aberdeen, UK).

Zimmerman, R. C. (2003). A biooptical model of irradiance distribution and photosynthesis in seagrass canopies. *Limnol. Oceanogr*. 48(1 pt. 2), 568–585. doi: 10.4319/lo.2003.48.1_part_2.0568

Conflict of Interest Statement: The authors declare that the research was conducted in the absence of any commercial or financial relationships that could be construed as a potential conflict of interest.

frontiers in Marine Science

ORIGINAL RESEARCH
published: 26 October 2017
doi: 10.3389/fmars.2017.00329

Application of Landsat 8 for Monitoring Impacts of Wastewater Discharge on Coastal Water Quality

Rebecca C. Trinh[1,2], Cédric G. Fichot[3], Michelle M. Gierach[1], Benjamin Holt[1], Nabin K. Malakar[1,4], Glynn Hulley[1] and Jayme Smith[5]*

[1] Jet Propulsion Laboratory, California Institute of Technology, Pasadena, CA, United States, [2] Lamont Doherty Earth Observatory, Department of Earth and Environmental Science, Columbia University, Palisades, NY, United States, [3] Department of Earth and Environment, Boston University, Boston, MA, United States, [4] Department of Earth, Environment, and Physics, Worcester State University, Worcester, MA, United States, [5] Department of Biological Sciences, University of Southern California, Los Angeles, CA, United States

In this study, we examine the capabilities of the Landsat 8 Operational Land Imager (OLI), Thermal Infrared Sensor (TIRS), and Aqua Moderate resolution Imaging Spectroradiometer (MODIS) for monitoring the environmental impact of the 2015 Hyperion Treatment Plant (HTP) wastewater diversion in Santa Monica Bay, California. From 21 September–2 November 2015, the HTP discharged $\sim 39 \times 10^3$ m^3 h^{-1} of treated wastewater into Santa Monica Bay through their emergency 1-mile outfall pipe. Multi-sensor satellite remote sensing was employed to determine the biophysical impact of discharged wastewater in the shallow nearshore environment. Landsat 8 TIRS observed decreased sea surface temperatures (SST) associated with the surfacing wastewater plume. Chlorophyll-a (*chl-a*) concentrations derived from Landsat 8 OLI and Aqua MODIS satellite sensors were used to monitor the biological response to the addition of nutrient-rich wastewater. *In situ chl-a* and *in situ* remote sensing reflectance (*Rrs*) were measured before, during, and after the diversion event. These *in situ* data were paired with coincident OLI and MODIS satellite data to yield a more comprehensive view of the changing conditions in Santa Monica Bay due to the wastewater diversion. Two new local *chl-a* algorithms were empirically derived using *in situ* data for the OLI and MODIS sensors. These new local *chl-a* algorithms proved more accurate at measuring *chl-a* changes in Santa Monica Bay compared to the standard open ocean OC2 and OC3M algorithms, and the regional southern California CALFIT algorithm, as validated by *in situ chl-a* measurements. Additionally, the local OLI algorithm outperformed the local MODIS algorithm, especially in the nearshore region. A time series of *chl-a*, as detected by the local OLI *chl-a* algorithm, illustrated a very large increase in *chl-a* concentrations during the wastewater diversion, and a subsequent decrease in *chl-a* after the diversion. Our study demonstrates the capability of using Landsat 8 TIRS and OLI sensors for the monitoring of SST and surface *chl-a* concentrations at high spatial resolution in nearshore waters and highlights the value of these sensors for assessing the environmental effects of wastewater discharge in a coastal environment.

Keywords: Landsat 8, Chlorophyll, coastal water quality, sea surface temperature (SST), wastewater diversion, satellite remote sensing

OPEN ACCESS

Edited by:
Kevin Ross Turpie, University of Maryland, Baltimore County, United States

Reviewed by:
Saumitra Mukherjee, Jawaharlal Nehru University, India
Oliver Zielinski, University of Oldenburg, Germany

****Correspondence:***
Rebecca C. Trinh
rtrinh@ldeo.columbia.edu

Specialty section:
This article was submitted to Coastal Ocean Processes, a section of the journal Frontiers in Marine Science

Received: *03 August 2017*
Accepted: *04 October 2017*
Published: *26 October 2017*

Citation:
Trinh RC, Fichot CG, Gierach MM, Holt B, Malakar NK, Hulley G and Smith J (2017) Application of Landsat 8 for Monitoring Impacts of Wastewater Discharge on Coastal Water Quality. Front. Mar. Sci. 4:329. doi: 10.3389/fmars.2017.00329

INTRODUCTION

The coastal waters of the Southern California Bight border one of the most densely populated regions in North America and are increasingly affected by pollution from both publicly owned treatment works (POTWs) and stormwater runoff due to increasing population growth and urbanization (McKinney, 2002; Bay et al., 2003; Creel, 2003; Schiff and Bay, 2003; Crossett et al., 2004; Lyon and Stein, 2009; Gierach et al., 2017; Holt et al., 2017). The Hyperion Treatment Plant (HTP) is the largest POTW in the Southern California Bight, discharging wastewater directly into Santa Monica Bay. Servicing the Los Angeles Metropolitan Area, HTP releases a daily average of 8.71×10^5 m^3 of secondary treated effluent into Santa Monica Bay via a 5-mile (8.1 km) outfall pipe (Southern California Coastal Water Research Project, 1973; Steinberger and Stein, 2004; Lyon and Stein, 2009). However, during diversion events, when their main 5-mile outfall pipe is temporarily shut down, HTP diverts the wastewater to their 1-mile (1.2 km) outfall pipe, discharging the wastewater into the nearshore environment of Santa Monica Bay (**Figure 1**). Based on the findings from a 2006 inspection and diversion event (Reifel et al., 2013; Gierach et al., 2017), HTP scheduled another diversion event in Fall 2015 in order to conduct necessary infrastructure repairs. During this 6-week diversion event from 21 September−2 November 2015, HTP discharged an average of 39×10^3 m^3 h^{-1} of treated wastewater through their backup 1-mile outfall pipe into the coastal environment.

Secondary treated effluent released in coastal waters not only contains contaminants (e.g., harmful chemicals, coliform bacteria, oils, and metals), but also organic matter and nutrients that can affect water quality (Steinberger and Stein, 2004). Wastewater effluent has been found to contribute as much nitrogen to coastal regions as wind-driven upwelling in several sub-regions of the Southern California Bight, including Santa Monica Bay, thereby doubling the nitrogen load (Howard et al., 2014; McLaughlin et al., 2017). A primary environmental concern of the release of nutrient-rich wastewater into the Southern California Bight is the stimulation of primary production, which can lead to eutrophication and the proliferation of toxic harmful algal blooms (Caron et al., 2017). Under typical density-stratification conditions for the region, the discharge of wastewater near the head of the Santa Monica Submarine Canyon (8.1 km offshore at 57 m depth), limits the likelihood that wastewater will surface and affect marine life and human health (Washburn et al., 1992; Uchiyama et al., 2014). In contrast, the 1-mile outfall pipe terminates within the shallow nearshore region of Santa Monica Bay, discharging the wastewater at 18 m depth. During diversion events, the discharge of wastewater through the 1-mile outfall pipe increases contaminant and nitrogen concentrations in the shallow and sunlit coastal waters of Santa Monica Bay, thereby increasing the probability of phytoplankton blooms and contaminant exposure to marine life and humans, as Santa Monica Bay is a major coastal recreation area (Caron et al., 2017; Gierach et al., 2017).

With the advent and continued advancement in satellite sensors, remote sensing has become an effective tool for monitoring the biophysical impacts of coastal pollution (e.g., DiGiacomo et al., 2004; Hu et al., 2004; Nezlin and DiGiacomo, 2005; Nezlin et al., 2005, 2008, 2012; Marmorino et al., 2010; Holt et al., 2017). Radar, thermal, and optical sensors have, respectively, been used to track the surface expression of wastewater plumes through reduced sea surface roughness, decreased temperature, and changes in surface-water reflectance due to increased organic matter (DiGiacomo et al., 2004; Marmorino et al., 2010; Nezlin et al., 2012). Most recently, Gierach et al. (2017) demonstrated the capabilities of the Moderate resolution Imaging Spectroradiometer (MODIS), on board NASA's Aqua satellite, launched in 2002, and the Advanced Spaceborne Thermal Emission and Reflection Radiometer (ASTER), on board NASA's Terra satellite, launched in 1999, in detecting changes in chlorophyll-*a* (*chl-a*) and sea surface temperature (SST) associated with the surfacing wastewater plume during the 2006 HTP diversion. *Chl-a*, a photosynthetic pigment present in phytoplankton, can be measured by optical satellite sensors, and is used as a proxy for phytoplankton biomass in the surface ocean.

Satellite remote sensing greatly expands the spatio-temporal coverage of the marine environment compared to *in situ* monitoring. However, the coarse spatial resolution (∼750–1 km at nadir) of current optical satellite sensors used to monitor marine environments, and the uncertainties associated with instrument calibration and data processing algorithms in optically complex water (McClain, 2009), have limited the ability to monitor water quality in urban coastal waters like Santa Monica Bay. While improvements have been made in on-orbit assessment of sensor characteristics, atmospheric correction, and sensor calibration procedures over time (Franz et al., 2007), the resolution of current ocean color sensors still remains one of the most limiting factors for water quality applications in nearshore areas, as they are unable to accurately resolve coastal ocean characteristics (Mouw et al., 2015). The Thermal Infrared Sensor (TIRS) and the Operational Land Imager (OLI) on board Landsat 8, launched in 2013, provide two high-resolution sensors with high signal-to-noise ratios to more precisely monitor biophysical changes in the coastal Santa Monica Bay. With 100 m and 30 m spatial resolution, respectively, TIRS and OLI are better suited to resolve detailed features of SST and surface *chl-a* in the nearshore region compared to MODIS (1 km) and other similar satellite sensors, e.g., SeaWiFS (1.1 km), AVHRR (1.1 km), and VIIRS (750 m). Additionally, improved sensor signal-to-noise ratio and radiometric resolution of OLI and TIRS, compared to its predecessors, e.g., Landsat 7 ETM+, permits use of these land-designed sensors for marine applications. For example, the ability to monitor water quality in coastal regions, as coastal waters are generally dark targets, requires better signal-to-noise ratio and radiometric resolution to accurately resolve coastal features (Vanhellemont and Ruddick, 2014).

Though high-resolution sensors are likely to yield more detailed measurements than their coarser resolution counterparts, discrepancies in satellite *chl-a* values continue to be common in optically complex nearshore waters, such as the Southern California Bight (Kim et al., 2009). Therefore, we argue

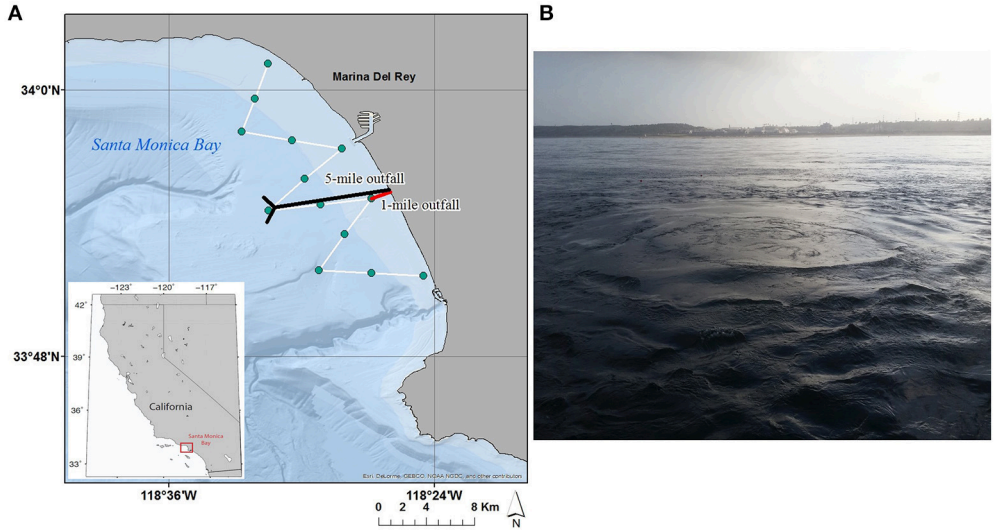

FIGURE 1 | (A) Map of Santa Monica Bay, California, with the 5-mile and 1-mile outfall pipes denoted as black and red lines, respectively, and *in situ* sampling stations denoted as green circles. **(B)** Photo of the wastewater plume surfacing at the terminus of the 1-mile outfall pipe during the diversion.

the necessity for the derivation and application of more locally derived empirical *chl-a* algorithms, as opposed to the standard open-ocean *chl-a* algorithms commonly used for each satellite sensor. In this study, we investigate the utility of high-resolution Landsat 8 TIRS and OLI satellite sensors, as compared to coarser resolution Aqua MODIS, in conjunction with corresponding *in situ* field measurements, to monitor the biophysical impacts of the Fall 2015 HTP wastewater diversion in Santa Monica Bay. Standard *chl-a* algorithms for each sensor are compared to newly derived empirical local *chl-a* algorithms, tuned specifically for the optically complex nearshore waters of Santa Monica Bay to accurately distinguish *chl-a* from other optical constituents in the water, such as suspended sediments and colored dissolved organic matter (CDOM). To the extent of our knowledge, this study is the first to develop, validate, and apply OLI *chl-a* retrievals for water quality monitoring in coastal waters.

The paper is organized as follows. Section Data and Methods describes the study region of Santa Monica Bay and the data utilized, including *in situ*, TIRS SST, satellite *chl-a* as detected by OLI and MODIS using standard and newly derived local *chl-a* algorithms. Section Data and Methods also describes the development of the local *chl-a* algorithms using *in situ chl-a* and *in situ* remote sensing reflectance (*Rrs*) measurements during the wastewater diversion. Results from the Fall 2015 HTP diversion are presented in section Results. Finally, in section Discussion we discuss the satellite findings and application of the newly derived local Landsat 8 OLI *chl-a* algorithm to more accurately monitor the evolution of the biological impact of the wastewater diversion.

DATA AND METHODS

Study Area

Santa Monica Bay is a semi-enclosed nearshore bay in the Southern California Bight whose coastal waters are directly influenced by the densely-populated Los Angeles basin. The bay is characterized by a relatively wide continental shelf and features a mixture of submarine outcrops and canyons (**Figure 1**). The unique geography and coastal processes in the region create favorable conditions for a relatively productive coastal environment and diverse ecosystem (Hickey, 1992; Eganhouse and Venkatesan, 1993; Hickey et al., 2003; Corcoran and Shipe, 2011). Though the seasonal supply of nutrients from coastal upwelling is a major driver of phytoplankton biomass variability in Santa Monica Bay, there is increasing evidence that anthropogenic nutrient point sources also contribute significantly to the phytoplankton dynamics of the bay (Nezlin and Li, 2003; Corcoran and Shipe, 2011; Nezlin et al., 2012; Howard et al., 2014; Gierach et al., 2017).

In Situ Measurements

In situ samples and measurements in Santa Monica Bay were collected before, during, and after the wastewater diversion as part of a large collaborative sampling effort led by the City of Los Angeles' Environmental Monitoring Division (CLAEMD) to monitor the impacts of the HTP diversion on water quality (**Figure 1** and **Table 1**). The samples and measurements were collected onboard the R/V *La Mer* and R/V *Surveyor* along a grid of 13 stations between 26 August and 11 November 2015 (**Figure 1**). Three main categories of samples/measurements were collected *in situ*: (1) hydrographic data from a Conductivity-Temperature-Depth (CTD) instrument, (2) surface water samples for lab-based *chl-a* concentration analyses, and (3) radiometric measurements to derive *in situ* hyperspectral remote sensing reflectance (*Rrs*). When possible, the *in situ* sampling was planned to coincide with satellite overpasses in order to facilitate comparison between *in situ* measurements and remote sensing retrievals.

TABLE 1 | *In situ* and remote sensing sampling dates before, during, and after the wastewater diversion event in Santa Monica Bay.

Date	*In situ Chl-a*	*In situ Rrs*	OLI	MODIS
26 August 2015		X		
8 September 2015			X	X
16 September 2015	X	X		
23 September 2015	X			
24 September 2015		X	X	X
30 September 2015	X	X		
7 October 2015	X			
10 October 2015			X	X
14 October 2015	X	X		
17 October 2015	X			
21 October 2015	X	X		
26 October 2015		X	X	X
28 October 2015	X			
5 November 2015	X	X		
11 November 2015	X	X	X	X
27 November 2015			X	X

The diversion period (21 September – 2 November 2015) is highlighted in gray.

Hydrographic Profiles

Vertical hydrographic profiles were collected at all stations along the sample grid (**Figure 1**) using a SBE 19-plus Conductivity-Temperature-Depth (CTD) package (Sea-Bird Electronics, Inc. Bellevue WA), mounted on a rosette also equipped with a C-star transmissometer (WET Labs, Inc. Philomath, OR), and WETStar *chl-a* and CDOM fluorometers (WET Labs, Inc. Philomath, OR) (City of Los Angeles, 2009; Reifel et al., 2013) to determine temperature and chlorophyll fluorescence from 1 m below the surface to 1 m above the ocean floor.

In Situ Surface Chlorophyll-*a* Concentrations

Discrete surface water samples were collected at 1 meter for *chl-a* analysis at selected stations along the sample grid before, during, and after the wastewater diversion (**Figure 1**, **Table 1**). Duplicate water samples were collected from Niskin bottles and filtered immediately onboard the ship by gentle filtration of 5–100 mL of water onto 0.7-μm GF/F glass fiber filters. The filtration volume was reduced incrementally from 100 mL based on the biomass indicated by *in situ* chlorophyll fluorescence measured at 1 meter by the CTD profiler. Filters were then stored at −20°C until they were analyzed fluorometrically for *chl-a* in the laboratory using the non-acidification method (Welschmeyer, 1994). Filters were extracted in 100% acetone at −20°C in the dark for 24 h. Filter extracts were analyzed on a Turner Designs Trilogy fluorometer (Turner Designs, Sunnyvale, CA).

In Situ Remote Sensing Reflectance

In situ hyperspectral remote sensing reflectance, $Rrs(\lambda,0^+)$, was measured in the λ = 350–700 nm wavelength range at selected stations before, during, and after the diversion event (**Table 1**). $Rrs(\lambda,0^+)$ was derived from field measurements of spectral downwelling irradiance, $E_d(\lambda)$, and upwelling radiance, $L_u(\lambda)$, acquired using a Satlantic® HyperPRO free-falling optical profiler equipped with a surface irradiance reference. The measured $E_d(\lambda)$ and $L_u(\lambda)$ were used to calculate $Rrs(\lambda,0^+)$ following Equation (1):

$$Rrs(\lambda,0^+) = \frac{L_w(\lambda)}{E_d(\lambda,0^+)} \quad (1)$$

where $E_d(\lambda,0^+)$ is the spectral downwelling irradiance just above the surface and $L_w(\lambda)$ is the spectral water-leaving radiance, equivalent to $L_u(\lambda)$ measured just above the surface: $L_u(\lambda,0^+)$.

About half of the $Rrs(\lambda,0^+)$ spectra were measured and derived using the HyperPRO in profiling mode. In this configuration, simultaneous profiles of $E_d(\lambda,z)$ and $L_u(\lambda,z)$ (where z is depth) were used to calculate $Rrs(\lambda,0^+)$. The maximum depth of the optical profiles ranged from a few meters in nearshore waters to 60 m in the more oligotrophic waters. Profiles were performed away from the influence of the ship, at a distance of at least 30 m and on the sunny side of the ship. Any data with an instrument tilt of $>5^\circ$ was discarded. At each sampled station, measurements of $E_d(\lambda,z)$ and $L_u(\lambda,z)$ were collected during three or four optical profiles in clear waters, and up to 10 optical profiles in more shallow and turbid waters. The data were processed to Level-2 with the Satlantic® Prosoft software. Our own MatLab® routine was then used to do a supervised processing of the $E_d(\lambda,z)$ and $L_u(\lambda,z)$ profiles and calculate $Rrs(\lambda,0^+)$. In this routine, $E_d(\lambda,0^-)$ was calculated as the exponential of the intercept ($z = 0$) of the least-square fit of the pooled profiles of $\ln[E_d(\lambda,z)]$ against depth z, and it was then converted to $E_d(\lambda,0^+)$ using the approximation: $E_d(\lambda,0^+) = 1.04\ E_d(\lambda,0^-)$ (Austin, 1974). Similarly, $L_u(\lambda,0^-)$ was calculated as the exponential of the intercept ($z = 0$) of the least-square fit of the pooled $\ln[L_u(\lambda,0^-)]$ profiles against depth z, and it was then converted to $L_w(\lambda)$ using the approximation $L_w(\lambda) = 0.54\ L_u(\lambda,0^-)$ (Austin, 1974). Data from the multiple profiles were pooled together in order to provide sufficient data density to derive reliable linear fits of $E_d(\lambda,z)$ and $L_u(\lambda,z)$ against depth, and supervised processing with our MatLab® routine allowed to select adequate depth ranges (between 0.5 m to several meters depth) for reliable fits. At each station, profiles were collected within a short period of time (<20–30 min) and, in most cases, the illumination conditions were very stable throughout the data collection. Any $E_d(\lambda,z)$ and $L_u(\lambda,z)$ profile that differed substantially was discarded in order to minimize errors in the fit. Note here that the spectral diffuse attenuation coefficient of upwelling radiance, $K_{Lu}(\lambda)$, was also derived from these optical profiles as the slope of the least-square fit of the pooled $\ln[L_u(\lambda,0^-)]$ profiles against depth z.

The remainder of the $Rrs(\lambda,0^+)$ were measured and derived by using the HyperPRO deployed in buoy mode. The use of the buoy-mode configuration was done for practical reasons and in the interest of saving time during the sampling cruises. In this configuration, $E_d(\lambda,0^+)$ and $L_u(\lambda,0^-)$ were measured directly for a short time period of ∼2 min and used as in equation (1) to estimate $Rrs(\lambda,0^+)$ assuming $L_w(\lambda) = 0.54\ L_u(\lambda,0^-)$. The $L_u(\lambda,0^-)$ measurements were corrected for the fact that upwelling radiance was measured ∼ 0.2 m below the

water surface rather than just below the surface. Estimates of $K_{Lu}(\lambda)$ were thus used following the equation $L_u(\lambda,0^-) = L_u(\lambda,0.2)^*\exp(K_{Lu}(\lambda)^*0.2)$ to correct for the diffuse attenuation of $L_u(\lambda)$ occurring in the top 20 cm. However, $K_{Lu}(\lambda)$ could not be measured using the HyperPRO configured in "buoy mode" and therefore had to be estimated from uncorrected $Rrs(\lambda,0^+)$ determined by assuming $L_u(\lambda,0.2) = L_u(\lambda,0^-)$. The estimation of $K_{Lu}(\lambda)$ from the uncorrected $Rrs(\lambda,0^+)$ was made possible by using a partial-least-squares (PLS) regression model specifically developed for this study. The PLS model was developed using the other data set collected with the HyperPRO in "profiling mode": First, the $K_{Lu}(\lambda)$ and $Rrs(\lambda,0^+)$ derived from the profiles were used to simulate uncorrected $Rrs(\lambda,0^+)$. Then, a model of $K_{Lu}(\lambda)$ applicable to uncorrected $Rrs(\lambda,0^+)$ was developed by doing a PLS regression of $K_{Lu}(\lambda)$ on the simulated uncorrected $Rrs(\lambda,0^+)$. This PLS regression model, developed from the "profiling mode" data, was then applied to the "buoy mode" uncorrected $Rrs(\lambda,0^+)$ to provide a first-order approximation of $K_{Lu}(\lambda)$ and derive corrected values of $Rrs(\lambda,0^+)$ for that data set. The approach presented above only provides an approximate correction. However, the differences between corrected and uncorrected $Rrs(\lambda,0^+)$ amounted to no more than a few percent for the stations sampled in this study, and the uncertainties linked to this correction therefore have a minimal impact on the measured $Rrs(\lambda,0^+)$ and especially on $Rrs(\lambda,0^+)$ ratios. For simplicity, *in situ* $Rrs(\lambda,0^+)$ will be further denoted in the paper as *in situ Rrs*.

Development of Local Chlorophyll-*a* Algorithms

The *in situ* hyperspectral *Rrs* spectra and simultaneously collected *in situ chl-a* concentrations were used to develop local blue-green band-ratio algorithms applicable to Landsat 8 OLI and Aqua MODIS. A total of 96 *in situ chl-a* concentrations and 49 *in situ Rrs* measurements were collected over the 14-week period, with 36 of these measurements coinciding in time and space for deriving the local algorithms (**Table 1**). Briefly, the natural log values of the measured surface *chl-a* concentrations were regressed on the natural log values of blue-green *Rrs* ratios following Equation (2):

$$ln(chl\text{–}a) = a_0 + a_1\, ln(\frac{Rrs\ (\lambda blue)}{Rrs\ (\lambda green)}) \quad (2)$$

The hyperspectral *in situ Rrs* facilitated the development of two different local algorithms using the respective blue and green wavebands of OLI and MODIS (**Table 2**). The highly correlated logarithmic relationship between *in situ Rrs* and *in situ chl-a,* including the regression coefficients (R^2 = 0.90 and 0.89, respectively) and the coefficients of determination, are presented in **Figure 2** and **Table 2**. These local algorithms were expected to perform better than the standard global, open ocean *chl-a* algorithms (e.g., OC2 and OC3M) for this study because of the unusual environmental conditions caused by the wastewater diversion.

TABLE 2 | Respective OLI and MODIS red, green, and blue band wavelengths, and derived local *chl-a* satellite algorithm coefficients.

Sensor	Red band (nm)	Green band (nm)	Blue band (nm)	a0	a1
OLI	665	561	482	0.9375	−1.8862
MODIS	667	547	488	0.8822	−2.3694

Satellite Retrievals of Chlorophyll-*a* Concentrations

Satellite *Rrs* from Aqua MODIS and Landsat 8 OLI were used to monitor potential changes in *chl-a* concentration in Santa Monica Bay associated with the diversion (**Table 1**). Data from Aqua MODIS and Landsat 8 OLI were obtained for the region, before, during, and after the diversion from the Ocean Biology Distributed Active Archive Center (OB.DAAC; https://oceancolor.gsfc.nasa.gov) and the United States Geological Survey (USGS) EarthExplorer (https://earthexplorer.usgs.gov/), respectively. All satellite data were processed using the SeaWiFS Data Analysis System (SeaDAS) version 7.4 (https://oceancolor.gsfc.nasa.gov/seadas).

Aqua MODIS

Daily Aqua MODIS Level 1 radiance data were obtained from the OB.DAAC. SeaDAS was used to atmospherically correct MODIS optical radiance data, using a standard multi-scattering and iterative near infrared (NIR) model (Bailey et al., 2010) with bidirectional reflectance correction (Morel and Gentili, 1996), and generate a standard 1-km OC3M *chl-a* product. The 1-km *chl-a* product was then interpolated to a 250-m product (Franz et al., 2006) for a more detailed evaluation of the wastewater plume in the nearshore environment. The standard open-ocean OC3M model (Maritorena et al., 2002; Hu et al., 2012) was used to obtain *chl-a* measurements using the MODIS specific *Rrs* wavelengths in **Table 2**. Additionally, a more regional *chl-a* algorithm (CALFIT) developed by Kahru et al. (2012) for MODIS was used to potentially improve *chl-a* accuracy in Santa Monica Bay. The CALFIT algorithm was empirically derived from a large archive of *in situ chl-a* data for the coastal waters of the greater southern California Current system.

The local *chl-a* algorithm for MODIS (**Table 2**, **Figure 2B**), as well as the standard OC3M algorithm, and regional CALFIT algorithm were then applied to the MODIS-specific blue-green *in situ Rrs* retrievals to estimate *chl-a* concentrations. These values were compared to corresponding *in situ chl-a* measurements to determine the accuracy of each algorithm in Santa Monica Bay during the wastewater diversion. Additionally, each local and standard *chl-a* algorithm was then applied directly to MODIS satellite *Rrs* data. These remotely-sensed *chl-a* values were then directly compared to *in situ chl-a* measurements in order to determine the capability of MODIS under each algorithm in accurately detecting *chl-a* concentrations during the diversion. Due to its relatively coarse spatial resolution of 1 km, a single MODIS *chl-a* pixel value was compared to surface *in situ chl-a* from the corresponding station.

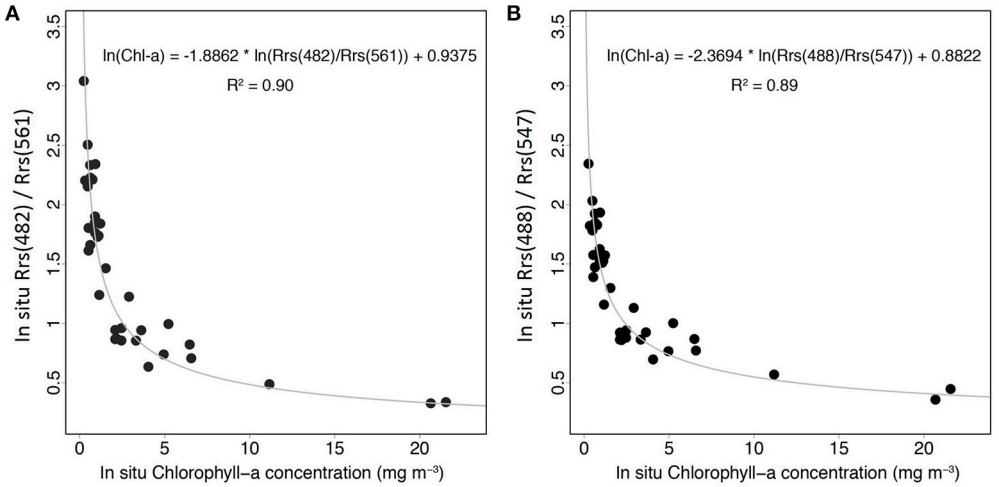

FIGURE 2 | Local empirical relationships between *in situ* surface *chl-a* concentrations and *in situ* blue-green *Rrs*: **(A)** OLI (blue: 482 nm and green: 561 nm), **(B)** MODIS (blue: 488 nm and green: 547 nm).

Landsat 8 OLI

Data from Landsat 8 OLI were obtained from the USGS EarthExplorer. The OLI radiance at the top of atmosphere data were atmospherically corrected, using the same methods described for MODIS, and processed to generate a standard OC2 *chl-a* product using SeaDAS (Werdell and Bailey, 2005). The local *chl-a* algorithm for OLI (**Table 2**, **Figure 2A**), as well as the standard OC2 OLI algorithm, were then applied to OLI-specific blue-green (**Table 2**) *in situ Rrs* retrievals to estimate *chl-a* concentrations. These values were compared to corresponding *in situ chl-a* measurements to determine the accuracy of each algorithm in Santa Monica Bay during the wastewater diversion. Additionally, each local and standard *chl-a* algorithm was then applied directly to OLI satellite *Rrs* data. These remotely-sensed *chl-a* values were then directly compared to *in situ chl-a* measurements in order to determine the capability of OLI under each algorithm in accurately detecting *chl-a* concentrations during the diversion. With its high spatial resolution of 30 m, a 3 × 3 pixel mean *chl-a* value around the sample station was compared to surface *in situ chl-a* from the corresponding station. A time series analysis was completed using the local *chl-a* algorithm for OLI in which maximum *chl-a* concentrations for each OLI scene were found within in Santa Monica Bay.

Landsat 8 TIRS Retrievals of Sea Surface Temperature

The effect of the surfacing wastewater plume on SST was monitored using Landsat 8 TIRS data obtained from the USGS EarthExplorer. TIRS has two longwave thermal bands, band 10 and 11 (10.3–11.3 μm and 11.5–12.5 μm, respectively), that can facilitate the retrieval of SSTs with a spatial resolution of 100 m, resampled to 30 m resolution. Stray light issues limit the applicability of the split-window algorithm traditionally used to derive SSTs from thermal imagery (Barsi et al., 2014; Montanaro et al., 2014). Therefore, we applied a single channel method developed by Malakar et al. (in preparation). The method uses physical emissivity data from ASTER GEDv3 (Hulley et al., 2015) and a radiative transfer model for atmospheric correction (Berk et al., 2005). Specifically, to estimate SST from observed thermal radiance data the measured radiance was (1) atmospherically corrected using a radiative transfer model (Berk et al., 2005), (2) the ASTER GEDv3 was spectrally adjusted to the TIRS wavebands, and (3) the temperature was retrieved by inverting the atmospherically and emissivity corrected TIRS radiances using a look-up table (Alley and Jentoft-Nilsen, 1999).

The TIRS band 10 data was used because it is less affected by the stray light issue than band 11 (Barsi et al., 2014). The correction algorithm of Montanaro et al. (2015), refined by Gerace and Montanaro (2017), was applied to the TIRS band 10 data to further reduce the effects of stray light. This stray light correction algorithm has since been implemented operationally into the Landsat Product Generation System in early 2017 by the USGS (Gerace and Montanaro, 2017), and methods are currently being developed to continually improve the accuracy of SST retrievals from the Landsat 8 TIRS. Herein, TIRS data are used solely to detect relative SST differences between plume and non-plume waters due to current limitations in TIRS-derived SST accuracy and lack of *in situ* skin temperature data collection during the diversion.

Additionally, MODIS Level 1 thermal infrared (TIR) radiance data were atmospherically corrected and processed to generate a standard 250-m product in SeaDAS, as described above in the Aqua MODIS section. However, given the spatially confined nature of the SST plume during the Fall 2015 diversion (**Figure 3B**), and the comparatively coarse spatial resolution of MODIS, MODIS TIR data were not able to detect changes in SST during the 2015 HTP wastewater diversion related to the wastewater plume (Supplemental Figure 1).

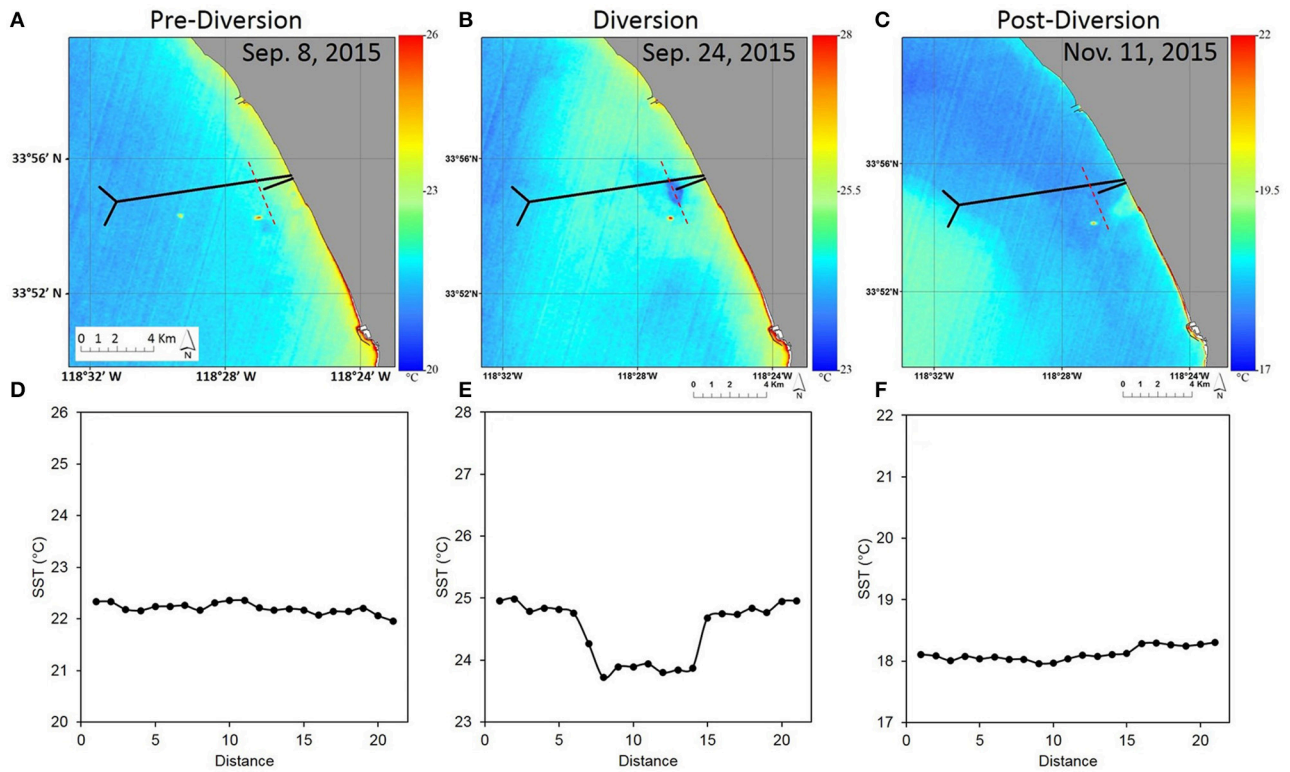

FIGURE 3 | (A–C) Landsat 8 TIRS-derived SST in Santa Monica Bay with the 5-mile and 1-mile outfall pipes shown as black lines and a 4 km alongshore transect at the terminus of the 1-mile outfall pipe denoted by red dashed lines. **(D–F)** SSTs across the 4 km alongshore transect, from north to south. **(A,D)** SST on 8 September 2015, pre-diversion; **(B,E)** SST on 24 September 2015, during the diversion; **(C,F)** SST on 11 November 2015, after the diversion. Cooler SSTs were detected at the terminus of the 1-mile outfall pipe during the diversion, due to entrainment of cold bottom water as the wastewater plume surfaced. Pre- and post-diversion, no SST anomalies were observed at the terminus of the 1-mile outfall pipe. The warm signature of an oil tanker to the southwest of the 1-mile outfall pipe is clearly visible. SSTs uniformly decreased from September to November due to seasonal cooling, therefore each image is shown on different temperature scales.

RESULTS

Wastewater Plume Detection via Sea Surface Temperature

The SST response to the wastewater plume was clearly detected by Landsat 8 TIRS (**Figure 3**). Before the diversion, on 8 September 2015, wastewater was being discharged from the 5-mile outfall pipe and no SST anomalies were detected in the vicinity of either the 5-mile or 1-mile outfall pipes (**Figure 3A**). **Figure 3D** shows no significant change in SST across an alongshore transect, shown as a dashed red line, in the vicinity of the 1-mile outfall pipe. During the diversion, on 24 September 2015, the wastewater was diverted from the 5-mile outfall pipe to the shallow (18 m depth) 1-mile outfall pipe and decreased SSTs were clearly detected at the terminus of the 1-mile outfall pipe in comparison to ambient waters (**Figures 3B,E**). The wastewater plume was ∼1°C colder than the surrounding water (**Figure 3B**). The depressed SSTs at the terminus of the 1-mile outfall pipe resulted from the entrainment of colder bottom water to the surface as the buoyant wastewater plume rose (Washburn et al., 1992; Marmorino et al., 2010; Rogowski et al., 2014). This cold SST signal was absent in MODIS TIR data from the same day, due to the coarse resolution of MODIS (Supplemental Figure 1). The wastewater was diverted back to the 5-mile outfall pipe on 2 November 2015, and by 11 November 2015, no SST anomalies were observed near either outfall pipe (**Figure 3C**) and no significant change in SST was detected across the alongshore transect (**Figure 3F**). By late fall, SSTs had uniformly decreased compared to September due to seasonal cooling.

TIRS SST data clearly show the relative temperature difference between the wastewater plume and ambient waters. The observed difference was similar to those detected by MODIS Aqua and ASTER during the 2006 HTP and 2012 Orange County Sanitation District diversions (Gierach et al., 2017). *In situ* CTD temperature data also showed colder water temperatures in the plume compared to ambient waters. Direct comparisons to *in situ* data are not provided herein as TIRS SST data provide skin temperature measurements of the top few millimeters of the ocean surface, whereas *in situ* CTD temperature measurements were taken at depths greater than 1 m below the surface.

Wastewater Impact on *chl-a* in Santa Monica Bay

Satellite and *In Situ Rrs* Comparison

To validate satellite retrievals for use in ocean color monitoring of the wastewater diversion, OLI and MODIS *Rrs* at the red, green, and blue wavelengths were compared to corresponding *in*

situ Rrs measurements (Supplemental Figures 2, 3). Respective OLI and MODIS blue-green *Rrs* wavelength ratios (**Table 2**) were compared to corresponding *in situ Rrs* as an initial measure of suitability for *chl-a* measurements in Santa Monica Bay during the diversion. **Figure 4A** shows OLI *Rrs*(482)/*Rrs*(561) retrievals compared to *in situ* measured *Rrs*(482)/*Rrs*(561). OLI and *in situ Rrs* values corresponded well ($R^2 = 0.78$), with most of the satellite retrievals falling within ±30% of *in situ* values. The mean percent error between OLI *Rrs* and *in situ Rrs* blue-green ratio was ±19%. **Figure 4B** shows MODIS *Rrs*(488)/*Rrs*(547) retrievals compared to *in situ* measured *Rrs*(488)/*Rrs*(547). MODIS greatly overestimated the *Rrs* blue-green ratio by over 30%, as seen in the inset showing the full range of MODIS *Rrs* ratio values compared to corresponding *in situ* values ($R^2 = 0.05$). The mean percent error between MODIS *Rrs* and *in situ Rrs* blue-green ratio was ±271%. OLI *Rrs* retrievals for each red, blue, green, wavelength (Supplemental Figure 2), as well as the blue-green ratio (**Figure 4A**), corresponded much more closely to *in situ Rrs* values than MODIS *Rrs* retrievals (Supplemental Figure 3 and **Figure 4B**), demonstrating the suitability of the higher resolution OLI sensor for the monitoring of surface *chl-a* in the nearshore coastal waters of Santa Monica Bay.

Local and Standard *chl-a* Algorithm Comparison

To demonstrate the performance capabilities of the standard OLI and MODIS *chl-a* algorithms (OC2 and OC3M, respectively), in comparison to the newly derived local OLI and MODIS *chl-a* algorithms (**Figure 2**), we applied the algorithms to *in situ* derived *Rrs* using respective OLI and MODIS *Rrs* blue-green wavelengths (**Table 2**) and compared the resulting estimated satellite *chl-a* values to corresponding surface *in situ chl-a* measurements (**Figure 5**).

When the standard OC2 *chl-a* algorithm was applied to OLI *in situ Rrs* wavelengths, the mean percent error between the estimated *chl-a* values and *in situ chl-a* values was ±40% (**Figure 5A**). The standard OC3M *chl-a* algorithm applied to MODIS *in situ Rrs* wavelengths yielded a mean percent error of ±35% (**Figure 5B**). Applying our local OLI-derived *chl-a* algorithm to OLI *in situ Rrs* wavelengths yielded a mean percent error between the estimated *chl-a* values and *in situ chl-a* values of ±30% (**Figure 5C**). When our local MODIS-derived *chl-a* algorithm was applied to MODIS *in situ Rrs* wavelengths, the mean percent error between the estimated *chl-a* values and *in situ chl-a* values was ±32%. The standard algorithms tended to underestimate midlevel *chl-a* values and overestimate high *chl-a* values in respect to measured values, with the highest values falling well above the +30% error dashed line (**Figures 5A,B**). The local OLI *chl-a* algorithm (**Figure 5C**), with the lowest mean percent error, estimated *chl-a* values more accurately than the standard OC2, standard OC3M, and local MODIS algorithms.

In addition to the standard open ocean algorithms (OC2 and OC3M), we applied the Kahru et al. (2012) Aqua MODIS CALFIT *chl-a* algorithm, empirically derived for the regional southern California Current system, to MODIS *in situ Rrs* wavelengths and compared it to corresponding *in situ chl-a* measurements (Supplemental Figure 4). This regional *chl-a* algorithm more accurately estimated *chl-a* values than the standard OC3M algorithm, but still greatly overestimated high *chl-a* values with respect to measured values, and performed less accurately than our local MODIS *chl-a* algorithm (**Figure 5**).

The local and standard *chl-a* algorithms were applied directly to OLI and MODIS scenes from 11 November 2015, which is the only date in our time series for which there were coincident *in situ chl-a* and *in situ Rrs* measurements with Landsat 8 OLI and Aqua MODIS overpasses (**Table 1**). **Figure 6** illustrates the differences between the local and standard *chl-a* algorithms for OLI and MODIS in comparison to *in situ chl-a* measurements at each sampling station. Comparison of *in situ chl-a* to remotely-sensed *chl-a* as detected by our local OLI *chl-a* algorithm (**Figure 6A**), standard OC2 *chl-a* algorithm (**Figure 6B**), our local MODIS *chl-a* algorithm (**Figure 6C**), and standard OC3M *chl-a* algorithm (**Figure 6D**) highlight the discrepancies in *chl-a*

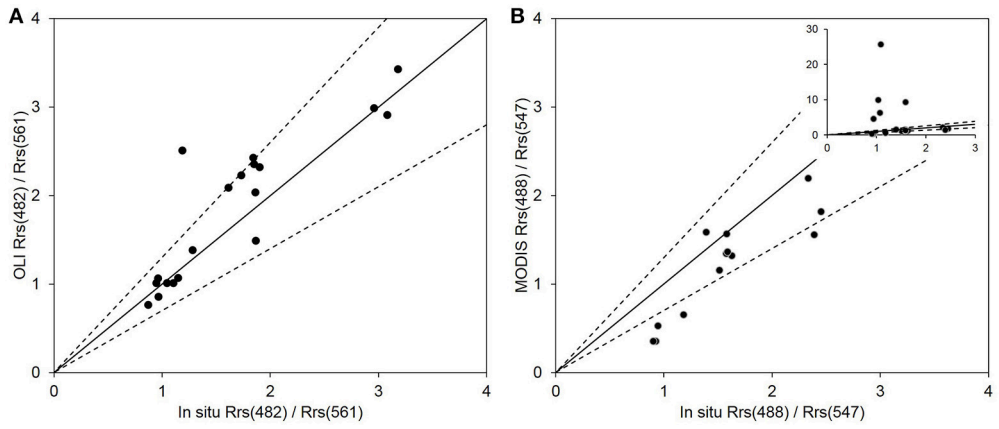

FIGURE 4 | Comparison between *in situ* and satellite-derived *Rrs* blue-green ratios. **(A)** OLI *Rrs*(482)/*Rrs*(561) vs. *in situ Rrs*(482)/*Rrs*(561). **(B)** MODIS *Rrs*(488)/*Rrs*(547) vs. *in situ Rrs*(488)/*Rrs*(547). The inset graph in panel **(B)** shows the full extent of MODIS data, indicating that several nearshore reflectance ratio values are significantly overestimated, a problem that is much less pronounced for the OLI data. The solid black line is the 1:1 line. Dashed lines are ± 30% from the 1:1 line.

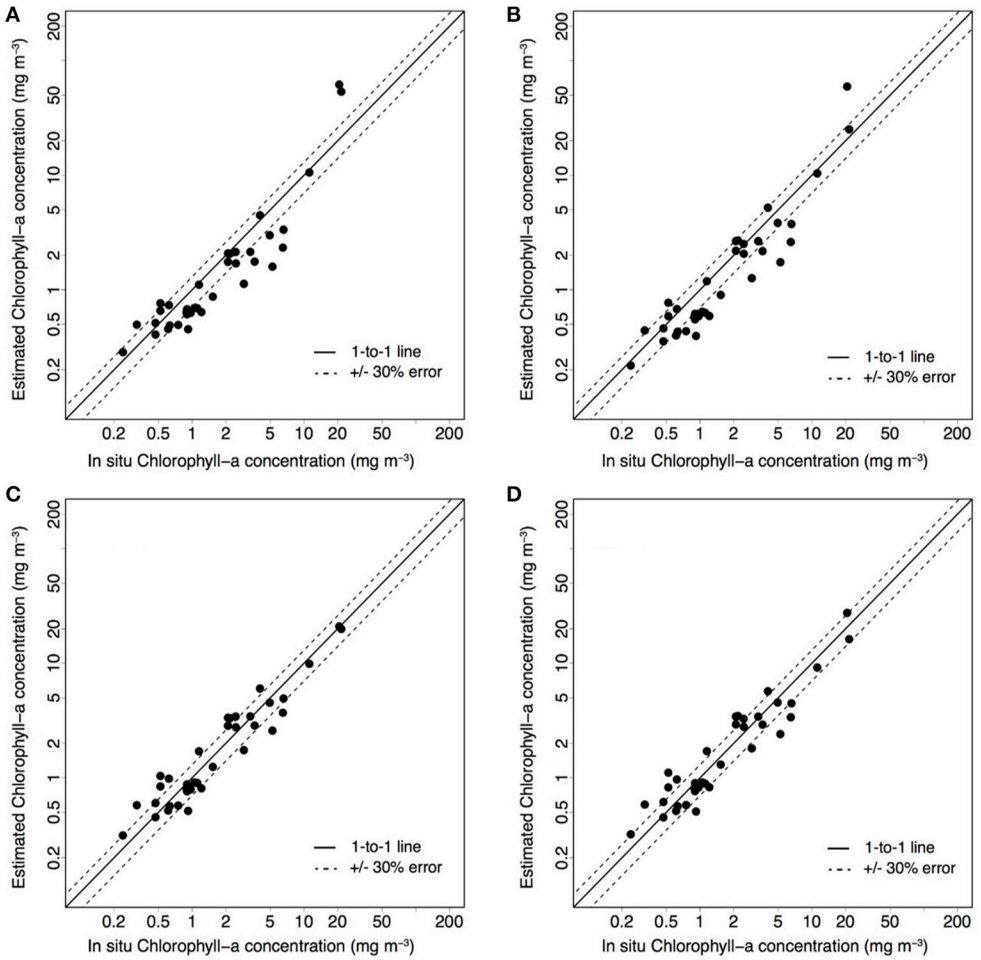

FIGURE 5 | Algorithm performance comparison using *in situ* data. Comparison of estimated *chl-a* derived from standard and local algorithms to *in situ chl-a* on a log-log scale. **(A)** Standard OC2 *chl-a* algorithm applied to OLI *Rrs*. **(B)** Standard OC3M *chl-a* algorithm applied to MODIS *Rrs*. **(C)** Local OLI-derived *chl-a* algorithm applied to OLI *Rrs*. **(D)** Local MODIS-derived *chl-a* algorithm applied to MODIS *Rrs*. Standard algorithms **(A,B)** tend to overestimate *chl-a* values in respect to measured values. The local OLI *chl-a* algorithm **(C)** estimates *chl-a* values more accurately than the standard OC2, standard OC3M, and local MODIS algorithms. The solid black line is the 1:1 line. Dashed lines are ± 30% from the 1:1 line.

conditions depending on which sensors and algorithms are used to monitor Santa Monica Bay.

On 11 November 2015, 9 days after the end of the diversion, there was no evidence of any *chl-a* response at either outfall pipe in association with excess nutrient availability from surfaced wastewater (**Figure 6**). Elevated *chl-a* levels were observed along the coastline, decreasing in concentration in the offshore direction. This trend is seen in both OLI and MODIS data, as well as *in situ chl-a* data. However, MODIS greatly overestimated *chl-a* concentrations, both inshore and offshore, with OC3M doing the worst job reconciling *in situ chl-a* concentrations. More fine scale details in *chl-a* distribution are visible in OLI data compared to MODIS. As seen in **Figure 6**, *in situ chl-a* samples most closely matched concentrations detected by OLI using our local *chl-a* algorithm. **Table 3** illustrates the statistical differences between the four *chl-a* algorithms analyzed for OLI and MODIS and *in situ chl-a* concentrations from **Figure 6**. Nine out of 10 corresponding observations present in both OLI and MODIS retrievals were analyzed as MODIS was unable to detect the southernmost nearshore *in situ* sampling location due to its coarser spatial resolution and inability to fully resolve the shoreline. Overall, OLI *chl-a* retrievals were more accurate than MODIS. The local OLI *chl-a* algorithm outperformed MODIS (local and OC3M) and OC2 algorithms with a mean percent error of ∼29% and the smallest RMSE of ∼0.36. The standard OC2 algorithm underestimated *chl-a* values and had a mean percent error of ∼26% and RMSE of ∼0.58. Our local MODIS *chl-a* algorithm performed better than the OC3M algorithm, but still overestimated *chl-a* concentrations with a mean percent error of ∼37% and RMSE of ∼0.67. The standard OC3M algorithm had a mean percent error of ∼349% and RMSE of ∼18.2, performing an order of magnitude poorer than our local MODIS *chl-a* algorithm and either OLI algorithm (local or OC2).

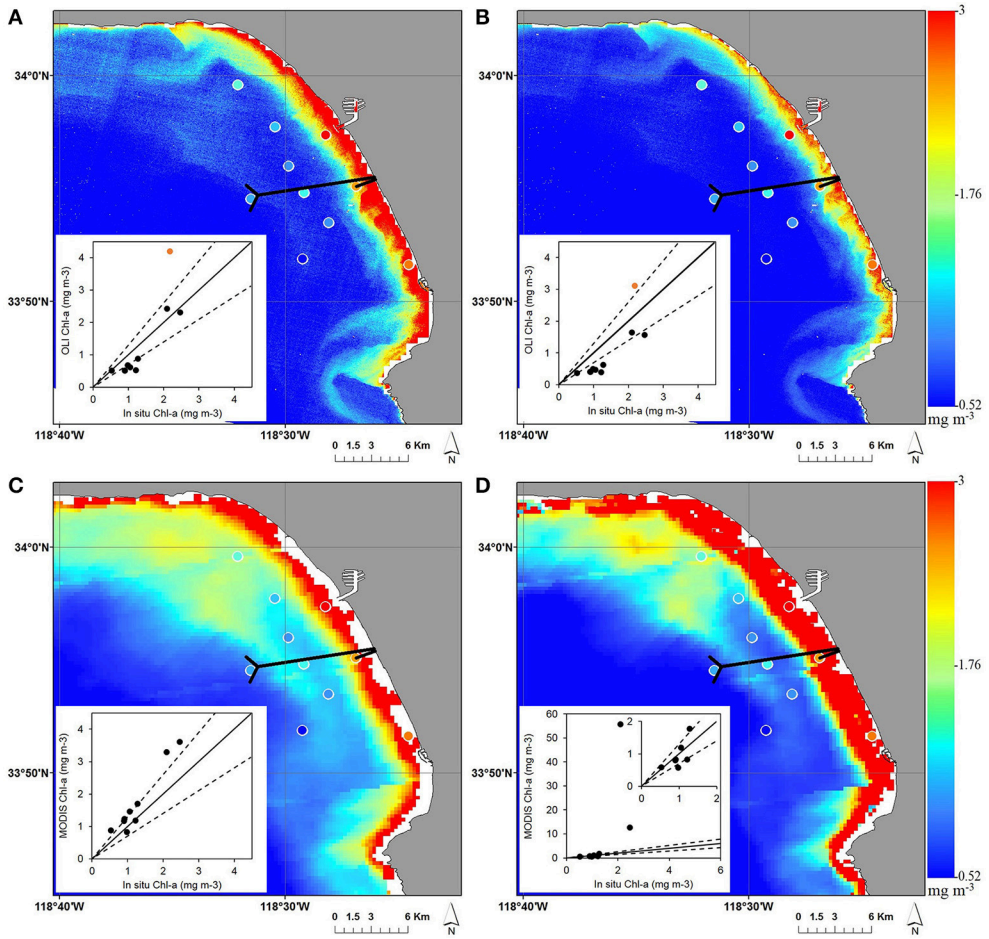

FIGURE 6 | Maps of *chl-a* concentrations on 11 November 2015, overlaid with 10 corresponding *in situ chl-a* measurements from sampling stations (denoted as circles using the same color scale as the satellite *chl-a* concentrations). **(A)** Local OLI *chl-a* algorithm. **(B)** Standard OC2 OLI *chl-a* algorithm. **(C)** Local MODIS *chl-a* algorithm. **(D)** Standard OC3M MODIS *chl-a* algorithm. Inset graphs show comparison between and *in situ chl-a* values. Orange data points in the insets of **(A,B)** denote the southernmost nearshore *in situ* sampling location, where there is no corresponding MODIS *chl-a* retrieval.

Chlorophyll-*a* Evolution in Response to the Wastewater Diversion

A time series of *chl-a* from before, during, and after the diversion using the local OLI algorithm is shown in **Figure 7**. The white box denotes a coastal region of interest (ROI) most affected by changes in *chl-a*, analyzed in **Figure 9**. Pre-diversion, on 8 September 2015, elevated *chl-a* levels were confined along the shore of Santa Monica Bay (**Figure 7A**). On 24 September 2015 (3 days into the diversion) elevated *chl-a* levels were detected in the vicinity of the 1-mile outfall pipe and extend northward along the coastline (**Figure 7B**). The area of enhanced *chl-a* concentration near the 1-mile outfall pipe increased in spatial extent on 10 October 2015 (19 days into the wastewater diversion), extending well offshore and alongshore (**Figure 7C**). Elevated *chl-a* concentrations remained visible alongshore on 26 October 2015 (35 days into the wastewater diversion) (**Figure 7D**). **Figure 8** shows an enlarged area view of *chl-a* data on 26 October 2015, in which the full extent of the *chl-a* bloom could be seen along the Santa Monica Bay coast wrapping around the peninsula to the south, then moving offshore and to the east. Post-diversion, *chl-a* concentrations returned to nominal levels along the shore of Santa Monica Bay (**Figures 7E,F**). Similar trends in *chl-a* were observed using the local MODIS algorithm (Supplemental Figures 5, 6); however, MODIS tended to overestimate *chl-a* concentrations and did not capture the fine scale structure shown by OLI. Additionally, MODIS was unable to resolve the shoreline as well as OLI, leaving gaps in the observed response to the diversion.

Figure 9 shows a boxplot distribution of *chl-a* concentration within the ROI denoted by the white box on each date of the time series shown in **Figure 7**.The period during the wastewater diversion is highlighted in gray. The ROI selected focuses on the coastal area most impacted by the wastewater diversion and *chl-a* blooms. Prior to the diversion, the maximum *chl-a* concentration detected by OLI in the ROI was 2.90 mg/m^3. There was a low range of variability in *chl-a* concentration prior to the diversion. During the diversion, the maximum

chl-a concentrations increased to 4.33 mg/m^3 on 24 September 2015 and peaked at 9.99 mg/m^3 on 10 October 2015. The small range of *chl-a* values in terms of the first quartile and third quartiles on 24 September 2015 can be attributed to the small spatial extent of the bloom and the high presence of low *chl-a* pixels. The greatest range of *chl-a* values occurred in the large *chl-a* patch in the ROI on 10 October 2015 during the diversion. The ROI does not fully encompass the *chl-a* bloom of 26 October 2015 (**Figure 7D**), in which the majority of the bloom was advected to the south, wrapping around the peninsula, as seen in **Figure 8**. Nevertheless, the part of the bloom captured in the ROI (**Figure 7D**) yielded high *chl-a* concentrations, with a maximum of 8.89 mg/m^3. After the diversion, *chl-a* concentration in Santa Monica Bay declined. On 11 November 2015, the maximum *chl-a* concentration in the ROI was 3.90 mg/m^3. By 27 November 2015, *chl-a* concentrations in the ROI declined to a maximum of 1.20 mg/m^3, and exhibited a very low *chl-a* range, as illustrated by the first quartile and third quartiles, similar to 8 September 2015, prior to the diversion.

TABLE 3 | Comparison of local and standard OLI and MODIS algorithm *chl-a* retrievals vs. *in situ chl-a* on 11 November 2015 for nine observations (see **Figure 6** for observation locations).

Chl-a Algorithm	Trend Line	R^2	Average % Error	RMSE
Local OLI	y=1.1925x-0.5002	0.89	29.0	0.38
OC2 OLI	y=0.7815x-0.271	0.89	26.4	0.58
Local MODIS	y=1.5973x-0.3062	0.93	37.0	0.67
OC3M MODIS	y=19.464x-16.233	0.44	348.7	18.2

DISCUSSION

Utility of Landsat 8 TIRS and OLI for Coastal Water Quality Monitoring

The scheduled maintenance work by HTP, as a result of the findings from their 2006 wastewater diversion event, allowed for foresight into planning monitoring efforts for the Fall 2015 diversion. This allowed for a large collaborative effort in which

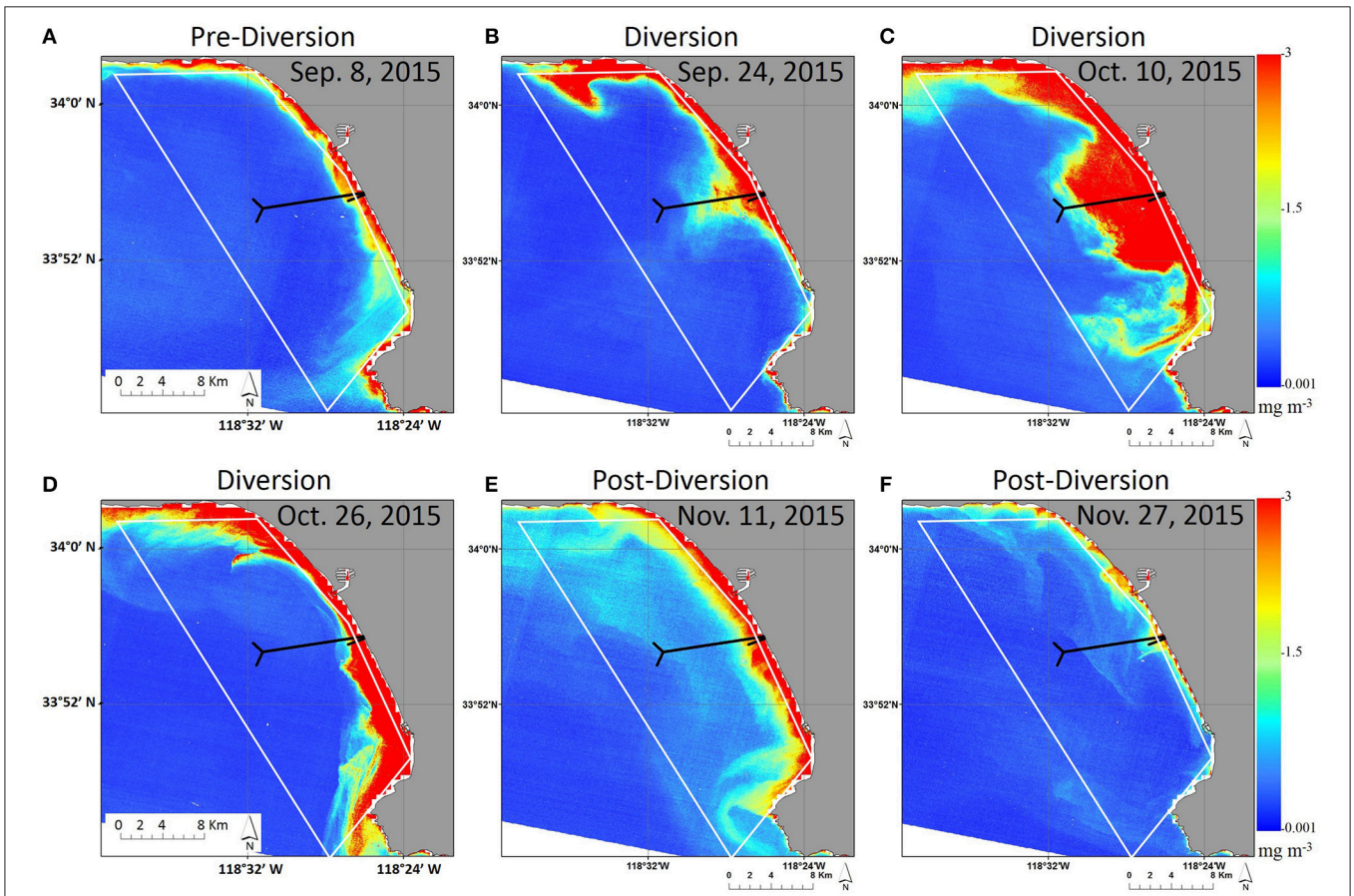

FIGURE 7 | Time series of *chl-a* in Santa Monica Bay using the local OLI algorithm. The white box denotes a coastal region of interest most affected by changes in *chl-a*, analyzed in **Figure 9**. **(A)** 8 September 2015, pre-diversion; **(B)** 24 September 2015, 3 days into the diversion; **(C)** 10 October 2015, 19 days into the diversion; **(D)** 26 October 2015, 35 days into the diversion; **(E)** 11 November 2015, 9 days post-diversion; **(F)** 27 November 2015, 25 days post-diversion. During the diversion, elevated *chl-a* levels were detected in the vicinity of the 1-mile outfall pipe, extending offshore, and along the coastline. Values returned to nominal levels post-diversion.

the pairing of satellite remote sensing and *in situ* sampling created a unique opportunity, not only for monitoring crucial changes in the environment in response to the shallow discharged wastewater, but also for creating and validating new and existing satellite remote sensing *chl-a* algorithms with coincident, high precision *in situ* data. Additionally, the Fall 2015 timeframe for the diversion minimized influences of upwelling nutrients, as well as incidences of cloud cover for the Southern California Bight region, which allowed for optimal satellite acquisitions with no sunglint issues.

Our results show that high-resolution thermal and optical sensors, such as Landsat 8 TIRS and OLI, with improved high signal-to-noise ratio, can facilitate the monitoring of SST and *chl-a* in complex nearshore coastal environments. Like many coastal environments, the nearshore waters of Santa Monica Bay are heterogeneous, dynamic, and optically complex due to high primary production and proximity to varied and multiple terrestrial inputs. The southward flowing California Current delivers relatively cold waters into Santa Monica Bay through the Santa Barbara Channel, with flow intensifying in spring in response to large-scale upwelling (e.g., Lynn and Simpson, 1987; Bray et al., 1999; DiGiacomo and Holt, 2001). The Southern California Countercurrent (Sverdrup and Fleming, 1941) penetrates the basin alongshore, bringing relatively warm waters from the southeast. SST gradients near the coast are enhanced by the effects of local wind-driven upwelling. This upwelling of cold, nutrient-rich waters injects nitrogen into surface waters along the coast and drives increased phytoplankton production (Cullen and Eppley, 1981; Hickey, 1992; Jones et al., 2002; Nezlin and Li, 2003; Kim et al., 2009; Nezlin et al., 2012). As a result, the bay is characterized by dynamic temperature gradients and relatively high primary production year-round compared to offshore oligotrophic waters. Furthermore, nutrient inputs associated with the wastewater diversion represent an additional source of biogeochemical and optical variability to this already complex system. Therefore, incorporating high-resolution satellite sensors into the monitoring of coastal Santa Monica Bay greatly increases the ability to detect environmental change, especially during pollution-related events.

In this study, we demonstrate the utility of TIRS in resolving small scale cold water plumes associated with surfacing wastewater. The buoyant wastewater, discharged at a temperature of about 25–29°C, entrains colder deep ocean water as it rises through the water column, resulting in a cold SST anomaly at the surface. Satellite SST has been available from a number of operational and experimental satellites for over 30 years (Guan and Kawamura, 2003). Sensors such as AVHRR (1.1 km) and MODIS (1 km) are widely used in global SST retrievals. However, these sensors, with comparatively coarser spatial resolution, are inadequate for detecting thermal plumes in complex coastal waters as they are unable to resolve features finer than a few kilometers (Thomas et al., 2002; Tang et al., 2003; Ahn et al., 2006). Radiometers optimized for terrestrial applications, such as the Landsat satellite series, deliver considerably higher spatial resolution (Thomas et al., 2002). The thermal infrared bands of Landsat-5 Thematic Mapper (TM), Landsat-7 Enhanced Thematic Mapper Plus (ETM+), and Terra ASTER, have high spatial resolutions of 120, 60, and 90 m, respectively, and have been adapted for use in coastal SST retrievals (Gibbons et al., 1989; Mustard et al., 1999; Chen et al., 2003; Suga et al., 2003; Gierach et al., 2017). Landsat 8 TIRS is the latest high-resolution thermal sensor for use in coastal monitoring. In this study, we found that the spatial resolution of TIRS was fine enough to detect not only the cold surfacing wastewater plume, but also the thermal signature of an oil tanker moored just offshore from the 1-mile outfall pipe (**Figure 3**). TIRS has great promise for application to coastal SST studies; however, at present further refinement to TIRS SST accuracy is necessary and is an ongoing effort.

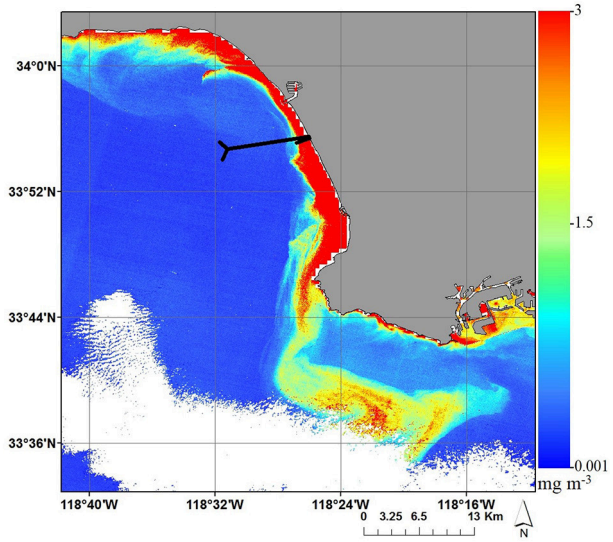

FIGURE 8 | Larger spatial extent of *chl-a* distribution on 26 October 2015, using the local OLI *chl-a* algorithm. Elevated *chl-a* values were detected along the coast that continue to wrap around the peninsula to the south. A large cloud region has been masked out in the bottom of the OLI frame.

Landsat 8 OLI has been shown to outperform its predecessors (e.g., TM and ETM+) in terms of waterbody classification (Ko et al., 2015; Kim et al., 2016). Before its launch, the suitability of OLI for coastal water monitoring was demonstrated using simulated data (Gerace et al., 2013; Pahlevan and Schott, 2013), as the suite of relatively narrow spectral bands and high spatial resolution in the visible to shortwave infrared made OLI a potential tool for ocean color radiometry (Franz et al., 2015). OLI ocean color monitoring in terms of total suspended solids was first analyzed by Vanhellemont and Ruddick (2014), in which they demonstrated the enhanced accuracy of OLI compared to dedicated wide-swath ocean color instruments such as MODIS, as well as TM and ETM+. Compared to its predecessors, OLI offers higher signal-to-noise ratios, due mainly to longer integration times on the push-broom scanner, better quantization due to 12-bit radiometric resolution, and the addition of a band centered at 443 nm (Knight and Kvaran, 2014; Pahlevan et al., 2014).

The presence of the high-quality SWIR bands on Landsat 8 facilitates more accurate quantification of aerosol contribution to the top of atmosphere radiance over very turbid waters, enabling more accurate remote sensing of ocean color and water quality monitoring (Franz et al., 2015; Garaba and Zielinski, 2015; Vanhellemont and Ruddick, 2015). These enhanced features of OLI allow for a more lucid characterization of *chl-a* and CDOM in open ocean and coastal waters (Franz et al., 2015). In Franz et al. (2015), standard *chl-a* algorithm coefficients were tuned for OLI using the NASA Bio-Optical Marine Algorithm Dataset (NOMAD) but no OLI data or coincident *in situ* measurements were used in the algorithm development. Here, we expand on the demonstrated applications of Landsat imagery in marine environments by validating the utility of OLI for coastal *chl-a* measurements as an indicator of changing water quality due to anthropogenic pollution with coincident *in situ* measurements of both *Rrs* and surface *chl-a*.

This study demonstrates the improved accuracy of *chl-a* from high-resolution OLI in comparison to coarser resolution MODIS for coastal *chl-a* detection, wherein the high-resolution of OLI enables detection of a large range of *chl-a* values found for a single MODIS pixel (**Figure 4**). Moreover, we show that the application of our local *chl-a* algorithms, developed using *in situ chl-a* and *in situ Rrs* measurements, improves *chl-a* retrievals in Santa Monica Bay during the 2015 HTP wastewater diversion in comparison to the standard open ocean algorithms (i.e., OC2 and OC3M) (**Figure 5**), and the regional CALFIT algorithm (Kahru et al., 2012; Supplemental Figure 4). The OC3M and OC2 algorithms are empirical algorithms developed for global applications and have been shown to overestimate *chl-a* in coastal environments, in part due to increased concentrations of other optical constituents (e.g., Muller-Karger et al., 2005). Within optically complex coastal waters such as Santa Monica Bay, CDOM, sediments, bottom reflectance (Maritorena et al., 1994; Cannizzaro and Carder, 2006), land adjacency effects (Santer and Schmechtig, 2000), and urban and absorbing aerosols (Moulin et al., 2001; Claustre et al., 2002; Ransibrahmanakul and Stumpf, 2006) can all interfere with the accurate detection of *chl-a*. This challenge is potentially exacerbated during the unusual conditions created by the wastewater diversion. The wastewater diversion increased the concentration of optical constituents in the water. Prior to the diversion, the beam attenuation coefficient at 650 nm was 0.89 m^{-1} at 1 meter depth at the sampling station at the terminus of the 1-mile outfall pipe. At the same sampling station, this increased to 1.78 m^{-1} during the wastewater diversion event. After the diversion ended, the beam attenuation coefficient decreased to 1.08 m^{-1}. Additionally, the absorption coefficient of CDOM at 400 nm prior to the diversion at the same sampling station was 0.29 m^{-1}. During the diversion, it increased to 0.57 m^{-1}. After the diversion, it decreased to 0.12 m^{-1}. Here, the development and application of our local OLI *chl-a* algorithm clearly improved *chl-a* retrievals relative to the standard OC2 and OC3M retrievals. Overall, our local OLI *chl-a* algorithm provided the best assessment of change in surface *chl-a* concentrations related to the 2015 HTP wastewater diversion.

Environmental Impacts of the 2015 HTP Wastewater Diversion

High-resolution TIRS and OLI were used to monitor two major environmental impacts of the Fall 2015 HTP wastewater diversion, SST and *chl-a*. Changes in SST were spatially limited to cold plumes near the terminus of the 1-mile outfall pipe, before mixing with warmer ambient surface water. The cold SST anomaly provides a physical indicator of whether or not the discharged wastewater has risen to the surface and provides some indication of its transport direction. The surfacing wastewater introduces excess nutrients, mainly ammonium, to the euphotic zone, where it has been shown to stimulate phytoplankton growth and production in the region (Reifel et al., 2013; Howard et al., 2014; Caron et al., 2017; Gierach et al., 2017).

During the diversion event, cold water plumes were detected by TIRS (**Figure 3**) and *in situ* measurements (not shown) at the terminus of the 1-mile outfall pipe, indicating that, throughout the diversion, the fresh wastewater plume consistently reached the surface, entraining cold bottom water with it as it rose through the water column. Pre- and post-diversion, when wastewater was discharged through the 5-mile outfall pipe, no SST anomalies were seen in the vicinity of either the 1-mile or 5-mile outfall pipes. The 5-mile outfall pipe terminates at 57 m depth, allowing the discharged wastewater to mix more thoroughly with ambient seawater and largely remain at depth in association with density stratification (Washburn et al., 1992; Uchiyama et al., 2014). TIRS data additionally shows warmer SSTs along the coast, cooling in the offshore direction, and an overall decrease in SST from September to November (**Figure 3**). These trends are consistent with the inshore-offshore temperature gradient and seasonally driven temperature decrease characteristic of the coastal Santa Monica Bay region (Corcoran and Shipe, 2011).

In the Southern California Bight, like many other coastal waters dominated by seasonal upwelling, nitrogen is generally the limiting nutrient for phytoplankton growth (Capone and Hutchins, 2013). Nitrate is the dominant form of nitrogen brought to surface waters via upwelling. Ammonium is overwhelmingly the dominant form of nitrogen (92%) in secondarily-treated wastewater discharged into the Southern California Bight (Howard et al., 2014). In Santa Monica Bay, the flux of nitrogen from upwelling and treated wastewater are about equal (102×10^2 kg N km^{-2} y^{-1} and 99×10^2 kg N km^{-2} y^{-1}, respectively), comprising over 95% of the total nitrogen flux for the region (Howard et al., 2017). During normal operations, treated wastewater is discharged from the 5-mile outfall pipe at the head of a submarine canyon that quickly drops off to over 100 m depth (**Figure 1**), allowing for dilution and mixing and limiting the impact on the near-surface phytoplankton community. During the diversion, there was major concern not only in regards to the magnitude of nitrogen being released into surface waters, but also in regards to the species of the nitrogen being released (Howarth and Marino, 2006) as it may cause shifts in phytoplankton community structure due to different nutrient preferences among algal taxa (Howard et al., 2007; Ryan et al., 2017). Ammonium is the most biologically available

form of nitrogen and is usually present in the euphotic zone in limited concentrations because it is assimilated so quickly. Therefore, such a large release of ammonium, specifically in the fall, a time in which nutrients tend to be limited, can rapidly stimulate phytoplankton blooms in this area. The preferential stimulation of harmful algal blooms was a particular concern as anthropogenic nutrients have been shown to be a factor in the increased occurrence of these outbreaks (Anderson et al., 2002; Heisler et al., 2008; Kudela et al., 2008). The increased frequency and duration of phytoplankton blooms related to anthropogenic nutrient loading have also coincided with increased incidents of eutrophication of coastal waters over the last several decades (Howarth, 2008; Paerl and Piehler, 2008).

During the 6-week 2015 HTP wastewater diversion, ∼1.61 × 10^6 kg of ammonium was released into the shallow coastal waters of Santa Monica Bay. This amount of nitrogen loading was likely to have greatly altered the composition of the nitrogen pool available to phytoplankton populations. With these concerns in mind, the main goal of this study was to use high-resolution satellite remote sensing to monitor changes in the biological response through *chl-a* concentrations in surface waters during the wastewater diversion. Given the immense amount of ammonium introduced into surface waters, the observed increase in *chl-a* during the diversion in Santa Monica Bay was not surprising (**Figure 7**). The maximum *chl-a* level during the diversion in the ROI, using our local OLI *chl-a* algorithm, was 9.99 mg/m^3 on 10 October 2015 (**Figure 9**), far exceeding the nominal *chl-a* value of 1.7 ± 0.33 mg/m^3 measured *in situ* (Corcoran and Shipe, 2011) and 0.61 mg/m^3 remotely-sensed by SeaWiFS (Nezlin and Li, 2003) for the same region and time of year. The *chl-a* enhancement seen during the 2015 HTP wastewater diversion was larger than that seen during the 2006 HTP diversion (Reifel et al., 2013; Gierach et al., 2017), not only in terms of concentration but also in terms of spatial extent. This can most likely be attributed to the much longer duration of the 2015 diversion (6 weeks as opposed to 3 days in 2006).

Prior to the diversion, the maximum *chl-a* concentration measured by OLI, was 2.90 mg/m^3 (**Figure 9**). After the diversion event, on 27 November 2015, the maximum *chl-a* concentration measured by OLI was 1.20 mg/m^3. These maximum *chl-a* values were found in the most nearshore region of Santa Monica Bay. The general inshore-offshore gradient in *chl-a* detected before and after the diversion is characteristic of the Southern California Bight, with higher values of *chl-a* observed at shallower depths (Kim et al., 2009; Corcoran and Shipe, 2011; Gierach et al., 2017). However, during the diversion, high *chl-a* values, were found further offshore and away from the terminus of the 1-mile outfall pipe (**Figures 7B–D**). As exemplified in **Figure 8** and Supplemental Figure 6, the effects of the wastewater diversion were not confined to the nearshore region. Given the complex nature of currents and wind in the region, as demonstrated by models of current velocity and direction, as well as by tracks of experimental drifters placed in the water near the 1-mile outfall pipe (City of Los Angeles, Environmental Monitoring Division, 2017), and the volume of wastewater being discharged, the nutrient- and organic matter-rich wastewater can be exported offshore into the more oligotrophic region of Santa Monica Bay where it can fuel primary production and heterotrophic processes in areas that may not commonly experience such conditions during the fall (Boehm et al., 2002; Landry et al., 2009). Fortunately, testing in areas with enhanced *chl-a* as identified by OLI found that no algal blooms produced harmful toxins during the wastewater diversion (City of Los Angeles, Environmental Monitoring Division, 2017).

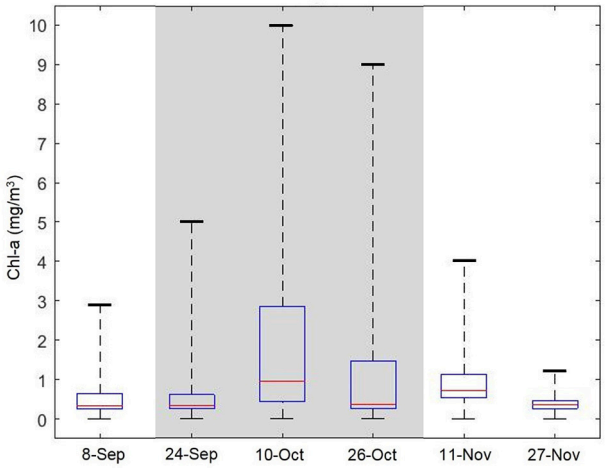

FIGURE 9 | OLI-derived *chl-a* concentration range in the region-of-interest for each date of the time series shown in **Figure 7**. Prior to the diversion, *chl-a* levels were relatively low with low variability within the ROI. During the diversion, gray region, *chl-a* levels increased well above nominal values. Post-diversion, *chl-a* values returned to nominal levels.

Satellite *chl-a* data clearly show the spatial contrast between productive coastal waters and oligotrophic offshore waters along the coast of California (Eppley, 1992; Thomas et al., 1994; Legaard and Thomas, 2006). However, as noted in previous studies (Kahru and Mitchell, 1999; Darecki and Stramski, 2004; Kim et al., 2009; Kahru et al., 2012; Gierach et al., 2017), satellite *chl-a* data in very nearshore waters have systematic and variable errors due to the proximity of land (e.g., adjacency effects, breaking waves) and due to the optical complexity of the waters caused by varying concentrations of CDOM and inorganic suspended particles, and bottom reflectance. Errors due to proximity of land appeared to be less pronounced in high-resolution Landsat 8 OLI (30 m) compared to MODIS. The newly derived local *chl-a* algorithm, tuned for the optically complex nearshore environment of Santa Monica Bay, helped reduce the discrepancy between satellite *chl-a* and *in situ chl-a*.

In this study, we demonstrated the enhanced performance of TIRS and OLI for detecting mesoscale nearshore features, in terms of SST and surface *chl-a* concentrations. Although TIRS and OLI show great promise for monitoring water quality indicators in coastal environments, Landsat 8 has a repeat cycle of 16 days. This infrequent coverage yielded a limited number of satellite overpasses during a diversion event and did not capture the complete biophysical response to the wastewater diversion event. Phytoplankton blooms and die-offs were captured by *in situ* monitoring on timescales less than the 16-day repeat cycle. In contrast to Landsat 8, MODIS has a coarser spatial

resolution but daily repeat cycle. In the future, coastal water quality monitoring efforts can employ additional high-resolution sensors with improved temporal resolutions, such as the two Sentinel-2 MultiSpectral Instruments (MSI) with a 5-day repeat cycle and Landsat-9, predicted to launch in December 2020, with an 8-day offset from Landsat 8 repeat cycle, to capture the environmental response over greater temporal resolution. This study was the first to use high-resolution Landsat 8 TIRS and OLI for coastal water quality monitoring of wastewater diversions. By employing satellite monitoring in concert with *in situ* sampling, we were able to develop local empirical *chl-a* algorithms for both OLI and MODIS to gain an improved understanding of the biophysical dynamics occurring within Santa Monica Bay during a wastewater diversion event.

AUTHOR CONTRIBUTIONS

BH and MG were the principal investigators for the study, and along with RT and CF, helped conceive, plan, and implement the study. RT and CF collected in situ remote sensing reflectance data each week. CF processed the in situ remote sensing reflectance data. RT obtained and processed satellite ocean color data and wrote the bulk of the manuscript with edits from co-authors. NM and GH helped process Landsat sea surface temperature data. JS collected and processed in situ chlorophyll samples used in this study.

ACKNOWLEDGMENTS

This work was performed at the Jet Propulsion Laboratory, California Institute of Technology, under contract with the National Aeronautics and Space Administration. The NASA DEVELOP program (http://develop.larc.nasa.gov/) provided the primary support for this project with additional support provided by the Physical Oceanography Distributed Active Archive Center. The authors would like to acknowledge the earlier contributions of Mark Barker and Lindsay Amaleh, who performed preliminary analysis of the satellite data collected during the 2015 HTP diversion. We would also like to acknowledge Matt Montanaro for his assistance in applying the stray-light correction to our TIRS data. Finally, we would like to acknowledge our project partners for assistance in the field sample collection, instrument deployment, and inclusion in the 2015 HTP diversion monitoring program: Curtis Cash and Mas Dojiri of the City of Los Angeles Environmental Monitoring Division, as well as the very helpful captain and crew of the R/V *La Mer* and R/V *Surveyor*.

SUPPLEMENTARY MATERIAL

The Supplementary Material for this article can be found online at: https://www.frontiersin.org/articles/10.3389/fmars.2017.00329/full#supplementary-material

REFERENCES

Ahn, Y. H., Shanmugam, P., Lee, J. H., and Kang, Y. Q. (2006). Application of satellite infrared data for mapping of thermal plume contamination in coastal ecosystem of Korea. *Mar. Environ. Res.* 61, 186–201. doi: 10.1016/j.marenvres.2005.09.001

Alley, R., and Jentoft-Nilsen, M. (1999). *Algorithm Theoretical Basis Document for: Brightness Temperature*. Pasadena, CA: Jet Propulsion Lab., California Inst. of Tech.

Anderson, D. M., Glibert, P. M., and Burkholder, J. M. (2002). Harmful algal blooms and eutrophication: nutrient sources, composition, and consequences. *Estuaries* 25, 704–726. doi: 10.1007/BF02804901

Austin, R. W. (1974). "The remote sensing of spectral radiance from below the ocean surface," in *Optical Aspects of Oceanography*, eds N. G. Jerlov and E. S. Nielsen (London: Academic Press), 317–344.

Bailey, S. W., Franz, B. A., and Werdell, P. J. (2010). Estimation of near-infrared water-leaving reflectance for satellite ocean color data processing. *Opt. Express* 18, 7521–7527. doi: 10.1364/OE.18.007521

Barsi, J. A., Schott, J. R., Hook, S. J., Raqueno, N. G., Markham, B. L., and Radocinski, R. G. (2014). Landsat-8 Thermal Infrared Sensor (TIRS) vicarious radiometric calibration. *Remote Sens.* 6, 11607–11626. doi: 10.3390/rs61111607

Bay, S., Jones, B. H., Schiff, K., and Washburn, L. (2003). Water quality impacts of stormwater discharges to Santa Monica Bay. *Mar. Environ. Res.* 56, 205–223. doi: 10.1016/S0141-1136(02)00331-8

Berk, A., Anderson, G. P., Acharya, P. K., Bernstein, L. S., Muratov, L., Lee, J., et al. (2005). "MODTRANTM 5, a reformulated atmospheric band model with auxiliary species and practical multiple scattering options: update," in *Algorithms and Technologies for Multispectral, Hyperspectral, and Ultraspectral Imagery XI*, eds S. S. Sylvia and P. E. Lewis (Bellingham, WA: Proceedings of SPIE).

Boehm, A. B., Sanders, B. F., and Winant, C. D. (2002). Cross-shelf transport at Huntington Beach. Implications for the fate of sewage discharged through an offshore ocean outfall. *Environ. Sci. Technol.* 36, 1899–1906. doi: 10.1021/es0111986

Bray, N. A., Keyes, A., and Morawitz, W. M. L. (1999). The California current system in the southern California bight and the Santa Barbara Channel. *J. Geophys. Res. Oceans* 104, 7695–7714. doi: 10.1029/1998JC900038

Cannizzaro, J. P., and Carder, K. L. (2006). Estimating chlorophyll a concentrations from remote-sensing reflectance in optically shallow waters. *Remote Sens. Environ.* 101, 13–24. doi: 10.1016/j.rse.2005.12.002

Capone, D. G., and Hutchins, D. A. (2013). Microbial biogeochemistry of coastal upwelling regimes in a changing ocean. *Nat. Geosci.* 6, 711–717. doi: 10.1038/ngeo1916

Caron, D. A., Gellene, A. G., Smith, J., Seubert, E. L., Campbell, V., Sukhatme, G. S., et al. (2017). Response of phytoplankton and bacterial biomass during a wastewater effluent diversion into nearshore coastal waters. *Estuar. Coast. Shelf Sci.* 186, 223–236. doi: 10.1016/j.ecss.2015.09.013

Chen, C., Shi, P., and Mao, Q. (2003). Application of remote sensing techniques for monitoring the thermal pollution of cooling-water discharge from nuclear power plant. *J. Environ. Sci. Heal. A, A*38, 1659–1668. doi: 10.1081/ESE-120021487

City of Los Angeles, Environmental Monitoring Division (2009). *2006 Hyperion Receiving Water Monitoring for Diversion of 5-Mile Discharge to 1-Mile Pipe during the 5-Mile Pipe Inspection*. California, CA: Department of Public Works, Bureau of Sanitation, Hyperion Treatment Plant, Playa del Rey.

City of Los Angeles, Environmental Monitoring Division (2017). *Fall 2015 Hyperion Treatment Plant Effluent Diversion to the 1-Mile Outfall Comprehensive Monitoring Program Final Report*. Environmental Monitoring Division, Bureau of Sanitation, Department of Public Works, City of Los Angeles, pp. 160 + appendicies.

Claustre, H., Morel, A., Hooker, S. B., Babin, M., Antoine, D., Oubelkheir, K., et al. (2002). Is desert dust making oligotrophic waters greener? *Geophys. Res. Lett.* 29, 107-1–107-4. doi: 10.1029/2001GL014056

Corcoran, A. A., and Shipe, R. F. (2011). Inshore–offshore and vertical patterns of phytoplankton biomass and community composition in Santa Monica Bay, CA (USA). *Estuar. Coast. Shelf Sci.* 94, 24–35. doi: 10.1016/j.ecss.2011.05.007

Creel, L. (2003). *Ripple Effects: Population and Coastal Regions*. Washington, DC: Population Reference Bureau.

Crossett, K. M., Culliton, T. J., Wiley, P. C., and Goodspeed, T. R. (2004). *Population Trends Along the Coastal United States: 1980—2008*. Coastal Trends Report Series. NOAA, National Oceanic Service Management Budget Off-Spec Project, Silver Spring, MD.

Cullen, J. J., and Eppley, R. W. (1981). Chlorophyll maximum layers of the Southern-California Bight and possible mechanisms of their formation and maintenance. *Oceanol. Acta*. 4, 23–32.

Darecki, M., and Stramski, D. (2004). An evaluation of MODIS and SeaWiFS bio-optical algorithms in the Baltic Sea. *Remote Sens. Environ.* 89, 326–350. doi: 10.1016/j.rse.2003.10.012

DiGiacomo, P. M., and Holt, B. (2001). Satellite observations of small coastal ocean eddies in the Southern California Bight. *J. Geophys. Res.* 106, 22521–22543. doi: 10.1029/2000JC000728

DiGiacomo, P. M., Washburn, L., Holt, B., and Jones, B. H. (2004). Coastal pollution hazards in southern California observed by SAR imagery: stormwater plumes, wastewater plumes, and natural hydrocarbon seeps. *Mar. Pollut. Bull.* 49, 1013–1024. doi: 10.1016/j.marpolbul.2004.07.016

Eganhouse, R. P., and Venkatesan, M. I. (1993). "Chemical oceanography and geochemistry," in *Ecology of the Southern California Bight: A Synthesis and Interpretation*, eds M. D. Dailey, D. J. Reish, and J. W. Anderson (Berkeley, CA: University of California Press), 71–189.

Eppley, R. W. (1992). Chlorophyll, photosynthesis and new production in the Southern California Bight. *Prog. Oceanogr.* 30, 117–150. doi: 10.1016/0079-6611(92)90010-W

Franz, B. A., Bailey, S. W., Kuring, N., and Werdell, P. J. (2015). Ocean color measurements with the Operational Land Imager on Landsat-8: implementation and evaluation in SeaDAS. *J. Appl. Remote Sens.* 9:096070. doi: 10.1117/1.JRS.9.096070

Franz, B. A., Bailey, S. W., Werdell, P. J., and McClain, C. R. (2007). Sensor-independent approach to the vicarious calibration of satellite ocean color radiometry. *Appl. Opt.* 46, 5068–5082. doi: 10.1364/AO.46.005068

Franz, B. A., Werdell, P. J., Meister, G., Kwiatkowska, E. J., Bailey, S. W., Ahmad, Z., et al. (2006). "MODIS land bands for Ocean Remote sensing applications," in *Proceedings of Ocean Optics XVIII* (Montreal, QC), 9–13.

Garaba, S. P., and Zielinski, O. (2015). An assessment of water quality monitoring tools in an estuarine system. *Remote Sens. Appl. Soc. Environ*. 2, 1–10. doi: 10.1016/j.rsase.2015.09.001

Gerace, A. D., Schott, J. R., and Nevins, R. (2013). Increased potential to monitor water quality in the near-shore environment with Landsat's next-generation satellite. *J. Appl. Remote Sens.* 7, 73558–73558. doi: 10.1117/1.JRS.7.073558

Gerace, A., and Montanaro, M. (2017). Derivation and validation of the stray light correction algorithm for the thermal infrared sensor onboard Landsat 8. *Remote Sens. Environ.* 191, 246–257. doi: 10.1016/j.rse.2017.01.029

Gibbons, D. E., Wukelic, G. E., Leighton, J. P., and Doyle, M. J. (1989). Application of Landsat thematic mapper data for coastal thermal plume analysis at Diablo Canyon. *Photogr. Eng. Rem. Sens*. 55, 903–909.

Gierach, M., Holt, B., Trinh, R., Pan, B., and Rains, C. (2017). Satellite detection of wastewater diversion plumes in Southern California. *Estuar. Coast. Shelf Sci.* 186, 171–182. doi: 10.1016/j.ecss.2016.10.012

Guan, L., and Kawamura, H. (2003). SST availabilities of satellite infrared and microwave measurements. *J. Oceanogr.* 59, 201–209. doi: 10.1023/A:1025543305658

Heisler, J., Glibert, P., Burkholder, J., Anderson, D., Cochlan, W., Dennison, W., et al. (2008). Eutrophication and harmful algal blooms: a scientific consensus. *Harmful Algae* 8, 3–13. doi: 10.1016/j.hal.2008.08.006

Hickey, B. M. (1992). Circulation over the Santa Monica-San Pedro basin and shelf. *Prog. Oceanogr.* 30, 37–115. doi: 10.1016/0079-6611(92)90009-O

Hickey, B. M., Dobbins, E. L., and Allen, S. E. (2003). Local and remote forcing of currents and temperature in the central Southern California Bight. *J. Geophys. Res.* 108:3081. doi: 10.1029/2000JC000313

Holt, B., Trinh, R., and Gierach, M. M. (2017). Stormwater runoff plumes in the Southern California Bight: a comparison study with SAR and MODIS imagery. *Mar. Pollut. Bull.* 118, 141–154. doi: 10.1016/j.marpolbul.2017.02.040

Howard, M. D. A., Cochlan, W. P., Ladizinsky, N., and Kudela, R. M. (2007). Nitrogenous preference of toxigenic Pseudo-nitzschia australis (Bacillariophyceae) from field and laboratory experiments. *Harmful Algae* 6, 206–217. doi: 10.1016/j.hal.2006.06.003

Howard, M. D. A., Kudela, R. M., and McLaughlin, K. (2017). New insights into impacts of anthropogenic nutrients on urban ecosystem processes on the Southern California coastal shelf: introduction and synthesis. *Estuarine Coast. Shelf Sci.* 186, 163–170. doi: 10.1016/j.ecss.2016.06.028

Howard, M. D. A., Sutula, M., Caron, D. A., Chao, Y., Farrara, J. D., Frenzel, H., et al. (2014). Anthropogenic nutrient sources rival natural sources on small scales in the coastal waters of the Southern California Bight. *Limnol. Oceanogr.* 59, 285–297. doi: 10.4319/lo.2014.59.1.0285

Howarth, R. W. (2008). Coastal nitrogen pollution: a review of sources and trends globally and regionally. *Harmful Algae* 8, 14–20. doi: 10.1016/j.hal.2008.08.015

Howarth, R. W., and Marino, R. (2006). Nitrogen as the limiting nutrient for eutrophication in coastal marine ecosystems: evolving views over three decades. *Limnol. Oceanogr.* 51, 364–376. doi: 10.4319/lo.2006.51.1_part_2.0364

Hu, C., Chen, Z., Clayton, T. D., Swarzenski, P., Brock, J. C., and Muller-Karger, F. E. (2004). Assessment of estuarine water-quality indicators using MODIS medium-resolution bands: initial results from Tampa Bay, FL. *Remote Sens. Environ.* 93, 423–441. doi: 10.1016/j.rse.2004.08.007

Hu, C., Lee, Z., and Franz, B. (2012). Chlorophyll *a* algorithms for oligotrophic oceans: a novel approach based on three-band reflectance difference. *J. Geophys. Res.* 117, C01011. doi: 10.1029/2011JC007395

Hulley, G. C., Hook, S. J., Abbott, E., Malakar, N., Islam, T., and Abrams, M. (2015). The ASTER Global Emissivity Dataset (ASTER GED): mapping earth's emissivity at 100 meter spatial scale. *Geophys. Res. Lett.* 42, 7966–7976. doi: 10.1002/2015GL065564

Jones, B. H., Noble, M. A., and Dickey, T. D. (2002). Hydrographic and particle distributions over the Palos Verdes Continental Shelf: spatial, seasonal and daily variability. *Cont. Shelf Res.* 22, 945–965. doi: 10.1016/S0278-4343(01)00114-5

Kahru, M., Kudela, R. M., Manzano-Sarabia, M., and Mitchell, B. G. (2012). Trends in the surface chlorophyll of the California Current: merging data from multiple ocean color satellites. *Deep Sea Res. II Top. Stud. Oceanog.* 77, 89–98. doi: 10.1016/j.dsr2.2012.04.007

Kahru, M., and Mitchell, B. G. (1999). Empirical chlorophyll algorithm and preliminary SeaWiFS validation for the California Current. *Int. J. Remote Sens.* 20, 3423–3429. doi: 10.1080/014311699211453

Kim, H. H., Ko, B. C., and Nam, J. Y. (2016). Predicting chlorophyll-a using Landsat 8 OLI sensor data and the non-linear RANSAC method–a case study of Nakdong River, South Korea. *Int. J. Remote Sens.* 37, 3255–3271. doi: 10.1080/01431161.2016.1196839

Kim, H. J., Miller, A. J., McGowan, J., and Carter, M. L. (2009). Coastal phytoplankton blooms in the Southern California Bight. *Prog. Oceanogr.* 82, 137–147. doi: 10.1016/j.pocean.2009.05.002

Knight, E. J., and Kvaran, G. (2014). Landsat-8 operational land imager design, characterization and performance. *Remote Sens.* 6, 10286–10305. doi: 10.3390/rs61110286

Ko, B. C., Kim, H. H., and Nam, J. Y. (2015). Classification of potential water bodies using Landsat 8 OLI and a combination of two boosted random forest classifiers. *Sensors* 15, 13763–13777. doi: 10.3390/s150613763

Kudela, R. M., Ryan, J. P., Blakely, M. D., Lane, J. Q., and Peterson, T. D. (2008). Linking the physiology and ecology of Cochlodinium to better understand harmful algal bloom events: a comparative approach. *Harmful Algae* 7, 278–292. doi: 10.1016/j.hal.2007.12.016

Landry, M. R., Ohman, M. D., Goericke, R., Stukel, M. R., and Tsyrklevich, K. (2009). Lagrangian studies of phytoplankton growth and grazing relationships in a coastal upwelling ecosystem off Southern California. *Prog. Oceanogr.* 83, 208–216. doi: 10.1016/j.pocean.2009.07.026

Legaard, K. R., and Thomas, A. C. (2006). Spatial patterns in seasonal and interannual variability of chlorophyll and sea surface temperature in the California Current. *J. Geophys. Res.* 111, C06032. doi: 10.1029/2005JC003282

Lynn, R. J., and Simpson, J. J. (1987). The California Current System: the seasonal variability of its physical characteristics. *J. Geophys. Res. Oceans* 92, 12947–12966. doi: 10.1029/JC092iC12p12947

Lyon, G. S., and Stein, E. D. (2009). How effective has the Clean Water Act been at reducing pollutant mass emissions to the Southern California Bight over the past 35 years? *Environ. Monit. Assess.* 154, 413–426. doi: 10.1007/s10661-008-0408-1

Maritorena, S., Morel, A., and Gentili, B. (1994). Diffuse reflectance of oceanic shallow waters: influence of water depth and bottom albedo. *Limnol. Oceanogr.* 39, 1689–1703. doi: 10.4319/lo.1994.39.7.1689

Maritorena, S., Siegel, D. A., and Peterson, A. R. (2002). Optimization of a semi analytical ocean color model for global-scale applications. *Appl. Opt.* 41, 2705–2714. doi: 10.1364/AO.41.002705

Marmorino, G. O., Smith, G. B., Miller, W. D., and Bowles, J. H. (2010). Detection of a buoyant coastal wastewater discharge using airborne hyperspectral and infrared imagery. *J. Appl. Remote Sens.* 4:043502. doi: 10.1117/1.3302630

McClain, C. R. (2009). A decade of satellite ocean color observations. *Ann. Rev. Mar. Sci.* 1, 19–42. doi: 10.1146/annurev.marine.010908.163650

McKinney, M. L. (2002). Urbanization, biodiversity, and conservation. *Bioscience* 52, 883–890. doi: 10.1641/0006-3568(2002)052[0883:UBAC]2.0.CO;2

McLaughlin, K., Nezlin, N. P., Howard, M. D., Beck, C. D., Kudela, R. M., Mengel, M. J., et al. (2017). Rapid nitrification of wastewater ammonium near coastal ocean outfalls, Southern California, USA. *Estuar. Coast. Shelf Sci.* 186, 263–275. doi: 10.1016/j.ecss.2016.05.013

Montanaro, M., Gerace, A., Lunsford, A., and Reuter, D. (2014). Stray light artifacts in imagery from the landsat 8 thermal infrared sensor. *Remote Sens.* 6, 10435–10456. doi: 10.3390/rs61110435

Montanaro, M., Gerace, A., and Rohrbach, S. (2015). Toward an operational stray light correction for the Landsat 8 thermal infrared sensor. *Appl. Opt.* 54, 3963–3978. doi: 10.1364/AO.54.003963

Morel, A., and Gentili, B. (1996). Diffuse reflectance of oceanic waters. III. Implication of bidirectionality for the remote-sensing problem. *Appl. Opt.* 35, 4850–4862. doi: 10.1364/AO.35.004850

Moulin, C., Gordon, H. R., Chomko, R. M., Banzon, V. F., and Evans, R. H. (2001). Atmospheric correction of ocean color imagery through thick layers of Saharan dust. *Geophys. Res. Lett.* 28, 5–8. doi: 10.1029/2000GL011803

Mouw, C. B., Greb, S., Aurin, D., DiGiacomo, P. M., Lee, Z., Twardowski, M., et al. (2015). Aquatic color radiometry remote sensing of coastal and inland waters: challenges and recommendations for future satellite missions. *Remote Sens. Environ.* 160, 15–30. doi: 10.1016/j.rse.2015.02.001

Muller-Karger, F. E., Hu, C., Andréfouët, S., Varela, R., and Thunell, R. (2005). "The color of the coastal ocean and applications in the solution of research and management problems," in *Remote Sensing of Coastal Aquatic Environments*, eds R. L. Miller, C. E. Del Castillo, and B. A. McKee (Dordrecht: Springer), 101–127.

Mustard, J. F., Carney, M. A., and Sen, A. (1999). The use of satellite data to quantify thermal effluent impacts. *Estur. Coast. Shelf S.* 49, 509–524. doi: 10.1006/ecss.1999.0517

Nezlin, N. P., and DiGiacomo, P. M. (2005). Satellite ocean color observations of stormwater runoff plumes along the San Pedro Shelf (southern California) during 1997–2003. *Cont. Shelf Res.* 25, 1692–1711. doi: 10.1016/j.csr.2005.05.001

Nezlin, N. P., DiGiacomo, P. M., Diehl, D. W., Jones, B. H., Johnson, S. C., Mengel, M. J., et al. (2008). Stormwater plume detection by MODIS imagery in the southern California coastal ocean. *Estuar. Coast. Shelf Sci.* 80, 141–152. doi: 10.1016/j.ecss.2008.07.012

Nezlin, N. P., DiGiacomo, P. M., Stein, E. D., and Ackerman, D. (2005). Stormwater runoff plumes observed by SeaWiFS radiometer in the Southern California Bight. *Remote Sens. Environ.* 98, 494–510. doi: 10.1016/j.rse.2005.08.008

Nezlin, N. P., and Li, B. L. (2003). Time-series analysis of remote-sensed chlorophyll and environmental factors in the Santa Monica–San Pedro Basin off Southern California. *J. Mar. Syst.* 39, 185–202. doi: 10.1016/S0924-7963(03)00030-7

Nezlin, N. P., Sutula, M. A., Stumpf, R. P., and Sengupta, A. (2012). Phytoplankton blooms detected by SeaWiFS along the central and southern California coasts. *J. Geophys. Res.* 117, C07004. doi: 10.1029/2011JC007773

Paerl, H. W., and Piehler, M. F. (2008). Nitrogen and marine eutrophication. *Nitrog. Mar. Environ.* 2, 529–567. doi: 10.1016/B978-0-12-372522-6.00011-6

Pahlevan, N., Lee, Z., Wei, J., Schaaf, C. B., Schott, J. R., and Berk, A. (2014). On-orbit radiometric characterization of OLI (Landsat-8) for applications in aquatic remote sensing. *Remote Sens. Environ.* 154, 272–284. doi: 10.1016/j.rse.2014.08.001

Pahlevan, N., and Schott, J. R. (2013). Leveraging EO-1 to evaluate capability of new generation of Landsat sensors for coastal/inland water studies. *Sel. Top. Appl. Earth Obs. Remote Sens. IEEE J.* 6. 360–374. doi: 10.1109/JSTARS.2012.2235174

Ransibrahmanakul, V., and Stumpf, R. P. (2006). Correcting ocean colour reflectance for absorbing aerosols. *Int. J. Remote Sens.* 27, 1759–1774. doi: 10.1080/01431160500380604

Reifel, K. M., Corcoran, A. A., Cash, C., Shipe, R., and Jones, B. H. (2013). Effects of a surfacing effluent plume on a coastal phytoplankton community. *Cont. Shelf Res.* 60, 38–50. doi: 10.1016/j.csr.2013.04.012

Southern California Coastal Water Research Project (1973). *The Ecology of the Southern California Bight: Implications for Water Quality Management*. Three-year Report of the Southern California Coastal Water Research Project, El Segundo, CA.

Rogowski, P., Terrill, E., Thomas, J., Rosenfeld, L., and Largier, J. (2014). *2012 Orange County Sanitation District (OCSD) Outfall Diversion – Summary Report*. Final Report Prepared for the Orange County Sanitation District, 92 pp, plus appendices.

Ryan, J. P., Kudela, R. M., Birch, J. M., Blum, M., Bowers, H. A., Chavez, F. P., et al. (2017). Causality of an extreme harmful algal bloom in Monterey Bay, California, during the 2014–2016 northeast Pacific warm anomaly. *Geophys. Res. Lett.* 44, 5571–5579. doi: 10.1002/2017GL072637

Santer, R., and Schmechtig, C. (2000). Adjacency effects on water surfaces: primary scattering approximation and sensitivity study. *Appl. Opt.* 39, 361–375. doi: 10.1364/AO.39.000361

Schiff, K., and Bay, S. (2003). Impacts of stormwater discharges on the nearshore benthic environment of Santa Monica Bay. *Mar. Environ. Res.* 56, 225–243. doi: 10.1016/S0141-1136(02)00332-X

Steinberger, A., and Stein, E. D. (2004). "Effluent discharges to the Southern California Bight from large municipal wastewater treatment facilities in 2001 and 2002," in *Southern California Coastal Water Research Project Biennial Report 2003-2004*, eds D. Elmore and S. B. Weisberg (Westminster, CA), 2–15.

Suga, Y., Ogawa, H., Ohno, K., and Yamada, K. (2003). Detection of surface temperature from Landsat-7/ETM+. *Adv. Space Res.* 32, 2235–2240. doi: 10.1016/S0273-1177(03)90548-5

Sverdrup, H. U., and Fleming, R. H. (1941). The waters off southern California March to July 1937. *Bull. Scripps Inst. Oceanogr.* 4, 261–378.

Tang, D. L., Kester, D. R., Wang, Z., Lian, J., and Kawamura, H. (2003). AVHRR satellite remote sensing and shipboard measurements of the thermal plume from the Daya Bay, nuclear power station, China. *Remote Sens. Environ.* 84, 506–515. doi: 10.1016/S0034-4257(02)00149-9

Thomas, A. C., Huang, F., Strub, P. T., and James, C. (1994). Comparison of the seasonal and interannual variability of phytoplankton pigment concentrations in the Peru and California Current systems. *J. Geophys. Res. Oceans* 99, 7355–7370. doi: 10.1029/93JC02146

Thomas, A., Byrne, D., and Weatherbee, R. (2002). Coastal sea surface temperature variability from Landsat infrared data. *Remote Sens. Environ.* 81, 262–272. doi: 10.1016/S0034-4257(02)00004-4

Uchiyama, Y., Idica, E. Y., McWilliams, J. C., and Stolzenbach, K. D. (2014). Wastewater effluent dispersal in Southern California Bays. *Cont. Shelf Res.* 76, 36–52. doi: 10.1016/j.csr.2014.01.002

Vanhellemont, Q., and Ruddick, K. (2014). Turbid wakes associated with offshore wind turbines observed with Landsat 8. *Remote Sens. Environ.* 145, 105–115. doi: 10.1016/j.rse.2014.01.009

Vanhellemont, Q., and Ruddick, K. (2015). Advantages of high quality SWIR bands for ocean colour processing: examples from Landsat-8. *Remote Sens. Environ.* 161, 89–106. doi: 10.1016/j.rse.2015.02.007

Washburn, L., Jones, B. H., Bratkovich, A., Dickey, T. D., and Chen, M. S. (1992). Mixing, dispersion, and resuspension in vicinity of ocean wastewater plume. *J. Hydraul. Eng.* 118, 38–58. doi: 10.1061/(ASCE)0733-9429(1992)118:1(38)

Welschmeyer, N. A. (1994). Fluorometric analysis of chlorophyll a in the presence of chlorophyll b and pheopigments. *Limnol. Oceanogr.* 39, 1985–1992. doi: 10.4319/lo.1994.39.8.1985

Werdell, P. J., and Bailey, S. W. (2005). An improved bio-optical data set for ocean color algorithm development and satellite data product validation. *Remote Sens. Environ.* 98, 122–140. doi: 10.1016/j.rse.2005.07.001

Conflict of Interest Statement: The authors declare that the research was conducted in the absence of any commercial or financial relationships that could be construed as a potential conflict of interest.

frontiers in Marine Science

ORIGINAL RESEARCH
published: 16 November 2017
doi: 10.3389/fmars.2017.00362

Remote Sensing of Seagrass Leaf Area Index and Species: The Capability of a Model Inversion Method Assessed by Sensitivity Analysis and Hyperspectral Data of Florida Bay

John D. Hedley[1], Brandon J. Russell[2], Kaylan Randolph[2], Miguel Á. Pérez-Castro[3], Román M. Vásquez-Elizondo[3], Susana Enríquez[3] and Heidi M. Dierssen[2]*

[1] Numerical Optics Ltd., Tiverton, United Kingdom, [2] Department of Marine Sciences, University of Connecticut, Groton, CT, United States, [3] Unidad Académica de Sistemas Arrecifales Puerto Morelos (Reef System Academic Unit), Instituto de Ciencias del Mar y Limnología, Universidad Nacional Autónoma de México, Cancún, Mexico

OPEN ACCESS

Edited by:
Steven G. Ackleson, United States Naval Research Laboratory, United States

Reviewed by:
Tom William Bell, University of California, Los Angeles, United States
William Philpot, Cornell University, United States

***Correspondence:**
John D. Hedley
j.d.hedley@numopt.com

Specialty section:
This article was submitted to Coastal Ocean Processes, a section of the journal Frontiers in Marine Science

Received: *04 August 2017*
Accepted: *30 October 2017*
Published: *16 November 2017*

Citation:
Hedley JD, Russell BJ, Randolph K, Pérez-Castro MÁ, Vásquez-Elizondo RM, Enríquez S and Dierssen HM (2017) Remote Sensing of Seagrass Leaf Area Index and Species: The Capability of a Model Inversion Method Assessed by Sensitivity Analysis and Hyperspectral Data of Florida Bay. Front. Mar. Sci. 4:362. doi: 10.3389/fmars.2017.00362

The capability for mapping two species of seagrass, *Thalassia testudinium* and *Syringodium filiforme*, by remote sensing using a physics based model inversion method was investigated. The model was based on a three-dimensional canopy model combined with a model for the overlying water column. The model included uncertainty propagation based on variation in leaf reflectances, canopy structure, water column properties, and the air-water interface. The uncertainty propagation enabled both a-priori predictive sensitivity analysis of potential capability and the generation of per-pixel error bars when applied to imagery. A primary aim of the work was to compare the sensitivity analysis to results achieved in a practical application using airborne hyperspectral data, to gain insight on the validity of sensitivity analyses in general. Results showed that while the sensitivity analysis predicted a weak but positive discrimination capability for species, in a practical application the relevant spectral differences were extremely small compared to discrepancies in the radiometric alignment of the model with the imagery—even though this alignment was very good. Complex interactions between spectral matching and uncertainty propagation also introduced biases. Ability to discriminate LAI was good, and comparable to previously published methods using different approaches. The main limitation in this respect was spatial alignment with the imagery with *in situ* data, which was heterogeneous on scales of a few meters. The results provide insight on the limitations of physics based inversion methods and seagrass mapping in general. Complex models can degrade unpredictably when radiometric alignment of the model and imagery is not perfect and incorporating uncertainties can have non-intuitive impacts on method performance. Sensitivity analyses are upper bounds to practical

capability, incorporating a term for potential systematic errors in radiometric alignment may be advisable. While *T. testudinium* and *S. filiforme* were too spectrally similar to be discriminated purely on spectral grounds, mapping of these, and other species may be achievable by exploiting co-incident factors based on ecological zonation.

Keywords: seagrass, remote sensing, inversion, hyperspectral, leaf area index, species

INTRODUCTION

Seagrasses are a key biotic component of coastal environments and provide numerous ecosystem services such as oxygen production, regulation of water quality, sediment stabilization, protection from wave energy (Fonesca and Cahalan, 1992), organic and inorganic carbon sequestration (Enríquez and Schubert, 2014), and nursery habitats for fish of commercial importance (Beck et al., 2001) or that have a role in associated habitats such as coral reefs (Nagelkerken et al., 2002; Verweij et al., 2008). Increasingly ecosystem services are recognized to have real economic value (Costanza et al., 1997) and seagrasses fall under a number of national and international initiatives for protection, such as the Water Framework Directive in Europe (Gobert et al., 2009), the Convention on Biological Diversity (United Nations, 1992), the Ramsar convention (Ramsar Convention Secretariat, 2013).

Using satellite or airborne imagery for monitoring and management of seagrasses is an attractive proposition given their global and spatial extent, estimated at 177,000 km^2 (Green and Short, 2003). Published demonstrations include estimation of canopy biophysical parameters such cover, biomass, leaf area index, and species (Mumby et al., 1997; Phinn et al., 2008; Knudby and Nordlund, 2011). The majority of approaches use classification or regression based on spectral reflectance in one or more wavelength bands. That these methods can deduce biophysical parameters indicates that, at least under some conditions, the information is present in the remote sensing reflectance to make these determinations. However, from empirical techniques it is difficult to infer the transferability and general limitations: would the same result be achievable at another site, for another species, with different depth or water conditions?

Another approach to benthic mapping by remote sensing is that of physics-based approaches, which rather than using *in-situ* empirical training data, rely on the parameterization of a physical model for spectral reflectance as seen by a remote sensing instrument. The model is then "inverted" by successive approximation (Lee et al., 1999) or look-up tables (Mobley et al., 2005) to deduce which biophysical parameter values can produce the reflectance in each pixel. The model incorporates a range of possibilities for bottom type and the optical properties of the water, this represents what is not known about the site or can vary from pixel to pixel. These variations can form the basis for uncertainty propagation, the possibility of multiple solutions within the bounds of instrument or environmental noise determines the fundamental limitation of the method (Hedley et al., 2012b). In addition, the underlying model can be used for sensitivity analysis before image processing. While sensitivity analyses and uncertainty propagation are key tools for predicting capability and informing on sensor design (Lubin et al., 2001; Hochberg and Atkinson, 2003; Hedley et al., 2012b, 2015; Botha et al., 2013) their results are not often directly compared to practical image analyses, to determine if the predictions of the sensitivity analysis are borne out in practice.

Physics-based inversion methods have been applied in seagrass environments (Dekker et al., 2011; Hedley et al., 2015) and are in theory more transferable, since they can be parameterized generically and are not linked to any specific site or imagery. Being based on a physical model rather than statistical inference, these methods also facilitate greater understanding of the fundamental limitations and uncertainties. However, applying physics-based methods presents a different set of challenges. In particular the input parameters and the model should encompass all the major sources of variation, otherwise spectra resulting from those variations may be non-physical from the point of view of the model, leading to errors in estimations and under-estimates of the uncertainty. For the same reason, atmospheric, and water interface corrections (sun-glint) must be performed with high accuracy (Goodman et al., 2008), any discrepancies in the radiometry of the imagery with respect to that of the model will lead to inaccurate results.

In this paper we present a two-species physics-based model for mapping seagrass species, canopy density (leaf area index, LAI), and depth. As an advance to previous work (Hedley et al., 2015) the new model incorporates two species, *Thalassia testudinum* and *Syringodium filiforme*, and incorporates uncertainty in the leaf reflectance of both species, in addition to variation in canopy structure, water optical properties and depth. Here we describe the application of the model in a sensitivity analysis and to hyperspectral imagery of Florida Bay. A key aim of the work was to gain insight into the relationship between the theoretical and practical method performance, in the context of the included uncertainties. For example, does including more uncertainties lead to an algorithm that has poor discrimination both theoretically and in practice? Which objectives: depth, LAI or species; are most compromised by the introduced uncertainties, and again does the theory (sensitivity analysis) match the practice (image application)? The results are relevant for improving the incorporation of uncertainties into physics-based methods, and for interpreting sensitivity analyses in the context of practical applications.

In summary the key objectives of the work presented here were:

1) Develop the conceptual framework for a multi-species model with variation in leaf reflectance, canopy structure, depth, and water optical properties, and parameterize that model.

2) Understand which sources of variation and factors are theoretically limiting in the mapping of species and leaf area index, with respect to that model.
3) Assess the capability of the method in a field test with hyperspectral airborne imagery.
4) Compare the predicted capability to the actual capability, and to understand the basis of discrepancies between theoretical and achievable performance.
5) Draw conclusions on the capability for mapping seagrass species and leaf area index by remote sensing.

METHODS

Overview

The following sections discuss successive components of the methods starting with the canopy reflectance model (**Figure 1A**); the above-water reflectance model which combines the canopy model and a water column model (**Figure 1B**); the sensitivity analysis used to understand the fundamental limitations of spectral separability, and finally the image analysis (**Figure 1C**). The steps in the development of the physics-based model are similar to those described in Hedley and Enríquez (2010), Hedley et al. (2015), so here the description is briefer and focuses on the key differences in the current work. The two species considered are *T. testudinium* and *S. filiforme*, for readability these are henceforth referred to simply as *Thalassia* and *Syringodium*.

Canopy Reflectance Model

The first step was to conduct many runs of a three-dimensional canopy model (**Figure 1**) for monospecific *Thalassia*, *Syringodium,* and 50:50 mixed canopies in terms of LAI, in order to establish the distribution of top of canopy spectral reflectance as a function of species, LAI, and canopy structure and position. Seagrass meadows are not monospecific in reality but often either *Thalassia* or *Syringodium* can represent greater than 70% of the total above-ground biomass of the macro-phyto-benthic community in Caribbean coastal habitats (Enríquez and Pantoja-Reyes, 2005). A range of community compositions are also common, associated with environmental conditions (Medina-Gómez et al., 2016). By including monospecific and 50:50 canopies in the model the idea was to cover the range of what might occur, with the concept of a mixed canopy included. The technical details of the model itself are described in Hedley (2008), Hedley and Enríquez (2010), and Hedley et al. (2014, 2015). **Table 1** gives the full details of the treatments included in the model.

The factors of canopy structure and position were considered a source of variation, leaves were modeled as flexible strips that under simple model of wave motion assume naturalistic canopy positions, of which four treatments were used, two of each termed loosely "upright" and "flattened" (**Table 1**). The leaves are modeled as reflecting and transmitting surfaces 0.9 cm wide for *Thalassia* and 0.25 cm wide for *Syringodium*. In reality *Syringodium* leaves are circular in cross-section, however most previous modeling work and measurements of reflection and transmission treat *Syringodium* leaves in the same way as flat leaves (Thorhaug et al., 2007; Stoughton, 2009). The optical data to model them as circular volumes is not available and would be difficult to obtain in practical terms. The canopy model is also designed such that all leaves originate at the substrate whereas, unlike *Thalassia*, *Syringodium* has a short shoot from which leaves branch (Eiseman, 1980). Since the application here is remote sensing and not within-canopy light fields for photobiology (Hedley et al., 2014) these compromises are most likely optically insignificant in the context of the other factors such as canopy position (**Figure 1**), depth, and water column optical properties.

An important consideration was to incorporate variation in leaf optical properties, since the previous model (Hedley et al., 2015) assumed every *Thalassia* leaf had the same reflectance. In reality leaf reflectance varies at many scales: along the leaf length, between leaves and between sites (Hedley and Enríquez, 2010). Using only a single reflectance and absorptance spectra for all leaves represents an underestimate in that component of spectral variation, but how to quantify the appropriate variation at given spatial scale is not obvious. In this study each species was represented by three pairs of reflectance and absorptance spectra, corresponding to low, medium and high reflectance, coupled with high, medium, and low absorptance (**Figure 2**). The reflectance and absorptance data for *Syringodium* and *Thalassia* leaves were collected using samples of clean leaves from the Puerto Morelos reef lagoon, Yucatan, Mexico. Leaf reflectance spectra were measured using an Ocean Optics USB2000 spectroradiometer according to the methods described in Vásquez-Elizondo et al. (2017). Reflection, $R_L(\lambda)$, was measured with a 2 mm diameter fiber optics placed over the surface of the sample at an angle of 45°C and a distance of 5 mm with a Teflon panel as a reference. Diffuse illumination was provided from light reflected from a semi-sphere coated with barium oxide (BaO) illuminated was with a white LED ring (450–650 nm) located around the sample, plus violet-blue LEDs and halogen lamps, to increase the diffuse illumination below 450 nm and above 650 nm (Vásquez-Elizondo et al., 2017). Transmission spectra were determined as $T_L(\lambda) = 10^{-D(\lambda)}$, where $D(\lambda)$ denotes absorbance, using a conventional spectrophotometer (AMINCO DW2, USA) controlled by an OLIS data collection system equipped with an opal-glass in front of the detector, following the methodology proposed by Shibata (1959) and described in Enríquez (2005) and Vásquez-Elizondo et al. (2017). Absorptance estimations were calculated as $A_L(\lambda) = 1 - T_L(\lambda) - R_L(\lambda)$. For *Syringodium*, leaves were sampled from six sites and the three reflectance and absorptance pairs were selected from 193 optical determinations as representative of the range in the data. For *Thalassia* absorptance the model described in Hedley and Enríquez (2010) was used to generate spectral absorptance based on 50, 60, and 70% PAR absorptance, a typical range as shown in that paper. Additional reflectance measurements of leaf samples, not included in Hedley and Enríquez (2010) were taken to provide the three reflectance spectra (**Figure 2A**). For each individual modeled top of canopy reflectance (**Table 1**) one of the reflectance-absorptance pairs was selected for each species. This means that the spatial scale of the variation that is included was assumed pixel-to-pixel in a remote sensing context. This

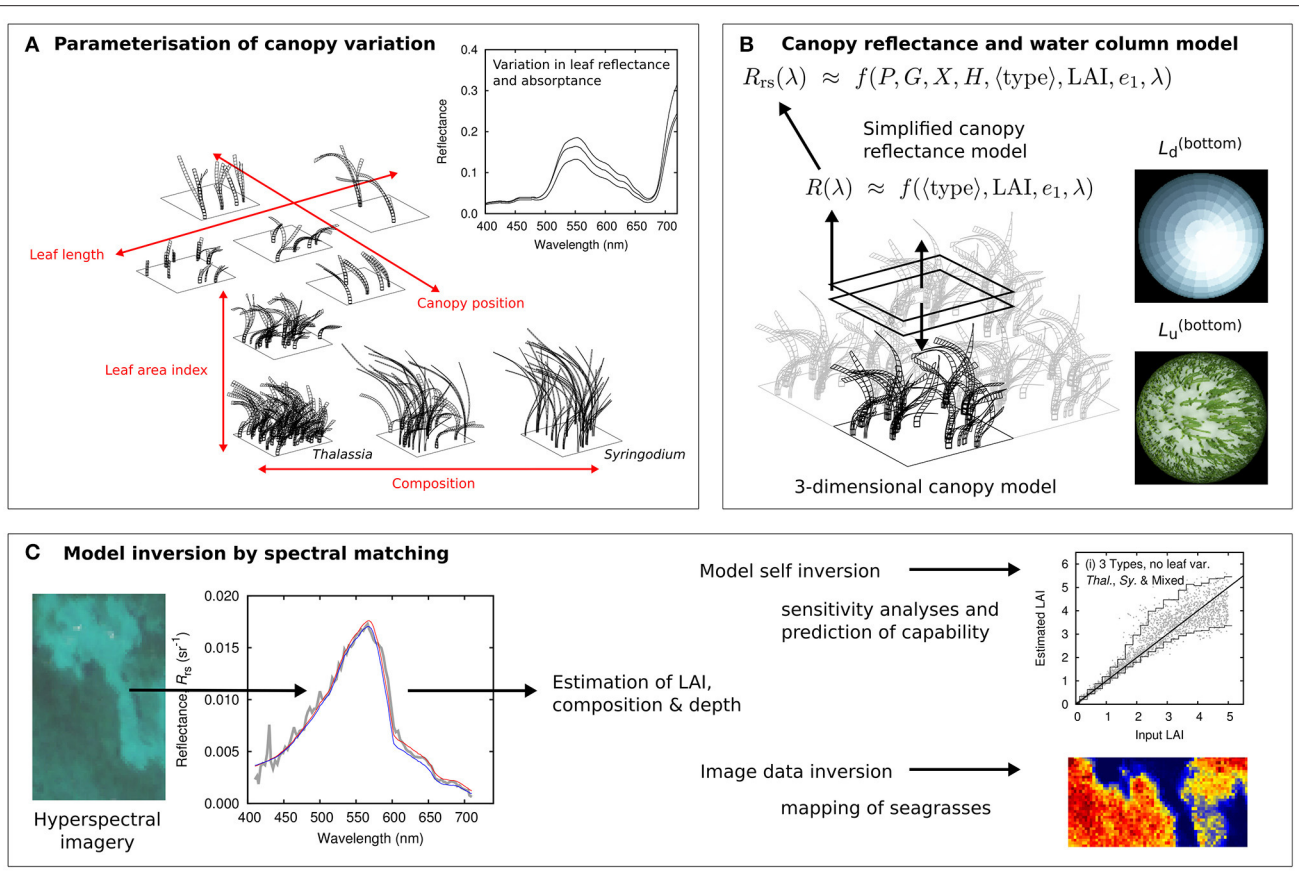

FIGURE 1 | Overview of seagrass reflectance model and analysis. **(A)** Canopies are parameterized by four factors: Composition, leaf area index (LAI), leaf lengths, and leaf position. **(B)** A three dimensional canopy model estimates the top of canopy reflectance over all conditions and the results are reduced to a simpler functional form that includes the water column. **(C)** A spectral matching procedure applies the simplified model in sensitivity analyses and image processing.

TABLE 1 | Experimental design of model runs for establishing the variation of above canopy diffuse reflectance with LAI and other factors.

	Leaf length	LAI	Position	Sand reflectance	Leaf reflectance	SZA	Depth	Random repeats	Total
Thal.	x 3 short medium long	x 11 Max. ~6.5	x 4 2 upright 2 flattened	x 1	x 1 A random choice of 1 out of 3 each time	x 2 26° 56°	x 3 1 m 5 m 10 m	x 5	3,960
Sy.	x 2 short long	x 9 max. ~5.5	x 4 2 upright 2 flattened	x 1	x 1 A random choice of 1 out of 3 each time	x 2	x 3	x 5	2,160
Mix	x 1 *Thal.* medium *Sy.* short	x 9	x 4 2 upright 2 flattened	x 1	x 1 A random choice of 1 out of 3 each time for *Thal.* and *Sy.*	x 2	x 3	x 5	1,080

Thal, were monospecific Thalassia canopies; Sy, Syringodium; and Mix was a mix of Thalassia and Syringodium that is on average 50:50 in terms of LAI. SZA denotes solar zenith angle. For Thalassia leaf length distributions in terms of mean and standard deviation were: short 6 ± 3 cm; medium 12 ± 6 cm; long 24 ± 12 cm, for Syringodium, short 25 ± 10 cm; long 50 ± 20 cm. Each column shows the number of treatments and the final column the number of canopy model runs used to characterize the distribution of top of canopy reflectances.

inclusion of variation in leaf reflectance is approximate, as the appropriate variation at a given spatial scale is unknown. However, to include no variation at all would be the weakest treatment because it could lead to spectral differences between the species for purely numerical reasons. Two spectra, as single data points, could have a distinguishing feature at

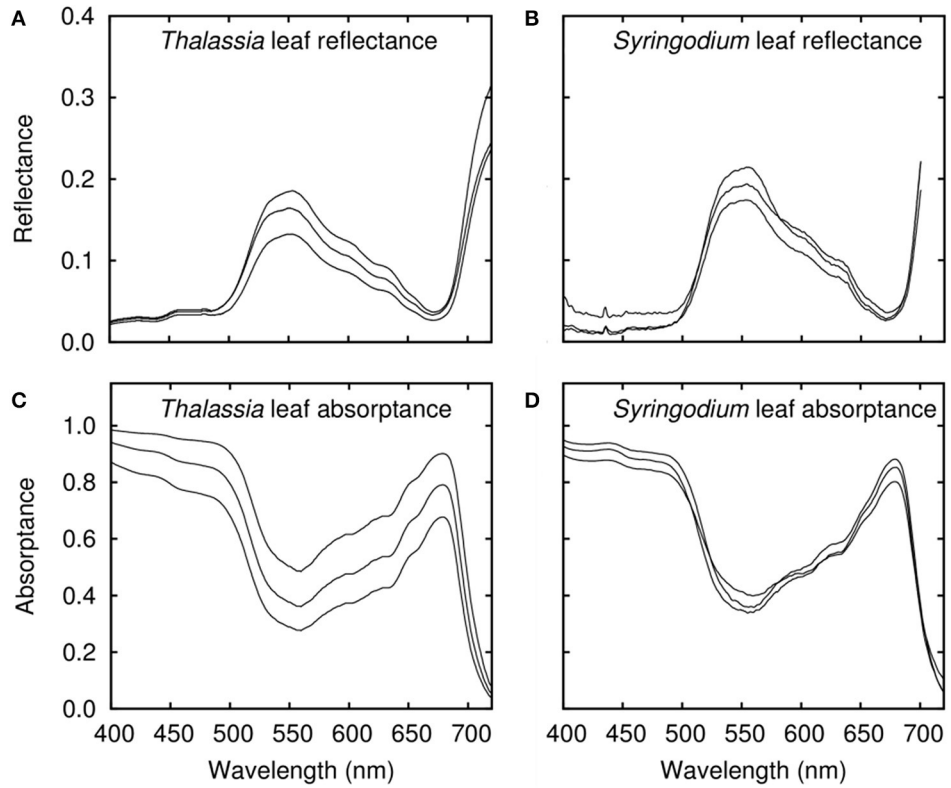

FIGURE 2 | Leaf level reflectances and absorptances as used in the modeling for **(A,C)** *Thalassia* and **(B,D)** *Syringodium*. Each plot shows three lines, corresponding to the high, medium, and low reflectance variants (high reflectance being paired with low absorptance etc.).

random. Further discussion of these questions is deferred to the Discussion but the key point is that the specification of this variation (**Figure 2**) must be borne in mind when interpreting the results.

The reflectance of the underlying sand was the same as that used in Hedley et al. (2015), being a typical calcium carbonate sand reflectance spectra with increasing reflectance in the red to a maximum of about 40% (Hedley et al., 2015). Note that in Hedley et al. (2015) the leaf reflectances were modified to include a component of sand reflectance to account for the observation that in some sparse *Thalassia* canopies there was sediment on the leaves, that term was not included here.

To factor in variations due to canopy BRDF (Bi-directional Reflectance Distribution Function) with repeat runs canopies were illuminated from two solar zenith angles, 26° and 56°, by sky radiance distributions computed by libRadtran, (Mayer and Kylling, 2005), and at three depths, 1, 5, 10 m, with the directional light field at depth computed by PlanarRad[1]. These factors are discussed in more detail in Hedley et al. (2015). In the incorporation of the water column to the image analysis algorithm by necessity the top of canopy reflectance is considered Lambertian. Hedley et al. (2015) showed this simplification was insignificant in comparison to other factors but the propagation of the BRDF related uncertainty is retained for completeness.

[1]www.planarrad.com

The canopy model was configured to calculate in 16 spectral bands of 20 nm width over the range 400–720 nm and all reflectances were resampled to these bands. The spectral reflectance properties of *Thalassia* and *Syringodium* are dominated by chlorophyll *a* and *b* therefore no species-dependent fine scale spectral features are lost by this process (**Figure 2**).

Top of Water Column Reflectance Model

The next step was to develop a model of top of water column reflectance that was fast enough in application to be used for image analysis. For each of the three canopy species structures, mono specific *Thalassia* and *Syringodium* and the 50:50 mix, the reflectance at each wavelength was fitted to an exponential model of the form,

$$R(\lambda) = A(\lambda) \exp\left[-k(\lambda) \times \mathrm{LAI}\right] + B(\lambda) + \varepsilon(\lambda) \qquad (1)$$

Where the $A(\lambda)$, $k(\lambda)$, and $B(\lambda)$ values were deduced by regression over all the canopy model results for each canopy type. An exponential decrease in reflectance with LAI was shown to work well in the previous study (Hedley et al., 2015). The term $\varepsilon(\lambda)$ represents a set of spectra, which are the residual differences between the regression model and the actual spectra, largely due to the factors that introduce variation. It is assumed that $\varepsilon(\lambda)$ can be treated as random since we are not interested to deduce factors such as canopy position. A model for the range of magnitude and shape of $\varepsilon(\lambda)$ is established by principle components analysis and

$\varepsilon(\lambda)$ is reduced to a wavelength independent single parameter e_1, which ranges from 0 to 1 (Hedley et al., 2015). A check is performed that the full model, including the component captured by e_1 can replicate all the top of canopy spectra to within acceptable accuracy (**Figure 3**). On this basis one error term was judged sufficient, so top of canopy spectral reflectance becomes a function of species composition (canopy type), leaf area index, and the random error term drawn from a uniform distribution of 0 to 1.

$$R(\lambda) \approx f\left(\langle type\rangle, \mathrm{LAI}, e_1, \lambda\right) \quad (2)$$

This expression was embedded into Lee et al.'s (1998, 1999) semi-analytical model for shallow water remote sensing. A input parameter of Lee et al.'s model is bottom spectral reflectance, $R(\lambda)$, so using Equation (2) this input can be eliminated and a function of the following form implemented,

$$R_{\mathrm{rs}}(\lambda) \approx f\left(P, G, X, H, \langle type\rangle, \mathrm{LAI}, e_1, \lambda\right) \quad (3)$$

where the remote sensing reflectance, $R\mathrm{rs}(\lambda)$, at wavelength λ is calculated dependent on the amount of phytoplankton (P), dissolved organic matter (G), backscatter (X), depth (H), and bottom reflectance $R(\lambda)$. LAI, <type>, and e_1 represent the canopy, where <type> is a categorical parameter (integer) taking the value 0, 1, or 2 for *Thalassia*, *Syringodium,* or mixed canopy type respectively. This model can be used in both forward mode, to estimate the remote sensing reflectance for a specific situation represented by the input parameters, or in inverse mode using a successive approximation technique such as Levenberg-Marquardt (Wolfe, 1978), where the input parameters that give the best least-squares match to a given remote sensing reflectance are deduced. Since <type> in Equation (3) is not a continuous parameter, for inversion three best-fit solutions are found for <type> = 0, 1, 2, and the overall best fit is considered the optimal solution and determines canopy composition type. The possible range of the parameter values for all inversions in this study were P [0, 0.2]; G [0, 0.5]; X [0, 0.05]; H [0, 20]; LAI [0, 6]; e_1[0, 1] (**Table 2**). The possible canopy type was in some cases restricted, or all three of *Thalassia*, *Syringodium,* or 50:50 mix were used. For further details of what underlies Equation (3) see Hedley et al. (2009, 2015).

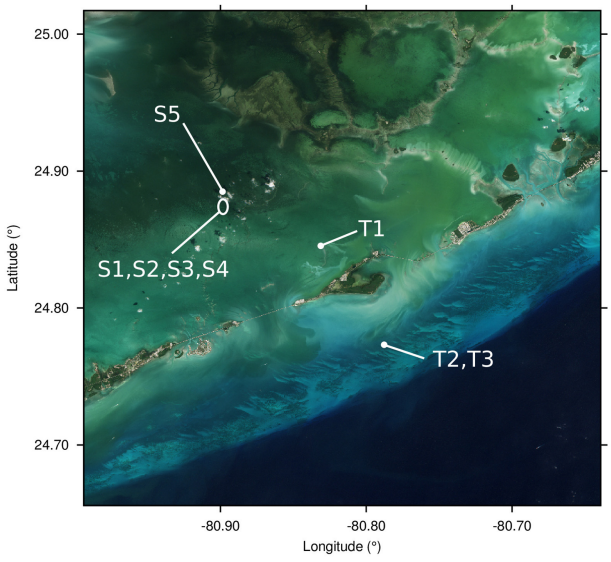

FIGURE 3 | The five *Syringodium* dominated locations (S1-S5) and three *Thalassia* dominated locations (T1-T3) where the *in situ* LAI and depth data points were located. Image produced using Sentinel-2A data from the European Space Agency.

In the sensitivity and image analyses, Equation (3) was evaluated at a wavelength resolution corresponding to a subset of the bands of the PRISM hyperspectral data, specifically 107 bands with centers from 410 to 710 nm. The canopy model results and other spectrally tabulated coefficient data were resampled to these wavelengths by linear interpolation. Local optima in the inversion were avoided by repeating each inversion five times with a random parameter start point, and the best matching solution of the five taken.

Sensitivity Analysis

The model for remote sensing reflectance (Equation 3) was applied in a sensitivity analysis to deduce the fundamental uncertainty, which occurs when two different physical situations lead to the same remote sensing reflectance within a tolerance that is negligible in practical terms. In other words, spectra are so close that they cannot be reliably differentiated. The model included sources of variation in spectra from components of the system up to the top of the water column, with the intention that it would be applied to atmospheric and glint corrected imagery. Optical processes that occur above the water column that cause pixel-to-pixel variation were outside the scope of the model and are effectively noise. In this context the fundamental uncertainty can be deduced by noise perturbed self-inversion of the model. i.e., a specific set of parameters are used to model remote sensing reflectance from Equation (3), a random noise term is added on, then the model is inverted to see if the input parameters can be recovered. The variability in the recovered parameters is the fundamental uncertainty of the model in the context of the noise. In the sensitivity analysis we used a spectrally correlated noise model (Hedley et al., 2012a; Garcia et al., 2014) based on the covariance matrix over a deep water area of the Florida Bay PRISM imagery (see next section). Being empirically derived, the covariance matrix captures all sources of pixel to pixel variation that occur over the deep water area, including both environmental effects and instrument noise. A spectrally correlated model is used because a large part of the noise is residual surface glint, even after images have been glint corrected (Kay et al., 2009), and so is not independently random in each band.

The model of Equation (3) was used to randomly generate spectral remote sensing reflectances with parameters being drawn from uniform distributions over the ranges in **Table 2.** Depth ranged from 0 to 10 m, LAI from 0 to 5. Five separate analyses were conducted, three where canopy type was fixed as only one of the basic classes: *Thalassia*, *Syringodium,* or a 50:50 mixture, one where canopy type could be one of either *Thalassia*

TABLE 2 | Sensitivity analysis design showing range of parameters used for forward modeling and for inversion.

	Forward modeling							Inversion						
Analysis	***P***	***G***	***X***	***H***	**LAI**	**<type>**	e_1	***P***	***G***	***X***	***H***	**LAI**	**<type>**	e_1
Thal.	0.03	0.05	0.01	0–10	0–5	1	0–1	0–0.2	0–0.5	0–0.05	0–20	0–6	1	0–1
Sy.						2							2	
50% Mixed						3							3	
Thal. & *Sy.*						1, 2							1, 2	
All 3						1, 2, 3							1, 2, 3	

These inversion parameters were also used for the image analysis. Canopy type <type> corresponds to: 1, Thalassia; 2, Syringodium; 3, 50% mixed by LAI.

and *Syringodium*, and one where each modeled spectra could arise from any of the three classes. The idea was to simulate varying degrees of canopy composition changes from pixel to pixel, and investigate the consequences of introducing canopy type variability. All five analyses were performed three times: (1) using results with leaf level reflectance variation (**Figure 2**); (2) using only canopies modeled with no leaf level variation in reflectance and absorptance: using the medium reflectance and absorptance (middle lines in **Figure 2**); and (3) using the canopy reflectances directly from the 3D canopy model, hence bypassing the simplified reflectance model (Equation 1) and using more "realistic" canopy reflectances in the forward model while retaining the simplified model in the inversion. The aim was to understand the consequences of introducing leaf level variation to the fundamental uncertainty, and also to verify if the performance of the simplified canopy model against the 3D canopy model which it is based. For the forward modeling the water optical properties were fixed at the values shown in **Table 2**. This is equivalent to assuming an area of spatially homogenous water optical properties.

For each analysis, 15 in all, 2,500 random spectra were generated by the forward model, random noise was added on and then the inversion model was applied to attempt to recover the input parameters. The resulting dataset facilitated an investigation into the various sensitivities of the model and is presented in the Results and Discussion section.

Image Data Analysis

The inversion model was applied to hyperspectral airborne imagery acquired by the Portable Remote Imaging Spectrometer (PRISM) instrument (Mouroulis et al., 2014) in Florida Bay, January 2014 (Dierssen et al., 2015), using 107 of the PRISM bands from 410 to 710 nm. Details of the imagery pre-processing are given in Hedley et al. (2015), but in short this consisted of: atmospheric correction and conversion to $R_{rs}(\lambda)$ using a modified version of the ATREM radiative transfer model (Gao and Davis, 1997); per-pixel sun-glint correction by use of the Rayleigh-corrected reflectance at 980 nm; and a vicarious calibration adjustment based on above-water spectral reflectance measurements taken with an ASD FieldSpec 4 co-incidentally with image acquisition (Dierssen et al., 2010). The imagery is at ∼1 m resolution. The above-surface solar zenith angle was ∼30° at the time of acquisition.

A number of flight lines were available, some of which covered sites at which canopy composition, LAI, and depth had been recorded co-incident with GPS data (see Hedley et al., 2015 for methods). The data included areas that were dominated by *Thalassia* or *Syringodium*, typically located ocean side or bay side respectively (**Figure 3**). The analysis utilized eight locations from three flight lines that covered the *in-situ* data locations, and varied in pixel size from ∼1 to 2 m. Five locations (S1-S5) were *Syringodium* dominated (close to monospecific) and three (T1-T3) where *Thalassia* dominated. Each location contained between two and 12 *in-situ* data points of LAI determinations based on 20 × 20 cm quadrats in transects spaced 2 m apart. In total 42 data points were available however the seagrass beds were patchy and in some cases visual inspection indicated that the location of the data in the imagery was only reliable to within a few meters. For this reason precise image to data registration of the 42 individual points was not possible and the data was processed as grouped into the eight locations. At each location the mean and standard deviation of LAI estimates from 4-pixel window (∼4–8 m dependent on pixel size) around the data points was taken, and compared to the mean and standard deviation of the *in-situ* data points at that location. Depth data was also available for each of the eight locations; this was assumed constant at each location.

Parameterization of the model for image processing was the same as described in the sensitivity analysis, inversion ranges as in **Table 2** and with all three bottom composition types included. A deep water area at the end of the flight line containing the *Thalassia* dominated canopies was used to characterize the above-surface noise covariance matrix (the same noise matrix as used in the sensitivity analysis), the other flight line did not have a suitable deep water area for noise assessment, so the same above surface noise was assumed. For each pixel 20 noise perturbed inversions were performed to provide the mean results and 90% confidence intervals for the parameters of interest, in particular LAI and depth.

RESULTS AND DISCUSSION

Variation in Modeled Top of Canopy Reflectance

The leaf level reflectance measurements of *Thalassia* and *Syringodium* (**Figure 2**) were consistent with those measured by others for those species and for other seagrasses

(Lüning and Dring, 1985; Zimmerman, 2003; Runcie and Durako, 2004; Enríquez, 2005; Thorhaug et al., 2007; Stoughton, 2009) although our reflectances tended to be higher at the peak of 550 nm. Consistent with Enríquez (2005) and Thorhaug et al. (2007) the spectral shapes of the leaf reflectance of *Thalassia* and *Syringodium* were almost identical to each other and the reflectance of *Syringodium* at 550 nm was slightly higher than *Thalassia* (**Figure 2**).

The first question of interest in this study is how the sources of variation in the 3D canopy model affected the top of canopy reflectances for *Thalassia* and *Syringodium*, and in particular the relative contribution of variation of leaf level reflectance. The input data on reflectance and absorptance of *Thalassia* and *Syringodium* leaves contains a wider variation for *Thalassia* than *Syringodium*, especially in terms of absorptance (**Figure 2**). This has a consequence for the variation in the top of canopy reflectance (**Figure 4**). For *Thalassia* at an LAI of 3 the variation in reflectance at 630 nm was around three times greater when leaf level variation is included (**Figure 4B** vs. **Figure 4A**), whereas for *Syringodium* the variation in reflectance was relatively unaffected by the introduction of leaf level variance (**Figure 4D** vs. **Figure 4C**). At a given LAI the "base level" variation induced by variation in canopy structure and position was similar for *Thalassia* and *Syringodium* (**Figures 4A,C**); a small level of variation in leaf optical properties is negligible in comparison (**Figure 4D**) but clearly above a certain threshold of leaf level variation the variation in canopy reflectance becomes much greater (**Figure 4C**). In our data *Syringodium* was below this threshold and *Thalassia* was above it. Whether this level of variation is appropriate for the spatial scale of the remote sensing

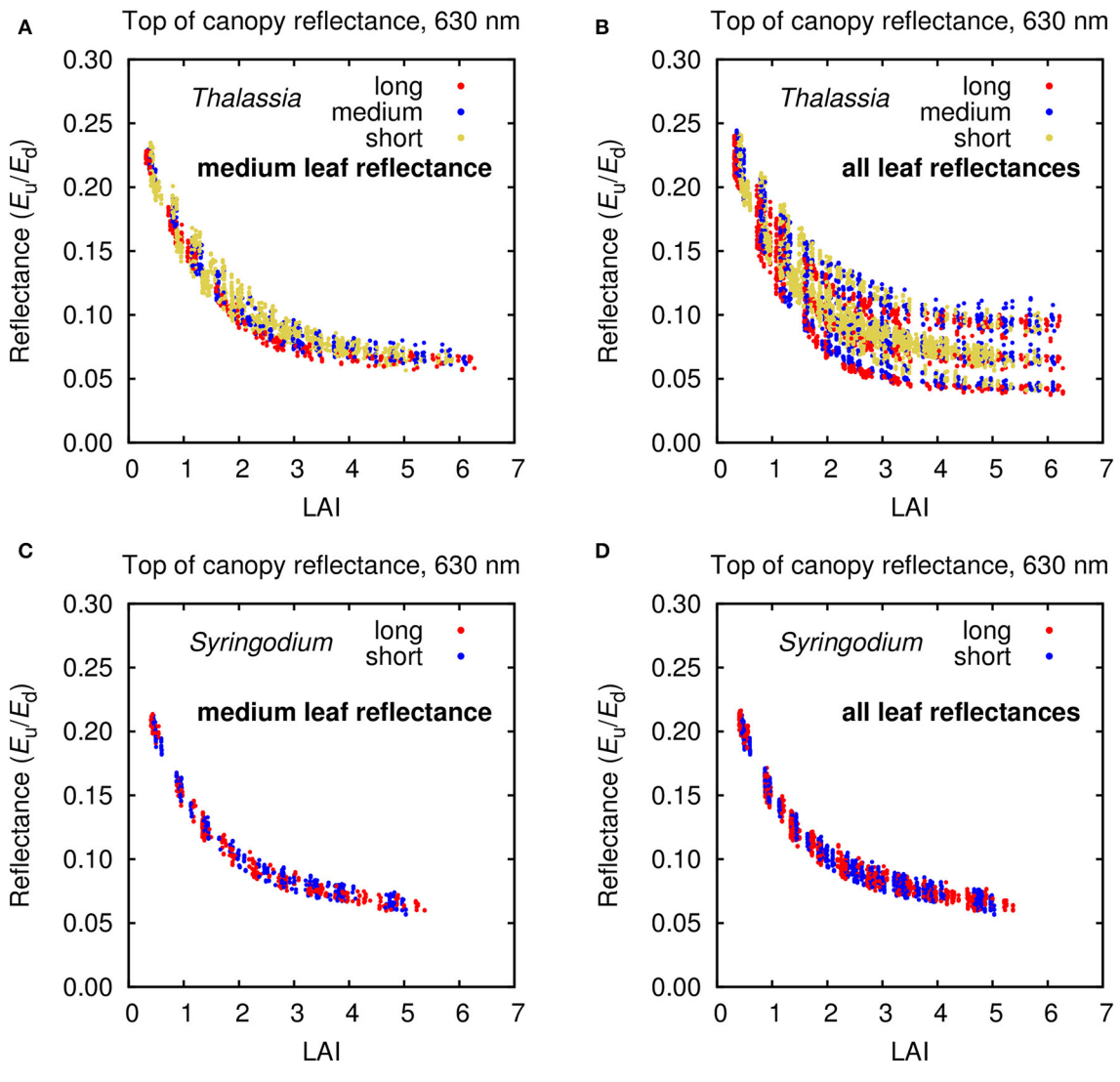

FIGURE 4 | Top of canopy (TOC) reflectance at 630 nm for modeled **(A,B)** *Thalassia* and **(C,D)** *Syringodium* canopies under all treatments but differentiated by **(A,C)** medium leaf reflectances only and **(B,D)** all three leaf reflectance and absorptance treatments.

analysis (1–2 m pixels) remains unknown, as the data were not collected with this objective in mind, this will be discussed later.

Spectral Separability in Top of Canopy Reflectance

Given the level of variation introduced by canopy position, structure, and leaf level variations (**Figure 4**) the next question is how much spectral separability for determining LAI or between canopy compositions of *Thalassia* and *Syringodium* remained in the top of canopy reflectances? While this will be answered more comprehensively by the sensitivity analysis an initial band ratio plot for 450 and 550 nm for all of the modeled canopy reflectances indicates that separability in the model data is possible (**Figure 5**). Considering LAI first (**Figure 5**B) there was a clear trend of darkening in both bands where LAI graduates across the plot area. Despite a few isolated places where, for example, LAIs of 5 were mixed with LAIs of 3, there is a monotonic trend in LAI in both bands up to LAIs of around 4. This is consistent with the previous *Thalassia* only model (Hedley et al., 2015) and suggests the introduction of *Syringodium* does not compromise this capability.

The ability to spectrally discriminate species in the modeled top of canopy reflectances is less clear (**Figure 5A**). *Syringodium* was distributed in the upper range of the variation with respect to reflectance at 550 nm, in part at least because leaf reflectance was generally higher at 550 nm (**Figure 2**), but still overlaps with *Thalassia* in the two-band space of 450 and 550 nm. At any specific LAI the species were separable by the ratio of reflectance at 550–450 nm (**Figure 5C**), but for ratio values less than around eight either species could be present but with different LAIs. There is a region on the left of **Figure 5A** where only *Syringodium* occurs, corresponding to an LAI greater than 3 (c.f. **Figure 5B**), this corresponds to reflectance ratios greater than 8, where only *Syringodium* occurs in **Figure 5C**. In this region *Syringodium* could be distinguished from *Thalassia* in top of canopy reflectance using only the bands at 450 and 550 nm. The basis of this is that in our data at 550 nm *Syringodium* leaves were slightly brighter than *Thalassia* to an extent that is beyond the incorporated variation, but at 450 nm they were similar. Capability for discrimination using all the spectral bands can only be greater, but water column variations and above surface noise will compromise that ability.

Simplified Model for Top of Canopy Reflectance

The next set of results verified that the simplified model for top of canopy reflectance (Equation 1) for each canopy composition adequately captured the variations previously discussed. The question is how much is "lost" going from the 3D model reflectances to the simplification of Equation (1). This is also checked later in the sensitivity analysis, but the first evaluation is to consider the magnitude of the residual spectra between the 3D canopy model reflectances and those that can be produced by the simplified model (**Figure 6**). In all cases the spread of the residuals was very small compared to the range of reflectances captured. For wavelengths lower than 700 nm, over all six models 70% of the 90% confidence intervals on the residuals were less than 5% of the reflectance range, and nowhere were the residual 90% confidence intervals greater than 10% of the reflectance range. Residual ranges greater than 5% of the reflectance only occur when leaf level optical variation is introduced. This indicates that leaf level optical variation does introduce different modes of variation that can't be captured by a single variation term (e_1, section Top of Water Column Reflectance Model). But since the effect is small a single error term was retained for this study.

Sensitivity Analysis—Bathymetry

The sensitivity analysis indicated that the fundamental uncertainty for bathymetry was very low under all treatments (**Figure 7**). Even for the treatment that included the most sources of variation, including all three canopy compositions of *Thalassia*, *Syringodium,* and 50% mixtures, 90% confidence intervals on bathymetry retrieval were better than ±1 m at 10 m depth (**Figure 7J**). For the other treatments the confidence intervals on bathymetry retrieval mirrored the amount of variation included in the model; the confidence intervals for canopy treatments of single composition types with no leaf

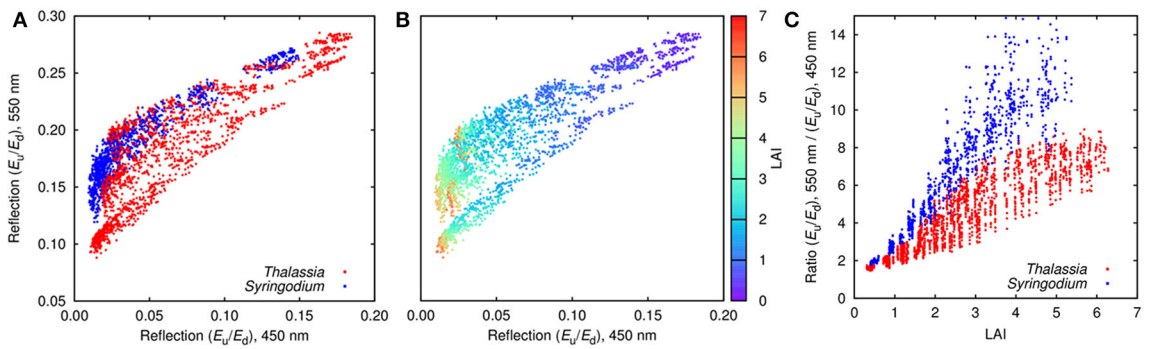

FIGURE 5 | Distribution of top of canopy (TOC) reflectance for all modeled *Thalassia* and *Syringodium* canopies with 26° solar zenith angle, in two band space: 450 and 550 nm. **(A)** Distribution by species, **(B)** distribution color coded by LAI, **(C)** band ratio of reflectance at 550–450 nm, as a function of LAI. Note that all points are plotted in a random order so the dominance of a color in particular area does not arise simply because other points are obscured.

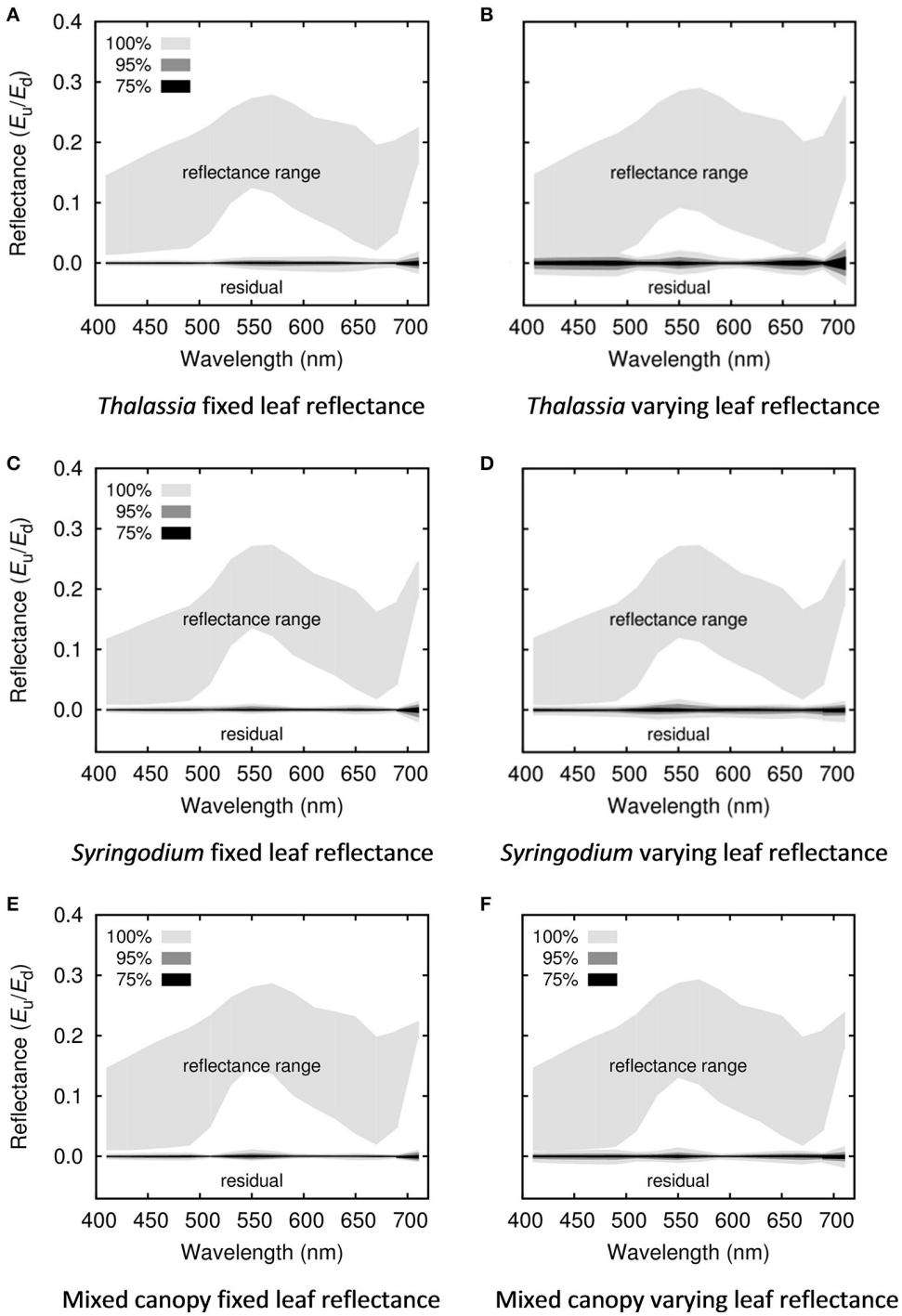

FIGURE 6 | Magnitude of discarded residuals for each of the simplified canopy models for **(A,B)** *Thalassia*, **(C,D)** *Syringodium*, **(E,F)** 50% mixed canopies of *Thalassia* and *Syringodium*, and for **(A,C,E)** canopies where leaf reflectance is fixed, **(B,D,F)** variable leaf reflectance. The upper region of each plot shows the full range of reflectances from all treatments in the 3D canopy model, the lower line shows the magnitude of the discarded residual error when the model is simplified, in terms of 100, 95, and 75% of the inputs, i.e., 75% of the residuals lie with the bounds of the 75% shaded region.

level variation were particularly narrow (**Figures 7A,C,E**). That bathymetry is a robust result under physics based inversion approaches is well-established (Dekker et al., 2011) and this result is as expected. What is important here is that introducing different canopy compositions and leaf level optical variation made very little difference to the fundamental uncertainty in

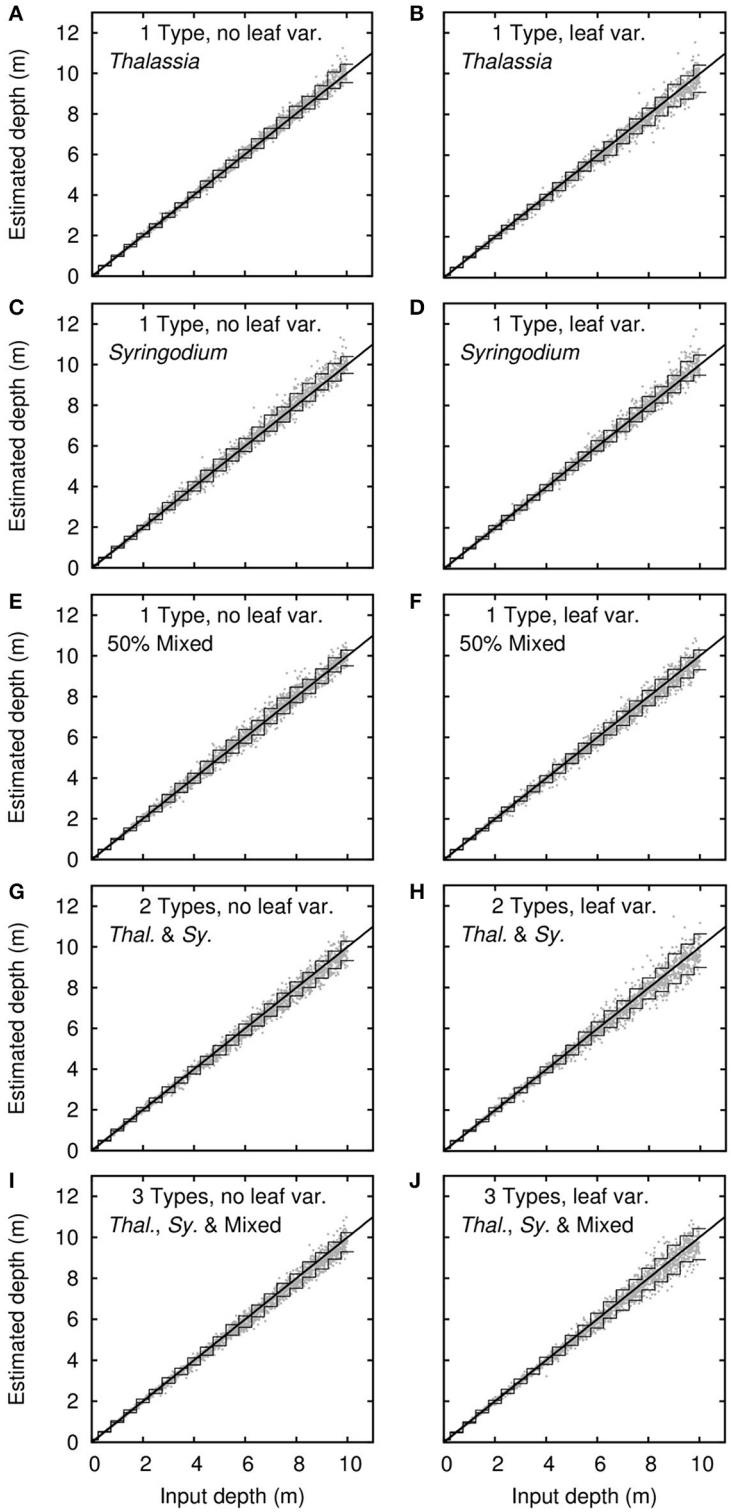

FIGURE 7 | Sensitivity analysis results for bathymetry. Dots are 2,500 noise-perturbed self-inversion results, lines are mean 90% confidence intervals binned in steps of 0.5 m. Treatments are **(A–F)** single benthic types of *Thalassia*, *Syringodium* and 50% mixed canopies, plus **(G–J)** models with multiple bottom types. Right and left columns are with and without variation in leaf reflectance.

bathymetry. However, being an estimate of the uncertainty from self-inversion of the model this is an upper bound on what could be expected in a real application. The possibility of errors in image pre-processing is neglected, for example.

Sensitivity Analysis—Leaf Area Index

Leaf area index was a less robust result than bathymetry (**Figure 8**). The confidence intervals for LAI retrieval are relatively large, especially for LAIs greater than 2. This corresponds to the increasing saturation of the LAI effect on reflectance as canopy reflectance becomes less, beyond a certain LAI no further darkening can occur and approaching this limit uncertainties become high (**Figure 5**) (Knyazikhin et al., 1998). In the inversion parameter limits (**Table 2**) the upper limit on the LAI confidence interval is capped at 6 and this explains why the upper confidence interval curves toward the horizontal for high LAIs (**Figure 8**). The upper limit acts to reduce the uncertainty and is akin to including the *a priori* information that LAIs greater than 6 cannot occur. Including *a priori* limits or probabilities is useful for reducing uncertainty in inversion methods (Jay and Guillaume, 2016) but is unsuitable if anomalies are of interest or the bounds are too restrictive. Other seagrass species such as *Posidonia sinuosa* and *Posidonia oceanica* can achieve much higher LAIs (e.g., >8 reported in Collier et al., 2007; and >12 reported in Olesen et al., 2002, respectively) and in that case it would be preferable that the uncertainty accurately reflects this.

Leaf area index was also more sensitive to the specific canopy composition treatment or inclusion of leaf level variation, but not exceptionally so and without any clear pattern (**Figure 8**). Introducing leaf level optical variation in general increased uncertainty in LAI retrievals, as expected, but the effect was relatively small. Interestingly, without leaf level variation *Syringodium* LAI determinations had higher uncertainty than for *Thalassia* (**Figure 8C** vs. **Figure 8A**). This was likely the result canopy position and structure, the longer and thinner leaves of *Syringodium* will have a greater effect on the apparent areal density as viewed from above, when they assume different positions. The higher leaf level variation in *Thalassia* (**Figure 2**) more than compensated for this factor and when leaf level variation was included *Thalassia* had slighter higher uncertainty (**Figures 8B,D**). Overall though, all treatments performed similarly, and introducing a model with two species (**Figures 8G,H**) or two species plus mixtures (**Figures 8I,J**) did not greatly increase the uncertainty in LAI estimation.

Sensitivity Analysis—Canopy Composition

Determining the canopy composition type, either monospecific *Thalassia* or *Syringodium*, or between the two monospecific canopies and 50:50 mixed canopies, would be expected to have high uncertainty since the spectral shapes of *Thalassia* and *Syringodium* leaf optical properties are almost identical (**Figure 2**, and Thorhaug et al., 2007). However, as previously mentioned, in our model a degree of species separability at the top of canopy exists because the *Syringodium* was relatively brighter than *Thalassia* at 550 nm (**Figure 2**). The sensitivity analysis also indicates some capability for species discrimination, in fact for depths less than 0.5 m the self-inversion analysis was able to accurately recover the canopy composition type 100% of the time (**Figure 9**), hence even including low LAI conditions that **Figure 5** indicated might be inseparable. Therefore, despite including above surface noise, the top of canopy reflectances were spectrally separable to a much greater extent than implied by the two-band analysis of **Figure 5**. This is partly a consequence of the simplified canopy reflectance model, which reduces variation by multiple factors into a single degree of freedom. However, this issue is not large, when using the original 3D canopy model reflectances in the forward model, accuracy in composition type for depths less than 0.5 m is in the range 60–80% for most treatments (**Figure 9**), but by a depth of 4 m the ability to distinguish canopy type has reduced to around 50–70% and any artefactual advantage in using the simplified canopy forward model is lost. This provides an alternative estimate of the "cost" of the simplified canopy model: At a depth of 4 meters the above surface noise in relation to the benthic "signal" was already greater than what was lost in simplifying the canopy model.

Ability to determine canopy composition decreases with increasing depth (**Figure 9**). For canopies that can be either *Thalassia* or *Syringodium* (**Figures 9A,B**) a random choice would be correct 50% of the time, so at 10 m depth separability of ∼60% indicates the ability to determine species is almost completely lost. Likewise for three bottom compositions of *Thalassia*, *Syringodium*, or mixed canopies ∼40% accuracy at 10 m is close to a random choice.

It might be expected that the ability to determine species would increase with LAI, since the "signal" of the species would be expected to increase with leaf area. This was true only for treatments that included leaf level optical variation, and the effect was small (**Figures 10B,D**). For multiple canopy types where there was no leaf variation, ability to discriminate canopy composition actually decreased slightly with LAI (**Figures 10A,C**). However, these results do not give any strong indication since overall ability to discriminate canopy type was averaged over all depths from 0 to 10 m, the primary conclusion is depth was the more significant factor (**Figure 9**).

The sensitivity analysis is therefore pessimistic as regards the ability to distinguish between *Thalassia* and *Syringodium* by remote sensing. These results should be considered upper bounds of what is achievable, in the context of what is included in the model. That is, in any application results can only be worse unless there is some aspect not included in the model that could be leveraged to facilitate species discrimination. In Florida Bay *Syringodium* tends to occur bay-side whereas *Thalassia* is ocean-side, therefore there could be systematic differences in water optical properties co-incident with species that would increase discrimination. Here, we have only considered clean leaves free of large epiphytes. *Thalassia* leaves have a longer life span than *Syringodium*, which facilitates the formation of more complex epiphyte communities on the leaves. The dominant epiphyte taxa are calcifying red coralline algae, although foraminifera, diatoms, and other small calcifiers have also been reported (Corlett and Jones, 2007). Epiphyte cover is greatest at the apical segments of *Thalassia* leaves, since these are the oldest part of the leaf. Being located at the top of the canopy there is good potential for epiphytes to contribute to the reflectance. On the other hand,

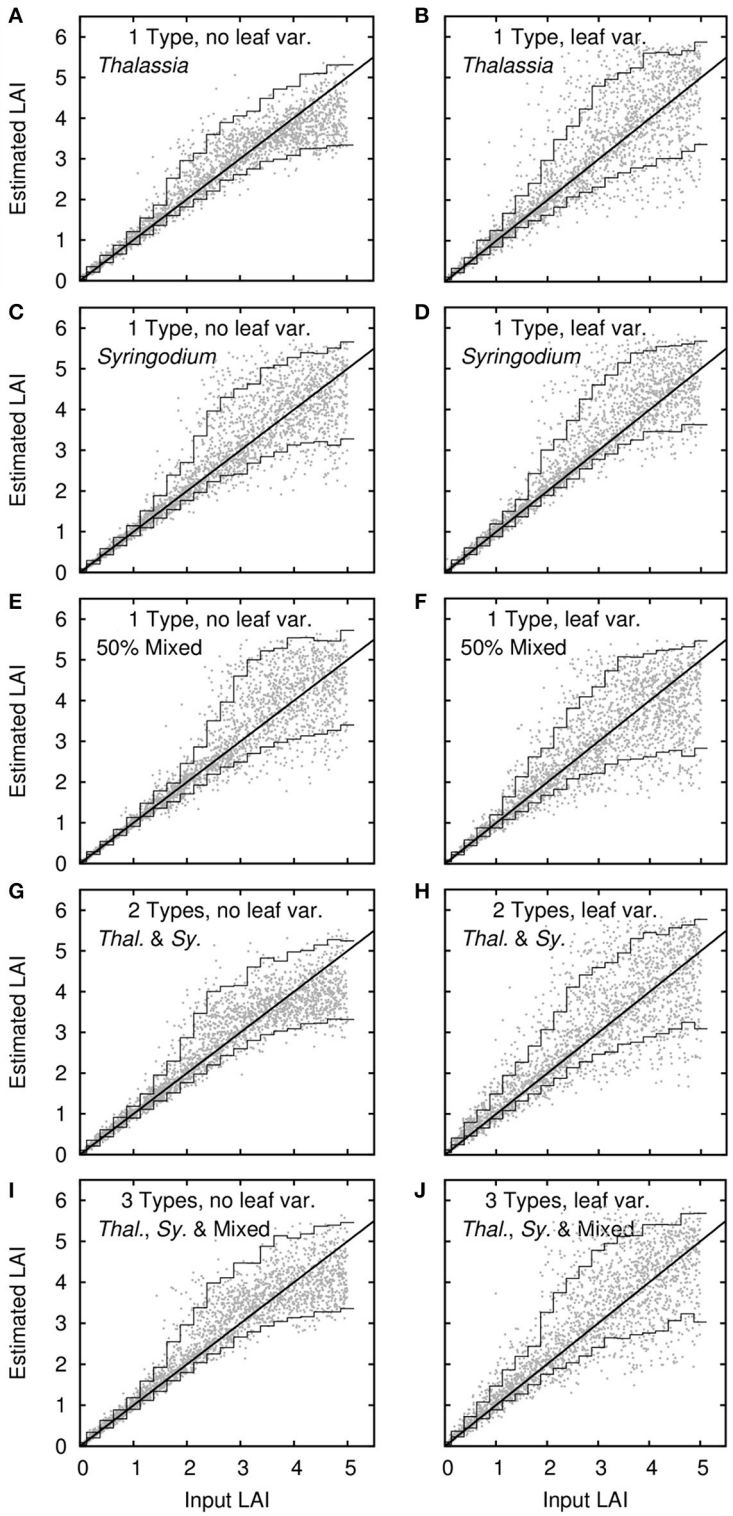

FIGURE 8 | Sensitivity analysis results for leaf area index (LAI). Dots are 2,500 noise-perturbed self-inversion results, lines are mean 90% confidence intervals binned in steps of 0.25 in LAI. Treatments are **(A–F)** single benthic types of *Thalassia*, *Syringodium* and 50% mixed canopies, plus **(G–J)** models with multiple bottom types. Right and left columns are with and without variation in leaf reflectance.

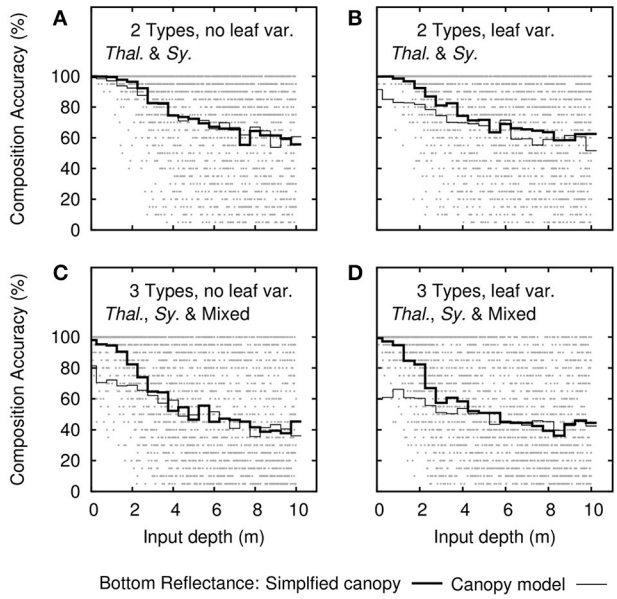

FIGURE 9 | Sensitivity analysis results for the accuracy of canopy composition type determination as function of depth. Each dot is the overall accuracy from the uncertainty propagation (20 repeats) of each of the 2,500 noise-perturbed self-inversions. Dark lines are the mean accuracy binned in steps of 0.5 m. Thin lines are the mean accuracy when input bottom reflectances are drawn directly from the canopy model results. Treatments include **(A,B)** the model of two bottom types and **(C,D)** three bottom types. Each is repeated **(B,D)** with and **(A,C)** without leaf level variance.

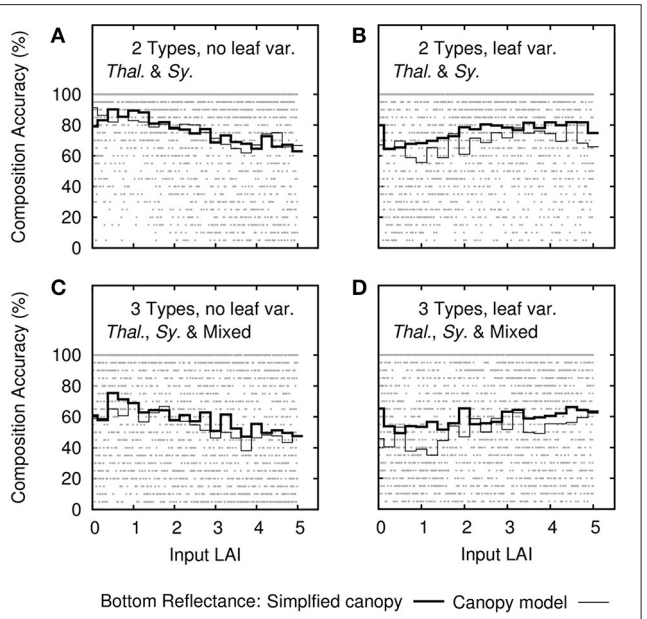

FIGURE 10 | Sensitivity analysis results for the accuracy of canopy composition type determination as function of leaf area index (LAI). Each dot is the overall accuracy from the uncertainty propagation (20 repeats) of each of the 2,500 noise-perturbed self-inversions. Dark lines are the mean accuracy binned in steps of 0.25 in LAI. Thin lines are the mean accuracy when input bottom reflectances are drawn directly from the canopy model results. Treatments include **(A,B)** the model of two bottom types and **(C,D)** three bottom types. Each is repeated **(B,D)** with and **(A,C)** without leaf level variance.

red wavelengths, where coralline algae are spectrally distinct, have low penetration in water so any discrimination advantage may be limited to the shallowest canopies. The situation will also vary between canopies since dependent on conditions some canopies are relatively free of epiphytes and the epiphyte community follows a progressive process of organization coupled with leaf age (Cebrián et al., 1999), Understanding the epiphyte contribution for the purposes of optical modeling is therefore a complicated task, but these kind of co-incident factors could explain the relatively reasonable performance of classification techniques applied to multispectral data (Phinn et al., 2008).

Image Data Analysis

Visually, LAI results from the hyperspectral imagery appeared reasonable over both the *Thalassia* and *Syringodium* dominated areas (**Figure 11**). Sand areas were identified as LAI close to zero, and denser seagrass areas, especially over *Syringodium* dominated locations, contained the full range of LAIs up to 5 or more, which was the limit of discrimination predicted by the sensitivity analysis (**Figure 8**). The algorithm output did highlight some artifacts in the source imagery such as a vertical line (**Figure 11**, left LAI image) presumably corresponding to detector anomaly such as dust contamination. Image-derived LAI corresponded well to *in situ* data in terms of both area-averaged LAI and standard deviation at each location (**Figure 12A**). Linear regression of the area-averaged estimated LAIs against the *in situ* data yielded an r^2 of only 0.32 with a *y*-intercept of 1.54 and slope of 0.48 (**Figure 12B**). However, it is clear that the method identifies areas of zero LAI very well (**Figure 11**) but there is no *in situ* data at zero LAI to represent this. Acknowledging this capability by constraining the regression to have an intercept at zero gives an r^2 of 0.86 and a slope of 1.01 (**Figure 12B**). This would seem a more sensible result given visual interpretation of **Figure 11**: zero LAI areas are not identifed as LAI of 1.54. In general the high variation exhibited by the *in situ* LAI point data at a scale of 2 m (the transect sampling distance at each location) is clearly a confounding factor for validation of a remote sensing analysis. It places a very high demand on the geo-correction of the imagery and accuracy of the GPS system. The *in situ* data used here was not collected with this study in mind, for future studies placing benthic markers that can be identified in the imagery may be a better solution (Mumby et al., 2004). Nevertheless, both visually and in comparison to the available data (**Figures 11**, **12**) LAI estimations from the image data analysis appear reasonably accurate.

Depths at the eight locations ranged from ∼1.5 m to 8 m, depth estimates from the inversion model agreed well in general but there was a dependency on LAI (**Figure 13**). All locations except T1 were highly heterogeneous in terms of canopy density, to generate **Figure 13** the mean estimated depth at 5 pixels with relatively low LAI within an approximate 20 m radius were taken, and likewise depth estimates from pixels with relatively high

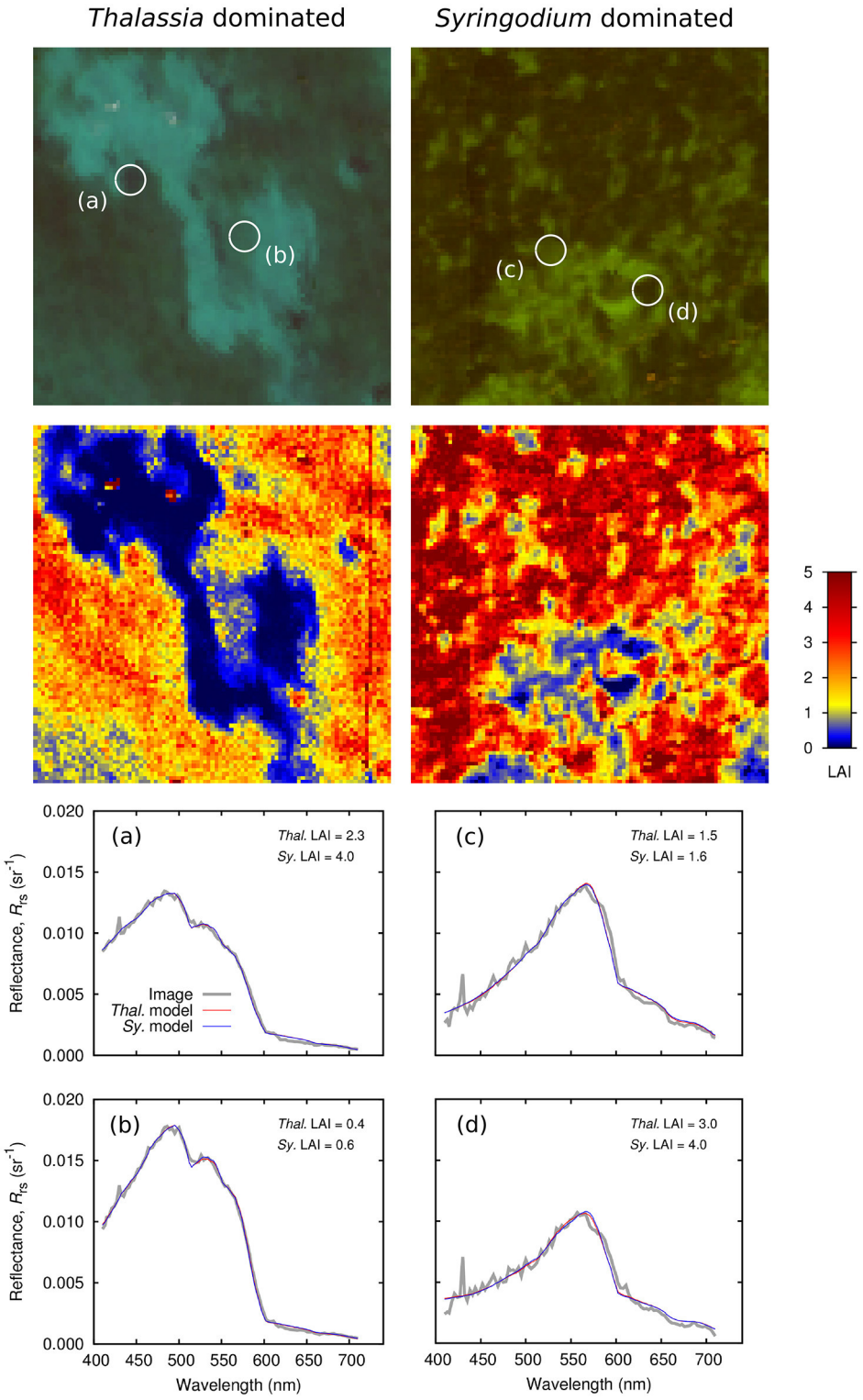

FIGURE 11 | Application of inversion model to hyperspectral PRISM imagery in (left) a *Thalassia* dominated area (T2 and T3) and (right) a *Syringodium* dominated area (S1). LAI image is from model containing all bottom compositions, **(a–d)** show spectral matches for models constrained to *Thalassia* or *Syringodium* only.

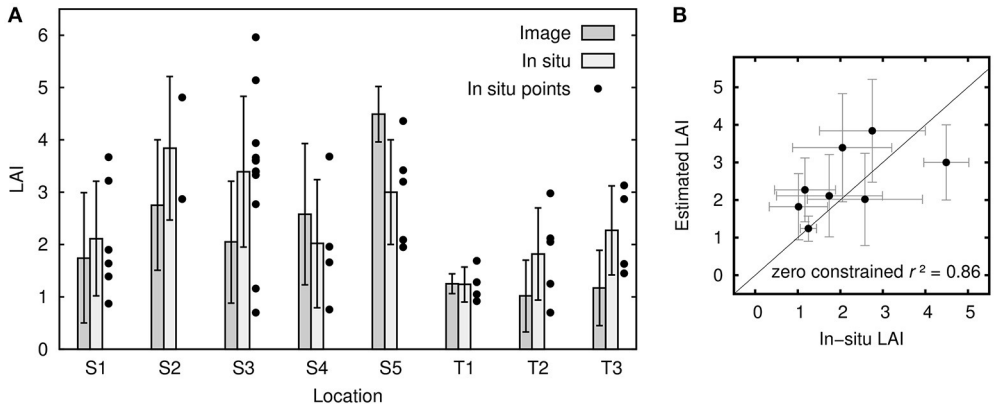

FIGURE 12 | (A) Leaf area index as estimated from imagery compared to *in-situ* data, for the five sites dominated by *Syringodium* (S1-S5) and the three by *Thalassia* (T1-T3). Bars show mean and standard deviation for *in-situ* data points and for a 4-pixel window around those points. The number of pixels contributing to each bar varies from 71 to 170. The individual data points at each location are plotted to show the variation that exists at each location. **(B)** Scatterplot of LAIs from *in-situ* data and 4-pixel window imagery estimates, i.e., the same information as in the bars in **(A)**.

LAI within that area. **Figure 13** therefore gives an indication of the effect of LAI on depth estimation at each location. A regression plot using both low and high LAI results (**Figure 13B**) gave an r^2 of 0.94 and slope of 1.10. Clearly this is a good result but the number of data points is too low to make any strong conclusions. It might be expected that high LAI, giving rise to darker pixels, would cause depth over-estimation. Indeed for most cases over low LAI areas (typically bare sand) depth estimates were quite accurate while for high LAI depth was over-estimated (**Figure 13A**, S1, S4, T2, T3, and **Figure 13B**). However, the pattern was not always consistent, in fact the highest LAI areas (S2, S3, LAI greater than 5) gave good depth estimates. It seems that intermediate LAIs give rise to the largest potential for depth over-estimation. The largest depth errors were greater than the uncertainty in depth estimation predicted by the sensitivity analysis over all LAIs (**Figure 7J**) and the uncertainty propagation (error bars in **Figure 13**). The sensitivity analysis of **Figure 7** covers LAIs from 0 to 5, but if the analysis is restricted to LAIs from 3 to 4 the plots appear almost identical and the depth uncertainty is still only around ± 1 m at 10 m depth. In comparison at S1 an LAI of 3 gave rise to error of $+1.5$ m in a depth of 2.4 m. The true depth at location S1 lies outside the uncertainty estimates for the high LAI pixels and so points to either an omission from the model or a radiometric discrepancy between the model and the image data. In other words, the spectral reflectance from the image data does not lie within the possibilities that can be produced for a depth of 2.4 m from the forward model. It is worth noting that the parameters for the optical properties of the water column, *P*, *G*, and *X*, are not estimated as their minimal or maximal values (**Table 2**) and so are not unduly constraining the inversion.

With respect to canopy composition, model inversion uniformly converged on a solution for monospecific *Thalassia* canopies. Even over the *Syringodium* dominated sites (**Figure 11**, right, S1) the model almost never selected *Syringodium* canopies or a 50:50 mix as giving the best spectral match. The only exceptions occurred on or around the edges of sand patches where LAI was close to zero so canopy composition is irrelevant. The sensitivity analysis suggested that discrimination of species would be subject to high uncertainty (**Figure 9**), but that one bottom type is systematically chosen in all cases indicates an issue of the radiometric alignment of the model with the image pixel reflectances, since the expected outcome under high uncertainty would be random bottom composition.

Sensitivity Analysis vs. Image Data Results

While overall the results for LAI and depth are reasonable, a few discrepancies have arisen between the performance predicted by the sensitivity analysis and the performance demonstrated by application to image data. The sensitivity analysis and uncertainty propagation are based on the assumption that the forward model is (1) radiometrically aligned with the image reflectances, i.e., ideally both the model is accurate and the image data is radiometrically accurate, or at least they are systematically comparable; and (2) that the model incorporates all possible sources of variation that could occur over the application area. If either condition is not met, then the behavior when applying the model to the image data will lead to results outside the scope of the sensitivity analysis.

The spectral matches achieved were in general very good (**Figures 11a–d**). Over either the *Thalassia* or *Syringodium* dominated sites when the model was constrained to only allow one composition type, then either *Thalassia* or *Syringodium* canopies were capable of generating spectra that matched the overall shape of the image reflectances, and which were virtually indistinguishable from each other (**Figures 11a–d**). It is therefore not surprising *Thalassia* and *Syringodium* could not be discriminated in the image data, any spectral difference in the forward model due to canopy composition was negligible in comparison to the residual fit between the model and image data. One reason that the *Thalassia* composition is preferentially selected may be that the *Thalassia* canopy model contains more

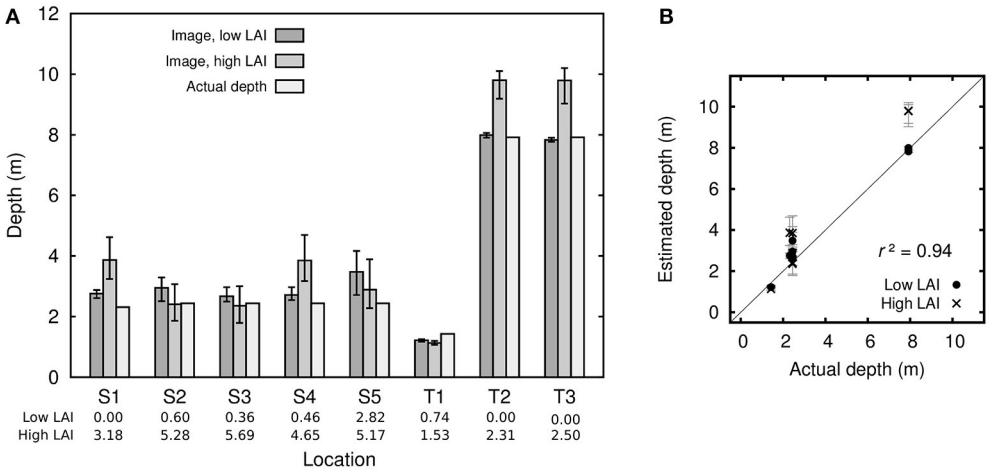

FIGURE 13 | (A) Depth estimates for the five sites dominated by *Syringodium* (S1-S5) and the three by *Thalassia* (T1-T3). Low LAI and high LAI are each averages over 5 pixels within an approximate 20 m radius of the location center, selected as examples of low and high LAI pixels. Error bars are the mean of the upper and lower 90% confidence intervals from the uncertainty propagation. **(B)** Scatterplot of actual depth against estimated depths over low and high LAI locations, i.e. the same data as **(A)**.

leaf level optical variation that does *Syringodium* (**Figure 2**) so the greater degree of freedom permits a marginally closer match than is possible with the *Syringodium* model. This implies that incorporating uncertainty could bias the inversion when the model and reflectances aren't exactly radiometrically aligned, and this may be a limitation of the approach. How much variation is the correct amount to include in the canopy modeling is also difficult to assess. Strictly it should be the pixel-to-pixel variation at the scale of image pixels within the spatial domain of the application, but to quantify this is unrealistic. A better approach may be to standardize the amount of optical variation between species, as this might remove the bias or at least reveal the extent by which the inversion was biased by differences in uncertainty.

The spectral matches from the model at the *Syringodium* dominated site S1 (**Figures 11c,d**) do not fully capture the chlorophyll absorption features in wavelengths from 570 nm upward (Jeffery et al., 1997). The model is a smoother approximation because the 3D canopy model operates at 20 nm resolution. Improving the spectral resolution of the canopy model may help match these chlorophyll features and disambiguate increased LAI from increased depth, although that issue primarily afflicted the deeper site where these features are almost absent in the image data (**Figures 11a,b**). These spectral features are unlikely to assist in species discrimination since they are also present in reflectances from the shallow *Thalassia* site (T3, data not shown). In particular the shoulder at 570 to 585 nm and reflectance peaks at ∼645 nm and ∼690 are ubiquitous and arise from features also visible in the leaf level reflectances for both species (**Figure 2**).

The flight line over the *Syringodium* site S1 (**Figures 11c,d**) contained much more spectral noise up to 550 nm than for the *Thalassia* sites (**Figures 11a,b**). However, the band-to-band noise appears to average out satisfactorily with respect to the overall spectral fit. The documented signal to noise ratio of the PRISM instrument is more than adequate for this application. By the sensitivity analysis parameterization (**Table 2**) the reflectance change at 550 nm to detect 1 m change in depth at a depth of 10 m over a canopy of LAI 4 is 0.8% of the reflectance for bare sand at zero depth (the brightest target required for subsurface applications). This dynamic range would be covered by a signal to noise ratio (SNR) of 120 and 8-bit digitization, while PRISM is 14-bit with an SNR of 200 per band, and much greater when bands are combined as they are here (since fitting a spectrum is a effectively a kind of band-averaging) (Mouroulis et al., 2014). So for hyperspectral imagers such as PRISM the radiometric limiting factors, especially for physics based aquatic applications, lie not in the instrument specifications but in the data processing (see also Goodman et al., 2008; Hedley et al., 2012b). Since here discrepancies between the sensitivity analyses and practical performance appear to be due to radiometric differences between the model and data, this suggests future model based sensitivity analyses should include a term for "radiometric discrepancy." That is, regardless of the cause of such a discrepancy (atmospheric correction issues, model inadequacy, etc.) it seems overly optimistic that such a term should be zero. The common practice of relying entirely on a sensor or environmental noise characterization (Brando et al., 2009; Hedley et al., 2012b, 2015; Garcia et al., 2014) is not really adequate to predict practical performance.

Implications for Remote Sensing of Seagrasses

In this study, the sensitivity analysis suggested the ability to discriminate between *T. testudinium* and *S. filiforme* by remote sensing is at best weak. In a practical application reflectance spectra arising from either canopy were virtually identical, with differences below the accuracy of the radiometric alignment

of the model with imagery data. The situation with respect to other species may be better, Fyfe (2003) indicated that *Zostera capricorni*, *Posidonia australis*, and *Halophila ovalis* were separable in terms of leaf reflectance, but that study did not include other sources of variability at remote sensing scales. For those species spectral matching may be more effective if the matching were weighted on wavelength regions in which discrimination is possible, but this would be at the cost of other factors such as depth determination.

On the other hand, a physics-based approach with spectral matching may not be the best way to extract species information. Phinn et al. (2008) demonstrated a weak ability to map seagrass species using a classification approach on 54-band CASI data (Compact Airborne Spectrographic Imager). Of eight classes of canopy composition (including five species) around three classes were identified with overall accuracies greater than around 40%. However, the classification applied in Phinn et al. (2008) was based on top of water column reflectances, so if for example species were associated with depth then the classification can use this information since it is also contained in the reflectance spectra. Classification approaches are in general able to use whatever information is present in the reflectances they are presented with, so results can be better but are site-specific and contingent on training data being representative of the entire site.

Phinn et al. (2008) were able to identify four classes of leaf projected area with around 50% accuracy in depths to 3 m. Direct comparison is difficult but if LAI here is treated as four classes from 0 to 6 with step 1.5, then 4 of the 8 locations in **Figure 12** represent correct classifications (so also 50%), but that includes depths to 8 m and the two deep points are those with greatest relative error. The performance of the physics-based method and the classification approach for LAI would certainly appear to be comparable, the physics based method is possibly better but the geolocation of *in situ* data in the imagery is insufficient conclude this. Empirical regression methods using band-pair depth invariant indices (Mumby et al., 1997) have reported calibration data correlations of $r = 0.83$ in depths to 10 m. However, being a calibration plot the figure from Mumby et al. (1997) (their **Figure 4**) is more directly comparable to the sensitivity analyses here (**Figure 8**). Together these underline that the information is present to achieve the LAI accuracy predicted by the sensitivity analysis, but practically accessing that information and relating it to *in situ* data is challenging. The most successful demonstrable benthic mapping results occurred in studies where *in situ* data collection was tailored for the objective in mind. In particular, with calibrated visual assessment methods the i*n situ* LAI estimation is performed in a way that is closer to remote sensing, i.e., by visual assessment (Mumby et al., 1997; Knudby and Nordlund, 2011), so it is likely that good match between remote sensing and *in situ* data can be achieved.

CONCLUSIONS

The capability for mapping two species of seagrass, *T. testudinium* and *S. filiforme*, using a physics-based model inversion method was investigated. A key aspect of the model was that variations (uncertainties) were included at all levels, from individual leaf reflectances, through canopy structure, the water column and the air-water interface. The results were consistent with the performance of a previously developed single species model that lacked leaf reflectance variation (Hedley et al., 2015). LAI estimates were reasonable within the limitations of the *in situ* data available for assessment. Depth estimates were in many cases accurate down to 8 m but increasing LAI tended to cause depth over-estimation, especially for intermediate LAI values. *T. testudinium* and *S. filiforme* could not be distinguished by remote sensing reflectance alone, due to their spectral similarity. Canopies of other seagrass species may be more spectrally distinct, and discrimination could be aided by making use of information on ecological zonation, perhaps in a Bayesian framework. The presence of epiphytes such as encrusting coralline red algae on *Thalassia* leaves but noton those of *Syringodium* may be worth investigating but any spectral features will be a small component of the reflectance and may not be detectable at remote sensing scales. Spectral matching to chlorophyll features of the canopy reflectance could be improved by increasing the spectral resolution of the 3D canopy model. Although this would be computationally expensive and there is no clear indication from this study that any improvements would result. With respect to environments dominated by *Thalassia* and *Syringodium* a better algorithm design might be to focus on LAI and relegate species as a contributor to variability in canopy structure rather than a remote sensing objective. Practical considerations of collecting and aligning *in situ* data with imagery are a major limiting factor in demonstrating the capability of methods, this aspect of the experimental design requires careful consideration in order to advance benthic remote sensing methods.

Examination of the sensitivity analysis and model parameterization highlighted the challenges involved in fully exploiting hyperspectral data using model inversion methods. In particular in the absence of exact radiometric alignment between model and the hyperspectral imagery, there can be a complex relationship between uncertainty and the spectral matching process: features with higher uncertainty may permit a closer spectral fit to "noise" and hence be preferentially selected. Sensitivity analyses should be interpreted with caution since they are always an upper bound on what can be achieved. Here, in practice there was a greater confusion between depth and LAI than was predicted by the sensitivity analysis. This suggests that future work on predicting remote sensing capability should consider a "radiometric discrepancy" term in addition to sensor and environmental noise. While the aim is that such a term should be zero, in practice, considering the challenges inherent in atmospheric and surface reflectance corrections, that is likely an overly optimistic assumption.

AUTHOR CONTRIBUTIONS

JH, HD, and SE contributed to manuscript preparation. MP-C, RV-E, and SE contributed to collection of leaf level optical properties and experimental design. BR, KR, and HD contributed

to *in situ* data collection and experimental design. JH and HD contributed to experimental design and data analysis. Modeling work was performed by JH.

ACKNOWLEDGMENTS

The work presented here was funded by NASA Ocean Biology and Biogeochemistry Program AWARD #NNX13AH88G. The PRISM instrument is supported NASA's Earth Science and Technology Office and the Airborne Science Programs. Bo-Cai Gao at the Naval Research Laboratory and the PRISM team at NASA Jet Propulsion Laboratories including P. Mouroulis, R. Greene, B. VanGorp, I. McCubbin, and D. Thompson provided image pre-processing. Field data collection was assisted by A. Chlus, R. Perry, J. Godfrey, and N. De Jesus Rivera from the University of Connecticut and the staff and facilities of the Keys Marine Laboratory. We thank two reviewers for their comments which helped us to improve the manuscript.

REFERENCES

Beck, M. W., Heck, Jr. K. L., Able, K. W., Childers, D. L., Eggleston, D. B., Gillanders, B. M., et al. (2001). The identification, conservation, and management of estuarine and marine nurseries for fish and invertebrates. *Bioscience* 51, 633–641. doi: 10.1641/0006-3568(2001)051[0633:TICAMO]2.0.CO;2

Botha, E. J., Brando, V. E., Anstee, J. M., Dekker, A. G., and Sagar, S. (2013). Increased spectral resolution enhances coral detection under varying water conditions. *Remote Sens. Environ.* 131, 247–261. doi: 10.1016/j.rse.2012.12.021

Brando, V. E., Anstee, J. M., Wettle, M., Dekker, A. G., Phinn, S. R., and Roelfsema, C. (2009). A physics based retrieval and quality assessment of bathymetry from suboptimal hyperspectral data. *Remote Sens. Environ*. 2009, 755–770. doi: 10.1016/j.rse.2008.12.003

Cebrián, J., Enríquez, S., Fortes, M., Agawin, N., Vermaat, J. E., and Duarte, C. M. (1999). Epiphyte accrual on *Posidonia oceanica* (L.) delile leaves: implications for light absorption. *Bot. Mar.* 42, 123–128. doi: 10.1515/BOT.1999.015

Collier, C. J., Lavery, P. S., Masini, R. J., and Ralph, P. J. (2007). Morphological, growth and meadow characteristics of the seagrass *Posidonia sinuosa* along a depth-related gradient of light availability. *Mar. Ecol. Prog. Ser.* 337, 103–115. doi: 10.3354/meps337103

Corlett, H., and Jones, B. (2007). Epiphyte communities on *Thalassia testudinum* from Grand Cayman, British West Indies: their composition, structure, and contribution to lagoonal sediments. *Sediment. Geol.* 194, 245–262. doi: 10.1016/j.sedgeo.2006.06.010

Costanza, R., d'Arge, R., de Groot, R., Farber, S., Grasso, M., Hannon, B., et al. (1997). The value of the world's ecosystem services and natural capital. *Nature* 387, 253–260. doi: 10.1038/387253a0

Dekker, A. G., Phinn, S. R., Anstee, J., Bissett, P., Brando, V. E., Casey, B., et al. (2011). Intercomparison of shallow water bathymetry, hydro-optics, and benthos mapping techniques in Australian and Caribbean coastal environments. *Limnol. Oceanogr. Methods* 9, 396–425. doi: 10.4319/lom.2011.9.396

Dierssen, H. M., Chlus, A., and Russsell, B. (2015). Hyperspectral discrimination of floating mats of seagrass wrack and the macroalgae Sargassum in coastal waters of greater Florida bay using airborne remote sensing. *Remote Sens. Environ.* 167, 247–258. doi: 10.1016/j.rse.2015.01.027

Dierssen, H. M., Zimmerman, R. C., Drake, L. A., and Burdige, D. (2010). Benthic ecology from space: optics and net primary production in seagrass and benthic algae across the Great Bahama Bank. *Mar. Ecol. Prog. Ser.* 411, 1–15. doi: 10.3354/meps08665

Eiseman N. J. (1980). *An Illustrated Guide to the Sea Grasses of the Indian River Region of Florida. Technical Report No. 31.HBOITR#31,* Harbor Branch Foundation Inc.

Enríquez, S. (2005). Light absorption efficiency and the package effect in the leaves of the seagrass *Thalassia testudinum*. *Mar. Ecol. Prog. Ser.* 289, 141–150. doi: 10.3354/meps289141

Enríquez, S., and Pantoja-Reyes, N. I. (2005). Form-function analysis of the effect of canopy morphology on leaf self-shading in the seagrass *Thalassia testudinum*. *Oecologia* 145, 235–243. doi: 10.1007/s00442-005-0111-7

Enríquez, S., and Schubert, N. (2014). Direct contribution of the seagrass *Thalassia testudinum* to lime mud production. *Nat. Commun.* 5:4835. doi: 10.1038/ncomms4835

Fonesca, M. S., and Cahalan, J. A. (1992). A preliminary evaluation of wave attenuation by four species of seagrass. *Estuar. Coast. Shelf Sci.* 35, 565–576. doi: 10.1016/S0272-7714(05)80039-3

Fyfe, S. K. (2003). Spatial and temporal variation in spectral reflectance: are seagrass species spectrally distinct? *Limnol. Oceanogr.* 48, 464–479. doi: 10.4319/lo.2003.48.1_part_2.0464

Gao, B.-C., and Davis, C. O. (1997). "Development of a line-by-line-based atmosphere removal algorithm for airborne and spaceborne imaging spectrometers," in *Optical Science, Engineering and Instrumentation'97* (San Diego, CA: International Society for Optics and Photonics), 132–141.

Garcia, R. A., McKinna, L. I. W., Hedley, J. D., and Fearns, P. R. C. S. (2014). Improving the optimization solution for a semi-analytical shallow water inversion model in the presence of spectrally correlated noise. *Limnol. Oceanoogr. Methods* 12, 651–669. doi: 10.4319/lom.2014.12.651

Gobert, S., Sartoretto, S., Rico-Raimodino, V., Andral, B., Chery, A., Lejeune, P., et al. (2009). Assessment of the ecological status of Mediterranean French coastal waters as required by the Water Framework Directive using the *Posidonia oceanica* Rapid Easy Index: PREI. *Mar. Pollut. Bull.* 11, 1727–1733. doi: 10.1016/j.marpolbul.2009.06.012

Goodman, J. A., Lee, Z. P., and Ustin, S. L. (2008). Influence of atmospheric and sea-surface corrections on retrieval of bottom depth and reflectance using a semi-analytic model: a case study in Kaneohe Bay, Hawaii. *Appl. Opt.* 47, F1–F11. doi: 10.1364/AO.47.0000F1

Green, E. P., and Short, F. T. (2003). *World Atlas of Seagrasses*. Berkeley, CA: University of California Press.

Hedley, J. (2008). A three-dimensional radiative transfer model for shallow water environments. *Opt. Exp*. 16, 21887–21902. doi: 10.1364/OE.16.021887

Hedley, J., and Enríquez, S. (2010). Optical properties of canopies of the tropical seagrass *Thalassia testudinum* estimated by a three-dimensional radiative transfer model. *Limnol. Oceanogr*. 55, 1537–1550. doi: 10.4319/lo.2010.55.4.1537

Hedley, J., Roelfsema, C., and Phinn, S. R. (2009). Efficient radiative transfer model inversion for remote sensing applications. *Remote Sens. Environ*. 113, 2527–2532. doi: 10.1016/j.rse.2009.07.008

Hedley, J. D., McMahon, K., and Fearns, P. (2014). Seagrass canopy photosynthetic response is a function of canopy density and light environment: a model for *Amphibolis griffithii*. *PLoS ONE* 9:e111454. doi: 10.1371/journal.pone.0111454

Hedley, J. D., Roelfsema, C., Koetz, B., and Phinn, S. (2012a). Capability of the Sentinel 2 mission for tropical coral reef mapping and coral bleaching detection. *Remote Sens. Environ.* 120, 145–155. doi: 10.1016/j.rse.2011.06.028

Hedley, J. D., Roelfsema, C., Phinn, S., and Mumby, P. J. (2012b). Environmental and sensor limitations in optical remote sensing of coral reefs: implications for monitoring and sensor design. *Remote Sens.* 4, 271–302. doi: 10.3390/rs4010271

Hedley, J. D., Russell, B., Randolph, K., and Dierssen, H. (2015). A physics-based method for the remote sensing of seagasses. *Remote Sens. Environ.* 174, 134–147. doi: 10.1016/j.rse.2015.12.001

Hochberg, E. J., and Atkinson, M. J. (2003). Capabilities of remote sensors to classify coral, algae, and sand as pure and mixed spectra. *Remote Sens. Environ.* 85, 174–189. doi: 10.1016/S0034-4257(02)00202-X

Jay, S., and Guillaume, M. (2016). Regularized estimation of bathymetry and water quality using hyperspectral remote sensing. *Int. J. Remote Sens.* 32, 2–27. doi: 10.1080/01431161.2015.1125551

Jeffery, S. W., Mantoura, R. F. C., and Wright, S. W. (1997). *Phytoplankton Pigments in Oceanography: Quidelines to Modern Methods*. Paris: UNESCO.

Kay, S., Hedley, J. D., and Lavender, S. (2009). Sun glint correction of high and low spatial resolution images of aquatic scenes: a review of methods for visible and near-infrared wavelengths. *Remote Sens.* 1, 697–730. doi: 10.3390/rs1040697

Knudby, A., and Nordlund, L. (2011). Remote sensing of seagrasses in a patchy multi-species environment. *Int. J. Remote Sens.* 32, 2227–2244. doi: 10.1080/01431161003692057

Knyazikhin, Y., Martonchik, J. V., Diner, D. J., Myneni, R. B., Verstraete, M., Pinty, B., et al. (1998). Estimation of vegetation leaf area index and fraction of absorbed photosynthetically active radiation from atmosphere-corrected MISR data. *J. Geophys. Res.* 103, 32239–32256. doi: 10.1029/98JD02461

Lee, Z. P., Carder, K. L., Mobley, C. D., Steward, R. G., and Patch, J. S. (1998). Hyperspectral remote sensing for shallow waters. I. A semi-analytical model. *Appl. Opt.* 37, 6329–6338. doi: 10.1364/AO.37.006329

Lee, Z. P., Carder, K. L., Mobley, C. D., Steward, R. G., and Patch, J. S. (1999). Hyperspectral remote sensing for shallow waters, 2. Deriving bottom depths and water properties by optimization. *Appl. Opt.* 38, 3831–3843. doi: 10.1364/AO.38.003831

Lubin, D., Li, W., Dustan, P., Mazel, C. H., and Stamnes, K. (2001). Spectral signatures of coral reefs: features from space. *Remote Sens. Environ.* 75, 127–137. doi: 10.1016/S0034-4257(00)00161-9

Lüning, K., and Dring, M. J. (1985). Action spectra and spectral quantum yield in marine macroalgae with thin and thick thalli. *Mar. Biol.* 87, 119–129. doi: 10.1007/BF00539419

Mayer, B. A., and Kylling, A. (2005). The libRadtran software package for radiative transfer calculations-description and examples of use. *Atmos. Chem. Phys*. 5, 1855–1877. doi: 10.5194/acp-5-1855-2005

Medina-Gómez, I., Madden, C. J., Herrera-Silveira, J., and Kjerfve, B. (2016). Response of *Thalassia testudinum* morphometry and distribution to environmental drivers in a pristine tropical lagoon. *PLoS ONE* 11:e0164014. doi: 10.1371/journal.pone.0164014

Mobley, C. D., Sundman, L. K., Davis, C., Bowles, J. H., Downes, T. V., Leathers, R. A., et al. (2005). Interpretation of hyperspectral remote-sensing imagery by spectrum matching and look-up tables. *Appl. Opt.* 44, 3576–3592. doi: 10.1364/AO.44.003576

Mouroulis, P., Van Gorp, B., Green, R. O., Dierssen, H., Wilson, D. W., Eastwood, M., et al. (2014). The Portable Remote Imaging Spectrometer (PRISM) coastal ocean sensor: design, characteristics and first flight results. *Appl. Opt.* 53, 1363–1380. doi: 10.1364/AO.53.001363

Mumby, P. J., Green, E. P., Edwards, A. J., and Clark, C. D. (1997). Measurement of seagrass standing crop using satellite and digital airborne remote sensing. *Mar. Ecol. Prog. Ser.* 159, 51–60. doi: 10.3354/meps159051

Mumby, P. J., Hedley, J. D., Chisholm, J. R. M., Clark, C. D., Ripley, H., and Jaubert, J. (2004). The cover of living and dead corals from airborne remote sensing. *Coral Reefs* 23, 171–183. doi: 10.1007/s00338-004-0382-1

Nagelkerken, I., Roberts, C. M., van der Velde, G., Dorenbosch, M., van Riel, M. C., Cocheret de la Morinière, E., et al. (2002). How important are mangroves and seagrass beds for coral-reef fish? The nursery hypothesis tested on an island scale. *Mar. Ecol. Prog. Ser.* 244, 299–305. doi: 10.3354/meps244299

Olesen, B., Enriquez, S., Duarte, C. M., and Sand-Jensen, K. (2002). Depth-acclimation of photosynthesis, morphology and demography of *Posidonia oceanica* and *Cymodocea nodosa* in the Spanish Mediterranean Sea. *Mar. Ecol. Prog. Ser.* 236, 89–97. doi: 10.3354/meps236089

Phinn, S. R., Roelfsema, C. M., Dekker, A., Brando, V., and Anstee, J. (2008). Mapping seagrass species, cover and biomass in shallow waters: an assessment of satellite multi-spectral and airborne hyper-spectral imaging systems in Moreton Bay (Australia). *Remote Sens. Environ.* 112, 3413–3425. doi: 10.1016/j.rse.2007.09.017

Ramsar Convention Secretariat (2013). *The Ramsar Convention Manual: A Guide to the Convention on Wetlands (Ramsar, Iran, 1971), 6th Edn.* Gland: Ramsar Convention Secretariat.

Runcie, M., and Durako, M. J. (2004). Among-shoot variability and leaf-spe- cific absorptance characteristics affect diel estimates of *in situ* electron transport of *Posidonia australis*. *Aquat. Bot.* 80, 209–220. doi: 10.1016/j.aquabot.2004.08.001

Shibata, K. (1959). Spectrophotometry of translucence biological materials: opal glass transmission method. *Method Biochem. Anal.* 7, 77–109.

Stoughton, M. A. (2009). *A Bio-optical Model for Syringodium filiforme Canopies*. Masters' Thesis, Old Dominion University.

Thorhaug, A., Berlyn, G. P., and Richardson, A. D. (2007). Spectral reflectance of the seagrasses: *Thalassia testudinum*, *Halodule wrightii*, *Syringodium filiforme* and five marine algae. *Int. J. Remote Sens.* 28, 1487–1501. doi: 10.1080/01431160600954662

United Nations (1992). *Convention on Biological Diversity*, 1760 UNTS 79; 31 *ILM* 818.

Vásquez-Elizondo, R. M., Legaria-Moreno, L., Pérez-Castro, M. A., Krämer, W. E., Scheufen, T., Iglesias-Prieto, R., et al. (2017). Absorptance determinations in multicellular tissues. *Photosyn. Res.* 132, 311–324. doi: 10.1007/s11120-017-0395-6

Verweij, M. C., Nagelkerken, I., Hans, I., Ruseler, S. M., and Mason, R. D. (2008). Seagrass nurseries contribute to coral reef fish populations. *Limnol. Oceangr.* 53, 1540–1547. doi: 10.4319/lo.2008.53.4.1540

Wolfe, M. A. (1978). *Numerical Methods for Unconstrained Optimization*. New York, NY: Van Nostrand Reinhold Company.

Zimmerman, R. C. (2003). A biooptical model of irradiance distribution and photosynthesis in seagrass canopies. *Limnol. Oceanogr.* 48(1 Pt 2), 568–585. doi: 10.4319/lo.2003.48.1_part_2.0568

Conflict of Interest Statement: JH was employed by the company Numerical Optics Ltd.

The other authors declare that the research was conducted in the absence of any commercial or financial relationships that could be construed as a potential conflict of interest.

frontiers in Marine Science

ORIGINAL RESEARCH
published: 21 November 2017
doi: 10.3389/fmars.2017.00372

Variability and 20-Year Trends in Satellite-Derived Surface Chlorophyll Concentrations in Large Marine Ecosystems around South and Western Central America

Marina Marrari[1, 2, 3]*, *Alberto R. Piola*[1, 2, 3, 4]* and *Daniel Valla*[1, 2, 3, 4]

[1] Departamento de Oceanografía, Servicio de Hidrografía Naval, Buenos Aires, Argentina, [2] Consejo Nacional de Investigaciones Científicas y Técnicas, Buenos Aires, Argentina, [3] Instituto Franco-Argentino sobre Estudios de Clima y sus Impactos, Universidad de Buenos Aires, Buenos Aires, Argentina, [4] Departamento de Ciencias de Atmósfera y los Océanos, Facultad de Ciencias Exactas y Naturales, Universidad de Buenos Aires, Buenos Aires, Argentina

OPEN ACCESS

Edited by:
Kevin Ross Turpie,
University of Maryland, United States

Reviewed by:
Alejandro Orfila,
Mediterranean Institute for Advanced Studies (CSIC), Spain
Vanesa Magar,
Center for Scientific Research and Higher Education at Ensenada, Mexico

***Correspondence:**
Marina Marrari
marumarrari@gmail.com
Alberto R. Piola
apiola@hidro.gov.ar

Specialty section:
This article was submitted to Coastal Ocean Processes, a section of the journal Frontiers in Marine Science

Received: 17 August 2017
Accepted: 06 November 2017
Published: 21 November 2017

Citation:
Marrari M, Piola AR and Valla D (2017) Variability and 20-Year Trends in Satellite-Derived Surface Chlorophyll Concentrations in Large Marine Ecosystems around South and Western Central America. Front. Mar. Sci. 4:372. doi: 10.3389/fmars.2017.00372

Marine ecosystems are under the increasing stress of natural and anthropogenic climate variability and change. Knowledge of the patterns of distribution of chlorophyll concentrations as an indicator of phytoplankton abundance, its spatial and temporal variability, and the processes that control this variability is required to better understand the dynamics of marine populations and their fluctuations, including species of ecological and commercial importance. The Patagonia (PLME), South Brazil (SBLME), Humboldt (HLME), and Pacific Coastal Central America (PCACLME) Large Marine Ecosystems (LMEs) around South and Western Central America support high primary productivity and fisheries catch. During the past few decades, climate change and warming in most ecosystems has become evident, which in combination with variations in production rates could impact the dynamics of marine ecosystems. The goal of this study is to assess the variability and longer-term trends in chlorophyll concentrations in the PLME, SBLME, HLME, and PCACLME, and to discuss implications for higher trophic levels. We use a combination of high-resolution satellite-derived chlorophyll concentration data from SeaWiFS (1997–2006) and MODIS Aqua (2002–2017) to examine spatial and temporal variability and analyze the record-length linear trends in these LMEs (25°N-60°S, 30–120°W). We use monthly composites with 2 × 2 km spatial resolution for the period of overlap between sensors (2002–2006) to compare retrievals and adjust the MODIS Aqua data series at all pixels using linear regressions. We then apply the corrections to the MODIS data and combine the SeaWiFS and adjusted MODIS datasets to generate the longest time series in chlorophyll concentrations to date in the region. Our results revealed significant increases in chlorophyll concentrations in large areas of the PLME (78.23%) and HLME (43.03%) during the last ~20 years, with large potential implications for trophic relationships and the reproductive success of fish. For the mostly subtropical SBLME (26.35%) and tropical PCACLME (13.35%), increasing trends were detected

only in relatively small regions, while changes in the PLME and HLME are widespread. Results from this study contribute to a better understanding of the potential effects of environmental change on ecosystem dynamics and provide new tools to assess longer-term trends in satellite chlorophyll concentrations.

Keywords: chlorophyll concentrations, SeaWiFS, MODIS, trends, climate change, Large Marine Ecosystems, South America, Central America

INTRODUCTION

Coastal marine ecosystems contribute ∼15% of the global carbon sequestration (Le Quéré et al., 2016) and more than 80% of the global fish catch (Pauly et al., 2008) and they are, therefore, a critically important component of our living planet. Large Marine Ecosystems (LMEs) are relatively large ocean regions of 200,000 km^2 or greater that encompass coastal areas from rivers and estuaries to the outer margins of continental shelves and major current systems, and are characterized by distinct bathymetry, hydrography, productivity, and trophically dependent populations (Sherman and Alexander, 1989; Sherman, 1993; Duda and Sherman, 2002). The world's oceans have been classified in 66 LMEs (IOC-UNESCO UNEP, 2016), which have been used since 1984 as a practical framework to evaluate and manage the global coastal ocean based on changing states of productivity, fisheries, pollution, and ecosystem health, socioeconomics, and governance (Duda and Sherman, 2002; Sherman and Hempel, 2008; Sherman, 2014a,b).

In recent decades, fisheries around South America have undergone accelerated growth and currently all commercially exploited stocks are either fully- or over-exploited, with large changes in catch potential predicted for upcoming decades (Cheung et al., 2010). In addition, populations show natural fluctuations in abundance, presumably due to environmental effects. Recent changes in the abundance and catch of crustacean, fish, and sea turtles were associated with regional climate variability in a variety of timescales, such as El Niño Southern Oscillation (ENSO) (Brander, 2007; Möller et al., 2009; Quiñones et al., 2010; Acha et al., 2012).

The South Brazil Shelf Large Marine Ecosystem (SBLME) extends from 22 to 34°S along the southwestern Atlantic Ocean with a surface area of ∼550,000 km^2. SBLME presents moderate to high productivity influenced by the meandering of the Brazil Current, wind driven coastal upwelling, the proximity to the Brazil/Malvinas Confluence, the plume of the Río de la Plata River, the discharge of the Patos-Mirim lagoon system, and the propagation of Subantarctic Shelf Water derived from the Argentine shelf (Ciotti et al., 1995; Zavialov et al., 2003; Piola et al., 2005; Möller et al., 2008; Palma et al., 2008; Matano et al., 2010; Campos et al., 2013). The Uruguayan and Brazilian fishing efforts are largely concentrated in the regions near the Río de la Plata and southern Brazil. The SBLME supports approximately one half of Brazil's fisheries (IBAMA, 2002), with sardines being the most important group over the continental shelf and the whitemouth croaker (*Micropogonias furnieri*), other scienids, skipjack tuna (*Katsuwonus pelamis*), and penaeids shrimps being important demersal species (Paiva, 1997; Valentini and Pezzuto, 2006).

The Patagonian Shelf Large Marine Ecosystem (PLME) lies south of the SBLME and extends along the western South Atlantic continental shelf, from the Río de la Plata to Tierra del Fuego, covering ∼1.2 million km^2. The continental shelf is one of the widest in the world and one of the most productive and complex marine regions in the Southern Hemisphere (Heileman, 2009). The high production of the PLME is associated with several shelf and shelf-break fronts controlled by the strong winds and large-amplitude tides, freshwater discharge, and the Malvinas Current (Acha et al., 2004; Romero et al., 2006; Matano and Palma, 2008; Palma et al., 2008; Matano et al., 2010). The high biological production of the PLME sustains an intense fishing activity. The species most targeted are the Argentine hake *Merluccius hubbsi*, the shrimp *Pleoticus muelleri*, and the Argentine shortfin squid *Illex argentinus* (Secretaría de Agricultura, Ganadería y Pesca, Ministerio de Agroindustria, Argentina, 2016). In addition, the high phytoplankton productivity of the PLME drives the uptake of large amounts of CO_2 (Bianchi et al., 2005, 2009).

The PLME and the SBLME are influenced by their proximity to two distinct western boundary currents: the Brazil and Malvinas currents, which flow in opposing directions along the margins of Brazil, Uruguay, and Argentina and collide near 38°S. This region is known as the Brazil-Malvinas Confluence (BMC) and is one of the most energetic globally (e.g., Chelton et al., 1990; Garzoli, 1993; Piola and Matano, 2001). The circulation is characterized by the northward flow of the Malvinas Current carrying cold nutrient-rich and relatively fresh water of subantarctic origin, and the southward flow of warmer nutrient-poor and saltier waters from the Brazil Current (Piola et al., 2000; Palma et al., 2008; Matano et al., 2010). The strong frontal zone that separates these distinct water masses presents high mesoscale variability in the BMC region (e.g., Saraceno et al., 2004), which has in turn a strong effect on species distribution (Brandini et al., 2000). The encounter of shelf waters of subantarctic and subtropical origin close to the mouth of the Río de la Plata near 32°S (**Figure 1**) also leads to a cross-shelf front known as the Subtropical Shelf Front (STSF), which appears to be an extension of the transition observed at the BMC over the shelf (Piola et al., 2000).

The Humboldt Large Marine Ecosystem (HLME) is an eastern boundary system that extends from northern Peru to southern Chile in the eastern South Pacific Ocean, where it is adjacent to the PLME (**Figure 1**). The large-scale circulation of the HLME includes the broad eastward flowing West Wind Drift at ∼43°S that reaching the coast of South America splits into the equatorward Humboldt Current and the poleward

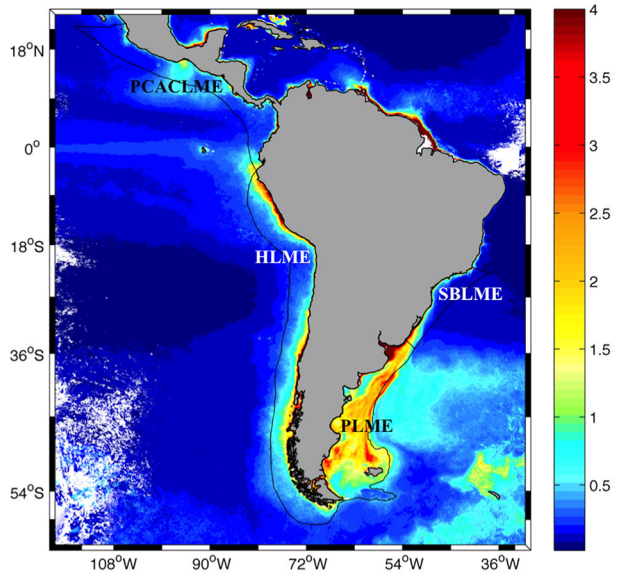

FIGURE 1 | Distribution of SeaWiFS climatological (1997–2006) surface chlorophyll concentrations in austral spring (October–December) around Central and South America (mg m^{-3}, 2 km $pixel^{-1}$). The locations of the South Brazil (SBLME), Patagonia (PLME), Humboldt (HLME), and Pacific Coastal Central American (PCACLME) Large Marine Ecosystems (LMEs) are indicated.

flowing Cape Horn Current (Strub et al., 1998). The oceanic circulation includes a complex pattern of intense surface jets, subsurface undercurrents, and eddies, meanders and filaments, which exchange mass, energy, and biota with the deep ocean (Strub et al., 1998). Ekman offshore divergence due to the trade winds north of ∼35°S results in the largest coastal upwelling system in the world, characteristic of this LME. This system shows large oceanographic and climatic variability and is strongly influenced by ENSO (Heileman et al., 2009). About 65% of the area of HMLE corresponds to the Humboldt Current System (HCS) and is under the influence of coastal upwelling from ∼4 to 40°S. The fishery off Peru is the most productive in the world, with harvests of anchoveta and sardine that peaked up to 12 million metric tons during 1994. The Chilean fishery concentrates primarily on horse mackerel, anchovy, sardine, and hake (Prado and Drew, 1999). The Cape Horn Current flows poleward along coast of southern Chile (40–55°S) next to a complex fiord system and is mostly under the influence of downwelling-favorable (poleward) winds. The HCS includes an extensive and pronounced oxygen minimum zone (OMZ) centered at 300–400 m and is characterized by high primary production at the surface and a permanent and sharp thermocline that restricts ventilation of subsurface waters (Karstensen et al., 2008) This OMZ has a strong impact on the local ecosystem as well as on global climate through the exchange of greenhouse gases with the atmosphere (Bertrand et al., 2010).

The Pacific Central-American Coastal LME (PCACLME) includes the Pacific Coast of Central America (22°N–4°S) from Mexico to Ecuador and covers ∼2 million km^2. The PCACLME is characterized by recirculating coastal currents and milder temperatures than those of the adjacent California Current and Humboldt Current LMEs. A large part of this LME is under the influence of the meridional displacements of the Inter-tropical Convergence Zone (Bakun et al., 1999) and is also vulnerable to ENSO variability at interannual time scales.

Several studies have observed recent changes in marine environmental conditions at both global and regional scales. Trend analyses of global sea surface temperature (SST) indicate mean increases of 0.71°C $century^{-1}$ since 1900 (Wu et al., 2012) and between 0.09° ± 0.03 and 0.18° ± 0.04°C $decade^{-1}$ since the 1980s (Lawrence et al., 2004; Good et al., 2007). Long-term trends in chlorophyll concentrations are variable, with areas of increasing and decreasing chlorophyll around the globe (Gregg et al., 2005; Demarcq, 2009; Saulquin et al., 2013; Boyce et al., 2014; Gregg and Rousseaux, 2014; O'Brien et al., 2017). The factors driving these changes in environmental conditions are not fully understood, and although climate driven changes can have a global effect (i.e., increased SST and more intense stratification), other factors have variable effects on regional scales. It has been shown that climate driven changes of marine ecosystems have a large impact on artisanal fisheries, which in turn have a substantial socio-economic impact in Central and South American countries (e.g., Castilla and Defeo, 2001; Caddy and Defeo, 2003; Defeo et al., 2009; Möller et al., 2009; Schroëder and Castello, 2010). The analysis of longer-term changes in environmental variables is essential for understanding the effects of climate change and ecosystems dynamics on marine populations. The recent increase in the number of ocean color missions allows a great variety of applications, although different durations and timing for the individual missions lead to relatively short datasets that are not appropriate for assessing changes at interdecadal scales. Thus, there is a need for longer time series, which can be obtained by applying a multi-sensor approach.

The VOCES Project (Variability of ocean ecosystems around South America) (CRN 3070) is aimed at assessing the impact of climate variability on the Humboldt, Patagonia, and South Brazil LMEs through collaborative research (http://www.iai.int). The Pacific Central-American Coastal LME is adjacent to HLME and includes the study area of the project "Study of the upwelling system in the Santa Elena Gulf, north Pacific coast of Costa Rica" (CONICIT FV-027-13, Costa Rica). Our study is part of these projects and analyzes the four LMEs as a contribution to the understanding of the processes controlling variability in chlorophyll concentrations and trends around South and Central America. The main objectives of this study are (1) to develop extended time series of satellite chlorophyll concentrations in four LMEs around South and Central America using a combination of SeaWiFS and MODIS high-resolution data, (2) to compare the spatial and temporal patterns and variability observed in chlorophyll concentrations in the different ecosystems, and (3) to determine statistically significant trends in chlorophyll concentrations and discuss their potential implications for the different LMEs.

MATERIALS AND METHODS

The study area includes the Patagonia (PLME), South Brazil (SBLME), Humboldt (HLME), and Pacific Central American Coastal (PCACLME) Large Marine Ecosystems around South and Central America between 25°N–60°S and 30–120°W (**Figure 1**). LMEs were defined according to the limits established in http://www.lme.noaa.gov. A preliminary analysis of chlorophyll concentrations within these regions revealed that the limits established originally for PLME excluded part of the shelf-break front where high chlorophyll concentrations of up to ∼20 mg m^{-3} often develop during spring and summer (Garcia et al., 2008; Lutz et al., 2010). For this reason, the offshore limit was extended to the 500 m isobath in order to include all high chlorophyll waters in the region.

Daily SeaWiFS Local Area Coverage (LAC) data with 1 × 1 km spatial resolution are available between August 1997 and December 2006. In addition, 9 km $pixel^{-1}$ data are available until December 2010, when the satellite stopped communicating. The MODIS Aqua dataset includes the period July 2002-present at 1 km $pixel^{-1}$ and, together, both sensors provide over 20 years of high spatial resolution surface chlorophyll concentration measurements with ∼5 years of temporally overlapping data (2002–2006, 54 months). Surface chlorophyll concentrations (CHL, mg m^{-3}) from SeaWiFS (SWF) and MODIS Aqua (AQ) were analyzed in the area bounded by 25°N–60°S and 30–120°W. All available high-resolution (∼1 km $pixel^{-1}$) level 2 data were processed with the standard flags and empirical algorithms (OC4v4 for SeaWiFS and OC3M for MODIS, O'Reilly et al., 2000), binned, and mapped to a 2 km $pixel^{-1}$ spatial resolution. Reprocessing versions 2014.0 (SWF) and 2014.0.1 (AQ) were used. To reduce errors caused by digitization and random noise without losing spatial resolution, a smoothing filter was applied by computing the mean chlorophyll concentration in a 3 × 3 box around each pixel (Hu et al., 2001). Chlorophyll concentrations <0.02 and >30 mg m^{-3} were excluded from the analyses. Monthly composites were generated from SWF (September 1997–December 2006) and AQ (July 2002-January 2017) data. Data are distributed by the Ocean Biology Processing Group (OBPG) at NASA's Goddard Space Flight Center.

It is well documented that ocean color satellite sensors overestimate chlorophyll concentrations in waters of the Río de la Plata (**Figure 1**) where high concentrations of sediment and terrigenous material are present (Armstrong et al., 2004; Garcia et al., 2005); thus, this area was excluded from all error and trend analyses. Since there is no significant seasonality in river discharge volume for the Río de la Plata (Piola et al., 2005), years of higher than normal discharge were selected (1998, 2002, 2003, 2010, and 2016; Piola et al., 2008a) and average chlorophyll concentrations for those years were calculated in the area. A mask was defined using the 5 mg m^{-3} isoline as the limit of the river waters and the area included within the mask was excluded from all quantitative analyses.

Previous comparisons of monthly CHL data from SWF and AQ data for the overlapping period (2002–2006) in the Patagonia LME region revealed differences between sensors (Marrari et al., 2016). Preliminary analyses of data for the larger study area included here revealed that in highly productive areas during spring and summer, both estimates agreed well at lower chlorophyll concentrations (<1 mg m^{-3}) but AQ systematically produced larger estimates than SWF at higher values (**Figure 2A**). For lower productivity waters, SWF produced somewhat higher estimates than AQ, although differences were smaller than for AQ > SWF. The spatial patterns observed in the relationship between SWF and AQ estimates showed a moderate association with the amplitude in spring chlorophyll concentrations ($r = 0.525$, $p < 0.0001$; **Figure 2B**), which in turn is associated with the distribution of spring SST ($r = -0.262$, $p < 0.0001$; **Figure 2C**). In general, warm oligotrophic waters with small spring chlorophyll amplitudes are characterized by higher SWF than AQ estimates, whereas nutrient-rich colder areas that support large phytoplankton blooms and large amplitudes in spring chlorophyll concentrations present the opposite pattern. Based on the high productivity of the LMEs analyzed here and previous reports of SWF performing better than AQ at higher chlorophyll concentrations (e.g., Werdell et al., 2009), the AQ dataset was corrected using SWF as reference. Model II ordinary least squares (OLS) regressions (Legendre and Legendre, 1998) were calculated at all pixels on the log-transformed chlorophyll data using monthly composites for the overlap period, between July 2002 and December 2006. Other analyses with higher order polynomials and other nonlinear fits did not reduce the errors; thus, we present results based on linear fits. Using the coefficients estimated from the regressions, corrections were applied to the entire AQ dataset at all pixels (2002–2017). Taking into consideration the lognormal distribution of chlorophyll data (Campbell, 1995), all error estimates and corrections were made to the log-transformed (base 10) data. The root mean square error (RMS) and bias were calculated at each pixel according to Gregg and Casey (2004) and Marrari et al. (2006):

$$log\_RMS = \sqrt{\frac{\sum [\log(AQ) - \log(SWF)]^2}{n}}$$

$$\log\_bias = \frac{\sum [\log(AQ) - \log(SWF)]}{n}$$

In addition, errors were calculated for different CHL ranges at the different LMEs and compared. Two types of time series were generated at each pixel, each using data from a different sensor for the overlapping period (2002–2006): a first time series combined data from SWF for the entire period available (September 1997–December 2006) with corrected data from AQ for January 2007–January 2017 (TS-A), while the second analysis included SWF data for September 1997–June 2002 and corrected AQ for the entire mission (July 2002–January 2017) (TS-B) ($n = 233$ months in both cases).

The analysis of trends was done at all pixels jointly for the SWF and AQ time series following the methodology developed in Saulquin et al. (2013). This method considers the noise autocorrelation in the time series, which affects the estimation of the uncertainty in the trend estimate and consequently the ability to detect a significant trend. The time series of chlorophyll concentration, y_t, is modeled as the sum of a long-term linear

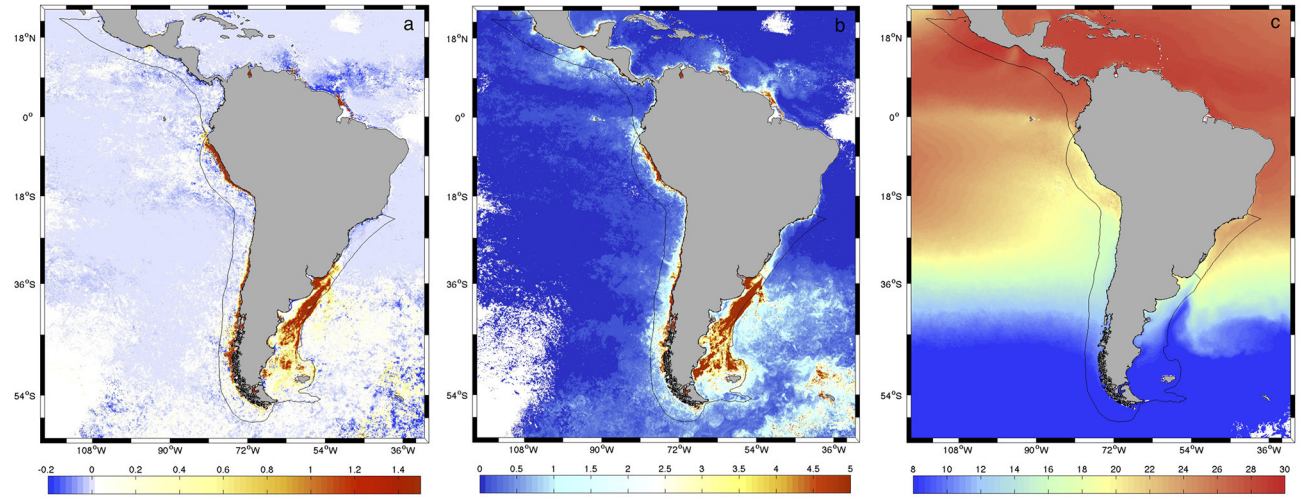

FIGURE 2 | (A) Differences in average spring (October–December) chlorophyll concentration retrievals from SWF and AQUA during the period of overlap of both sensors (2002–2006) (AQ-SWF, mg m^{-3}). The geographic limits for the four LMEs analyzed in this study are indicated. **(B)** Amplitude in climatological spring chlorophyll concentrations from SeaWiFS (maximum-minimum at each pixel, mg m^{-3}) for the period 2002–2006 **(C)** Distribution of average spring sea surface temperature (SST, °C) from MODIS Aqua for the period 2002–2006.

trend (ω), a seasonal pattern (S_t), and a noise process (N_t) (Weatherhead et al., 1998):

$$y_t = \mu + \omega t + S_t + N_t, \quad t = 1 \ldots . n$$

where n is the length of the time series and μ is the y-intercept term. N_t is the correlated noise, assumed to be first-order autoregressive process: $N_t = \phi N_{t-1} + \varepsilon_t$, with ε_t representing a white noise and ϕ the noise autocorrelation. For two sensors, the assumption is that both datasets share a long-term trend and seasonal pattern but include an unknown level shift, δ, and correlated noise processes. The seasonal component is removed from all time series and the equations are then transformed to remove the autocorrelation (Cochrane and Orcutt, 1949). Spectral analyses conducted on the chlorophyll concentration extended time series show no significant concentration of energy at time periods longer than 12 months. Therefore, we have not included an interannual component other than the linear trend.

For periods when only one time series is available, the equations for SeaWiFS (y^*_{1t}) and MODIS (y^*_{2t}) are:

$$y^*_{1t} = \mu(1-\phi_1) + \omega\phi_1 + \omega(1-\phi_1)t + \varepsilon_{1t}$$
$$y^*_{2t} = \mu(1-\phi_2) + \omega\phi_2 + \omega(1-\phi_2)t + \delta(1-\phi_2) + \varepsilon_{2t}$$

where t is time relative to each time series. When both time series are available:

$$y^*_t = \mu(1-\alpha) + \omega(1-\alpha)t - \alpha\delta + \varepsilon_{3t}$$

with α representing the correlation between N_1 and N_2. The transformed equation can be expressed in matrix form as:

$$Y^* = X^*A + \varepsilon$$

where X^* is the Tx3 coefficient matrix for the equation system, A is the parameter vector (μ, δ, ω), and ε is the residual white noise. The OLS estimator of A yields estimates of μ, δ, and ω. In practice, the equation is solved through iteration until convergence, with initial parameter values estimated from the data. Then, all parameters are revaluated. The variable $|\omega|/\sigma_\omega$ is used to detect significant trends, and the 95% confidence level is reached for $|\omega|/\sigma_\omega > 1.96$. Only trends satisfying the 95% detection threshold are considered in the analyses. More details on the numerical resolution of the equations can be found in Tiao et al. (1990) and Saulquin et al. (2013).

RESULTS

The correction of the AQ dataset (AQ_{corr}) improved the relationship between SWF and AQ for most of the region and allowed the combination of SWF and AQ_{corr} data to develop the longest time series of high-resolution chlorophyll concentrations in the region to date. Although the correction did not greatly improve the root mean squared error (log_RMS) for the SWF vs. AQ regression, the bias (log_Bias) was significantly reduced in the entire study area and the ratios AQ/SWF were greatly improved (closer to 1) for all LMEs examined (**Figure 3** and **Table 1**).

The differences between SeaWiFS and MODIS retrievals varied between LMEs, with the highest ratios AQ/SWF occurring in HLME followed by SBLME and PLME, and the best agreement observed at PCACLME. Before applying the corrections to AQ, the ratio AQ/SWF was >1 for the entire chlorophyll concentration range at HLME and PLME. High ratios between 1.30 and 1.57 (indicating an overestimation of AQ relative to SWF of 30–57%) occurred for chlorophyll concentration values between 1 and 9 mg m^{-3} at HLME. At SBLME, an overestimation

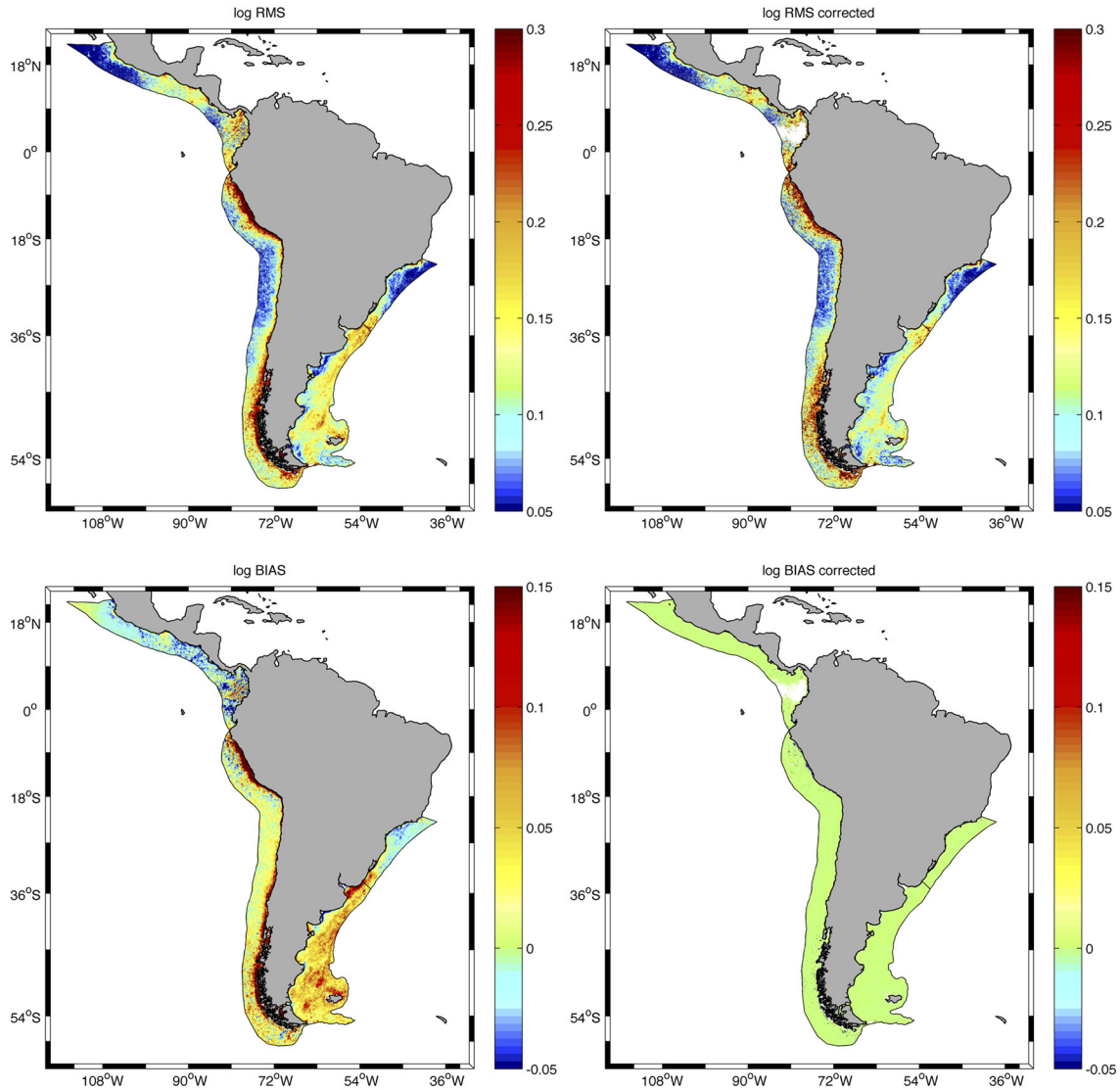

FIGURE 3 | Distribution of root mean squared error (log_RMS) (upper panels) and bias (lower panels) for the regression of SWF vs. AQ chlorophyll concentrations before (left) and after (right) correction of the AQ dataset at all pixels in the LMEs examined. Statistics are presented in **Table 1**.

TABLE 1 | Area (km^2), mean ± standard deviation (SD) spring (October–December) chlorophyll concentration (mg m^{-3}) and SST (°C) from MODIS Aqua (2007–2017) for the LMEs analyzed.

LME	Area (km^2)	Spring CHL (mg m^{-3})	Spring SST (°C)	AQ/SWF ± SD	AQ_{corr}/SWF ± SD	log_RMS ± SD	log_RMS_{corr} ± SD	log_Bias ±S D
SBLME	547,393	0.800 ± 0.538	22.195 ± 0.231	1.045 ± 0.092	1.029 ± 0.077	0.093 ± 0.016	0.091 ± 0.030	0.004 ± 0.008
PLME	1,126,103	3.037 ± 0.862	11.058 ± 1.322	1.181 ± 0.040	1.054 ± 0.038	0.140 ± 0.008	0.124 ± 0.011	0.047 ± 0.007
HLME	2,468,858	1.233 ± 0.606	13.587 ± 2.987	1.215 ± 0.081	1.110 ± 0.080	0.162 ± 0.020	0.181 ± 0.041	0.040 ± 0.021
PCACLME	1,945,330	0.406 ± 0.275	27.346 ± 0.388	1.005 ± 0.061	1.044 ± 0.070	0.098 ± 0.018	0.108 ± 0.035	−0.010 ± 0.017

Different measures of average errors before (AQ/SWF, log_RMS, log_Bias) and after correction of the AQ dataset (AQ_{corr}/SWF, log_RMS_{corr}) are also indicated.

ranging between 10 and 20% was observed for chlorophyll concentrations between 1.5 and 8 mg m^{-3}, while at PLME, ratios of ∼1.15 occurred between 1 and 6 mg m^{-3} (**Figure 4A**). On the other hand, for PCACLME, AQ/SWF ratios were ∼1 for most of the chlorophyll concentration range examined, only decreasing to values <1 at >5 mg m^{-3}. After applying the corrections, the relationship between sensor retrievals was greatly improved, with ratios AQ_{corr}/SWF closer to 1 for all chlorophyll

concentration values examined at all LMEs (**Figure 4B**). For HLME, AQ_{corr}/SWF remained high (∼1.2) for chlorophyll values within the 1.5–4 mg m^{-3} range.

The distribution of ratios AQ/SWF before and after correction of AQ showed some interesting spatial patterns (**Figure 5**). Before corrections, AQ/SWF ratios were predominantly >1 at PLME and HLME, and mostly <1 at SBLME and PCACLME, in coincidence with the spatial patterns observed in chlorophyll concentrations at those LMEs, which are evident from the spring climatology presented in **Figure 1**. In areas where chlorophyll reaches high spring and summer values, AQ tends to overestimate concentrations relative to SWF, whereas the opposite is true for areas where chlorophyll concentrations remain relatively low, such as the mostly subtropical SBLME and the tropical PCACLME areas. It is interesting to note that even though the mean ratio AQ/SWF at SBLME was >1 for most of the chlorophyll range examined (**Figure 4A**), the majority of the pixels (63.89%) had values <1 (**Figure 5A**). After applying corrections, ratios became closer to 1 at all LMEs, except for some areas of HLME where the ratios AQ_{corr}/SWF >1 observed in **Figure 4B** are evident (**Figure 5B**).

The correction of AQ and improvement of the agreement between sensors allowed the combination of both datasets to generate extended time series of chlorophyll concentrations at all pixels of the LMEs examined. The newly extended time series TS-A and TS-B represent the longest records of high-resolution chlorophyll concentration data in the region. At each LME, monthly mean chlorophyll concentrations were calculated and time series were generated, which revealed important differences between the regions examined for both sets of time series (**Figure 6**). For both TS-A (SWF 1997–2006 + AQ_{corr} 2007–2017), and TS-B (SWF 2997–2002 + AQ_{corr} 2002–2017), the highest monthly mean chlorophyll concentrations occurred consistently at PLME, followed by HLME and SBLME, while the lowest values were prevalent at PCACLME. Even though overall chlorophyll concentrations at HLME were higher than those at SBLME, chlorophyll maxima were regularly higher at the latter, most likely driven by the high winter values often observed in the southern part of SBLME. A seasonal pattern was evident in all regions, although more marked at PLME and SBLME, with peaks during austral spring for PLME (October–December) and HLME (September–November) (**Figure 6**). Maxima at SBLME occurred during July–September, in coincidence with the period of maximum extension of the Río de la Plata river plume, whereas at PCACLME, they were observed during late boreal winter-early spring (February–April). For both TS-A and TS-B, significant increasing trends were observed in the areal mean chlorophyll concentrations at PLME and HLME, whereas no trends were detected at SBLME or PCACLME (**Table 2**). The strongest positive trends occurred at PLME (0.0032 mg m^{-3} $month^{-1}$ for both TS-A and TS-B) and HLME (0.0009 mg m^{-3} $month^{-1}$ for TS-A and TS-B) and represent average increases of ∼66% and 32% since 1997, respectively.

To further examine the differences between the LMEs, an analysis of the climatology of monthly mean chlorophyll concentrations (1997–2017) clearly shows the highest values at PLME throughout the year, with austral spring and summer concentrations up to 2.5 times higher than any other LMEs, followed by HLME during austral spring, summer and fall (**Figure 7**). During winter, SBLME shows higher average concentrations than HLME, with climatological areal mean values of 1.19 and 1.17 mg m^{-3} for July and August, respectively. PCACLME presented the lowest monthly chlorophyll concentrations of all LMEs during austral winter and spring, but slightly higher values than SBLME during summer and fall. It is interesting to note that PLME and SBLME had the highest seasonality, with peaks in austral spring and winter, respectively, while both HLME and PCACLME showed little to no seasonal variability in chlorophyll concentrations (**Figure 7**).

A more detailed analysis of the spatial distribution of trends within each LME revealed that significant trends occurred in 78.23% of PLME and 43.03% of HLME, whereas only smaller subareas of SBLME (26.35%) and PCACLME (13.35%) showed significant changes since 1997 (**Table 3**). The largest trends were observed at PLME (median slope = 0.0011 mg m^{-3} $month^{-1}$), where 99.22% of the pixels with significant trends showed increasing chlorophyll concentrations (**Figure 8**). At HLME, the median trend was 0.0009 mg m^{-3} $month^{-1}$, and again 88.98% presented positive values. For SBLME and PCACLME, changes in chlorophyll concentrations over time were less evident. At SBLME, 26.35% of the pixels showed significant trends, 97.69% of which were positive. The median trend for SBLME was 0.0005 mg m^{-3} $month^{-1}$, while at PCACLME the median trend was 0.0011 mg m^{-3} $month^{-1}$ but only 13.35% of the pixels showed changes corresponding to 62.64% increases and 37.36% decreases in overall chlorophyll concentrations since 1997 (**Figure 8** and **Table 3**).

DISCUSSION

Variability in Chlorophyll Concentrations

Globally, the distribution of phytoplankton is primarily controlled by the degree of stratification, which in turn affects nutrient supply and light exposure: while in warm and permanently stratified waters nutrients limit phytoplankton growth, in seasonally stratified areas, nutrient-rich waters from below the mixed layer supply nutrients to the illuminated layer after the breakdown of the thermocline, supporting phytoplankton growth during spring and summer (Behrenfeld et al., 2006; Doney, 2006). The comparison of average conditions between LMEs confirmed this inverse relationship between surface temperature and chlorophyll, with the coldest area (PLME) supporting the highest chlorophyll concentrations and seasonality in the study area. At PLME the maximum climatological monthly CHL concentration of 2.76 mg m^{-3} was observed in November, and a minimum of 1.15 mg m^{-3} in August, which is noteworthy considering this value is higher than the maxima observed at HLME and PCACLME, and very similar to the maximum at SBLME. The high productivity of PLME has been long recognized, especially in the shelf-break area where large blooms develop during summer, supporting some of the largest fisheries in the world and serving as foraging areas for higher trophic levels (e.g., Campagna et al., 2006).

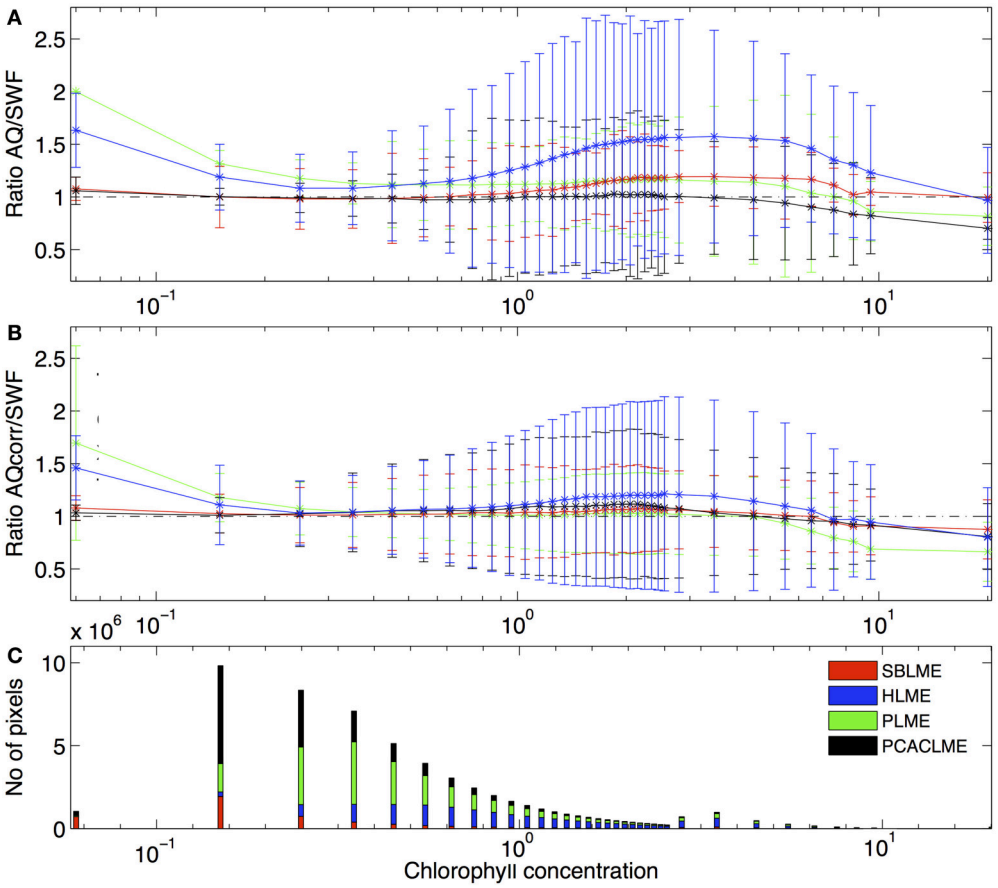

FIGURE 4 | Mean ratio of **(A)** AQ/SWF before and **(B)** after correction of the AQ dataset as a function of chlorophyll concentration ranges (mg m^{-3}) from SWF for the period 2002–2006 at the LMEs examined: PLME (green), SBLME (red), HLME (blue) and PCACLME (black). Error bars represent 1 standard deviation. **(C)** Frequency of SWF chlorophyll concentration values at each LME.

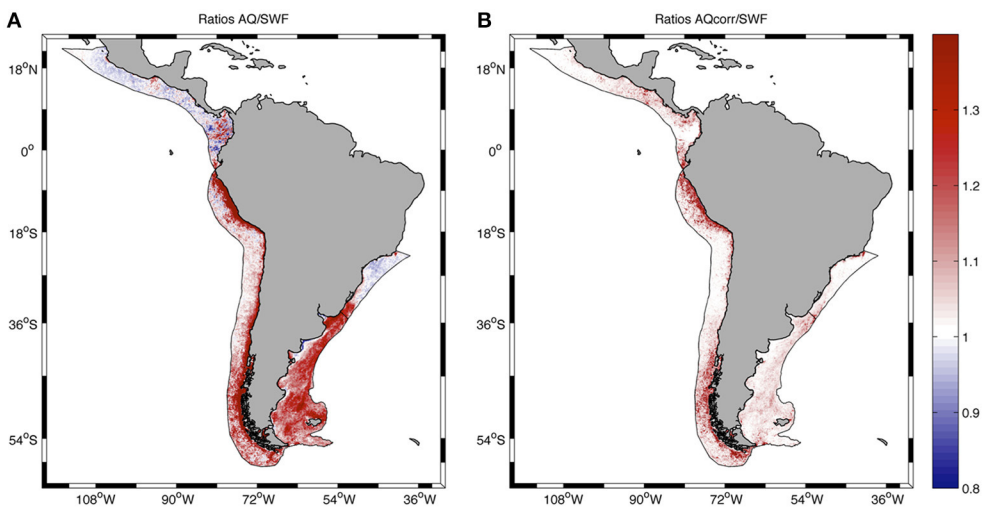

FIGURE 5 | Spatial distribution of the ratio AQ/SWF before **(A)** and after **(B)** correcting the AQ dataset at all pixels in the LMEs examined. Statistics are presented in **Table 1**.

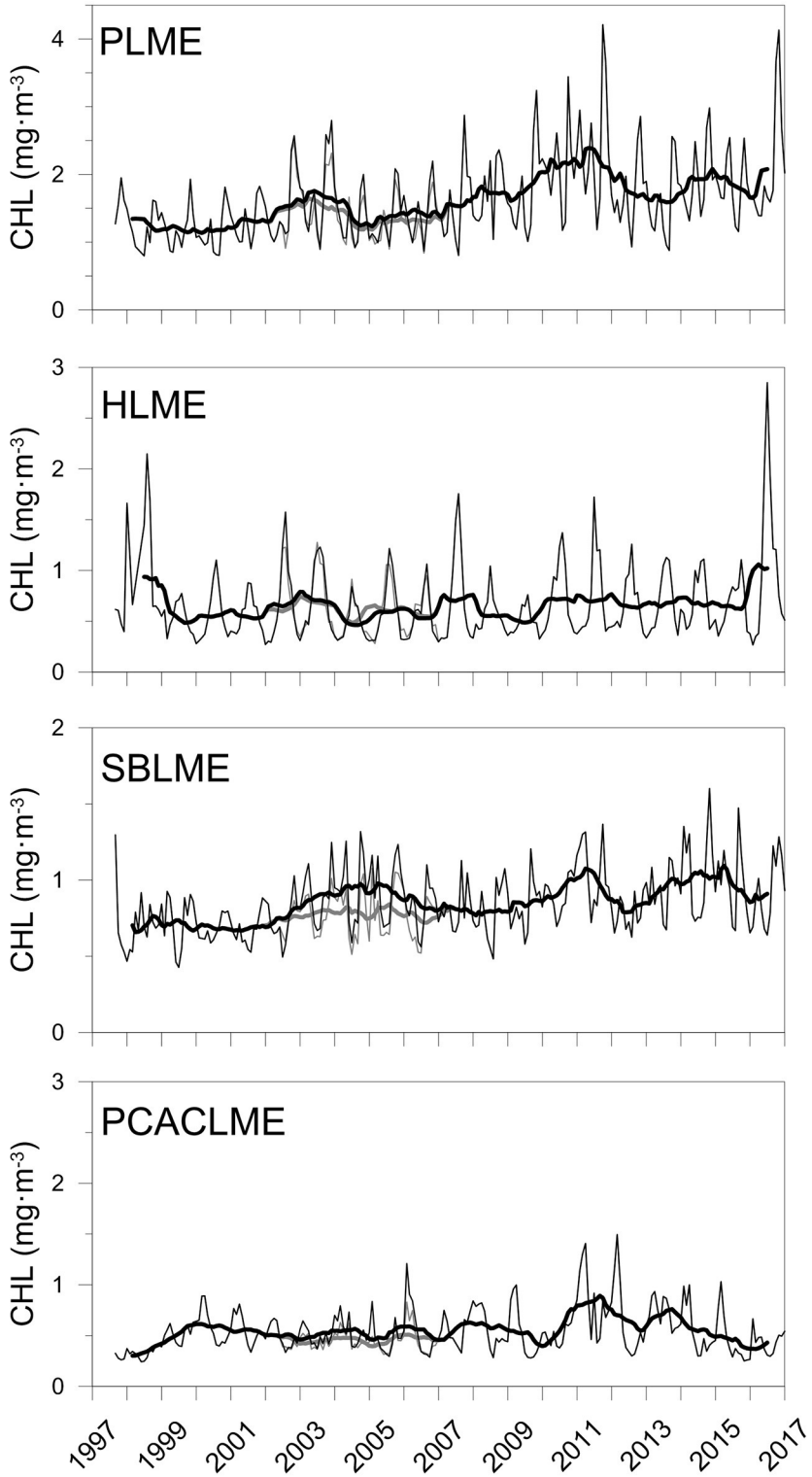

FIGURE 6 | Extended time series (1997–2017) of monthly mean CHL (mg m^{-3}, $n = 233$) at the PLME, HLME, SBLME, and PCACLME using a combination of SWF data for the period September 1997-December 2006 and AQ_{corr} for January 2007-January 2017 (TS-A, gray), and SWF data for September 1997-June 2002 and AQ_{corr} for July 2002-January 2017 (TS-B, black). The thick lines represent the 13-month running mean. Regression parameters are presented in **Table 2**.

TABLE 2 | Regression parameters for extended time series of monthly mean chlorophyll concentrations at the four LMEs analyzed for the period September 1997-January 2017 ($n = 233$ months).

LME	TS-A (SWF 9/1997-12/2006 + AQ_{corr} 1/2007-1/2017)				TS-B (SWF 9/1997-6/2002 + AQ_{corr} 7/2002-1/2017)			
	Intercept	Slope	Total change (% mg m^{-3})	Change per year (% mg m^{-3} $year^{-1}$)	Intercept	Slope	Total change (% mg m^{-3})	Change per year (% mg m^{-3} $year^{-1}$)
SBLME	0.6055	0.0006	21.588	1.112	0.6013	0.0006	22.784	1.174
PLME	1.1270	**0.0032***	66.158	3.407	1.1251	**0.0032***	66.270	3.414
HLME	0.6682	**0.0009***	32.488	1.674	0.6683	**0.0009***	32.283	1.663
PCACLME	0.4554	0.0002	12.537	0.646	0.4545	0.0003	13.006	0.670

Results for the two types of time series generated are presented. Significant trends (*) are indicated in bold. Trend significance was determined following the methods in Saulquin et al. (2013).

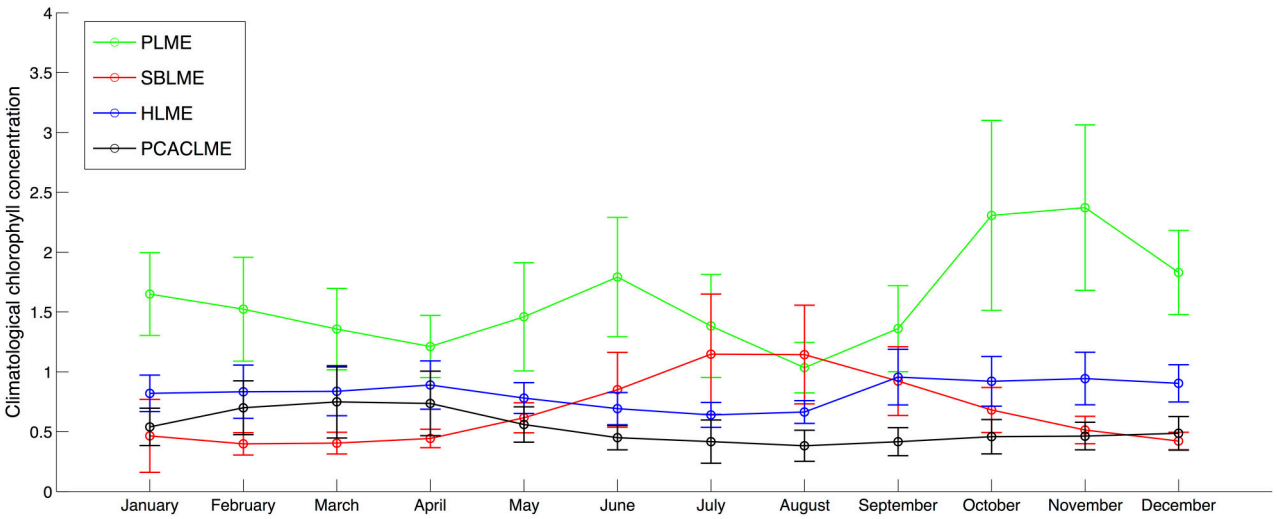

FIGURE 7 | Monthly climatological chlorophyll concentrations (mg m^{-3}) for the period September 1997-January 2017 using TS-A (SeaWiFS data for 1997–2006 and MODIS Aqua data for 2007–2017). For each LME, values represent the climatology of the areal mean chlorophyll concentration for each month. Errorbars represent 1 standard deviation.

TABLE 3 | Statistics for the trends estimated at the four LMEs examined, including the area of each LME (km^2), the percentage (%) of the area that presented significant trends, the percentage (%) of those significant trends that were positive (increasing chlorophyll concentrations), and the median trend for each LME (mg m^{-3} $month^{-1}$).

LME	Area (km^2)	% Area	% Increasing trends (+ slopes)	Median slope
SBLME	547,393	26.35	97.69	0.0005
PLME	1,126,103	78.23	99.22	0.0011
HLME	2,468,858	43.03	88.98	0.0009
PCACLME	1,945,330	13.35	62.64	0.0011

HLME has been characterized as moderately productive, even though localized areas of high productivity occur along the coast (Heileman et al., 2009). HLME includes a large area of wide latitudinal range and high spatial variability in physical and biological processes: while the northern part is affected by ENSO, the southern sector is not directly impacted by this phenomenon. The most prominent area is the HCS, one of the four major global eastern boundary current systems, characterized by coastal upwelling of cool nutrient-rich waters and dramatically increased biological production, including ~10% of the global fish catch (Chavez et al., 2008). High variability in this region is associated with ENSO, with El Niño (warm) conditions resulting in elevated sea level, a deeper thermocline, and warmer temperatures. Alongshore winds and offshore Ekman transport persist during El Niño (Carr et al., 2002; Escribano et al., 2004), but bring waters from above the deepened thermocline, which is nutrient-depleted, resulting in decreased production. On average, HLME supports about half of the monthly mean chlorophyll concentration of PLME throughout the year, with monthly climatological chlorophyll concentrations ranging between 0.75 and 1.8 mg m^{-3}, and an overall ratio PLME/HLME of 1.92 ± 0.44. However, HLME encompasses about twice the area, which translates into a monthly mean integrated chlorophyll concentration 14% higher than that recorded at PLME. In addition, HLME presents low seasonality, with the variability between monthly chlorophyll

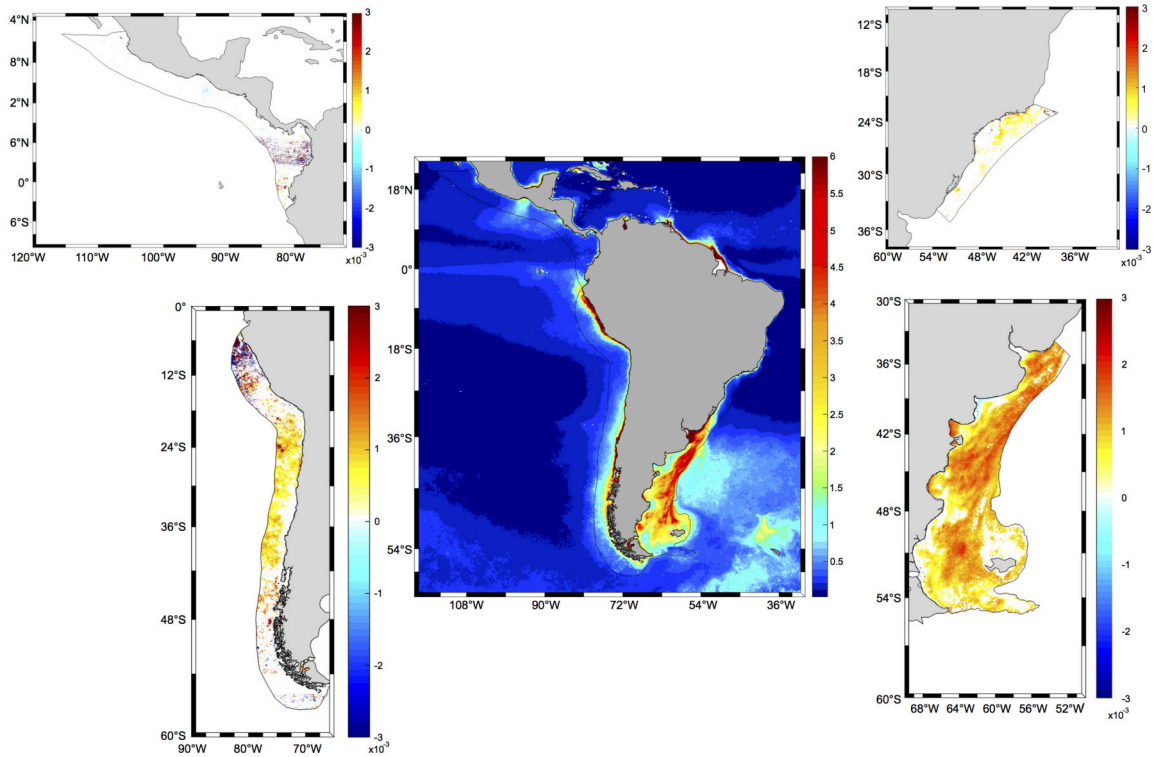

FIGURE 8 | Spatial distribution of significant trends in CHL (mg m^{-3} $month^{-1}$) in the four LMEs examined around South and Central America for the period 1997–2017. The central panel presents the distribution of climatological spring chlorophyll concentrations from MODIS Aqua for the period 2002–2017 (mg m^{-3}). Black solid lines represent the limits of each LME. White areas in LME panels indicate that the trend is not significantly different from zero at the 95% confidence level. Statistics for each LME are presented in **Table 3**.

values being ∼25% of that observed at PLME, and comparable to that of the oligotrophic PCACLME. Previous studies showed that off northern Chile, chlorophyll concentrations are somewhat higher in winter and early spring, while in central southern Chile (30–40°S), the chlorophyll peak develops during the summer months (Thomas et al., 2001). Another study observed a peak in biomass during summer north of 22°S and during spring further south, with maximum values >5 mg m^{-3} north of 20°S and south of 35°S. Primary production followed the same pattern, with minimum values (∼2 g C m^{-2} day^{-1}) in the central area of HLME (∼27°S) and maxima north of 18°S and south of 34°S (>4 g C m^{-2} day^{-1}) (Carr and Kearns, 2003).

At PCACLME, SST values are the highest and chlorophyll concentrations the lowest of the LMEs analyzed. Waters in this region are permanently stratified and nutrient availability limits photosynthesis throughout the year. Chlorophyll concentrations at PCACLME remain relatively low throughout the year and do not exceed 0.66 mg m^{-3} for the climatological monthly mean. However, within PCACLME there are areas of localized increased chlorophyll concentrations as a result of a combination of regional atmospheric and oceanographic processes. The Gulf of Papagayo on the Pacific coast of Costa Rica, for example, is a dynamic area characterized by high seasonal productivity and sustains ∼45% of the fisheries in the country (www.incopesca.go.cr). Other localized areas of high production include the Gulf of Tehuantepec off Mexico and the Gulf of Panama. In these regions, primary production is determined by vertical mixing and upwelling, which supply nitrate-rich waters to the surface. The regional climate is dominated by the north-south migration of the Intertropical Convergence Zone (ITCZ) located between the equator and 10°N and by the influence of cold air masses moving in from North America. During boreal winter (December–February), the ITCZ moves south, the easterlies intensify, and cold fronts move through the Caribbean, leading to strong winds blowing from the Atlantic to the Pacific Ocean and inducing coastal upwelling and the formation of large cyclonic and anticyclonic eddies that propagate offshore. The result is a sharp increase in coastal chlorophyll concentrations that can extend up to 900 km offshore and have a strong influence on the biology of the area (McClain et al., 2002). Results from numerical models reproduce the variability observed in chlorophyll concentrations and its relationship with Ekman pumping velocities and ENSO (Sasai et al., 2012).

SBLME is the smallest of the LMEs examined here and presented intermediate chlorophyll concentrations. In austral fall and winter freshwater runoff from the Río de La Plata and Lagoa dos Patos move northward along the coast supplying nutrients to the area and promoting primary production in the

southern sector of the SBLME (Brandini, 1990). In addition, SBLME showed moderate seasonal variability, with a winter peak in chlorophyll concentrations that can be accounted for by the tongue of chlorophyll-rich waters from the Río de la Plata that migrate northward along the coast and lead to high chlorophyll concentrations of up to $>3.5\,mg\,m^{-3}$ in this area (Garcia and Garcia, 2008; Piola et al., 2008b). Although high concentrations of suspended matter likely cause an overestimation of chlorophyll in the estuary, *in situ* data have confirmed that the Río de la Plata supports values of up to $7.7\,mg\,m^{-3}$ (e.g., Carreto et al., 1986). Our results agree with previous studies that indicate that the slope and continental shelf in the northern part of SBLME are characterized by low chlorophyll concentrations throughout the year (Brandini, 1990; Castro et al., 2006).

Trends in Large Marine Ecosystems

The corrections made to the MODIS Aqua dataset in this study allowed the combination of multi-sensor data to generate the longest time series of satellite chlorophyll concentrations available to date around South and Western Central America. The newly developed extended time series include almost 20 years of data at high spatial resolution and revealed significant trends in chlorophyll concentrations. Previous studies observed varying trends in global average chlorophyll concentrations, with reports of a general decline (e.g., Behrenfeld et al., 2006; Vantrepotte and Mélin, 2009; Boyce et al., 2014; Lorenzoni et al., 2017), as well as no detectable trends (Beaulieu et al., 2013) or even a global increase of 4.13% (Gregg et al., 2005). However, there is general consensus in that there is high global variability, with regions of increasing and decreasing trends. For example, Hammond et al. (2017) detected a small global decline in chlorophyll between 1997 and 2013, but observed regional variability with both positive and negative trends present across the globe ranging from ~ -2 to 1% $year^{-1}$. Our results indicate that within the LMEs analyzed the greatest changes have occurred at the Patagonia (PLME) and Humboldt (HLME) Large Marine Ecosystems, where the largest and almost exclusively increasing trends were recorded and the largest percent areas showed significant changes. On the other hand, the warmer SBLME and PCACLME showed no significant trends in areal mean chlorophyll concentrations, and only smaller percent areas showed significant trends. The increasing chlorophyll concentrations observed on the Patagonian Shelf and in the Humboldt upwelling system have been reported in previous global studies (Gregg et al., 2005; Saulquin et al., 2013; Siegel et al., 2013; Muller-Karger et al., 2017), although these analyses were based on shorter time series with coarser resolution. The high resolution data used in this study allows a more detailed analysis of the variability in the distribution of trends within the LMEs and the relationship with other variables, leading to a better understanding of the mechanisms controlling chlorophyll distribution and the changes occurring over the past two decades.

At PMLE, maximum chlorophyll concentrations occur during austral summer over the mid-shelf and in proximity of the shelf-break, where a sharp thermal front system develops separating vertically stratified warm shelf waters from weakly stratified waters of the Malvinas Current (Acha et al., 2004; Romero et al., 2006). Our results revealed that large positive trends also occurred mostly in these areas that support high spring and summer chlorophyll, suggesting that the processes that favor production most likely have intensified. Although rich in nutrients, the Malvinas Current is characterized by low phytoplankton abundances presumably due to intense mixing and light limitation. On the seasonally stratified shelf, phytoplankton growth is limited by nutrient concentrations. As the Malvinas Current flows northward, upwelling along the shelf-break supplies cold nutrient-rich waters onto the shelf (Matano and Palma, 2008; Piola et al., 2010; Valla and Piola, 2015) favoring increased primary production in the vicinity of the shelf break and adjacent shelf waters. Model results suggest that the Malvinas Current controls cross-shelf exchanges at the shelf-break as well as the circulation over the continental shelf (Matano et al., 2010). In turn, the shelf break upwelling is controlled by the along-shelf pressure gradient associated with the presence of a slope current (Matano and Palma, 2008). The increasing trends observed in the shelf-break area and over the continental shelf could be an indication of changes affecting the supply of nutrients onto the shelf via changes in the interaction between the shelf break and the Malvinas Current (e.g., Matano and Palma, 2008). Alternatively, changes in along-slope winds over the outer shelf can modulate the intensity and location of shelf break upwelling (e.g., Carranza et al., 2017). To the best of our knowledge there are no published reports of increased transport of the Malvinas Current or changes in the along-slope winds that might lead to a more intense upwelling during the last two decades. The factors leading to the large positive trends in chlorophyll in the PLME should be further investigated.

Most of HMLE also presented increasing trends in chlorophyll concentrations. Based on the primary productivity of coastal waters, previous studies described four provinces along HLME (Montecino and Pizarro, 2006; Quiñones et al., 2009; Gutiérrez et al., 2016). The most productive province is located off Peru, followed by the area off central Chile, which shows stronger seasonality associated with changes in wind stress. The coastal areas off northern Chile and the Magellanic region have the lowest production rates. This description coincides, in general, with the spatial distribution of CHL trends observed at HLME, where the largest positive trends occurred off Peru and central Chile, smaller increases were observed off northern Chile, and no trends were detected off the southern Chilean coast, in the area under the influence of the Cape Horn Current. North of 40°S, the increasing trends in chlorophyll concentrations were associated with negative trends in SST. HLME is one of two LMEs in the world showing a cooling trend, the other being the California Current LME (Chavez et al., 2008; Belkin, 2009). Within HLME, there are two regions of persistent cooling close to the continent: a larger one off northern Chile and southern Peru ($\sim$10–30°S) and a smaller one at $\sim$40–50°S (Gutiérrez et al., 2016; Thompson et al., 2017), which largely coincide with the areas of maximum positive trends in chlorophyll. HLME is under the influence of the Humboldt upwelling system, where cold nutrient-rich waters from below the thermocline are upwelled to the surface as a result of the prevailing easterlies, favoring increased phytoplankton concentrations. It has been suggested

that upwelling intensity has increased as a result of climate change (Bakun, 1990; Demarcq, 2009; Sydeman et al., 2014), and that an observed cooling of 0.10°C for the period 1982–2006 is the result of increased upwelling, which ultimately translates into higher nutrient supply and chlorophyll concentrations in the area (Belkin, 2009). Gutiérrez et al. (2011) used sediment core data spanning 150 years to reconstruct the SST record from an upwelling area off Peru and confirmed a temperature decrease since the 1950s, which was in phase with an increase in productivity and also coincided with strengthened alongshore winds and intensified upwelling.

Global warming has the potential to increase stratification, affecting phytoplankton distribution and abundance and has been suggested as the cause of the expansion of the low-chlorophyll, low-productivity central ocean gyres (McClain et al., 2004; Polovina et al., 2008; Irwin and Oliver, 2009). Signorini et al. (2015) used a combination of satellite and model data to analyze trends in chlorophyll concentration, primary production, SST, mixed layer depth (MLD), and sea level anomaly (SLA) in five oligotrophic gyres for the period 1998–2013. They observed that, in general, the oligotrophic waters are expanding, with positive trends in SST, MLD and SLA, and reduced chlorophyll concentrations and primary production, with important implications for atmospheric CO_2 uptake and the biological pump. In an analysis of SST change in the world ocean LMEs, SBLME showed the strongest warming among the four LME's considered here, with a net increase in SST of 0.53°C during the period 1982–2006, while PCACLME and PLME showed milder changes of 0.14 and 0.08°C, respectively (Belkin, 2009). The observation of mostly positive trends in chlorophyll concentrations at the four LMEs examined in this study is an unexpected result considering the general surface warming recorded for the global ocean. A recent IOC-UNESCO report that examined global trends in SST and chlorophyll concentrations for the period 1998–2012 using monthly averaged satellite data with a $0.5^\circ \times 0.5^\circ$ spatial resolution described mixed relationships, with warming and cooling areas associated with both increasing and decreasing chlorophyll concentrations (O'Brien et al., 2017). In general, reduced chlorophyll concentrations associated with warmer SSTs can be explained in terms of increased vertical stability and changes in mixed layer depth (e.g., Behrenfeld et al., 2006). As the surface layer warms, the mixed layer becomes shallower and the thermocline stronger, which constrains the nutrient input from sub-thermocline water and ultimately reduces phytoplankton abundance. However, although most of our study area showed warming trends, decreasing chlorophyll concentrations were only observed in a small area of PCACLME. This suggests that no single factor can be identified as controlling changes in these LMEs but that a variety of mechanisms besides changes in stratification and mixed layer depth due to warming must be operating regionally at different scales. An alternative proposed mechanism that might explain, at least in part, increasing chlorophyll concentrations in a warming environment include changes in the composition and physiology of the phytoplankton community. Behrenfeld et al. (2015) pointed out that due to photoacclimation, chlorophyll variability is not simply a measure of phytoplankton biomass, but is also modulated by changes in pigmentation and as a physiological response to variability in nutrient supply. The study also concluded that relationships between trends in chlorophyll concentration and ocean warming do not represent proportional changes in primary production, as declines in chlorophyll can be related to constant or increased photosynthesis.

Implications for Higher Trophic Levels

The changes occurring in SST and chlorophyll concentrations have important implications for ecosystem dynamics and trophic interactions. For fish and many invertebrates, the highest mortality occurs during the early developmental stages of egg and larva, which are highly susceptible to changes in environmental conditions, such as temperature and oxygen concentrations, food availability (i.e., phyto- and zooplankton concentrations), and physical processes (turbulence and advection) (Cushing, 1975; Cury and Roy, 1989; Bakun, 1998; Mann and Lazier, 2005). Fluctuations in the environment will affect the timing of the onset of the spring bloom, with early or delayed blooms having a negative impact on the survival of fish larvae and recruitment (match-mismatch hypothesis, Cushing, 1990). Previous studies have shown that interannual variability in chlorophyll concentrations during the reproductive season can have strong effects on recruitment (Platt et al., 2003; Fuentes-Yaco et al., 2007; Marrari et al., 2008, 2013), with not only the concentration of chlorophyll having an effect on reproductive success, but also other aspects of phytoplankton dynamics, such as the timing and duration of the spring bloom. At HLME, the fish community is dominated by four pelagic species: the anchoveta *Engraulis ringens*, the sardine *Sardinops sagax*, the jack mackerel *Trachurus murphyi*, and the chub mackerel *Scomber japonicus*. These species feed on phytoplankton and/or zooplankton for part or all of their life cycles; thus, changes in the abundance and composition of the phytoplankton community can have a direct impact on their population via changes in the availability of food.

At PLME, the increases in chlorophyll concentrations observed at the shelf break and in some coastal areas are of special interest in terms of fisheries. The northern population of the argentine anchovy *Engraulis anchoita* spawns in coastal waters shallower than ∼50 m between 34 and 41°S, in the vicinity of a thermal front that separates mixed coastal waters from seasonally stratified mid-shelf waters. At the front, high chlorophyll concentrations develop during spring. A recent study showed that variability in the timing, magnitude, and duration of the spring bloom explained a large fraction of the variability in anchovy recruitment (Marrari et al., 2013). On the other hand, the area of Isla Escondida and the San Jorge Gulf (43–47°S) represent the main spawning and nursery grounds for the argentine hake *Merluccius hubbsi*, the main demersal fishery in the region. Recent results indicated that larval survival was related to spring chlorophyll concentrations and the timing of the chlorophyll maximum in the main spawning area, suggesting that phytoplankton dynamics likely affects the reproductive success of hake via de production of zooplanktonic prey for the larvae (Marrari et al., under review).

Changes in phytoplankton abundances can have a direct effect on the biological pump and global carbon budget. Kahl et al. (2017) analyzed the distribution of sea-air CO_2 fluxes on the Patagonia shelf and observed that on the mid- and outer-shelf areas fluxes were dominated by biological processes, leading to a strong sink of atmospheric CO_2 of -6.0×10^{-3} m^{-2} day^{-1}, equivalent to -20 TgC $year^{-1}$, with the maximum uptake occurring in spring. This suggests that an analysis of the seasonality in the trends observed should be included in future studies to more accurately describe the effects of long-term changes in chlorophyll concentrations on the ecosystem. Increased phytoplankton abundances will intensify carbon export to the deep ocean with a direct effect on benthic-pelagic interactions. Franco et al. (2017) used particle-tracking models and observed that 80% of the particles released at the surface in proximity of shelf break at PLME settled on the bottom in areas where scallop beds are known to occur; thus an increase in surface phytoplankton abundances could positively impact benthic communities.

The changes occurring in chlorophyll concentrations over the last two decades have important ecological and economic implications for marine populations. In light of the ongoing climate change, further changes in phytoplankton dynamics are anticipated. This highlights the need to continue the analysis of trend in key environmental variables in order to better understand and predict the effects on ecosystem dynamics and the economy of the LMEs.

AUTHOR CONTRIBUTIONS

All authors (MM, AP, and DV) contributed substantially to the design of this study, the analysis of the data, drafting the work, interpreting results and revising it critically. All authors have approved the final version and agreed to be accountable for all aspects of the work in ensuring that questions related to the accuracy or integrity of any part of the work are appropriately investigated and resolved.

ACKNOWLEDGMENTS

We thank John Wilding for assisting with data processing. SeaWiFS and MODIS data were distributed by the NASA Ocean Biology Processing Group. This study was funded by grants PICT-2013-1243 from Fondo para la Investigación Científica y Tecnológica (Argentina) and CRN3070 from the Inter-American Institute for Global Change Research through the US National Science Foundation grant GEO-1128040.

REFERENCES

Acha, E. M., Mianzán, H. W., Guerrero, R. A., Favero, M., and Bava, J. (2004). Marine fronts at the continental shelves of austral South America. Physical and ecological processes. *J. Mar. Syst*. 44, 83–105. doi: 10.1016/j.jmarsys.2003.09.005

Acha, E. M., Simionato, C. G., Carozza, C., and Mianzán, H. W. (2012). Climate-induced year-class fluctuations of whitemouth croaker *Micropogonias furnieri* (Pisces, Sciaenidae) in the Rio de la Plata estuary, Argentina-Uruguay. *Fish. Oceanogr*. 21, 58–77. doi: 10.1111/j.1365-2419.2011.00609.x

Armstrong, R. A., Gilbes, F., Guerrero, R., Lasta, C., Benavidez, H., and Mianzán, H. (2004). Validation of SeaWiFS-derived chlorophyll for the Rio de la Plata Estuary and adjacent waters. *Int. J. Remote Sens.* 25, 1501–1505. doi: 10.1080/01431160310001592517

Bakun, A. (1990). Global climate change and intensification of coastal ocean upwelling. *Science* 247, 198–201. doi: 10.1126/science.247.4939.198

Bakun, A. (1998). "Ocean triads and radical interdecadal stock variability: bane and boon for fishery management science," in *Reinventing Fisheries Management*, eds T. J. Pitcher, P. J. B. Hart, and D. Pauly (Dordrecht: Kluwer Academic Publishers), 331–358.

Bakun, A., Csirke, J., Lluch-Belda, D., and Steer-Ruiz, R. (1999). "The Pacific Central American coastal LME," in *Large Marine Ecosystems of the Pacific Rim: Assessment, Sustainability and Management*, eds K. Sherman and Q. Tang (Malden: Blackwell Science Inc.,), 268–280.

Beaulieu, C., Henson, S. A., Sarmiento, J. L., Dunne, J. P., Doney, S. C., Rykaczewski, R. R., et al. (2013). Factors challenging our ability to detect long-term trends in ocean chlorophyll. *Biogeosciences* 10, 2711–2724. doi: 10.5194/bg-10-2711-2013

Behrenfeld, M. J., O'Malley, R. T., Boss, E. S., Westberry, T. K., Graff, J. R., Halsey, K. H., et al. (2015). Revaluating ocean warming impacts on global phytoplankton. *Nat. Clim. Chang.* 6, 323–330. doi: 10.1038/nclimate2838

Behrenfeld, M. J., O'Malley, R. T., Siegel, D. A., McClain, C. R., Sarmiento, J. L., Feldman, G., et al. (2006). Climate-driven trends in contemporary ocean productivity. *Nature* 444, 752–755. doi: 10.1038/nature05317

Belkin, I. M. (2009). Rapid warming of large marine ecosystems. *Prog. Oceanogr.* 81, 207–213. doi: 10.1016/j.pocean.2009.04.011

Bertrand, A., Fréon, P., Chaigneau, A., Echevin, V., Estrella, C., Demarcq, H., et al. (2010). *Impactos del Cambio Climático en las Dinámicas Oceánicas, el Funcionamiento de los Ecosistemas y las Pesquerías en el Perú: Proyección de Escenarios e Impactos Socio Económicos.* Embajada Británica en Lima. Available online at: http://humboldt.iwlearn.org/en/information-and-publication-1/Bertrandetal2010escenariospesquerosCCPeru.pdf.

Bianchi, A. A., Bianucci, L., Piola, A. R., Ruiz Pino, D., Schloss, I., Poisson, A., et al. (2005). Vertical stratification and air–sea CO_2 fluxes in the Patagonian shelf. *J. Geophys. Res.* 110:C07003. doi: 10.1029/2004JC002488

Bianchi, A. A., Ruiz Pino, D., Isbert Perlender, H. G., Osiroff, A. P., Segura, V., Lutz, V., et al. (2009). Annual balance and seasonal variability of sea–air CO_2 fluxes in the Patagonian Sea: their relationship with fronts and chlorophyll distribution. *J. Geophys. Res.* 114:C03018. doi: 10.1029/2008JC004854

Boyce, D. G., Dowd, M., Lewis, M. R., and Worm, B. (2014). Estimating global chlorophyll changes over the past century. *Prog. Oceanogr.* 122, 163–173. doi: 10.1016/j.pocean.2014.01.004

Brander, K. M. (2007). Global fish production and climate change. *Proc. Natl. Acad. Sci. U.S.A.* 104, 19709–19714. doi: 10.1073/pnas.0702059104

Brandini, F., Boltovskoy, D., Piola, A. R., Kocmur, S., Rottgers, R., Abreu, P., et al. (2000). Multiannual trends in fronts and distribution of nutrients and chlorophyll in the southwestern Atlantic. *Deep Sea Res. I* 47, 1015–1033. doi: 10.1016/S0967-0637(99)00075-8

Brandini, F. P. (1990). Hydrography and characteristics of the phytoplankton in shelf and oceanic waters off southeastern Brazil during winter (July/August 1982) and summer (February/March 1984). *Hydrobiologia* 196, 111–148. doi: 10.1007/BF00006105

Caddy, J. F., and Defeo, O. (2003). *Enhancing or Restoring the Productivity of Natural Populations of Shellfish and Other Marine Invertebrate Resources.* FAO Fisheries Technical Paper, Vol. 448. (Rome: FAO), 159.

Campagna, C., Piola, A. R., Marin, M. R., Lewis, M., and Fernández, T. (2006). Southern elephant seal trajectories, ocean fronts and eddies in the Brazil/Malvinas Confluence. *Deep Sea Res. I* 53, 1907–1924. doi: 10.1016/j.dsr.2006.08.015

Campbell, J. W. (1995). The lognormal distribution as a model for bio-optical variability in the sea. *J. Geophys. Res.* 100, 13237–13254. doi: 10.1029/95JC00458

Campos, P., Möller, O. O., Piola, A. R., and Palma, E. D. (2013). Seasonal variability and western boundary upwelling: cape Santa Marta (Brazil). *J. Geophys. Res. Oceans* 118, 1420–1433. doi: 10.1002/jgrc.20131

Carr, M. E., and Kearns, E. J. (2003). Production regimes in four eastern boundary current systems. *Deep Sea Res. II* 50, 3199–3221. doi: 10.1016/j.dsr2.2003.07.015

Carr, M. E., Strub, P. T., Thomas, A. C., and Blanco, J. L. (2002). Evolution of 1996-1999 La Niña and El Niño conditions off the western coast of South America: a remote sensing perspective. *J. Geophys. Res.* 107, 3236. doi: 10.1029/2001JC001183

Carranza, M. M., Gille, S. T., Piola, A. R., Charo, M., and Romero, S. I. (2017). Wind modulation of upwelling at the shelf-break front off Patagonia: observational evidence. *J. Geophys. Res. Oceans* 122, 2401–2424. doi: 10.1002/2016JC012059

Carreto, J. I., Negri, R. M., and Benavides, H. R. (1986). Algunas características del florecimiento del fitoplancton en el frente del Río de la Plata. Parte I: los sistemas nutritivos. *Rev. Investigac. Y Desarrollo Pesquero* 5, 7–29.

Castilla, J. C., and Defeo, O. (2001). Latin-American benthic shellfisheries: emphasis on comanagement and experimental practices. *Rev. Fish Biol. Fish.* 11, 1–30. doi: 10.1023/A:1014235924952

Castro, B. M., Brandini, F. P., Pires-Vanin, A. M. S., and Miranda, L. B. (2006). "Multidisciplinary oceanographic processes on the Western Atlantic continental shelf between 4°N and 34°S," in *The Sea, Vol. 14, The Global Coastal Ocean: Interdisciplinary Regional Studies and Syntheses, Chapter 8*, eds A. R. Robinson and K. Brink (Cambridge, MA: Harvard University Press), 259–294.

Chavez, F. P., Bertrand, A., Guevara-Carrasco, R., Soler, P., and Csirke, J. (2008). The northern Humboldt Current System: brief history, present status and a view towards the future. *Prog. Oceanogr.* 79, 95–105. doi: 10.1016/j.pocean.2008.10.012

Chelton, D. B., Schlax, M. G., Witter, D. L., and Richman, J. G. (1990). Geosat altimeter observations of the surface circulation of the Southern Ocean. *J. Geophysical. Res. 95:*17877. doi: 10.1029/JC095iC10p17877

Cheung, W. W. L., Lam, V. W. Y., Sarmiento, J. L., Kearney, K. R., Watson, R., Zeller, D., et al. (2010). Large-scale redistribution of maximum fisheries catch potential in the global ocean under climate change. *Glob. Chang. Biol.* 16, 24–35. doi: 10.1111/j.1365-2486.2009.01995.x

Ciotti, A. M., Odebrecht, C., Fillmann, G., and Möller, O. O. (1995). Freshwater outflow and Subtropical Convergence influence on phytoplankton biomass on the southern Brazilian continental shelf. *Cont. Shelf Res.* 15, 1737–1756. doi: 10.1016/0278-4343(94)00091-Z

Cochrane, D., and Orcutt, G. H. (1949). Application of least squares regression to relationships containing auto-correlated error terms. *J. Am. Stat. Assoc.* 44, 32–61.

Cury, P., and Roy, C. (1989). Optimal environmental window and pelagic fish recruitment success in upwelling areas. *Cana. J. Fish. Aqu. Sci*. 46, 670–680. doi: 10.1139/f89-086

Cushing, D. H. (1975). *Marine Ecology and Fisheries*. Cambridge: Cambridge University Press. 287.

Cushing, D. H. (1990). Plankton production and year-class strength in fish-populations: an update of the match/mismatch hypothesis. *Adv. Mar. Biol.* 26, 249–293. doi: 10.1016/S0065-2881(08)60202-3

Defeo, O., Horta, S., Carranza, A., Lercari, D., de Álava, A., and Gómez, J., Martínez, G., et al. (2009). *Hacia un manejo ecosistémico de pesquerías. Áreas marinas protegidas en Uruguay*. Montevideo: Facultad de Ciencias-DINARA, 122.

Demarcq, H. (2009). Trends in primary production, sea surface temperature and wind in upwelling systems (1998–2007). *Prog. Oceanogr.* 83, 376–385. doi: 10.1016/j.pocean.2009.07.022

Doney, S. C. (2006). Oceanography-Plankton in a warmer world. *Nature* 444, 695–696, doi: 10.1038/444695a

Duda, A., and Sherman, K. (2002). A new imperative for improving management of large marine ecosystems. *Ocean Coastal Manag.* 45, 797–833. doi: 10.1016/S0964-5691(02)00107-2

Escribano, R., Daneri, D., Farías, L., Gallardo, V. A., Gonzalez, H. E., and Gutierrez, D., et al. (2004). Biological and chemical consequences of the 1997-1998 El Niño in the Chilean coastal upwelling system: a synthesis. *Deep Sea Res. II* 51, 2389–2411. doi: 10.1016/j.dsr2.2004.08.011

Franco, B. C., Palma, E. D., Combes, V., and Lasta, M. L. (2017). Physical processes controlling passive larval transport at the Patagonian Shelf Break Front. *J. Sea Res*. 124, 17–25. doi: 10.1016/j.seares.2017.04.012

Fuentes-Yaco, C., Koeller, P. A., Sathyendranath, S., and Platt, T. (2007). Shrimp (*Pandalus borealis*) growth and timing of the spring phytoplankton bloom on the Newfoundland-Labrador Shelf. *Fish. Oceanogr.* 16, 116–129. doi: 10.1111/j.1365-2419.2006.00402.x

Garcia, C. A. E., and Garcia, V. M. T. (2008). Variability of chlorophyll-a from ocean color images in the La Plata continental shelf region. *Cont. Shelf Res.* 28, 1568–1578. doi: 10.1016/j.csr.2007.08.010

Garcia, C. A. E., Garcia, V. M. T., and McClain, C. R. (2005). Evaluation of SeaWiFS chlorophyll algorithms in the Southwestern Atlantic and Southern Oceans. *Remote Sens. Environ.* 95, 125–137. doi: 10.1016/j.rse.2004.12.006

Garcia, V. M. T., Garcia, C. A. E., Mata, M. M., Pollery, R., Piola, A. R., Signorini, S., et al. (2008). Environmental factors controlling the phytoplankton blooms at the Patagonia shelf-break in spring. *Deep Sea Res. I* 55, 1150–1166. doi: 10.1016/j.dsr.2008.04.011

Garzoli, S. L. (1993). Geostrophic velocity and transport variability in the Brazil-Malvinas Confluence. *Deep Sea Res. I. Oceanogr. Res. Pap.* 40, 1379–1403, doi: 10.1016/0967-0637(93)90118-M

Good, S. A., Corlett, G. K., Remedios, J. J., Noyes, E. J., and Llewellyn-Jones, D. T. (2007). The global trend in sea surface temperature from 20 years of advanced very high resolution radiometer data. *J. Clim.* 20, 1255–1264. doi: 10.1175/JCLI4049.1

Gregg, W. W., and Casey, N. W. (2004). Global and regional evaluation of the SeaWiFS chlorophyll dataset. *Remote Sens. Environ.* 93, 463–479. doi: 10.1016/j.rse.2003.12.012

Gregg, W. W., Casey, N. W., and McClain, C. R. (2005). Recent trends in global chlorophyll. *Geophys. Res. Lett.* 32:L03606. doi: 10.1029/2004GL021808

Gregg, W. W., and Rousseaux, C. S. (2014). Decadal trends in global pelagic ocean chlorophyll: a new assessment integrating multiple satellites, *in situ* data, and models. *J. Geophys. Res. Oceans* 119, 5921–5933. doi: 10.1002/2014JC010158

Gutiérrez, D., Akester, M., and Naranjo, L. (2016). Productivity and sustainable management of the humboldt current large marine ecosystem under climate change. *Environ. Dev.* 17, 126–144. doi: 10.1016/j.envdev.2015.11.004

Gutiérrez, D., Bouloubassi, I., Sifeddine, A., Purca, S., Goubanova, K., Graco, M., et al. (2011). Coastal cooling and increased productivity in the main upwelling zone off Peru since the mid-twentieth century. *Geophys. Res. Lett.* 38:L07603. doi: 10.1029/2010GL046324

Hammond, M. L., Beaulieu, C., Sahu, S. K., and Henson, S. A. (2017). Assessing trends and uncertainties in satellite-era ocean chlorophyll using space-time modeling. *Global Biogeochem. Cycles* 31, 1103–1117. doi: 10.1002/2016GB005600

Heileman, S. (2009). "XVI-55 Patagonian Shelf LME," in *The UNEP Large marine Ecosystem Report: A perspective on changing conditions in LMES of the world's Regional Seas. UNEP Regional Seas Report and Studies N° 182. United Nations Environment Programme*, eds K. Sherman and G. Hempel (Nairobi: UNDP). 735–746.

Heileman, S., Guevara, R., Chavez, F., Bertrand, A., and Soldi, H. (2009). "XVII-56 Humboldt Current: LME 13," in *The UNEP Large marine Ecosystem Report: A perspective on changing conditions in LMES of the world's Regional Seas. UNEP Regional Seas Report and Studies N° 182. United Nations Environment Programme*, eds K. Sherman and G. Hempel (Nairobi: UNDP). 749–762.

Hu, C., Carder, K. L., and Müller-Karger, F. E. (2001). How precise are SeaWiFS ocean color estimates? Implications of digitization-noise errors. *Remote Sens. Environ.* 76, 239–249. doi: 10.1016/S0034-4257(00)00206-6

IBAMA (2002). *Geo-Brasil 2002: Perspectivas do Meio Ambiente no Brasil*. Brasilia: Instituto Brasileiro de Meio Ambiente.

IOC-UNESCO and UNEP (2016). *Large Marine Ecosystems: Status and Trends, Summary for Policy Makers*. Nairobi: Environment Programme (UNEP).

Irwin, A. J., and Oliver, M. J. (2009). Are ocean deserts getting larger? *Geophys. Res. Lett.* 36:L18609. doi: 10.1029/2009GL039883

Kahl, L. C., Bianchi, A. A., Osiroff, A. P., Ruiz Pino, D., and Piola, A. R. (2017). Distribution of sea-air CO_2 fluxes in the Patagonian Sea: seasonal, biological and thermal effects. *Cont. Shelf Res.* 143, 18–28. doi: 10.1016/j.csr.2017.05.011

Karstensen, J., Stramma, L., and Visbeck, M. (2008). Oxygen minimum zones in the eastern tropical Atlantic and Pacific oceans. *Prog. Oceanogr.* 77, 331–350. doi: 10.1016/j.pocean.2007.05.009

Lawrence, S. P., Llewellyn-Jones, D. T., and Smith, S. J. (2004). The measurement of climate change using data from the advanced very high

resolution and along track scanning radiometers. *J. Geophys. Res.* 109:C08017. doi: 10.1029/2003JC002104

Legendre, P., and Legendre, L. (1998). *Numerical Ecology*, 2nd Edn. Amsterdam: Elsevier Scientific Publishing Company, 870.

Le Quéré, C., Andrew, R. M., Canadell, J. G., Sitch, S., Korsbakken, J. I., Peters, G. P., et al. (2016). Global Carbon Budget 2016. *Earth Syst. Sci. Data* 8, 605–649. doi: 10.5194/essd-8-605-2016

Lorenzoni, L., O'Brien, T., Isensee, K., Benway, H., Muller-Karger, F. E., Thompson, P. A., et al. (2017). "Global Overview," in *What are Marine Ecological Time Series Telling us About the Ocean? A Status Report*, eds T. O'Brien, L. Lorenzoni, K. Isensee and L. Valdés (Paris: IOC-UNESCO), 171–190. IOC Technical Series, No. 129.

Lutz, V. A., Segura, V., Dogliotti, A. I., Gagliardini, D. A., Bianchi, A., and Balestrini, C. F. (2010). Primary production in the Argentine Sea during spring estimated by field and satellite models. *J. Plankton Res.* 32, 181–195. doi: 10.1093/plankt/fbp117

Mann, K. H., and Lazier, J. R. N. (2005). *Dynamics of Marine Ecosystems. 3rd Edn*. Oxford, UK: Wiley-Blackwell, 512

Marrari, M., Daly, K. L., and Hu, C. (2008). Spatial and temporal variability of SeaWiFS chlorophyll a distributions west of the Antarctic Peninsula: implications for krill production. *Deep Sea Res. II* 53, 377–392. doi: 10.1016/j.dsr2.2007.11.011

Marrari, M., Hu, C., and Daly, K. L. (2006). Validation of SeaWiFS chlorophyll a concentrations in the Southern Ocean: a revisit. *Remote Sens. Environ.* 105, 367–375. doi: 10.1016/j.rse.2006.07.008

Marrari, M., Piola, A. R., Valla, D., and Wilding, J. G. (2016). Trends and variability in extended ocean color time series in the main reproductive area of the Argentine hake, *Merluccius hubbsi* (Southwestern Atlantic Ocean). *Remote Sens. Environ.* 177, 1–12. doi: 10.1016/j.rse.2016.02.011

Marrari, M., Signorini, S., McClain, C. R., Pájaro, M., Martos, P., Viñas, M. D., et al. (2013). Reproductive success of the Argentine anchovy, *Engraulis anchoita*, in relation to environmental variability at a mid-shelf front (Southwestern Atlantic Ocean). *Fish. Oceanogr.* 22, 247–261. doi: 10.1111/fog.12019

Matano, R. P., and Palma, E. D. (2008). The Upwellling of Downwelling Currents. *J. Phys. Oceanogr*. 38, 2482–2500. doi: 10.1175/2008JPO3783.1

Matano, R. P., Palma, E. D., and Piola, A. R. (2010). The influence of the Brazil and Malvinas currents on the southwestern Atlantic shelf. *Ocean Sci*. 6, 983–995. doi: 10.5194/os-6-983-2010

McClain, C. R., Christian, J. R., Signorini, S. R., Lewis, M. R., Asanuma, I., Turk, D., et al., (2002). Satellite ocean-color observations of tropical Pacific Ocean. *Deep Sea Res. II* 49, 2533–2560. doi: 10.1016/S0967-0645(02)00047-4

McClain, C. R., Signorini, S. R., and Christian, J. R. (2004). Subtropical gyre variability observed by ocean-color satellites. *Deep Sea Res. Part II* 51, 281–301. doi: 10.1016/j.dsr2.2003.08.002

Möller, O. O., Castello, J. P., and Vaz, A. C. (2009). The effect of river discharge and winds on the interannual variability of the Pink Shrimp Farfantepenaeus paulensis production in Patos Lagoon. *Estuar. Coasts* 32, 787–796. doi: 10.1007/s12237-009-9168-6

Möller, O. O., Piola, A. R., Freitas, A. C., and Campos, E. J. D. (2008). The effects of river discharge and winds on the shelf off southeastern South America. *Cont. Shelf Res.* 28, 1607–1624. doi: 10.1016/j.csr.2008.03.012

Montecino, V., and Pizarro, G. (2006). "Productividad primaria, biomasa y tamaño del fitoplancton en canales y fiordos australes: patrones primavera-verano," in *Avances en el conocimiento oceanográfico de las aguas interiores chilenas, Puerto Montt a cabo de Hornos,* eds N. Silva and S. Palma, (Valparaíso: Comité Oceanográfico Nacional, Pontificia Universidad Católica de Valparaíso), 93–97.

Muller-Karger, F. E., Piola, A., Verheye, H. M., O'Brien, T. D., and Lorenzoni, L. (2017). "South Atlantic Ocean," in *What are Marine Ecological Time Series telling us about the ocean? A Status Report,* eds T. O'Brien, L. Lorenzoni, K. Isensee and L. Valdés (Paris: IOC-UNESCO), 83–96. IOC Technical Series, No. 129.

O'Brien, T. D., Lorenzoni, L., Isensee, K., and Valdés, L. (eds.). (2017). *What are Marine Ecological Time Series telling us about the ocean? A status Report,* (Paris: IOC-UNESCO), 297. IOC Technical Series, No. 129.

O'Reilly, J. E., Maritorena, S., O'Brien, M. C., Siegel, D. A., Toole, D., Menzies, D., et al. (2000). "SeaWiFS postlaunch calibration and validation analyses: Part 3. SeaWiFS postlaunch technical report series," in *NASA technical memorandum 2000–206892*, Vol. 11, eds S. B. Hooker and R. E. Firestone (Greenbelt, MD: NASA Goddard Space Flight Center), 49.

Paiva, M. P. (1997). *Recursos pesqueiros estuarinos e marinhos do Brasil*. Fortaleza: Universidade Federal do Ceará-UFC.

Palma, E. D., Matano, R. P., and Piola, A. R. (2008). A numerical study of the Southwestern Atlantic Shelf circulation: stratified ocean response to local and offshore forcing. *J. Geophys. Res.* 113:C11010. doi: 10.1029/2007JC004720

Pauly, D., Alder, J., Booth, S., Cheung, W. W. L., Christensen, V., Close, C., et al. (2008). "Fisheries in Large Marine Ecosystems: Descriptions and Diagnoses," in *The UNEP Large Marine Ecosystem Report: A Perspective on Changing Conditions in LMEs of the World's Regional SeasL*, eds Sherman and G. Hempel (UNEP Regional Seas Reports and Studies No. 182), 23–40.

Piola, A. R., Campos, E. J. D., Möller, O. O., Charo, M., and Martinez, C. (2000). Subtropical shelf front off eastern South America. *J. Goephys. Res*. 105, 6566–6578. doi: 10.1029/1999JC000300

Piola, A. R., Martínez Avellaneda, N., Guerrero, R. A., Jardón, F. P., Palma, E. D., and Romero, S. I. (2010). Malvinas-slope water intrusions on the northern Patagonia continental shelf. *Ocean Sci*. 6, 345–359. doi: 10.5194/os-6-345-2010

Piola, A. R., and Matano, R. P. (2001). "Brazil and Falklands (Malvinas) Currents," in *Encyclopedia of Ocean Sciences,* Vol. 1, eds J. H. Steele, S. A Thorpe, and K. K. Turekian, (London: Academic Press), 340–349.

Piola, A. R., Matano, R. P., Palma, E. D., Möller, O. O., and Campos, E. J. D. (2005). The influence of the Plata River discharge on the western South Atlantic shelf. *Geophys. Res. Lett.* 32:L01603. doi: 10.1029/2004GL021638

Piola, A. R., Möller, O. O. Jr., Guerrero, R. A., and Campos, E. J. D. (2008a). Variability of the subtropical shelf front off eastern South America: winter 2003 and summer 2004. *Cont. Shelf Res.* 28, 1639–1648. doi: 10.1016/j.csr.2008.03.013

Piola, A. R., Romero, S. I., and Zajaczkowski, U. (2008b). Space-time variability of the Plata plume inferred from ocean color. *Cont. Shelf Res.* 28, 1556–1567. doi: 10.1016/j.csr.2007.02.013

Platt, T., Fuentes-Yaco, C., and Frank, K. T. (2003). Spring algal bloom and larval fish survival. *Nature* 423, 398–399. doi: 10.1038/423398b

Polovina, J. J., Howell, E. A., and Abecassis, M. (2008). Ocean's least productive waters are expanding. *Geophys. Res. Lett*. 35:L03618. doi: 10.1029/2007GL031745

Prado, J., and Drew, S. (1999). *Research and development in fishing technology in Latin America.* Rome: FAO Fisheries Circular No. 944, Food and Agriculture Organization of the United Nations (FAO). 31.

Quiñones, J., Gonzáles Carman, V., Zeballos, J., Purca, S., and Mianzán, H. W. (2010). Effects of El Niño-driven environmental variability on black turtle migration to Peruvian foraging grounds. *Hydrobiologia* 645, 69–79. doi: 10.1007/s10750-010-0225-8

Quiñones, R. M. H., Gutiérrez, G., Daneri, D., Gutiérrez Aguilar, H., and González Chavez, F. (2009). "Pelagic carbon fluxes in the Humboldt Current System," in Carbon and Nutrient Fluxes in Continental Margins: a Global Synthesis, eds K. K. Liu, L. Atkinson, R. Quiñones, and L. Talaue-McManus, (Weinheim: Springer-Verlag), 44–64.

Romero, S. I., Piola, A. R., Charo, M., and Garcia, C. A. E. (2006). Chlorophyll-a variability off Patagonia based on SeaWiFS data. *J. Geophys. Res.* 111:C05021. doi: 10.1029/2005JC003244

Saraceno, M., Provost, C., Piola, A. R., Bava, J., and Gagliardini, A. (2004). Brazil Malvinas Frontal System as seen from 9 years of advanced very high resolution radiometer data. *J. Geophys. Res.* 109:C05027. doi: 10.1029/2003JC002127

Sasai, Y., Richards, K. J., Ishida, A., and Sasaki, H. (2012). Spatial and temporal variabilities of the chlorophyll distribution in the northeastern tropical Pacific: the impact of physical processes on seasonal and interannual time scales. *J. Marine Syst*. 96–97, 24–31. doi: 10.1016/j.jmarsys.2012.01.014

Saulquin, B., Fablet, R., Mangin, A., Mercier, G., Antoine, D., and Fanton d'Andon, O. (2013). Detection of linear trends in multisensor time series in the presence of autocorrelated noise: application to the chlorophyll-a SeaWiFS and MERIS data sets and extrapolation to the incoming Sentinel 3-OLCI mission. *J. Geophys. Res.* 118, 3752–3763. doi: 10.1002/jgrc.20264

Schroëder, F. A., and Castello, J. P. (2010). An essay on the potential effects of climate change on fisheries in Patos Lagoon, Brazil. *Pan. Am. J. Aquatic Sci.* 5, 320–330.

Sherman, K. (1993). "Large Marine Ecosystems as Global Units for Marine Resources Management-An Ecological Perspective," in *Large Marine Ecosystems,* eds K. Sherman, L. M. Alexander and B. Gold, (Washington, DC: American Association for the Advancement of Science-AAAs), 3–14.

Sherman, K. (2014a). Adaptive management institutions at the regional level: the case of large marine ecosystems. *Ocean and Coast. Manag.* 90, 38–49. doi: 10.1016/j.ocecoaman.2013.06.008

Sherman, K. (2014b). Toward ecosystem-based management (EBM) of the world's large marine ecosystems during climate change. *Environ. Develop.* 11, 43–66. doi: 10.1016/j.envdev.2014.04.006

Sherman, K., and Alexander, L. (eds.). (1989). "Variability and management of large marine ecosystems," in *AAAS Symposium 99*, (Boulder: Westview Press CO). 319.

Sherman, K., and Hempel, G. (eds.). (2008). *The UNEP Large Marine Ecosystem Report: a Perspective on Changing Conditions in LMES of the World's Regional Seas UNEP Regional Seas Report and Studies, No 182*. (Nairobi; United Nations Environment Programme), 2009.

Siegel, D. A., Behrenfeld, M. J., Maritorena, S., McClain, C. R., Antoine, D., Bailey, S. W., et al. (2013). Regional to global assessments of phytoplankton dynamics from the SeaWiFS mission. *Remote Sens. Environ.* 135, 77–91. doi: 10.1016/j.rse.2013.03.025

Signorini, S. R., Franz, B. A., and McClain, C. R. (2015). Chlorophyll variability in the oligotrophic gyres: mechanisms, seasonality and trends. *Front. Mar. Sci.* 2:1. doi: 10.3389/fmars.2015.00001

Strub, P. T., Mesias, J. M., Montecino,-B., V., Rutllant,-C., J., and Salinas-M, S. (1998). "Coastal ocean circulation off western South America," in *The Sea*, Vol. 11, eds A. R. Robinson and K. H. Brink (New York, NY: John Wiley and Sons), 273–313.

Sydeman, W. J., García-Reyes, M., Schoeman, D. S., Rykaczewski, R. R., Thompson, S. A., Black, B. A., et al. (2014). Climate change and wind intensification in coastal upwelling ecosystems. *Science* 345, 77–80. doi: 10.1126/science.1251635

Thomas, A. C., Carr, M. E., and Strub, P. T. (2001). Chlorophyll variability in Eastern Boundary Currents. *Geophys. Res. Lett.* 28, 3421–3424. doi: 10.1029/2001GL013368

Thompson, P. A., O'Brien, T. D., Lorenzoni, L., and Richardson, A. J. (2017). "South Pacific Ocean," in *What are Marine Ecological Time Series Telling us about the Ocean? A Status Report* Vol, 129, eds T. O'Brien, L. Lorenzoni, K. Isensee and L. Valdés (Paris: IOC-UNESCO), 133–152. IOC Technical Series, No.129.

Tiao, G. C., Reinsel, G. C., Xu, D., Pedrick, J. H., Zhu, X., Miller, A. J., et al. (1990). Effects of autocorrelation and temporal sampling schemes on estimates of trend and spatial correlation. *J. Geophys. Res.* 95, 20507–20517. doi: 10.1029/JD095iD12p20507

Valentini, H., and Pezzuto, P. R. (2006). *Análise das Principais Pescarias Comerciais da Regiao Sudeste-Sul do Brasil com base na Produção Controlada do Periodo 1986-2004.* Série Documentos REVIZEE-SCORE Sul, 56.

Valla, D., and Piola, A. R. (2015). Evidence of upwelling events at the northern Patagonian shelf break. *J. Geophys. Res.* 120, 7635–7656, doi: 10.1002/2015JC011002

Vantrepotte, V., and Mélin, F. (2009). Temporal variability of 10-year global SeaWiFS time-series of phytoplankton chlorophyll a concentration. *ICES J. Mar. Sci.* 66, 1547–1556. doi: 10.1093/icesjms/fsp107

Weatherhead, E. C., Reinsel, G. C., Tiao, G. C., Meng, X., Choi, D., Cheang, W., et al. (1998). Factors affecting the detection of trends: statistical considerations and applications to environmental data. *J. Geophys. Res.* 103, 17149–17161. doi: 10.1029/98JD00995

Werdell, P. J., Bailey, S. W., Franz, B. A., Harding, L. W. Jr., Feldman, G. C., and McClain, C. R. (2009). Regional and seasonal variability of chlorophyll-a in Chesapeake Bay as observed by SeaWiFS and MODIS-Aqua. *Remote Sens. Environ.* 113, 1319–1330. doi: 10.1016/j.rse.2009.02.012

Wu, L., Cai, W., Zhang, L., Nakamura, H., Timmermann, A., Joyce, T., et al. (2012). Enhanced warming over the global subtropical western boundary currents. *Nat. Clim. Change* 2, 161–166. doi: 10.1038/nclimate1353

Zavialov, P., Kostianoy, A., and Möller, O. O. (2003). Safari Cruise: mapping river discharge effects on southern Brazil. *Geophys. Res. Lett.* 30, 71–74. doi: 10.1029/2003GL018265

Conflict of Interest Statement: The authors declare that the research was conducted in the absence of any commercial or financial relationships that could be construed as a potential conflict of interest.

frontiers in Marine Science

ORIGINAL RESEARCH
published: 20 December 2017
doi: 10.3389/fmars.2017.00233

Estuarine Suspended Sediment Dynamics: Observations Derived from over a Decade of Satellite Data

Anthony Reisinger[1]*, *James C. Gibeaut*[1]* and *Phillippe E. Tissot*[2]

[1] Coastal and Marine Geospatial Laboratory, Harte Research Institute, Texas A&M University—Corpus Christi, Corpus Christi, TX, United States, [2] Conrad Blucher Institute, Texas A&M University—Corpus Christi, Corpus Christi, TX, United States

Suspended sediment dynamics of Corpus Christi Bay, Texas, USA, a shallow-water wind-driven estuary, were investigated by combining field and satellite measurements of total suspended solids (TSS). An algorithm was developed to transform 500-m Moderate Resolution Imaging Spectroradiometer (MODIS) Aqua satellite reflectance data into estimated TSS values. The algorithm was developed using a reflectance ratio regression of MODIS Band 1 (red) and Band 3 (green) with TSS measurements ($n = 54$) collected by the Texas Commission on Environmental Quality for Corpus Christi Bay and other Texas estuaries. The algorithm was validated by independently collected TSS measurements during the period of 2011–2014 with an uncertainty estimate of 13%. The algorithm was applied to the period of 2002–2014 to create a synoptic time series of TSS for Corpus Christi Bay. Potential drivers of long-term variability in suspended sediment were investigated. Median and IQR composites of suspended sediments were generated for seasonal wind regimes. From this analysis it was determined that long-term, spatial patterns of suspended sediment in the estuary are related to wind-wave resuspension during the predominant northerly and prevalent southeasterly seasonal wind regimes. The impact of dredging is also apparent in long-term patterns of Corpus Christi Bay as concentrations of suspended sediments over dredge spoil disposal sites are higher and more variable than surrounding areas, which is most likely due to their less consolidated sediments and shallower depths requiring less wave energy for sediment resuspension. This study highlights the advantage of how long-synoptic time series of TSS can be used to elucidate the major drivers of suspended sediments in estuaries.

Keywords: suspended sediments, MODIS, wind-driven estuary, wind-wave resuspension, Corpus Christi Bay, dredging influence

OPEN ACCESS

Edited by:
Steven G. Ackleson, United States Naval Research Laboratory, United States

Reviewed by:
Matthew Lewis, Bangor University, United Kingdom
Sachidananda Mishtra, National Oceanic and Atmospheric Administration (NOAA), United States

***Correspondence:**
Anthony Reisinger
anthony.reisinger@gmail.com
James C. Gibeaut
james.gibeaut@tamucc.edu

Specialty section:
This article was submitted to Coastal Ocean Processes, a section of the journal Frontiers in Marine Science

Received: *22 February 2017*
Accepted: *10 July 2017*
Published: *20 December 2017*

Citation:
Reisinger A, Gibeaut JC and Tissot PE (2017) Estuarine Suspended Sediment Dynamics: Observations Derived from over a Decade of Satellite Data. Front. Mar. Sci. 4:233. doi: 10.3389/fmars.2017.00233

INTRODUCTION

Estuaries are highly dynamic environments. They exist in transitional zones where riverine systems combine with oceanic systems and exhibit characteristics of both, such as floods and droughts as well as tides and waves. Suspended sediments are an integral part of estuarine systems; their flux within estuaries is a result of interplay between freshwater inflow, tidal currents, wind-wave resuspension, commercial fishing, and dredging operations (Ward and Montague, 1996). The relative importance of physical processes influencing the spatial distributions of suspended sediments varies as a function of time and space, morphology, bathymetry, and regional climate, however, the influence of anthropogenic activities is largely unknown (Ward and Montague, 1996; Green and Coco, 2014).

Most US state and federal agencies use a few point measurements within estuarine systems to characterize overall conditions. Typically, suspended sediment concentrations have been quantified by collecting water samples from discrete locations within an estuary and measuring their total suspended solids (TSS) concentrations (Ward and Montague, 1996). For temporal studies, the sampling is repeated at the same station over time, thus providing insight into the processes ongoing in the area (Shideler, 1984). The spatial resolution of this approach, however, is limited by time and expense thus restricting the number of regularly sampled locations. Conditions observed at a single point, however, can be the result of many complex and interrelated processes. Early attempts to bridge this spatial gap in Texas included eight repeated sample collections at 14 locations within 5 h, in Corpus Christi Bay using a helicopter (Shideler, 1984). Shideler's study produced some of the first quasi-synoptic measurements of suspended sediments in this region and documented the dominant spatial patterns of suspended sediment distributions including the bay's response to wind-wave resuspension from prevalent northerlies associated with frontal passage and predominant southeasterlies. While these measurements provided much-improved coverage, their relatively limited spatial and temporal resolutions and their fair-weather bias created impediments when trying to characterize the complexity and heterogeneity of the Corpus Christi Bay estuarine system.

A major advance in the monitoring of suspended sediments came when Stumpf and Pennock (1989) discovered that weather satellites were able to quantify suspended sediments in the Chesapeake and Delaware Bays. Satellite remote sensing has increasingly provided synoptic views of suspended sediment dynamics leading to some of the first Environmental Data Records (EDR) of suspended sediments acquired daily and spanning decades (Stumpf and Pennock, 1989; Ruhl et al., 2001). More recently, satellites have been used to monitor suspended sediment and other water quality parameters such as chlorophyll-a (CHL-α) and colored dissolved organic matter (CDOM) (Matthews, 2011). While most of this research based on satellite imagery has focused on oceanic areas (McClain, 2009), there is now much interest in studying suspended sediments in estuaries and coastal areas (Miller and McKee, 2004; D'sa and Miller, 2005; Zawada et al., 2007; Doxaran et al., 2009; Chen et al., 2010; Petus et al., 2010; Feng et al., 2014).

This study was conducted to gain a better understanding of estuarine sedimentary processes in Texas estuaries using satellite-derived TSS data by taking advantage of the spatial and temporal resolution data provided by the MODIS-Aqua almost-daily 500-m data. These measurements allow for the identification of prevalent and predominant controls that force the distribution of estuarine suspended sediments in shallow-water estuaries. The study starts with the development and assessment of an inversion algorithm to create an EDR of suspended sediment. The algorithm is calibrated by comparing MODIS-Aqua satellite reflectance data with a long term data set of TSS collected by the Texas Commission on Environmental Quality (TCEQ) in Texas estuaries. The algorithm is then validated using independent *in situ* measurements collected by Paudel and Montagna (2014). The study area and *in situ* measurement locations are illustrated in **Figure 1**. The 12-year EDR is analyzed for a case study in Corpus Christi Bay. For this analysis, seasonal patterns of suspended sediment are identified as well as their main forcings. The influence of dredging is also considered.

STUDY AREA

Climate and Sedimentary Processes

Numerous shallow-water estuaries are found along the Texas coast (see **Figure 1**). These estuaries are drowned river valleys that formed during the Holocene after the last sea-level low stand. They are separated from the Gulf of Mexico by a thin chain of barrier islands and spits that span the length of the Texas Coast (Davis and FitzGerald, 2004; Davis, 2011). Small tidal inlets, the majority of which are jettied and dredged, connect the estuaries to the Gulf. These estuaries are in a microtidal (0.6 m Gulf and less than 0.3 m estuary tidal range), wave-dominated mixed energy coastal setting, and are affected by a climatic gradient with wetter conditions to the north and drier to the south (McKee and Baskaran, 1999; Davis, 2011; Montagna et al., 2011). For all bays, marine sediment input is thought to be relatively small due to the microtidal setting (Yeager et al., 2006). The bottom sediments and those in suspension mostly consist of fine-grained silt and clay (McKee and Baskaran, 1999). Average grain size for Texas bays range from 2.3 to 8 phi (Folger, 1972). For Corpus Christi Bay, the predominant bay bottom sediments range in grain size from 4.0 to 8.0 phi (Shideler, 1984). Average depths in Texas estuaries range from 2 to 4 m.

This case study focuses on the suspended sediment dynamics of Corpus Christi Bay (**Figure 2**). Corpus Christi Bay is about 284 km^2 and the deepest of the Texas bays with an average depth of 4 m (McKee and Baskaran, 1999). This estuary was chosen for comparison with a previous study by Shideler (1984). Relatively little freshwater enters this estuary from the Nueces River and Oso Creek. Low amounts of freshwater inflows coupled with high rates of evaporation cause the estuary to become hyper-saline for much of the year (Montagna et al., 2012).

Wind along the Texas coast is prevalently from the southeast for the majority of the year (spring-summer) complemented by predominant northerlies (fall-winter). The prevalent southeasterlies are stronger in the south and decrease in speed moving northeastward along the coast. The wind is strongest during spring and progressively decreases in speed during the summer. In contrast, frontal passages, "northers" or winter storms, bring the dominant wind from the north with wind speed often greater than 15 m/s. During these frontal passages, northerly wind gusts are generally preceded by high southerly wind speeds (Ward, 1997). Shideler (1984) showed that wind-waves is the most important forcing of suspended sediments in Corpus Christi Bay.

Dredging and Related Impacts

Substantial modifications have occurred within Texas estuaries through the dredging of deep ship channels. In Corpus Christi Bay, the main channel is 14 m deep, spans the length of the estuary in an east-west direction and is maintained for

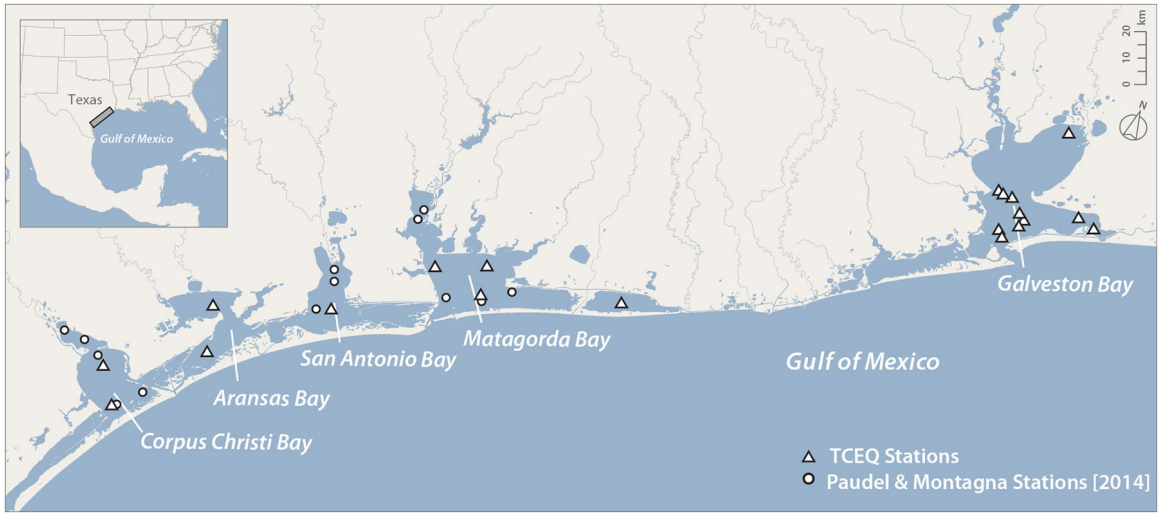

FIGURE 1 | Texas estuaries and *in situ* data collection sites of the TCEQ and Paudel and Montagna (2014).

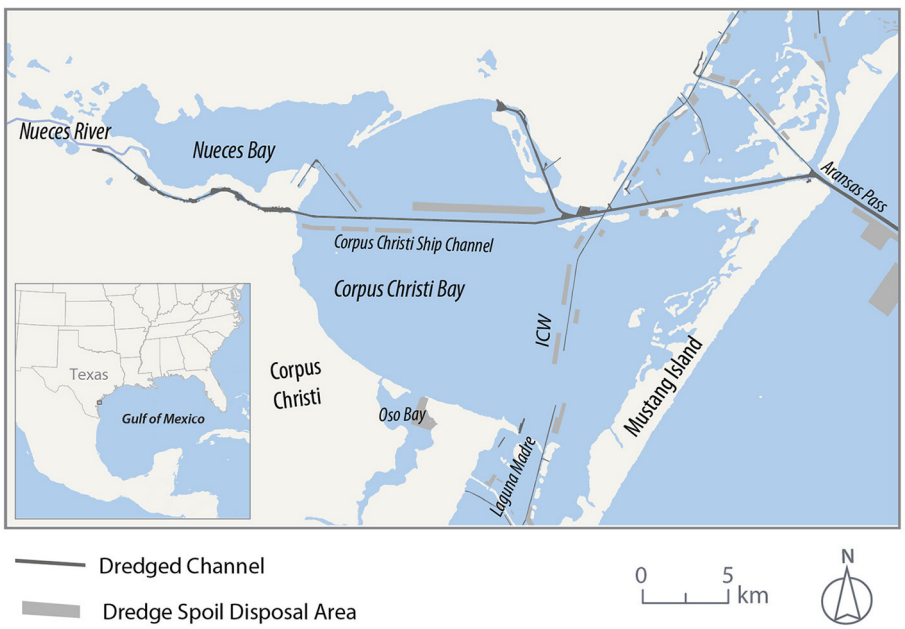

FIGURE 2 | Detailed map of Corpus Christi Bay.

navigation (Kraus, 2007). Other shallower dredged channels are scattered throughout these estuarine systems (**Figure 2**). In Corpus Christi Bay, the Intracoastal Waterway (ICW) bisects the eastern portion of the bay. Sediment from routine dredging for channel maintenance are placed in subaqueous disposal areas next to navigation channels. While active dredging operations suspend large amounts of sediment, the materials are typically contained in boomed-off areas resulting in small impacted areas relative to the size of the estuary. Dredging operations are conducted over short periods of time for up to a few months. A lasting effect of dredging, however, is the alteration of the Bay bathymetry through the creation of subaqueous disposal areas. Sediments of placement areas may have a higher propensity to be suspended by wind-wave action as less wave energy is needed to suspend these materials due to their shallower depth relative to the rest of the bay.

DATASETS

The main data sets for this study consisted of two *in situ* data sets for the calibration and independent validation of the algorithm and MODIS satellite imagery processed to remove sun glint. The

in situ suspended sediment data used to calibrate the study's model for transforming MODIS imagery to TSS was collected by the TCEQ. The TCEQ catalogs its surface water samples in the Surface Water Quality Monitoring Information System (SWQMIS) (Texas Commission on Environmental Quality, 2008). TCEQ *in situ* measurements are collected following the Total Suspended Solid (TSS) EPA STORET Standard Method 2450b. This measurement involves taking a volume of water from a point within an estuary and passing it through a pre-weighed glass fiber filter. The filter is then dried and weighed with the mass of the sample divided by the volume of water filtered, normally denoted in mg/l. These measurements are typically made quarterly, however, some sites in the dataset are sampled sporadically for special projects. Data were extracted from the SWQMIS (Texas Commission on Environmental Quality, 2008) for the period spanning 2002–2010. For this analysis, only TSS data collected from the primary and secondary bays (**Figure 1**) were used. If coincident sampling of CHL-α was present, this too was extracted. To avoid mixed land-water pixels in the MODIS data, TCEQ data were omitted if stations were within a kilometer of the shoreline. Measurements were also removed if they were located within or near Sabine Lake and any points south of Corpus Christi Bay. Sabine Lake data were removed because the CDOM-rich water coming from the Neches River may bias the optical signal. Areas south of Corpus Christi Bay were left out of the input dataset because the area is relatively shallow, and the possibility for bottom reflectance contaminating the TSS signal is high. As a result, a total of 704 *in-situ* samples were selected for inputs for model development.

Overflights from the polar-orbiting satellite Aqua carrying National Aeronautics and Space Administration's (NASA)'s Moderate-Resolution Imaging Spectroradiometer (MODIS) provide almost-daily images of estuaries and coastal areas. The MODIS sensor onboard NASA's Aqua satellite has been in orbit since 2002. MODIS was designed with 36 spectral channels to support observations of oceans, land, and clouds (McClain, 2009). There are nine 1-km bands designed for ocean color observations in the visible to near-infrared (NIR) (412–816 nm) portion of the electromagnetic spectrum. Over turbid waters of inland and coastal areas, however, the dynamic range of the sensor can be exceeded, leaving the actual signal to be unknown (Franz et al., 2006). Many researchers are now using the land/cloud bands to quantify suspended sediment concentrations in coastal waters (Matthews, 2011). The land (1 and 2) and cloud bands (3–9) have spatial resolutions of 250 and 500 m, respectively. These land/cloud bands are less sensitive than the 1-km ocean color bands, have broader dynamic ranges and do not suffer from the problems of the l-km resolution ocean color bands (Franz et al., 2006). Band 1 is optimal for detecting suspended sediment due to high reflectance from sediment in the water column around the red portion of the spectrum centered at 645 nm. Using the red portion of the spectrum, quantifying suspended sediments has little impact from phytoplankton pigments, such as CHL-α, in low concentrations (Bukata, 1995). Recently, MODIS land bands have been used to quantify suspended sediments in coastal estuaries with 250 and 500-m MODIS data (Doxaran et al., 2009; Feng et al., 2014).

The 500-m MODIS-Aqua Surface-Reflectance Product (MYD09GA) was chosen for use in this study because it includes atmospherically corrected bands 1–4, red, near infrared blue, and green, mostly used for ocean color applications and a cloud detection flag. The MYD09GA product is generated from MODIS Level 1B for land bands 1–7 and are estimates of surface spectral reflectance corrected for both atmospheric scattering and absorption (Vermote and Kotchenova, 2008). Doxaran et al. (2009) used the MYD09 and its counterpart MOD09 to quantify suspended sediments accurately in the Gironde estuary, France. Doxaran et al. (2009) developed an algorithm using a remote sensing reflectance (*Rrs*) ratio of Bands 1 and 2, red and near-infrared, respectively. In their study, they found that the atmospheric correction used by the land data community was sufficient to quantify suspended sediment concentration ranging from 77 to 2,182 g/m^3. The combination of high spatial resolution, daily-repeat time, and a greater than 12-year data period, makes these land products ideal for creating an EDR of suspended sediments in estuaries and coastal water bodies.

Wind speed and direction data were extracted from the National Center for Environmental Prediction (NCEP) North American Regional Reanalysis model (NARR) (Mesinger et al., 2006). These data were used for creation of the wind roses and the implementation of the sun glint algorithm. Over water, significant areas of remotely-sensed satellite imagery can be contaminated with sun glint, a disk-like spot that has higher reflectance values than the surrounding area in the satellite imagery. Fresnel reflection causes sun glint and its magnitude is dependent on a combination of complex interactions of surface roughness of the water that is influenced by wind speed and direction, and solar and sensor viewing geometries (Zhang and Wang, 2010). MODIS data are routinely contaminated by sun glint because the satellite does not have a glint tilting avoidance strategy (Wang and Bailey, 2001). The MYD09GA data product does not include a glint coefficient because its use is for land applications; thus, *Rrs* data over water is sometimes contaminated by sun glint. We, therefore, implemented the sun glint algorithm created by Wang and Bailey (2001). Use of this algorithm allowed for the removal of contaminated *Rrs* data from inputs into algorithm development and the removal of contaminated data in the TSS EDR created for this study. Wind speed data were extracted from the NCEP NARR (Mesinger et al., 2006) for the locations and time of the MODIS image capture for input into the sun glint algorithm.

An independent dataset collected by Paudel and Montagna (2014) was used to validate the final TSS algorithm. These data were collected in Matagorda, San Antonio, and Corpus Christi Bays, and follow the same methods as the TCEQ SWQMIS. Sampling sites are spread over these estuaries and provide quarterly sampling from 2011 to 2013. In total, there were 137 cloud free data points that were available prior to sunglint filtering. Surface water samples for TSS and CHL-α were collected for every *in situ* location. Use of this independent dataset gave an impartial assessment of the final algorithm's accuracy and illustrated its robustness.

METHODS

Model Development for Transforming *Rrs* to TSS

The TSS reflectance model was developed using *in situ* and remote sensing reflectance data derived from the MYD09GA data product. These data products were downloaded using NASA's Reverb data discovery tool (http://reverb.echo.nasa.gov/) for each day data were available in the SQWMIS database. From the 709 *in-situ* samples, a total of 294 unique days of satellite data were available. Satellite data collected from Reverb spanned from 8-13-2002 to thru 5-3-2010. NASA's SeaDAS 7.0.1 software was used to extract atmospherically corrected reflectance, viewing geometries, and flags from MYD09GA files over the SWQMIS collection sites when concurrent collections were within 4 h of the overflight of the satellite. Atmospherically corrected reflectance data were then multiplied by pi to derive *Rrs* data.

After data extraction was complete, MYD09GA data were combined with SQWMIS *in situ* data. To avoid the influence of bottom reflectance and algal absorption on *Rrs* data, individual TSS measurements were removed from the calibration data if (1) the collection depth was <3 m unless TSS values were greater than 50 mg/l, and (2) the sample's CHL-α values were greater than 30 mg/l following suggestions from Bukata (1995). To avoid sun glint and other interference, data were removed if (1) it was flagged as cloud reflectance in the MYD09 dataset, (2) sun glint coefficient was >0.001 (Wang and Bailey, 2001), and (3) sensor zenith angles were greater than or equal to 60 degrees. After these data had been filtered, 55 of the 704 data points remained for the development of the TSS model with TSS values ranging from 4 to 178 mg/l.

Spearman rank correlation coefficients were generated from *Rrs* Bands 1–4 and combinations of *Rrs* ratios between TSS to determine the best candidates for inputs into the model. Spearman correlation was used because it is less influenced by outliers and can show non-linear relationships among data (Wilks, 2011). Using the first three highest ranked correlation coefficients, linear and exponential regression models were fit to satellite and TSS data. Finally, the MYD09GA data over the *in situ* sites of Paudel and Montagna (2014) were extracted. The dataset was filtered following the same procedure as the calibration dataset with the difference that high CHL-α samples were not removed. This step was omitted as only one data point would have been excluded, and this portion of the data is used for validation only. The high CHL-α content collected in this sample shows how the algorithm is influenced in algal bloom conditions. After filtering had been applied to the validation set, 35 of the 137 data points were left in this validation dataset. The models' fit to the calibration dataset was quantified using the Root Mean Squared Error (RMSE) and the R-squared metrics. The validation dataset was used to quantify the Mean Absolute Error (MAE) and mean bias of the model.

TSS Time Series Development

The TSS reflectance model with the best performance was then applied to all available scenes of the MYD09GA land product over the study areas. These data were downloaded from https://lpdaac.usgs.gov/ and totaled 4,503 analyzed scenes for this study. Each image was then filtered for clouds, sun glint, and satellite geometries following the methodologies mentioned above, and daily cloud-free TSS maps were created at 500-m resolution. There was a maximum of 1,444 scenes of cloud free, glint free, and geometrically compatible imagery, however, on a pixel-by-pixel basis, this number varied due to the cloud mask and on average there were 1,226 scenes available for Corpus Christi Bay. Both individual scenes and composites were produced to show suspended sediment patterns in the estuaries (see **Figure 5**). Composite images were generated by computing medians and interquartile ranges (IQR) of satellite-derived TSS data for the entirety of the valid scenes of the satellite dataset. Seasonal comparisons were generated for Corpus Christi Bay for wind patterns to highlight the respective temporal variability, and show the different distributions and patterns of TSS for the different time periods. Here satellite data within 1 km of land are removed to avoid mixed pixels of land and water. Also, to avoid data contamination from bottom reflectance, any data occurring in water shallower than 1 m was removed.

Seasonal Wind Analysis

To investigate wind-wave resuspension, wind speed data at 10 m height for the study period were extracted from the NCEP NARR model (Mesinger et al., 2006) over Corpus Christi Bay. The NARR's 32-km spatial and 3-h temporal resolutions were considered sufficient for this analysis. Wind data were analyzed to determine seasonal patterns. Data were split into seasonal wind regimes, and wind roses were plotted and compared to TSS composites for each regime. The period of November—February is characterized by frontal passages and dominant northerly winds and is referred to as the frontal passages period. The March–June period is characterized by weaker fronts at the beginning of the period and prevalent southeasterlies, and is referred to as the southeasterly period. The last period of July–October is also characterized by prevalent southeasterlies, however, their magnitude is lower when compared to the southeasterly period and referred to as the quiet period (quiet period). Wind data were then plotted as wind roses for each regime. Composites of satellite-derived TSS patterns are compared to the related wind rose plots for the three identified wind regimes in **Figure 6** to determine if the wind speed and directional component influences the sediment distributions in the estuary.

RESULTS AND DISCUSSION

TSS Model Results and Discussion

Spearman rank correlations identified the highest correlations between individual bands and band ratios with the TSS data collected by the TCEQ. The correlation analysis found that *Rrs 645, Rrs 645*/*Rrs 555*, and *Rrs 645*/*Rrs 469* had the highest correlations with TSS, at 0.65, 0.79, and 0.63, respectively. These radiometric values were then fit to derive TSS using linear and exponential models. In total there were six models tested three linear and three exponential (**Table 1**). A comparison of the empirical models tested to derive TSS from *Rrs* and *Rrs* ratios are

TABLE 1 | Model fit statistics for calibration dataset and validation dataset error metrics for linear and exponential models for estimating TSS from *Rrs* and *Rrs* band ratios.

Fit type	Band input	Calibration data		Validation data	
		R-square	RMSE	MAE	Mean bias
Exponential	*Rrs 645/Rrs 469*	0.46	27.06	22.74	−18.39
Exponential	*Rrs 645*	0.19	33.13	258.56	240.20
Exponential	*Rrs 645/Rrs 555*	0.81	16.06	17.52	−13.40
Linear	*Rrs 645/Rrs 469*	0.45	27.22	24.63	−19.64
Linear	*Rrs 645*	0.28	31.15	43.22	24.03
Linear	*Rrs 645/Rrs 555*	0.70	20.26	18.06	−9.63

presented in **Table 1** along with their fit statistics. The model with lowest MAE of validation dataset was selected to create the TSS EDR. As indicated in **Table 1**, the best model was an exponential function using the band reflectance ratio of *Rrs 645/ Rrs 555*. The equation for this algorithm is:

$$y = a^* e^{b*x} \quad (1)$$

Where y is the estimate for TSS in mg/l and x is the *Rrs 645/Rrs 555* reflectance ratio from the MYD09GA dataset. Coefficients a and b and their 95% confidence intervals were 1.696 (0.703, 2.689) and 3.562 (3.030, 4.094), respectively. The model fits quite well to the data with an R-square of 0.81 and RMSE of 16.1 ($n = 55$) for the TCEQ calibration data (**Figure 3**). The MAE for the validation dataset is 17.52 ($n = 35$) with a mean bias of −13.40. Model fit to the data is illustrated in **Figure 3**. The uncertainty in this model is estimated to be 13% according to the RMSE compared to the range of the calibrated data. It is interesting to note that the model underestimates 66% of the validation dataset, however, these values still fall with the 95% confidence interval of the model fit. While exact cause of the bias is unknown, potential reasons for the bias include radiometer drift and slight differences in TSS processing. The model was fit to data spanning 2003 to 2010 and validation data was collected from 2011 to 2013, a drift in the satellite radiometer could account for this difference. Slight differences in the TSS sampling methods may also account for the differences.

In order to gain more confidence in this model high concentration TSS measurements are needed in both the calibration and validation dataset to achieve a more robust quantification of error. While this model performs well over a range of TSS values in several Texas estuaries, more validation data is needed to quantify the true error of the model. Individual models tuned for individual estuaries may reduce the error using the same method, but this was not possible due to an insufficient number of *in situ* data points within each estuary.

Usage of this algorithm for deriving TSS from *Rrs* will cause over- and under-estimations of TSS in high concentrations of CDOM and CHL-α, respectively. An example is included in the validation data set where a high concentrations of CHL-α causes the algorithm to underestimate the true concentration of sediment in the water (**Figure 3**). The TSS value of 133.7 mg/l in the validation data set occurred during an algal bloom with

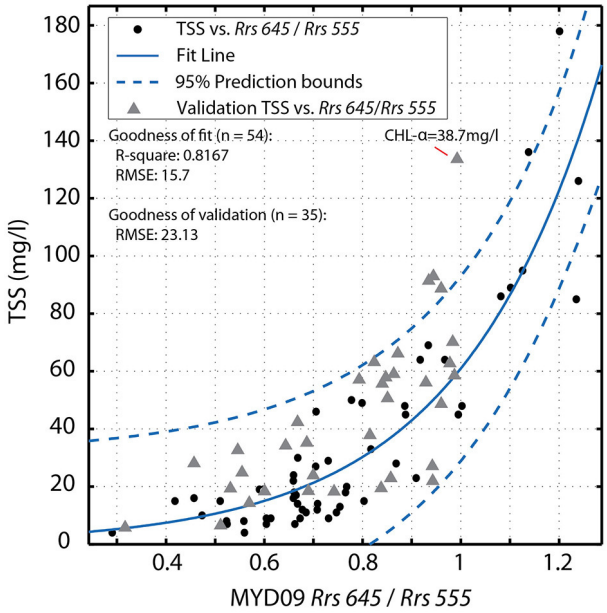

FIGURE 3 | Model produced by Equation 1 for the estimation of TSS from MYD09 reflectance with *in situ* data collected by TCEQ (black circles) and validation dataset (gray triangles) collected by Paudel and Montagna (2014).

a CHL-α density of 38.4 mg/l. For this case, the modeled TSS was 59.8 mg/l, which underestimates the actual measurement by 73.9 mg/l. While this is a large error, algal blooms in these estuarine waters are infrequent events. To further illustrate CHL-α influence on the model a sensitivity analysis was conducted on CHL-α vs. modeled TSS residuals for both the calibration and validation datasets (**Figure 4**). We found no systematic influence of CHL-α on predicted TSS values, except for the aforementioned high concentration sample of CHL-α. For the majority of the year, the suspended sediments in these Texas estuaries are mostly composed of suspended inorganic particles (McKee and Baskaran, 1999). Thus, the influence of algal blooms will only impact the EDR created from this algorithm for a small percentage of the time allowing for analysis of suspended sediment dynamics in Texas estuaries. The influence of CDOM on the algorithm could not be quantified because neither TCEQ nor Paudel and Montagna (2014) collected such measurements. With these limitations, this algorithm shows promise in creating a TSS EDR for Texas estuaries.

Development of this model enables the creation of synoptic suspended sediment maps in Texas estuaries. **Figure 5** compares a MODIS-Aqua true color image with estimated TSS concentrations for the same scene, the Texas estuaries and coast, following the passage of a cold front. The largest TSS concentrations along the coast are observed for Galveston Bay and Matagorda Bay.

TSS Patterns and Forcings for Corpus Christi Bay

TSS composites and wind roses for Corpus Christi Bay are presented in **Figure 6**. During the frontal passages period,

median, and IQR TSS are higher in the southern portion of the estuary, windward of the predominant north-northeast wind direction. Median TSS and IQR values increase as the fetch lengths increase. The similar patterns of both IQR and median TSS with values increasing with fetch length and highest on the windward side of the estuary suggest that wind-wave resuspension from frontal passages is the dominant process controlling suspended sediment concentrations during this period. These patterns are similar to those reported by Shideler (1984) during the same wind regime. TSS median values are the lowest during this period when compared to other wind regimes in this estuary, possibly resulting from the combination of low wind speeds between frontal passages and a relatively low frequency of such events. The majority of wind speeds during this period are <7.5 m/s (**Figure 6**) while there are typically 10 frontal passages during the frontal passages period (Ward, 1997). Low wind speeds between frontal passages are likely not significant enough to generate waves that impart sufficient bed shear stress for resuspension as the bay is 4 m deep on average, the deepest along the Texas coast. Another area that exhibits a behavior similar to the southern portion of the estuary during the same period are the dredge spoil deposition sites along the ICW (**Figure 6**). Elevated median TSS and higher IQR values compared to the rest of the bay occur at these locations. Yet these areas fetch lengths are considerably smaller in the direction of the prevalent wind. These areas have more unconsolidated dredged sediments and are shallower than the rest of the estuary thus sediments are more readily suspended.

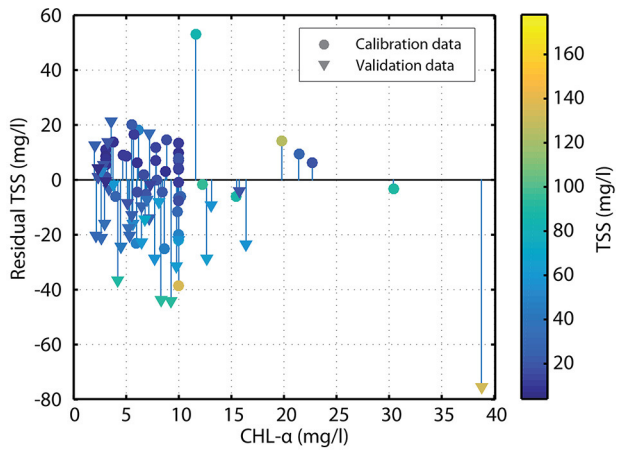

FIGURE 4 | Residual TSS from TSS model plotted against CHL-a sampled concurrently for both the calibration (triangles) and validation dataset (circles). Calibration and validation datasets are colored based on in situ TSS-values.

Another factor that may influence the measured patterns is bias due to cloud presence (Eleveld et al., 2014). Higher wind periods may be under represented compared to the actual resuspension events that occur because the majority of cold fronts are accompanied by cloud-cover that obscures the satellites view of the estuary. The frontal passages period composites of Corpus Christi Bay support Shideler's (1984) hypothesis that Nueces Bay is a fluvial sediment storage basin having a control valve activated by strong northerly wind. Suspended sediments are released into Corpus Christi Bay during frontal passages as indicated by the higher median and IQR TSS values near the entrance to Nueces Bay. These higher TSS values compared to those of the surrounding area are consistent with suspended sediments spilling into Corpus Christi Bay when strong wind is blowing for a prolonged period from the north.

The influence of tides is more difficult to identify using the composite patterns, however, some observations can be made. Lower IQR values are observed along the length of the Corpus Christi Ship Channel (**Figure 6**). Additionally, median and IQR values are lower than surrounding values at the entrance of the Corpus Christi Ship Channel into the main portion of the bay. Both observations are consistent with flood plumes that are

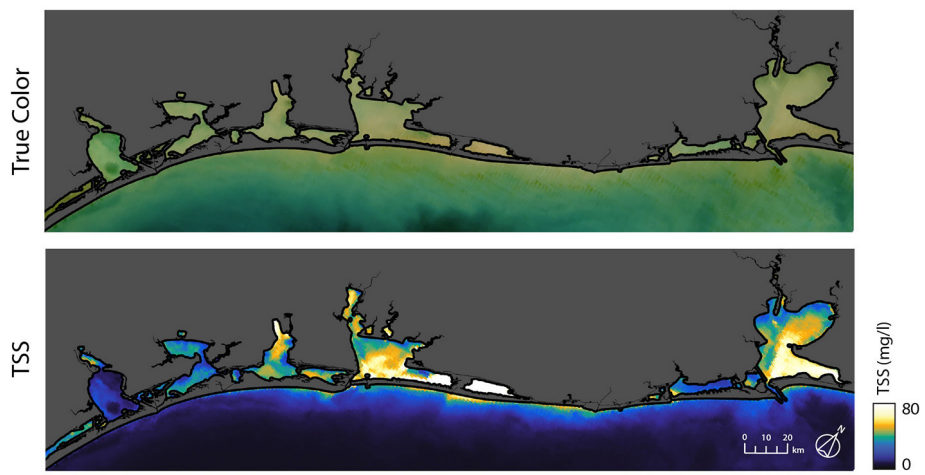

FIGURE 5 | MODIS-Aqua 500-m True Color RGB image and example of output from TSS algorithm for same scene following the passage of a cold front on January 10th 2006.

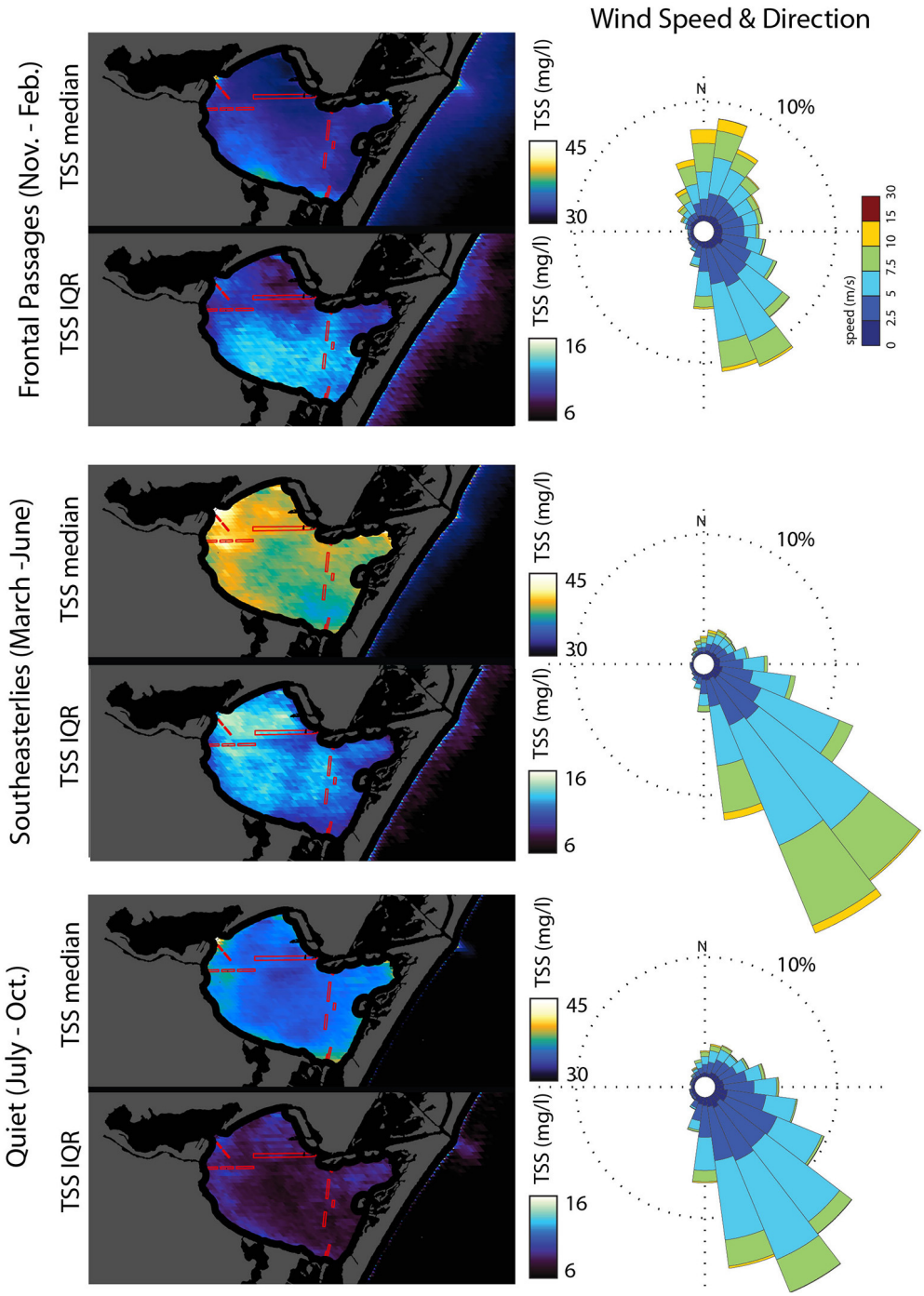

FIGURE 6 | Corpus Christi Bay TSS Median and IQR with corresponding wind rose for each wind regime. Red rectangular polygons are dredge spoil deposition sites.

lower in suspended sediment concentration originating in the Gulf of Mexico. These lower values indicate that, for Corpus Christi Bay, inflow of Gulf waters reduces the concentration of sediment within and surrounding the ship channel but not for the bay at large. Export of suspended sediments from the Bay to the Gulf of Mexico is evident from an ebb plume at the exit of the ship channel into the Gulf of Mexico for all wind regimes with the largest plumes observed for the frontal passages period (**Figure 6**). Higher TSS concentrations are observed along the shorelines of the Gulf of Mexico for the frontal passages period as compared to the other wind regimes consistent with strong offshore northerly winds often accompanying frontal passages. It is hypothesized that wave action generated by the southerly winds preceding frontal passages results in resuspension of nearshore

sediments and that offshore northerly winds then transport the suspended sediments further offshore.

The southeasterly period has the highest concentrations of median and IQR TSS values. Similar to the frontal passages period, both Median and IQR TSS values increase along fetch length in the dominant wind direction. Highest median and IQR TSS values are located along and near the windward shore in the northwestern quadrant of Corpus Christi Bay. This area is where the predominant and prevalent wind of this wind regime has the longest fetch lengths, ∼18 km. Similarly to the frontal passages period, this pattern indicates that wind-wave resuspension is the dominant process influencing estuarine suspended sediment distribution during this period. The median TSS composite resembles the pattern in Shideler's (1984) southeasterly mode. Similar to Shideler's (1984) observations, the southeastern quadrant of Corpus Christi Bay has very low concentrations of TSS. These low TSS concentrations are attributed to a flux of sediment free waters from the Upper Laguna Madre being pushed into the southern portion of Corpus Christi Bay by the southeasterly wind.

Dredge spoil placement sites exhibit similar behavior to those during the frontal passages period. The dredge spoil area located on the ICW has higher median and IQR TSS values than the surrounding area (**Figure 6**). These higher values during both the frontal passages period and southeasterly period illustrate that these areas are more prone to wind-wave resuspension. The dredge spoil site next to the entrance of the port of Corpus Christi also has higher median and IQR values than those of the surrounding area.

During the quiet period (**Figure 6**), the Corpus Christi Bay median and IQR values are relatively uniform. Areas near and along the windward shore have slightly elevated values when compared to the rest of Corpus Christi Bay. The low concentrations of median and IQR TSS values are compatible with a wave dominated TSS with less sediment than during any of the other time periods. The IQR pattern also displays the lowest values indicating consistently low TSS concentrations during the quiet period. The highest concentrations of median TSS values are located over the dredge spoil deposition area near the Port of Corpus Christi similar to during the southeasterly period.

Potential Limitations of the Study

It is important to note that the seasonal median TSS composites may be biased by cloud presence obscuring satellite view of estuaries and thus providing lower representation of scenes associated with frontal passages, southeasterlies, sea breeze, and thunderstorms. While these biases likely influence total estimated suspended sediment concentrations, the overall seasonal changes in resuspended sediment concentration patterns are unlikely to be substantially affected by these biases and are still clearly identifiable permitting assessment of the importance of the respective forcing mechanisms.

Another potential limitation of this study is the influence that CDOM and high CHL-α have on the reflectance ratio algorithm. Areas with high CDOM concentrations cause overestimates of TSS concentrations while areas of high CHL-α cause underestimates of TSS concentrations. This bias is believed to be minimal for Corpus Christi Bay.

CONCLUSIONS

A TSS algorithm was created to quantify suspended sediment in estuaries of the Texas Coast based on MODIS reflectance data and a comparison with two *in situ* data sets collected in the study area during the period 2002–2014. The algorithm includes filtering of the data for geometries, sun glint, and water depth, and an exponential function that gives the best fit for TSS concentrations ranging from 4 to 176 mg/l. After calibration based on a long-term TCEQ data set, the algorithm was further validated with an independent data set, acquired outside of the model's calibration period. However, we did find that the algorithm does not provide accurate results for cases with CHL-α values greater than 30 mg/l. Future users of the model and TSS EDR generated for this study should be aware of this and other limitations of the method.

The model was applied to create an EDR of suspended sediments for Corpus Christi Bay. Analysis of the EDR reveals that the bay is influenced by wind-wave resuspension with different patterns during the predominant northerlies and prevalent southeasterlies seasons. The impact of dredging is apparent in long-term TSS patterns as concentrations of suspended sediments over dredge spoil disposal sites are higher and more variable than surrounding areas, which is most likely due to their less consolidated nature and shallower depths requiring less wave energy for sediment resuspension. This study highlights the advantage of how long-synoptic time series of TSS can be used to elucidate the major drivers of suspended sediments in estuaries.

AUTHOR CONTRIBUTIONS

AR wrote the article, collected field data, developed algorithm, and performed analysis. PT aided in algorithm development, analysis of data, and writing of article. JG aided in algorithm development, analysis of data, and editing of text.

FUNDING

This study was supported by grant number NA09NMF4720179 from the National Oceanic and Atmospheric Administration under the Comparative Assessment of Marine Ecosystem (CAMEO) program, and National Aeronautics and Space Administration Headquarters under the NASA Earth and Space Science Fellowship Program—Grant NNX12AO09H. Partial support was also provided by the Harte Research Institute for Gulf of Mexico Studies at Texas A&M University-Corpus Christi. The funders had no role in study design, data collection and analysis, decision to publish, or preparation of the manuscript.

ACKNOWLEDGMENTS

The authors would like to thank the reviewers, Sachidananda Mishtra and Matthew Lewis for their helpful and constructive comments that greatly contributed to improving the final version of the paper.

REFERENCES

Bukata, R. P. (ed.) (1995). *Optical Properties and Remote Sensing of Inland and Coastal Waters*. Boca Raton, FL: CRC Press.

Chen, Z., Hu, C., Muller-Karger, F. E., and Luther, M. E. (2010). Short-term variability of suspended sediment and phytoplankton in Tampa Bay, Florida: observations from a coastal oceanographic tower and ocean color satellites. *Estuar. Coast. Shelf Sci.* 89, 62–72. doi: 10.1016/j.ecss.2010.05.014

D'sa, E. J., and Miller, R. L. (2005). "Bio-optical properties of coastal waters," in *Remote Sensing of Coastal Aquatic Environments*, eds R. L. Miller, C. E. Del Castillo, and B. A. Mckee (Dordrecht: Springer), 129–155.

Davis, R. A. (2011). *Sea-Level Change in the Gulf of Mexico*. College Station: Texas A&M University Press.

Davis, R. A., and FitzGerald, D. M. (2004). *Beaches and Coasts*. Oxford: Blackwell Publ.

Doxaran, D., Froidefond, J. M., Castaing, P., and Babin, M. (2009). Dynamics of the turbidity maximum zone in a macrotidal estuary (the Gironde, France): observations from field and MODIS satellite data. *Estuar. Coast. Shelf Sci.* 81, 321–332. doi: 10.1016/j.ecss.2008.11.013

Eleveld, M. A., van der Wal, D., and van Kessel, T. (2014). Estuarine suspended particulate matter concentrations from sun-synchronous satellite remote sensing: tidal and meteorological effects and biases. *Remote Sens. Environ.* 143, 204–215. doi: 10.1016/j.rse.2013.12.019

Feng, L., Hu, C., Chen, X., and Song, Q. (2014). Influence of the three Gorges Dam on total suspended matters in the Yangtze Estuary and its adjacent coastal waters: observations from MODIS. *Remote Sens. Environ.* 140, 779–788. doi: 10.1016/j.rse.2013.10.002

Folger, D. W. (1972). *Characteristics of Estuarine Sediments of the United States*. U.S. Govt. Print. Off. Available online at: https://pubs.er.usgs.gov/publication/pp742742 (Accessed November 20, 2016).

Franz, B. A., Werdell, P. J., Meister, G., Kwiatkowska, E. J., Bailey, S. W., Ahmad, Z., et al. (2006). "MODIS land bands for ocean remote sensing applications," in *Proceedings of Ocean Optics XVIII* (Montreal, QB).

Green, M. O., and Coco, G. (2014). Review of wave-driven sediment resuspension and transport in estuaries. *Rev. Geophys.* 52, 77–117. doi: 10.1002/2013RG000437

Kraus, N. C. (2007). "Coastal inlets of Texas, USA," in *Coastal Sediments'07*, eds N. C. Kraus and J. D. Rosanti (Reston, VA: American Society of Civil Engineers), 1475–1488.

Matthews, M. W. (2011). A current review of empirical procedures of remote sensing in inland and near-coastal transitional waters. *Int. J. Remote Sens.* 32, 6855–6899. doi: 10.1080/01431161.2010.512947

McClain, C. R. (2009). A decade of satellite ocean color observations*. *Annu. Rev. Mar. Sci.* 1, 19–42. doi: 10.1146/annurev.marine.010908.163650

McKee, B. A., and Baskaran, M. (1999). "Sedimentary processes of Gulf of Mexico Estuaries," in *Biogeochemistry of Gulf Mexico Estuaries*, eds T. S. Bianchi, J. R. Pennock , and R. R. Twilley (New York, NY: Wiley), 63–85.

Mesinger, F., DiMego, G., Kalnay, E., Mitchell, K., Shafran, P. C., Ebisuzaki, W., et al. (2006). North American regional reanalysis. *Bull. Am. Meteorol. Soc.* 87, 343–360. doi: 10.1175/BAMS-87-3-343

Miller, R. L., and McKee, B. A. (2004). Using MODIS Terra 250 m imagery to map concentrations of total suspended matter in coastal waters. *Remote Sens. Environ.* 93, 259–266. doi: 10.1016/j.rse.2004.07.012

Montagna, P. A., Brenner, J., Gibeaut, J., and Morehead, S. (2011). "Coastal impacts," in *The Impact of Global Warming on Texas*, eds J. Schmandt, J. Clarkson, and G. R. North (Austin: University of Texas Press), 97–123.

Montagna, P., Palmer, T. A., and Pollack, J. (2012). *Hydrological Changes and Estuarine Dynamics*. New York, NY: Springer Science & Business Media.

Paudel, B., and Montagna, P. A. (2014). Modeling inorganic nutrient distributions among hydrologic gradients using multivariate approaches. *Ecol. Inform.* 24, 35–46. doi: 10.1016/j.ecoinf.2014.06.003

Petus, C., Chust, G., Gohin, F., Doxaran, D., Froidefond, J.-M., and Sagarminaga, Y. (2010). Estimating turbidity and total suspended matter in the Adour River plume (South Bay of Biscay) using MODIS 250-m imagery. *Cont. Shelf Res.* 30, 379–392. doi: 10.1016/j.csr.2009.12.007

Ruhl, C. A., Schoellhamer, D. H., Stumpf, R. P., and Lindsay, C. L. (2001). Combined use of remote sensing and continuous monitoring to analyse the variability of suspended-sediment concentrations in San Francisco Bay, California. *Estuar. Coast. Shelf Sci.* 53, 801–812. doi: 10.1006/ecss.2000.0730

Shideler, G. L. (1984). Suspended sediment responses in a wind-dominated estuary of the Texas Gulf Coast. *J. Sediment. Res.* 54, 731–745.

Stumpf, R. P., and Pennock, J. R. (1989). Calibration of a general optical equation for remote sensing of suspended sediments in a moderately turbid estuary. *J. Geophys. Res.* 94:14363. doi: 10.1029/JC094iC10p14363

Texas Commission on Environmental Quality (2008). *TCEQ Surface Water Quality Monitoring Procedures Volume 1: Physical and Chemical Monitoring Methods for Water*, 202.

Vermote, E. F., and Kotchenova, S. Y. (2008). *MOD09 (Surface Reflectance) User's Guide, Version 1.1, March, 2008*. Greenbelt, MD.

Wang, M., and Bailey, S. W. (2001). Correction of sun glint contamination on the SeaWiFS ocean and atmosphere products. *Appl. Opt.* 40, 4790–4798. doi: 10.1364/AO.40.004790

Ward, G. H. (1997). *Processes and Trends of Circulation within the Corpus Christi Bay National Estuary Program Study Area*. Corpus Christi, TX: Corpus Christi Bay National Estuary Program.

Ward, G., and Montague, C. (1996). *Estuaries*. New York, NY: McGraw-Hill Book Company.

Wilks, D. S. (2011). *Statistical Methods in the Atmospheric Sciences*. Oxford: Academic press.

Yeager, K. M., Santschi, P. H., Schindler, K. J., Andres, M. J., and Weaver, E. A. (2006). The relative importance of terrestrial versus marine sediment sources to the Nueces-Corpus Christi Estuary, Texas: an isotopic approach. *Estuar. Coasts* 29, 443–454. doi: 10.1007/BF02784992

Zawada, D. G., Hu, C., Clayton, T., Chen, Z., Brock, J. C., and Muller-Karger, F. E. (2007). Remote sensing of particle backscattering in Chesapeake Bay: a 6-year SeaWiFS retrospective view. *Estuar. Coast. Shelf Sci.* 73, 792–806. doi: 10.1016/j.ecss.2007.03.005

Zhang, H., and Wang, M. (2010). Evaluation of sun glint models using MODIS measurements. *J. Quant. Spectrosc. Radiat. Transf.* 111, 492–506. doi: 10.1016/j.jqsrt.2009.10.001

Conflict of Interest Statement: The authors declare that the research was conducted in the absence of any commercial or financial relationships that could be construed as a potential conflict of interest.

frontiers in Marine Science

PERSPECTIVE
published: 30 January 2018
doi: 10.3389/fmars.2018.00008

AOPs Are Not Additive: On the Biogeo-Optical Modeling of the Diffuse Attenuation Coefficient

Zhongping Lee[1]*, *Shaoling Shang*[2] and *Robert Stavn*[3]

[1] School for the Environment, University of Massachusetts Boston, Boston, MA, United States, [2] State Key Laboratory of Marine Environmental Science, College of Ocean and Earth Sciences, Xiamen University, Xiamen, China, [3] Department of Biology, The University of North Carolina at Greensboro, Greensboro, NC, United States

Commonly we see the diffuse attenuation coefficient of downwelling irradiance (K_d) expressed as a sum of the contributions of various constituents. We show here that, both theoretically and numerically, because K_d is an apparent optical property (AOP), this approach is not consistent with radiative transfer. We further advocate the application of models of K_d developed in past decades that are not only consistent with radiative transfer but also provide more accurate estimates, in particular for coastal turbid waters.

Keywords: solar radiation, apparent optical properties, inherent optical properties, diffuse attenuation coefficient, optical additivity

OPEN ACCESS

Edited by:
Kevin Ross Turpie, University of Maryland, Baltimore County, United States

Reviewed by:
Emmanuel Devred, Fisheries and Oceans Canada, Canada
Knut Barthel, University of Bergen, Norway

***Correspondence:**
Zhongping Lee
zhongping.lee@umb.edu

Specialty section:
This article was submitted to Coastal Ocean Processes, a section of the journal Frontiers in Marine Science

Received: *14 July 2017*
Accepted: *11 January 2018*
Published: *30 January 2018*

Citation:
Lee Z, Shang S and Stavn R (2018) AOPs Are Not Additive: On the Biogeo-Optical Modeling of the Diffuse Attenuation Coefficient. Front. Mar. Sci. 5:8. doi: 10.3389/fmars.2018.00008

BACKGROUND

Solar radiation is the energy source for the entire earth system. In aquatic environments, unlike terrestrial environments, solar radiation can penetrate to great depths to fuel photosynthesis and to heat up the upper layer (Zaneveld et al., 1981; Platt, 1986; Lewis et al., 1990). The propagation of solar radiation from surface to greater depths can be expressed as (Mobley, 1994)

$$E_d(z,\lambda) = E_d(0^-,\lambda)\, e^{-K_d(\lambda)\, z}. \quad (1)$$

Here E_d (W/m^2/nm) is the downwelling irradiance, z (m) is the depth from the surface (0^- for subsurface), K_d (m^{-1}) is the attenuation coefficient of downwelling irradiance between surface and depth z, and λ (nm) for wavelength. Since the variation of $E_d(0^-)$ is independent of water properties (except extremely turbid waters where the enhanced upwelling flux will result in significant contributions to $E_d(0^-)$ due to internal reflection), it is then imperative to describe the variation of K_d for various aquatic environments when quantifying the impact of water constituents on the heat budget (Morel and Antoine, 1994; Ohlmann et al., 2000), the feedback of oceanic systems on climate changes (Rochford et al., 2001; Gnanadesikan and Anderson, 2009), as well as the vertical variation of primary production (Sathyendranath and Platt, 1995).

Historically, with an objective of easy modeling and efficient calculation for large scale applications, K_d is commonly expressed as (Smith and Baker, 1978; Morel, 1988; Morel and Maritorena, 2001),

$$K_d(\lambda) = K_w(\lambda) + K_{bio}(\lambda), \quad (2)$$

with K_w the contribution of pure (sea)water, and K_{bio} the contributions of phytoplankton. In this expression, i.e., the so-called "Case-1" scheme (Morel and Prieur, 1977), the attenuation of pure

(sea)water is considered as a background, while other constituents that are actively changing, such as phytoplankton and suspended mineral solids, are considered as added contributions. In addition, the contributions of colored dissolved organic matter (CDOM) and organic detritus are considered as co-varying with phytoplankton, and lumped into the K_{bio} term. So their contributions are not ignored or omitted as might be implied by the equation, although its application is limited to "Case-1" waters.

In order to explicitly evaluate and understand the impact of constituents such as CDOM and/or suspended mineral particles or particulate inorganic matter (PIM) on the propagation of solar radiation, K_d in many studies is expanded as a sum of more components, although there are subtle variations among these models (Smith and Baker, 1978; Baker and Smith, 1982; Gallegos et al., 1990; Devlin et al., 2009; Kim et al., 2015),

$$K_d(\lambda) = K_w(\lambda) + K_{bio}(\lambda) + K_{CDOM}(\lambda) + K_{PIM}(\lambda). \quad (3)$$

Here K_{CDOM} and K_{PIM} are the diffuse attenuation coefficients resulted from CDOM and PIM, respectively. In essence, these biogeo-optical models of K_d effectively treat K_d, an apparent optical property (AOP) (Preisendorfer, 1976), as an inherent optical property (IOP) (Preisendorfer, 1976), which is not consistent with the definitions and the nature of variations of K_d (Stavn, 1988). The attitude of treating K_d as an IOP might stem from that K_d of "Case 1" water, after correcting for the sun angle effect, can be considered as a "quasi" IOP (Gordon, 1989). However, it was never claimed that this would work in any other water types than "Case 1" water. Many subsequent studies have, for the most part, somehow ignored these limitations in applications.

Fundamentally K_d is sun-angle dependent (Stavn, 1988; Mobley, 1994) (also weakly dependent on atmospheric properties). So, considering the model of Morel and Maritorena (2001), it is specifically stated that the model and the empirical coefficients (Equation 3 in Morel and Maritorena, 2001) are *valid just for low zenith sun angles*. But this restriction has in fact largely been ignored by the research community, which leads to inconsistent applications and errors. For instance, if we use this model for early morning or late afternoon situations, because of the likely large sun angle, this can easily result in 30% or greater errors in estimating K_d (Morel et al., 2002; Lee et al., 2005b). In the following, we demonstrate the non-additive nature of K_d theoretically and numerically.

THEORETICAL MODEL OF K_d

Based on radiative transfer, K_d is a function of IOPs (especially the absorption, a, and backscattering, b_b, coefficients) as (Lee et al., 2005b),

$$K_d = \frac{1}{\mu_d}\, a + \left(\frac{r_d}{\mu_d} - \frac{r_u\, R}{\mu_u}\right)\, b_b. \quad (4)$$

Here μ_d (μ_u) is the average cosine and r_d (r_u) is the shape factor for the downwelling (upwelling) light field (Stavn and Weidemann, 1989), respectively. R is the irradiance reflectance (Gordon et al., 1975). Through numerical simulations via Hydrolight, it was found that the above expression could be simplified as (Lee et al., 2005b)

$$K_d(\lambda) = m_0\, a(\lambda) + m_1\, \left(1 - m_2\, e^{-m_3\, a(\lambda)}\right)\, b_b(\lambda), \quad (5)$$

with m_{0-3} constants that are independent of wavelength and water properties. Note that these model parameters vary weakly with depth (Lee et al., 2005b) due to changes of light field structure, consistent with the change of μ_d with depth (Stavn, 1988; Berwald et al., 1995; McCormick, 1995). Also note that for large zenith angles, the forward scattering coefficient will also contribute to the diffuse attenuation coefficient through its contribution to μ_d, μ_u, r_d and r_u (Stavn and Weidemann, 1989). Mathematically, Equation (5) can be rewritten as,

$$K_d(\lambda) = m_0\, a(\lambda) + m_1\, b_b(\lambda) - m_1\, m_2\, e^{-m_3\, a(\lambda)}\, b_b(\lambda). \quad (6)$$

Consequently, although $a(\lambda)$ and $b_b(\lambda)$ are additive, a nature of IOPs, the interaction term between $a(\lambda)$ and $b_b(\lambda)$ (the third term on the right side of Equation 6) is *not* additive, thus K_d cannot be additive—a general nature of AOPs. This characteristic is further highlighted in details below.

For simplicity, let's consider a medium has just two constituents: pure seawater and suspended inorganic mineral particles (PIM). For pure seawater alone, following Equation (6), there is

$$K_w(\lambda) = m_0\, a_w(\lambda) + m_1\, b_{bw}(\lambda) - m_1\, m_2\, e^{-m_3\, a_w(\lambda)}\, b_{bw}(\lambda). \quad (7)$$

Here $a_w(\lambda)$ and $b_{bw}(\lambda)$ are the spectral absorption and backscattering coefficients of pure seawater.

For suspended inorganic mineral particles alone,

$$K_{PIM}(\lambda) = m_0\, a_{PIM}(\lambda) + m_1\, b_{bPIM}(\lambda) - m_1\, m_2\, e^{-m_3\, a_{PIM}(\lambda)}\, b_{bPIM}(\lambda), \quad (8)$$

with a_{PIM} and b_{bPIM} being the absorption and backscattering coefficients of suspended mineral particles.

Therefore, a sum ($K_d^{sum}(\lambda)$) of the two contributions to K_d following Equations (2) and (3) resulted in,

$$K_d^{sum}(\lambda) = m_0(a_w(\lambda) + a_{PIM}(\lambda)) + m_1(b_{bw}(\lambda) + b_{bPIM}(\lambda)) - m_1\, m_2\, \left(e^{-m_3\, a_w(\lambda)}\, b_{bw}(\lambda) + e^{-m_3\, a_{PIM}(\lambda)}\, b_{bPIM}(\lambda)\right). \quad (9)$$

However, when the medium is composed of both pure seawater and suspended mineral particles, its K_d following radiative transfer (Equation 6) is

$$K_d(\lambda) = m_0(a_w(\lambda) + a_{PIM}(\lambda)) + m_1(b_{bw}(\lambda) + b_{bPIM}(\lambda)) - m_1\, m_2\, \left(e^{-m_3\, a_w(\lambda) - m_3\, a_{PIM}(\lambda)}\right)\, (b_{bw}(\lambda) + b_{bPIM}(\lambda)). \quad (10)$$

Clearly, as shown above, when there are more constituents, because the light field is determined by the bulk properties (Stavn, 1988; Stavn and Weidemann, 1989; Lee et al., 2005b), a_w and a_{PIM} will affect the contribution of both b_{bw} and b_{bPIM} to K_d. However, when K_d is treated as an additive property of K_w and K_{PIM}, the effect of a_w on the contribution of b_{bPIM} and the effect of a_{PIM} on the contribution of b_{bw} are excluded.

NUMERICAL DEMONSTRATION

To demonstrate the above point numerically, **Figure 1** compares K_d spectra from Hydrolight (Mobley and Sundman, 2013) simulations with K_d^{sum}, where the two component spectra (K_w and K_{PIM}) were also obtained from Hydrolight simulations using the same constituents as for K_d. Specifically, spectral (400–800 nm, 10 nm interval) $E_d(z)$ were simulated with Hydrolight, and K_d between surface and z is calculated following

$$K_d(\lambda) = \frac{1}{z} \ln\left(\frac{E_d(0^-, \lambda)}{E_d(z, \lambda)}\right) \tag{11}$$

For the derivation of K_w from Hydrolight, all other constituents were held to 0 except for the properties of pure seawater. Values of a_w are a combination of Lee et al. (2015) and Pope and Fry (1997) while values of b_{bw} are those of Morel (1974). For the derivation of K_{PIM} from Hydrolight, PIM was set as 10 g/m^3 and the default optical model parameters for suspended minerals included in Hydrolight were used to get the absorption and scattering coefficients of PIM. Note that this PIM concentration is just a low-medium value for turbid coastal waters (Babin et al., 2003; Doxaran et al., 2009). For this simulation, an idealized "transparent pure seawater" was used where very low values of a_w (0.1×10^{-4} m^{-1}) and b_{bw} (0.5×10^{-5} m^{-1}) were employed. With such a setup the contribution of this "transparent pure seawater" to the calculated K_d (Equation 11) is then negligible, and the resultant K_d from Hydrolight simulations can be considered as K_{PIM}. The sun angle for all simulations for both K_w and K_{PIM} was set as 30° from zenith along with a clear sky.

There are distinct differences in K_d (at least for this case) in the longer wavelengths (~10–15% for the 600–800 nm range), where a_w makes significant contributions to the total a; and this contribution, when there are sediments, to K_d is not represented in the additive descriptions of K_d (the red curve). For the shorter wavelengths (<~500 nm), because most (>~98%) of the contributions to K_d comes from PIM, the sum of the two terms match the bulk results well. Certainly the impact of the non-additive nature of K_d depends on the values of both a and b_b. For "Case-1" waters or waters where the scattering coefficients are relatively small, it might be applicable, without great errors, to treat $K_d(\lambda)$ as an additive property. However, this will depend on the validity of the above-mentioned assumptions. While not based on any assumptions of "Case-1" conditions or dependencies, the modeled K_d spectrum following Equation 5 is in an excellent agreement with the Hydrolight K_d spectrum

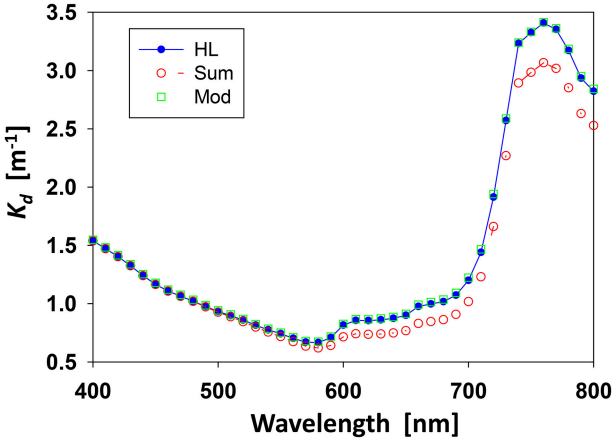

FIGURE 1 | Comparison of K_d spectra between Hydrolight simulation (blue), sum of individual components (red), and that from semi-analytical model based on bulk IOPs (green). The range for K_d is between surface and 5 m.

(~1% differences, see **Figure 1**), which highlights the much wider applicability of models based on radiative transfer. And, the robust performance of this model was also demonstrated in Zimmerman et al. (2015) for the quite turbid Chesapeake Bay waters.

Historically (Lorenzen, 1972; Smith and Baker, 1978; Woodruff et al., 1999; Gallegos, 2001; Devlin et al., 2008), there are also studies that treat the attenuation coefficient (K(PAR)) of the photosynthetic available radiation (PAR) as being additive of the contributions of individual constituents,

$$K(PAR) = K_w(PAR) + K_{bio}(PAR) + K_x(PAR), \tag{12}$$

with K_x(PAR) for contributions except phytoplankton and pure (sea)water. Following the above logic and discussion regarding spectral K_d, we easily observe that this model is not consistent with radiative transfer either (Morel, 1988). In particular, it is ambiguous of the light spectra that should be used for the calculation of K_w(PAR) or K_{bio}(PAR). Further, because K(PAR) is the attenuation coefficient of solar radiation of a wide spectral range (400–700 nm, i.e., the PAR spectral range), while the spectral quality of $E_d(z)$ changes significantly from surface to depths, which then causes K(PAR) to change greatly (as much as a factor of 4) from surface to depth (Lee et al., 2005a; Lee, 2009). Consequently, the applicability of such biogeo-optical models for K(PAR) is ambiguous at the very least.

CONCLUSIONS

Because the interaction term (the third term on the right side of Equation 6) of $K_d(\lambda)$ (or K(PAR)) depends on the values of both a and b_b, the contribution of this term to K_d is not always small or negligible. Also, this interaction term is not a linear function of a and b_b. Therefore, for consistency with radiative transfer and for more accurate estimation, and also to incorporate advancements in ocean optics of recent decades, it is better to

get bulk IOPs first from biogeochemical properties, and then to calculate K_d based on IOPs. In short, IOPs are additive, but AOPs are not.

AUTHOR CONTRIBUTIONS

All authors contributed to the hypothesis and overall discussions regarding diffuse attenuation of solar radiation. ZL drafted the manuscript and both SS and RS commented and edited the manuscript before submission.

ACKNOWLEDGMENTS

Funding support provided by the National Key Research and Development Program of China (2016YFC1400905, 2016YFC1400904, #2016YFA0601201, SS), the National Oceanic and Atmospheric Administration (NOAA) JPSS VIIRS Ocean Color Cal/Val Project (NA11OAR4320199, ZL), the National Aeronautic and Space Administration (NASA) Water and Energy Cycle, Ocean Biology and Biogeochemistry Programs (NNX14AK08G, NNX14AQ47A, ZL), and the University of Massachusetts Boston are greatly appreciated.

REFERENCES

Babin, M., Morel, A., Fournier-Sicre, V., Fell, F., and Stramski, D. (2003). Light scattering properties of marine particles in coastal and open ocean waters as related to particle mass concentration. *Limnol. Oceanogr.* 48, 843–859. doi: 10.4319/lo.2003.48.2.0843

Baker, K. S., and Smith, R. C. (1982). Bio-optical classification and model of natural waters. 2. *Limnol. Oceanogr.* 27, 500–509. doi: 10.4319/lo.1982.27.3.0500

Berwald, J., Stramski, D., Mobley, C. D., and Kiefer, D. A. (1995). Influences of absorption and scattering on vertical changes in the average cosine of the underwater light field. *Limnol. Oceanogr.* 40, 1347–1357. doi: 10.4319/lo.1995.40.8.1347

Devlin, M. J., Barry, J., Mills, D. K., Gowen, R. J., Foden, J., and Tett, P. (2008). Relationships between suspended particulate material, light attenuation and Secchi depth in UK marine waters. *Estuarine Coastal Shelf Sci.* 79, 429–439. doi: 10.1016/j.ecss.2008.04.024

Devlin, M. J., Barry, J., Mills, D. K., Gowen, R. J., Foden, J., and Tett, P. (2009). Estimating the diffuse attenuation coefficient from optically active constituents in UK marine waters. *Estuarine Coastal Shelf Sci.* 82, 73–83. doi: 10.1016/j.ecss.2008.12.015

Doxaran, D., Ruddick, K., McKee, D., Gentili, B., Tailliez, D., Chami, M., et al. (2009). Spectral variations of light scattering by marine particles in coastal waters, from visible to near infrared. *Limnol. Oceanogr.* 54, 1257–1271. doi: 10.4319/lo.2009.54.4.1257

Gallegos, C., Correll, D., and Pierce, J. (1990). Modeling spectral diffuse attenuation, absorption, and scattering coefficients in a turbid estuary. *Limnol. Oceanogr.* 35, 1486–1502. doi: 10.4319/lo.1990.35.7.1486

Gallegos, C. L. (2001). Calculating optical water quality targets to restore and protect submersed aquatic vegetation: overcoming problems in partitioning the diffuse attenuation coefficient for photosynthetically active radiation. *Estuaries* 24, 381–397. doi: 10.2307/1353240

Gnanadesikan, A., and Anderson, W. G. (2009). Ocean water clarity and the ocean general circulation in a coupled climate model. *J. Phys. Oceanogr.* 39, 314–332. doi: 10.1175/2008JPO3935.1

Gordon, H. R. (1989). Can the Lambert-Beer law be applied to the diffuse attenuation coefficient of ocean water?. *Limnol. Oceanogr.* 34, 1389–1409. doi: 10.4319/lo.1989.34.8.1389

Gordon, H. R., Brown, O. B., and Jacobs, M. M. (1975). Computed relationship between the inherent and apparent optical properties of a flat homogeneous ocean. *Appl. Optics* 14, 417–427. doi: 10.1364/AO.14.000417

Kim, G. E. M., Pradal, A., and Gnanadesikan, A. (2015). Quantifying the biological impact of surface ocean light attenuation by colored detrital matter in an ESM using a new optical parameterization. *Biogeosciences* 12, 5119–5132. doi: 10.5194/bg-12-5119-2015

Lee, Z. P. (2009). KPAR: An optical property associated with ambiguous values. *J. Lake Sci.* 21, 159–164. doi: 10.18307/2009.0202

Lee, Z. P., Du, K., Arnone, R., Liew, S. C., and Penta, B. (2005a). Penetration of solar radiation in the upper ocean - A numerical model for oceanic and coastal waters. *J. Geophys. Res.* 110:C09019. doi: 10.1029/2004JC002780

Lee, Z. P., Du, K. P., and Arnone, R. (2005b). A model for the diffuse attenuation coefficient of downwelling irradiance. *J. Geophys. Res.* 110:C0201. doi: 10.1029/2004JC002275

Lee, Z., Wei, J., Voss, K., Lewis, M., Bricaud, A., and Huot, Y. (2015). Hyperspectral absorption coefficient of "pure" seawater in the range of 350–550 nm inverted from remote sensing reflectance. *Appl. Optics* 54, 546–558. doi: 10.1364/AO.54.000546

Lewis, M. R., Carr, M., Feldman, G., Esaias, W., and McMclain, C. (1990). Influence of penetrating solar radiation on the heat budget of the equatorial pacific ocean. *Nature* 347, 543–545. doi: 10.1038/347543a0

Lorenzen, C. J. (1972). Extinction of light in the ocean by phytoplankton. *J. Cons. Int. Explor. Mar.* 34, 262–267.

McCormick, N. J. (1995). Mathematical models for the mean cosine of irradiance and the diffuse attenuation coefficient. *Limnol. Oceanogr.* 40, 1013–1018. doi: 10.4319/lo.1995.40.5.1013

Mobley, C. D. (1994). *Light and Water: Radiative Transfer in Natural Waters.* New York, NY: Academic Press.

Mobley, C. D., and Sundman, L. K. (2013). *HydroLight 5.2 User's Guide.* Bellevue, WA: Sequoia Scientific, Inc.

Morel, A. (1974). "Optical properties of pure water and pure sea water," in *Optical Aspects of Oceanography*, eds N. G. Jerlov and E. S. Nielsen (New York, NY: Academic), 1–24.

Morel, A. (1988). Optical modeling of the upper ocean in relation to its biogenous matter content (Case I waters). *J. Geophys. Res.* 93, 10749–10768. doi: 10.1029/JC093iC09p10749

Morel, A., and Antoine, D. (1994). Heating rate within the upper ocean in relation to its bio-optical state. *J. Phys. Oceanogr.* 24, 1652–1665. doi: 10.1175/1520-0485(1994)024<1652:HRWTUO>2.0.CO;2

Morel, A., Antoine, D., and Gentili, B. (2002). Bidirectional reflectance of oceanic waters: accounting for Raman emission and varying particle scattering phase function. *Appl. Optics* 41, 6289–6306. doi: 10.1364/AO.41.006289

Morel, A., and Maritorena, S. (2001). Bio-optical properties of oceanic waters: a reappraisal. *J. Geophys. Res.* 106, 7163–7180. doi: 10.4319/lo.1977.22.4.0709

Morel, A., and Prieur, L. (1977). Analysis of variations in ocean color. *Limnol. Oceanogr.* 22, 709–722. doi: 10.1029/2000JC000319

Ohlmann, J. C., Siegel, D. A., and Mobley, C. D. (2000). Ocean radiant heating. Part I: Optical influences. *J. Phys. Oceanogr.* 30, 1833–1848. doi: 10.1175/1520-0485(2000)030<1833:ORHPIO>2.0.CO;2

Platt, T. (1986). Primary production of ocean water column as a function of surface light intensity: algorithms for remote sensing. *Deep-Sea Res.* 33, 149–163. doi: 10.1016/0198-0149(86)90115-9

Pope, R., and Fry, E. (1997). Absorption spectrum (380–700 nm) of pure waters: II. Integrating cavity measurements. *Appl. Optics* 36, 8710–8723. doi: 10.1364/AO.36.008710

Preisendorfer, R. W. (1976). *Hydrologic optics vol. 1: introduction, National Technical Information Service*. Office of Naval Research, Springfield.

Rochford, P. A., Kara, A. B., Wallcraft, A. J., and Arnone, R. A. (2001). Importance of solar subsurface heating in ocean general circulation models. *J. Geophys. Res.* 106, 30923–30938. doi: 10.1029/2000JC000355

Sathyendranath, S., and Platt, T. (1995). "Remote sensing of water-column primary production," in *Measurement Of Primary Production from the Molecular to the Global Scale*, eds W. K. Li and W. Maestrini (Copenhagen: ICES Marine Science Symposia), 236–243.

Smith, R. C., and Baker, K. S. (1978). The bio-optical state of ocean waters and remote sensing. *Limnol. Oceanogr.* 23, 247–259. doi: 10.4319/lo.1978.23.2.0247

Stavn, R. (1988). Lambert-Beer law in ocean waters: optical properties of water and of dissolved/suspended materials, optical energy budgets. *Appl. Optics* 27, 222–231. doi: 10.1364/AO.27.000222

Stavn, R. H., and Weidemann, A. D. (1989). Shape factors, two-flow models, and the problem of irradiance inversion in estimating optical parameters. *Limnol. Oceanogr*. 34, 1426–1441. doi: 10.4319/lo.1989.34.8.1426

Woodruff, D. L., Stumpf, R. P., Scope, J. A., and Paerl, H. W. (1999). Remote estimation of water clarity in optically complex estuarine waters. *Remote Sens. Environ*. 68, 41–52. doi: 10.1016/S0034-4257(98)00108-4

Zaneveld, J. R. V., Kitchen, J. C., and Pak, H. (1981). The influence of optical water type on the heating rate of a constant depth mixed layer. *J. Geophys. Res.* 86, 6426–6428. doi: 10.1029/JC086iC07p06426

Zimmerman, R. C., Hill, V. J., and Gallegos, C. L. (2015). Predicting effects of ocean warming, acidification, and water quality on Chesapeake region eelgrass. *Limnol. Oceanogr*. 60, 1781–1804. doi: 10.1002/lno.10139

Conflict of Interest Statement: The authors declare that the research was conducted in the absence of any commercial or financial relationships that could be construed as a potential conflict of interest.

frontiers in Marine Science

ORIGINAL RESEARCH
published: 23 February 2018
doi: 10.3389/fmars.2017.00437

Modeling Net Growth of *Phaeocystis antarctica* Based on Physiological and Optical Responses to Light and Temperature Co-limitation

Tiffany A. Moisan[1†] *and B. Greg Mitchell*[2*]

[1] Wallops Flight Facility, Goddard Space Flight Center (NASA), Wallops Island, VA, United States, [2] Scripps Institution of Oceanography, University of California, San Diego, La Jolla, CA, United States

OPEN ACCESS

Edited by:
François G. Schmitt, Centre National de la Recherche Scientifique (CNRS), France

Reviewed by:
Fabrice Lizon, Lille University of Science and Technology, France
Raghab Ray, UMR6539 Laboratoire des Sciences de L'environnement Marin (LEMAR), France

***Correspondence:**
B. Greg Mitchell
gmitchell@ucsd.edu

[†]*Deceased.*

Specialty section:
This article was submitted to Coastal Ocean Processes, a section of the journal Frontiers in Marine Science

Received: *06 July 2017*
Accepted: *20 December 2017*
Published: *23 February 2018*

Citation:
Moisan TA and Mitchell BG (2018) Modeling Net Growth of Phaeocystis antarctica Based on Physiological and Optical Responses to Light and Temperature Co-limitation. Front. Mar. Sci. 4:437. doi: 10.3389/fmars.2017.00437

Temperature and light are fundamental environmental variables which regulate phytoplankton growth rates when nutrients are in excess. For polar coastal oceans that are undergoing changes in sea ice cover and warming, light, and temperature are particularly important for bloom dynamics. Using colonial *Phaeocystis antarctica* cultures grown at steady-state, we assessed the combined effect of these two environmental controls on net growth rate (μ_n), chlorophyll-specific absorption of light (a^*_{ph} (λ)), and quantum yields for growth (ϕ_μ). Specific net growth rates (μ_n) varied from 0.04 to 0.34 day^{-1} within a matrix of light and temperature ranging from 14 to 542 μmol quanta m^{-2} s^{-1} and −1.5 to 4°C. Values of a^*_{ph} (λ) varied significantly with light but only slightly with temperature. Values of ϕ_μ ranged from 0.003 to 0.09 mol C (mol quanta absorbed)$^{-1}$ with highest values at low light and 4°C. For excess irradiances or low temperatures where growth rate is inhibited, quantum yields were low. The low ϕ_μ values are attributed both to increased absorption by photoprotective pigments compared to photosynthetic pigments and thermodynamic control of dark reaction enzymes. The systematic changes in photophysiological properties of *P. antarctica* in relation to temperature and light were used to develop a series of nested light- and temperature-dependent models for μ_n, a^*_{ph} (λ), and ϕ_μ. A model for a^*_{ph} (300–700 nm) was developed that takes into account the systematic changes in a^*_{ph} (λ) due to pigment packaging effects and cellular concentrations of chlorophylls and photoprotective pigments. Also, a model for ϕ_μ was developed based on a cumulative one-hit Poisson probability function. These model parameterizations for absorption and quantum yield are combined into an overall model of net growth that can be applied easily to *P. antarctica* bloom dynamics using remote sensing data for temperature, light, and chlorophyll *a*. Furthermore, modeling based on the biophysical variables a^*_{ph} (λ), and ϕ_μ that are shown to regulate the growth rate provides a more fundamental mechanistic approach compared to other modeling methods that do not explicitly resolve photon flux into the cell or the quantum yield.

Keywords: *Phaeocystis*, phytoplankton, photosynthesis, modeling, co-limitation, photophysiology, quantum yield, absorption

INTRODUCTION

The colonial prymnesiophyte *Phaeocystis* can dominate coastal, ice edge, and open ocean blooms in polar and temperate waters with significant implications for carbon export (Smith et al., 1991; DiTullio et al., 2000; van Leeuwe et al., 2007; Pavlov et al., 2017). The importance of light, temperature, and nutrients in governing phytoplankton growth and bloom formation has motivated research on metabolic and cellular characteristics of phytoplankton in response to environmental stressors. Singly, the light-, temperature-, and nutrient- dependence of phytoplankton growth has been well-characterized for a variety of species under a wide range of experimentally controlled laboratory conditions providing the basis for generalized models of phytoplankton growth for temperature, nutrients, and light limitation. Nutrient-limited growth has been described as a function of cell quota which is determined by Michaelis-Menten uptake kinetics (Droop, 1983). These kinetic models have been modified to account for multiple nutrients by invoking Leibig's Law of the minimum (Falkowski and Raven, 2007). Temperature-dependent growth has been modeled with the Arrhenius equation (Li, 1980) and maximal growth has been based on empirical derivations determined from cultures (Eppley, 1972). Light-dependent growth has been modeled as a variety of different formulations which allows growth to increase with irradiance, saturate, and decrease at high irradiances (Goldman and Carpenter, 1974; Laws and Bannister, 1980; Moisan et al., 2002). While nutrient limitation is generally modeled on the basis of the "limiting" nutrient, phytoplankton must also acclimate to large variations in light and temperature (Behrenfeld et al., 2002; Ciotti et al., 2002). Often these regulate growth in an interactive co-limitation matrix (Sosik and Mitchell, 1994; Sunda and Huntsman, 1997, 2011) however there is lacking a mechanistic framework for modeling phytoplankton growth rate based on the biophysical variables of cellular absorption and quantum yield under simultaneous co-limitation.

Blooms of *Phaeocystis* sp. have been reported in diverse oceanic provinces for temperature ranging from less than 0°C to greater than 35°C and for both shallow and deep mixed layers (Gieskes et al., 2007; Gypens et al., 2007). Data sets required to specify physiological parameters for growth at various environmental conditions are relatively rare. A review of Chl:C ratios in polar and temperate microalgae at different acclimation states is found in Lacour et al. (2017)Various mathematical descriptions for modeling phytoplankton growth that include multiple limitations establish the foundations for our approach (Shuter, 1979; Laws and Bannister, 1980; Rhee and Gotham, 1981a,b; Geider et al., 1998; Behrenfeld et al., 2002; Edwards et al., 2016). These concepts have been extended to the estimates of primary production and growth rates from satellites (Behrenfeld et al., 2005; Arteaga et al., 2014, 2016). Growth rates regulated by irradiance, temperature, and nutrients have been modeled using different approaches based on algal metabolism (Laws and Bannister, 1980), elemental ratios of chlorophyll or carbon (Geider et al., 1998; Graff et al., 2016), or cell carbon quota (Zonneveld et al., 1997). Some of these models have limited ecological applicability because they require parameters that are not easily measured in natural systems. We model steady-state growth based on the mechanistic biophysical parameters of chl-a specific spectral absorption and photosynthetic quantum yeield (a^*_{ph} (λ) and ϕ_μ,) which are directly regulated by light, temperature, and nutrients (Kiefer and Mitchell, 1983; Sakshaug et al., 1989; Cullen, 1990; Moisan and Mitchell, 1999). For brevity, all symbols are defined in **Table 1**. For steady-state growth, a^*_{ph} (λ) and ϕ_μ vary in response to temperature, light, and nutrient regulation of growth (Mitchell and Kiefer, 1988; Nelson and Prézelin, 1990; Sosik and Mitchell, 1991, 1995; Moisan and Mitchell, 1999; Westberry et al., 2008). Combining estimates of phytoplankton absorption (Kishino et al., 1985) with rates of carbon fixation allows for validation of models based on a^*_{ph} (λ) and ϕ_μ for natural communities (Cleveland et al., 1989; Smith et al., 1989; Marra et al., 1995; Sosik and Mitchell, 1995; Sosik, 1996). Thus, the model we describe here to predict a^*_{ph} (λ) and ϕ_μ for light and temperature co-limitation can easily be applied and validated for natural communities in polar regions using routine methods and is most applicable when blooms dominated by *Phaeocystis* are forming and nutrients are in excess. The model is most likely not as robust during pre-bloom situations with a mixed community assemblage and for post bloom conditions when nutrients are exhausted.

Modeling growth rates of phytoplankton over large geographical scales will require parameterizations that take into account the taxonomic diversity of the phytoplankton community and variability driven by physiological acclimation (Moisan et al., 2017). In this paper, we have developed a model of growth rate using the colonial prymnesiophyte, *P. antarctica*, an ecologically and biogeochemically important organism in the polar and subpolar carbon cycle (Stuart et al., 2000; Smith et al., 2003; Pabi and Arrigo, 2006; Smith et al., 2006; Gieskes et al., 2007) and is responsible for significant amounts of new production (Arrigo et al., 1999). Temperature, light, and iron are major limiting factors that control the initiation and development of phytoplankton blooms in the Southern Ocean. We describe the range of variability and relationships of μ_n, a^*_{ph} (λ), and ϕ_μ for *P. antarctica* for a realistic range of temperature, light, and nutrient conditions that occur during the Antarctic spring bloom. Using steady-state experimental data, we developed a series of nested models that together form a photophysiological model of net growth. Our model is based on contemporary bio-optical models for photosynthesis (Kiefer and Mitchell, 1983; Cullen, 1990; Moisan and Mitchell, 1999) which utilize a^*_{ph} (λ) and ϕ_μ as photophysiological variables to describe phytoplankton net growth,

$$\mu_n = \frac{chl\ a}{C} \int_{350nm}^{700nm} a^*_{ph}(\lambda) E_0(\lambda) \phi_\mu \, d\lambda. \quad (1a)$$

We determined the environmental control of a^*_{ph} (λ), and ϕ_μ by assessing their magnitude for co-limitation using controlled light and temperature experiments. Our model for ϕ_μ is based on a cumulative one-hit Poisson probability distribution and introduces the concept that both light and temperature regulate the maximal quantum yield of growth for any acclimated state.

TABLE 1 | Symbols used throughout the text.

λ	Wavelength (nm)
chl a	Chlorophyll a (mg m^{-3})
T	Temperature (°C)
P_{net}	Net primary production
μ_n	Specific rate of net growth (day^{-1})
μ_m	Maximal specific rate of net growth (day^{-1})
C	Particulate carbon (mg m^{-3})
$E_o(\lambda)$	Spectral quantum scalar irradiance (mol quanta m^{-2} s^{-1} nm^{-1})
PAR	Photosynthetically available radiation defined as $\int_{350nm}^{700nm} E_o(\lambda)d\lambda$ (μmol quanta m^{-2} s^{-1})
F_{DCMU}	*In vivo* DCMU-enhanced fluorescence (relative units)
a_{ph} (λ)	Absorption by phytoplankton (m^{-1})
a^*_{ph} (λ)	Chl-specific absorption of phytoplankton (m^2 mg chl a^{-1})
a^*_{ps} (λ)	Chl-specific absorption due to photosynthetic pigments (m^2 mg chl a^{-1})
a^*_{pp} (λ)	Chl-specific absorption due to photo-protective pigments (m^2 mg chl a^{-1})
ϕ_μ	Quantum yield for growth [mol C fixed (mol quanta absorbed)$^{-1}$]
ϕ_m	Maximal quantum yield [mol C fixed (mol quanta absorbed)$^{-1}$]
$\phi_{mE_0,T}$	Maximal quantum yield at a steady state irradiance and temperature [mol C fixed (mole quanta absorbed)$^{-1}$]
$E_{k\mu}$	Photoacclimation parameter (m^2/μmol quanta m^{-2} s^{-1})
a, b	Coefficients of power function fit for $\phi_{mE_o,T}$
C_0, C_E, C_T	Coefficients for intercepts, irradiance and temperature multiple-linear regression fit for a^*_{ph} (λ)
α, $\mu_s{}^\beta$, β	Coefficients for fitting light-dependent growth
α_1, α_2	Coefficients for temperature-dependence of α
P_{sb}	Curve fitting parameter for a P vs. E curve

In general, the maximal quantum yield for any acclimated state should be modeled as a function of the limiting growth conditions (Moisan and Mitchell, 1999) rather than using the theoretical maximum (Sakshaug et al., 1989). Our formulation is based on Cullen (1990) and we extend our previous model of ϕ_μ (Moisan and Mitchell, 1999) as a variable dependent on both light and temperature,

$$\phi_\mu = \phi_{mE_o,T} \frac{1 - \exp^{-E_o/E_{k\mu}}}{E_o/E_{k\mu}} \quad (1b)$$

where ϕ_μ is the quantum yield of growth, $\phi_{m,Eo,T}$ is the maximal quantum yield for growth for an acclimated state within the light and temperature limitation matrix, $E_{k\mu}$ is the photoacclimation parameter (Falkowski and Raven, 2007), and E_0 is photosynthetically available radiation.

The culture experiments were designed to assess the broad range of temperature and light that Antarctic phytoplankton experience in nature that is relevant to formation of blooms. Since a bloom cannot form unless there are excess nutrients to support the growth of the bloom, we do not model nutrients although clearly macronutrients and iron can regulate the crop size and productivity (Sedwick, 2007; van Leeuwe and Stefels, 2007). By characterizing the light and temperature response of phytoplankton absorption and quantum yield over a realistic environmental range, we have parameterized a bio-optical model for μ_n for application to ocean color satellites and buoys. This effort to describe and model the variability in the biophysical parameters that mediate temperature and light control of phytoplankton growth provides important details related to phytoplankton acclimation when multiple environmental variables are regulating growth simultaneously.

MATERIALS AND METHODS

Cultures of colonial *P. antarctica* (CCMP 1374) were grown semi-continuously at −1.5, 0, 2, and 4°C for 5–8 generations in f/2 medium (Gulliard and Ryther, 1962) under continuous blue light ranging from 14 to 542 mol quanta m^{-2} s^{-1}. The spectrum of the light source was similar to the light quality observed in the upper ocean (Moisan and Mitchell, 1999). Cultures were maintained at ∼30% of the carrying capacity of the culture medium. This protocol results in a steady-state acclimated condition at the time of experimental sampling. Details of the illumination source, blue filter and culturing system and our method to estimate spectral quantum flux in the cultures can be found in Moisan and Mitchell (1999).

Specific Growth Rate (μ_n)

Specific growth rate was estimated by a linear regression of $\log_e$ transformed daily determinations of *in vivo* fluorescence intensity ($n = 2$) measured with a Turner Model 10 fluorometer at the same time each day. POC data was also collected during mid-log phase growth at the time of the experiments, allowing an estimate of the carbon-based growth rate for each experimental culture.

Fluorometric Estimates of Chl *a*

Chl *a* concentrations ($n = 3$) were estimated fluorometrically using a Turner Model 10-AU fluorometer according to (Welschmeyer, 1994).

High Performance Liquid Chromatography (HPLC)

Duplicate samples ($n = 2$) were concentrated onto Whatman GF/F filters and extracted in cold 100% acetone by grinding with a teflon-tip grinding rod. After centrifugation, the supernatant was mixed with 20% (v/v) HPLC-grade water and analyzed on a Shimadzu LC10-AD HPLC system (Wright et al., 1991). Pigment concentrations were based on absorption at 440 nm (Dynamax Model UV-1). Integrated HPLC peak area was quantified with external standards. Canthaxanthin was used as an internal standard. A spectral diode detector provided spectral absorption of peaks which were used to confirm the individual pigments by reference to a spectral library of standards. Duplicate samples ($N = 2$) differed by less than 2% of each other on replicate filtered samples. Note that there was a small difference (2–20%) between HPLC samples and fluorometric samples. For this reason, we have averaged the HPLC and fluorometric samples.

Chl-Specific Absorption Coefficient (a^*_{ph} (λ))

For experiments at −1.5, 2, and 4°C, *in vivo* whole cell absorption spectra were determined ($n = 4$) on concentrated samples from 300 to 800 nm at 1 nm intervals with an integrating sphere accessory in a dual beam Perkin Elmer Lambda 6 UV/Vis spectrophotometer. Fresh f/2 medium was used as a reference and a blank. For cultures grown at 0°C, the integrating sphere failed and we estimated the absorption coefficient with the glass fiber filter method of Mitchell (1990) which has been shown to agree well with the integrating sphere methods after corrections for pathlength amplification (Mitchell et al., 2000). The chl-specific absorption coefficient was estimated by dividing $\log_e$ absorption, aph (λ), by the corresponding chl *a* value:

$$a^*_{ph}(\lambda) = a_{ph}(\lambda)\,[\text{chl } a]^{-1}. \quad (2)$$

Particulate Carbon and Nitrogen Content

Samples ($n = 3$) were filtered onto pre-combusted GF/F filters, stored at −20°C and run on a Carlo Erba carbon analyzer. Samples of acetanilide were used to validate the system's calibration. See Moisan and Mitchell (1999) for details.

Cell Concentrations

Cell concentrations were estimated in Palmer Maloney chambers both fresh (unfixed) and observed at a magnification of 400X. See Moisan and Mitchell (1999) for details.

Quantum Yield for Growth

Quantum yield for growth was based on the carbon-specific net growth rate, whole cell *in vivo* spectral absorption, and the spectral irradiance in each treatment (Sosik and Mitchell, 1991; Moisan and Mitchell, 1999) and is a rearrangement of Equation (1a).

Non-linear Curve Fitting

Coefficients for P-E curves, and temperature and light dependent equations for growth and quantum yield for growth were fit using a Marquardt-Levenberg non-linear least squares minimization routine (Marquardt, 1963). See Moisan and Mitchell (1999) for details.

RESULTS AND DISCUSSION

The Relationship between Growth Rate, Temperature, and Light

Growth rates of *P. antarctica* varied ∼8-fold ranging from 0.04 day^{-1} to 0.34 day^{-1} under conditions which were limiting to inhibiting for growth (**Figure 1A**). Specific net growth rates (μ_n) increased in response to light and approached photoinhibition at higher irradiances (**Table 2**). The initial slope of the light-dependent growth was lowest at 4°C (0.007 average± S.E. 0.001) and highest at 0°C (0.030 average ± S.E. 0.006). A photoacclimation parameter ($E_{k\mu}$) was derived utilizing a curve-fitting scheme of all of the light treatments for a single temperature and other studies. Values of $E_{k\mu}$ were both temperature- and light- dependent (**Figure 1A**).

Relative growth rates (μ_n/μ_m) for our treatments exhibited a strong dependence on temperature, with maximal values between 0 and 2°C except at photoinhibiting intensities (**Figure 1B**, Tilzer and Dubinsky, 1987). In general, μ_n had a parabolic response to temperature, with a 1.5-fold change between minima and maxima with the exception of the treatments at 14 μmol quanta m^{-2} s^{-1}. At low temperatures under moderate light intensities, *P. antarctica* achieved maximal growth similar to those grown at high light at 4°C. For example, the maximal growth rates, μ_m (0.98 ± 0.05, average ± S.E.) achieved at 37 μmol quanta m^{-2} s^{-1} at temperatures <2°C were lower than those observed at inhibiting growth conditions at 542 μmol quanta m^{-2} s^{-1} at 4°C (**Figure 1A**, *t*-test; $p > 0.05$).

Empirical Model of Growth Rate

The systematic dependence of net growth rate (μ_n) on temperature and light allowed for the derivation of a simple empirical model for μ_n (**Figure 1C**). We modeled the light-dependence of growth with a hyperbolic tangent equation commonly used for photosynthesis-irradiance relationships (Platt et al., 1980, **Figure 1A**) which allows μ_n to increase with irradiance and become saturated or photoinhibited at higher irradiances (**Table 3**). We modeled μ_m as a function of temperature (Eppley, 1972). Values of α were fit as linear functions of temperature and light ($R^2 = 0.85$) as has been observed for Antarctic phytoplankton (Lizotte and Sullivan, 1991). Net growth for *P. antarctica* can be estimated with knowledge of light and temperature using the following equations,

$$\mu_m = \log(2)0.851^*(1.066^T), \quad (3a)$$

$$\alpha = \alpha 1 + (\alpha 2 T), \quad (3b)$$

$$\mu_n = \mu s^b[1 - \exp(\frac{-\alpha PAR}{\mu s^b})]\exp(\frac{-\beta PAR}{\mu s^b}) \quad (3c)$$

$$\mu s^b = \frac{\mu_{max}[\alpha + \beta/\alpha]}{[\beta/\alpha + \beta]^{\beta/\alpha}} \quad (3d)$$

where μ_n is net growth rate, μ_m is the maximal growth rate (day^{-1}), T is temperature (°C), α is the initial slope of the μ_n vs. irradiance relationship, β is the inhibition of growth at high irradiance, α1 and α2 are the y-intercepts and slope for α with temperature, respectively, μs^b (analogous to P_{sb} in Platt et al., 1980) is a fitting parameter and PAR is photosynthetically available radiation (350–700 nm). Equations (3c,d) represent a growth equation originally derived by Platt et al. (1980) as a function of P vs. I. parameters. The values for α1 and α2 are 0.0069 ± 0.001 and (−0.001 ± 0.0003), respectively ($p < 0.00001$). We have very few treatments where irradiance was sufficient to inhibit growth. However, other investigators have clearly documented that phytoplankton growth is inhibited at higher irradiances (Goldman and Carpenter, 1974; Laws and Bannister, 1980; Platt et al., 1980). Therefore, we allow β to be constrained in a relatively large range to accomodate photoinhibition at high light under low temperature. These dynamics are in general agreement with increases in photoinhibition of short-term photosynthetic carbon fixation at high light (Platt et al., 1980).

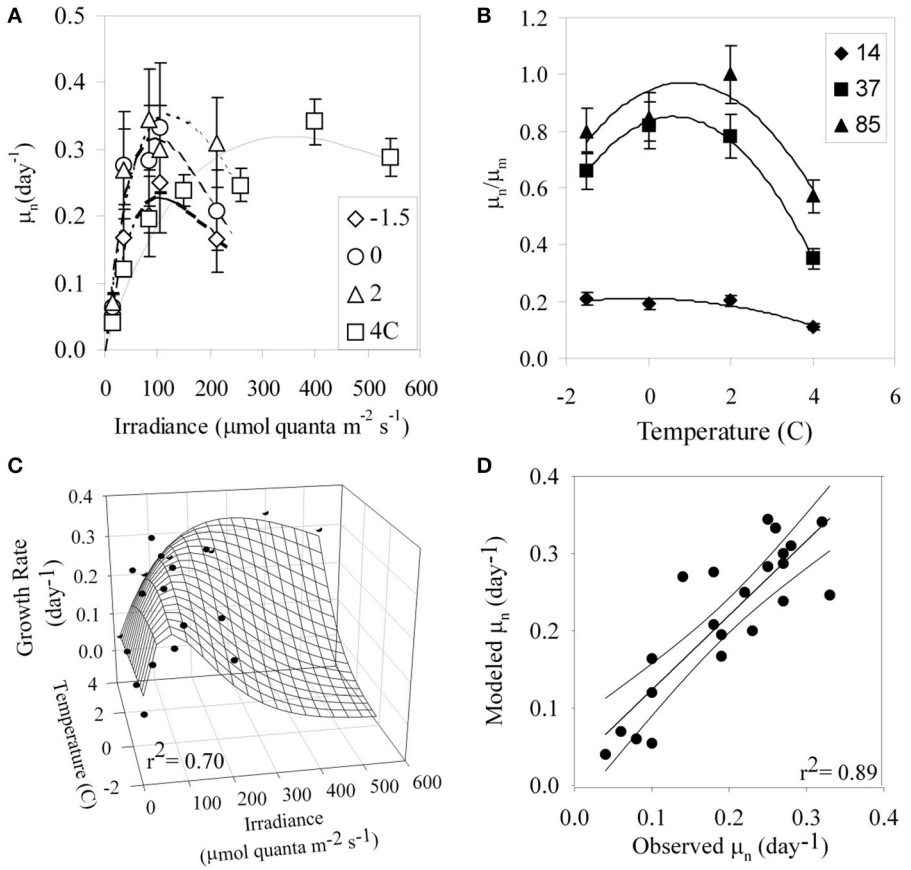

FIGURE 1 | (A) Specific growth rates (μ_n, day^{-1}) of *P. antarctica* with respect to irradiance for growth temperatures ranging from −1.5 to 4°C. **(B)** Relative growth rate (μ_n/μ_m) with respect to temperature for irradiances in units of µmol quanta m^{-2} s^{-1}. **(C)** An empirically-derived model for growth rate based on combined limitation of light and temperature. The continuous surface is the model prediction and discrete points are experimental observations. **(D)** Modeled vs. observed µ (day^{-1}) based on Equation (4).

This simple empirical model has an excellent ability for predicting μ_n based only on light and temperature as input (**Figure 1D**; $r^2 = 0.89$, $p < 0.05$). However, it does not include explicit information about mechanisms of physiological acclimation. Therefore, we have also developed a model to predict growth using a series of nested models that predict the biophysical parameters, $a^*_{ph}(\lambda)$ and ϕ_μ, based on acclimation to temperature and light.

Temperature and Light Dependence of $a^*_{ph}(\lambda)$: Observations and Modeling of Variability

The *in vivo* whole cell chlorophyll-specific absorption properties, $a^*_{ph}(\lambda)$, of *P. antarctica* varied with both irradiance and temperature (**Figures 2A,B**). Values of $a^*_{ph}(\lambda)$ increased with increasing irradiance (**Figures 2C–E**). Values of $a^*_{ph}(\lambda)$ at 436 and 676 nm generally increased with decreasing temperature but the magnitude of the temperature dependence was less than the irradiance dependence (**Figures 2C,D**, ANOVA $p > 0.05$). Values of $a^*_{ph}(330)$, due to mycosporine-like amino acids (Moisan and Mitchell, 2001), had less dependence on temperature than estimates at 436 and 676 nm (**Figure 2E**). Our observations are within the range of $a^*_{ph}(\lambda)$ observed during *Phaeocystis*-dominated blooms (Cota et al., 1994; Arrigo et al., 1998; Reynolds et al., 2001).

Pigment package effects, changes in pigment ratios (**Table 2**), and thylakoid stacking played an important role in determining both the spectral shape and large changes in the magnitude of $a^*_{ph}(\lambda)$ (Moisan and Mitchell, 1999; Moisan et al., 2006). Ratios of $a_{ph}(330)$ to $a_{ph}(676)$ increased linearly from 1.8 to 13 due to changes in MAA to Chl *a* concentrations as a photo-protective response to increased irradiance (Moisan and Mitchell, 2001).

We explored the dependence of $a^*_{ph}(\lambda)$ on irradiance and temperature in an attempt to specify a simple parameterization for spectral absorption that could accurately capture the changes in both shape and magnitude caused by changes in pigment ratios and packaging. Singly, $a^*_{ph}(676)$ was highly predictable by a linear regression with either irradiance ($r^2 = 0.62$, **Figure 3A**) or temperature ($r^2 = 0.63$, data not shown). However, the accuracy

TABLE 2 | Growth and pigmentation of *P. antarctica* grown under nutrient-replete conditions.

Irradiance μmol quanta m^{-2} s^{-1}	μ	Chl *a* Pg $(cell)^{-1}$	Ratio to HPLC Chl a						Total Pigment Per cell	PS/total Pig (w/w)	PP/ total Pig of total (w/w)
			Chl (c1+c2+c3)	19′hex	Fuco	19′but	β-car	DD+DT			
T = 4°C											
14	0.04	0.38	0.415	0.609	0.008	ND	0.003	0.015	0.76	0.99	0.01
37	0.12	0.45	0.407	0.640	0.031	ND	0.003	0.016	0.92	0.99	0.01
85	0.19	0.45	0.307	0.268	0.010	ND	0.010	0.070	0.82	0.95	0.05
151	0.24	0.35	0.325	0.368	0.012	ND	0.011	0.099	0.60	0.94	0.06
259	0.25	0.37	0.380	0.386	0.009	ND	0.011	0.077	0.69	0.95	0.05
400	0.34	0.28	0.264	0.298	0.042	ND	0.016	0.120	0.50	0.92	0.08
542	0.29	0.17	0.204	0.230	0.015	ND	0.028	0.371	0.38	0.78	0.22
T = 2°C											
14	0.07	0.10	0.503	0.725	0.217	0.010	0.006	0.038	0.22	0.98	0.02
37	0.27	0.31	0.528	1.254	0.076	0.028	0.005	0.053	0.74	0.98	0.02
85	0.34	0.36	0.519	1.585	0.052	0.035	0.010	0.189	1.04	0.94	0.06
106	0.30	0.30	0.489	1.529	0.057	0.039	0.012	0.199	0.86	0.94	0.06
214	0.31	0.06	0.525	1.624	0.070	0.039	0.010	0.183	0.17	0.94	0.06
T = 0°C											
14	0.06	0.26	0.508	1.305	0.061	0.019	0.005	0.085	0.65	0.97	0.03
37	0.28	0.37	0.511	1.079	0.079	0.020	0.006	0.065	0.85	0.97	0.03
85	0.28	0.41	0.473	0.933	0.023	0.025	0.009	0.097	1.15	0.96	0.04
106	0.33	0.34	0.470	0.834	0.027	0.023	0.006	0.087	0.65	0.96	0.04
214	0.21	0.05	0.402	0.797	0.022	0.017	0.011	0.180	0.11	0.92	0.08
T = −1.5°C											
14	0.05	0.02	0.461	0.529	0.164	0.014	0.004	0.028	0.05	0.99	0.01
37	0.17	0.03	0.529	1.425	0.048	0.044	0.009	0.159	0.77	0.95	0.05
85	0.20	0.27	0.533	1.528	0.051	0.042	0.008	0.135	0.79	0.96	0.04
106	0.25	0.30	0.539	1.340	0.047	0.042	0.008	0.133	0.96	0.95	0.05
214	0.16	0.10	0.475	1.386	0.038	0.046	0.012	0.321	0.26	0.90	0.10

Photosynthetic pigments (PS) include Chlorophyll (Chl), 19′hexanoyloxyfucoxanthin (19′hex), and fucoxanthin (Fuco). Photo-protective pigments (PP) include diadinoxanthin (DD), β-carotene (β-car), and diatoxanthin (DT). Chl a values are the average of HPLC and fluorometric (Fluor) values. HPLC values (N = 2) were within 2% of each other.

of modeled estimates of a^*_{ph} (λ) was improved by using a multiple linear regression with light and temperature,

$$a^*_{ph}(\lambda) = C_o + C_E PAR + C_T T, \quad (4)$$

where PAR is in units of μmol quanta m^{-2} s^{-1}, temperature (T) is in °C, C_o is the intercept of the multiple linear regression, C_E and C_T are the multiple linear regression coefficients for PAR and T. The multiple regression fit for a^*_{ph} (676) for temperature and light had an $r^2 = 0.82$ (**Figure 3B**), a considerable improvement compared to the fit for only irradiance ($r^2 = 0.62$, data not shown). A comparison of modeled (10 nm resolution) and observed (1 nm hyperspectral) a^*_{ph} (λ) are shown in **Figures 3C,D**. Our modeled values are in excellent agreement with measured a^*_{ph} (λ) in the visible region. Variability in a^*_{ph} (λ) between 300 and 400 nm is dominated by irradiance (Moisan and Mitchell, 2001) with negligible dependence on temperature (data not shown). For consistency, a single parameterization based on PAR and T is used for the full spectrum (300–700 nm). Coefficients for the model based on light and temperature are given in **Table 4**. The model does an excellent job of describing a^*_{ph} (λ) as illustrated for an extreme range of acclimation states representing high (**Figure 3C**) and low (**Figure 3D**) degrees of pigment packaging and changes in photosynthetic and photo-protective pigments relative to chlorophyll *a*. High relative error in the UV for the high light sample (**Figure 3C**) is caused in part because a^*_{ph} (330) is ∼10 times smaller than the low light example (**Figure 3D**) caused by changes in cellular concentrations of mycosporine-like amino acids relative to chlorophyll a (Moisan and Mitchell, 2001). There was insignificant irradiance in the system below 350 nm so the large variance in the a^*_{ph} (λ) model for data between 300 and350 nm did not affect the estimates of ϕ_μ or μ_n; see section Performance of the Biophysical Model of Net Growth for *P. antarctica* for dertails on model application and **Figures 5C,D** for results modeling ϕ_μ and μ_n .

Temperature and Light Dependence of the Quantum Yield for Growth: Observations and Modeling

The quantum yield for growth, ϕ_μ, is the molar ratio of carbon fixed for net growth to the quanta absorbed. Understanding

TABLE 3 | Growth fitting parameters of *Phaeocystis* grown between −1.5 and 4°C.

Temperature °C	α_μ	μ_{nm}	$E_{k\mu}$
−1.5	0.026 ± 0.003	0.95 ± 0.06	37
0	0.030 ± 0.006	0.99 ± 0.01	34
2	0.026 ± 0.006	1.06 ± 0.12	41
4	0.007 ± 0.001	0.93 ± 0.06	128

how ϕ_μ varies as a function of environmental conditions that are easily measured either *in situ* or remotely is critical in the parameterization of photosynthetic bio-optical models that have ecological relevance. We have chosen to estimate ϕ_μ in relation to light and temperature because they limit bloom formation, control cellular absorption, and enzymatic activity. Although phytoplankton may exhibit chromatic adaptation that optimizes the absorbing pigments to selectively absorb the modified under water light spectrum (Dubinsky and Stambler, 2009), the quantum yield of photosynthesis (oxygen evolved or carbon fixed per photon absorbed) is relatively flat from about 400–650 nm (Luning and Dring, 1985). In the classic review *Photosynthesis* by Rabinowitch and Govindjee (1969) they show the spectral quantum yield determined by Emerson and Lewis (1943) for *Chlorella pyrenoidosa* ranged from 0.07 to 0.09 over the spectral range 400–680 nm with the lowest values in the area of photoprotective carotenoids 480–510 nm. While this classic work shows very modest spectral variation in the spectral quantum yield of ±15% from 400 to 680 nm, there are other articles that show larger variations more like ±30%, including our work on the chlorophyll-a fluorescence yield of *P. antarctica* (Moisan and Mitchell, 2001) with a similar dip in the photoprotective carotenoid band and very low yields below 350 nm where mycosporine amino acids absorb. The work by (Luning and Dring, 1985) for 4 genera of macro algae indicated quantum yield varied by ±15% from 400 to 670 nm. There is spectral variation in the quantum yield that we did not determine in this study, but for the PAR region below 680 nm the variations are modest, depending on which study is cited.

We spectrally quantified total photon absorption and total carbon growth so we do not have resolution of the spectral dependence of ϕ_μ. The quantum yield for growth at steady state for experimental samples was estimated by rearranging Equation (1a),

$$\phi_\mu = \frac{\mu_n}{Chl : C \int_{350nm}^{700nm} a^*_{ph}(\lambda) E_0(\lambda) d\lambda}. \quad (5)$$

For our study, ϕ_μ varied by 30-fold (**Figure 4A**) ranging from 0.003 to 0.09 mol C (mol quanta absorbed)$^{-1}$. Values of ϕ_μ were highest at low irradiances and decreased at high light intensity but with a large difference in the relationship with light for different temperatures. For a given light level, ϕ_μ generally decreased with decreasing temperature (**Figure 4A**); the curve fitted to the 4°C was consistently higher than all other temperatures. Values of ϕ_μ for the 0 and 2°C treatments were similar to each other for the corresponding light treatments (t-test, $p > 0.05$). Our values for ϕ_μ are in the range previously reported for *Phaeocystis*-dominated blooms (SooHoo et al., 1987; Cota et al., 1994; Carder et al., 1995; Vaillancourt et al., 2003).

The quantum yield for net photosynthesis has previously been modeled as a product of the maximal quantum yield for net photosynthesis, ϕ_m and a Poisson probability function that an open photosynthetic unit will be hit. This model was originally formulated and validated with experiments on O_2 evolution by short-term flashes of light (Dubinsky et al., 1986; Falkowski and Raven, 2007) and adopted to model the quantum yield for growth (Sakshaug et al., 1989; Cullen, 1990). Typically, ϕ_m has been set for all acclimation states to the theoretical maximal value which is equal to 0.125 mol C (mol quanta absorbed)$^{-1}$ (e.g., Sakshaug et al., 1989). However, as reviewed by Laws et al. (2002), absorption by non-photosynthetic pigments will automatically result in quantum yields of photosynthesis less than the theoretical maximum. To address this important modeling issue, Moisan and Mitchell (1999) proposed a novel approach where the maximal quantum yield (ϕ_m) for each acclimated state was dependent on the irradiance. Here, we extend this concept of an environmentally controlled maximal quantum yield by also parameterizing it based on temperature which controls the thermodynamics of photosynthetic enzymes and therefore affects the quantum yield for growth. Thus, as we have shown for a^*_{ph} above, here we present a mechanistic control of ϕ_m based on co-limitation by light and temperature.

We found lower quantum yield for growth values at low light (<20 μmol quanta $m^{-2}s^{-1}$) whereas the cumulative hit Poisson Probability does not allow this roll off at low light. Johnsen and Barber (2003)have shown excellent experimental data that demonstrates that there are different photophysiological mechanisms at reduced light levels which contribute to a reduced quantum yield. Despite low quantum yields for growth and photosynthesis, there is experimental evidence that photosynthetic efficiency is not always maximal at low irradiances (Johnsen and Barber, 2003). Low photosynthetic quantum yield has been attributed to the Kok effect, S-state decay (S3 to S2), and imbalances in photosystem excitation (Diner and Mauzerall, 1973). Furthermore, it is expected that the ratio of respiration to photosynthesis may increase at very low light, leading to the observed reduction in quantum yield at very low light.

Given observed values of ϕ_μ, a function for $\phi_{mEo,T}$ was derived which exponentially decreased from low to high irradiances (**Figure 4B**). The equations used to predict $\phi_{mEo,T}$ are given below and the final estimate of ϕ_μ compared to observed values are plotted in in **Figure 5C**. Values of $\phi_{mEo,T}$ were described as a function of irradiance (**Figure 4B**) and the temperature dependence was incorporated into the coefficients a and b which are modeled as linear functions of temperature (**Table 5**),

$$\phi_{mEo,T} = ae^{-bEo}, \quad (6a)$$

$$a = 0.0125T + 0.058 \quad r^2 = 0.70 \quad (6b)$$

$$b = -0.0010T + 0.0075 \quad r^2 = 0.85 \quad (6c)$$

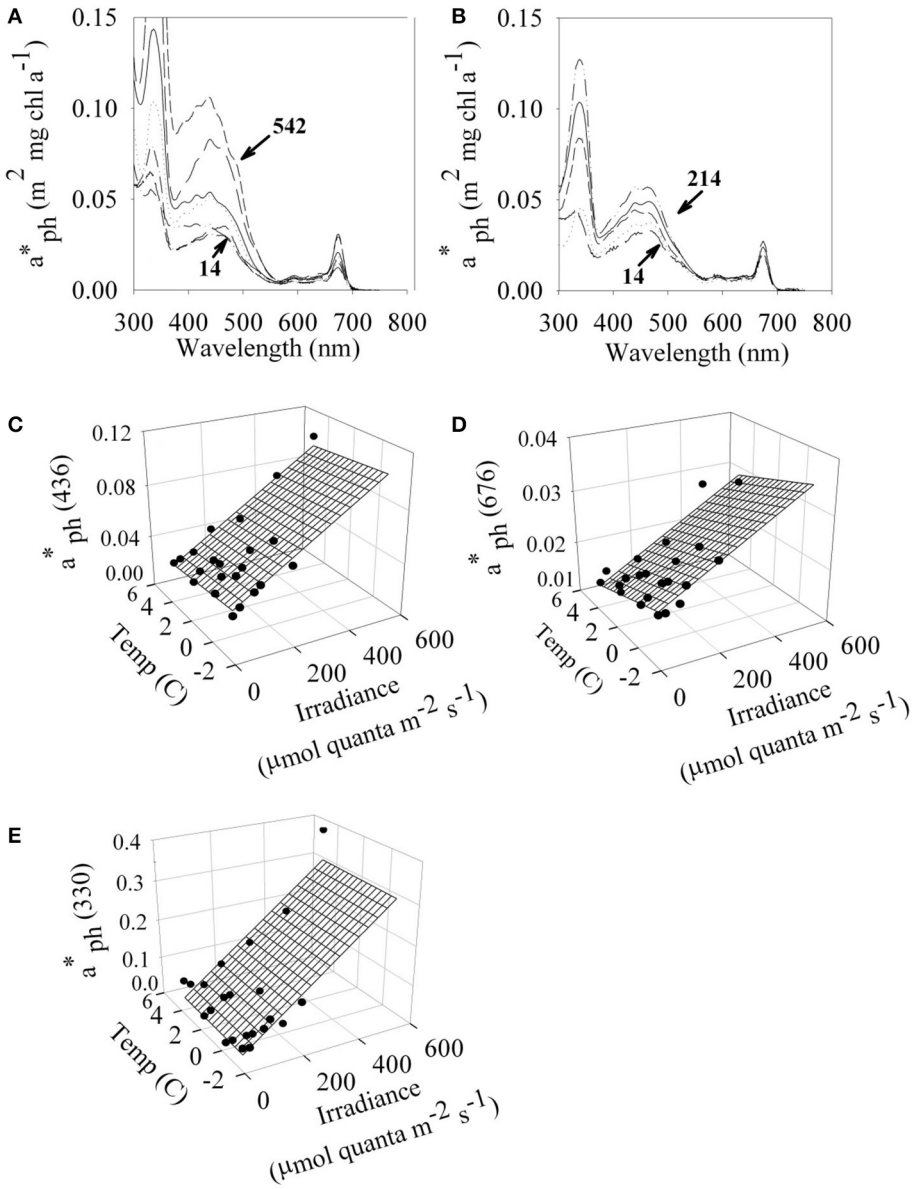

FIGURE 2 | Absorption characteristics of *P. antarctica*. *In vivo* chl-specific absorption spectrum (a^*_{ph} (λ)) for *P. antarctica* grown at **(A)** 4C and **(B)**−1.5°C between a range of irradiances (µmol quanta m^{-2} s^{-1}). Irradiance- and temperature- dependent values of a^*_{ph} (circles) at **(C)** 436 nm **(D)** 676 nm and **(E)** 330 nm. Multiple linear regressions based on temperature and light (continuous surface) are overlaid on the discrete points of a^*_{ph} (λ). Each point represents the average of 4 replicates. C.V. for a^*_{ph} (λ) values are 5%.

where T is temperature in °C and E_o is in units of µmol quanta m^{-2} s^{-1}. Values of a and b which are in Equation (6a) are linear relationships of parameters that rely on temperature. Values of $\phi_{mEo,T}$ and for Ekµ as estimated below were introduced into Equation (1b) to estimate ϕ_μ.

Performance of the Biophysical Model of Net Growth for *P. antarctica*

To test the performance of the biophysical model for net photosynthesis, we predicted a^*_{ph} (λ) and ϕ_μ using the temperature and light dependent model parameterizations as described above. Overall, the predicted values of a^*_{ph} (λ) underestimate the observed values by about 10% (**Figures 3C,D**, **5A**) with greatest accuracy achieved in the region between 350 and 700 nm. Relatively more scatter was seen in the UV region between 300 and 350 nm. **Figure 5B** is a compilation of net growth normalized to the maximum value of the experiment vs. irradiance for the data presented here, Moisan and Mitchell (1999), and data from the literature for the genus *Phaeocystis*. To estimate an $E_{k\mu}$ value to introduce into Equation (1b), we used a non-linear curve fit (Platt et al., 1980) for the full data synthesis in

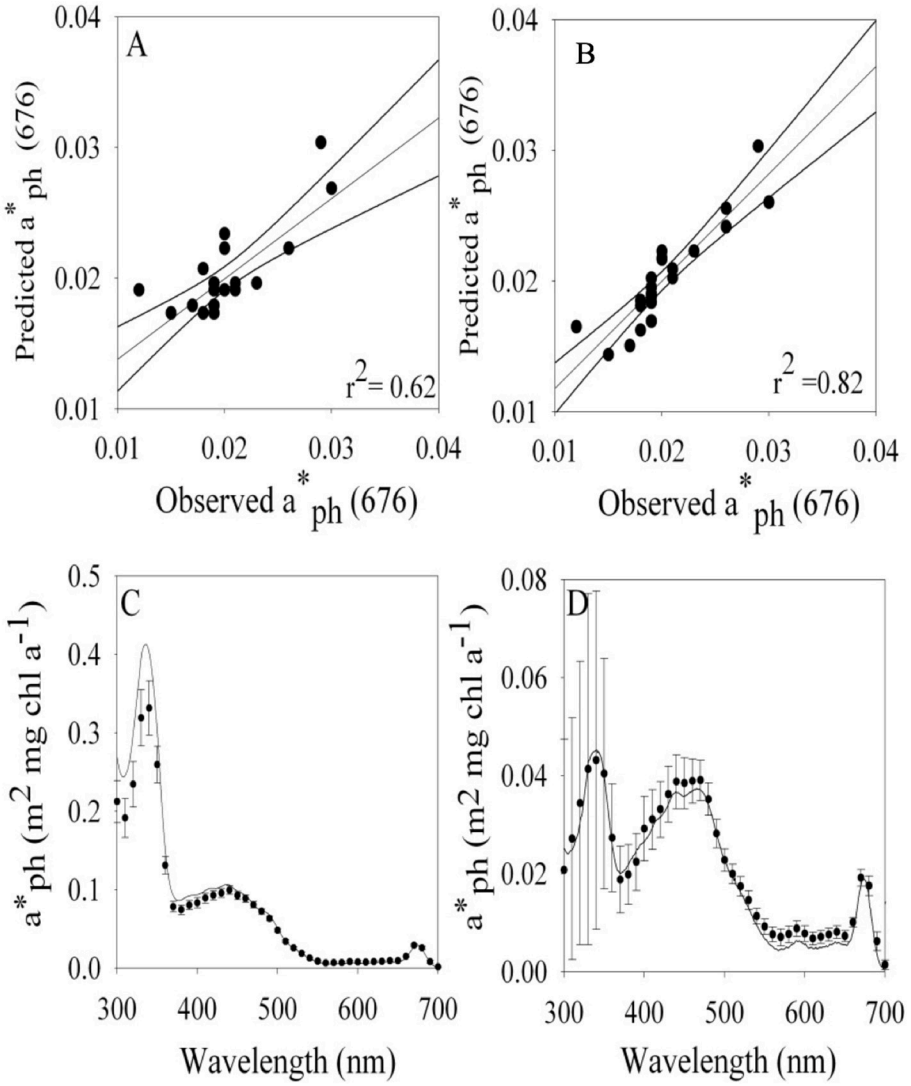

FIGURE 3 | Modeled vs. observed values of a^*_{ph} at 676 nm based on a linear regression using **(A)** light and **(B)** a multiple linear regression based on temperature and light. Comparison of a^*_{ph} (λ) observed (1 nm resolution continuous line) vs. modeled values (10 nm resolution) based on temperature and light for cultures grown at **(C)** 4°C 542 μmol quanta m^{-2} s^{-1} and −1.5°C and **(D)** 37 μmol quanta m^{-2} s^{-1}. Note scale difference in a^*_{ph} in **(C,D)**. Standard error bars are shown for model estimates.

Figure 5B. This fit resulted in a single value of μ_m and α for the full data set in **Figure 5B** that we used to estimate a generalized value of $E_{k\mu}$ (μ_m/α) for *Phaeocystis* spp. This resulted in a $E_{k\mu}$ value of 110 μmol quanta m^{-2} s^{-1} overall fit with $r^2 = 0.83$ (**Figure 5B**). We also explored modeling using $E_{k\mu}$ determined from each individual growth vs. irradiance data set at the different temperatures (**Figure 1A**) but that did not improve the overall variance in our biophysical model so we kept the model simpler by using one generalized value determined from our data and literature synthesis (**Figure 5B**).

We predicted values of ϕ_μ using a cumulative one hit Poisson probability parameterization where $\phi_{mEo,T}$ in Equation (1b) is predicted from temperature and light (Equation 5). The ϕ_μ model also requires an input variable for $E_{k\mu}$. **Figure 5B** combines data for *Phaeocystis* spp. presented in Moisan and Mitchell (1999) and the new data for −1.5, 0, and 2°C treatments that are presented here. Using the combined data set, we have derived an $E_{k\mu}$. Our sensitivity analysis shows that the ϕ_μ is the most sensitive to $\phi_{mEo,T}$ as compared to $E_{k\mu}$.We prefer the use of a composite $E_{k\mu}$ at this time although in principle it should depend on environmental acclimation, in this case the steady-state conditions we imposed in our experiment. Although we acknowledge that in nature both light and temperature may fluctuate on time scales faster than division rates and hence impact acclimation, our experiments were not designed to resolve that additional, and potentially important, variability. We conducted a sensitivity analysis of ϕ_μ that indicates that the relative magnitude of the error is greatest at high intensities; however, the absolute error is minor. These assumptions are justified on the basis that the entire equation is dependent on

TABLE 4 | Coefficients for multiple-linear regression model for a^*_{ph} (λ) based on temperature and light.

λ (nm)	C_0	C_E	C_T	Standard error of estimate	R^2
300	0.016	3.25E-04	0.0050	0.000715	0.79
310	0.020	2.96E-04	0.0027	0.000609	0.77
320	0.022	3.84E-04	0.0011	0.000834	0.79
330	0.022	5.42E-04	0.0007	0.001282	0.83
340	0.022	5.72E-04	−0.0001	0.001190	0.85
350	0.023	4.41E-04	−0.0007	0.000553	0.88
360	0.019	2.07E-04	−0.0002	0.000121	0.88
370	0.016	1.09E-04	0.0008	4.69E-05	0.85
380	0.017	9.93E-05	0.0008	3.71E-05	0.86
390	0.019	1.08E-04	0.0006	3.37E-05	0.89
400	0.021	1.11E-04	0.0004	2.83E-05	0.91
410	0.026	1.19E-04	−0.0004	3.72E-05	0.87
420	0.028	1.24E-04	−0.0006	3.27E-05	0.89
430	0.030	1.29E-04	−0.0010	3.21E-05	0.90
440	0.032	1.32E-04	−0.0011	3.05E-05	0.90
450	0.032	1.21E-04	−0.0013	2.74E-05	0.90
460	0.033	1.14E-04	−0.0014	2.07E-05	0.91
470	0.033	9.90E-05	−0.0015	1.66E-05	0.90
480	0.030	8.94E-05	−0.0015	1.12E-05	0.92
490	0.023	8.21E-05	−0.0012	8.63E-06	0.93
500	0.019	6.05E-05	−0.0010	5.40E-06	0.91
510	0.017	3.95E-05	−0.0011	3.92E-06	0.86
520	0.015	2.77E-05	−0.0011	4.49E-06	0.74
530	0.012	1.87E-05	−0.0010	3.63E-06	0.65
540	0.010	1.12E-05	−0.0008	2.64E-06	0.54
550	0.008	6.36E-06	−0.0007	2.42E-06	0.41
560	0.007	4.36E-06	−0.0006	2.21E-06	0.34
570	0.006	4.46E-06	−0.0005	2.76E-06	0.23
580	0.007	4.16E-06	−0.0005	2.76E-06	0.22
590	0.008	5.02E-06	−0.0006	2.45E-06	0.34
600	0.007	4.29E-06	−0.0004	2.41E-06	0.19
610	0.006	4.70E-06	−0.0003	1.79E-06	0.21
620	0.006	6.50E-06	−0.0004	1.57E-06	0.33
630	0.007	6.18E-06	−0.0004	1.57E-06	0.33
640	0.007	5.83E-06	−0.0003	1.68E-06	0.26
650	0.007	6.40E-06	−0.0002	1.13E-06	0.34
660	0.009	1.23E-05	−0.0003	2.28E-06	0.49
670	0.017	2.79E-05	−0.0008	3.04E-06	0.80
680	0.015	2.57E-05	−0.0009	4.18E-06	0.72
690	0.005	7.53E-06	−0.0004	3.77E-06	0.16
700	0.001	8.76E-07	−0.0001	9.27E-07	−0.03

See Equation (6) for abbreviated terms.

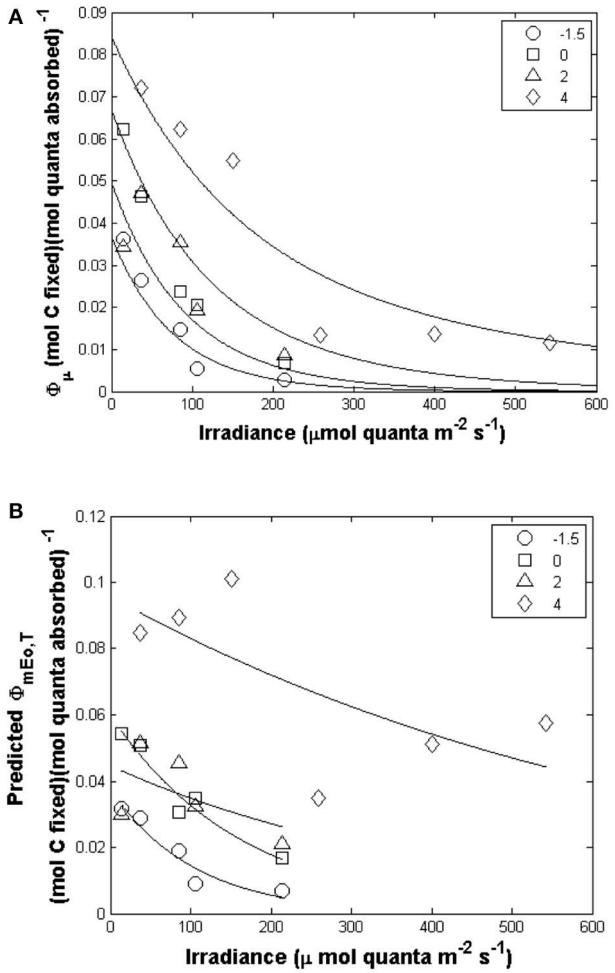

FIGURE 4 | (A) Light and temperature dependence of ϕ_μ (mol C (mol quanta absorbed)$^{-1}$) for *P. antarctica* (symbols). Our modeled ϕ_μ relationship with light and temperature (solid line) is calculated with a constant $E_{k\mu}$ and a modeled $\phi_{mEo,T}$ (Equation 6). **(B)** $\phi_{mEo,T}$ response to different temperature and irradiance treatments (Symbols are experimental observations, lines are model predictions). A fixed $E_{k\mu}$ value was used to calculate $\phi_{mEo,T}$.

φ_{max}. We do observe some variability in $E_{k\mu}$ between the lower temperature treatments and the 4°C treatment (**Figure 1A**). We derived a composite $E_{k\mu}$ from the intersection between the initial slope of the growth curve and the maximal growth rate (**Figure 5B**). The use of a generic $E_{k\mu}$ is appropriate because of the overall variability in growth curves with respect to irradiance for various *Phaeocystis* spp. Also, a sensitivity analysis of $E_{k\mu}$ within the model revealed that ϕ_μ was relatively insensitive to the changes that we observed in $E_{k\mu}$. Using an $E_{k\mu}$ value of 110 μmol quanta m^{-2} s^{-1} and a temperature-light dependent model of $\phi_{mEo,T}$ results in an excellent prediction of ϕ_μ (**Figure 5C**, $r^2 = 0.80$). Using these individual component models for a^*_{ph} (λ) and $\phi_{mEo,T}$ in Equations (1a,b), a comparison between observed and predicted values of μ_n (**Figure 5D**; $r^2 = 0.66$). The simple empirical model using only temperature and light resulted in a slightly better estimate ($r^2 = 0.70$; **Figure 1C**) however that empirical approach does not include the mechanistic dynamics of changes in a^*_{ph} (λ) and $\phi_{mEo,T}$ that represent how light and temperature co-limitation regulate the cellular physiology.

Although we used a single value of $E_{k\mu}$ a sensitivity analysis proved that using the estimated $E_{k\mu}$ for the different temperatures did not improve our model fit. Also, our quantum yields for growth are a net process of growth after respiration which can be important in nature (Grégori et al., 2002; Siegel et al., 2002; Marra and Barber, 2004; López-Urrutia et al., 2006).

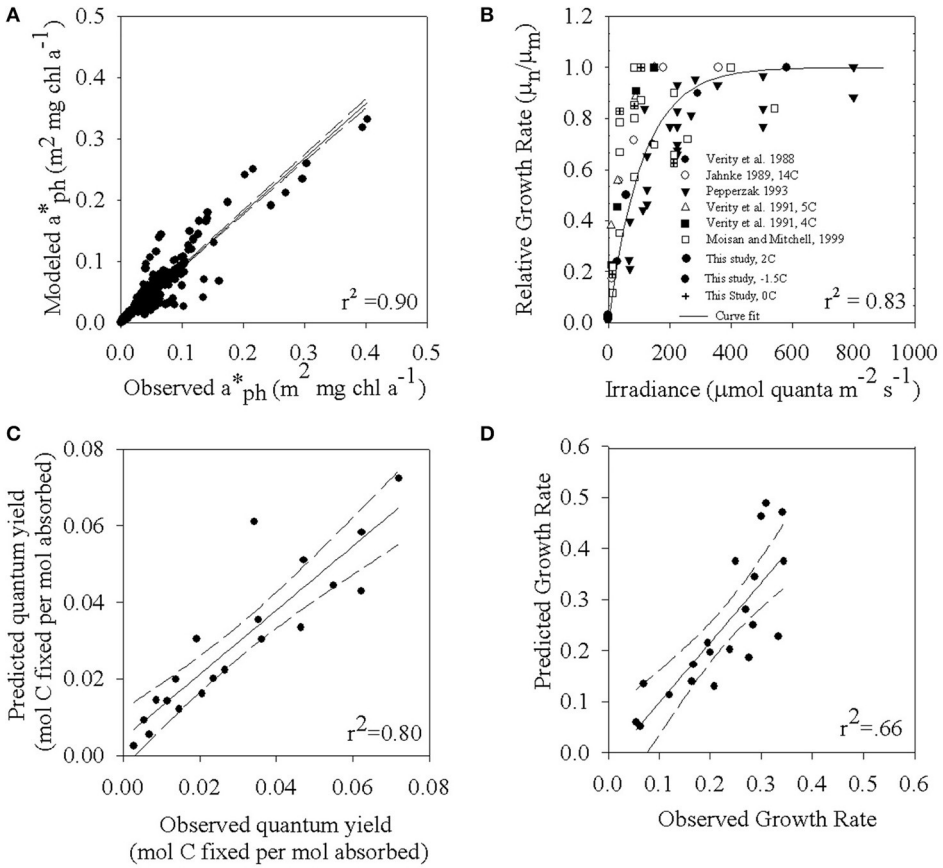

FIGURE 5 | (A) The relationship between modeled a^*_{ph} (λ) based on temperature and light (Equation 6, **Table 4**) and observed values at individual wavelengths. **(B)** Relative growth rates measured from various *Phaeocystis* species grown under a variety of temperature and irradiance regimes. Note that there are overlapping data points. **(C)** Modeled ϕ_μ vs. observed values. There are overlapping points. **(D)** Relationship between the observed carbon-specific growth rate and model predictions of carbon-specific rate of net growth (μ_n). Model is based on Equation (1) and **Table 4**.

TABLE 5 | Model variables for maximal quantum yield based on irradiance at discrete temperatures.

Temperature	*a* value	*b* value	r^2 value
−1.5	0.0377	−0.0095	0.90
0	0.0600	−0.0061	0.93
2	0.0447	−0.0025	0.09
4	0.0958	−0.0014	0.32

Values of ϕ_m are described as an exponential function of irradiance with the form, $\phi_{mE_o}=ae^{-bE_o}$.

Our quantum yield for net growth calculations can be defined by:

$$\phi_{\mu n} = \frac{\mu_n C}{E_{absorbed}} = \frac{P-R}{E_{absorbed}}.$$

Although respiration is often modeled as a fixed ratio to growth rate, or a basal a rate plus a fixed fraction of growth rate, this likely is not so simple. There are relatively few data sets in the literature for phytoplankton respiration over a range of growth conditions and we did not estimate respiration for our study. Respiration data that is commonly used in models is very noisy (Laws and Bannister, 1980; Geider et al., 1998) and is mostly limited to a modest range of intensity from about 50–200 μmol quanta m^{-2} s^{-1} so the fidelity of respiration models may not be robust over the full range of light intensity that is relevant to phytoplankton communities. One expects that the ratio of respiration to net growth (R/μ_n) will actually go to infinity at the limit as light goes to zero where there is no photosynthesis but basal respiration continues. Also, for the growth inhibiting irradiances greater than about 150 μmol quanta m^{-2} s^{-1} we observed at lower temperatures (**Figure 1A**), we speculate that the ratio of R/μ_n also must increase. Models that assume a basal respiration rate plus a fixed fraction of growth rate will not predict this increase in R/μ_n at higher growth inhibiting irradiances but will instead predict lower respiration as growth rate decreases. This seems flawed since inhibiting irradiances would cause damage from oxidative stress and hence very likely a greater respiration rate, not a lower rate. These two thought experiments based on simple logic indicate that it is important to obtain more data that includes respiration at very low light that and also at high growth inhibiting irradiances, but such data is lacking in the literature.

Our biophysical model includes explicit descriptions of the regulation of absorption and quantum yield by environmental controls which results both in an accurate model of net growth and captures details of light and temperature regulation of the biophysical variables that mediate light utilization. Our quantum yields for growth were calculated in a traditional way of modeling based on carbon, chlorophyll a, phytoplankton absorption, and spectral irradiance flux. However, our estimates are relatively high compared to other phytoplankton; our high C: chl a ratios are above the typical ratio of 75–150 for phytoplankton (Falkowski and Raven, 2007). This is likely due to the fact that *Phaeocystis* can accumulate a carbohydrate/glucan-rich mucilage that is not metabolically active in addition to metabolically active cellular carbon. Mathot et al. (2000) estimates that mucus-related carbon at peak bloom is about 14 ± 4% of total colony carbon but mucus-related carbon may be as high as 90% for a senescent bloom (Verity and Medlin, 2003). The colonial matrix acts as a spillover mechanism probably for storage of low molecular weight compounds (Lancelot and Mathot, 1985) and hence may accumulate when there is excess light.

Although natural systems may have substantial variations in both light and temperature over time-scales that are much less than the doubling times that will affect acclimation of algae in a more complicated way than the simple steady-state experiments we conducted, it is very time consuming to try to add that complexity to the matrix of growth and acclimation control. There is a relatively small literature for the steady-state co-limitation of light, nutrients and temperature acclimation of cellular pigments, absorption, quantum yield and growth (Laws and Bannister, 1980; Kiefer and Mitchell, 1983; Sosik and Mitchell, 1991, 1994; Geider et al., 1997). There is even more limited knowledge for cold water obligate psychrophiles like *P. antarctica*, for example the study of Luxem et al. (2017) who explored light and iron limitation for this organism. In the area of applied phycology aimed at commercial production, recent work with a similar experimental design for light and temperature as ours, for the seaweed *Gracilaria*, Nejrup et al. (2013), reported growth rates and metabolic capacity. Grobbelaar et al. (1996) have explored microalgae acclimated to different light levels, then exposed to light fluctuations that would be found in commercial cultivation. However, neither of these studies quantified spectral absorption or quantum yield, that ultimately underlie the responses for growth and bulk PvsE relationships. Our work advances the state of knowledge with greater detail of how light and temperature combined affect acclimation of the fundamental biophysical parameters light absorption and quantum yield of algae and provides a level of detail not previously reported for the ecologically important prymnesiophyte, *Phaeocystis antarctica*, that is a key structural component of the Southern Ocean and that may show changes in its role as stratification and heating of the Southern Ocean change both light and temperature climate in the future.

CONCLUSIONS

Understanding the contribution of *Phaeocystis* in the overall global carbon cycle is important because this genus can dominate mesoscale blooms and make a significant contribution to the carbon and sulfur cycle for open and coastal oceans as well in the vicinity of ice edges. The strain of *P. antarctica* we used for these experiments exhibits flexibility in its ability to absorb light due to changes in cell size and the cellular concentrations of photoprotective and photosynthetic pigments that are regulated by light and temperature co-limitation. These cellular changes have consequences for how *P. antarctica* captures light required for carbon fixation. Photo-protective pigments that divert absorbed photons from the photosynthetic reaction centers will automatically result in photosynthetic quantum yields below the theoretical maximum. Using data from our controlled laboratory experiments, we have developed both empirical and biophysical models that predict growth rates based on knowledge of chlorophyll a, light, and temperature. It is important to note that unlike some proposed models that depend only on easily measured variables our biophysical model, a^*_{ph} (λ) and ϕ_μ is parameterized based on light and temperature since nutrients are not regulating during the onset and development of blooms. We propose a conceptually important improvement over previous models by accepting the fact that the maximum quantum yield for any acclimated state may be considerably less than the theoretical maximum (Moisan and Mitchell, 1999) and that it should be regulated by environmental control, in this case light and temperature co-regulation. In general, a^*_{ph} (λ), E_{km} and ϕ_μ, should all be modeled as variables determined by the simultaneous interaction of light, temperature, and nutrients. Furthermore, future ocean color missions with hyperspectral ability, such as PACE, may be capable of remote sensing phytoplankton spectral shape that we document changes significantly with different acclimation states (**Figure 2**). Such a capability might allow a link between community structure, photosynthetic processes and the biophysical model for absorption, cellular pigmentation and pigment packaging that is dependent on light and temperature co-limitation (see also Wang et al., 2016; Moisan et al., 2017). While this level of detail remains aspirational for our community, an accurate understanding of how biophysical variables (Equation 1) depend on the full matrix of environmental forcing requires these essential but time-consuming laboratory studies for representative taxa over the full range of environmental variability experienced by phytoplankton to advance our ability to apply advanced remote sensing methods to coastal processes of primary production and the carbon cycle.

AUTHOR CONTRIBUTIONS

TM: Supervised all experiment, sample analysis and data analysis; TM and BGM: Contributed equally to writing, editing, graphics, and tables.

FUNDING

Support for this work was provided by ONR grant N00014-91-J-1186 and NASA Award # NNX15AC98G (BGM) and the NASA Biodiversity Program (05-TEB/05-0016) (TM).

ACKNOWLEDGMENTS

We thank S. Cheng for excellent technical assistance; M. Vernet for insightful recommendations throughout this study and comments on earlier versions of the manuscript; M. Olaizola and R. Goericke for assistance with HPLC analysis and thoughtful discussions regarding pigment data; N. Delaney, N. Crawford, M. Cape, and M. Linkswiler for programming assistance; and M. Anderson for final manuscript preparation.

REFERENCES

Arrigo, K. R., Robinson, D. H., Worthen, D. L., Dunbar, R. B., DiTullio, G. R., VanWoert, M., et al. (1999). Phytoplankton community structure and the drawdown of nutrients and CO_2 in the southern ocean. *Science* 283, 365–367. doi: 10.1126/science.283.5400.365

Arrigo, K. R., Worthen, D., Schnell, A., and Lizotte, M. P. (1998). Primary production in Southern Ocean waters. *J. Geophys. Res.* 103, 15587–15600.

Arteaga, L., Pahlow, M., and Oschlies, A. (2014). Global patterns of phytoplankton nutrient and light co-limitation inferred from an optimality GÇÉ based model. *Glob. Biogeochem. Cycle* 28, 648–661. doi: 10.1002/2013GB004668

Arteaga, L., Pahlow, M., and Oschlies, A. (2016). Modeled Chl: C ratio and derived estimates of phytoplankton carbon biomass and its contribution to total particulate organic carbon in the global surface ocean. *Glob. Biogeochem. Cycle* 30, 1791–1810. doi: 10.1002/2016GB005458

Behrenfeld, M. J., Boss, E., Siegel, D. A., and Shea, D. M. (2005). Carbon-based ocean productivity and phytoplankton physiology from space. *Glob. Biogeochem. Cycle* 19:GB1006. doi: 10.1029/2004GB002299

Behrenfeld, M. J., Marañón, E., Siegel, D. A., and Hooker, S. B. (2002). Photoacclimation and nutrient-based model of light-saturated photosynthesis for quantifying oceanic primary production. *Mar. Ecol. Prog. Ser.* 228, 103–117. doi: 10.3354/meps228103

Carder, K. L., Lee, Z. P., Marra, J., Steward, R. G., and Perry, M. J. (1995). Calculated quantum yield of photosynthesis of phytoplankton in the marine light-mixed layers (59oN, 21oW). *J. Geophys. Res.* 100, 6655–6663.

Ciotti, A. M., Lewis, M. R., and Cullen, J. J. (2002). Assessment of the relationships between dominant cell size in natural phytoplankton communities and the spectral shape of the absorption coefficient. *Limnol. Oceanogr.* 47, 404–417. doi: 10.4319/lo.2002.47.2.0404

Cleveland, J. S., Perry, M. J., Kiefer, D. A., and Talbot, M. C. (1989). Maximum quantum yield of photosynthesis in the northwestern Sargasso Sea. *J. Mar. Res.* 47, 869–892. doi: 10.1357/002224089785076055

Cota, G. F., Smith, W. O. Jr., and Mitchell, B. G. (1994). Photosynthesis of *Phaeocystis* in the Greenland Sea. *Limnol. Oceanogr.* 39, 948–953. doi: 10.4319/lo.1994.39.4.0948

Cullen, J. J. (1990). On models of growth and photosynthesis in phytoplankton. *Deep Sea Res. Part A* 37, 667–683.

Diner, B., and Mauzerall, D. (1973). Feedback controlling oxygen production in a cross-reaction between two photosystems in photosynthesis. *Biochim. Biophys. Acta* 305, 329–352.

DiTullio, G. R., Grebmeier, J. M., Arrigo, K. R., Lizotte, M. P., Robinson, D. H., Leventer, A., et al. (2000). Rapid and early export of *Phaeocystis antarctica* blooms in the Ross Sea, Antarctica. *Nature* 404, 595–598. doi: 10.1038/35007061

Droop, M. R. (1983). 25 years of algal growth kinetics: a personal view. *Bot. Mar.* 26, 99–112.

Dubinsky, Z., Falkowski, P. G., and Wyman, K. (1986). Light harvesting and utilization by phytoplankton. *Plant Cell Physiol.* 27, 1335–1349. doi: 10.1093/oxfordjournals.pcp.a077232

Dubinsky, Z. V., and Stambler, N. (2009). Photoacclimation processes in phytoplankton: mechanisms, consequences, and applications. *Aquat. Microb. Ecol.* 56, 163–176. doi: 10.3354/ame01345

Edwards, K. F., Thomas, M. K., Klausmeier, C. A., and Litchman, E. (2016). Phytoplankton growth and the interaction of light and temperature: a synthesis at the species and community level. *Limnol. Oceanogr.* 61, 1232–1244. doi: 10.1002/lno.10282

Emerson, R., and Lewis, C. M. (1943). The dependence of the quantum yield of photosynthesis on the wavelength of light. *Am. J. Bot.* 30, 165–178.

Eppley, R. W. (1972). Temperature and phytoplankton growth in the sea. *Fish. Bull. Nat. Ocean. Atmos. Adm.* 70, 1063–1085.

Falkowski, P. G., and Raven, J. (2007). *Aquatic Photosynthesis, 2nd Edn*. Princeton, NJ: Princeton University Press.

Geider, R. J., MacIntyre, H. L., and Kana, T. M. (1997). Dynamic model of phytoplankton growth and acclimation: responses of the balanced growth rate and the chlorophyll *a*: carbon ratio to light, nutrient-limitation and temperature. *Mar. Ecol. Prog. Ser.* 148l, 187–200.

Geider, R. J., MacIntyre, H. L., and Kana, T. M. (1998). A dynamic regulatory model of phytoplanktonic acclimation to light, nutrients, and temperature. *Limnol. Oceanogr.* 43, 679–694.

Gieskes, W. W. C., Leterme, S. C., Peletier, H., Edwards, M., and Reid, P. C. (2007). Phaeocystis colony distribution in the North Atlantic Ocean since 1948, and interpretation of long-term changes in the *Phaeocystis* hotspot in the North Sea. *Biochemistry* 83, 49–60. doi: 10.1007/s10533-007-9082-6

Goldman, J. C., and Carpenter, E. J. (1974). A kinetic approach to the effect of temperature on algal growth. *Limnol. Oceanogr.* 19, 756–766.

Graff, J. R., Westberry, T. K., Milligan, A. J., Brown, M., Dall'Olmo, G., Reifel, K. M., et al. (2016). Photoacclimation of natural phytoplankton communities. *Mar. Ecol. Prog. Ser.* 542, 51–62. doi: 10.3354/meps11539

Grégori, G., Denis, M., Lefèvre, D., and Beker, B. (2002). A flow cytometric approach to assess phytoplankton respiration. *Methods Cell Sci.* 24, 99–106. doi: 10.1023/A:1024110418448

Grobbelaar, J. U., Nedbal, L., and Tichy, V. (1996). Influence of high frequency light/dark fluctuations on photosynthetic characteristics of microalgae photoacclimated to different light intensities and implications for mass algal cultivation. *J. Appl. Phycol.* 8, 335–343. doi: 10.1007/BF02178576

Gulliard, R. R., and Ryther, J. H. (1962). Studies on marine planktonic diatoms. I. *Cyclotella nana* Hustedt and *Detonula confervacea* (Cleve) Gran. *Can. J. Microbiol.* 8, 229–239.

Gypens, N., Lacroix, G., and Lancelot, C. (2007). Causes of variability in diatom and Phaeocystis blooms in Belgian coastal waters between 1989 and 2003: a model study. *J. Sea Res.* 57, 19–35. doi: 10.1016/j.seares.2006.07.004

Johnsen, Z., and Barber, R. T. (2003). The low-light reduction in the quantum yield of photosynthesis: potential errors and biases when calculating the maximal quantum yield. *Photosyn. Res.* 75, 85–95. doi: 10.1023/A:1022440305765

Kiefer, D. A., and Mitchell, B. G. (1983). A simple steady state description of phytoplankton growth based on absorption cross section and quantum efficiency. *Limnol. Oceanogr.* 28, 770–776.

Kishino, M., Takahashi, M., Okami, N., and Ichimura, S. (1985). Estimation of spectral absorption coefficients of phytoplankton in the sea. *Bull. Mar. Sci.* 37, 634–642.

Lacour, T., Lariviere, J., and Babin, M. (2017). Growth, Chl a content, photosynthesis, and elemental composition in polar and temperate microalgae. *Limnol. Oceanogr.* 1, 43–48. doi: 10.1002/lno.10369

Lancelot, C., and Mathot, S. (1985). Biochemical fractionation of primary production by phytoplankton in Belgian coastal waters during short- and long-term incubations with C-bicarbonate II. *Phaeocystis poucheti* colonial population. *Mar. Biol.* 86, 227–232.

Laws, E. A., and Bannister, T. T. (1980). Nutrient- and light-limited growth of *Thalassiosira fluviatilis* in continuous culture, with implications for phytoplankton growth in the ocean. *Limnol. Oceanogr.* 25, 457–473.

Laws, E., Sakshaug, E., Babin, M., Dandonneau, Y., Falkowski, P., Geider, R., et al. (2002). *Photosynthesis and primary productivity in marine ecosystems: Practical aspects and application of techniques*. Scientific Committee on Oceanic Research, JGOFS Report No. 36, 1–89.

Li, W. K. W. (1980). "Temperature adaptation in phytoplankton: cellular and photosynthetic characteristics," in *Primary Productivity in the Sea,* ed P. G. Falkowski (New York, NY: Plenum), 259–279.

Lizotte, M. P., and Sullivan, C. W. (1991). Photosynthesis-irradiance relationships in microalgae associated with Antarctic pack ice: evidence for *in situ* activity. *Mar. Ecol. Prog. Ser*. 71, 175–184. doi: 10.3354/meps071175

López-Urrutia, A., San Martin, E., Harris R. P., and Irigoien, X. (2006). Scaling the metabolic balance of the oceans. *Proc. Natl. Acad. Sci. U.S.A*. 103, 8739–8744. doi: 10.1073/pnas.0601137103

Luning, K., and Dring, M. J. (1985). Action spectra and spectral quantum yield of photosynthesis in marine macroalgae with thin and thick thalli. *Mar. Biol*. 87, 119–129. doi: 10.1007/BF00539419

Luxem, K. E., Ellwood, M. J., and Strzepek, R. F. (2017). Intraspecific variability in *Phaeocystis antarctica*'s response to iron and light stress. *PLoS ONE* 12:e0179751. doi: 10.1371/journal.pone.0179751

Marquardt, D. W. (1963). An algorithm for least squares estimations of parameters. *J. Soc. Ind. Appl. Math*. 11, 431–441.

Marra, J., and Barber, R. T. (2004). Phytoplankton and heterotrophic respiration in the surface layer of the ocean. *Geophys. Res. Lett*. 31:L09314. doi: 10.1029/2004GL019664

Marra, J., Langdon, C., and Knudson, C. A. (1995). Primary production, water column changes, and the demise of *Phaeocystis* bloom at the Marine Light-Mixed Layers site (59oN, 21oW) in the northeast Atlantic Ocean. *J. Geophys. Res.* 100, 6633–6643.

Mathot, S., Smith,W. O. Jr., Carlson,. C. A., Garrison, D. L., Gowing, M. M., and Vickers, C. L. (2000). Carbon partitioning within *Phaeocystis antarctica* (Prymnesiophyceae) colonies in the Ross Sea, Antarctica. *J. Phycol*. 36, 1049–1056. doi: 10.1046/j.1529-8817.2000.99078.x

Mitchell, B. G. (1990). "Algorithms for determining the absorption coefficient of aquatic particulates using the quantitative filter technique (QFT)," in *Ocean Optics X*, ed R. Spinrad (Bellingham, WA: SPIE), 37–148.

Mitchell, B. G., Bricaud, A., Carder, K., Cleveland, J., Ferrari, G., Gould, R., et al. (2000). "Determination of spectral absorption coefficients of particles, dissolved material and phytoplankton for discrete water samples," in *Ocean Optics Protocols For Satellite Ocean Color Sensor Validation* (Greenbelt, MD: NASA/TM-2000-209966), 125–153.

Mitchell, B. G., and Kiefer, D. A. (1988). Variability in pigment specific particulate fluorescence and absorption spectra in the northeastern Pacific Ocean. *Deep Sea Res. Part I* 35, 665–689.

Moisan, J. R., Moisan, T. A., and Abbot, M. R. (2002). Modeling the effects of temperature on the maximum growth rates of phytoplankton growth. *Ecol. Model*. 153, 197–215. doi: 10.1016/S0304-3800(02)00008-X

Moisan, T. A., Ellisman, M. H., Buitenhuys, C. W., and Sosinsky, G. E. (2006). Differences in chloroplast ultrastructure of *Phaeocystis antarctica* in low and high light. *Mar. Biol*. 149, 1281–1290. doi: 10.1007/s00227-006-0321-5

Moisan, T. A., and Mitchell, B. G. (1999). Photophysiological adaptation of *Phaeocystis antarctica* Karsten under PAR light limitation. *Limnol. Oceanogr*. 44, 247–258. doi: 10.4319/lo.1999.44.2.0247

Moisan, T. A., and Mitchell, B. G. (2001). UV absorption by mycosporine-like amino acids in *Phaeocystis antarctica* Karsten. *Mar. Biol*. 138, 217–227. doi: 10.1007/s002270000424

Moisan, T. A., Rufty, K. M., Moisan, J. R., and Linkswiler, M. A. (2017). Satellite observations of phytoplankton functional type spatial distributions, phenology, diversity, and ecotones. *Front. Mar. Sci*. 4:189. doi: 10.3389/fmars.2017.00189

Nejrup, L. B., Staehr, P. A., and Thomsen, M. S. (2013). Temperature- and light-dependent growth and metabolism of the invasive red algae *Gracilaria vermiculophylla* - a comparison with two native macroalgae. *Eur. J. Phycol*. 48, 295–308. doi: 10.1080/09670262.2013.830778

Nelson, N. B., and Prézelin, B. B. (1990). Chromatic light effects and physiological modeling of absorption properties of *Heterocapsa pygmaea* (= *Glenodinium* sp.). *Mar. Ecol. Prog. Ser*. 63, 37–46.

Pabi, S., and Arrigo, K. R. (2006). Satellite estimation of marine particulate organic carbon in waters dominated by different phytoplankton taxa. *J. Geophys. Res*. 111:C09003,

Pavlov, A. K., Taskjelle, T., Kauko, H. M., Hamre, B., Hudson, S. R., Assmy, P., et al. (2017). Altered inherent optical properties and estimates of the underwater light field during an Arctic under-ice bloom of *Phaeocystis pouchetii*. *J. Geophys. Res. Oceans* 122, 4939–4961. doi: 10.1002/2016JC012471

Platt, T., Gallegos, C. L., and Harrison, W. G. (1980). Photoinhibition of photosynthesis in natural assemblages of marine phytoplankton. *J. Mar. Res*. 38, 687–701.

Rabinowitch, E., and Govindjee, R. (1969). *Photosynthesis*. New York, NY: J.Wiley.

Reynolds, R. A., Stramski, D., and Mitchell, B. G. (2001). A chlorophyll-dependent semi-analytical reflectance model derived from field measurements of absorption and backscattering coefficients within the Southern Ocean. *J. Geophys. Res*. 106, 7125–7138. doi: 10.1029/1999JC000311

Rhee, G. Y., and Gotham, I. J. (1981a). The effect of environmental factors on phytoplankton growth: light and the interactions of light with nitrate limitation. *Limnol. Oceanogr*. 26, 649–659.

Rhee, G. Y., and Gotham, I. J. (1981b). The effect of environmental factors on phytoplankton growth: temperature and the interactions of temperature with nutrient limitation. *Limnol. Oceanogr*. 26, 635–648.

Sakshaug, E., Andresen, K., and Kiefer, D. A. (1989). A steady state description of growth and light absorption in the marine planktonic diatom *Skeletonema costatum*. *Limnol. Oceanogr*. 34, 198–205. doi: 10.4319/lo.1989.34.1.0198

Sedwick, P. N. (2007). Evidence of high iron requirements of colonial *Phaeocystis antarctica* at low irradiance. *Biochemistry* 83, 83–97. doi: 10.1007/s10533-007-9081-7

Shuter, B. (1979). A model of physiological adaptation in unicellular algae. *J. Theor. Biol*. 78, 519–552.

Siegel, D. A., Doney, S. C., and Yoder, J. A. (2002). The North Atlantic spring Phytoplankton bloom and Sverdrup's critical depth hypothesis. *Science* 296, 730–733. doi: 10.1126/science.1069174

Smith, R. C., Prézelin, B. B., Bidigare, R. R., and Baker, K. S. (1989). Bio-optical modeling of photosynthetic production in coastal waters. *Limnol. Oceanogr*. 34, 1524–1544.

Smith, W. O. Jr., Codispoti, L. A., Nelson, D. M., Manley, T., Buskey, E. J., Niebauer, H. J., et al. (1991). Importance of *Phaeocystis* blooms in the high-latitude ocean carbon cycle. *Nature* 352, 514–516.

Smith, W. O., Dennett, M. R., Mathot, S., and Caron, D. A. (2003). The temporal dynamics of the flagellated and colonial stages of *Phaeocystis antarctica* in the Ross Sea. *Deep Sea Res. Part II* 50, 605–617. doi: 10.1016/S0967-0645(02)00586-6

Smith, W. O., Shields, A. R., Peloquin, J. A., Catalano, G., Tozzi, S., Dinniman, M. S., et al. (2006). Interannual variations in nutrients, net community production, and biogeochemical cycles in the Ross Sea. *Deep Sea Res. Part II* 53, 815–833. doi: 10.1016/j.dsr2.2006.02.014

SooHoo, J. B., Palmisano, A. C., Kottmeier, S. T., Lizotte, M. P., SooHoo, S. L., and Sullivan, C. W. (1987). Spectral light absorption and quantum yield of photosynthesis in sea ice microalgae and a bloom of Phaeocystis pouchetii from McMurdo Sound, Antarctica. *Mar. Ecol. Prog. Ser*. 39, 175–189.

Sosik, H. M. (1996). Bio-optical modeling of primary production: consequences of variability in quantum yield and specific absorption. *Mar. Ecol. Prog. Ser*. 143, 225–238.

Sosik, H. M., and Mitchell, B. G. (1991). Absorption, fluorescence and quantum yield for growth in nitrogen limited *Dunaliella tertiolecta*. *Limnol. Oceanogr*. 36, 910–921. doi: 10.4319/lo.1991.36.5.0910

Sosik, H. M., and Mitchell, B. G. (1994). Effects of temperature on growth, light absorption, and quantum yield in *Dunalliela tertiolecta* (chlorophyceae). *J. Phycol*. 30, 833–840.

Sosik, H. M., and Mitchell, B. G. (1995). Light absorption by phytoplankton, photosynthetic pigments, and detritus in the California current system. *Deep Sea Res. Part I* 42, 1717–1748. doi: 10.1016/0967-0637(95)00081-G

Stuart, V., Sathyendranath, S., Head, E. J. H., Platt, T., Irwin, B., and Maass, H. (2000). Bio-optical characteristics of diatoms and prymnesiophyte populations in the Labrador Sea. *Mar. Ecol. Prog. Ser*. 201, 91–106. doi: 10.3354/meps201091 (Sverdrup's Critical Depth Hypothesis. Science 296, 730–733).

Sunda, W. G., and Huntsman, S. A. (1997). Interrelated influence of iron, light and cell size on marine phytoplankton growth. *Nature* 390, 389–392. doi: 10.1038/37093

Sunda, W. G., and Huntsman, S. A. (2011). Interactive effects of light and temperature on iron limitation in a marine diatom: implications for marine productivity and carbon cycling. *Limnol. Oceanogr*. 56, 1475–1488. doi: 10.4319/lo.2011.56.4.1475

Tilzer, M. M., and Dubinsky, Z. (1987). Effects of temperature and day length on the mass balance of Antarctic Phytoplankton. *Polar Biol.* 7, 35–42.

Vaillancourt, R. D., Marra, J., Barber, R. T., and Smith, W. O. (2003). Primary productivity and *in situ* quantum yields in the Ross Sea and Pacific Sector of the Antarctic circumpolar current. *Deep Sea Res. Partt. II* 50, 559–578. doi: 10.1016/S0967-0645(02)00584-2

van Leeuwe, M. A., and Stefels, J. (2007). Photosynthetic responses in *Phaeocystis antarctica* towards varying light and iron conditions. *Biochemistry* 83, 61–70. doi: 10.1007/s10533-007-9083-5

van Leeuwe, M. A., Stefels, J., Belviso, S., Lancelot, C., Verity, P. G., and Gieskes, W. W. C. (2007). *Phaeocystis, Major Link in the Biogeochemical Cycling of Climate-Relevant Elements*. Dordrecht: Springer.

Verity, P. G., and Medlin, L. K. (2003). Observations on colony formation by the cosmopolitan phytoplankton genus Phaeocystis. *J. Mar. Syst.* 43, 153–164. doi: 10.1016/j.jmarsys.2003.09.001

Wang, G., Lee, Z. P., Mishra, D. R., and Ma, R. (2016). Retrieving absorption coefficients of multiple phytoplankton pigments from hyperspectral remote sensing reflectance measured over cyanobacteria bloom waters. *Limnol.Oceanogr. Methods* 14, 432–447. doi: 10.1002/lom3.10102

Welschmeyer, N. A. (1994). Fluorometric analysis of chlorophyll a in the presence of chlorophyll b and phaeopigments. *Limnol. Oceanogr.* 39, 1985–1992.

Westberry, T., Behrenfeld, M. J., Siegel, D. A., and Boss, E. (2008). Carbon-based primary productivity modeling with vertically resolved photoacclimation. *Glob. Biogeochem. Cycle* 22:GB2024. doi: 10.1029/2007GB003078

Wright, S. W., Jeffrey, S. W., Mantoura, R. F. C., Llewellyn, C. A., Björnland, T., Repeta, D., et al. (1991). Improved HPLC method for the analysis of chlorophylls and carotenoids from marine phytoplankton. *Mar. Ecol. Prog. Ser.* 77, 183–196.

Zonneveld, C., van den Berg, H. A., and Kooijaman, S. A. L. M. (1997). Modeling carbon cell quota in light-limited phytoplankton. *J. Theor. Biol.* 188, 215–222.

Conflict of Interest Statement: The authors declare that the research was conducted in the absence of any commercial or financial relationships that could be construed as a potential conflict of interest.

Advantages of publishing in Frontiers

OPEN ACCESS
Articles are free to read for greatest visibility and readership

FAST PUBLICATION
Around 90 days from submission to decision

HIGH QUALITY PEER-REVIEW
Rigorous, collaborative, and constructive peer-review

TRANSPARENT PEER-REVIEW
Editors and reviewers acknowledged by name on published articles

Frontiers
Avenue du Tribunal-Fédéral 34
1005 Lausanne | Switzerland

Visit us: www.frontiersin.org
Contact us: frontiersin.org/about/contact

REPRODUCIBILITY OF RESEARCH
Support open data and methods to enhance research reproducibility

DIGITAL PUBLISHING
Articles designed for optimal readership across devices

FOLLOW US
@frontiersin

IMPACT METRICS
Advanced article metrics track visibility across digital media

EXTENSIVE PROMOTION
Marketing and promotion of impactful research

LOOP RESEARCH NETWORK
Our network increases your article's readership